AD-A050 762 ADVISORY GROUP FOR AEROSPACE RESEARCH AND DEVELOPMENT--ETC F/G 20/4
THREE DIMENSIONAL AND UNSTEADY SEPARATION AT HIGH REYNOLDS NUMB--ETC(U)
FEB 78

UNCLASSIFIED AGARD-LS-94 NL

1 OF 4
AD
A050762

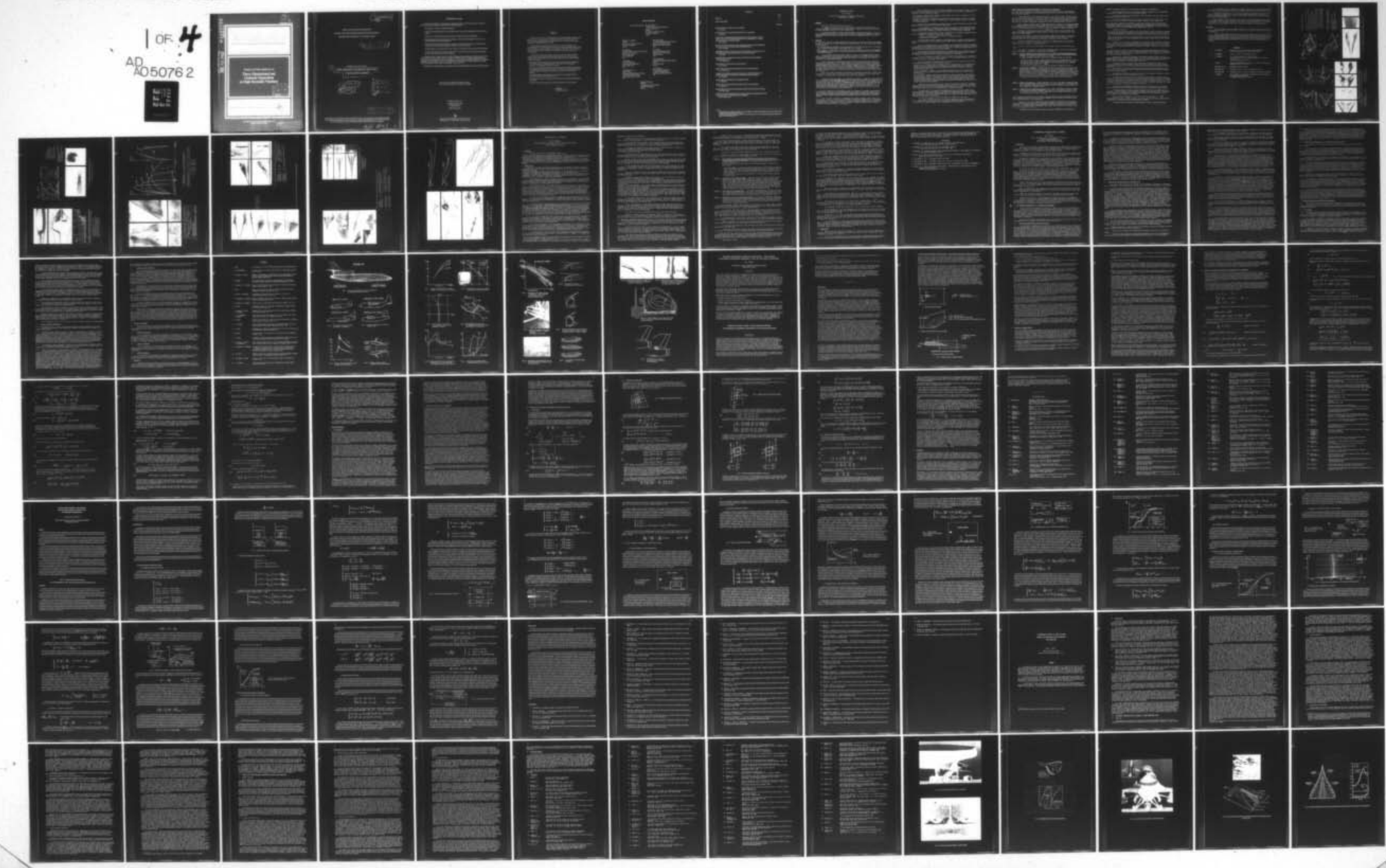

AGARD-LS-94

AGARD

ADVISORY GROUP FOR AEROSPACE RESEARCH & DEVELOPMENT

7 RUE ANCELLE 92200 NEUILLY SUR SEINE FRANCE

AGARD LECTURE SERIES No. 94

Three Dimensional and Unsteady Separation at High Reynolds Numbers

NORTH ATLANTIC TREATY ORGANIZATION

DISTRIBUTION AND AVAILABILITY
ON BACK COVER

① ⑭ AGARD-LS-94

NORTH ATLANTIC TREATY ORGANIZATION

ADVISORY GROUP FOR AEROSPACE RESEARCH AND DEVELOPMENT

(ORGANISATION DU TRAITE DE L'ATLANTIQUE NORD)

⑨ Lecture series.

AGARD Lecture Series No.94

⑥

THREE DIMENSIONAL AND UNSTEADY SEPARATION AT HIGH REYNOLDS NUMBERS.

⑪ Feb 78

⑫ 247p.

DDC
RECEIVED
MAR 6 1978
A

DISTRIBUTION STATEMENT A
Approved for public release;
Distribution Unlimited

The material in this publication was assembled to support a Lecture Series under the sponsorship of the Fluid Dynamics Panel and the Consultant and Exchange Programme of AGARD presented on 20–24 February at the Von Kármán Institute, Rhode-Saint-Genèse, Belgium.

400 043

THE MISSION OF AGARD

The mission of AGARD is to bring together the leading personalities of the NATO nations in the fields of science and technology relating to aerospace for the following purposes:

- Exchanging of scientific and technical information;
- Continuously stimulating advances in the aerospace sciences relevant to strengthening the common defence posture;
- Improving the co-operation among member nations in aerospace research and development;
- Providing scientific and technical advice and assistance to the North Atlantic Military Committee in the field of aerospace research and development;
- Rendering scientific and technical assistance, as requested, to other NATO bodies and to member nations in connection with research and development problems in the aerospace field;
- Providing assistance to member nations for the purpose of increasing their scientific and technical potential;
- Recommending effective ways for the member nations to use their research and development capabilities for the common benefit of the NATO community.

The highest authority within AGARD is the National Delegates Board consisting of officially appointed senior representatives from each member nation. The mission of AGARD is carried out through the Panels which are composed of experts appointed by the National Delegates, the Consultant and Exchange Program and the Aerospace Applications Studies Program. The results of AGARD work are reported to the member nations and the NATO Authorities through the AGARD series of publications of which this is one.

Participation in AGARD activities is by invitation only and is normally limited to citizens of the NATO nations.

The content of this publication has been reproduced
directly from material supplied by AGARD or the authors.

Published February 1978

ISBN 92-835-0210-8

Printed by Technical Editing and Reproduction Ltd
Harford House, 7–9 Charlotte St, London, W1P 1HD

PREFACE

This Lecture Series No.94 on "Three Dimensional Unsteady Separation at High Reynolds Numbers" has been co-sponsored by the Fluid Dynamics Panel of AGARD and by the von Kármán Institute for Fluid Dynamics, and implemented by the Consultant and Exchange Programme of AGARD together with the VKI.

The aim of this lecture series is to review the present state of knowledge of three-dimensional flows which contain regions of quasi-steady or unsteady separation and to provide a critical appraisal of current methods for the investigation of such flows. Both experimental and theoretical aspects will be considered and particular emphasis will be placed on the transonic regime.

After lectures devoted to the problems which flows of this type present during the design and performance prediction of civil and military aircraft and to a review of recent progress in the numerical solution of two-dimensional separated flows, the following topics will be treated in detail.

- Quasi-stationary three-dimensional separations: phenomenological aspects; application to wings with moderate or high sweep and to slender bodies; various interaction phenomena; instrumentation; control of separation.
- A general review and physical aspects of unsteady separations; application to the problems of the trailing edge conditions for slender bodies, of the dynamic stall (oscillating aerofoil, helicopter blade), and of shock wave-boundary layer interaction; the prediction of buffeting.
- Inviscid fluid models based on rolled-up vortex sheets for the computation of three-dimensional separation at high Reynolds number.
- The structure of turbulence in complex flows. Boundary layer calculations and prediction of separation.
- Numerical methods for separated flows. The present position and future prospects.

M.SIRIEIX
Lecture Series Director

LIST OF SPEAKERS

Lecture Series Director: Monsieur M.Sirieix
Directeur Adjoint de l'Aérodynamique
pour les Recherches
ONERA
29, Avenue de la Division Leclerc
Châtillon-sous-Bagneux
France

Monsieur J-C. le Balleur
ONERA
29, Avenue de la Division Leclerc
Châtillon-sous-Bagneux
France

Dr P.Bradshaw
Imperial College of Science and Technology
Department of Aeronautics
Prince Consort Road
London SW7 2BY
UK

Dr D.G.Mabey
Dynamics Laboratory
Royal Aircraft Establishment
Bedford MK41 6AE
UK

Mr R.W.MacCormack
Assistant Chief
Computational Fluid Dynamics Branch
NASA Ames Research Center
Moffett Field, California 94035
USA

Mr W.J.McCroskey
US Army Air Mobility R&D Laboratory
NASA Ames Research Center
Moffett Field, California 94035
USA

Dr D.J.Peake
NASA Ames Research Center
Mail Stop 227-8, Moffett Field
California 94035
USA

Monsieur M.Perrier
Avions Marcel Dassault Breguet Aviation
B.P. 23
92214 Saint Cloud
France

Dr J.H.B.Smith
Royal Aircraft Establishment
Aerodynamics Department
Farnborough, Hants GU14 6TD
UK

Monsieur H.Viviand
ONERA
29, Avenue de la Division Leclerc
Châtillon-sous-Bagneux
France

CONTENTS

*** Note**

- Papers presented at Lecture Series are either in French or English (the official NATO languages) and simultaneous interpretation is provided during the presentation of the Lecture.
- Translation of texts from one language to the other is not provided, and in the case of these three papers only the Introductions appear in both English and French.

PRESENTATION DU SUJET

par M. SIRIEIX

Office National d'Etudes et de Recherches Aérospatiales
92320 Châtillon (FRANCE)

----

1 - PREAMBULE

Cette brève conférence introductive a pour but :

- de dégager les objectifs de cette "Lecture séries", d'en préciser l'articulation et le contenu, en insistant sur les points autour desquels pourrait s'engager la discussion de table ronde qui traditionnellement clôture un tel cycle de conférences,

- de présenter de manière concrète, essentiellement à l'aide de visualisations, ce que sont les décollements tridimensionnels ou instationnaires, comment ils apparaissent notamment sur des configurations schématiques d'avions, enfin quels sont les problèmes fondamentaux auxquels on se trouve confronté.

2 - OBJECTIFS

2.1 La décision prise par le "Fluid Dynamic Pannel" de consacrer une "Lecture séries" aux écoulements décollés, un peu moins de 3 ans après la réunion de Spécialistes qui s'est tenue à Goettingen, comporte un double dessein :

- tout d'abord diffuser de la manière la plus large possible les progrès réalisés dans la compréhension et le traitement des décollements, spécialement dans le cas turbulent,
- ensuite centrer ces informations dont bon nombre relèvent de recherches à caractère trop fondamental sinon académique, sur des objectifs rattachés aux applications aéronautiques (avions, hélicoptères) ou spatiales (missiles).

Il ne s'agissait donc pas seulement de faire le bilan de nos connaissances dans certains domaines de Mécanique des Fluides souvent peu explorés par suite de leur extrême complexité mais surtout de faire face à des besoins d'économie comme d'accroissement de la qualité et de la sécurité des produits de l'Industrie Aéronautique.

Pour le constructeur, la nécessité d'accepter dans certaines circonstances l'existence de décollements est une évidence. Son rôle consiste alors soit à en contrôler et minimiser les effets, lorsque ces décollements constituent un élément nuisible, générateur de pertes et/ou d'instabilités sévères dégradant les qualités de vol, soit au contraire à organiser à priori le décollement de manière à ce qu'il constitue une source naturelle d'accroissement de performances. Un choix convenable des formes peut conduire en effet, à la formation de structures tourbillonnaires très organisées, avec le cas échéant des effets d'interaction favorables entre certaines d'entre elles (strake, adaptation d'un plan canard etc...).

Dans un tel travail les aspects instationnaires du décollement représentent un élément essentiel inhérent à la nature même du décollement, par le biais de la turbulence, ou encore associé aux mouvements d'un dispositif qui les pilote (gouvernes, pales d'hélicoptère etc...).

Pour mener à bien cette tâche, il est nécessaire d'accroître le niveau encore très insuffisant de nos connaissances, sur le plan expérimental pour une compréhension plus grande des phénomènes mis en jeu et des facteurs qui les influencent, sur le plan du calcul pour établir un juste compromis entre le traitement complet des effets visqueux et turbulents que leur complexité rend irréalisable même dans un avenir lointain, malgré les progrès attendus des ordinateurs comme des méthodes numériques, et, la "modélisation" des phénomènes que l'expérience peut suggérer à divers niveaux. Dans ce but, il est permis d'espérer que les échanges et discussions que cette "Lecture Séries" provoquera, susciteront des orientations nouvelles de l'activité des chercheurs.

1.2 C'est dans ce contexte qu'a été organisé ce cycle de conférences. Le programme quoique ambitieux est limité pour l'essentiel, au cas des écoulements à grand nombre de Reynolds et à nombre de Mach faible ou modéré. Par ailleurs les applications envisagées concernent des problèmes d'Aérodynamique externe, mis à part quelques exemples relatifs aux écoulements dans les prises d'air ou les turbomachines.

Pour ce qui est du contenu de ce programme je me bornerai à quelques brèves remarques sur son organisation. Celui-ci comporte en gros 3 parties. La première relativement courte (3 conférences) est introductive, la seconde (7 conférences) est consacrée aux aspects expérimentaux des décollements tridimensionnels et instationnaires, enfin la troisième (7 conférences) passe en revue et discute les moyens de prévision existants ou envisageables.

Dans la première partie, c'est d'une manière délibérée et pour souligner l'aspect très concret des besoins à partir desquels s'ordonnent les sujets traités, qu'a été confiée à un représentant de l'Industrie, la tâche importante de définir :

- les différents problèmes liés à la présence de décollements sur un avion ou un missile, au niveau des performances, qualités de vol etc...
- les moyens en usage chez le constructeur pour déterminer ces décollements, en assurer le contrôle, en réduire les nuisances et notamment la manière dont il utilise ou entend utiliser le calcul dans ces diverses opérations.

D'autre part, il lui appartient de formuler des voies possibles de Recherches futures autour desquelles pourra se développer la discussion de table ronde.

Il a paru également utile dans cette introduction, de dresser le bilan des progrès substantiels qui ont été enregistrés ces dernières années dans le traitement par voie numérique des décollements bidimensionnels, notamment en écoulement transsonique et à grand nombre de Reynolds.

2 conférences sont consacrées à ce sujet : chacune d'elles correspond à une approche différente du traitement des écoulements à grand nombre de Reynolds :

- résolution des équations de Navier-Stokes convenablement moyennées,
- méthodes dites de "couplage".

Une discussion des mérites comparés de ces deux approches, des apports que la seconde peut fournir à la première parait un bon thème de discussion parmi ceux qui concernent les méthodes de calcul.

Pour ce qui est des parties 2 et 3 du Programme, une très large part du temps de conférence a été consacrée aux décollements instationnaires en raison de l'importance pratique du sujet mais aussi pour répondre à un voeu exprimé lors de la Discussion qui a suivi la réunion de spécialistes de 1975 au cours de laquelle très peu avait été dit sur la question.

Dans les exposés à caractère expérimental, les conférenciers se sont attachés à fournir sur des exemples intéressant les applications, une description aussi complète que possible des mécanismes conduisant au décollement et des conséquences pratiques d'un tel phénomène.

C'est ainsi par exemple que dans le cas des décollements instationnaires les problèmes de "tremblement" on fait l'objet d'une conférence spéciale et que le décrochage dynamique a été traité en liaison étroite avec les problèmes d'hélicoptère.

En ce qui concerne les méthodes de calcul, les conférences sont réparties suivant différents niveaux de "modélisation" des décollements turbulents.

- en premier lieu, la schématisation d'écoulements décollés tridimensionnels et/ou instationnaires par des structures tourbillonnaires non visqueuses ; cette schématisation est bien adaptée au traitement de décollements tridimensionnels organisés à grand nombre de Reynolds, lorsque la ligne de séparation est fixée.
- ensuite les méthodes de couplage, encore insuffisamment développées par suite des difficultés inhérentes au calcul des lignes de séparation mais qui devraient constituer un support naturel des précédentes.
- enfin les méthodes fondées sur la résolution numérique des équations complètes, convenablement moyennées, par une méthode instationnaire, mettant en jeu une discrétisation à partir des techniques de différences finies ou volumes finis. Compte tenu des réductions considérables de temps de calcul obtenues récemment, peut-on admettre avec un certain optimisme que d'ici dix ans le traitement numérique d'une configuration complète sera devenu possible grâce aux progrès des ordinateurs comme des méthodes numériques ?

Dans tous les cas, le succès ne pourra intervenir que lorsque le problème de la modélisation de la Turbulence aura progressé de façon suffisante. Ce sujet très important qui intervient en dénominateur commun pour limiter le développement des méthodes de calcul, fera l'objet d'une conférence consacrée à la structure de la Turbulence dans les écoulements complexes.

On notera que s'il n'est pas fait expressement référence aux méthodes d'éléments finis pour le traitement numérique de problèmes où la complexité des formes peut inciter à les utiliser préférentiellement, c'est que ces méthodes sont encore d'un usage relativement limité et conduisent pour l'instant à des performances moins satisfaisantes, sur le plan de la durée des calculs que les méthodes de différences ou volumes finis.

Ce point de vue pourra d'ailleurs être débattu en discussion de table ronde.

Ces dernières remarques concernant le contenu du programme terminent la première partie de cet exposé. Dans la seconde partie nous nous proposons d'introduire de manière plus concrète notre sujet, avec l'appui extrêmement riche d'enseignements de la visualisation.

3 - COMMENT ABORDER LES PROBLEMES DE DECOLLEMENT ? D'ABORD PAR LA VISUALISATION

3.1 Cette méthode est en effet une source d'inspiration féconde aussi bien pour l'expérimentateur comme guide dans la compréhension des mécanismes physiques que pour le théoricien dans l'élaboration et le contrôle de "modèles".

L'expérience montre que les essais effectués dans l'eau à faible vitesse ($R_e \sim 10^4$) peuvent pourtant fournir dans de nombreux cas une description fine et précise d'écoulements très complexes (dont les décollements tridimensionnels sont un exemple), qui n'est pas démentie par les analyses que l'on peut effectuer plus difficilement et avec moins de finesse, sur une maquette géométriquement semblable placée dans un écoulement aérodynamique incompressible à nombre de Reynolds beaucoup plus élevé.

Cette technique a été développée à l'ONERA depuis 1952 sous l'impulsion de M. ROY, R. LEGENDRE et P. CARRIERE. Depuis, les travaux de grande qualité effectués sous la direction de H. WERLE (4) sont connus de tous les Mécaniciens des Fluides et l'étude détaillée de la structure d'écoulement décollés tridimensionnels et/ou instationnaires constitue l'une des activités privilégiées du tunnel hydrodynamique.

Réservant la présentation de documents filmés (5,6,7) à l'exposé oral, nous nous bornerons ici à commenter brièvement quelques images caractéristiques qui pourront servir d'introduction aux conférences de D.J. PEAKE notamment.

3.2 Les traceurs utilisés sont, soit des filets de liquide coloré de même densité et viscosité que l'eau émis à partir d'orifices situés sur la surface même du modèle, soit de fines bulles d'air en suspension dans l'eau, cette technique étant associée à la méthode du plan de lumière.

Les émissions pariétales de colorant visualisent les lignes de courant de l'écoulement lorsque celui-ci est permanent, à l'extérieur ou au sein de la couche limite et à la limite par réduction du débit du traceur, l'écoulement pariétal.

Les bulles définissent l'aspect général de l'écoulement, dans de minces tranches transversales.

Les figures 1 à 4 montrent un certain nombre d'exemples servant à illustrer les différentes causes qui provoquent le décollement d'un écoulement tridimensionnel :

Figure 1 : l'effet des gradients de pression adverses sur des corps à caractéristiques géométriques continues. La configuration représentée ici est celle d'une aile delta moyennement épaisse et à bord d'attaque arrondi placée à incidence variable.
Le schéma d'écoulement construit à partir de la visualisation permet de distinguer :

- un certain nombre de points et lignes caractéristiques de l'écoulement pariétal (lignes de décollement, points et lignes de partage, point de convergence spirale etc...) qui ont été analysés géométriquement par R. LEGENDRE (1,2,3) à partir des travaux de POINCARE et seront discutés en détail par D.J. PEAKE.
- les conditions de formation de tourbillons concentrés qui s'échappent du modèle.

Figure 2 : l'effet d'arête ou de Bord : analysé ici dans le cas d'une aile delta mince, à bord d'attaque aigu, mise en incidence. La visualisation met ici en évidence la belle organisation du décollement autour d'un tourbillon principal qui résulte de l'enroulement "en cornet" de la nappe se détachant le long du bord d'attaque. Un tourbillon secondaire moins intense se forme à partir d'un décollement de la couche limite, cette configuration appelle deux remarques. Tout d'abord, dans une telle organisation, les effets liés à la turbulence et à la viscosité tiennent une place relativement réduite tout au moins pour le tourbillon principal, ensuite l'organisation du décollement est pratiquement la même en écoulement supersonique.

Figure 3 : l'effet de protubérance : L'exemple présenté ici est celui d'un ressaut d'envergure limitée placé sur une paroi plane. Le caractère dominant de cette configuration très complexe réside dans l'échappement transversal tourbillonnaire du fluide provenant de la couche limite qui la distingue du cas bidimensionnel pur.

Figure 4 : l'effet d'un jet non parallèle à la paroi. Dans ce cas le décollement s'organise de manière à satisfaire deux exigences opposées, d'une part l'effet de protubérance qui tend à créer le décollement, d'autre part l'effet d'entrainement du jet d'autant plus marqué que celui-ci est plus intense, qui tend à le réduire.

3.3 Ces différents exemples mettent en évidence l'existence, dans bon nombre de configurations décollées tridimensionnelles, d'une structure fortement organisée autour de tourbillons concentrés, assurant une grande stabilité à ces configurations.

Toutefois, sous l'effet de gradients de pression antagonistes importants, ces structures peuvent se désorganiser et on assiste alors au phénomène d'éclatement du tourbillon qui est représenté figures 5 à 7. Ce phénomène apparait par exemple dans le cas d'une aile delta mince, lorsque l'incidence croît. Il se traduit par une désagrégation chaotique du noyau, associée une décroissance rapide de la vitesse axiale (figure 5.).

Ce phénomène est particulièrement sensible aux effets de dissymétrie de l'écoulement et notamment de dérapage (figure 6) et peut contribuer à entretenir ces dissymétries.

Parmi les moyens d'éviter ou tout au moins de retarder l'apparition d'un tel phénomène, le contrôle par soufflage est l'un des plus efficaces (figure 7).

En écoulement transsonique et supersonique l'effet des ondes de choc peut conduire à des phénomènes d'éclatement de même nature.

L'étude de l'éclatement des tourbillons (dont l'interaction choc-tourbillon est un cas particulier) constitue un thème de recherches extrêmement important pour les applications.

3.4 Les diverses circonstances d'écoulement que nous venons de décrire sur des configurations géométriquement simples, se retrouvent bien évidemment dans les études effectuées sur des maquettes d'avions, la visualisation permettant de mieux apprécier la complexité et l'importance relative des phénomènes mis en jeu. De tels exemples sont présentés figures 8 et 9.

Ils servent à montrer :

- tout d'abord que les phénomènes observés au tunnel hydrodynamique ont été confirmés à de nombreuses reprises par des essais en vol, notamment dans le cas de Concorde (clichés a et b de la figure 8) et de l'avion Douglas F5D, (clichés c à f de la figure 8 , les clichés c et e étant pris en vol).
- ensuite (figure 9) les interactions complexes existant entre diverses structures tourbillonnaires formées sur le fuselage et la voilure, notamment lorsque celle-ci comporte des variations rapides de la forme en plan.

L'étude de ces interactions, des phénomènes de stabilité liés aux interférences entre ces diverses structures est l'un des problèmes majeurs pour la réalisation d'un bon projet. Cela nécessite la mise en oeuvre sur le plan expérimental de moyens d'analyse du champ et sur le plan théorique la définition des méthodes permettant de représenter correctement l'évolution de ces structures complexes.

3.5 Après avoir montré l'apport de la visualisation des phénomènes physiques dans l'analyse des écoulements décollés, je voudrais clore cette présentation sur un dernier exemple où la visualisation intéresse à la fois l'expérience numérique, les aspects physiques et les comparaisons que l'on peut faire entre le "modèle" et la réalité.

Dans le cadre d'une approche numérique des décollements tridimensionnels à très grand nombre de Reynolds par un modèle de fluide parfait, sujet qui sera traité en détail par J.H.B. SMITH, REHBACH (8) a récemment développé à l'ONERA une méthode dont je me bornerai simplement à donner les grandes lignes, en reprenant les intentions mêmes de l'auteur.

L'approche utilisée est fondée sur une discrétisation volumique du tourbillon qui, en écoulement tridimensionnel, évoluera dans le temps en fonction des distorsions locales du champ des vitesses pour respecter les théorèmes de conservation propres aux écoulements tourbillonnaires. (HELMHOLTZ).

La formulation utilisée est une formulation intégro-différentielle Lagrangienne permettant de suivre l'évolution dans le temps d'une répartition discrète de particules fluides chargées chacune d'un vecteur tourbillon.

Les conditions d'émission de ces particules sur le contour attaché à l'obstacle sont définies par les conditions aux limites imposées sur ce contour.

L'intérêt de cette méthode est tout d'abord d'être instationnaire, le cas stationnaire constituant un cas limite. A ce titre elle peut tirer avantage de conditions initiales correspondant à une situation physique bien déterminée et permettrait une remise en question naturelle de la ligne d'émission par adjonction d'une procédure de calcul de la ligne de décollement à partir d'un calcul de couche limite lui-même instationnaire. Ensuite, par sa forme intrinsèque, elle permet de s'affranchir de tout maillage de calcul dans le domaine de résolution.

Cette méthode a été appliquée notamment au calcul de l'écoulement autour d'une plaque plane d'allongement 1 placée à différentes incidences α et mise en mouvement de façon impulsive.

Une visualisation sur console des lignes d'émission c'est-à-dire des lignes joignant à un instant t donné les particules fluides émises d'une même source a été effectuée avec la possibilité d'obtenir une vue perspective de l'ensemble de ces lignes ou une vue des projections sur un plan quelconque, le plan de symétrie par exemple.

Quelques résultats typiques pour $\alpha = 15°$ et $30°$ et un temps réduit $\tau = \frac{V_\infty t}{c} \sim 3$ sont présentés figure 10 et comparés cliché par cliché à ceux qui ont été obtenus lors d'une étude expérimentale de ce phénomène au Tunnel hydrodynamique de l'ONERA.

L'analogie entre ces résultats est assez frappante et mérite quelques commentaires.

A l'incidence $\alpha = 15°$, la régularité des lignes d'émission dans l'expérience comme dans le calcul montre qu'un état stationnaire a été assez rapidement atteint du moins au voisinage de l'aile.

Par contre à l'incidence $\alpha = 30°$, l'allure tourmentée voire chaotique des lignes d'émission est l'indice d'une configuration fortement instationnaire conduisant pour des temps plus longs à un véritable éclatement des structures tourbillonnaires aussi bien dans l'expérience numérique que dans l'expérience physique.

Peut-on induire de cette analogie que par le jeu de la viscosité numérique introduite par l'algorithme de calcul, ce dernier peut fournir une indication au moins qualitative sur la tendance à l'éclatement d'un noyau tourbillonnaire en fluide réel ? La réponse sera fournie lorsque les recherches en cours auront permis de traiter des configurations réalistes en nombre suffisant.

4 - CONCLUSION

Avant de laisser la parole aux autres conférenciers, je voudrais insister sur le rôle de catalyseur que doit jouer cette Lecture Séries tant par son contenu que par les orientations qu'elle peut susciter.

Il faut en effet engager beaucoup de conviction et entreprendre beaucoup d'efforts sur le plan des méthodes numériques comme de la recherche expérimentale spécialement dans le domaine de la turbulence pour que dans un avenir pas trop lointain, les progrès déjà importants réalisés notamment pour le traitement des décollements bidimensionnels à grand nombre de Reynolds soient étendus et complétés par des résultats de même niveau dans le cas des décollements tridimensionnels et instationnaires.

REFERENCES

1	R. LEGENDRE	Séparation de l'écoulement laminaire tridimensionnel La recherche Aéronautique n° 54 (Novembre 1956).
2	R. LEGENDRE	Lignes de courant d'un écoulement continu
3	R. LEGENDRE	La recherche Aérospatiale n° 105 (Mars 1965). Ligne de courant dans un écoulement permanent : décollement et séparation. La recherche Aérospatiale 1977-6
4	H. WERLE	Le tunnel hydrodynamique au service de la Recherche Aérospatiale ONERA Publication n° 156 (1977).
5	FILM ONERA n° 817	Ecoulements décollés (1975).
6	FILM ONERA 888	Ecoulement autour d'un avion à voilure delta (1977).
7	FILM ONERA 869	Ecoulement autour d'une aile rectangulaire de faible allongement.
8	C. REHBACH	Calcul numérique d'écoulements tridimensionnels instationnaires avec nappes tourbillonnaires. La Recherche Aérospatiale n° 1977-5.

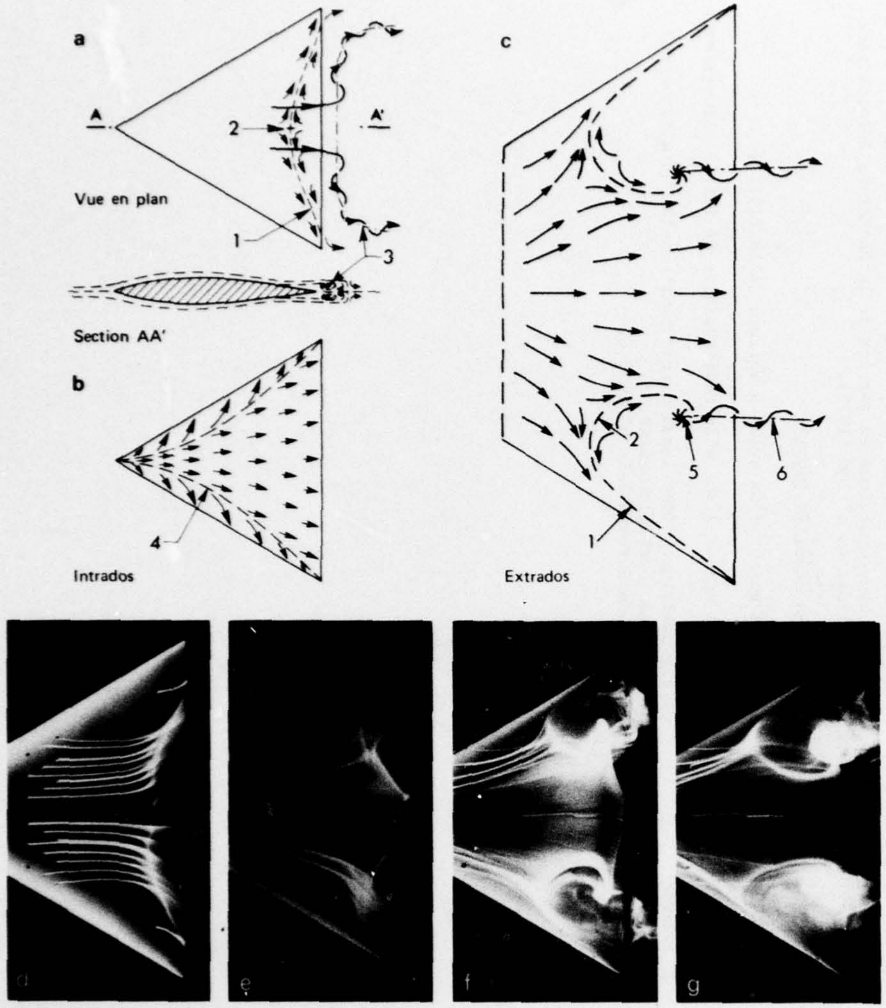

Fig. 1 – Ecoulement pariétal autour d'une aile delta moyennement épaisse.

a) et d) aile delta sans incidence b) c) e) f) et g) aile delta avec incidence.

1. ligne de décollement.
2. point de partage de l'écoulement pariétal.
3. tourbillon de bord de fuite.
4. ligne de partage.
5. point de convergence spirale.
6. tourbillon d'extrados issu de 5.

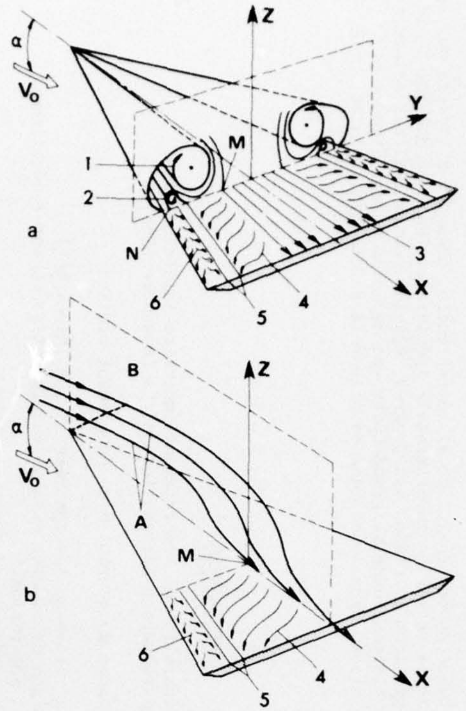

a écoulement à incidence moyenne

1. nappe en «cornet» formant le tourbillon principal d'extrados.
2. nappe en «cornet» formant le tourbillon secondaire.
3. zone médiane non tourbillonnaire.
4. zone balayée par le tourbillon principal.
5. lignes d'accumulation de bulles d'air (ou d'enduit) situées entre les zones 4 et 6.
6. zone balayée par le tourbillon secondaire.

M frontière entre les zones 3 et 4 (ou entre les zones 4 après disparition de la zone 3 aux incidences élevées).

N frontière entre la zone 6 et la zone située près du bord d'attaque et soumise à l'effet de la nappe 1.

A allure des lignes de courant dans le plan de symétrie B.

b schéma de l'écoulement dans le plan de symétrie et sur l'extrados à incidence élevée

c visualisation des nappes en cornet
d écoulement pariétal
e écoulement dans une coupe transversale située au bord de fuite

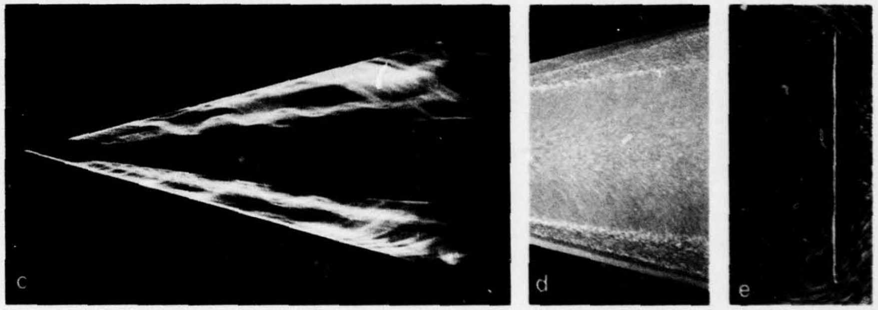

Fig. 2 – Ecoulement sur l'extrados d'une aile delta mince avec incidence.

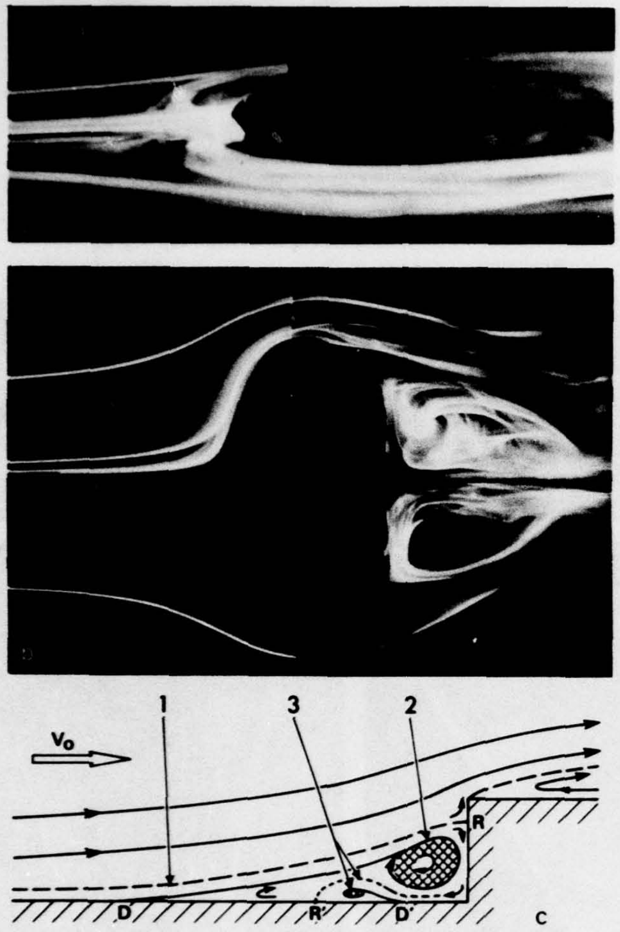

Fig. 3 – Ecoulement le long d'une paroi plane avec ressaut d'envergure limitée.
a) Vue perspective b) Vue en plan c) Coupe suivant le plan de symétrie.

1. surface de séparation aboutissant le long de la ligne de recollement R.
2. tourbillon-puits principal (échappement transversal) autour duquel s'enroule la surface de séparation issue *le long de la ligne de décollement D.*
3. tourbillon-puits et surface de séparation secondaires.

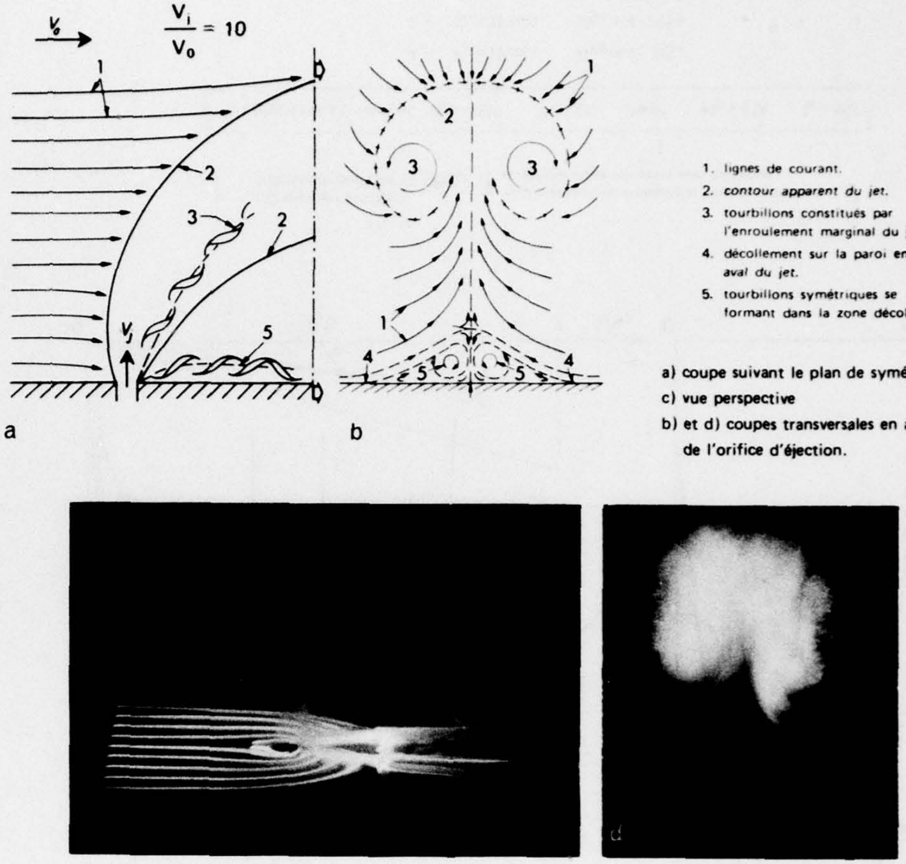

1. lignes de courant.
2. *contour apparent du jet.*
3. tourbillons constitués par l'enroulement marginal du jet.
4. décollement sur la paroi en *aval du jet.*
5. tourbillons symétriques se formant dans la zone décollée 4.

a) coupe suivant le plan de symétrie
c) vue perspective
b) et d) coupes transversales en aval de l'orifice d'éjection.

Fig. 4 – Ecoulement le long d'une paroi plane avec jet normal.

(jet de section circulaire $\overline{V}_i \simeq 10\ V_0$)

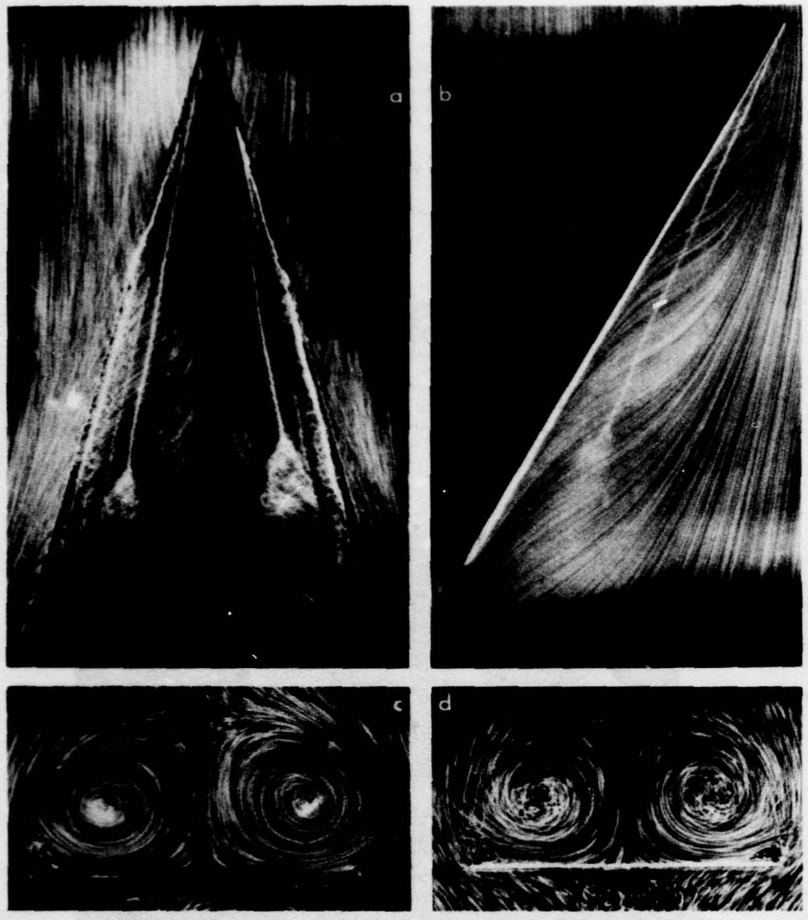

Fig. 5 – Ecoulement sur l'extrados d'une aile delta mince aux incidences élevées.

$\varphi_{BA} = 75°$ $j = 0°$ $l_a = 200$ $\mathcal{R}e_{l_a}$ de $2 \cdot 10^4$ à $4 \cdot 10^4$

$i_{\text{géométrique}} = 30°$ soit $i_{\text{effective}} = 32°,6$ après correction de l'effet d'obstruction
(sauf contre-indic.) (voir *fig. 20*).
visualisation par bulles d'air

a, écoulement au voisinage de l'extrados
b, écoulement dans le plan de symétrie
c, écoulement dans le plan transversal situé à la mi-corde } axe de prises de vues
d, écoulement dans le plan transversal situé au bord de fuite } parallèle à l'axe de l'aile.

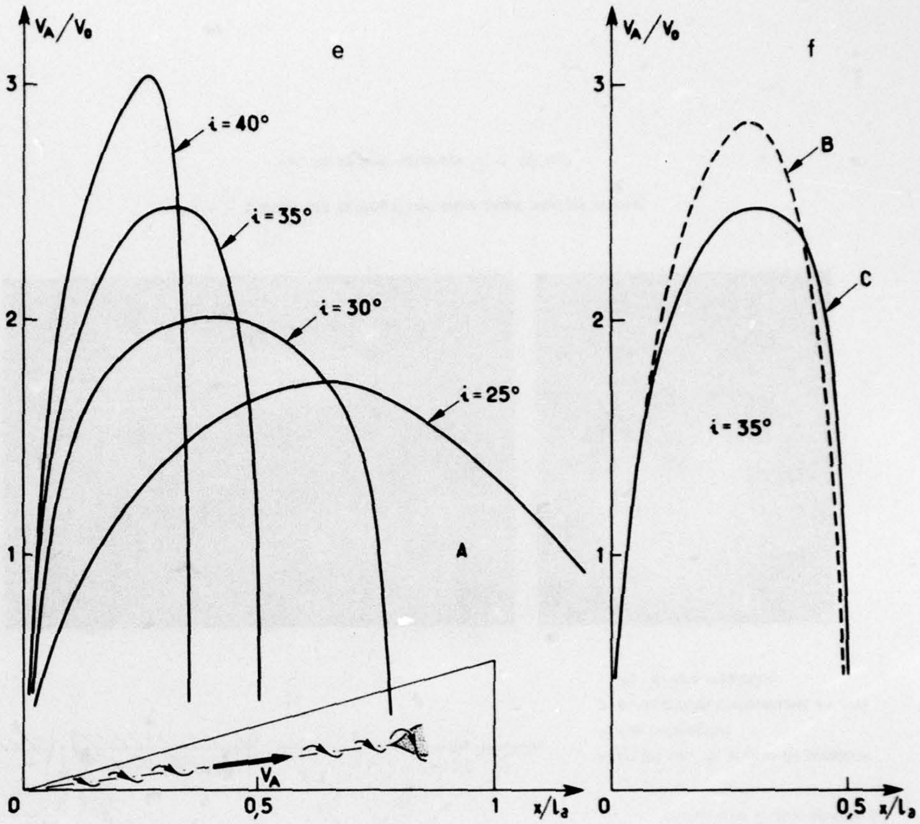

e influence de l'incidence. } sur l'évolution de la vitesse le long de l'axe du
f influence de la vitesse V_0 ($\mathcal{R}e_{l_a}$) } tourbillon d'une aile delta avec incidence

Aile delta mince à bords aigus $\varphi_{BA} = 75°$ $\lambda = 1,07$ $j = 0°$ $e/l_a = 1\ \%$ $l_a = 200$

A – $V_0 = 10$ cm/s $\mathcal{R}e_{l_a} \simeq 2 \cdot 10^4$
B – $V_0 = 20$ cm/s $\mathcal{R}e_{l_a} \simeq 4 \cdot 10^4$
C – $V_0 = 10$ cm/s $\mathcal{R}e_{l_a} \simeq 2 \cdot 10^4$

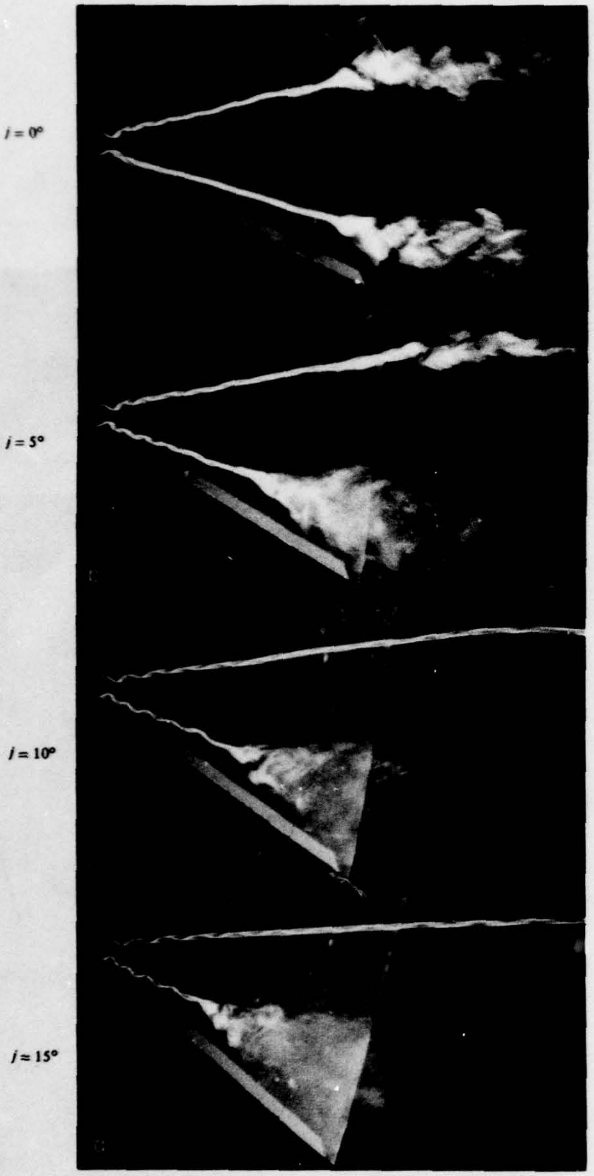

$i = 20°$ $\varphi_{BA} = 65°$
$l = 130$ $\mathcal{R}e_{l_a} \simeq 1,3 \cdot 10^4$

Fig. 6 – Evolution de l'éclatement des tourbillons d'une aile delta mince avec incidence en fonction du dérapage.

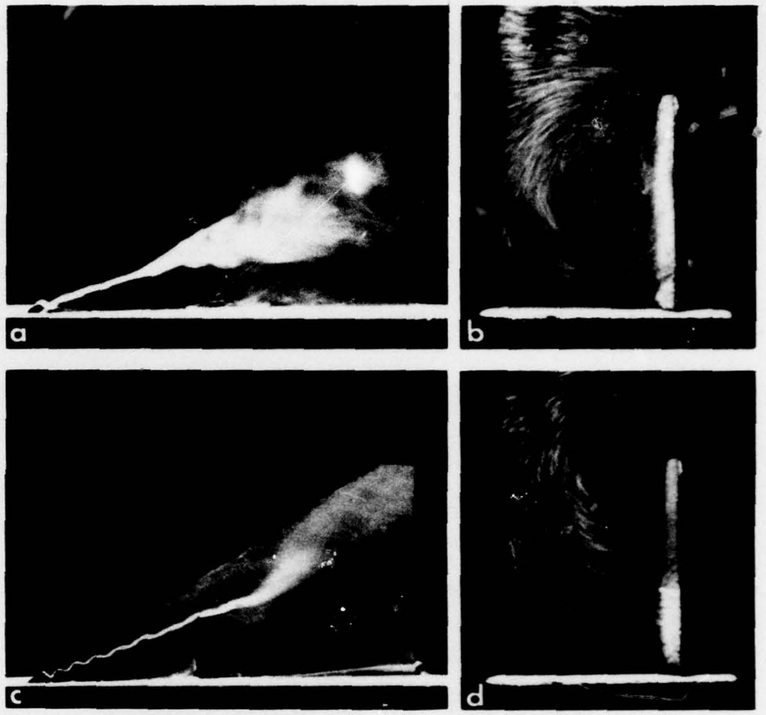

Fig. 7 – Influence d'un jet émis suivant l'axe du tourbillon sur l'écoulement autour d'une aile delta mince avec incidence.

a, vue de l'extrados ;
b, écoulement dans un plan transversal situé au voisinage du bord de fuite ; } essai sans jet.

c, vue de l'extrados ;
d, écoulement dans un plan transversal situé au voisinage du bord de fuite ; } essai avec jet (ϕ_{jet} 1,5 – soufflage effectué à la mi-corde).
$c_\mu \simeq 0,5$ ($V_j \simeq 30\ V_0$).

1/2 modèle monté à la paroi $\alpha = 25°$
plaque ($e = 2$) à bords biseautés côté intrados
$\varphi_{BA} = 60°$ effilement = 0,1
$l_a = 150$ $\mathcal{R}e_{l_a} \simeq 1,5 \cdot 10^4$

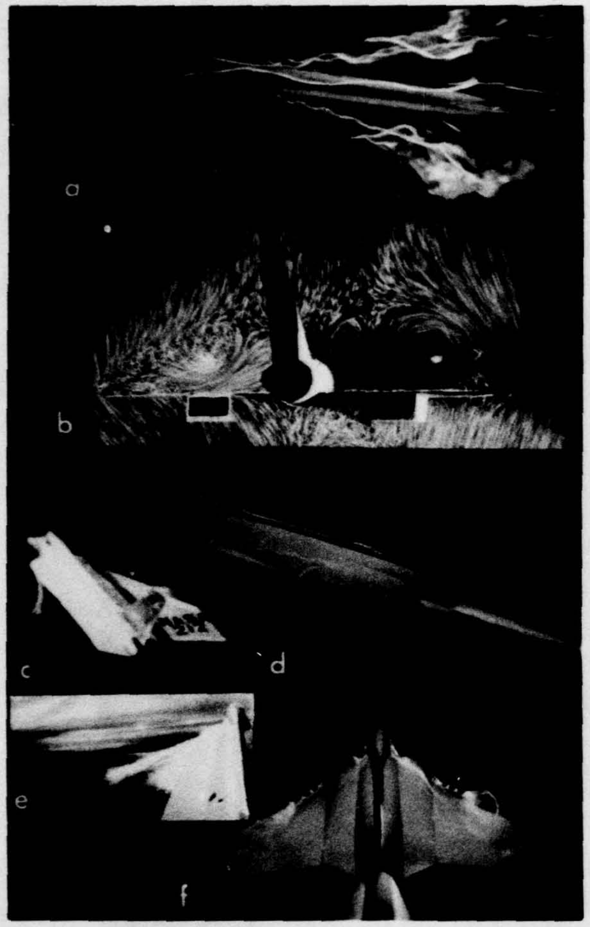

Fig. 8 – Éclatement de tourbillons sur maquettes d'avion à ailes en flèche et avec simulation des réacteurs.

a, vue de l'extrados
b, écoulement dans un plan transversal situé au voisinage du bord de fuite.
} avion du type "Concorde" avec incidence et dérapage *modèle au 1/140ème, corde sur l'axe avion* $l_a = 225$
$i = 12°$ $j = 10°$ $\mathcal{R}e_{l_a} \simeq 2 \cdot 10^4$

d, vue de profil *(côté extrados)*
f, vue perspective depuis l'arrière
} *avion* Douglas F5D à aile ogivale *modèle* au 1/72,5ème,
corde moyenne $\bar{l} \simeq 95$ $i = 15°$ $j = 0°$ $\mathcal{R}e_{\bar{l}} \simeq 10^4$

c, vue perspective (côté extrados)
e, vue perspective depuis l'arrière
} essai en vol de l'avion Douglas F5D [31] ;
images extraites du film de la NASA [66]

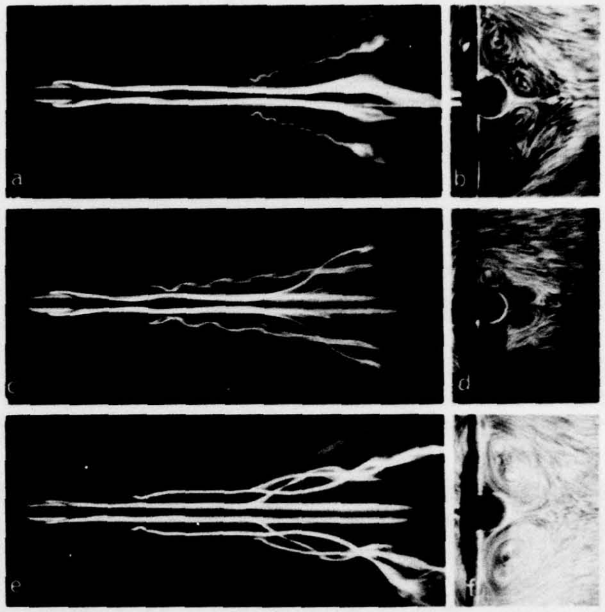

Fig. 9 – Comparaison entre différents types de voilure ($\alpha = 15°$).

a) b) delta avec fuselage long
c) d) double delta
e) f) delta avec nageoires

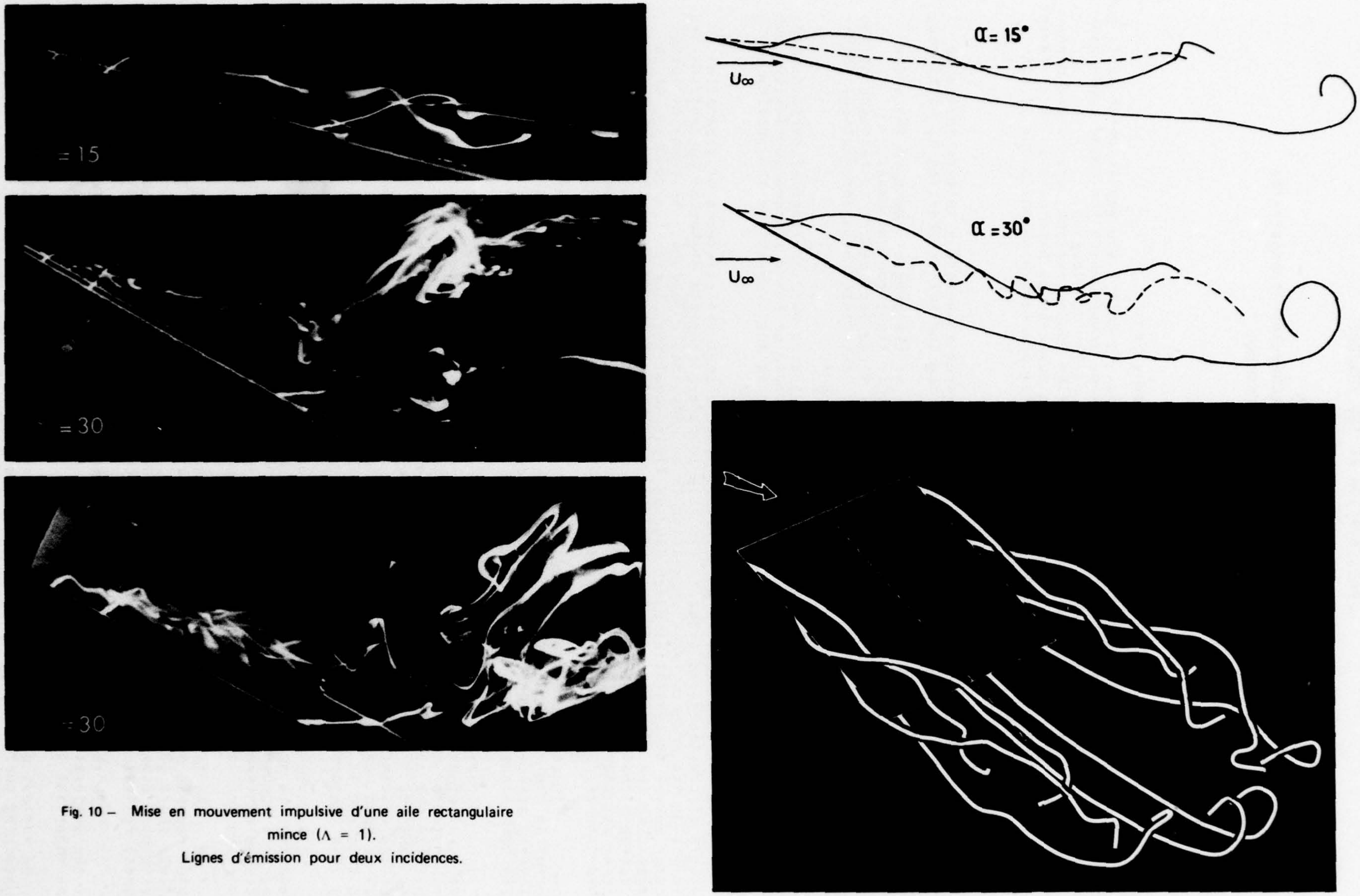

Fig. 10 – Mise en mouvement impulsive d'une aile rectangulaire mince (Λ = 1).
Lignes d'émission pour deux incidences.

PRESENTATION OF THE SUBJECT

by M. SIRIEIX
Office National d'Etudes et de Recherches Aérospatiales
92320 Châtillon (France)

1 - PREAMBLE

The aims of this short introductory lecture are :

- to bring out the objectives of the lecture series, to detail the way in which it is put together and its content, and to emphasize the points around which the round table discussion which traditionally closes such a lecture series can develop,
- to explain in a concrete way, with the help of flow visualizations, what three-dimensional or unsteady separation is, how it makes its appearance, particularly on different aircraft configurations, and finally the fundamental problems with which one is confronted.

2 - OBJECTIVES

2.1 The decision taken by the Fluid Dynamics Panel to devote a lecture series to separated flows, a little less than 3 years after the Specialists Meeting at Göttingen, had a double purpose :

- firstly, to spread as widely as possible details of the progress made in the understanding and treatment of separation, particularly in the turbulent case,
- secondly, to relate this information, of which a large part refers to research of too fundamental if not academic a nature, to objectives associated with aeronautical (aircraft,helicopters) or spatial (missiles) applications.

It is therefore not only a matter of reviewing our knowledge of certain areas of fluid mechanics which are often not studied because of their extreme complexity, but above all to face up to economic requirements such as improvements in the quality and safety of the products of the aeronautical industry.

For the manufacturer, the necessity to accept the existence of separation in certain circumstances is evident. His role therefore consists either of controlling and minimizing the effects, when separation is an undesirable feature, the cause of losses and/or severe instabilities which degrade flying qualities, or on the contrary of so organizing the separation that it constitutes a natural way of improving performance. A suitable choice of geometry can lead, in fact, to the formation of well-organized vortex structures, with in some cases favourable interaction effects between certain of them (strake, use of a canard layout, etc.).

In such work the unsteady aspects of separation are an essential feature inherent in the very nature of the separation, through the effects of turbulence, or alternatively associated with the movements of a device which controls them (control surfaces, helicopter blades, etc.).

To carry out this task successfully it is necessary to raise the still far too low level of out knowledge, from the experimental point of view to obtain a greater comprehension of the phenomena called into play and of the factors which influence them, and from the computational point of view to establish an acceptable compromise between the complete treatment of viscous and turbulent effects, which cannot be envisaged even for the distant future in spite of the progress to be expected in computers and numerical methods, and in the various levels of "modelling" which experience can suggest. To this end it is reasonable to hope that the exchange of views and discussions provoked by this lecture series will lead to new directions for research activities.

2.2 It is in this context that this lecture series has been organized. Although far-reaching the programme is essentially limited to the consideration of flows at high Reynolds numbers and at low or moderate Mach numbers. Furthermore, the applications envisaged concern problems of external aerodynamics, with the exception of some examples relating to flows in intakes or turbomachines.

As far as the content of this programme is concerned I limit myself to a few brief remarks on its arrangement. It is divided broadly into 3 parts. The first is relatively short (3 lectures) and introductory, the second (7 lectures) is devoted to experimental aspects of three-dimensional and unsteady separation, and the third (7 lectures) reviews and discusses existing and contemplated methods of prediction.

In the first part, with the considered intention of underlying the relevance of the subjects treated for current needs, a representative of industry is charged with the important task of defining :

- the various problems related to the occurrence of separation on an aircraft or missile, concerning performance, flying qualities, etc.
- the methods used by the manufacturer to predict and control separation and to reduce its adverse effects, with emphasis on the way in which he uses or plans to use numerical

methods for these various operations.

On another point, he will formulate the possible directions for future research which can guide the development of the round table discussion.

It was also felt to be useful in this introduction to review the significant progress made during the last few years in the numerical treatment of two-dimensional separation, particularly in transonic flow and at high Reynolds number.

2 lectures are devoted to this topic; each of them deals with a different approach to the treatment of flows at high Reynolds number :
- solution of the suitably-averaged Navier-Stokes equations
- so-called "coupling" methods.

A discussion of the comparative merits of these two approaches and of the contribution which the second can make to the first would appear to be a fruitful theme for discussion among others concerning numerical methods.

As far as parts 2 and 3 of the programme are concerned, a large amount of time will be devoted to unsteady separation because of the practical importance of the topic but also in response to a wish expressed during the discussion which followed the Specialists Meeting in 1975 when very little was said on this question.

In the presentations dealing with experimental work, the lecturers will seek to present, using examples which illustrate applications, as complete a description as possible of the mechanisms leading to separation and the practical consequences of the phenomenon.

Thus, for example,in the case of unsteady separation the problems of buffeting form the subject of a special lecture and dynamic stall is dealt with in the context of helicopter problems.

Regarding computational methods, the lectures may be classified in terms of the various levels of "modelling" of turbulent separation.
- in the first place, the representation of three-dimensional and/or unsteady separated flows by inviscid vortex structures; this representation is well-adapted to the handling of organized three-dimensional separation at high Reynolds number when the separation line is fixed.
- secondly, coupling methods, still insufficiently developed because of the difficulties inherent in the calculation of separation lines but which ought to be able to provide a natural back-up for the preceding methods.
- finally, methods based on the numerical solution of the complete equations, suitably averaged, by an unsteady method, making use of the techniques of finite differences or finite volumes to effect discretization. Taking into account the considerable reductions in computing time obtained recently, may one optimistically expect that ten years from now the numerical treatment of a complete configuration will have become possible thanks to progress in both computers and numerical methods ?

In all cases, success will not be achieved until turbulence modelling has progressed to a sufficient extent. This very important topic, which is a common factor limiting the development of numerical methods, forms the subject of a lecture devoted to the structure of turbulence in complex flows.

It will be noted that finite element methods for the numerical solution of problems in which the geometrical complexity may suggest them to be appropriate are not referred to explicitly. These methods are still not used extensively and lead at the present time to computing times which are long in comparison with those needed using finite difference or finite volume methods.

This point of view can be debated during the round table discussion.

These last remarks concerning programme content conclude the first part of this presentation. In the second part we shall introduce our subject in a more concrete way, with the invaluable help of information provided by flow visualization.

3 - HOW SHOULD SEPARATION PROBLEMS BE TACKLED ? IN THE FIRST PLACE BY FLOW VISUALIZATION

3.1 This method is in fact a source of fruitful inspiration as much for the experimenter who is trying to understand physical mechanisms as for the theoretician in the formulation and verification of "models".

Experience shows that tests done in water at low speeds ($Re \sim 10^4$) can nevertheless provide in many cases a precise and detailed description of very complex flows (three-dimensional flows being an example) which is not falsified by more difficult and less precise analyses made for a geometrically similar model placed in an incompressible air flow with a much higher Reynolds number.

This technique has been developed at ONERA since 1952, the stimulus being provided by M. Roy, R. Legendre and P. Carrière. Since that time the high quality work done under the direction of H. Werle (4) has become known to all workers in fluid mechanics and the detailed investigation of the structure of separated three-dimensional and/or unsteady flows is one of the activities entrusted to the hydrodynamic tunnel.

Filmed records (5, 6, 7) will be shown during the spoken presentation; we confine ourselves here to brief comments on some characteristic situations which will serve by way of introduction, in particular to the lectures of D.J. Peake.

3.2 The tracers used are either coloured liquid filaments of the same density and viscosity as water emitted from holes on the surface of the model itself, or small air bubbles in suspension in the water, these being used in conjunction with the light sheet technique.

The coloured emissions from the wall visualize the streamlines of the flow when this is steady, in the outer flow or within the boundary layer and, in the limit when the flow of tracer is reduced, the flow at the wall.

The bubbles reveal the general appearance of the flow in transverse sections.

Figures 1 to 4 show a certain number of examples which serve to illustrate the various causes of separation of a three-dimensional flow :

Figure 1 : The effect of an adverse pressure gradient on bodies with continuously varying geometrical characteristics. The configuration shown here is that of a delta wing of moderate thickness and rounded leading edge placed at a variable incidence.
The flow pattern constructed from the visualization makes it possible to distinguish :

- a certain number of points and lines characteristic of the flow at the surface (separation lines, dividing points and lines, point of spiral convergence, etc.) which have been analyzed geometrically by R. Legendre (1, 2, 3) starting from the work of Poincaré and which will be discussed in detail by D.J. Peake.
- The conditions leading to the formation of concentrated vortices emitted from the model.

Figure 2 : The effect of a corner or edge : analyzed here in the case of a thin delta wing with a sharp leading edge, placed at incidence. Visualizations show clearly the organization of the separation around a primary vortex which results from spiral rolling-up of the sheet springing from the entire leading edge. A secondary weaker vortex forms following separation of the boundary layer, this pattern calling for two comments. Firstly, in such an organized flow, effects arising from turbulence and viscosity occupy a relatively unimportant place at least for the primary vortex, and secondly, the organization of separation is practically the same in supersonic flow.

Figure 3 : The effect of a protuberance : The example presented here is that of a step of limited breadth placed on a flat wall. The dominant characteristic of this very complex pattern is the transverse vortical flow of fluid from the boundary layer which distinguishes it from the purely two-dimensional case.

Figure 4 : The effect of a jet inclined to the wall. In this case separation organises itself in such a way as to satisfy two opposing demands - on the one hand the protuberance effect which tends to cause separation, on the other hand the effect of jet entrainment which increases with the strength of the jet and which tends to oppose separation.

3.3 These different examples make apparent the existence, in a large number of three-dimensional separation patterns, of a strongly-organized structure around concentrated vortices, ensuring high stability of these configurations.

All the same under the effect of important adverse pressure gradients these structures can break up, so giving rise to the phenomenon of vortex bursting which is shown in figures 5 to 7. This phenomenon occurs, for example, in the case of a thin delta wing when incidence increases. It reveals itself in a chaotic disintegration of the core, associated with a rapid decrease in axial velocity (figure 5).

This phenomenon is particularly sensitive to the effects of assymmetry of the flow and notably of sideslip (fig.6) and can contribute to maintaining these assymetries.

Among the methods for avoiding or at least delaying the onset of such a phenomenon, control by blowing is one of the most effective (figure 7).

In transonic and supersonic flow the effects of shock waves can lead to bursting phenomena of the same type.

Investigation of vortex bursting (of which shock-vortex interaction is a particular case) is a research topic of extreme importance for many applications.

3.4 The various flow conditions which we have been describing on geometrically simple configurations occur also, of course, in studies made on aircraft models, visualization making it possible better to appreciate the complexity and relative importance of the phenomena which play a part. Such examples are shown in figures 8 and 9.

Thev serve to show :

- firstly, that the phenomena observed in the hydrodynamic tunnel have been confirmed many times by flight tests, notably in the case of Concorde (figure 8 a and b) and of the Douglas F5D (figure 8, c to f, c and e being taken in flight).
- secondly, (figure 9) the complex interactions existing between various vortex structures formed on the fuselage and wings, particularly when the latter displays abrupt variations in planform.

Investigation of these interactions and of the stability phenomena related to interference between the various structures is one of the major problems in the achievement of a good project. It necessitates the implementation of experiments designed to analyze the field of flow and, on the theoretical side, of the development of methods which provide the correct representation of the evolution of these complex structures.

3.5 Having shown the contribution made by visualization of physical phenomena to the analysis of separated flows, I would now like to close this presentation with a final example in which visualization has an interest at the same time for numerical experiments, physical aspects and the comparisons which can be made between the "model" and reality.

Within the framework of a numerical approach to three-dimensional separation at very high Reynolds number by means of a perfect fluid model, a subject treated in detail by J.H.B. Smith, Rehbach (8) has recently developed at ONERA a method for which I will content myself simply with giving the broad outline as stated by the author.

The approach used is based on a volume discretization of the vortex which, in three-dimensional flow, evolves in time as a function of the local distortions of the velocity field, in such a way as to respect the conservation theorems appropriate to vortex flows (Helmholtz).

The formulation employed is a Lagrangian integro-differential one which makes it possible to follow the evolution in time of a discrete distribution of fluid particles each of which carries a vorticity vector.

The emission conditions of these particles on a contour describing the obstacle are defined by the boundary conditions imposed on the contour.

The method is of interest in the first place because it is unsteady, the steady case being a limiting case. Because of this it can take into account the initial conditions corresponding to a well-determined physical situation and then update a streak line in a natural way by the addition of a procedure for calculating the separation line, starting from a calculation of the boundary layer which is itself unsteady. Furthermore, the very nature of the method makes it independent of the computational mesh in the solution domain.

This method has been used for the calculation of the flow around a flat plate of unit aspect ratio placed at different incidences α and set into motion in an impulsive way.

Visualization of the streak lines, that is to say the lines joining at a given time t the fluid particles emitted from the same source, has been made on a computer display and has provided the possibility of obtaining a general perspective view of these lines or a picture of their projections on any required plane, such as the plane of symmetry.

Some typical results for $\alpha = 15°$ and 30° and a reduced time $\tau = \frac{V_\infty t}{c} \sim 3$ are presented on figure 10 and compared case by case with those obtained during an experimental investigation of this phenomenon in the ONERA hydrodynamic tunnel.

The agreement between these results is fairly striking and warrants comment.

At an incidence $\alpha = 15°$, the smoothness of the streak lines both in the experiment and in the computation shows that a steady state is attained fairly quickly at least in the neighbourhood of the wing.

At an incidence $\alpha = 30°$, on the other hand, the twisted, indeed chaotic, appearance of the streak lines is an indication of an extremely unsteady pattern leading at greater times to a true bursting of the vortex structures for both the computational and the physical experiments.

Is it permissible to infer from this agreement that through the effect of numerical viscosity introduced by the computational algorithm, this last can provide at any rate a qualitative indication of the bursting tendency of a vortex core in a real fluid ? The answer will be given when research now in progress has made it possible to study a sufficient number of realistic configurations.

4 - CONCLUSION

Before calling on the other lecturers to speak, I would like to emphasize the catalytic role which this lecture series must play, as much by its content as by the orientations to which it can lead.

In fact it is necessary to have conviction and to undertake strenuous efforts in the fields of both numerical methods and experimental research, particularly as

regards the study of turbulence, in order that the already important progress made in the handling of two-dimensional separation at high Reynolds number should be extended and completed, in the not too distant future, to provide results of the same quality for cases of three-dimensional and unsteady separation.

REFERENCES

**1. LEGENDRE, R.: Séparation de l'écoulement laminaire tridimensionnel.
La Recherche Aéronautique, N° 54, Novembre 1956.**

**2. LEGENDRE, R.: Lignes de courant d'un écoulement continu.
La Recherche Aérospatiale, N° 105, Mars 1965.**

**3. LEGENDRE, R.: Ligne de courant dans un écoulement permanent : décollement et séparation.
La Recherche Aérospatiale 1977-6.**

**4. WERLE, H.: Le tunnel hydrodynamique au service de la recherche aérospatiale.
ONERA Publication N° 156, 1977.**

5. FILM ONERA N° 817 : Ecoulements décollés, 1975.

6. FILM ONERA N° 888 : Ecoulement autour d'un avion à voilure delta, 1977.

7. FILM ONERA N° 869 : Ecoulement autour d'une aile rectangulaire de faible allongement.

**8. REHBACH, C.: Calcul numérique d'écoulements tridimensionnels instationnaires avec nappes tourbillonnaires.
La Recherche Aérospatiale N° 1977-5.**

LES PROBLEMES DE DECOLLEMENTS POSES A L'AVIONNEUR

par
Pierre PERRIER

Chef du Département des Etudes Théoriques Aérodynamiques
Division des Etudes Avancées
AVIONS MARCEL DASSAULT-BREGUET AVIATION
78, quai Carnot - 92214 ST CLOUD (France)

1. INTRODUCTION

1.0. Il n'y a pas si longtemps, l'avionneur dessinait les avions pour réduire autant que possible les décollements dans les zones courantes de vol et demandait aux pilotes d'éviter les zones exceptionnelles de décrochage ou de buffeting pour lesquelles quelques méthodes, voire quelques recettes, permettaient de rendre le vol sinon acceptable du moins sans danger excessif.

L'augmentation du prix des avions et la recherche d'une sécurité plus grande ont conduit parallèlement à la recherche d'une meilleure qualité du produit dans les zones d'utilisation courante et à la recherche d'un comportement totalement sans danger dans les zones exceptionnelles.

Pour prendre un exemple simple, on est passé ainsi en peu d'années d'avions école(Fouga-Magister), dont le décrochage était acceptable et suffisamment franc et agité pour que le pilote sache qu'il avait "décroché" et qu'il devait "rendre la main", à des avions dessinés pour avoir un décrochage sans accident de stabilité aucun et dessinés pour avoir une récupération de vrille toujours effective en deux rotations (Alpha-Jet) et on prépare des avions dont les caractéristiques longitudinales et transversales rendent l'entrée en vrille involontaire improbable et le pilotage acceptable dans tout le domaine de vol décroché, grâce à des commandes de vol électriques adaptées (Contrôle Automatique Généralisé).

Un objectif aussi ambitieux se retrouve au niveau du contrôle des décollements plus localisés.

Cet objectif peut être atteint de deux façons complémentaires : d'une part, on peut expérimentalement modifier les configurations jusqu'à ce que les caractéristiques demandées soient atteintes ; d'autre part, on peut, en partant d'une certaine compréhension de la structure fine de phénomènes de décollement, modifier les formes pour réaliser des champs aérodynamiques acceptables d'abord sur des modèles numériques, puis vérifier par essais en soufflerie. Ces deux approches doivent rester, encore un certain temps, complémentaires car on n'a pas encore atteint un niveau suffisant de modélisation numérique des décollements pour permettre à une approche rationnelle, confirmée et orientée par des calculs, de suffire à la définition initiale d'un avion.

1.1. Dans cet exposé, nous allons tout d'abord distinguer les différentes formes sous lesquelles se posent les problèmes liés aux décollements suivant le point de vue où l'on se place : performance, qualité de vol, etc ..., à l'aide d'exemples. Les solutions recherchées peuvent présenter des incompatibilités suivant ces points de vue.

Dans une deuxième partie, nous passerons en revue les moyens dont nous disposons pour résoudre ces problèmes d'un point de vue purement expérimental et d'un point de vue analytique où un bagage numérique, non négligeable, est déjà disponible.

Enfin, nous indiquerons quelques voies de recherche qui semblent prometteuses et qui permettraient de rendre plus efficaces les moyens de prévision non négligeables dont nous disposons.

1.2. On séparera dans la suite - les décollements avec eau morte importante, quasi isobares en général - les décollements fortement turbulents inorganisés qui admettent des gradients de pression moyens non négligeables - les décollements tridimensionnels organisés où coexistent des grosses structures souvent en spirale avec un bruit de fond turbulent à plus faible fréquence et à nettement plus haute fréquence que la fréquence de base des décollements bidimensionnels.

2. LES DIFFERENTS PROBLEMES LIES A LA PRESENCE DE DECOLLEMENTS

2.1. Les pilotes de planeur savent bien le silence et la douceur des vols à bord d'une machine de compétition où les décollements ont été systématiquement supprimés. Les niveaux de finesse atteints par ces planeurs rappellent qu'un écoulement propre est une condition nécessaire pour avoir des performances élevées et une finesse de pilotage suffisante. Malheureusement, on ne peut ni dessiner un avion usuel comme un planeur de compétition par suite de nécessaires compromis où l'aérodynamicien ne peut pas avoir toujours le dernier mot, ni toujours voler dans les conditions où l'avion a été optimisé. On séparera donc toujours les décollements liés au dessin de l'avion dans les conditions d'adaptation et les décollements hors adaptation.

Nous allons distinguer les décollements suivant les quatre points de vue usuels des quatre principaux spécialistes qui, ensemble, essayent de faire le meilleur produit.

2.2. - Influence des décollements sur les performances

Les performances sont dégradées par la présence de zones décollées trop étendues. L'évaluation des zones décollées était autrefois faite uniquement en soufflerie principalement à l'aide de visualisations, exceptionnellement à l'aide de mesures de pressions pariétales ou de sillage dont l'interprétation est moins évidente. Cette évaluation peut maintenant être faite par le calcul. On présente sur la figure 1 un calcul ayant servi à l'optimisation du fuselage arrière du Falcon 50 supercritique. Ce calcul peut être fait en conditions de vol et en conditions de soufflerie, les recoupements effectués sont excellents entre calculs et essais ; la corrélation entre soufflerie et vol est moins bonne , la couche limite étant plus épaisse au nombre de Reynolds plus faible en soufflerie, ce qui diminue les recompressions suivant un processus bien connu de sous-estimation des décollements sur les rétreints. Sur un avion comme le MD-315, dont les performances étaient excellentes pour l'époque de sa conception (1947), on admettait des zones décollées dont la surface était incomparablement plus grande. Remarquons que l'évaluation du coût en trainée des zones décollées n'est pas simple (cf. plus bas § 3.) et souvent elle est assez imprécise par le calcul.

Les exemples les plus simples de problèmes posés à l'avionneur couvrent les décollements de rétreint de fuselage dont on vient de parler, spécialement d'avions cargo (Bréguet 941), les décollements de coins, spécialement de Karman ou de jonction de mâts réacteur. Des augmentations de trainée de l'ordre de 20 % par rapport au résultat non décollé sont couramment la conséquence de mauvais dessins locaux qui ne devraient plus être acceptés grâce aux méthodes de calcul disponibles actuellement.

Cependant, en général, les augmentations de trainée importantes liées au décollement se produisent en transsonique. Ceci est dû à l'accroissement très important de trainée lié à une variation importante de courbure en transsonique où s'accrochent des ondes de choc dont on peut se rendre compte, par exemple, en regardant la variation de trainée d'un culot en fonction du nombre de Mach (figure 4) pour lequel les dépressions sont multipliées par des facteurs de l'ordre de 2 à 4 par rapport au subsonique. Beaucoup de travail a été fait sur les profils pour réduire ces accroissements de trainée de forme ou d'onde parasites que tout le monde connaît bien. On voudrait cependant rappeler qu'un dessin tridimensionnel très correct est nécessaire pour éviter les décollements liés aux focalisations de chocs et aux gradients très élevés dus à l'accumulation des rétreints par effets de lois des aires. Ces décollements, par nature tridimensionnels et organisés, donnent souvent naissance à des augmentations de trainée très importantes liées aux dépressions ainsi générées : on verra donc les rétreints de jonction voilure-fuselage après la correction, par effet de lois des aires, apporter en fait un gain beaucoup plus important que la simple suppression du volume occupé par les zones décollées.

Enfin, on rappelle qu'en supersonique coexistent avec les décollements tridimensionnels des zones de décollements d'eau morte dont l'effet est, en général, de réduire la trainée d'onde, ce qui a un effet bénéfique sur les performances. Ce schéma est systématiquement utilisé dans les arrières corps d'avions militaires à grand Mach et permet qu'une part de l'effet de convergent-divergent de l'arrière corps soit récupérée sur le fuselage arrière sans avoir à matérialiser le divergent optimum(fig.5 et réf.12).

De la même façon, on pourrait rappeler que les décollements d'eau morte ou de zones fortement turbulentes sont l'occasion de forts déficits par rapport aux performances théoriques en fluide parfait. Ces types de décollement commencent cependant maintenant à être correctement représentés, ce qui permet en particulier une approche analytique relativement correcte du problème des décollements dans les hypersustentateurs (cf. réf. 5 et 9). Il n'en est pas de même pour les décollements organisés (cf. réf. 2,3 et 4) qui permettent d'intéressantes performances de portance tant que les dépressions qu'ils induisent ne sont pas limitées par le voisinage de la vitesse limite du fluide (figure 6).

2.3. - Influence des décollements sur les qualités de vol

Nous allons séparer trois types de problèmes liés à l'irrégularité stationnaire et instationnaire de l'écoulement : les problèmes de non-linéarité, de métastabilité et d'hystérésis et de tremblement.

2.3.1. - En fluide parfait sans décollement, les différentes caractéristiques de portance et moment ne sont pas linéaires en général, soit que les grandes incidences ou le transsonique mettent en jeu des non-linéarités, soit que les positions relative des sillages et empennages introduisent ces non-linéarités en fonction de l'incidence ou du dérapage. Bien que les caractéristiques de base ne soient pas linéaires, on en minimise les conséquences par le choix de la configuration (position d'empennage, forme en plan ...). La figure 7 montre un écran interactif travaillant sur un programme d'optimisation de position d'empennages. En fait, ce programme inclut l'effet des décollements sur la voilure car on tente souvent de réaliser une compensation entre ces deux effets. La figure 7 montre un exemple classique de tendance à l'autocabrage en cours de mise au point du Falcon 50 dû à un décollement d'extrémité d'aile qui pose de gros problèmes de qualité de vol. La diminution de stabilité a été corrigée par un nouveau dessin des profils d'extrémité de voilure moyennant une légère pénalisation en trainée. Sur la figure 8 est présenté un cas contraire (Mirage G) où la configuration empennages bas, choisie pour les grandes incidences, crée des pertes de stabilité autour des C_z nuls ou négatifs (vol dos) auxquelles s'ajoute l'instabilité supplémentaire créée par les décollements d'intrados liés à la cambrure. On voit ainsi que l'avionneur ne peut pas réussir partout la compensation des non-linéarités de fluide parfait et de décollement.

Une non-linéarité courante correspond au cas des décollements non établis à petit angle d'attaque et disparaissant rapidement. Cela donne lieu aux courbes en S caractéristiques (figure 9 : résultats caractéristiques de stabilité de route à très grande incidence) qui peuvent provoquer des cycles limites très désagréables en qualité de vol si la zone à grande incidence est stable ou des stabilités pointues favorables aux vrilles dans le cas inverse. Curieusement ce même phénomène existe souvent aussi sur les avions à aile épaisse en soufflerie lié aux décollements laminaires autour des incidences d'adaptation. Il est courant pour les corps élancés ou les corps de réentrée d'engins (figure 17).

2.3.2. - Si les non-linéarités sont faibles en fin d'optimisation de l'avion en soufflerie, ou régulières, mais que l'avion est équipé de C.A.G., il n'y aura pas de problème à obtenir de bonnes qualités de vol ; il n'en est pas de même si l'avion présente des décollements métastables que l'on ne pourra pas, en général, simuler dans les fonctions de transfert correctrices de pilotage automatique.

L'exemple classique de la figure 10 relatif au décrochage d'un avion par éclatement de bulle de transition (Alpha Jet) peut être précisé en signalant que :

- la position en incidence du décrochage dépend du dérapage de l'avion et de la vitesse de tangage.

- les effets latéraux induits par le décrochage dissymétrique d'une aile sont prépondérants. Ces effets existent pour une dissymétrie minime géométrique des deux ailes et l'on sait bien que le décrochage d'une aile décharge suffisamment l'autre en chargement dissymétrique pour retarder son décrochage et donc le retour à des coefficients de roulis faibles.

- il y a hystérésis du processus, ce qui rend le retour au régime sans décollement généralisé aussi cahotique que l'aller, à moins d'optimiser l'aile ce qui est contradictoire avec la performance.

Un grand effort de clarification de cette notion de métastabilité, une expression de la probabilité ou de la stabilité comparée des différents régimes éclairerait beaucoup ce problème actuellement abordé de façon trop sommaire.

Un exemple très complexe en est donné par la stabilité en incidence et dérapage des décollements de culot d'un avion en transsonique. La figure 21 schématise la modification ainsi apportée au détriment de la trainée à l'arrière corps du Mirage IV pour supprimer une instabilité à $M = 0.92 - 0.95$. Le même processus a été appliqué au MRCA récemment (cf. réf. 21).

2.3.3. - Nous avons parlé dans les paragraphes précédents de l'apparition de décollements sous leur aspect stationnaire. En fait, l'aspect instationnaire est souvent aussi important. On l'évaluera sur un avion civil par la variation du confort et sur un avion militaire par la modification de la facilité à remplir une mission, sur les deux par l'agrément de pilotage (cf. réf. 6).

2.3.3.1. Pour un avion civil, il est criticable qu'en croisière les décollements que l'on n'a pas pu éliminer induisent un tremblement notable désagréable pour le confort du passager, ou un bruit dans la cabine excessif pour le personnel navigant. En approche, à l'atterrissage, également doivent être éliminées les vibrations excessives qui peuvent être liées à l'accord entre les fréquences discrètes de structure et le spectre inducteur des fluctuations de pression. Les volets multiéléments séparés en envergure sont, par exemple, mieux placés que les grands volets uniques très braqués par réduction des dimensions caractéristiques des décollements et comportement plus tridimensionnel, ce qui atténue nettement les spectres inducteurs. Il en est de même pour les aérofreins. Le comportement des avions à forte flèche, où les décollements sont plus stables, est globalement meilleur, mais dans les zones de stabilité des configurations à vortex (cf. le buffeting de configuration de Concorde en approche) seulement.

Il faut également considérer les conditions anormales de vol et rappeler le vieux problème des limites de buffeting en transsonique et à grande incidence, mal expliqué en général. Rappelons à ce propos que les intensités d'accélérations perçues (pour ne pas parler des spectres qui dépendent de la structure directement) ont, en fonction du paramètre incidence ou nombre de Mach, trois types principaux d'évolution donnés figure 11.

La courbe (1) est caractéristique des décollements brutaux en subsonique (ou transsonique sur des avions sans flèche) ; elle est souvent considérée comme inacceptable si le pic d'accélération est supérieur à 0,1 g, à moins de servir d'interdiction au pilote, par contre elle est souhaitable si ce pic est inférieur à 0,05 g et supérieur à 0,02 g et sert d'indicateur au pilote. Sur le Mercure nous avons trop bien réussi la courbe de type (1) associée au décrochage lisse puisqu'elle est considérée comme limite par les pilotes ($> 0,1$ g) et que le travail effectué au-delà, pour rendre excellentes les qualités de vol après décrochage, n'est pratiquement jamais reconnu par les pilotes. Le recours aux dispositifs artificiels (branleur de manche, signal sonore) toujours moins sûrs (sensibilité aux dérapages, vitesses de tangage) peut ainsi être évité. Une courbe de type (1) avec un niveau de l'ordre de 0,02 à 0,05 g est souhaitable pour signaler la sortie des becs, des volets,du train, le pilote étant alors parfaitement capable de reconnaître sa configuration. On ne souhaite pas une courbe de type (1) en transsonique car elle risque d'être induite par les variations de vitesse en atmosphère turbulente.

On souhaiterait plutôt une courbe de type (2) qui correspond à un établissement progressif du buffeting initial piloté par une extension progressive des zones décollées et une structure initiale non bidimensionnelle ; cependant, les "impuretés" correspondant au début de la courbe ne doivent être trop précoces ni à un niveau trop élevé. L'idéal serait que la croissance plus brutale ait bien lieu à 0,05 g environ 1 point de Mach après le début du buffeting.

Enfin, avec des décollements de type fortement tridimensionnels, on a souvent une courbe très progressive de type (3), c'est par exemple le cas d'un avion à géométrie variable (Mirage G) à forte flèche et l'on a beaucoup de mal à définir une incidence au-dessus de laquelle le buffeting est inacceptable.

2.3.3.2. Pour les avions militaires, le niveau acceptable ne peut être placé comme pour les avions civils à une valeur forfaitaire (0,05 g) car on a préféré l'inclure dans la totalité des effets qui dégradent la capacité de remplir la mission en augmentant la charge de travail du pilote (pilotage nécessaire simultané ou non à cause d'une dégradation des qualités de vol liées à la présence des décollements) ou la précision du tir. La première notion reste proche du confort civil mais l'aspect qualité de vol est important ; dans la seconde, au contraire, la distribution spectrale du tremblement est prépondérante par rapport à son niveau pour les vibrations relatives des yeux et du viseur par rapport au siège du pilote.

Entre la détermination a priori des courbes (1) (2) ou (3) et de leur intensité et les mesures actuelles en soufflerie, il y a un écart bien connu. On a donné figure 12 une comparaison sur un Falcon des courbes d'iso-accélération moyenne de buffeting mesurées en vol et des courbes dites de "limite de buffeting" que l'on obtient en exploitant divers signaux enregistrés en soufflerie à grands Reynolds (Réf.7). A l'exception des jauges de moment sur la voilure, les signaux exploités ont des accidents créés par les décollements mais non liés à l'aspect instationnaire des phénomènes, ce qui limite les conclusions que l'on peut tirer de l'énorme discordance des signes précurseurs. Pour remédier à cet état de fait, il semble important de tenter la mesure directe des efforts instationnaires. Nous avons initié une telle méthode de mesure (cf. réf. 8) mais elle sera de portée limitée tant que le niveau de turbulence des souffleries rendra imprécises les mesures à l'équivalent de 0,01 g près (soit 1 % du C_z étudié).

2.3.3.3. Nous n'avons pas parlé spécifiquement des engins à propos des effets de décollements sur la trainée, la portance et les autres coefficients, car ils ne posent pas de problèmes spécifiques à l'exception, peut-être, du problème du décollement en pied de jupe sur les corps de réentrée. Par contre, il est nécessaire de parler des forts buffetings engendrés en transsonique par les formes assez peu aérodynamiques souvent retenues pour des raisons de devis de masse. Ces mêmes problèmes sont également souvent rencontrés avec les charges externes d'un avion militaire et leurs supports et mâts également dans la zone de nombre de Mach 0.9 - 1.05. Les décollements correspondants intéressent l'avion autant que les charges par les champs induits réciproques. Enfin, il ne faut pas oublier les buffetings induits par les sorties d'aérofreins.

2.4. - Influence des décollements sur le dimensionnement des structures

Cette influence peut à nouveau être séparée en dimensionnement aux charges stationnaires et instationnaires.

2.4.1. - Sur les avions civils, les charges de dimensionnement font exceptionnellement intervenir les zones décollées sur l'avion lisse. Par contre, sur l'avion hypersustenté, on retrouve la nécessité de prédire les efforts sur les différents éléments des volets en présence des décollements toujours existants dès que les braquages sont suffisants. Les méthodes de calcul approchées dont nous disposons en tridimensionnel sont suffisantes pour ce genre de prédiction (cf. réf. 13) dans la plupart des cas et permettent d'économiser des essais coûteux en soufflerie ou en vol.

Sur avion militaire, au contraire, le fonctionnement en régime décollé est systématique et il est nécessaire d'évaluer les charges dans ces conditions où les calculs sont nettement moins précis, en particulier en transsonique et supersonique.

2.4.2. - Les charges instationnaires font surtout intervenir des problèmes de fatigue de la structure, ils sont liés à la coïncidence d'un spectre de niveau très élevé avec la réponse de la structure, soit que la fréquence principale soit renforcée (résonance) , soit que le spectre ait une répartition blanche mais de niveau exceptionnellement élevé. Sur l'exemple de la figure 13 , l'économie de la tôle d'intrados, pour obturer les fentes de volets de l'Alpha Jet, a conduit à une rupture prématurée des supports de goutte et des tôles de voûte, rupture supprimée par l'étanchéité de la solution II. Ce phénomène est souvent rencontré avec des décollements confinés bidimensionnels qui ont souvent un spectre avec une raie très marquée.

De même, un cas dimensionnant pour les engins correspond souvent à la tenue au vent au sol. Outre la tenue statique, les charges alternées produites par l'échappement des tourbillons du cylindre normal au vent constitué par l'engin sont souvent critiques.

Citons également les fatigues créées dans les trappes ouvertes d'avions militaires ou au culot des engins, ou chaque fois qu'un décollement important et peu tridimensionnel existe (tôles de fuselage ou de voilure au voisinage des aérofreins). C'est souvent un cas dimensionnant de la structure quand on ne peut éviter les décollements. On trouve dans ces cas par exemple les zones des manches à air qui sont le siège de décollements importants : effets des vents latéraux au point fixe en avion civil, des grandes incidences (vrille en particulier) en avion militaire transsonique et les pompages d'entrée d'air en vol supersonique hors adaptation.

Il est bon d'insister à nouveau pour finir sur les problèmes d'interaction entre manche à air et réacteur dont nous venons de parler du point de vue des effets sur la structure de l'avion, mais qui jouent un rôle encore plus grand sur le moteur lui-même. Un grand progrès a été fait dans la compréhension et la caractérisation de ces problèmes d'interface, qui se ramènent à la description de l'écoulement d'un fluide partiellement décollé et fortement turbulent pour que le motoriste puisse mieux prévoir l'effet sur le moteur, mais le chemin, là particulièrement, reste très long jusqu'à une maîtrise suffisante des phénomènes complexes mis en jeu (cf. figure 14 montrant un écoulement transsonique dans une entrée d'air à grande incidence prise en strioscopie éclair).

3. LES MOYENS D'ETUDE ET DE REDUCTION DES DECOLLEMENTS

3.0. - Nous allons passer en revue successivement et sommairement les remèdes dont nous disposons et les moyens de contrôler leur efficacité. La panoplie des moyens d'évaluation est assez élevée quoique son efficacité soit liée à la validité des moyens (limitation de nombre de Reynolds ou de schématisation principalement).

3.1. - Les remèdes

3.1.1. - Les remèdes à appliquer dépendent principalement du but à atteindre et nous rappelons la distinction essentielle que nous avons exposée au chapitre précédent entre les régimes de fonctionnement, où il est possible et souhaitable de limiter ou supprimer les décollements, et ceux où il faut se limiter à en réduire les conséquences (stabilisation-diffusion).

Si l'on essaye de supprimer les décollements, il faut d'abord s'assurer qu'avec les contraintes de construction données il n'existe pas de modifications simples de formes qui répondent à la question. La méthode consiste par approximations successives à réaliser des distributions de pression évitant le décollement des couches limites (cf. figure 1). C'est le travail habituel de l'avionneur sur toutes les zones de rétreint de fuselage et de jonction de volume mâts, empennages. Cette voie de travail est loin d'être encore exploitée complètement car il est évident que ce travail réagit fortement sur le dessin général de l'avion et que les rétreints optimaux sont loin d'être facilement évaluables dans tous les cas.

Cependant les gradients de pression, conséquence du dessin subsonique, ne permettent pas toujours de trouver simplement des formes qui "marchent". A défaut de réduire les gradients de pression absolus, on peut réduire les gradients de pression relatifs aux zones visqueuses $\frac{dKp}{ds/\delta}$ (Kp coefficient de pression, s abcisse curviligne en suivant la ligne de courant sur laquelle l'épaisseur de couche limite locale est δ) en réduisant δ. Dans les cas importants on fait appel à des pièges à couche limite qui permettent de redémarrer la couche limite au voisinage de la recompression (cf. figure 15 les pièges d'entrée d'air de l'Etendard et de l'Alphat Jet) ou à des aspirations à travers des plaques perforées moins efficaces mais de réalisation souvent plus simple en rattrapage.

On peut également utiliser un moyen de soufflage qui permet de réduire le paramètre de forme de la couche limite avec un gradient réduit $dKp/ds/\delta$ un peu augmenté en général par suite de l'épaississement lié à l'introduction de l'air soufflé. Comme cet effet de stabilisation est de durée limitée, ce type de contrôle de la couche limite est mieux adapté à la correction de problèmes locaux sinon le débit mis en jeu peut devenir rapidement excessif pour le réacteur sur lequel il est prélevé.

Le fonctionnement des hypersustentateurs modernes fait appel, par l'intermédiaire de fentes jouant le rôle de piège à couche limite et de dispositifs de soufflage, à des moyens dont l'efficacité est très grande pour la réduction des décollements (cf. réf. 9) et, par exemple, l'hypersustentation classique mais optimisée par le calcul du Super Etendard apporte une amélioration de la portance de cet avion supérieure à celle qui était obtenue par l'hypersustentation à volets soufflés qui avait été essayée, mais non retenue par suite des sujétions qu'elle introduisait sur l'Etendard.

Une voie analogue consiste à réduire le paramètre de forme de la couche limite par mélange plus énergique que le processus turbulent normal entre l'extérieur à grande vitesse de la couche limite et l'intérieur proche du décollement. Ce mélange est effectué de la meilleure façon possible par des tourbillons d'axes colinéaires à la vitesse, générés par des ailettes de faibles allongements dits générateurs de tourbillons. Ce moyen est très efficace en rattrapage mais le prix à payer est souvent grand en trainée.

Rappelons pour mémoire que l'on peut également réduire les décollements locaux en supprimant le frottement des sous-couches par cylindre tournant ou tourbillon captif.

3.1.2. - Pour stabiliser des décollements, les deux voies habituelles consistent, soit à assurer une stabilité suffisante du point de recollement ou des zones turbulentes de mélange le long du décollement, soit à recourir à une stabilisation tridimensionnelle.

Pour stabiliser le point de recollement, on utilise habituellement une survitesse locale si cela est possible sous forme d'un arrondi au point de recollement. On peut aussi essayer de stabiliser la ligne de jet, instable par nature en subsonique, en la rendant extrêmement turbulente par des tourbillons amonts de la taille de la zone de mélange et non de la zone décollée (cf. figure 17).

Cependant chaque fois qu'un effet de flèche favorise l'existence de tourbillons tridimensionnels dont la stabilité est beaucoup plus grande que celle d'une nappe, il devient intéressant de favoriser les grosses structures de tourbillons en cornet en utilisant des arêtes à fortes flèches ou simplement des bords d'attaque ; voir par exemple les flèches internes d'avion tel le Mirage G ou le fonctionnement des entrées d'air noyées de type NACA (cf. planche 18).

On peut également favoriser les structures en hélices par soufflage transversal (procédé Lockeed).

3.2. - Les moyens d'études expérimentaux

3.2.0. - Nous présentons dans la revue rapide suivante les moyens d'études expérimentaux et théoriques disponibles ou à mettre au point pour aider au travail de l'avionneur dans la réduction et le contrôle des décollements.

3.2.1. - Les moyens les plus simples de contrôle et d'étude des décollements sont pariétaux. Les visualisations par enduits visqueux permettent, en général, de bien détecter les décollements, mais la technique mise au point à l'O.N.E.R.A. d'injection continue de fluides colorés est probablement la plus riche en information à la fois sur l'étude des zones décollées et sur la stabilité de ces zones (cf.fig.19: visualisations colorées à la soufflerie S2 de Modane de l'O.N.E.R.A. au cours de la mise au point du Mirage F1 en transsonique grande incidence). Les pressions sont un guide utile surtout avec des capsules instationnaires type Kulite pour l'étude des spectres de fluctuations, mais elles sont d'interprétation plus difficile et le coût des maquettes équipées de centaines de prises de pression les réservent à des maquettes chères disponibles assez tardivement dans le processus de conception de l'avion.

3.2.2. - Nous commençons à équiper également nos maquettes assez systématiquement de jauges de contraintes et d'accéléromètres permettant de mieux préciser l'importance des fluctuations d'efforts et complètant les indications des efforts globaux donnés par la balance.

3.2.3. - Enfin, il devient de plus en plus nécessaire d'étudier le champ aérodynamique autour de l'avion pour mieux appréhender les dimensions des zones décollées et turbulentes. Pour cela, les visualisations tridimensionnelles renseignent mieux sur ce champ. Initialement on disposait surtout des très belles visualisations colorées effectuées par l'équipe de Monsieur Werlé à l'O.N.E.R.A. aux très faibles nombres de Reynolds (1000 - 5000) du tunnel hydrodynamique ou des sondages sommaires au fil de laine ou à la fumée, et aux mesures locales de pressions totales et statiques obtenues par des peignes fixes multiprises. Maintenant les visualisations tridimensionnelles sont complétées par l'emploi de dispositifs d'émission de bulle d'hélium (réf. 22) et la motorisation des peignes de sillage rend leur emploi plus économique donc courant. Citons l'emploi systématique de tels peignes tournants pour l'étude des champs de pression stationnaire et instationnaire dans les maquettes d'entrée d'air et l'emploi de sondes dont le déplacement en XYZ est commandé grâce à des moteurs pas à pas par l'ordinateur de la soufflerie. Un tel dispositif rend l'exploration de grandes zones décollées accessible à l'essai industriel, il peut être équipé de diverses sondes de pression statique, totale, directionnelle et même de dispositifs spéciaux tel le tourbillomètre (cf. réf. 20) dont l'intérêt est grand surtout dans l'étude des décollements très organisés tridimensionnels. On donne figure 20 le résultat d'un sondage de ce type effectué sur un

Super Mirage Delta à très grande incidence au bord de fuite montrant que la totalité de l'aile est envahie par le décollement turbulent dont la structure est très loin de la structure classique en cornet.

3.3. - Les moyens d'étude théorique

3.3.1. - Outre les calculs de limite de zones décollées, par calcul des couches limites tridimensionnelles amont, que nous avons déjà présentés sur la figure 1, il est possible assez simplement de calculer la forme des zones décollées isobares et la pression correspondante. Ces calculs sont de type couplage ou itératif : ou bien l'on se donne un moyen d'évaluer une zone séparée de l'écoulement, et il faut la rendre compatible suivant une limite à l'intérieur du fluide avec l'écoulement extérieur (cf. réf. 11 et 13), ou bien on résoud l'ensemble de l'écoulement en plaçant simplement une ligne de discontinuité par itération à la frontière de la zone isobare. Le travail de l'avionneur consiste alors à réduire la dimension maximale de la zone décollée ou bien à rapprocher la valeur de la pression correspondante de la pression en l'absence de décollements. En supersonique l'optimisation peut être plus compliquée, en particulier à cause de l'effet de réduction de trainée lié aux décollements et principalement dans les problèmes d'arrière-corps.

3.3.2. - Malheureusement, les zones décollées sont rarement isobares en dehors des zones fortement bidimensionnelles que l'on trouve sur les ailes et les culots. Il est alors de la plus grande importance d'utiliser un modèle théorique pour analyser le résultat des mesures et visualisations et choisir parmi les différentes modifications de forme possibles celles qui joueront sur les phénomènes en cause à défaut de savoir les influences.

Pour cela les méthodes de calcul les plus pratiques font intervenir les singularités dans le fluide, soit suivant le schéma, initialement proposé par Belotserkovskii, de nappes de tourbillons (cf. réf. 2 et 3 , soit suivant le schéma de tourbillons discrétisés de Rehbach (réf. 4). Ces méthodes fournissent un moyen de calcul précieux pour l'avionneur limité par la discrétisation (temps de calcul excessifs sur des configurations complexes) et surtout par leur principe mal adapté à la structure réelle très turbulente des phénomènes, bien que l'on puisse les perfectionner dans ce sens (réf. 16).

Il est alors préférable de partir de solutions directes des équations de Navier-Stokes auxquelles on ajoute un modèle de turbulence dont la validité est à améliorer constamment. Les AMD-BA (réf. 19) ont trouvé, dans l'utilisation courante des solutions de ce type, une aide importante à l'analyse des écoulements décollés non isobares.

3.3.3. - Enfin, très peu de moyens théoriques ont une précision, des temps de calculs, acceptables pour étudier l'aspect instationnaire et analyser les résultats expérimentaux de Mabey et autres(réf.13) Alors que l'on a insisté sur l'importance de ce problème pour l'avionneur, peu de moyens d'analyse aident ainsi la prévision de la stabilité des écoulements décollés. Rappelons comme exemple bien connu l'instabilité du décollement sur des pointes avant de révolution d'avions militaires qui influent beaucoup sur le départ en vrille. Ce phénomène, attaché au phénomène de l'échappement tourbillonnaire autour de cylindre, a été bien vu en vol sur le Mirage F1, comme en soufflerie, et sur nombre d'autres avions analogues. Les contraintes de construction des radômes de radar principalement limitent les modifications de forme acceptables et font là-aussi souhaiter l'aide d'une meilleure compréhension des phénomènes et de calculs a priori.

4. LES VOIES DE RECHERCHE

4.0. - Nous avons rencontré et recensé beaucoup de problèmes posés à l'avionneur par les décollements. Beaucoup de recherches consacrées à la compréhension fine du mécanisme des décollements sont donc souhaitables. Pouvons-nous cependant recommander que les trois approches suivantes soient utilisées conjointement ?

4.1 - Approche bas Reynolds

Il est très important de caractériser globalement les écoulements moyens décollés dans de nombreux cas et de les comparer à des solutions des équations des fluides visqueux : on en tirera des méthodes de calcul qui éviteront de trop recommencer des expériences sur des cas trop sommaires ou accessibles avec des hypothèses simples ; ces cas ne couvrent qu'une part très limitée des décollements que rencontre l'avionneur - spécialement pour les cas bidimensionnels - surtout en supersonique. D'autres, plus tridimensionnels ne sont pas moins importants dans la pratique.

4.2. - Approche turbulente

Il est très important de considérer comme des écoulements turbulents, très inhomogènes et non isotropes certes, ces zones décollées et d'appliquer les connaissances de base acquises récemment dans la compréhension des écoulements turbulents pour analyser, mesurer et calculer les décollements et leur aspect instationnaire.

4.3. - Approche dynamique

Une connaissance plus approfondie de la dynamique des décollements devra consister en un approfondissement et une clarification des idées de stabilité et de changement de forme des décollements Beaucoup d'expériences et de recherches théoriques sont nécessaires dans cette approche.

5. CONCLUSION

L'avionneur n'a pas fini de passer le plus clair de la mise au point aérodynamique d'un engin volant au contrôle des décollements et de leurs effets stationnaires et instationnaires. Mais, après avoir essayé de les supprimer ou à défaut de les réduire aux points d'adaptation, son souci sera de plus en plus, dans le futur, de les rendre stables et progressifs.

REFERENCES

1. AGARD — Fluid dynamics of Aircraft Stalling Agard Conference proceeding n°102.

2. S.BELOTSERKOVSKII — Calculation of the flow about arbitrary wings at high angle of attack. M.Z.G.-4-1968.

3. P.PERRIER et W.VITTE — Eléments d'aérodynamique tridimensionnelle en fluide parfait. Enroulement de la nappe tourbillonnaire. 7ème Colloque d'Aérodynamique appliquée AFITAé (AAAF) 1970.

4. C.REHBACH — Calculs numériques d'écoulements tridimensionnels instationnaires avec nappes tourbillonnaires. La Recherche Aérospastiale n°1977-5.

5. P.PERRIER et J.J.DEVIERS — Calculs tridimensionnels d'hypersustentation. 9ème Colloque d'Aérodynamique appliquée AAAF nov.1972.

6. AGARD — Advisory Report n°82. The effects of buffeting and other transonic phenomena on maneuvering combat Aircraft.

7. R.HOPPS et E.DANFORTH — Correlation of W.T and F.T Data for Lockeed L-1011 Tristar. AGARD.FMP Meeting Paris octobre 1977.

8. E.GAIGNEBET et G.HECKMANN — Nouvelles méthodes d'acquisition du buffeting. 12ème Colloque d'Aérodynamique appliquée AAAF nov.1975.

9. P.PERRIER et M.LAVENANT — Progrès récents en hypersustentation mécanique. AGARD CP 143. 1974.

10. M.SIRIEX — Décollement turbulent en écoulement bidimensionnel. AGARD Conference on Flow Separation. May 1975.

11. P.CARRIERE, M.SIRIEX et J.DELERY — Méthode de calcul des écoulements décollés en supersonique. Progress in Aerospace Science 1976.

12. G. de RICHEMONT et J. DELERY — Effets des conditions extérieures sur le fonctionnement d'une tuyère supersonique à double flux. AGARD CP 150 1974.

13. D. MABEY — Analysis and Correlation of Data on Pressures Fluctuations in Separated Flow. Journal of Aircraft Vol.6 n°9.

14. P. CAUPENNE — Etudes expérimentales et théoriques sur les décollements de profils. 13ème Colloque d'Aérodynamique appliquée AAAF nov. 1976.

15. H. WERLÉ — Ecoulements décollés. Etude phénoménologique à partir de visualisations hydrodynamiques. AGARD CP 168 May 1975.

16. REYNOLDS — Recent Advances in the computation of Turbulent Flows. ADV.CHEM.EN.9 : 193-246. 1974.

17. J. FROMM — A method for computing nonsteady, Incompressible, Viscous Fluid Flows. Los Alamos Scientific Laboratory Report LA 1910 Sep.1963.

18. P.PERRIER, J.PERIAUX et O.PIRONNEAU — Finite Elements Methods Applied to non-linear fluid dynamics equations. Short course on numerical fluid dynamics. Von Karman Institute. 1976.

19. J.PERIAUX et O.PIRONNEAU — Optimal control formulation for non-linear P.D.E. and applications to transonic inviscid flows and to incompressible viscous flows. To appear in proceeding of the conference on numerical methods in applied fluid dynamics, Reading. January 1978.

20. M. AIELLO — Mesures d'intensité de tourbillons dans la soufflerie AMD-BA de Vélizy. 14ème Colloque d' Aérodynamique appliquée AAAF nov.1977.

21. O.FRIEDRICH, B.YOUNG — Tornado, an advanced Stol fighter-bomber design. 10th Congress of I.C.A.S. 1976.

22. J. DRIVIERE — Caractérisation des décollements tridimensionnels. Mémoire ENSAM 331 3617. 1974-1975.

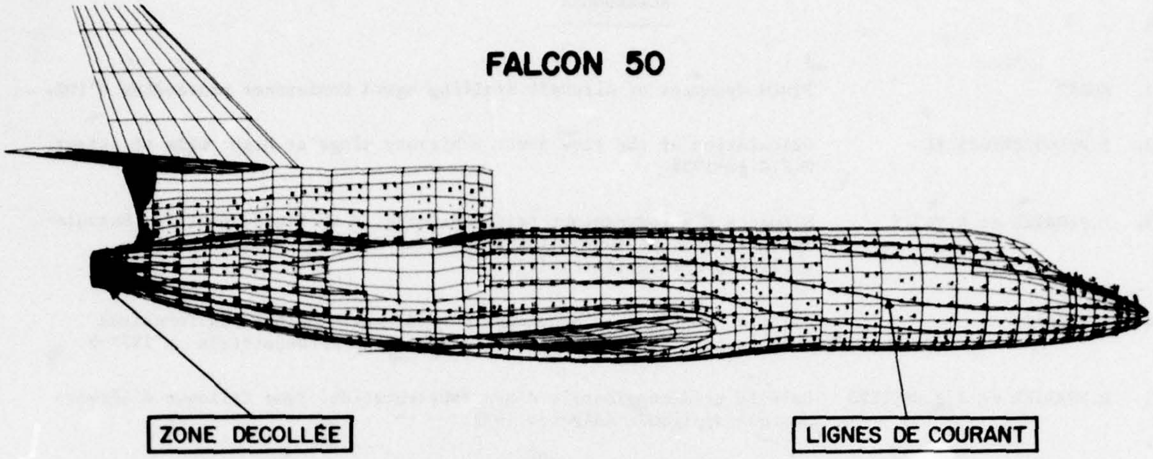

Fig.1 Calcul de décollements en cours d'optimisation du fuselage arrière du Falcon 50

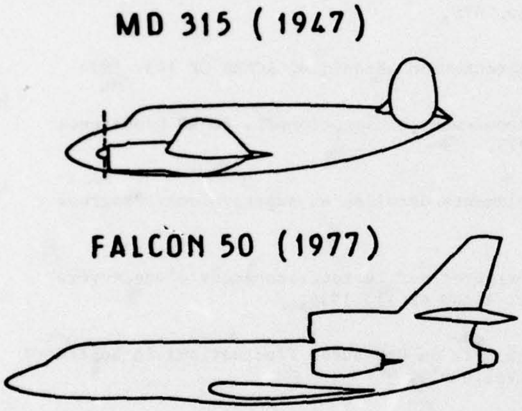

Fig.2 Evolution des formes des avions de transport de passagers.

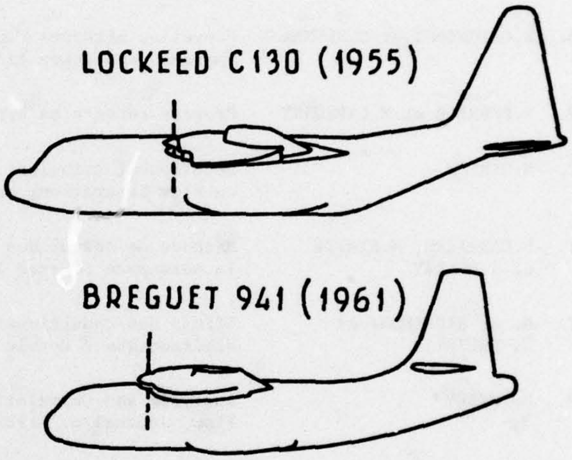

Fig.3 Evolution des dessins de fuselage d'avions cargo.

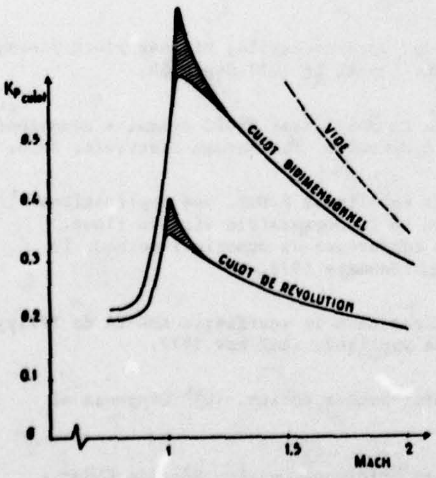

Fig.4 Trainées caractéristiques de décolts du culot, aile ou fuselage.

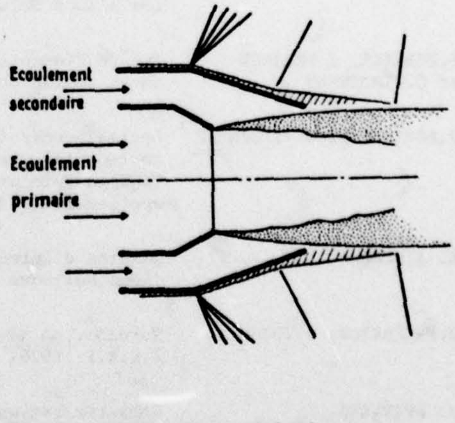

Fig.5 Schémas caractéristiques d'arrière-corps en supersonique.

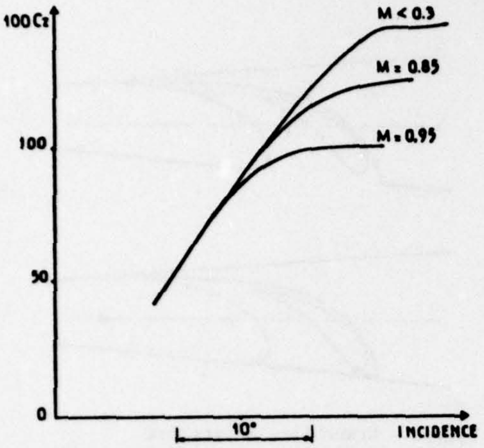

Fig.6 Influence caractéristique du nombre de Mach sur les portances d'un chasseur.

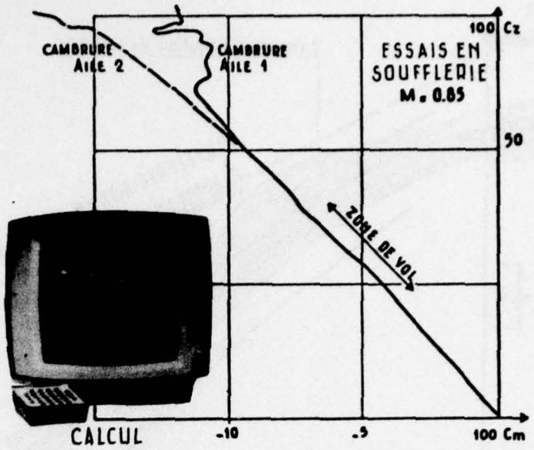

Fig.7 Optimisation de la courbe de moment en écoulement transsonique décollé.

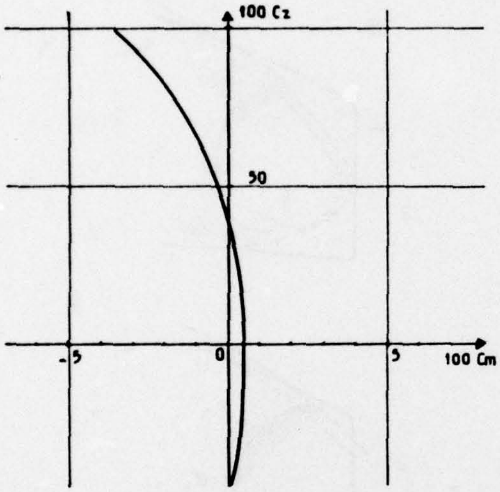

Fig.8 Pente typique de stabilité en portance négative sur un avion à géométrie variable.

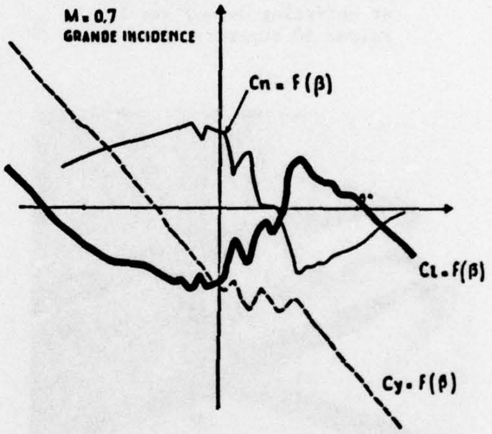

Fig.9 Non-linéarité typique autour des dérapages nuls des coefficients de stabilité en transsonique.

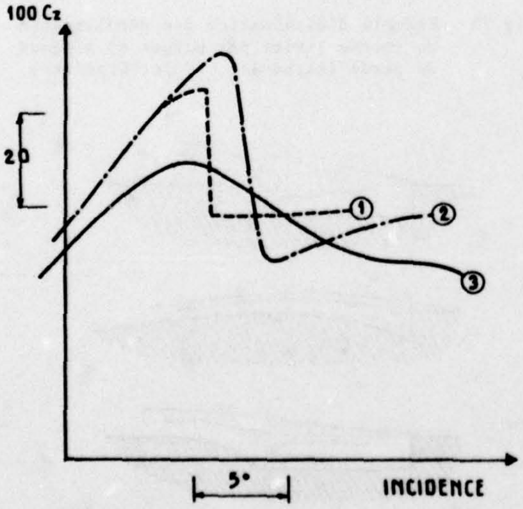

Fig.10 Echange typique entre les performances en portances et les non-linéarités au décrochage d'un avion école sans bec.

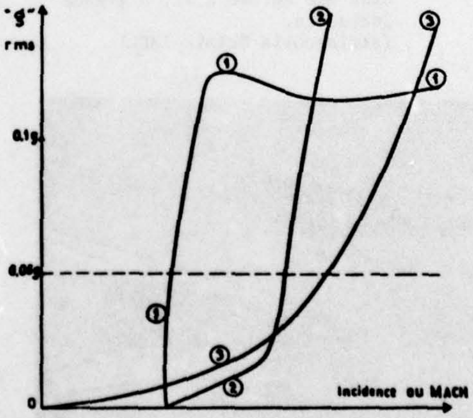

Fig.11 3 évolutions caractéristiques du buffeting ressenti sur un avion.

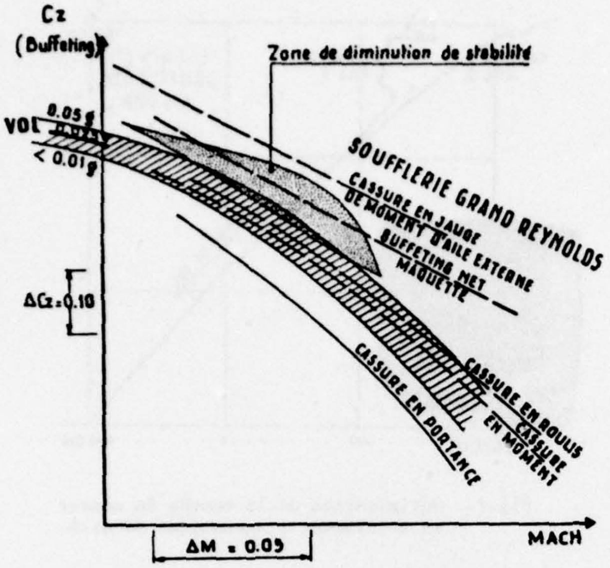

Fig.12 Comparaison des signaux mesurés en soufflerie à grands Reynolds et buffeting de vol sur le Falcon 50 supercritique.

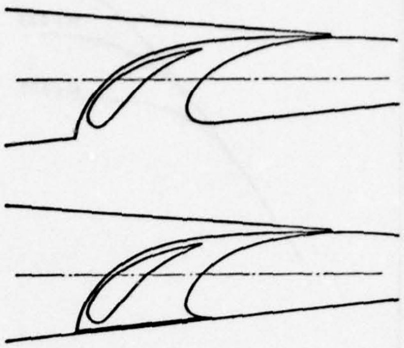

Fig.13 Etanchéité d'intrados anti-vibratoire sur Alpha Jet.

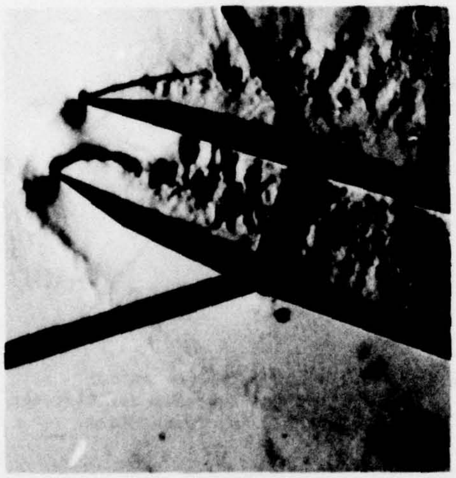

Fig.14 Schéma d'écoulement transsonique dans une entrée d'air à grande incidence. (strioscopie éclair IMFL)

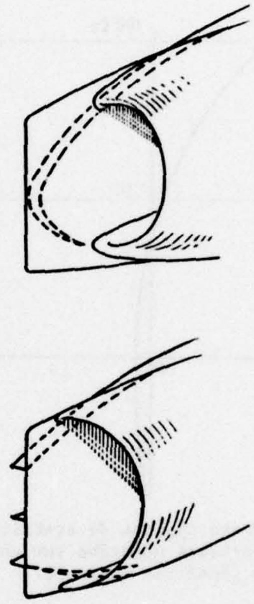

Fig.15 Exemple d'élimination des décollements de couche limite par pièges et plaques de garde (Alpha Jet - Super Etendard)

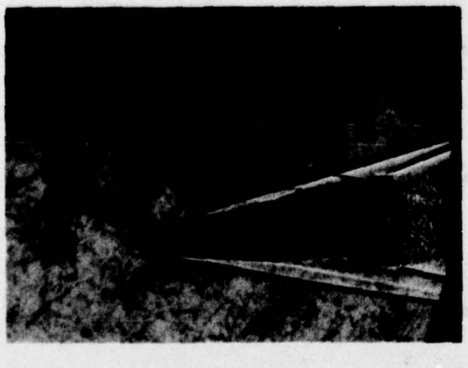

Fig.16 Décollements caractéristiques sur un corps de réentrée (strioscopie éclair au tunnel de tir).

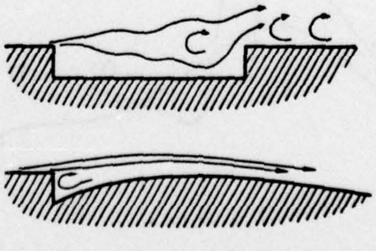

Fig.17 Stabilisation d'un décollement de cavité.

Fig.18 Décollements à grande incidence sur Mirage G8 stabilisés par augmentation de flèche à l'emplanture.

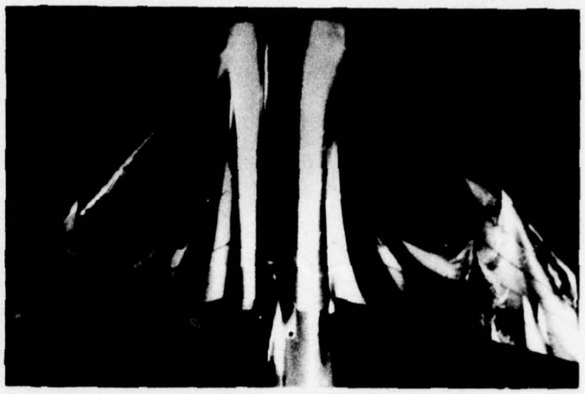

Fig.19 Visualisation par injections de fluides colorés pour étude des décollements organisés transsoniques du Mirage F1 à la soufflerie S2 de l'ONERA.

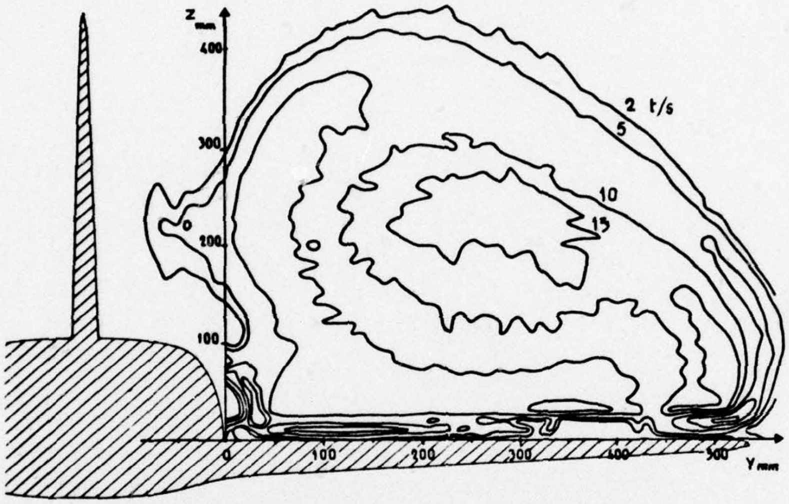

Fig.20 Mesure par tourbillomètre de la rotation du fluide dans le tourbillon d'apex du Delta Super Mirage à grande incidence.

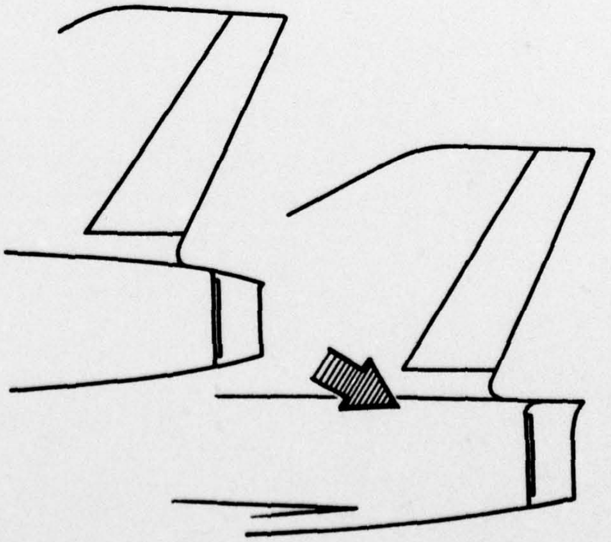

Fig.21 Modifications à l'arrière du Mirage IV pour stabiliser les décollements.

TRAITEMENT DES PROBLEMES D'INTERACTION FLUIDE PARFAIT – FLUIDE VISQUEUX EN ECOULEMENT BIDIMENSIONNEL COMPRESSIBLE A PARTIR DES EQUATIONS DE NAVIER-STOKES

Henri VIVIAND

Office National d'Etudes et de Recherches Aérospatiales (ONERA)
92320 Châtillon (France)

RESUME

On se propose de faire le point sur le traitement des problèmes d'interaction fluide parfait-fluide visqueux en écoulement bidimensionnel compressible, à grand nombre de Reynolds, par résolution numérique des équations de Navier-Stokes (N.S.). Cette approche globale comporte deux volets distincts : d'une part la résolution numérique des équations et, d'autre part la modélisation de la turbulence pour les écoulements décollés compressibles, la comparaison entre les prédictions du calcul numérique et les résultats expérimentaux étant nécessaire pour établir la validité des modèles de turbulence. La discussion de ces domaines de recherche, très vastes et en rapide évolution, déborde largement le cadre d'une conférence, et nous avons choisi d'une part de donner une idée d'ensemble des problèmes traités et des résultats obtenus, et d'autre part de présenter seulement les grandes lignes des méthodes numériques et des modèles de turbulence utilisés.

Les progrès récents réalisés dans les deux domaines qu'on vient de citer sont dus en grande partie aux travaux d'équipes de la NASA, travaux basés sur les méthodes numériques développées par MacCormack et ses collaborateurs. Notre exposé sera donc centré sur ces travaux, mais nous ferons état aussi d'autres travaux plus limités.

Nous passons d'abord en revue les problèmes d'interaction en écoulement compressible qui ont été ou sont traités par cette approche globale, à savoir :

- écoulement transsonique autour d'un profil,
- interaction choc droit-couche limite en transsonique,
- interactions choc oblique-couche limite en supersonique ou en hypersonique, soit sur une plaque plane, ou sur un cylindre circulaire, soit dans un angle de compression.

On présente ensuite une discussion de la formulation des équations de Navier-Stokes moyennées en temps en les comparant avec les équations correspondantes dans le cas incompressible. Le problème de la modélisation de la turbulence est seulement abordé, en faisant état des types de modèles utilisés dans les applications sans les décrire en détail.

En ce qui concerne les méthodes numériques de résolution des équations de Navier-Stokes, nous présentons le principe de la méthode actuellement la plus utilisée, c'est-à-dire la méthode de MacCormack, dans la formulation volumes-finis, valable dans un maillage quelconque. Divers aspects - importants en pratique - de cette méthode, ainsi que certains développements récents, ne sont que mentionnés avec renvoi aux publications correspondantes. Nous indiquons aussi plus rapidement d'autres méthodes de discrétisation dans des maillages quelconques, basées aussi sur le schéma de MacCormack.

NUMERICAL SOLUTION OF VISCOUS – INVISCID INTERACTION PROBLEMS IN TWO-DIMENSIONAL COMPRESSIBLE FLOWS BASED ON THE NAVIER-STOKES EQUATIONS

SUMMARY

A review is presented of the approach based on the numerical solution of the Navier-Stokes (N.S.) equations for the treatment of viscous-inviscid interaction problems in two-dimensional high Reynolds number compressible flows. This global approach involves two distincts problems : on the one hand the numerical solution of the equations used, and on the other hand turbulence modeling to close the system of the averaged N.S. equations for the case of compressible separated flows, the validity of turbulence models being tested through comparisons between numerical predictions and experimental results. The discussion of these rapidly evolving domains goes much beyond the limits of one conference and we have chosen here first to give a general presentation of the problems and of the results which have been obtained, and secondly to discuss only the essential features of the numerical methods and of the turbulence models which have been used.

Recent progress in these domains is due in large part to research works carried out at NASA and based on numerical methods which have been developped by MacCormack and his co-workers. Our report will thus be centred round these works, but we shall also mention other less extensive works.

First we present a review of interaction problems which have been treated by this global approach, i.e. :

- transonic flow about a profile,
- shock-boundary layer interaction in transonic flow,
- oblique shock-boundary layer interactions in supersonic or hypersonic flow, either over a flat plate (or a circular cylinder), or over a compression ramp.

Then the time-averaged compressible N.S. equations are discussed and compared to their incompressible counter part. The problem of turbulence modelling is only outlined ; the types of turbulence models which are actually used in the applications are only mentionned without detailed description.

Concerning the numerical methods for solving the N.S. equations, we present the fundamentals of the most widely used method, i.e. MacCormack's method, in its finite-volume form. Various practically important features of this method as well as some recent developments, are only mentioned with reference to the litterature. We give also brief indications about other discretization techniques, based on MacCormack's scheme and which can be used with arbitrary mesh systems.

---

1 - INTRODUCTION -

Tous les écoulements, laminaires ou turbulents, de gaz usuels comme l'air sont décrits avec une très grande précision par les équations de Navier-Stokes (dénotées N.S. dans ce qui suit), à l'exception des écoulements ou des régions d'écoulement où le libre parcours moyen des molécules n'est plus suffisamment petit devant une longueur caractéristique des gradients locaux instantanés. Les équations de N.S. permettent donc en principe, si on peut les résoudre avec une précision suffisante, de déterminer par le calcul numérique la grande majorité des écoulements rencontrés en aérodynamique.

Les problèmes que ces équations ne permettent pas de traiter sont les écoulements de gaz dits raréfiés, la structure d'une onde de choc de forte intensité, et éventuellement les voisinages très restreints de points singuliers des solutions des équations de N.S., comme, par exemple, à un angle de détente, si le comportement singulier de la solution n'est pas physiquement acceptable. En dehors des écoulements de gaz raréfiés qui sortent du cadre de cet exposé,ces zones de non-validité des équations de N.S. ont au moins une dimension extrêmement petite devant une longueur caractéristique de l'écoulement, telle qu'une épaisseur de couche limite, et on admet que la solution des équations de N.S. n'est pas affectée par la structure interne de ces zones, du moins au niveau de précision recherché dans l'étude d'un problème type d'interaction fluide parfait-fluide visqueux.

La turbulence, par contre, phénomène le plus souvent présent et d'une importance pratique considérable, est décrite par les équations de N.S., mais elle fait intervenir des échelles de temps et d'espace trop petites pour être prises en compte dans une représentation discrétisée de l'espace et du temps, même sur les ordinateurs les plus puissants.

Des études récentes font appel à une discrétisation partielle, pour les échelles suffisamment grandes, et à une modélisation (c'est-à-dire une représentation mathématique complémentaire) pour les échelles plus petites. Cette simulation numérique de la turbulence [1], qui reste très coûteuse en temps de calcul et n'est pas encore applicable aux problèmes concrets, ne sera pas discutée ici ; nous ne considérons que l'approche basée sur les équations de N.S. moyennées en temps et complétées de relations algébriques ou d'équations aux dérivées partielles qui constituent ce qu'on appelle un modèle de turbulence et qui permettent la fermeture du système d'équations. Dans cette approche, l'écoulement turbulent n'est décrit que par des valeurs moyennes en temps, ce qui suppose implicitement qu'on peut séparer les effets instationnaires propres à la turbulence d'autres effets instationnaires plus globaux et à fréquences nettement plus basses : l'écoulement moyen est donc soit stationnaire, soit instationnaire mais à une fréquence assez basse pour qu'il n'y ait pas interférence avec la turbulence proprement dite. Cette hypothèse est donc acceptée, par force, dans les calculs qu'on peut faire actuellement, mais les limites de sa validité sont mal connues. En tout cas, elle paraît exclure l'étude de décollements très étendus dans toutes les directions, et dans lesquels les grosses structures tourbillonnaires sont de dimensions comparables à une dimension géométrique du problème (corde d'un profil, rayon d'une sphère ...).

Les calculs d'écoulements de fluide visqueux compressible par résolution numérique des équations de N.S. se sont développés particulièrement depuis une dizaine d'années. On trouvera une revue des méthodes numériques utilisées et des applications traitées jusqu'à 1975 dans les références [2] à [4]. Dans le présent exposé nous nous proposons de faire le point sur le traitement des problèmes d'interaction fluide parfait-fluide visqueux à grand nombre de Reynolds, en écoulement compressible bidimensionnel, par résolution numérique des équations de N.S.

Le sujet est très vaste et nous n'en présentons ici qu'une discussion très générale, aussi bien en ce qui concerne les applications traitées qu'en ce qui concerne les méthodes numériques utilisées. La bibliographie à laquelle nous renvoyons pour des discussions détaillées est, sinon complète, du moins représentative de l'état actuel de développement de cette approche globale basée sur les équations de N.S.

2 - LA RESOLUTION DES EQUATIONS DE NAVIER-STOKES : UNE APPROCHE GLOBALE DES PROBLEMES D'INTERACTION -

Lorsqu'il s'agit de calculer des écoulements à faible nombre de Reynolds, la nécessité de faire appel aux *équations de N.S. est évidente. Par contre, pour les écoulements à grand nombre de* Reynolds que nous considérons ici, et en excluant le cas de décollements très étendus dans toutes les directions, l'utilisation des équations de N.S. complètes n'est pas indispensable et l'intérêt d'une approche basée sur ces équations est en fait dû à des raisons que nous discutons dans ce paragraphe.

La décomposition classique entre écoulement de fluide parfait et couche visqueuse de faible épaisseur reste valable pour les problèmes d'interaction considérés ici. Il y a interaction lorsque l'écoulement de fluide parfait est plus ou moins fortement influencé par la couche visqueuse, c'est-à-dire qu'il ne peut être déterminé indépendamment de celle-ci. Ce phénomène est toujours présent lorsqu'il y a décollement de la couche limite, et l'on sait que la théorie classique de la couche limite est alors mise en défaut. Cet échec n'est cependant pas imputable aux équations de Prandtl elles-mêmes, *mais plutôt aux conditions aux limites utilisées à la frontière de la couche limite et qui supposent* l'écoulement extérieur connu. On peut en effet, en première approximation, continuer à utiliser les équations de Prandtl pour la couche visqueuse même en interaction, à condition de coupler l'écoulement de fluide parfait et la couche visqueuse par des conditions de raccord sur leur frontière commune. Ces conditions, appelées relations de couplage, peuvent être établies de façon rigoureuse dans le cadre d'une *théorie asymptotique bien précise mais impliquant alors des restrictions* d'application, ou de façon plus heuristique et en même temps plus générale (par ex., [5],[6], [7]). On aboutit ainsi à une approche des problèmes d'interaction basée sur le calcul couplé des solutions dans la région du fluide parfait et dans la couche visqueuse. Cette approche fait l'objet de l'exposé de J.C. Le Balleur dans ce cycle de conférences.

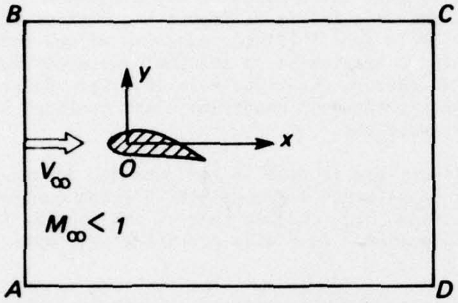

sur DABC : écoulement uniforme
sur DC : écoulement uniforme ou $\partial/\partial x = 0$.

a – Calcul de l'écoulement complet

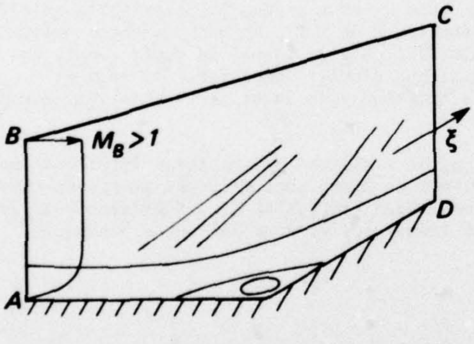

sur AB : écoulement donné
sur BC : écoulement donné, ou ondes simples
sur CD : $\partial/\partial\xi = 0$, ou pas de condition (schéma décentré en amont)

b – Domaine limité avec conditions aux limites fixées

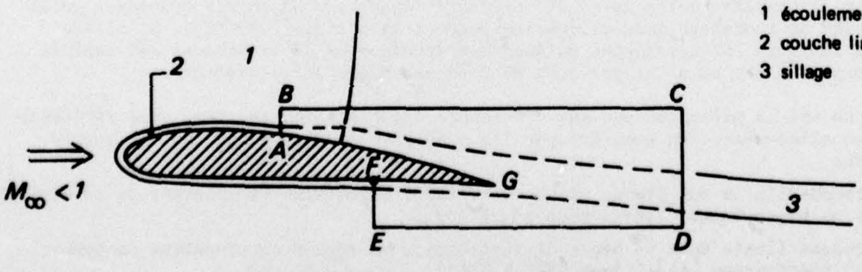

1 écoulement non visqueux
2 couche limite
3 sillage

(ABCDEFGA) : domaine "Navier-Stokes"

c – Domaine limité avec raccord numérique

Fig. 1 – Domaines de calcul de l'approche globale.

L'approche globale, basée sur les équations de N.S., peut être distinguée des méthodes de couplage par les deux propriétés suivantes :

1) le domaine de calcul dans l'approche globale est :

   a) soit la quasi-totalité de l'écoulement étudié (ex., figure 1-a),

   b) soit un domaine limité qui déborde sur l'écoulement de fluide parfait et sur les couches visqueuses au-delà de la *zone* d'interaction (ex., figures 1-b et 1-c).

La frontière entre fluide parfait et couche visqueuse, qui est l'une des inconnues dans les méthodes de couplage, est située à l'intérieur de ce domaine de calcul, mais sa position n'a pas à être précisée.

2) L'écoulement dans ce domaine est déterminé par un traitement numérique unique, ce qui implique l'utilisation d'un système d'équations unique, mais n'exclut pas par exemple l'utilisation de schémas numériques différents dans différentes parties de ce domaine.

Nous n'imposons pas, avec la propriété 2), l'utilisation des équations de N.S. complètes, la seule condition requise étant que le système d'équations soit également valable dans la couche visqueuse et dans la région de fluide parfait. C'est pourquoi nous préférons parler d'approche globale plutôt que de résolution des équations de N.S., même si dans les applications ce sont le plus souvent ces dernières qui sont mises en oeuvre. Des exemples d'approche globale avec des équations de N.S. tronquées sont fournis par les références [19] et [50].

Les conditions aux limites sur la frontière extérieure du domaine de calcul (paroi exclue) peuvent être fixées (cas des figures 1-a et 1-b), ou elles peuvent dépendre d'un raccord numérique avec des écoulements de fluide parfait et de couche limite qu'il faut alors calculer simultanément (cas de la figure 1-c). Le cas de la figure 1-c se distingue de celui de la figure 1-a surtout par le fait que, pour le premier, les traitements numériques de la zone 1 (fluide parfait) et des zones 2 et 3 (couche limite et sillage) sont supposés différents du traitement du domaine "Navier-Stokes", ce qui oblige à mettre en oeuvre une technique spéciale de raccord numérique à la frontière de ce domaine. Pour le cas de la figure 1-a au contraire, le même traitement numérique étant appliqué à tout l'écoulement, ce problème de raccord numérique ne se pose pas.

Le mode de calcul qui correspond au schéma de la figure 1-c a été proposé en [8] pour des écoulements incompressibles et il a été mis en oeuvre pour des écoulements compressibles à grand nombre de Reynolds, mais sous une forme quelque peu simplifiée, dans [51], [52] et [53] où une zone N. S. est effectivement calculée, mais où son influence sur l'écoulement de fluide parfait n'est représentée que par un effet de déplacement.

L'approche globale ne fait donc pas de distinction entre la couche visqueuse et la zone de fluide parfait incluse dans le domaine de calcul. De ce point de vue, elle fournit une description du *phénomène d'interaction plus proche de la réalité* que les méthodes de couplage, même si elle est utilisée avec des équations dont les termes visqueux sont approchés et non exacts. Paradoxalement, on peut dire que le principal avantage de l'approche globale n'est pas dans la possibilité qu'elle offre de tenir compte de tous les termes visqueux des équations de N.S., ce qui néanmoins présente un intérêt pour les zones décollées, mais plutôt dans le fait qu'elle permet de tenir compte de tous les termes de fluide parfait, c'est-à-dire des équations d'Euler complètes, car ceux-ci peuvent être particulièrement importants dans la partie extérieure de la couche limite (par exemple, le gradient de pression normal peut être important).

Ajoutons, pour conclure ces remarques, que l'existence de deux régions à caractères différents ne peut cependant être ignorée dans l'approche globale. Il est en effet nécessaire de mettre en oeuvre une discrétisation de l'espace adaptée aux gradients locaux des propriétés de l'écoulement, et le maillage doit être beaucoup plus fin, dans la direction transversale, dans la couche visqueuse que dans l'écoulement de fluide parfait.

3 - REVUE DES PROBLEMES TRAITES -

Nous avons rassemblé dans la bibliographie une liste de travaux récents (à partir de 1971, mais la plus grande partie correspond à la période 1975-1977) concernant le calcul d'écoulements bidimensionnels compressibles visqueux à grand nombre de Reynolds par cette approche globale. Cette revue reprend en partie et complète celle qui a été présentée dans [4]. On pourra constater qu'il y a eu une forte activité de recherche dans ce domaine pendant la période 1975-1977, et qu'une grande partie de cette activité est développée au Ames Research Center de la NASA et est centrée sur les méthodes numériques mises au point par R.W. MacCormack et ses collaborateurs.

L'objet de ce paragraphe est de présenter une vue d'ensemble des problèmes traités, sans référence aux méthodes numériques elles-mêmes. On peut grouper les problèmes étudiés selon les catégories d'écoulements suivantes:

A - Interaction choc-couche limite sur plaque plane ou cylindre circulaire (écoulement de révolution), en régime supersonique ou hypersonique (*références* [9] à [32]).

B - Interaction choc-couche limite dans un angle de compression en régime supersonique ou hypersonique (écoulement plan) (références [14]-(1) et [32] à [39]).

C - Interaction choc droit-couche limite dans un canal circulaire en régime transsonique (écoulement de révolution) (références [31], [32] et [40]).

D - Ecoulement complet autour d'un profil portant ou non en régime transsonique (références [41] à [53]).

E - Divers (références [27] et [54] à [59]).

Nous n'avons pas repris dans cette liste les problèmes classiques de l'écoulement de culot en supersonique et de l'écoulement sur le bord d'attaque d'une plaque plane en supersonique ou en hypersonique. Ces problèmes qui ont été parmi les premières applications numériques des méthodes de résolution des équations de N.S., en général à des nombres de Reynolds modérés, sont passés en revue dans [4].

Presque tous les problèmes traités concernent des écoulements stationnaires (laminaires ou turbulents), à l'exception de calculs récents d'écoulements transsoniques instationnaires autour de profils (références [49] et [50]).

Les problèmes A et B sont particulièrement intéressants pour tester des méthodes de calcul car les configurations géométriques sont simples et ils permettent d'obtenir des nombres de Reynolds assez élevés en régime laminaire. Les premières études, [9], [12], [15], [33], [34], [35], ont donc naturellement porté sur ces problèmes. En particulier le problème de l'interaction choc-couche limite sur plaque plane en régime supersonique ou hypersonique a été souvent traité pour tester des méthodes numériques nouvelles, [16], [17], [23] à [27], ou pour étudier de façon plus approfondie les questions de convergence et de précision [20], [28]. Les applications à des écoulements turbulents, tentées dès 1973-1974, [10], [11, [13], [14], se sont beaucoup développées à partir de 1975, [18], [21] à [24], [29] à [32], [36] à [39] pour étudier et tester, par comparaison avec des résultats expérimentaux, des modèles de turbulence adaptés aux écoulements supersoniques ou hypersoniques soumis à de forts gradients de pression et éventuellement décollés.

Le problème C, qui a été considéré plus tard que les problèmes A et B, présente les mêmes avantages que la configuration axisymétrique du problème A, à savoir la simplicité géométrique pour le calcul, et l'absence d'effets tridimensionnels parasites pour l'expérience. Ce problème est donc intéressant pour tester des modèles de turbulence dans le régime transsonique.

Pour les problèmes A, B et C, le domaine de calcul est limité de façon naturelle à un voisinage de la zone d'interaction, avec conditions aux limites connues aux frontières, comme sur l'exemple de la figure 1-b. Eventuellement, l'écoulement de couche limite sur la totalité de la paroi en amont de cette zone peut être calculé par la même méthode pour déterminer des conditions aux limites juste en amont de la zone d'interaction.

Pour le problème D, on peut définir un domaine de calcul limité, incluant les zones d'interaction qui apparaissent au niveau des chocs ainsi qu'au bord de fuite, mais on ne peut pas faire correspondre à ce domaine des conditions aux limites fixées, c'est-à-dire indépendantes de l'écoulement à l'extérieur du domaine, car on sait que tout le profil peut être affecté par des effets d'interaction locale. Il faut donc soit appliquer l'approche globale à la quasi-totalité de l'écoulement (cas de la figure 1-a), soit n'utiliser cette approche que dans un domaine limité, mais en assurant un raccord numérique avec l'écoulement, calculé par d'autres méthodes, à l'extérieur du domaine (cas de la figure 1-c) (pour la commodité de la discussion, nous appellerons D.a la première méthode et D.c la seconde). D'une façon générale, la difficulté supplémentaire que présente le problème D par rapport aux problèmes A, B et C tient à l'étendue du domaine de calcul comparée, par exemple, à l'épaisseur de la couche limite, qui conduit à des temps de calcul très importants. C'est dans le but de réduire les temps de calcul que la méthode D.c a été étudiée et mise en oeuvre dans [51], [52], [53], mais,comme nous l'avons déjà dit au paragraphe 2,avec une technique de raccord approchée. Des comparaisons faites dans [53] entre les méthodes D.a et D.c, il ressort que la méthode D.c est beaucoup plus rapide que la méthode D.a, tout en donnant des résultats aussi précis.

On peut cependant se demander si le raccord approché présentement utilisé donnera dans tous les cas une précision équivalente à celle de la méthode D.a, particulièrement dans le cas de décollements importants, et si la mise en oeuvre d'un raccord exact dans la méthode D.c ne provoquera pas une augmentation sensible des temps de calcul.

Le problème D a été étudié en écoulement symétrique, pour un profil biconvexe de 18 % d'épaisseur relative à incidence nulle (références [41] à [46]), ainsi qu'en écoulement portant (profil NACA 0012 en incidence, profil Garabedian-Korn , profil NACA 64 A010, un profil supercritique , références [47], [48], [50]). Le cas du profil biconvexe à incidence nulle a été repris dans [49], sans imposer de condition de symétrie et en tenant compte des parois de la veine (mais sans les couches limites de ces parois) ; le calcul à $M_\infty = 0{,}754$ et $\mathcal{R}e_{\infty,c} = 11 \times 10^6$ donne une solution instationnaire oscillatoire présentant les mêmes caractéristiques que les écoulements observés en soufflerie à des nombres de Mach légèrement plus élevés.

Le calcul met en évidence le mouvement alternatif du point de décollement, lié au choc lorsque l'intensité de celui-ci est assez forte, et revenant près du bord de fuite dans le cas contraire; les phénomènes se reproduisent identiquement à l'extrados et à l'intrados mais avec un déphasage de 180°.

Des calculs d'écoulements transsoniques instationnaires sont aussi présentés dans [50] (en utilisant une approximation de couche mince pour tronquer les termes visqueux des équations de N.S.), pour le profil NACA 64A010 animé d'un mouvement de battement vertical sinusoïdal, ainsi que pour le profil biconvexe de 18 % à incidence nulle en atmosphère infinie. Pour ce dernier cas, le calcul donne une solution stationnaire à $M_\infty = 0{,}754$, et instationnaire à $M_\infty = 0{,}783$, contrairement à ce qui est obtenu dans [49], et en meilleur accord avec l'expérience au moins pour le premier nombre de Mach. Etant donné que ces calculs sont effectués avec un modèle algébrique très simple de viscosité tourbillonnaire, l'interaction choc-couche limite ainsi que les zones décollées ne sont pas décrites de façon très précise ; on voit que le calcul permet néanmoins de reproduire les caractéristiques essentielles du phénomène instationnaire. Une description fine de l'interaction fluide parfait-fluide visqueux reste sans doute indispensable si l'on veut prédire correctement les conditions dans lesquelles se manifeste le régime instationnaire.

Dans la catégorie "divers",nous avons regroupé des travaux qui, à l'exception de [59], ne concernent pas directement des problèmes d'interaction à grand nombre de Reynolds, mais qu'il nous semble intéressant de signaler ici comme exemples d'applications de l'approche globale, parce-que soit les problèmes traités, soit les méthodes numériques utilisées, présentent des aspects originaux.

4 - EQUATIONS DE NAVIER-STOKES MOYENNES ET MODELISATION DE LA TURBULENCE -

Dans ce paragraphe nous présentons les équations de N.S. moyennées en temps pour le cas des écoulements turbulents, et nous discutons, en comparant avec le cas incompressible, certaines complications introduites par la compressibilité dans les équations moyennes. Nous donnons ensuite quelques indications sommaires sur les modèles de turbulence utilisés jusqu'à présent avec les équations de N.S. en fluide compressible. La justification de ces modèles repose principalement sur la comparaison entre le calcul numérique et l'expérience, d'où l'importance de méthodes de calcul suffisamment précises.

En fluide compressible, les fluctuations de masse volumique introduisent des termes supplémentaires de corrélation dans les équations moyennes. L'utilisation des moyennes pondérées par la masse, [60] à [62], permet de réduire au minimum le nombre de ces termes. Pour une quantité fluctuante quelconque φ , on définit d'une part une valeur moyenne $\bar{\varphi}$ et une fluctuation φ' au sens habituel, et d'autre part une valeur moyenne pondérée par la masse, $\tilde{\varphi}$, à laquelle correspond une fluctuation φ'' . Ces définitions conduisent aux formules suivantes :

$$\left\{\begin{aligned} &\varphi = \bar{\varphi} + \varphi' \quad , \quad \overline{\varphi'} = 0 \\ &\overline{\rho\varphi} = \bar{\rho}\tilde{\varphi} \quad , \quad \varphi = \tilde{\varphi} + \varphi'' \quad , \quad \overline{\rho\varphi''} = 0 \\ &\overline{\rho'\varphi'} = \overline{\rho'\varphi''} = -\bar{\rho}\,\overline{\varphi''} \end{aligned}\right. \tag{1}$$

On pourra constater les simplifications introduites par la pondération par la masse en comparant les formules suivantes :

$$\left\{\begin{aligned} &\overline{\rho\varphi\psi} = \bar{\rho}\tilde{\varphi}\tilde{\psi} + \overline{\rho\varphi''\psi''} \\ &\overline{\rho\varphi\psi^2} = \bar{\rho}\tilde{\varphi}\tilde{\psi}^2 + \tilde{\varphi}\,\overline{\rho\psi''^2} + 2\tilde{\psi}\,\overline{\rho\varphi''\psi''} + \overline{\rho\varphi''\psi''^2} \end{aligned}\right. \tag{2}$$

aux formules correspondantes en fonction de $\bar{\varphi}$, φ', $\bar{\psi}$ et ψ'.

Les équations de N.S. instantanées s'écrivent, sous forme vectorielle conservative, et avec les notations habituelles :

$$\frac{\partial \rho}{\partial t} + div\left(\rho\vec{V}\right) = 0 \quad , \qquad \text{équation de continuité} \tag{3}$$

$$\frac{\partial}{\partial t}\left(\rho\vec{V}\right) + div\left[\left(\rho\vec{V};\vec{V}\right) + p\underline{\underline{I}}\right] = div\,\underline{\underline{\tau}} \quad , \qquad \text{équation de quantité de mouvement} \tag{4}$$

$$\underline{\underline{\tau}} = \left(\lambda\, div\,\vec{V}\right)\underline{\underline{I}} + \mu\, def\,\vec{V} \;,\; def\,\vec{V} = grad\,\vec{V} + \left(grad\,\vec{V}\right)^t \;,\; \underline{\underline{I}} = \text{tenseur unité} \tag{5}$$

$$\frac{\partial}{\partial t}\left[\rho\left(E + \frac{1}{2}\vec{V}^2\right)\right] + div\left[\rho\left(E + \frac{1}{2}\vec{V}^2\right)\vec{V} + p\vec{V}\right] = div\left[\vec{V}\,\underline{\underline{\tau}} - \vec{q}\right] \quad , \qquad \text{équation de l'énergie} \tag{6}$$

avec

$$\vec{q} = -k\; grad\, T = -\frac{\gamma}{P_r}\,\mu\; grad\, E \tag{7}$$

où le nombre de Prandtl, $P_r = \mu C_p / k$ est supposé constant.

Il faut compléter ce système par une loi d'état et par des formules donnant les variations de λ ,

μ , k en fonction de la température T ou de E. On considère ici le cas d'un gaz parfait à chaleurs spécifiques constantes, de rapport γ :

$$p = (\gamma - 1)\, \rho E \tag{8}$$

Dans les applications, on admet toujours la relation de Stokes, $3\lambda + 2\mu = 0$.

Effectuant l'opération de moyenne dans le temps sur le système des équations (3), (4) et (6), on obtient :

$$\frac{\partial \bar{\rho}}{\partial t} + div\,(\bar{\rho}\, \tilde{\vec{V}}) = 0 \tag{9}$$

$$\frac{\partial}{\partial t}(\bar{\rho}\tilde{\vec{V}}) + div\left[(\bar{\rho}\,\tilde{\vec{V}}\,;\,\tilde{\vec{V}}) + \bar{p}\,\underline{\underline{I}}\right] = div\,(\overline{\underline{\underline{\tau}}} + \underline{\underline{\tau}}_R) \tag{10}$$

où

$$\underline{\underline{\tau}}_R = -\,\overline{(\rho\,\vec{V}''\,;\,\vec{V}'')} \tag{11}$$

est le tenseur des contraintes de Reynolds en fluide compressible.

$$\begin{aligned}\frac{\partial}{\partial t}\left[\bar{\rho}\left(\tilde{E} + \frac{1}{2}\tilde{\vec{V}}^2 + e\right)\right] + div\left[\bar{\rho}\left(\tilde{E} + \frac{1}{2}\tilde{\vec{V}}^2 + e\right)\tilde{\vec{V}} + \bar{p}\,\tilde{\vec{V}}\right] = \\ div\left[\left(\overline{\underline{\underline{\tau}}} + \underline{\underline{\tau}}_R\right)\tilde{\vec{V}} - \overline{\vec{q}} - \overline{(\rho\, h''\vec{V}'')} + \overline{(\underline{\underline{\tau}}\,\vec{V}'')} - \frac{1}{2}\overline{(\rho\,\vec{V}''^2\,\vec{V}'')}\right]\end{aligned} \tag{12}$$

où e est l'énergie cinétique de la turbulence, définie par :

$$\bar{\rho}\, e = \frac{1}{2}\,\overline{\rho\,\vec{V}''^2} = -\frac{1}{2}\, Trace\, \underline{\underline{\tau}}_R \tag{13}$$

et h'' est la fluctuation d'enthalpie spécifique h ($h = E + p/\rho$, $h = \tilde{h} + h''$).

La pression moyenne $\bar{p}$ s'exprime immédiatement en fonction de $\bar{\rho}$ et de $\tilde{E}$ par une formule identique à (8) :

$$\bar{p} = (\gamma - 1)\,\bar{\rho}\,\tilde{E} \tag{14}$$

L'équation moyenne de l'énergie totale (12) fait intervenir au premier membre l'énergie cinétique de la turbulence, e , pour laquelle on peut obtenir une équation indépendante à partir de l'équation moyenne de l'énergie mécanique :

$$\begin{aligned}\frac{\partial}{\partial t}(\bar{\rho}\, e) + div\,(\bar{\rho}\, e\,\tilde{\vec{V}}) = \underline{\underline{\tau}}_R \cdot grad\,\tilde{\vec{V}} + \\ \overline{div\left[\vec{V}''\,\underline{\underline{\tau}} - \left(p + \rho\,\frac{\vec{V}''^2}{2}\right)\vec{V}''\right]} - \overline{\underline{\underline{\tau}} \cdot grad\,\vec{V}''} + \overline{p\; div\,\vec{V}''}\end{aligned} \tag{15}$$

En retranchant (15) de (12), on obtient une équation pour l'énergie totale de l'écoulement moyen, $\tilde{E} + \tilde{\vec{V}}^2/2$, dont le premier membre a même forme que le premier membre de (6), mais dont le second membre contient des termes sous forme non conservative. Pour la suite de la discussion, nous utiliserons l'équation (12). On peut développer les termes du second membre de l'équation (15) de façon à mettre en évidence les termes supplémentaires dus à la compressibilité ; il vient :

$$\begin{aligned}\frac{\partial}{\partial t}(\bar{\rho}\, e) + div\,(\bar{\rho}\, e\,\tilde{\vec{V}}) &= \underline{\underline{\tau}}_R \cdot grad\,\tilde{\vec{V}} \\ &+ div\left\{\overline{\vec{V}''\,\underline{\underline{\tau}}'} - \overline{\left[p' + \left(\rho\,\frac{\vec{V}''^2}{2}\right)\right]\vec{V}''}\right\} - \overline{\underline{\underline{\tau}}' \cdot grad\,\vec{V}''} \\ &+ \boxed{\overline{\vec{V}''} \cdot \left[div\,\overline{\underline{\underline{\tau}}} - grad\,\bar{p}\right] + \overline{p'\, div\,\vec{V}''}}\end{aligned} \tag{16}$$

où les termes encadrés sont nuls en incompressible, soit parce que $\overline{\vec{V}''} = 0$, soit parce que div $\vec{V}'' = 0$.

En écoulement compressible, les variations de μ et k avec la température, ainsi que l'utilisation des moyennes pondérées par la masse de E et $\vec{V}$, introduisent des complications pour les expressions de $\overline{\underline{\underline{\tau}}}$ et de $\overline{\vec{q}}$. Par exemple, pour une composante caractéristique de $\underline{\underline{\tau}}$ telle que $\mu\,\partial V_i/\partial x_j$

en coordonnées cartésiennes, on a rigoureusement, en incompressible et à μ constant :

$$\overline{\mu\ \partial V_i/\partial x_j} = \mu\ \partial\overline{V_i}/\partial x_j$$

En compressible, par contre, et avec μ fonction donnée de E, on a :

$$\mu(E)\frac{\partial V_i}{\partial x_j} = \left[\mu(\tilde{E}) + E''\frac{d\mu}{dE}(\tilde{E}) + \dots\right]\left[\frac{\partial \tilde{V}_i}{\partial x_j} + \frac{\partial V_i''}{\partial x_j}\right]$$

d'où :

(17) $$\overline{\mu(E)\frac{\partial V_i}{\partial x_j}} = \mu(\tilde{E})\frac{\partial \tilde{V}_i}{\partial x_j} + \mu(\tilde{E})\frac{\partial \overline{V_i''}}{\partial x_j} + \overline{E''}\frac{d\mu}{dE}(\tilde{E})\frac{\partial \tilde{V}_i}{\partial x_j} + \dots$$

avec

$$\overline{V_i''} = -\overline{(\rho' V_i')}/\overline{\rho}\ ,\quad \overline{E''} = -\overline{(\rho' E')}/\overline{\rho}$$

En pratique, on ne retient que le premier terme de ce développement, ce qui semble tout à fait justifié compte tenu de l'état de développement actuel des modèles de turbulence. En outre $\overline{\underline{\underline{\tau}}}$ est négligeable devant $\underline{\underline{\tau}}_R$ dans la majeure partie d'une couche turbulente, et ne redevient important que dans la sous-couche visqueuse où les fluctuations diminuent d'intensité lorsqu'on s'approche de la paroi. De façon générale, on écrit donc :

(18) $$\overline{\underline{\underline{\tau}}} = \mu(\tilde{E})\left[\mathrm{def}\,\vec{\tilde{V}} - \frac{2}{3}\,\mathrm{div}\,\vec{\tilde{V}}\,\underline{\underline{I}}\right]$$

et de façon analogue, pour le flux de chaleur moyen :

(19) $$\overline{\vec{q}} = -\frac{k(\tilde{E})}{C_v}\,\mathrm{grad}\,\tilde{E} = -\frac{\gamma}{P_r}\,\mu(\tilde{E})\,\mathrm{grad}\,\tilde{E}$$

Les modèles de turbulence mis en oeuvre avec les équations de N.S. en fluide compressible sont, à notre connaissance, tous des modèles de viscosité turbulente où le tenseur des contraintes de Reynolds $\underline{\underline{\tau}}_R$ est, comme $\overline{\underline{\underline{\tau}}}$, supposé fonction linéaire du tenseur des vitesses de déformation de l'écoulement moyen. En tenant compte de ce que la trace de $\overline{\underline{\underline{\tau}}}$ est nulle (avec $3\lambda + 2\mu = 0$) alors que celle de $\underline{\underline{\tau}}_R$ est égale à $-2\bar{\rho}e$, il vient :

(20) $$\underline{\underline{\tau}}_R = \varepsilon\,\overline{\underline{\underline{\tau}}} - \frac{2}{3}\,\bar{\rho}\,e\,\underline{\underline{I}}$$

où $\varepsilon = \mu_t/\mu$, μ_t étant la viscosité turbulente.

Portons (20) dans (10) ; l'équation moyenne de quantité de mouvement s'écrit :

(21) $$\frac{\partial}{\partial t}(\bar{\rho}\vec{\tilde{V}}) + \mathrm{div}\left[(\bar{\rho}\vec{\tilde{V}};\vec{\tilde{V}}) + p^*\underline{\underline{I}}\right] = \mathrm{div}\left[(1+\varepsilon)\,\overline{\underline{\underline{\tau}}}\right]$$

où l'on a reporté la contribution de la trace de $\underline{\underline{\tau}}_R$ dans le terme de pression en posant :

(22) $$p^* = \bar{p} + \frac{2}{3}\bar{\rho}e = \bar{\rho}\left[(\gamma-1)\tilde{E} + \frac{2}{3}e\right]$$

Pour l'équation de l'énergie (12), la diffusion turbulente d'enthalpie est prise proportionnelle à grad $\tilde{E}$:

(23) $$\overline{\rho\, h''\vec{V}''} = -\frac{k_t}{C_v}\,\mathrm{grad}\,\tilde{E} = -\frac{\gamma}{Pr_t}\,\mu_t\,\mathrm{grad}\,\tilde{E}$$

où k_t est une conductivité turbulente variant comme μ_t, et où $Pr_t = \mu_t C_p/k_t$ est le nombre de Prandtl turbulent, pris égal en général à 0,9. Les deux autres termes de corrélation au second membre de (12) sont négligés, et il vient :

(24) $$\frac{\partial}{\partial t}\left[\bar{\rho}(\tilde{E} + \frac{1}{2}\vec{\tilde{V}}^2 + e)\right] + \mathrm{div}\left[\bar{\rho}(\tilde{E} + \frac{1}{2}\vec{\tilde{V}}^2 + e)\vec{\tilde{V}} + p^*\vec{\tilde{V}}\right] = \mathrm{div}\left[(1+\varepsilon)\,\overline{\underline{\underline{\tau}}}\,\vec{\tilde{V}} - \gamma\left(\frac{1}{Pr} + \frac{\varepsilon}{Pr_t}\right)\mu(\tilde{E})\,\mathrm{grad}\,\tilde{E}\right]$$

La modélisation de $\underline{\underline{\tau}}_R$ selon l'équation (20) laisse e indéterminé. Il apparaît ici une différence importante par rapport au cas incompressible, car dans ce dernier cas la contribution de e à p^* ne joue aucun rôle dans la résolution de l'équation de quantité de mouvement pour le champ des vitesses moyennes. En compressible, il n'en est plus de même puisque $\bar{p}$ est calculé en fonction de $\bar{\rho}$ et de $\tilde{E}$.

La prise en compte de e dans les premiers membres des équations (21) et (24) est d'importance relative secondaire par rapport à l'effet de ε dans les seconds membres. Néanmoins l'erreur commise en négligeant e peut ne pas être tout à fait négligeable pour les écoulements à nombre de Mach élevé. Si le modèle de turbulence utilisé inclut une équation pour e , alors il n'y a pas de difficulté à tenir compte des termes en e dans (21) et (24) ; sinon, et c'est le cas le plus fréquent dans les modèles étudiés jusqu'à maintenant, il faut négliger ces termes.

Trois types de modèles de viscosité turbulente ont été étudiés et utilisés dans des applications :

A - Les modèles, dits algébriques, qui ne font pas intervenir e , et où μ_t est calculé en fonction de données locales ou intégrales de l'écoulement moyen, à l'aide de relations algébriques qui constituent le modèle (références [10], [11], [18], [21] à [24], [29] à [32], [36] à [53], [59]).

B - Les modèles à une équation pour l'énergie cinétique de la turbulence, obtenue par modélisation des termes de corrélation au second membre de (15), où μ_t est calculé en fonction de e et d'une longueur caractéristique de turbulence L, fonction donnée de la distance à la paroi. (références [31], [32] [39-(2)]).

C - Les modèles à deux équations, respectivement pour e et pour une autre quantité (pseudo-tourbillon, ou dissipation de l'énergie cinétique de la turbulence), μ_t s'exprimant alors simplement en fonction de e et de cette autre quantité. (références [10], [11], [13],]14], [32]).

Les modèles algébriques utilisés sont, pour la plupart, dérivés du modèle à deux couches développé par Cebeci et Smith, [63], pour les couches limites attachées. Dans les équations qui suivent, pour simplifier l'écriture, les grandeurs relatives à l'écoulement moyen sont notées sans barre ni tilde. Le modèle de base peut être pris sous la forme suivante (par exemple [38], [39]) :

région intérieure : $\eta < \eta^*$

$$\mu_t = \mu_{t_i} = \rho\, \ell^2\, |\mathrm{rot}\, \vec{V}| \quad , \quad \ell = 0,4\ \eta\,(1 - \exp(-\eta/A)\,) \tag{25}$$

$$A = 26\, \mu\, [\rho\, |\tau_p|]^{-1/2} \quad , \quad \tau_p = [\mu\,(\partial u/\partial \eta)]_{\eta=0}$$

où η est la distance normale à la paroi, et u la composante de la vitesse parallèle à la paroi.

région extérieure : $\eta > \eta^*$

$$\mu_t = \mu_{t_e} = 0{,}0168\ \rho\, u_e\, \delta^* \beta \quad , \quad \beta = \left[1 + 5{,}5\left(\frac{y}{\delta}\right)^6\right]^{-1} \tag{26}$$

$$\delta^* = \int_{\eta_0}^{\delta} \left(1 - \frac{u}{u_e}\right) d\eta \quad , \quad u_e = u\,(\eta = \delta)$$

où η_o est la valeur de η (> 0 pour une couche décollée) où u s'annule et où δ est la frontière de la couche visqueuse ; la définition de δ dans une région de forte interaction peut être délicate, [38]. La limite η^* des deux régions est définie comme la plus petite valeur de η où $(\mu_{t_i} - \mu_{t_e})$ devient positif.

Ce modèle n'étant pas adapté aux couches turbulentes soumises à de forts gradients ou, a fortiori, décollées, l'objet principal des travaux cités est d'étudier des modifications de ce modèle et de les tester sur des applications numériques par comparaison avec des résultats expérimentaux. Ainsi l'histoire de la turbulence doit être prise en compte lorsque celle-ci n'est pas en équilibre avec l'écoulement moyen local. Une façon approchée de représenter cet effet de "mémoire" consiste à modifier le calcul de μ_t selon la formule ([18], [22], [31], [36], [37], [39]) :

$$\mu_t = \mu_{t_{eq}} - (\mu_{t_{eq}} - \mu_{t_o})\ \exp\cdot\left[-(\xi - \xi_o)/\lambda\right] \tag{27}$$

où ξ est la distance le long de la paroi (ou,plus précisément, le long d'une ligne de courant), $\mu_{t_{eq}}$ est la valeur de μ_t fournie par le modèle de base, et ξ_o est un point fixé au début de la zone d'interaction ($\mu_{t_o} = \mu_{t_{eq}}$ en $\xi = \xi_o$) ; λ est une longueur de relaxation de l'ordre de une à vingt épaisseurs de couche limite. Une formule de relaxation "point par point" a aussi été utilisée ([38], [40], [43]) :

$$\mu_t(\xi) = \mu_{t_{eq}}(\xi) - \left[\mu_{t_{eq}}(\xi) - \mu_t(\xi - \Delta\xi)\right] \exp\cdot\left[-\Delta\xi/\lambda\right] \tag{28}$$

Des modifications ont aussi été introduites dans l'expression de la longueur de mélange ℓ , pour tenir compte de l'effet du gradient de pression [18], [39], ou dans l'expression de la vitesse de frottement pour éviter un comportement singulier quand τ_p tend vers zéro, [21]. D'autres modifications sont encore discutées dans [21] et [18].

Pour le cas de l'écoulement transsonique autour d'un profil, il faut introduire une modélisation particulière pour le sillage. Un modèle récemment utilisé, [43], [46], [49], fait intervenir les formules suivantes :

région intérieure de la couche limite non décollée:

formule (25) mais avec $A = 26\ \mu_p \left[\rho_p \left|\tau_p\right|\right]^{-1/2}$

région extérieure de la couche limite et sillage (zone décollée exclue) :

$$\mu_t = 0{,}0168\ \rho\, u_e\, \delta_s^* \left[1+\left(\frac{\eta-\eta_s}{\delta}\right)^6\right]^{-1} \tag{29}$$

où $\eta = \eta_s$ est la ligne de courant séparatrice qui limite la zone de recirculation, et $\eta_s = 0$ en dehors de la zone décollée,

$$\delta_s^* = \int_{\eta_s}^{\delta}\left(1-\frac{u}{u_e}\right)d\eta$$

zone décollée $(\eta < \eta_s)$

$$\mu_t = 0{,}0168\ \rho\, u_e\, \delta_s^*\, Z^2 \tag{30}$$

avec $Z = \frac{\eta}{\eta_s}\left(1-\exp\left(-\frac{\eta}{A}\right)\right)$ sur le profil, et $Z = 1$ dans le sillage.

Ce modèle a aussi été utilisé dans [43] avec un effet de relaxation dans la région extérieure et le sillage, calculé le long des lignes de courant selon la formule (28), $\mu_{t_{eq}}$ étant alors donné par (29). L'effet dû à la suppression de la viscosité turbulente dans la zone décollée a été examiné dans [52] et [53], et une certaine amélioration des résultats a été observée.

Les modèles du type B, à une équation pour e, sont la version originale et des versions modifiées du modèle de Rubesin [64]. Le rapport ε de la viscosité tourbillonnaire à la viscosité laminaire est une *fonction donnée* du nombre de Reynolds de la turbulence r, défini par :

$$r = \sqrt{e}\, L\, \rho/\mu \tag{31}$$

où L est une échelle de longueur caractéristique de la turbulence, fonction donnée de la distance η à la paroi et de l'épaisseur δ de la couche limite :

$$L = \delta\, f(\eta/\delta) \tag{32}$$

Le coefficient ε dans (21) et dans le terme $(1+\varepsilon)\,\overline{\underline{\underline{\tau}}}\,\tilde{\vec{V}}$ de (24) est donc pris égal à $\varepsilon(r)$, alors que le coefficient ε/P_{r_t} dans le terme proportionnel à grad $\tilde{E}$ dans (24) est remplacé par $\varepsilon(\Gamma r)$ où Γ est une constante prise égale à $1/P_{r_t}$. Dans le modèle de Rubesin, l'équation (16) pour e est modélisée à l'aide des relations suivantes :

$$\overline{\left(p' + \rho\frac{\vec{V}''^2}{2}\right)\vec{V}''} = -\,\mu(E)\ \varepsilon(\lambda r)\ \mathrm{grad}\, e$$

$$\mathrm{div}\left(\overline{\vec{V}''\underline{\underline{\tau}}'}\right) - \overline{\underline{\underline{\tau}}'\cdot \mathrm{grad}\,\vec{V}''} = \mathrm{div}\left[\mu(E)\,\mathrm{grad}\, e\right] - \mu(E)\left[1+\varepsilon(\lambda r)\right]\cdot C\, e/L^2$$

et, pour les termes encadrés dans (16), qui s'annulent en incompressible :

$$\overline{\vec{V}''} = \frac{\gamma-1}{n-1}\ \frac{1}{p}\ \mu(E)\ \varepsilon(\Gamma r)\ \mathrm{grad}\, E$$

$$\overline{p'\,\mathrm{div}\,\vec{V}''} = \zeta\ p\ \frac{\vec{V}^2}{a^2}\ \frac{e}{a^2}\ \mathrm{div}\,\vec{V}\ , \quad a^2 = \gamma\frac{p}{\rho}$$

où λ, C, n, ζ sont des constantes numériques.

En regroupant tous ces termes, et en posant :

$$\mu_e = \mu\left[1+\varepsilon(\lambda r)\right] \tag{33}$$

on obtient l'équation suivante pour e :

$$\frac{\partial}{\partial t}(\rho e) + \mathrm{div}(\rho e \vec{V}) = \varepsilon(r)\,\underline{\underline{\tau}}\cdot \mathrm{grad}\,\vec{V} + \mathrm{div}\left[\mu_e\, \mathrm{grad}\, e\right] \tag{34}$$

$$+\left(\frac{\zeta}{\gamma}\ \frac{\vec{V}^2}{a^2} - \frac{2}{3}\right)\rho\, e\, \mathrm{div}\,\vec{V} - \mu_e\, C\,\frac{e}{L^2} + \overline{\vec{V}''}\cdot\left[\mathrm{div}\,\underline{\underline{\tau}} - \mathrm{grad}\, p\right]$$

où les grandeurs caractéristiques de l'écoulement moyen sont notées sans barre ni tilde.

Ce modèle est utilisé dans [31] pour traiter deux problèmes d'interaction choc-couche limite en régime transsonique et en régime hypersonique (en écoulement de révolution), et dans [39-(2)] pour traiter un problème d'interaction dans un angle de compression en régime supersonique. Les modifications étudiées portent sur la forme de la fonction f qui définit L (équation (32)), sur les valeurs des constantes numériques dont dépend le modèle, et sur l'utilisation de $\lambda\,\varepsilon(r)$ et $\Gamma\varepsilon(r)$ au lieu de $\varepsilon(\lambda r)$ et $\varepsilon(\Gamma r)$ respectivement pour simplifier les calculs.

Le modèle de Rubesin est utilisé à nouveau dans [32] pour traiter les trois problèmes précités, mais sans les termes $\overline{V}''$ et $\mu'\,div\,\overline{V}''$ ($n = \infty$ et $\zeta = 0$) et en prenant $\mu_e = \mu\,[1 + 0{,}4\,\varepsilon(r)\,]$.

En ce qui concerne les modèles du type C, à deux équations de transport, on peut remarquer que les travaux cités correspondent soit au début ([10], [11], [13], [14]), soit à la fin, [32], de cette période 1973-1977 qui a vu un important développement de l'approche globale pour les écoulements compressibles à grand nombre de Reynolds. Le fait que l'étude de tels modèles n'ait pas été poursuivie après les premières tentatives est sans doute dû à l'importance des temps de calcul requis pour traiter ces modèles avec des méthodes explicites. L'intérêt récent manifesté à nouveau pour des modèles à une ou deux équations de transport s'explique à la fois par l'utilisation d'une nouvelle méthode beaucoup plus rapide, [23], [24], par le développement des études de modèles à plusieurs équations de transport pour les couches limites compressibles, (par exemple, [65]), et par les difficultés rencontrées pour construire des modèles algébriques de validité suffisamment générale pour les problèmes d'interaction avec décollement.

Deux modèles de type C ont, à notre connaissance, été utilisés avec les équations de Navier-Stokes en fluide compressible. Les premiers calculs, [10], [11], [13], [14], ont été effectués avec le modèle de Saffman-Wilcox, [66], qui comprend une équation pour e et une équation pour un pseudo-tourbillon Ω, la viscosité turbulente étant simplement le rapport de ces deux quantités : $\mu_t = e/\Omega$. Le calcul le plus récent, [32], met en oeuvre le modèle de Jones-Launder, [67], qui comprend une équation pour e et une équation pour le taux de dissipation de l'énergie turbulente $s\,(\rho s = \tau'.\,grad\,\overline{V}'')$; la longueur caractéristique L est donnée en fonction de e et s par l'expression $L = e^{3/2}/s$, d'où $r = \rho e^2/(\mu s)$, et $\varepsilon = \mu_t/\mu$ est donné comme une fonction explicite de r.

On trouvera dans [68] une discussion approfondie du problème de la modélisation de la turbulence pour les écoulements compressibles en interaction, ainsi qu'une discussion des études expérimentales nécessaires à l'évaluation des modèles.

5 - METHODES NUMERIQUES -

5.1 - Revue générale -

Nous donnons ici un aperçu seulement des méthodes de résolution numérique des équations de N.S. mises en oeuvre dans les travaux passés en revue au paragraphe 3. Ces méthodes sont toutes des méthodes de différences finies ou de volumes finis et, à l'exception d'une seule, [27], elles sont de type instationnaire : les équations de N.S. instationnaires sont intégrées pas à pas dans le temps, jusqu'à une convergence vers un état stationnaire si celui-ci existe ; sinon l'évolution dans le temps de la solution numérique représente un écoulement instationnaire réel à condition que le traitement numérique des équations soit consistant dans le temps et que les conditions aux limites sur des frontières non matérielles ainsi que les conditions initiales aient un sens physique pour le régime instationnaire.

La méthode la plus utilisée dans les applications citées est la méthode de MacCormack dont on trouvera une description détaillée dans [12]. Dans la forme initiale de cette méthode, [69], les équations de N.S. écrites en coordonnées cartésiennes sont discrétisées dans un maillage rectangulaire à l'aide d'un schéma aux différences finies à deux pas en temps précis au second ordre. Cette méthode a ensuite été combinée avec une technique de pas fractionnaires qui en accroît l'efficacité, [9]. L'extension à un maillage curviligne quelconque peut être réalisée de diverses façons : nous décrivons au paragraphe 5.3 le principe de la méthode de volumes finis utilisée en particulier pour le calcul d'écoulements autour de profils (voir par exemple, [3], [41]), et nous indiquerons comment cette extension peut aussi être réalisée dans la méthode de différences finies.

Ces diverses variantes auxquelles nous venons de faire allusion sont toutes des méthodes explicites dans lesquelles la stabilité numérique limite la valeur du pas de temps, et ce d'autant plus que le maillage est plus fin (voir par exemple, le critère donné en [12]). Divers auteurs ont cherché à rendre la condition de stabilité moins restrictive en utilisant des schémas à caractère implicite plus ou moins prononcé. L'étude de telles méthodes pour les équations de N.S. n'est pas nouvelle (voir revue [4]), mais leur mise en oeuvre pour traiter des écoulements en interaction à grand nombre de Reynolds est récente. Nous nous bornerons à signaler les travaux qui ont été menés jusqu'à des applications de ce type, en distinguant les méthodes partiellement implicites utilisant de façon extensive la technique de décomposition des opérateurs (références [16], [17], [23], [24], [25]), et les méthodes à caractère fortement implicite utilisant des techniques de factorisation pour la résolution des systèmes algébriques (références [26], [50]). Dans toutes ces méthodes, qui rentrent dans la grande famille des méthodes à pas fractionnaires, l'idée directrice est de se ramener à la résolution de systèmes linéaires tridiagonaux, ou tridiagonaux par blocs, pour que l'avantage acquis par l'utilisation de grands pas de temps ne soit pas perdu dans le temps de calcul nécessaire pour la résolution des systèmes.

Cependant, nous mentionnerons plus spécialement la nouvelle méthode partiellement implicite proposée par MacCormack, [23], [24], car elle a déjà été utilisée pour des applications très diverses, [21], [31], [32], [39], [49], et même pour un problème tridimensionnel [70]. Dans cette nouvelle méthode, la technique de décomposition est utilisée non seulement pour séparer les dérivées en x (direction principale de l'écoulement, maille large) des dérivées en y (direction transversale dans la couche visqueuse, maille fine), comme dans la première méthode , mais aussi pour traiter séparément dans les termes des dérivées en y ceux qui appartiennent aux équations d' Euler et ceux qui sont de nature dissipative : le premier groupe (termes de fluide parfait) est traité par une combinaison d'une méthode de caractéristiques et du schéma de MacCormack, telle que le critère de stabilité devient de type purement convectif : $\Delta t < \Delta y / |v|$ où v, la vitesse transversale,est très petite et Δt est donc grand ; le deuxième groupe de termes (termes dissipatifs) est traité par un schéma implicite qui ne demande que des inversions de matrices tridiagonales simples. Cette nouvelle méthode n'est mise en oeuvre que dans une zone à maillage très fin en y, située près de la paroi. Le rapport des temps de calcul entre l'ancienne et la nouvelle méthode est de l'ordre de dix à plusieurs dizaines.

Indiquons enfin, pour mémoire, les autres méthodes mises en oeuvre dans les applications passées en revue au paragraphe 3. Il s'agit d'une part de deux méthodes instationnaires explicites, l'une basée sur le schéma à deux pas en temps de Braïlovskaya (références [15], [33], [34]), l'autre basée sur une formulation intégrale des équations (méthode AFTON, références [13], [14], [54]), et d'autre part d'une méthode stationnaire, [27], où les équations discrétisées, obtenues à partir d'une formulation intégrale des équations stationnaires, sont résolues par une techniquo itérative ne comportant que des résolutions de systèmes tridiagonaux.

5.2 - Problèmes de précision et de convergence -

Il est indispensable, pour des raisons de temps de calcul, d'adapter au mieux la taille des mailles aux gradients locaux de l'écoulement, et pour cela on utilise toujours un maillage tel que la couche visqueuse suive l'une des lignes du maillage, qui coïncide alors soit avec la paroi soit avec une ligne moyenne d'un sillage. Les techniques de raffinement de maillage sont un aspect important des méthodes de résolution des équations de N.S. à grand nombre de Reynolds, car il faut assurer une variation de la taille de la maille, dans la direction transversale de la couche visqueuse, par un facteur de l'ordre de plusieurs centaines. D'autre part, la condition de stabilité, avec des méthodes explicites, conduit à une valeur du pas de temps beaucoup plus petite pour la couche visqueuse que pour la région extérieure à maillage moins fin. On a donc intérêt à décomposer le domaine de calcul en au moins deux régions dans chacune desquelles on utilisera le pas de temps optimum pour cette région, ou voisin de l'optimum si l'on veut conserver la consistance dans le temps sinon la précision, car il faut alors assurer le raccord dans le temps des solutions aux frontières de ces régions ([12]). Une loi exponentielle est souvent utilisée pour contracter le maillage transversalement près de la paroi, ou pour le dilater à grande distance dans les deux directions du maillage dans le cas du profil en atmosphère infinie. Dans [56], une procédure générale de raffinement du maillage est obtenue en décomposant transversalement le domaine de calcul en un nombre de zones qui peut être aussi élevé que l'on veut, chaque zone étant à maillage constant (dans le plan physique ou dans un plan transformé) et d'étendue transversale réglable ; la taille transversale de la maille varie d'un facteur 2 d'une zone à la suivante, et une technique de raccord entre zones adjacentes permet d'assurer une précision du second ordre dans l'espace.

Le problème de la convergence, vers une solution unique, des résultats de calculs effectués dans des maillages de plus en plus fins est discuté dans [20], où un problème d'interaction choc-couche limite laminaire est traité par deux méthodes, celle de MacCormack [12], et celle de Carter [33]. Ces calculs montrent que chaque méthode conduit à une solution convergée lorsque le maillage est assez fin, et que les deux solutions convergées fournies par les deux méthodes sont en bon accord. Il faut aussi retenir de ce travail qu'il est très difficile d'apprécier la précision d'un calcul unique, c'est-à-dire effectué avec un seul maillage ; ainsi, pour le problème traité dans [20], le passage d'un maillage (64 x 33) qui pourrait être considéré comme suffisant, à un maillage (64 x 42) conduit à un déplacement sensible du point de recollement.

Un autre problème relatif à la précision des résultats numériques est celui de l'influence de la viscosité artificielle. En effet des instabilités non linéaires apparaissent dans certaines zones sous forme d'oscillations croissantes, lors du calcul d'un écoulement à grand nombre de Reynolds soumis à un gradient de pression adverse assez fort, et pour éviter que ces oscillations ne conduisent finalement à une divergence du calcul, il est nécessaire d'ajouter aux équations des termes d'amortissement dits termes de viscosité artificielle (voir exemple dans [12]). L'influence de ces termes sur la précision est toujours déclarée comme négligeable, mais on ne trouve pas dans la littérature, à notre connaissance, d'étude numérique détaillée permettant d'apprécier cette influence. Une vérification directe peut cependant être aisément réalisée, pour un écoulement stationnaire, en effectuant, à partir de la solution numérique considérée comme stationnaire, une seule itération en temps sans les termes de viscosité artificielle et en comparant les résidus correspondants (c'est-à-dire les dérivées en temps des inconnues de base) à ceux obtenus à la fin du calcul avec viscosité artificielle.

Ajoutons que des modifications locales du schéma numérique sont aussi utilisées dans la méthode de MacCormack, [3], [11], [12], pour combattre des instabilités non linéaires se développant dans les zones décollées.

La principale cause d'erreur dans les méthodes numériques actuelles est sans doute celle qui résulte de l'étalement des ondes de choc. C'est la viscosité numérique, qu'elle soit implicite dans le schéma ou explicite dans les termes de viscosité artificielle, qui permet aux ondes de choc de se former d'elles-mêmes dans la solution numérique et qui en même temps leur donne une épaisseur artificielle de l'ordre de quelques mailles. Cet étalement numérique des chocs modifie le phénomène d'interaction choc-couche limite d'une façon difficile à apprécier, et pour le moins entraîne une indétermination sur la position exacte du choc par rapport à la couche visqueuse. On peut sans doute diminuer fortement l'étalement du choc en utilisant un maillage très fin au voisinage du choc, mais celà oblige à adapter le maillage au choc pour que celui-ci reste parallèle à l'une des lignes du maillage, et les complications sont telles que cette technique n'a pas encore été mise en oeuvre, à notre connaissance, dans l'approche globale pour des problèmes d'interaction à grand nombre de Reynolds.

La solution complète, encore plus difficile à mettre en oeuvre, consiste à traiter le choc comme une discontinuité mobile, vérifiant les relations de Rankine-Hugoniot ; deux techniques peuvent être envisagées : adaptation du maillage au choc, ou choc flottant dans un maillage fixe, mais elles n'ont été utilisées jusqu'ici que dans des problèmes relativement simples. Ce problème du traitement numérique des chocs n'est évidemment pas particulier à l'approche globale, et il se pose aussi dans les méthodes de couplage.

Le passage du cas laminaire au cas turbulent, avec les modèles de viscosité tourbillonnaire utilisés jusqu'à présent, ne pose pas de difficulté de principe en ce qui concerne les méthodes numériques. Néanmoins, le traitement d'écoulements turbulents s'avère nettement plus délicat en pratique, compte tenu des très fortes variations des quantités caractérisant la turbulence (la viscosité tourbillonnaire et, éventuellement, les quantités décrites par des équations de transport complémentaires) dans la sous-couche visqueuse. Une technique spéciale de discrétisation, basée sur une interpolation de type exponentiel, a été utilisée, [3], [10], [11], pour obtenir une bonne représentation de la sous-couche visqueuse avec un nombre réduit de points. Dans [13], [14], le problème de la résolution de la sous-couche visqueuse est évité en raccordant la solution des équations de N.S. près de la paroi avec une loi de la paroi valable en fluide compressible et déduite du modèle à deux équations de transport utilisé avec les équations de N.S., [66].

5.3 - Extensions de la méthode de MacCormack en maillage quelconque -

5.3.1 - Généralités -

Pour ne pas alourdir la présentation, nous nous limiterons au cas d'écoulements plans. Un système de coordonnées cartésiennes notées indifféremment (x, y) ou (x_1, x_2) sert à projeter la vitesse $\vec{V}$ de composantes (u, v) ou (u_1, u_2), ainsi que l'équation de quantité de mouvement. La discrétisation des équations est effectuée dans un maillage curviligne quelconque dont les noeuds sont repérés par leurs coordonnées cartésiennes.

Nous considérons les équations de N.S. moyennes (9), (21) et (24), sans équation complémentaire de transport, et dans tout ce qui suit les valeurs moyennes seront écrites sans barre ni tilde. Après projection de l'équation de quantité de mouvement sur les axes ox_1, ox_2 on obtient un système de quatre équations scalaires qu'on peut écrire sous forme condensée à l'aide de matrices colonnes U et F_i :

$$\frac{\partial U}{\partial t} + \frac{\partial F_i}{\partial x_i} = 0 \qquad (i = 1,2) \tag{35}$$

avec

$$U = \begin{pmatrix} \rho \\ \rho u_1 \\ \rho u_2 \\ \rho\left(E + \frac{u_1^2 + u_2^2}{2}\right) \end{pmatrix} , \quad F_i = \begin{pmatrix} \rho u_i \\ \rho u_i u_1 + p\delta_{i1} \\ \rho u_i u_2 + p\delta_{i2} \\ \left(\rho E + p + \rho\frac{u_1^2 + u_2^2}{2}\right) u_i \end{pmatrix} + D_i \tag{36}$$

où δ_{ij} est le symbole de Kronecker, et D_i représente les termes dissipatifs :

$$\left\{ \begin{aligned} & D_i = - \begin{pmatrix} 0 \\ (1+\varepsilon)\,\tau_{i1} \\ (1+\varepsilon)\,\tau_{i2} \\ (1+\varepsilon)\,\tau_{ij}\,u_j + q_{t_i} \end{pmatrix} \\ & \tau_{ij} = \mu(E)\left[\frac{\partial u_i}{\partial x_j} + \frac{\partial u_j}{\partial x_i} - \frac{2}{3}\,\frac{\partial u_k}{\partial x_k}\,\delta_{ij}\right] \\ & q_{t_i} = -\,\gamma\,\mu(E)\left(\frac{1}{Pr} + \frac{\varepsilon}{Pr_t}\right)\frac{\partial E}{\partial x_i} \end{aligned} \right. \tag{37}$$

Ce système peut s'écrire sous une forme intégrale traduisant directement les lois de conservation pour un système limité par une surface de contrôle fixe S, de frontière ∂S , soit :

$$\frac{\partial}{\partial t}\iint_S U\,dS + \oint_{\partial S} \vec{H}\cdot\vec{n}\;ds = 0 \tag{38}$$

où, pour chacune des équations scalaires correspondant aux composantes de U , $\vec{H}$ est un vecteur de composantes F_1 et F_2 , soit $\vec{H}\cdot\vec{n} = F_1 n_1 + F_2 n_2$, n_1 et n_2 étant les composantes de la normale unitaire $\vec{n}$ sur ∂S orientée vers l'extérieur de S.

5.3.2 - Méthodes de volumes finis -

Le maillage découpe le domaine de calcul en éléments de surface quadrangulaires, appelés aussi cellules, chacun d'eux étant complètement défini par les coordonnées de ses quatre sommets. Une cellule $S_{i,j}$, ou S_M, est repérée par un couple d'indices (i, j), ou par le point M centre de la cellule. On numérote de (1) à (4) les côtés de la cellule S_M, et on note O, E, S et N les centres des cellules ayant un côté commun avec S_M (voir figure 2).

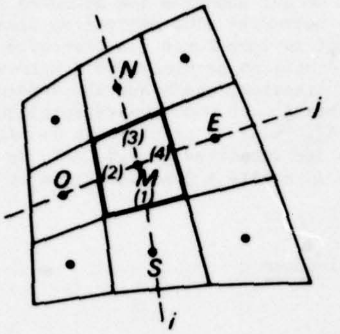

Fig. 2 – Maillage dans la méthode de volumes finis.

Les inconnues du problème discrétisé sont les valeurs moyennes de U dans chacune des cellules, valeurs que l'on considère comme égales aux valeurs de U aux centres des cellules. Soit $\vec{H}^{(k)}$ la valeur moyenne de $\vec{H}$ sur le côté (k) de la cellule S_M. L'équation (38) appliquée à cette cellule donne :

$$\frac{\partial U_M}{\partial t} + \sum_{k=1}^{4} \vec{H}^{(k)} \cdot \vec{\nu}^{(k)} = 0 \tag{39}$$

où

$$\vec{\nu}^{(k)} = \vec{n}^{(k)} \int_{\partial S_M^{(k)}} ds \Big/ \int_{S_M} dS$$

est calculé une fois pour toutes. Groupons dans (39) les contributions des faces opposées (1) et (3) d'une part, et (2) et (4) d'autre part, en posant :

$$\left\{\begin{array}{ll} a) & A_M = \vec{H}^{(2)} \cdot \vec{\nu}^{(2)} + \vec{H}^{(4)} \cdot \vec{\nu}^{(4)}, \text{ flux net à travers les cotés (2) et (4)} \\ b) & B_M = \vec{H}^{(1)} \cdot \vec{\nu}^{(1)} + \vec{H}^{(3)} \cdot \vec{\nu}^{(3)}, \quad \text{"} \quad \text{"} \quad \text{"} \quad \text{"} \quad \text{"} \quad \text{(1) et (3)} \end{array}\right. \tag{40}$$

En intégrant (39) par rapport au temps, de t à $t + \Delta t$, il vient :

$$U_M(t + \Delta t) = U_M(t) - \int_t^{t+\Delta t} \left[A_M(U) + B_M(U)\right] dt \tag{41}$$

Le calcul de $U_M(t + \Delta t)$ nécessite de définir des expressions approchées de $A_M(U)$ et $B_M(U)$ à partir du champ des valeurs discrètes de U au voisinage de M, ainsi qu'une technique d'intégration numérique en temps. Puisque U n'est pas défini sur les côtés (k) où l'on doit calculer $\vec{H}$, on construit des approximations de A et B en remplaçant $\vec{H}^{(k)}$ par la valeur de $\vec{H}$ en l'un des deux points les plus voisins du côté (k) ; on a ainsi deux approximations possibles, précises au premier ordre :

$$\left\{\begin{array}{lll} A_M^-(U) = \vec{H}_O^{(2)} \cdot \vec{\nu}^{(2)} + \vec{H}_M^{(4)} \cdot \vec{\nu}^{(4)} & , & \text{approximation "à gauche"} \\ A_M^+(U) = \vec{H}_M^{(2)} \cdot \vec{\nu}^{(2)} + \vec{H}_E^{(4)} \cdot \vec{\nu}^{(4)} & , & \text{approximation "à droite"} \end{array}\right. \tag{42}$$

$$\left\{\begin{array}{lll} B_M^-(U) = \vec{H}_S^{(1)} \cdot \vec{\nu}^{(1)} + \vec{H}_M^{(3)} \cdot \vec{\nu}^{(3)} & , & \text{approximation "en bas"} \\ B_M^+(U) = \vec{H}_M^{(1)} \cdot \vec{\nu}^{(1)} + \vec{H}_N^{(3)} \cdot \vec{\nu}^{(3)} & , & \text{approximation "en haut"} \end{array}\right. \tag{43}$$

où $\vec{H}_P^{(k)}$ désigne une approximation de $\vec{H}$ calculée au point P et qu'il reste à définir.

Séparons dans $\vec{H}_P$ les termes de fluide parfait, qui ne dépendent que de U et sont donc calculés à partir de la valeur de U en P, et les termes dissipatifs $\vec{D}$, de composantes D_1 et D_2 définies par les relations (37). $\vec{D}$ étant fonction linéaire des dérivées premières de u_1, u_2 et E, pour calculer $\vec{D}_P^{(k)}$ il faut évaluer des quantités de la forme $\partial\phi/\partial x$, $\partial\phi/\partial y$ en P, ce que l'on fait à partir des valeurs de ϕ en P et aux points voisins de P, mais selon une approximation qui dépend de la position respective de P par rapport au côté (k), de façon à compenser en partie l'erreur du 1er ordre introduite dans les approximations (42) et (43).

Si l'on admet que les centres des cellules sont répartis sur deux familles de courbes, $i = c^{te}$ et $j = c^{te}$, d'équations respectives $\xi(x, y) = c^{te}$ et $\eta(x,y) = c^{te}$, on peut exprimer ϕ_x et ϕ_y en fonction de ϕ_ξ et ϕ_η à l'aide des relations :

$$\frac{\partial\phi}{\partial x} = \frac{\phi_\xi\, y_\eta - \phi_\eta\, y_\xi}{x_\xi\, y_\eta - x_\eta\, y_\xi}, \quad \frac{\partial\phi}{\partial y} = \frac{\phi_\xi\, x_\eta - \phi_\eta\, x_\xi}{y_\xi\, x_\eta - y_\eta\, x_\xi} \tag{44}$$

qui permettent de ne pas avoir à expliciter les fonctions ξ (x,y) et η (x,y) si les dérivées de ϕ, x et y par rapport à ξ et η sont représentées par des différences finies.

En P passent deux lignes $\xi = \xi_P$ et $\eta = \eta_P$ l'une étant parallèle à la face *(k)* considérée, soit par exemple $\xi = \xi_P$, l'autre, $\eta = \eta_P$, coupant la face *(k)* (voir figure 3).

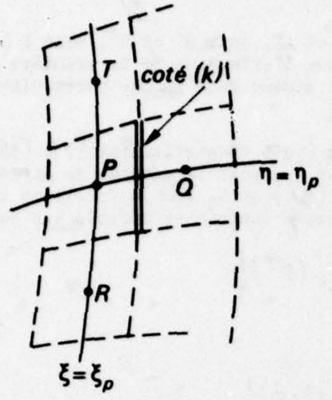

Fig. 3 – Notations pour le calcul des termes visqueux.

On définit les points Q, T et R, centres de cellules adjacentes à la cellule de centre P, disposés selon la figure 3 (*noter que le point M est confondu soit avec P, soit avec Q, mais il n'est pas nécessaire ici de le préciser*). On utilise alors les expressions aux différences suivantes :

$$(45)\quad \begin{cases} (\phi_\xi)_P = (\phi_Q - \phi_P) \,/\, (\xi_Q - \xi_P) \\ (\phi_\eta)_P = (\phi_T - \phi_R) \,/\, (\eta_T - \eta_R) \end{cases}$$

et ce aussi bien pour les dérivées de ϕ que pour celles de x et y dans (44), de telle sorte que les valeurs de ξ et η en Q, P, T et R disparaissent des expressions finales de ϕ_x et ϕ_y :

$$(46)\quad \begin{cases} \left(\dfrac{\partial \phi}{\partial x}\right)_P = \dfrac{(\phi_Q - \phi_P)(y_T - y_R) - (\phi_T - \phi_R)(y_Q - y_P)}{(x_Q - x_P)(y_T - y_R) - (x_T - x_R)(y_Q - y_P)} \\[2ex] \left(\dfrac{\partial \phi}{\partial y}\right)_P = \dfrac{(\phi_Q - \phi_P)(x_T - x_R) - (\phi_T - \phi_R)(x_Q - x_P)}{(y_Q - y_P)(x_T - x_R) - (y_T - y_R)(x_Q - x_P)} \end{cases}$$

Ces formules servent donc à calculer les dérivées de u_1, u_2 et E intervenant dans les termes dissipatifs $\vec{D}_P^{(k)}$ inclus dans les $\vec{H}_P^{(k)}$ des expressions (42) et (43). Ceci complète la définition des approximations A^-, A^+ de A, et B^-, B^+ de B. La figure 4 montre, à titre d'exemple, les domaines de dépendance numérique de A_M^- et de A_M^+

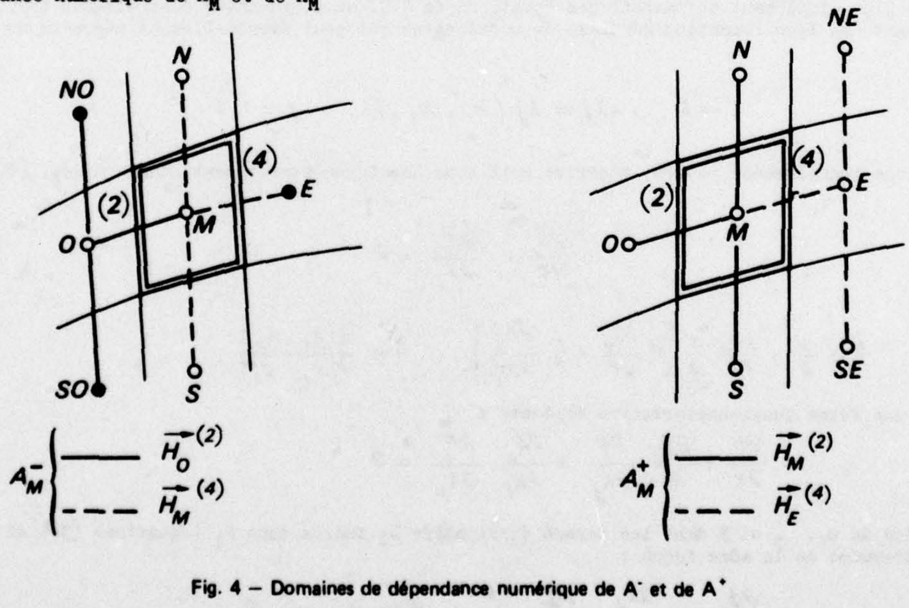

Fig. 4 – Domaines de dépendance numérique de A⁻ et de A⁺

Chacune des approximations A^-, A^+, et B^-, B^+ ainsi définies est précise au 1er ordre seulement. Mais on peut, en les utilisant dans (41) selon la méthode prédicteur-correcteur de MacCormack, aboutir à une approximation de U_M $(t + \Delta t)$ précise au second ordre dans l'espace et dans le temps. Ainsi, l'une des quatre variantes possibles du schéma s'écrira :

$$(47)\qquad \begin{cases} U_M^* = U_M(t) - \Delta t\left[A_M^-(U(t)) + B_M^-(U(t))\right] \\ U_M(t+\Delta t) = \frac{1}{2}\left\{U_M(t) + U_M^* - \Delta t\left[A_M^+(U^*) + B_M^+(U^*)\right]\right\} \end{cases}$$

les autres variantes s'obtenant en interchangeant soit A$^-$ et A$^+$, soit B$^-$ et B$^+$, soit à la fois A$^-$ et A$^+$, et B$^-$ et B$^+$. Cette méthode de volumes finis constitue l'extension de la première méthode de différences finies de MacCormack, [69], à laquelle elle se ramène dans le cas particulier d'un maillage cartésien uniforme.

La méthode de volumes finis utilisée dans les applications (voir en particulier [3], [35], [41], [42]) met en oeuvre la technique de décomposition, comme en [9] pour la méthode de différences finies. Pour en donner le principe, définissons les opérateurs L$_A$ (Δt) et L$_B$ (Δt), fonctions du pas de temps Δt , par les relations suivantes où ϕ est une fonction quelconque définie aux centres des cellules :

$$(48)\qquad \begin{cases} \left[L_A(\Delta t)\phi\right]_M = \frac{1}{2}\left\{\phi_M + \phi_M^* - \Delta t\, A_M^+(\phi^*)\right\} \\ \phi_P^* = \phi_P - \Delta t\, A_P^-(\phi) \end{cases}$$

$$(49)\qquad \begin{cases} \left[L_B(\Delta t)\phi\right]_M = \frac{1}{2}\left\{\phi_M + \tilde{\phi}_M - \Delta t\, B_M^+(\tilde{\phi})\right\} \\ \tilde{\phi}_P = \phi_P - \Delta t\, B_P^-(\phi) \end{cases}$$

où P et M représentent des centres de cellules quelconques. (On peut définir une autre variante de chacun de ces opérateurs en interchangeant A$^-$ et A$^+$, et B$^-$ et B$^+$).

On obtient alors une approximation de (41) en appliquant successivement L$_A$ et L$_B$, par exemple :

$$(50)\qquad U_M(t+\Delta t) = \left\{L_A(\Delta t)\left[L_B(\Delta t)\, U(t)\right]\right\}_M$$

mais cette approximation est seulement précise au premier ordre. Pour obtenir une précision du second ordre, il est nécessaire d'utiliser une suite symétrique des opérateurs L$_A$ et L$_B$, telle que, par exemple :

$$(51)\qquad U_M(t+\Delta t) = \left\{L_B\left(\frac{\Delta t}{2}\right)\left[L_A(\Delta t)\left(L_B\left(\frac{\Delta t}{2}\right) U(t)\right)\right]\right\}_M$$

5.3.3 - Méthodes de différences finies -

L'adaptation de la méthode aux différences finies de MacCormack a un maillage curviligne quelconque se fait le plus simplement en partant des équations de N.S. en coordonnées cartésiennes (35), et en effectuant une transformation générale de coordonnées qui peut éventuellement dépendre du temps, soit :

$$(52)\qquad \tau = t \quad , \quad X_j = X_j(x_1, x_2, t) \quad , \quad j = 1,2$$

Les équations transformées peuvent s'écrire soit sous une forme strictement conservative, [72], [4] :

$$(53)\qquad \frac{\partial \bar{U}}{\partial \tau} + \frac{\partial \bar{F}_j}{\partial X_j} = 0$$

avec :

$$(54)\qquad \bar{U} = \frac{U}{D} \; , \; \bar{F}_j = \frac{1}{D}\left[U\frac{\partial X_j}{\partial t} + F_i\frac{\partial X_j}{\partial x_i}\right] \quad , \quad D = \frac{\partial(X_1, X_2)}{\partial(x_1, x_2)}$$

soit sous une forme quasi-conservative évidente :

$$(55)\qquad \frac{\partial U}{\partial \tau} + \frac{\partial X_j}{\partial t}\frac{\partial U}{\partial X_j} + \frac{\partial X_j}{\partial x_i}\frac{\partial F_i}{\partial X_j} = 0$$

Les dérivées de u$_1$, u$_2$ et E dans les termes dissipatifs D$_i$ inclus dans F$_i$ (équations (36) et (37) sont transformées de la même façon :

$$(56)\qquad \frac{\partial \phi}{\partial x_i} = \frac{\partial X_j}{\partial x_i}\frac{\partial \phi}{\partial X_j} \qquad\qquad \phi = u_1, u_2, E$$

Le maillage est formé de lignes des deux familles des courbes coordonnées $X_1 = Cte$, $X_2 = Cte$. La discrétisation des équations transformées, sous la forme (53) ou sous la forme (55), dans le plan de calcul (X_1 , X_2) à l'aide du schéma de MacCormack s'effectue sans difficulté comme pour les équations en coordonnées cartésiennes. Notons que la capture correcte des ondes de choc dans une région de fluide parfait est tout aussi possible avec la forme quasi-conservative (55) qu'avec la forme conservative (53), à condition que les coefficients $\partial X_j/\partial x_i$ varient assez lentement pour qu'ils puissent être considérés comme constants dans la zone sur laquelle le choc se trouve étalé par l'effet de la viscosité numérique.

La forme strictement conservative (53) a été récemment utilisée avec une nouvelle méthode implicite, [50], pour le calcul d'écoulements autour de profils.

La forme quasi-conservative (55) a été utilisée avec la méthode de MacCormack :

- sans décomposition, dans [56] pour un problème de corps émoussé en supersonique, et plus récemment dans [71] pour un problème d'écoulement tridimensionnel dans un dièdre de compression ;
- avec décomposition, dans [58] et [59] pour des problèmes d'écoulements internes.

La nouvelle méthode implicite proposée dans [25] est aussi formulée à partir des équations sous la forme (55) étendue au cas tridimensionnel, pour une transformation de coordonnées indépendante du temps.

Dans [56], la forme quasi-conservative (55) est préférée à la forme (53), à la suite d'essais qui ont montré que, lorsque les dérivées de la transformation, $\partial X_j/\partial x_i$, sont calculées aux noeuds du maillage de façon exacte, alors des oscillations peuvent apparaître, même dans un écoulement qui devrait rester uniforme, lorsqu'on utilise (53) avec un maillage très déformé dans le plan physique ; ces oscillations n'apparaissent pas lorsqu'on utilise (55), avec le même maillage déformé. Ce phénomène est dû à une erreur de troncature supplémentaire dans la discrétisation de (53), causée par les variations des coefficients $\partial X_j/\partial x_i$ dans $\overline{F}_j$; cette erreur est indépendante des variations de l'écoulement et peut être importante même en écoulement uniforme.

On peut écrire (53) et (55) un peu différemment, en fonction des dérivées de la transformation inverse, $\partial x_i/\partial X_j$, à l'aide des relations :

$$\frac{1}{D}\,\frac{\partial X_j}{\partial x_i} = (-1)^{i+j}\,\frac{\partial x_{i'}}{\partial X_{j'}} \quad , \; i' \neq i \; , \; j' \neq j$$

où, en bidimensionnel, les indices i, i', j et j' ne prennent que les valeurs 1 ou 2. On retrouve de cette façon exactement les formules de transformation (44). On peut alors calculer les dérivées de la transformation numériquement, en discrétisant $\partial x_{i'}/\partial X_{j'}$ directement dans le plan de calcul : il suffit de connaître les coordonnées cartésiennes des noeuds du maillage. Cette méthode se rapproche de celle des volumes finis et présente les mêmes avantages. On peut montrer aussi que les difficultés mentionnées au sujet de l'utilisation de (53) avec les dérivées $\partial X_j/\partial x_i$ calculées exactement disparaissent dans cette nouvelle formulation si les dérivées $\partial x_{i'}/\partial X_{j'}$ sont représentées par des différences décentrées comme les $\partial \overline{F}_j/\partial X_j$.

On peut, à la place de (53) et (55), utiliser les équations de N.S. écrites directement dans un système de coordonnées curvilignes, comme dans [55] où un problème de corps émoussé est traité à partir des équations de N.S. écrites dans le système des coordonnées intrinsèques liées à la paroi, puis transformées. Les équations résultantes sont assez compliquées, surtout du fait que les termes visqueux sont exprimés en fonction des composantes de la vitesse sur les axes locaux (voir par exemple [4]). Néanmoins, de ce fait même, une telle formulation peut être intéressante si l'on veut utiliser des équations de N.S. tronquées où ne subsistent que les termes dissipatifs prépondérants dans une approximation de couche mince (et à la limite, que les termes dissipatifs des équations de Prandtl). L'avantage principal des formulations (53) ou (55) est surtout d'allier une relative simplicité à une grande généralité, puisque le programme de calcul peut être écrit pour une transformation de coordonnées arbitraire, celle-ci n'intervenant lors d'une application que par la mise au point d'un sous-programme spécifique de la transformation utilisée et fournissant au programme principal les valeurs des dérivées de cette transformation.

6 - CONCLUSION -

Des progrès importants ont été réalisés ces dernières années dans le traitement numérique, par l'approche globale basée sur les équations de N.S., des problèmes de forte interaction entre fluide parfait et fluide visqueux en écoulement bidimensionnel compressible à grand nombre de Reynolds. Ces progrès ressortent particulièrement d'une part de la diversité des problèmes traités, et d'autre part de la réduction des temps de calcul qui a pu être obtenue avec de nouvelles méthodes à caractère implicite.

La qualité des résultats obtenus dans le cas d'écoulements turbulents décollés, avec interaction choc-couche limite, est limitée par l'état actuel des connaissances sur la modélisation de la turbulence pour de tels écoulements. L'approche globale constitue justement un outil précieux pour l'étude et l'évaluation de nouveaux modèles de turbulence adaptés à ce type d'écoulements. On peut penser que, suivant la même évolution que pour les écoulements incompressibles, les recherches s'orienteront vers des modèles plus élaborés, à équations de transport pour les contraintes de Reynolds. Cette évolution est évidemment liée aux progrès futurs dans les méthodes numériques.

Parallèlement, il est nécessaire de chercher à comprendre les limitations de méthodes de calcul basées sur les équations de N.S. moyennes, afin d'en définir le domaine de validité et la précision. La modélisation de la turbulence dans le cadre de ces équations repose sur l'hypothèse, déjà évoquée dans l'introduction, selon laquelle il est possible de séparer les effets instationnaires qui constituent la turbulence proprement dite de ceux qui, à des fréquences beaucoup plus basses, sont propres à l'écoulement moyen. Si des fluctuations importantes apparaissent à des fréquences intermédiaires, affectant plus particulièrement les chocs et les décollements comme certaines expériences semblent l'indiquer, [29], [46], [73], alors le bien-fondé d'une description basée sur les équations de N.S. moyennes peut être remis en question.

Une autre façon de considérer le problème consiste à se demander jusqu'à quel degré de complexité il est justifié de pousser le développement de modèles de turbulence dans lesquels les seules quantités caractéristiques de la turbulence qui interviennent sont des corrélations à un point. La simulation numérique de la turbulence apportera sans doute *les réponses à ces questions*, mais dans un avenir difficilement prévisible.

REFERENCES

[1] RUBESIN M.W. — Numerical Turbulence Modeling,
AGARD-VKI Lecture Series No 86 on Computational Fluid Dynamics,
March 21-25, 1977, von Karman Institute for Fluid Dynamics,
Rhode St Genèse, Belgium.

[2] PEYRET R., VIVIAND H. — Numerical Solution of the Navier-Stokes Equations for Compressible Fluids,
AGARD-LS-73, 1975, pp. 6.1-6.14.

[3] BALDWIN B.S., MacCORMACK R.W., DEIWERT G.S. — Numerical Techniques for the Solution of the Compressible Navier-Stokes Equations and Implementation of Turbulence Models,
AGARD-LS-73, 1975, pp. 2.1-2.24.

[4] PEYRET R., VIVIAND H. — Computation of Viscous Compressible Flows Based on the Navier-Stokes Equations,
AGARD-AG-212, 1975.

[5] ROM J. — Flows with Strong Interaction Between the Viscous and Inviscid Regions,
SIAM J. Appl. Math, vol. 29, No 2, September 1975, pp. 309-328.

[6] STEWARTSON K. — On the Asymptotic Theory of Separated and Unseparated Fluid Motion,
SIAM J. Appl. Math., Vol. 28, No 2, March 1975, pp. 501-518.

[7] LE BALLEUR J.C. — Couplage visqueux-non visqueux : analyse du problème incluant décollements et ondes de choc,
A paraître dans la Recherche Aérospatiale, 1977.

[8] BRUNE G.W., RUBBERT P.E., FORESTER C.K. — The Analysis of Flow Fields with Separation by Numerical Matching,
AGARD-CP-168, Flow Separation, 1975, pp. 16.1-16.8.

[9] MacCORMACK R.W. — Numerical Solution of the Interaction of a Shock Wave With a Laminar Boundary Layer,
Lecture Notes in Physics, Vol. 8, Springer-Verlag, 1971, pp.151-161.

[10] BALDWIN B.S., MacCORMACK R.W. — Numerical Solution of the Interaction of a Strong Shock Wave with a Hypersonic Turbulent Boundary Layer,
AIAA Paper No. 74-558, June 1974.

[11] BALDWIN B.S., MacCORMACK R.W. — Interaction of Strong Shock Wave with Turbulent Boundary Layer,
Lecture Notes in Physics, Vol. 35, pp. 51-56, Springer Verlag, 1975.

[12] MacCORMACK R.W., BALDWIN B.S. — A Numerical Method for Solving the Navier-Stokes Equations with Application to Shock-Boundary Layer Interactions,
AIAA Paper, 75-1, January 1975.

[13] WILCOX D.C. — Calculation of Turbulent Boundary Layer Shock-Wave Interaction,
AIAA J., vol. 11, No. 11, 1973, pp. 1592-1594.

[14] WILCOX D.C. — Numerical Study of Separated Turbulent Flows,
(1) AIAA Paper No. 74-584, Juno 1974 et (2) AIAA J., Vol. 13, No. 5, 1975, pp.555-556.

[15] HANIN M., WOLFSHTEIN M., LANDAU U.E. — Numerical Solution of Navier-Stokes Equations for Interaction of Shock Wave with Laminar Boundary Layer,
ICAS Paper, No. 74-17, August 1974.

[16] LI C.P. — A mixed Explicit-Implicit Splitting Method for the Compressible Navier-Stokes Equations,
Lecture Notes in Physics, Vol. 59, Springer Verlag, 1976.

[17]	LI C.P.	A Numerical Study of Separated Flows Induced by Shock-Wave/Boundary Layer Interaction , AIAA Paper 77-168, 1977 .
[18]	BALDWIN B.S. ROSE W.C.	Calculation of Shock Separated Turbulent Boundary Layers , NASA-SP-347, "Aérodynamic Analysis Requiring Advanced Computers", Part I, 1975, pp. 401-417.
[19]	MURPHY J.D. PRESLEY L.L. ROSE W.C.	On the Calculation of Supersonic Separating and Reattaching Flows , AGARD-CP-168, Flow Separation, 1975, pp. 22.1-22.12, et NADA-SP-347, "Aérodynamic Analyses Requiring Advanced Computers, Part I, 1975, pp. 151-175 .
[20]	ROSE W.C.	Practical Aspects of Using Navier-Stokes Codes for Predicting Separated Flows , AIAA Paper No. 76-96, 1976 .
[21]	BALDWIN B.S. MacCORMACK R.W.	Modifications of the law of the Wall and Algebraic Turbulence Modelling for Separated Boundary Layers , AIAA Paper, No. 76-350, 1976 .
[22]	SHANG J.S. HANKEY W.L. Jr. LAW C.H.	Numerical Simulation of Shock-Wave - Turbulent Boundary Layer Interaction , AIAA Paper 76-95, 1976 et AIAA J., Vol. 14, No. 10, 1976, pp.1451-1457 .
[23]	MacCORMACK R.W.	A Rapid Solver for Hyperbolic Systems of Equations , Lecture Notes in Physics, Vol. 59, Springer-Verlag, 1976, pp;307-317.
[24]	MacCORMACK R.W.	An Efficient Numerical Method for Solving the Time-Dependent Compressible Navier-Stokes Equations at High Reynolds Number , NASA TM X-73 129, July 1976 .
[25]	SHANG J.S.	An Implicit-Explicit Method for Solving the Navier-Stokes Equations , AIAA Paper 77-646, AIAA 3rd Comput. Fluid Dyn. Conf., Albuquerque, N.M., 1977 .
[26]	BEAM R.M. WARMING R.F.	An Implicit Factored Scheme for the Compressible Navier-Stokes Equations , AIAA Paper 77-645, AIAA 3rd Comput. Fluid Dyn. Conf., Albuquerque, N.M., 1977 .
[27]	ISSA R.I. LOCKWOOD F.C.	On the Prediction of Two-Dimensional Supersonic Viscous Interactions Near Walls , AIAA J., Vol. 15, No. 2, 1977, pp. 182-188 .
[28]	HODGE B.K.	Prediction of Hypersonic Laminar Boundary Layer/ Shock-Wave Interactions , AIAA J., Vol. 15, No.7, 1977, pp. 903-904 .
[29]	HORSTMAN C.C. KUSSOY M.I. COAKLEY T.J. RUBESIN M.W. MARVIN J.G.	Shock Wave Induced Turbulent Boundary Layer Separation at Hypersonic Speeds , AIAA Paper 75-4, January 1975 .
[30]	MARVIN J.G. HORSTMAN C.C. RUBESIN M.W. COAKLEY T.J. KUSSOY M.I.	An Experimental and Numerical Investigation of Shock-Wave Induced Turbulent Boundary-Layer Separation at Hypersonic Speeds , AGARD-CP-168, Flow Separation, 1975 et NASA-SP-347, "Aerodynamic Analyses Requiring Advanced Computers, Part I, pp.377-399, 1975 .
[31]	VIEGAS J.R. COAKLEY T.J.	Numerical Investigation of Turbulence Models for Shock Separated Boundary-Layer Flows , AIAA Paper, 77-44, 1977 .
[32]	COAKLEY T.J. VIEGAS J.R. HORSTMAN C.C	Evaluation of Turbulence Models for Three Primary Types of Shock Separated Boundary Layers , AIAA Paper 77-692, 1977 .
[33]	CARTER J.E.	Numerical Solutions of the Navier-Stokes Equations for the Supersonic Laminar Flow over a two-dimensional Compression Corner , NASA TR R.385, July 1972 .
[34]	CARTER J.E.	Numerical Solution of the Supersonic Laminar Flow over a Two-Dimensional Compression Corner , Lecture Notes in Physics, vol. 19, pp. 69-78, Springer Verlag, 1973.

[35] HUNG C.M.
MacCORMACK R.W.
Numerical Solutions of Supersonic and Hypersonic Laminar Flows over a two-Dimensional Compression Corner,
AIAA Paper 75-2, January 1975 et AIAA J., vol. 14, No. 4, 1976, pp. 475-481 .

[36] SHANG J.S.
HANKEY W.L. Jr.
Numerical Solution of the Navier-Stokes Equations for Supersonic Turbulent Flow over a Compression Corner ,
AIAA Paper 75-3, January 1975, et AIAA J., Vol. 13, No. 10, 1975, pp. 1368-1374 .

[37] SHANG J.S.
HANKEY W.L. Jr.
Supersonic Turbulent Separated Flows Utilizing the Navier-Stokes Equations ,
AGARD-CP-168, Flow Separation, 1975 .

[38] HUNG C.M.
MacCORMACK R.W.
Numerical Simulation of Supersonic and Hypersonic Turbulent Compression Corner Flows Using Relaxation Models ,
AIAA Paper, No. 76-410, 1976, et AIAA J., Vol. 15, No. 3, 1977, pp. 410-416 .

[39] HORSTMAN C.C.
HUNG C.M.
SETTLES G.S.
VAS I.E.
BOGDONOFF S.M.
Reynolds Number Effects on Shock-Wave Turbulent Boundary-Layer Interactions - A Comparison of Numerical and Experimental Results,
AIAA Paper 77-42, 1977 et (2) AIAA J., Vol. 15, No. 8, 1977, pp. 1152-1158 .

[40] MATEER G.G.
BROSH A.
VIEGAS J.R.
A normal Shock-Wave Turbulent Boundary-Layer Interaction at Transonic Speeds ,
AIAA Paper, No. 76-161, 1976 .

[41] DEIWERT G.S.
Numerical Simulation of High Reynolds Number Transonic Flows ,
AIAA Paper No. 74-603, 1974 et AIAA J., Vol. 13, No. 10, 1975, pp. 1354-1359 .

[42] DEIWERT G.S.
High Reynolds Number Transonic Flow Simulation,
Lecture Notes in Physics, vol. 35, Springer Verlag, 1975, pp. 132-137.

[43] DEIWERT G.S.
Computation of Separated Transonic Turbulent Flows ,
AIAA Paper No. 75-829, 1975 et AIAA J., Vol. 14, No. 6, 1976, pp. 735-740 .

[44] DEIWERT G.S.
McDEVITT J.B.
LEVY L.L. Jr.
Simulation fo Turbulent Transonic Separated Flow over an Airfoil ,
NASA SP-347 - Aerodynamic Analyses Requiring Advanced Computers Part I, 1975, pp. 419-436 .

[45] McDEVITT J.B.
LEVY L.L. Jr.
DEIWERT G.S.
Transonic Flow about a Thick Circular-Arc Airfoil ,
AIAA Paper No. 75-878, 1975, et AIAA J., Vol. 14, No. 5, 1976, pp. 606-613 .

[46] RUBESIN M.W.
OKUNO A.F.
LEVY L.L. Jr.
McDEVITT J.B.
SEEGMILLER H.L.
An Experimental and Computational Investigation of the Flow Field About a Transonic Airfoil in Supercritical Flow with Turbulent Boundary-Layer Separation ,
Proceed. of 10th Congress of the ICAS, 4-8 oct. 1976, pp. 149-158 .

[47] DEIWERT G.S.
On the Prediction of Viscous Phenomana in Transonic Flows ,
presented et project SQUID Workshop on Transonic Flow Problems In Turbomachinery, Monterey, Calif., Feb. 11-13, 1975 .

[48] DEIWERT G.S.
Recent Computation of Viscous Effects in Transonic Flow ,
Lecture Notes in Physics, Vol. 59, Springer-Verlag, 1976, pp.159-164.

[49] LEVY L.L. Jr.
An Experimental and Computational Investigation of the Steady and Unsteady Transonic Flow Field About an Airfoil in a Solid-Wall Test Channel ,
AIAA Paper 77-678, 1977 .

[50] STEGER J.L.
Implicit Finite Difference Simulation of Flow About Arbitrary Geometrics with Application to Airfoils ,
AIAA Paper 77-665, 1977 .

[51] SEGINER A.
ROSE W.C.
A Numerical Solution of the Flow Field Over a Transonic Airfoil Including Strong Shock-Induced Flow Separation ,
AIAA Paper No. 76-330, 1976 .

[52] SEGINER A.
ROSE W.C.
An Approximate Calculation of Strong Interaction on a Transonic Airfoil,
AIAA Paper 77-210, 1977 .

[53] ROSE W.C.
SEGINER A.
Calculation of Transonic Flow Over Supercritical Airfoil Sections ,
AIAA Paper 77-681, 1977 .

[54] WALITT L.
LIU C.Y.
Numerical Solution of the Hypersonic Wake behind a Wedge ,
Aeron. Quart., Vol. XXV, pt. 4, pp. 313-330, 1974 .

[55] TANNEHILL J.C.
HOLST T.L.
RAKICH J.V.
Numerical Computation of Two-Dimensional Viscous Blunt Body Flow with an Impinging Shock ,
AIAA Paper 75-154 et AIAA J., Vol. 14, No.2, 1976, pp.204-211 .

[56] VIVIAND H.
GHAZZI W.
Numerical Solution of the Compressible Navier-Stokes Equations at High Reynolds Number with Applications to the Blunt Body Problem ,
Lecture Notes in Physics, Vol. 59, Springer-Verlag, 1976, pp.434-439.

[57] McRAE D.S.
A Numerical Study of Supersonic Viscous Cone Flow at High Angle of Attack ,
AIAA Paper No 76-97, 1976 .

[58] KNIGHT D.D.
HANKEY W.L. Jr.
Numerical Simulation of Non Chemically Reacting Radial Supersonic Diffusion Laser ,
AIAA Paper No. 76-60, 1976 .

[59] KNIGHT D.D.
Numerical Simulation of a High Speed Inlet Using the Navier-Stokes Equations,
AIAA Paper 77-146, 1977 .

[60] FAVRE A.J.
Equations des gaz turbulents compressibles ,
Journal de Mécanique, vol. 4, N° 3, septembre 1965, pp. 361-390

[61] RUBESIN M.W.
ROSE W.C.
The Turbulent Mean-Flow, Reynolds Stress, and Heat Flux Equations in Mass-Averaged Dependent Variables ,
NASA-TM-X-62248, March 1973 .

[62] FAVRE A.J.
Equations statistiques des fluides turbulents compressibles ,
Proceed. of the Vth Canadian Congress of Applied Mech., May 26-30 1975, Univ. of New Brunswick, N.B. Canada .

[63] CEBECI T.
SMITH A.M.O.
MOSINSKIS G.
Calculation of Compressible Adiabatic Turbulent Boundary Layers ,
AIAA J., Vol. 8, No 11, 1970, pp.1974-1982 .

[64] RUBESIN M.W.
A One-Equation Model of Turbulence for Use with the Compressible Navier-Stokes Equations,
NASA-TM-X-73128, April 1976 .

[65] RUBESIN M.W.
CRISALLI A.J.
HORSTMAN C.C.
ACHARYA M.
LANFRANCO M.J.
A Critique of Some Recent Second Order Closure Models for Compressible Boundary Layers ,
AIAA Paper 77-128, 1977 .

[66] SAFFMAN P.G.
WILCOX D.C.
Turbulence Model Predictions for Turbulent Boundary Layers ,
AIAA J., Vol. 12, No. 4, 1974, pp. 541-546 .

[67] JONES W.P.
LAUNDER B.E.
The Prediction of Laminarization with a Two-Equation Model of Turbulence ,
Int. J. Heat Mass Transfer, Vol. 15, 1972, pp. 301-314 .

[68] MARVIN J.G.
Turbulence Modeling for Compressible Flows ,
NASA-TM-X-73188, Jan. 1977 .

[69] MacCORMACK R.W.
The Effect of Viscosity in Hypervelocity Impact Cratering ,
AIAA Paper No. 69-354, 1969 .

[70] HUNG C.M.
MacCORMACK R.W.
Numerical Solution of Supersonic Laminar Flow Over a Three-Dimensional Compression Corner ,
AIAA Paper 77-694, 1977 .

[71] SHANG J.S.
HANKEY W.L.
Numerical Solution of the Compressible Navier-Stokes Equations for a Three-Dimensional Corner ,
AIAA Paper 77-169, 1977 .

[72] VIVIAND H.
Formes conservatives des équations de la dynamique des gaz ,
La Recherche Aérospatiale No. 1974-1, 1974, pp. 65-66 .

[73] HOLDEN M.S.
Shock Wave-Turbulent Boundary Layer Interaction in Hypersonic Flow ,
AIAA Paper 77-45, 1977 .

CALCULS COUPLÉS VISQUEUX – NON VISQUEUX
INCLUANT DÉCOLLEMENTS ET ONDES DE CHOC
EN ÉCOULEMENT BIDIMENSIONNEL

par Jean-Claude LE BALLEUR

Office National d'Etudes et de Recherches Aérospatiales (ONERA)
92320 Châtillon (France)

◆

RÉSUMÉ

Considérant des écoulements laminaires stationnaires, ou turbulents moyennés, on passe en revue les méthodes de calcul capables de décrire le fluide visqueux lorsque les nombres de Reynolds sont assez élevés pour que l'approximation de fluide parfait soit justifiée dans la plus grande partie de l'écoulement.

On caractérise d'abord brièvement différentes approches utilisées pour définir une approximation des équations de Navier-Stokes : méthodes asymptotiques rationnelles pour des couches limites en faible ou en forte interaction, couplage numérique "Euler-Navier Stokes" à grande distance des régions visqueuses, équations de Navier-Stokes tronquées, couplage visqueux-non visqueux au voisinage des couches dissipatives selon le concept de couche limite en forte interaction, méthodes simplifiées avec modèles empiriques de décollements.

On met l'accent sur les progrès récents obtenus dans les méthodes de couche limite en forte interaction. Ils portent sur leur justification par les analyses asymptotiques, sur le traitement des bulles de recirculation et de l'influence aval-amont en supersonique. D'un point de vue pratique, ces méthodes peuvent maintenant être associées à diverses techniques de calcul du fluide parfait, en subsonique, transsonique ou supersonique. Elles peuvent traiter des écoulements non-visqueux complexes, de même que des décollements multiples, sans qu'aucune connaissance préalable sur la solution ne soit nécessaire. Les conditions aux limites usuellement imposées au fluide parfait en présence de couches visqueuses sont discutées sur l'exemple du profil transsonique, en considérant les problèmes d'influence amont en supersonique, de résolution directe ou inverse, d'application de méthodes intégrales de couche limite, d'interaction onde de choc-couche limite, d'échelle des maillages.

On tente ensuite de classer les techniques numériques réalisant le couplage visqueux-non visqueux : méthodes de conditions initiales en supersonique avec tâtonnement pour respecter les conditions imposées à l'aval, méthodes stationnaires itératives de type direct pour les écoulements non décollés, itérations de type mixte direct-inverse en cas de décollement (Klineberg), itération mixte directe ou semi-inverse (ONERA), itération sur une résolution exacte du problème couplé linéarisé (Brune, Rubbert, Nark), méthodes pseudo-instationnaires (Werle, Vatsa - Briley, Mc Donald).

On discute enfin des performances actuelles de ces méthodes. Des améliorations de même nature que dans la résolution des équations de Navier-Stokes sont nécessaires. Elles concernent la turbulence dans les interactions couche limite-onde de choc, les décollements de bord de fuite, les bulles de décollement transitionnelles. Des études complémentaires sont aussi nécessaires pour définir le degré de validité des méthodes en cas de décollement turbulent, ainsi que pour traiter les gradients de pression normaux et les ondes de chocs internes aux couches dissipatives turbulentes.

VISCID – INVISCID INTERACTION METHODS
FOR TWO-DIMENSIONAL FLOWS, INCLUDING SEPARATION AND SHOCK WAVES

SUMMARY

Restricting to steady laminar or turbulent mean flows, review will be done of various methods able to predict viscous flows when the Reynolds number is large enough for the inviscid approximation to be applied in most part of the flow field.

Firstly, the different approaches used to approximate the Navier-Stokes equations will be shortly outlined : rational asymptotic methods both for weak and singular boundary layer interactions, truncated Navier-Stokes equations, numerical matching at large distance of boundary layer regions, viscid-inviscid patching in the vicinity of boundary layer according to the strong interaction or interacting boundary layer concept, simplified methods with empirical models of separation.

Emphasis will be put on progress recently achieved with the interacting boundary layer methods. On one hand, advances deal with the degree of rationality, the inclusion of separated bubbles, the upstream influence in supersonic flows. On the other hand, progress has been achieved in making this approach a practical tool for various inviscid codes, subsonic, transonic or supersonic. Concerning this point, we consider the requirements of initial guess of the solution, the practical possibilities of multiple separations, of complex flow fields. Usual inviscid boundary conditions used for matching the viscous layers will be discussed on a transonic airfoil example, with attention to supersonic upstream influence, direct-inverse alternative, integral methods for boundary layer, shock wave-boundary layer interaction and mesh size.

A tentative classification of numerical techniques for viscid-inviscid interaction will be given : supersonic marching methods with shooting on downstream condition (integral and differences methods), direct iterative methods for attached flows, mixed direct-inverse iterations for separated flows (Klineberg), mixed direct-half inverse iteration (ONERA), iteration on the exact solution of the linearized viscid-inviscid problem (Brune, Rubbert, Nark), pseudo-unsteady methods (Werle, Vatsa - Briley, Mc Donald).

Present status of the results is finally discussed. Required improvements are very much the same as in the Navier-Stokes approach and related to turbulence within shock-wave boundary layer interactions, trailing edge separation, transitional bubbles. Additional knowledge on the validity of viscid-inviscid methods is also needed for turbulent separation. Investigations on normal pressure gradient or shock-waves inside turbulent layers need to be continued.

INTRODUCTION

Les écoulements à grands nombres de Reynolds sont connus pour valider l'approximation d'Euler presque partout, à l'exception de couches minces où le caractère dissipatif redevient important. Cette structure non-uniforme est une source de difficultés pour la résolution numérique des équations de Navier-Stokes. Elle est aussi à l'origine de nombreuses techniques de résolution approchées, dont le point commun est de calculer le fluide visqueux comme un fluide parfait **perturbé**.

Dans le cadre des approximations retenues, le fluide parfait perturbé coïncide avec l'écoulement réel au loin des couches dissipatives. Une première technique de perturbation consiste à enrichir les équations d'Euler d'un certain nombre de termes visqueux. On définit ainsi des équations de Navier-Stokes tronquées, permettant de respecter la condition d'adhérence aux parois. La seconde technique ne perturbe le fluidè parfait que dans ses conditions aux limites, et élimine la condition de glissement au profit d'une condition déduite d'un traitement disjoint des phénomènes dissipatifs. Il peut s'agir d'un simple raccordement visqueux-non visqueux sur une interface placée hors des couches dissipatives, ou encore d'un prolongement fictif du fluide parfait à l'intérieur de celles-ci. Une telle approche permet, si nécessaire, d'appliquer aux régions visqueuses des équations de Navier-Stokes assez incomplètes, et l'interaction entre les régions visqueuses et non visqueuses reste souvent suffisamment faible pour qu'un couplage simplifié inspiré des méthodes asymptotiques puisse suffire. En revanche, la présence de décollements ou d'ondes de choc ramène au problème le plus général, dit de forte interaction, pour lequel l'analyse des singularités ou des domaines d'influence mathématiques associés aux équations ne peut être effectuée sans inclure l'effet de couplage.

Nous limitant aux écoulements bidimensionnels stationnaires, nous passerons brièvement en revue les principales méthodes utilisées. On examinera plus en détail les possibilités offertes par l'application des équations de Prandtl, ainsi que les méthodes numériques permettant leur couplage fort aux équations d'Euler.

1. Principales techniques d'approximation utilisées

1.1. Développements asymptotiques raccordés

Ces méthodes remarquent que l'inverse du nombre de Reynolds $\varepsilon = R^{-1}$ est un petit paramètre, et tirent avantage du passage à la limite $\varepsilon \rightarrow 0$. On construit pour ε petit un développement formel, dont la convergence et l'importance relative des divers termes sont seulement assurées à la limite $\varepsilon \rightarrow 0$. Renvoyant à *Van Dyke* [1] pour une introduction détaillée, on obtient dans le cas laminaire un problème de perturbation singulière avec une couche limite simple. En incompressible, affectant une barre aux variables de couche limite, on obtient dans un repère xOy tangent à la paroi :

$$\left[\begin{array}{l} x = \bar{x} \\ y = \varepsilon^{\frac{1}{2}}.\bar{y} \end{array}\right.$$

$$\left[\begin{array}{l} u(x,y) = u_0(x,y) + \varepsilon^{\frac{1}{2}}.u_1(x,y) + \dots. \\ v(x,y) = v_0(x,y) + \varepsilon^{\frac{1}{2}}.v_1(x,y) + \dots. \\ p(x,y) = p_0(x,y) + \varepsilon^{\frac{1}{2}}.p_1(x,y) + \dots. \end{array}\right.$$

$$\left[\begin{array}{l} \bar{u}(x,\bar{y}) = \bar{u}_0(x,\bar{y}) + \varepsilon^{\frac{1}{2}}.\bar{u}_1(x,\bar{y}) + \dots. \\ \bar{v}(x,\bar{y}) = \varepsilon^{\frac{1}{2}}.\bar{v}_0(x,\bar{y}) + \dots. \\ \bar{p}(x,\bar{y}) = p_0(x,0) + \varepsilon^{\frac{1}{2}}.\bar{p}_1(x,\bar{y}) + \dots. \end{array}\right.$$

Le fluide parfait au premier ordre (u_0, v_0, p_0), comme aux premier et second ordres réunis, vérifie les équations d'Euler. La couche limite présente un changement d'échelle pour les variables y et v. Ses équations sont celles de Prandtl au premier ordre des nouvelles variables $[\bar{u}_0, \bar{v}_0, \bar{p}_0 = p(x,0)]$. *Elles sont encore valables, second ordre inclus, si la courbure de la paroi ou du sillage est nulle au premier ordre.* Un gradient de pression normal existe en cas de courbure non nulle K_0:

$$\frac{\partial \bar{p}_1}{\partial \bar{y}} = K_0 \, \bar{\rho}_0 \bar{u}_0^2$$

Cette équation rappelle son homologue du fluide parfait avec deux simplifications supplémentaires. La première est mineure et remplace $\bar{u}(x, \bar{y})$ par sa partie principale $\bar{u}_0(x, \bar{y})$. La seconde remplace la courbure locale $K(x, \bar{y})$ de l'écoulement par une courbure moyenne $K_0(x)$ indépendante de $\bar{y}$, donnée par la paroi ou par le fluide parfait du premier ordre. *Baum* et *Denison* [2] ont montré que cette approximation est déterminante et qu'elle permet au problème parabolique de la couche limite, parcourue dans le sens amont-aval, de demeurer un problème bien posé dans les régions subsoniques.

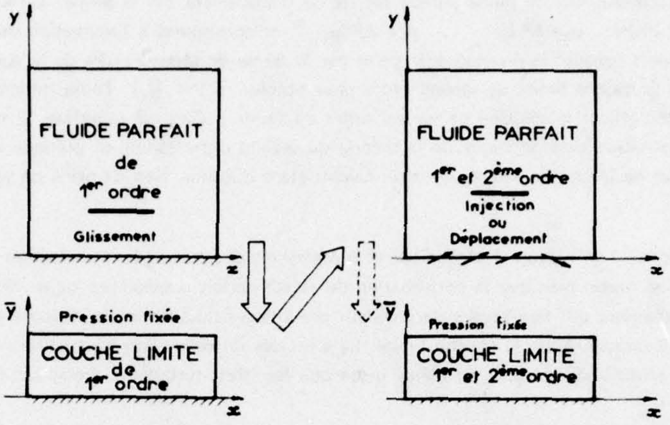

Fig. 1 – Interaction faible laminaire : couplage asymptotique hiérarchisé.

Les relations asymptotiques de couplage s'écrivent :

$$\left[\begin{aligned} v_0(x,0) &= 0 \\ u_0(x,0) &= \lim_{\bar{y}\to\infty} \bar{u}(x,\bar{y}) \\ p_0(x,0) &= \bar{p}_0(x,\bar{y}) = \bar{p}_0(x,0) \end{aligned}\right.$$

$$\left[\begin{aligned} u_1(x,0) &= \lim_{\bar{y}\to\infty} \left[\bar{u}_1(x,\bar{y}) - \bar{y}\cdot\left(\frac{\partial u_0}{\partial y}\right)_{(x,0)} \right] \\ v_1(x,0) &= \lim_{\bar{y}\to\infty} \left[\bar{v}_0(x,\bar{y}) - \bar{y}\cdot\left(\frac{\partial v_0}{\partial y}\right)_{(x,0)} \right] \\ p_1(x,0) &= \lim_{\bar{y}\to\infty} \left[\bar{p}_1(x,\bar{y}) - \bar{y}\cdot\left(\frac{\partial p_0}{\partial y}\right)_{(x,0)} \right] \end{aligned}\right.$$

Classiquement, les relations de second ordre, sont transformées en introduisant des épaisseurs de déplacement $\delta^*(x) = \varepsilon^{\frac{1}{2}} . \bar{\delta}^*$ et de quantité de mouvement $\delta^{**}(x) = \varepsilon^{\frac{1}{2}} . \bar{\delta}^{**}$. Posons :

$$\left[\begin{aligned} \bar{\delta}^* . (\rho_0 u_0)_{(x,0)} &= \lim_{\bar{y}\to\infty} \int_0^{\bar{y}} \left[(\rho_0 u_0)_{(x,0)} - (\bar{\rho}_0 \bar{u}_0)_{(x,\bar{y})} \right] . d\bar{y} \\ (\bar{\delta}^* + \bar{\delta}^{**}) . (\rho_0 u_0^2)_{(x,0)} &= \lim_{\bar{y}\to\infty} \int_0^{\bar{y}} \left[(\rho_0 u_0^2)_{(x,0)} - (\bar{\rho}_0 \bar{u}_0^2)_{(x,\bar{y})} \right] . d\bar{y} \end{aligned}\right.$$

Il vient alors :

$$\left[\begin{array}{ll} (\rho_0 v_1)_{(x,0)} & = \dfrac{d}{dx}\left[\,\overline{\delta^*}.(\rho_0 u_0)_{(x,0)}\right] \\ \bar{p}_1\,(x,0) & = p_1(x,0) + K_0\left[\overline{\delta^*}+\overline{\delta^{**}}\right].(\rho_0 u_0^2)_{(x,0)} \end{array}\right.$$

Ces relations de couplage ont pour particularité d'être hiérarchisées (Fig. 1). Le fluide parfait de premier ordre est déterminé par la condition de glissement $v_0(x, 0) = 0$. La couche limite de premier ordre peut ensuite être calculée avec une pression fixée $p_0(x, 0)$. Un second calcul de fluide parfait corrigé de déplacement *par le terme* $v_1(x, 0)$ *inclut alors les solutions de premier et de second ordre* $u_0 + \varepsilon^{\frac{1}{2}}.u_1$, $p_0 + \varepsilon^{\frac{1}{2}}.p_1$ *et correspond* à l'estimation définitive de la pression dans le fluide parfait. On peut alors corriger la pression à la paroi par le terme de second ordre de la couche limite $\bar{p}_1(x, 0)$, et facultativement résoudre la couche limite de second ordre pour obtenir $\bar{u}_1(x, \bar{y})$. Toute itération sur le terme de déplacement $v_1(x, 0)$ dans le but d'affiner la solution de second ordre du fluide parfait est superflue. Si elle ne l'est pas la théorie n'est plus valide. Cette hiérarchisation caractéristique de la théorie du second ordre réduit en pratique le couplage à une double résolution du fluide parfait et de la couche limite, les deux calculs étant disjoints. Son domaine de validité est qualifié d'interaction faible.

En régime turbulent, où l'on renvoit à *Mellor* [3] et à *Melnik* et *Grossman* [4], l'interaction faible est encore souvent qualifiée de théorie du second ordre, bien que la perturbation du fluide parfait n'apparaisse qu'au troisième. Il est nécessaire d'introduire un second petit paramètre *qui fixe l'ordre de grandeur des vitesses fluctuantes* par rapport à la vitesse de référence, et qui coïncide avec la jauge d'épaisseur δ de la couche limite. La structure de celle-ci est plus complexe et comporte une sous-couche d'épaisseur $\delta.\hat{\delta}$ où les effets visqueux sont du même ordre que les effets turbulents. Désignant par C_f le coefficient de frottement à la paroi, on a :

$$\delta^2.\hat{\delta} \sim \mathcal{O}(R^{-1}) \qquad\qquad \delta \sim \mathcal{O}\left(\sqrt{\frac{C_f}{2}}\right) \sim \mathcal{O}\left(\frac{1}{\operatorname{Log} R}\right)$$

Les développements sont conduits suivant les puissances de δ , voir réf. 3. Les développements par rapport à $\hat{\delta}$ n'apparaissent pas, car $\hat{\delta} \ll \delta^n$ pour tout n , d'après les relations précédentes. Surlignant d'un $\wedge$ les variables de la sous-couche, nous retiendrons en incompressible sur paroi plane :

$$\left[\begin{array}{l} x = \bar{x} = \hat{x} \\ y = \delta.\bar{y} = \delta\hat{\delta}.\hat{y} \end{array}\right.$$

$$\left[\begin{array}{l} \bar{u}\,(x,\bar{y}) = \bar{u}_0(x,\bar{y}) + \delta.\,\bar{u}_1(x,\bar{y}) + \delta^2.\bar{u}_2(x,\bar{y}) + \ldots. \\ \hat{p}\,(x,\hat{y}) = \hat{p}_0(x,\hat{y}) + \delta.\,\hat{p}_1(x,\bar{y}) + \delta^2.\hat{p}_2(x,\hat{y}) + \ldots. \\ \ldots\ldots. \end{array}\right.$$

$$\left[\begin{array}{ll} v_0(x,0) = v_1(x,0) = 0 & v_2(x,0) \neq 0 \\ \bar{v}_0(x,0) = \bar{v}_1(x,0) = \bar{v}_2(x,0) = 0 & \\ \dfrac{b_1}{\bar{y}} = \lim\limits_{\bar{y}\to 0}\left(\dfrac{\partial \bar{u}_1}{\partial \bar{y}}\right) & \dfrac{b_1}{\hat{y}} = \lim\limits_{\hat{y}\to\infty}\left(\dfrac{\partial \hat{u}_1}{\partial \hat{y}}\right) \end{array}\right.$$

$$\left[\begin{array}{l} \hat{p}_0(x,\hat{y}) = \bar{p}_0(x,\bar{y}) = p_0(x,0) \\ \bar{u}_0(x,\bar{y}) = u_0(x,0) \\ \hat{u}_0(x,\hat{y}) = \hat{v}_0(x,\hat{y}) = 0 \end{array}\right.$$

$$\left[\begin{array}{l} u_1(x,y) = v_1(x,y) = p_1(x,y) = 0 \\ \bar{p}_1(x,\bar{y}) = 0 \\ \hat{p}_1(x,\hat{y}) = 0 \end{array}\right.$$

Ces relations indiquent que le glissement sur la paroi s'applique au fluide parfait aux deux premiers ordres. Il s'applique à la couche limite externe à tous les ordres, le déplacement dû à la sous-couche étant négligeable. Le raccordement de la vitesse entre la couche limite et la sous-couche est logarithmique. La sous-couche est essentiellement une zone à frottement apparent constant, tandis que la couche limite est une région déficitaire de faible perturbation de l'écoulement externe. Aux deux premiers ordres, la pression est partout imposée par le fluide parfait de premier ordre et ne dépend que de x. Contrairêment à l'analyse laminaire, il apparaît au troisième ordre une variation de la pression dans la direction normale, indépendamment de la courbure de la paroi. Cet effet intéresse la région déficitiare mais n'affecte pas la paroi elle-même, $\hat{y} = 0$, où l'on a simplement $\hat{p}_2(x,0) = p_2(x,0)$ Si l'on réunit les deux premiers ordres assujettis au même champ de pression, les équations de la couche déficitaire et de la sous-couche sont incluses dans celles de Prandtl. Sur le plan pratique, la procédure hiérarchisée définie en laminaire peut donc être intégralement maintenue dans le cas de l'interaction faible turbulente. La correction de troisième ordre du fluide parfait est calculée directement après un premier calcul de couche limite, traitée par les équations de Prandtl et donnant $\bar{u}(x, \bar{y})$. L'effet de déplacement s'écrit :

$$\left[\begin{aligned} \bar{\delta}^{*} . \, u_0(x,0) &= \lim_{\bar{y} \to \infty} \int_0^{\bar{y}} \left[u_0(x,\delta\bar{y}) - \bar{u}(x,\bar{y}) \right] . d\bar{y} \\ v_2(x,0) &= \frac{d}{dx} \left[\bar{\delta}^{*} . u_0(x,0) \right] \end{aligned}\right.$$

avec :

$$\left[\begin{aligned} u_0(x,\delta\bar{y}) &\equiv u_0(x,0) + \delta\,\bar{y} \left(\frac{\partial u_0}{\partial y} \right)_{(x,0)} \\ \bar{u}(x,\bar{y}) &\equiv \bar{u}_0(x,\bar{y}) + \delta\,\bar{u}_1(x,\bar{y}) \end{aligned}\right.$$

Notons que $u_0(x,\delta\bar{y}) = u_0(x,0)$ pour une paroi plane et un fluide parfait irrotationnel. Notons encore que si l'épaisseur de déplacement laminaire est $\mathcal{O}(\varepsilon^{1/2}) \sim \mathcal{O}(\delta)$, elle devient en turbulent $\delta^{*} \sim \mathcal{O}(\delta^2)$ puisqu'il s'agit du déplacement de second ordre de la couche déficitaire. Indiquons enfin que la simplification apportée au problème du couplage par les ordres de grandeur de l'interaction faible cesse généralement dans le cas des couches visqueuses libres, comme l'indique *Viviand* [5].

Les phénomènes d'interaction visqueuse *invalident non seulement la procédure simplifiée de couplage*, mais encore les divers ordres de grandeur de l'interaction faible. Ce retour à une interaction forte coïncide avec la présence de singularités dans les théories précédentes. Pour le fluide parfait, elles résultent par exemple des discontinuités de paroi, des impacts d'ondes de choc ou des bords de fuite. Pour les couches dissipatives, on note l'effet de perte d'adhérence au bord de fuite, ainsi que la singularité de décollement de *Goldstein* [6]. Celle-ci est liée aux équations de Prandtl lorsque, pour un ordre de grandeur donné, la *pression se trouve imposée à la couche limite (couplage faible). L'investigation par les méthodes asymptotiques indique alors des* structures de couche limite beaucoup plus complexes, comportant des changements d'échelle à la fois en x et en y. Elles ont fait l'objet de quelques *investigations numériques*, voir dans [7, 8]. Dans le cas laminaire, une analyse détaillée de l'état de l'art est donnée par *Stewartson* dans [9] et surtout [10]; voir aussi [1] et [12, 13, 14, 15]. Dans le cas turbulent, beaucoup moins avancé, on pourra se reporter à *Melnik* [4, 7, 13, 15] et à l'analyse non-asymptotique [16].

La première remarque que l'on peut faire est que les décollements éventuellement mis en jeu dans ces analyses sont minces, en ce sens que leur jauge d'épaisseur tend vers zéro lorsque $R \to \infty$. En second lieu, parmi les passages à la limite simultanés, (tels que $M \to 1$, $R \to \infty$, en transsonique), la géométrie des obstacles elle-même doit souvent être incluse pour que la solution soit cohérente. Dans le cas du bord de fuite laminaire, on montre ainsi par exemple que le décollement sous l'effet d'épaisseur relative e apparaît si $e \sim R^{-\frac{1}{4}}$, que le décrochage sous l'effet d'incidence α apparaît si $\alpha \sim R^{-\frac{1}{16}}$ en subsonique, si $\alpha \sim R^{-\frac{1}{4}}$ en supersonique. Dans le cas laminaire, le résultat le plus remarquable, intervenant dans le traitement du bord de fuite et du décollement naissant, est la structure en triple couche (Fig. 2) introduite par *Neiland* et *Stewartson* pour le décollement

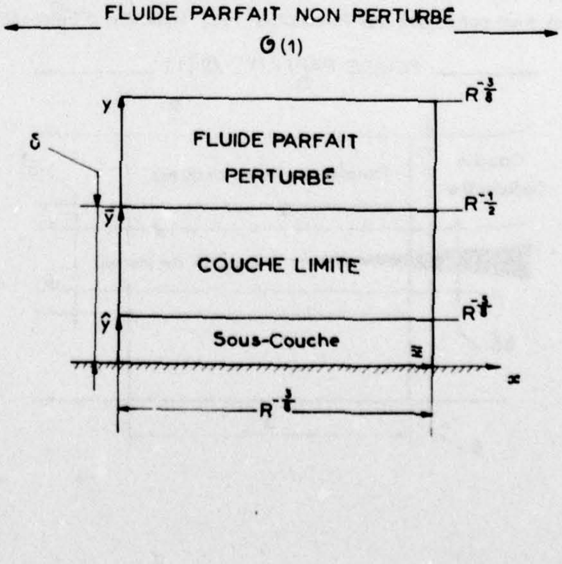

Fig. 2 – Triple couche laminaire (Stewartson - Neiland).

libre supersonique. L'étendue longitudinale et normale du domaine singulier est $\mathcal{O}(R^{-3/8})$, perturbant ainsi le fluide parfait. La couche limite principale $\mathcal{O}(R^{-1/2})$ comporte une sous-couche $\mathcal{O}(R^{-5/8})$. Les développements sont construits avec $R^{-1/8}$. Ne retenant que le premier terme de perturbation par rapport à la solution d'interaction faible valable en amont $[\bar{u}_0(\bar{y}),\ \bar{v}_0(\bar{y}) = 0,\ \bar{p}_0(\bar{y}) = p_0,\ \bar{\rho}_0(\bar{y})]$, on obtient dans la couche limite principale :

$$\left[\begin{array}{lllll} \bar{u}(\bar{x},\bar{y}) & = & \bar{u}_0(\bar{y}) & + R^{-\frac{1}{8}}.\bar{u}_1(\bar{x},\bar{y}) & + \dots \\ \bar{v}(\bar{x},\bar{y}) & = & & R^{-\frac{1}{4}}.\bar{v}_1(\bar{x},\bar{y}) & + \dots \\ \bar{p}(\bar{x},\bar{y}) & = & p_0 & + R^{-\frac{1}{4}}.\bar{p}_2(\bar{x}) & + \dots \\ \bar{\rho}(\bar{x},\bar{y}) & = & \bar{\rho}_0(\bar{y}) & + R^{-\frac{1}{8}}.\bar{\rho}_1(\bar{x},\bar{y}) & + \dots \end{array}\right. \qquad \frac{\partial \bar{p}_2}{\partial \bar{y}} = 0$$

$$\left[\begin{array}{l} \bar{u}_1 = A(\bar{x}).\dfrac{d\bar{u}_0}{d\bar{y}} \\ \bar{v}_1 = -\dfrac{dA}{dx}.\bar{u}_0(\bar{y}) \end{array}\right. \qquad \left[\begin{array}{l} \bar{\rho}_1 = A(\bar{x}).\dfrac{d\bar{\rho}_0}{d\bar{y}} \\ 0 = \lim\limits_{\bar{x}\to-\infty} A(\bar{x}) \end{array}\right.$$

Cette couche est non-visqueuse, ne dépend que de la fonction de déplacement $A(\bar{x})$ et transporte la pression de la sous-couche au fluide parfait externe où l'on obtient, M_∞ étant le nombre de Mach de référence :

$$\left[\begin{array}{lllll} u(\bar{x},y) & = & 1 & + R^{-\frac{1}{4}}.u_2(\bar{x},y) & + \dots \\ v(\bar{x},y) & = & & R^{-\frac{1}{4}}.v_2(\bar{x},y) & + \dots \\ p(\bar{x},y) & = & p_0 & + R^{-\frac{1}{4}}.p_2(\bar{x},y) & + \dots \\ \rho(\bar{x},y) & = & 1 & + R^{-\frac{1}{4}}.\rho_2(\bar{x},y) & + \dots \end{array}\right.$$

$$(M_\infty^2 - 1)\frac{\partial^2 p_2}{\partial \bar{x}^2} + \frac{\partial^2 p_2}{\partial y^2} = 0$$

La sous-couche vérifie des équations de Prandtl incompressibles de sorte que la pression à la pression à la paroi $p_0 + R^{-\frac{1}{4}}.p_2(x,0)$ résulte d'une interaction auto-induite entre l'équation externe précédente et la sous-couche, où :

$$\left[\begin{array}{lllll} \hat{u}(\bar{x},\hat{y}) & = & & R^{-\frac{1}{8}}.\hat{u}_1(\bar{x},\hat{y}) & + \dots \\ \hat{v}(\bar{x},\hat{y}) & = & & R^{-\frac{3}{8}}.\hat{v}_2(\bar{x},\hat{y}) & + \dots \\ \hat{\rho}(\bar{x},\hat{y}) & = & \bar{\rho}_0(0) & + \dots\dots\dots & \\ \hat{p}(\bar{x},\hat{y}) & = & p_0 & + R^{-\frac{1}{4}}.\hat{p}_2(\bar{x}) & + \dots \end{array}\right. \qquad \frac{\partial \hat{p}_2}{\partial \hat{y}} = 0$$

Si globalement les équations de la couche limite et de la sous-couche sont incluses dans celles de Prandtl, le décollement peut néanmoins être franchi sans singularité, car la pression $p_2(\bar{x}, 0)$ n'est plus imposée à la sous-couche et résulte d'un couplage fort avec l'écoulement externe. En contre partie, on doit noter qu'en dépit de l'écriture de développements asymptotiques, la simplification du couplage hiérarchisé n'apparaît plus et que, même à l'ordre le moins élevé, le problème à résoudre est aussi compliqué que le couplage fort "équations d'Euler–équations de Prandtl". Il est donc légitime d'un point de vue pra-

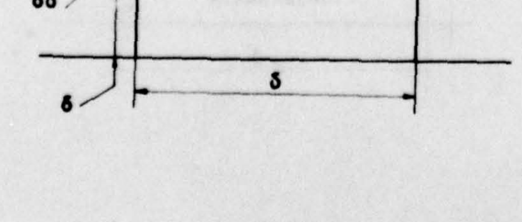

Fig. 3 – Bord de fuite turbulent non-décollé (Melnik - Chow).

tique de préférer cette dernière technique, dont la portée est plus générale. Il existe en effet des structures décollées plus complexes que la triple couche qui sont incluses dans les équations de Prandtl, voir [10].

La *figure 3 reproduit la structure donnée par* Melnik *pour le* bord de fuite turbulent incompressible non décollé. Le domaine singulier $\mathcal{O}(\delta)$ n'atteint pas le fluide parfait. La couche de paroi $\mathcal{O}(\delta.\hat{\delta})$ s'y prolonge, de même que dans le sillage. La couche déficitaire prend localement un comportement non-visqueux et une couche intermédiaire $\mathcal{O}(\delta^2)$ est nécessaire pour raccorder les tensions de *Reynolds. Au premier ordre de perturbation* $\mathcal{O}(\delta^{3/2})$ *l'effet de déplacement des sous-couches est négligeable*, de sorte que le problème de confluence ne résulte que des couches rotationnelles non visqueuses où existe un gradient de pression normal. La référence de vitesse étant prise au bord de fuite, on a :

$$\left|\begin{array}{l} x = \delta . \bar{x} \\ y = \delta . \bar{y} \\ \bar{u}(\bar{x},\bar{y}) = 1 + \delta^{1/2} . u(\bar{x},\bar{y}) + \delta . \bar{u}_0(\bar{y}) + \delta^{3/2} . \bar{u}_1(\bar{x},\bar{y}) + \dots \end{array}\right.$$

Le *premier terme* $u(\bar{x},\bar{y})$ est le prolongement du fluide parfait externe. Le second $\bar{u}_0(\bar{y})$ est le terme de couche limite amont. La perturbation apparaît seulement à l'ordre $\delta^{3/2}$. La fonction de courant correspondante $\bar{\Psi}_1(\bar{x},\bar{y})$ vérifie une équation de Poisson :

$$\frac{\partial^2 \bar{\Psi}_1}{\partial \bar{x}^2} + \frac{\partial^2 \bar{\Psi}_1}{\partial \bar{y}^2} = - \frac{d^2 \bar{u}_0}{d \bar{y}^2} . \psi(\bar{x},\bar{y}) \qquad \bar{p}_1(\bar{x},\bar{y}) = - \frac{\partial \bar{\Psi}_1}{\partial \bar{y}}$$

où $\psi(\bar{x},\bar{y})$ représente le prolongement du fluide irrotationnel externe.

1.2. Couplage numérique d'un domaine Navier-Stokes

L'idée de base (Fig. 4) est de résoudre les équations de Navier-Stokes sur un domaine surabondant, incluant largement les régions dissipatives, et de les coupler à une région externe de fluide parfait en raccordant simplement les valeurs discrétisées des solutions aux nœuds de recouvrement des maillages. On doit remarquer que le recouvrement naturel sur une maille conduit en fait à une condition de raccordement assez forte, portant sur toutes les grandeurs ainsi que leurs dérivées partielles premières. Elle ne convient en toute rigueur que si les équations sont identiques dans les deux domaines. Son utilisation demande donc que la région de recouvrement soit placée à une distance des parois très supérieure à l'épaisseur physique habituelle δ des couches dissipatives, de telle sorte que l'inconsistance soit de l'ordre de l'imprécision numérique. La pénalité de calcul correspondant à cette dilatation du domaine Navier-Stokes doit alors être amoindrie par une adaptation des maillages. On peut également lever l'inconsistance en imposant un raccordement plus faible où certaines dérivées partielles ne sont pas raccordées. Le problème ne se distingue alors de l'approche classique (section 1.4) que par le choix d'une région de raccordement non voisine de δ.

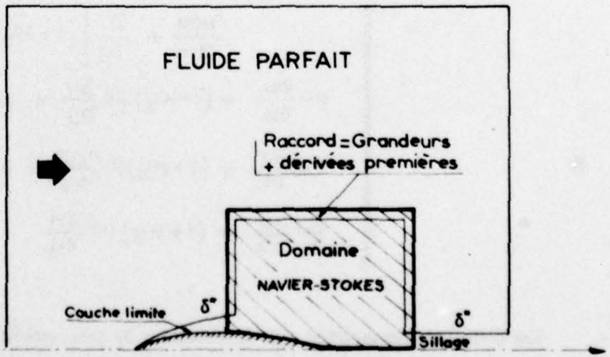

Fig. 4 – Couplage numérique "Euler-Navier Stokes" (profil symétrique).

Les problèmes soulevés par cette approche sont liés à l'application d'équations d'ordres différents dans les deux régions, et aux nombres différents de conditions aux limites qu'il est nécessaire de leur imposer. De plus, le nombre des conditions fixé, *elles doivent être sélectionnées de manière à résoudre itérativement chaque région* [18], et à obtenir un cycle convergent. A titre d'exemple, on peut imaginer de résoudre un problème de fluide parfait de type direct en imposant la vitesse normale sur l'interface, où seraient calculées la pression, la masse volumique, la vitesse tangentielle. Prescrivant alors celles-ci au domaine visqueux, *et ajoutant la dérivée normale de la vitesse tangentielle, on calculerait une nouvelle vitesse normale sur l'interface, etc. . .* Le problème soulevé par la convergence d'une telle itération ne semble éliminé que si les domaines d'Euler et Navier-Stokes sont

traités par des méthodes instationnaires consistantes, les deux calculs étant menés simultanément. Dans l'approche stationnaire itérative, l'investigation semble encore à ses débuts [18, 19, 20], et l'on note le recours à une surface de déplacement équivalente pour le calcul non visqueux.

1.3. Equations de Navier-Stokes tronquées

L'écoulement de fluide parfait sous-jacent est ici perturbé dans ses équations aux dérivées partielles, de sorte que le traitement est applicable à la fois aux régions visqueuses et non-visqueuses (Fig. 5), le raccordement à une région de fluide parfait externe non perturbé étant facultatif. En l'absence d'un tel raccordement externe, le problème peut sembler de même nature que la résolution des équations de Navier-Stokes complètes, et l'on peut imaginer d'appliquer les mêmes méthodes, voir [21,29]. L'économie de calcul est cependant relative, et l'intérêt surtout d'ordre fondamental. L'objectif pratique recherché est une simplification de la technique de résolution, obtenue en se ramenant soit à *un problème purement parabolique*, soit à un problème semblable au couplage d'un système parabolique et des équations d'Euler. Dans le premier cas, on peut résoudre d'amont en aval un simple problème de conditions initiales, une itération sur ce même problème étant nécessaire dans le second. On notera dans ces formulations que les difficultés de couplage, délibérément écartées par le choix de systèmes d'équations communs aux fluides visqueux et non-visqueux, resurgissent néanmoins au niveau de la sélection des équations approchées et de *leur résolution numérique*.

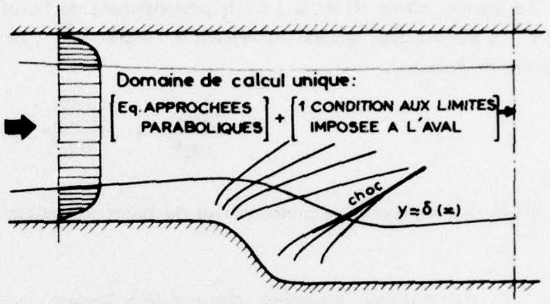

Fig. 5 – Equations de Navier Stokes tronquées.

La parabolisation tantôt complète tantôt partielle des équations de Navier-Stokes présente avec la couche limite l'analogie de privilégier une direction dite longitudinale, où les effets de diffusion matérialisés par les termes de dérivées secondes sont négligés. Cette direction privilégiée [23, 24, 25] est rattachée par exemple à une composante dominante de la vitesse, à la présence d'une paroi, ou encore au choix des lignes de courant pour coordonnées. Si les équations ainsi définies sont paraboliques, le problème de conditions initiales obtenu n'est pas *toujours bien posé, et des simplifications* supplémentaires doivent être adjointes. Par rapport aux équations d'Euler, ces méthodes ajoutent au moins le terme dissipatif des équations de Prandtl. Par rapport à ces dernières, on tente dans la mesure des possibilités numériques de retenir au moins le comportement non visqueux du gradient de pression normal. A titre d'exemple, notons les équations utilisées par *Baum* [22] en supersonique, xOy étant un repère tangent à une paroi de courbure $K(x)$:

$$\left[\begin{array}{l} \dfrac{\partial \rho u}{\partial x} + \dfrac{\partial}{\partial y}\Big[(1+Ky)\rho v\Big] = 0 \\[2ex] \rho u \dfrac{\partial u}{\partial x} + (1+Ky)\rho v \dfrac{\partial u}{\partial y} + K\rho u v = -\dfrac{\partial p}{\partial x} + \dfrac{\partial}{\partial y}\Big[\mu(1+Ky)\dfrac{\partial u}{\partial y}\Big] \\[2ex] \rho u \dfrac{\partial v}{\partial x} + (1+Ky)\rho v \dfrac{\partial v}{\partial y} - K\rho u^2 = -(1+Ky)\dfrac{\partial p}{\partial y} \\[2ex] \rho u \dfrac{\partial H}{\partial x} + (1+Ky)\rho v \dfrac{\partial H}{\partial y} = \dfrac{\partial}{\partial y}\Big[\mu(1+Ky)\dfrac{\partial H}{\partial y}\Big] \end{array}\right.$$

Les difficultés rencontrées dans la résolution de tels systèmes d'équations par une intégration simple de l'amont vers l'aval provient des régions subsoniques. Dans le cas d'un écoulement totalement subsonique, *Spalding* [26] remarque que l'ellipticité du problème ne porte cependant que sur la variable pression et que, celle-ci figée, le problème de conditions initiales est bien posé d'amont en aval. Il suggère alors une remise en cause itérative de la pression au cours de balayages amont-aval, où seul le champ de pression est stocké en mémoire, et où l'influence de l'aval sur l'amont est prise en compte par une technique spéciale de correction de la pression, décentrée vers l'amont. Une autre technique d'itération est également suggérée par *Mahgoub* et *Bradshaw* [30] . Lorsque l'influence de l'aval est moins sévère, Spalding propose des techniques simplifiées, à la fois par la discrétisation *numérique et par le recours à des équations totalement parabolisées.* Pour des écoulements subsoniques confinés, l'artifice conduisant à ce résultat est fondé sur l'idée que, en se rapprochant au maximum d'un écoulement monodimensionnel, l'ellipticité pourra être restreinte au principe de conservation du débit global, et pourra dès lors être traitée comme un problème de condition initiale sitôt le débit amont fixé. Pratiquement, Spalding introduit à cet effet un léger dédoublement de la variable pression, dissociant celle qui pilote l'équation de mouvement longitudinal ainsi que la vitesse longitudinale, de la pression pilotant les autres équations, voir *réf.* [24].

Dans le cas supersonique, on doit noter avant tout que les couches limites introduisent toujours des régions subsoniques. La clé des règles d'influence paraît alors être indiquée par *Baum, Denison, Ohrenberger* [27, 25]. Ils montrent d'abord par passage aux variables de von Misès que des équations du type indiqué plus haut conduisent pour les termes de plus haut degré à une équation de la chaleur :

$$\frac{\partial Z}{\partial x} = A \frac{\partial^2 Z}{\partial \psi^2} \qquad Z = u^2 \qquad A = k\,\frac{Z^{1/2}}{M^2-1}$$

Le problème parabolisé est de ce fait mal posé dans les régions subsoniques des couches limites, $(A<0)$, ce qui indique qu'une influence de l'aval sur l'amont est présente dans les équations de Navier-Stokes, indépendamment des termes de dérivées secondes longitudinales $\partial^2/\partial x^2$, termes très petits et ici négligés. Baum se ramène à un problème parabolique bien posé dans ces régions subsoniques de paroi en appliquant des approximations semblables à la couche limite ordinaire, soit au premier ordre $\partial p/\partial y = 0$ soit au second $\partial p/\partial y = K\rho u^2$. Cette simplification, appliquée aux seules régions subsoniques, permet l'intégration d'amont en aval. Le problème reste cependant encore mal posé, au sens où des **solutions de branchement** divergentes apparaissent pour des perturbations infinitésimales des conditions initiales, selon un processus similaire aux couplages des équations de Prandtl et des équations d'Euler supersoniques, (voir section 2.3). Dans le cas présent, le phénomène doit sans doute résulter d'un effet de couplage entre les deux problèmes paraboliques bien posés que constituent les régions subsoniques et supersoniques. Ce phénomène est favorable car il montre qu'en dépit des approximations faites, le modèle retenu contient non seulement des solutions d'où l'influence de l'aval est exclue, *mais aussi des solutions où celle-ci est présente indépendamment de tous courants de retour.* Lorsqu'elle existe, l'influence de l'aval doit être pilotée par une condition aux limites spéciale, qui peut par exemple être la pression $p(1)$ dans le cas de la plaque plane supersonique de longueur unité (Fig. 6). Si le domaine de calcul est suffisamment étendu vers l'amont, cette condition peut même en pratique être **excédentaire**, car son influence sur l'amont possède une décroissance exponentielle. La parabolisation des équations montre donc qu'à grand Reynolds l'influence de l'aval sur l'amont dans les équations de Navier-Stokes n'est dominée ni par les termes en $\partial^2/\partial x^2$, ni par les termes de gradient de pression normaux des régions subsoniques. La *solution parabolisée exempte d'influence de l'aval est l'**enveloppe** des précédentes, figurée en pointillés sur* la figure 6. Sa détermination numérique en tant que telle demande des tâtonnements laborieux. On a pu montrer [25] qu'elle peut être obtenue directement, à la simple condition de discrétiser le terme $\partial p/\partial x$ dans les régions subsoniques par des schémas ne faisant appel qu'aux points situés en amont de l'abscisse de calcul. Indiquons enfin que la résolution d'équations de Navier-Stokes tronquées peut être recherchée dans une extension de la méthode des caractéristiques ; on se reportera à [28] bien que les problèmes de couplage et de branchement n'y soient pas encore résolus.

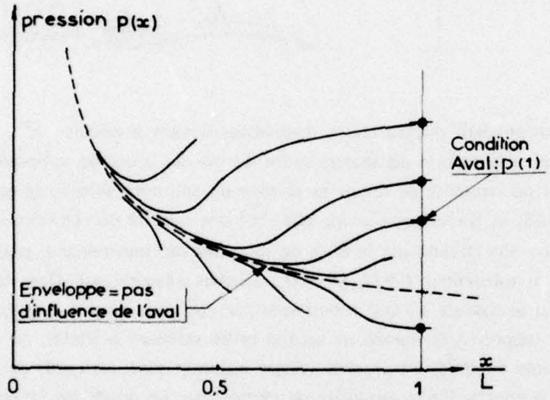

Fig. 6 – Aspect des solutions de branchement en supersonique.

1.4. Couplage classique : couche dissipative en forte interaction

L'écoulement de fluide parfait est ici perturbé uniquement dans ses conditions aux limites, de même que dans le couplage numérique à un domaine Navier-Stokes. Toutefois, les conditions de couplage imposées étant plus faibles, il est ici possible de raccorder en toute région les équations d'Euler à d'autres équations sans faire apparaître d'inconsistance. Cette propriété est exploitée pour limiter les zones dissipatives au strict minimum, en s'appuyant sur les frontières physiques habituelles $y = \delta(x)$ des couches limites. Le domaine de fluide parfait peut, ou non, avoir pour frontières les lignes $y = \delta(x)$, mais il doit toujours les inclure. Le couplage est fort au sens où il n'est restreint ni à la procédure hiérarchisée, ni aux ordres de grandeurs de l'interaction faible (voir section 1.1). Les couches dissipatives peuvent inclure des bulles de décollement.

Indépendamment de l'approximation d'Euler au delà de $y = \delta(x)$, toute simplification est fondée sur la petitesse de l'épaisseur δ . On applique ainsi aux couches dissipatives tantôt des équations de Navier-Stokes parabolisées dans la direction longitudinale Ox , tantôt les équations de Prandtl, tantôt les formes intégrales de ces mêmes équations. La formulation des conditions de couplage la plus simple est rappelée figure 7. On imagine une frontière libre $y = \delta(x)$ où sont raccordées les variables communes aux deux domaines, le transfert de masse étant possible le long de $\delta(x)$ au profit de la couche limite. Il existe en δ une discontinuité des dérivées partielles qui disparaît seulement à la limite $R \to \infty$. *La consistance avec les analyses asymptotique* dépend des équations retenues par la couche dissipative, et sera évoquée plus bas pour celles de Prandtl. Le couplage en vitesse normale est encore souvent écrit au moyen d'une épaisseur de déplacement. Les variables de couche limite étant barrées, on a dans le repère de paroi xOy ; la courbure de la paroi étant $K(x)$:

$$\left[\!\!\left[\begin{array}{ll} & \left[\dfrac{v}{u}\right]_{(x,\delta)} = \left\{\dfrac{d\delta^*}{dx} - (\delta - \delta^*) \cdot \left[\dfrac{1}{\rho u} \cdot \dfrac{d\rho u}{dx}\right]_{(x,\delta)}\right\} \cdot \dfrac{1}{1 + K\delta} \\ \text{si} & \delta^* \cdot [\rho u]_{(x,\delta)} = \displaystyle\int_0^{\delta} \left[\rho u_{(x,\delta)} - \bar{\rho}\bar{u}_{(x,y)}\right] \cdot dy \qquad \bar{u}(x,\delta) = u(x,\delta) \end{array}\right.$$

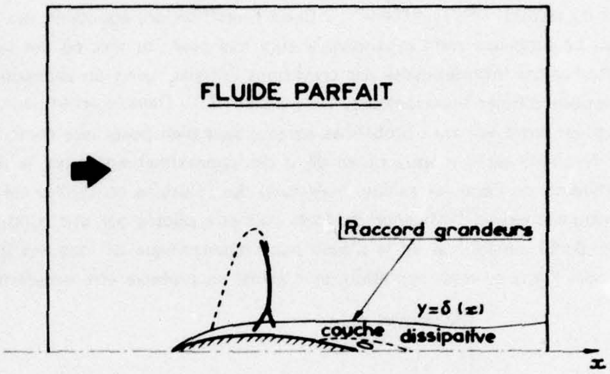

Fig. 7 – Couplage classique : couche dissipative en forte interaction (profil symétrique).

Cette relation est exacte, et toute approximation provient des *équations dissipatives servant à calculer* δ^* *.* Même s'il s'agit des équations de Prandtl, la méthode ne se réduit pas à la théorie du second ordre du fait du couplage, supposé fort et non hiérarchisé. Elle traite l'influence transmise de l'aval par les courants de retour et élimine les solutions singulières au point de décollement (R fini). *Crocco, Lees, Klineberg* [31, 32, 33] et *Weinbaum-Garvine* [34, 35] ont montré qu'elle contient encore *une influence de l'aval sur l'amont en régime supersonique non décollé* par le biais de solutions de branchement, pourvu que la couche limite se comporte comme un tube de courant subsonique ($dp/d\delta^* > 0$, couches subcritiques). Dans le cas contraire (supercritique), cet effet de couplage disparaît et seul le passage à l'état subcritique par des sauts de pression discontinus autorise l'influence de l'aval. Ces éléments nouveaux par rapport à *la théorie de second ordre suffisent à traiter, au moins qualitativement,* le décollement, l'interaction couche limite-onde de choc, les proches sillages supersoniques, les bords de fuite, etc. . .
Les premières méthodes, citées plus haut, traitaient la couche limite laminaire de Prandtl par ses équations intégrales dynamiques et thermiques, voir [38]. L'adjonction d'une équation intégrale auxiliaire (énergie cinétique) permettait d'utiliser les *relations intégrales des solutions de similitude sans faire l'hypothèse que l'écoulement soit localement semblable.* Le fluide parfait supersonique, enfin, était réduit à une onde simple. Généralement subcritiques pour une paroi adiabatique, les configurations pouvaient être rendues supercritiques pour des parois très refroidies. Ce résultat semble maintenant inexact à la lumière de traitements plus raffinés des équations de Prandtl [36], *mais l'erreur affecte essentiellement le voisinage immédiat* du saut de pression anormal de ces résolutions. Les configurations supercritiques deviennent en revanche plausibles dans le cas turbulent où elles constituent la situation la plus fréquente, et il nous semble [37] que les sauts de pression de ces solutions sont alors en rapport avec une pénétration des ondes de choc dans la couche limite. Ajoutons enfin que diverses variantes ont été proposées pour le traitement intégral des équations de Prandtl, voir par exemple [46, 47].

Globalement, les résultats des méthodes intégrales supersoniques laminaires sont très favorables [39 , 40], sauf pour la prédiction des flux de chaleur. *Leur transposition directe au cas turbulent,* dont on trouvera une revue détaillée dans [41] est moins satisfaisante. Les méthodes ont été étendues aux problèmes subsoniques et transsoniques par *Klineberg* et *Steger* [42] en utilisant une méthode de résolution itérative du fluide parfait et de la couche limite. Des méthodes de même nature résolvant les équations de Prandtl par différences finies ont aussi été établies, en supersonique puis en subsonique, voir par exemple [43, 44, 45]. Le perfectionnement de ces méthodes grâce à des équations plus complètes que celles de Prandtl a fait l'objet de diverses études. Notons la recherche d'une méthode intégrale laminaire précise au second ordre par *Crocco* [48], l'introduction d'un gradient de pression normal dans des méthodes aux différences [27, 28, 30], la subdivision de la couche limite en une couche rotationnelle non visqueuse *et une sous-couche* de Prandtl [36, 49, 50]. On doit remarquer que cette dernière solution est une simplification de la précédente, et que son investigation est demeurée imparfaite dans le choix de la sous-couche. Mentionnons enfin qu'il est possible de modéliser un gradient de pression normal dans les méthodes intégrales. On se reportera à l'analyse donnée par *Holden* [38], voir aussi [51, 52]. Le résultat le plus intéressant *dans une telle approche* est alors la disparition des comportements laminaires supercritiques, ainsi que des sauts de pression qui leur sont associés lorsque $\partial p/\partial y = 0$.

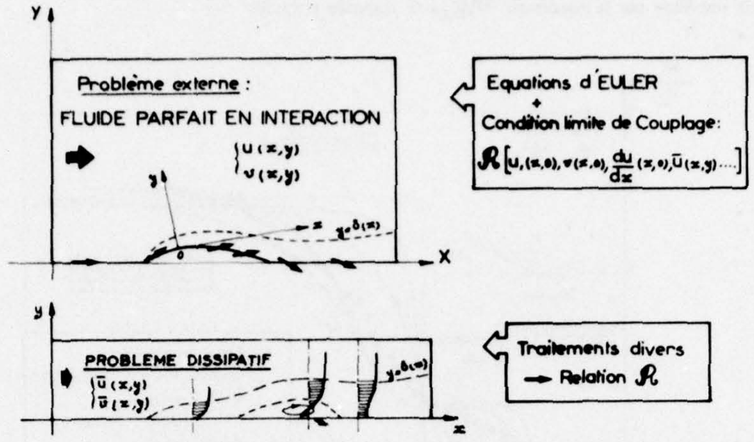

Fig. 8 – Couplage classique : option du fluide parfait prolongé à la paroi.

L'inclusion d'une équation de quantité de mouvement normale dans les méthodes intégrales constitue cependant leur élément le plus arbitraire, attaché à un choix sommaire de profils de pression statique $p(y)$. Nous pensons qu'il est pour cette raison plus satisfaisant et plus simple d'approcher $p(y)$ en prolongeant le calcul de fluide irrotationnel externe à l'intérieur de la couche limite $[0 < y < \delta(x)]$. Tacitement, ce procédé est utilisé de longue date en calculant les effets visqueux par glissement du fluide parfait sur l'épaisseur de déplacement. Il ignore l'influence des effets rotationnels sur la pression statique mais fournit, régime hypersonique exclu, une bonne estimation de celle-ci dans la région externe de la couche dissipative, où le gradient normal prend effectivement de l'importance. D'un point de vue pratique, le formalisme des méthodes intégrales à $\partial p/\partial y = 0$ peut alors être conservé. On résoud les équations de bilans globaux dans la direction longitudinale sans ajouter de termes nouveaux par rapport aux équations de Prandtl, mais, au lieu de piloter les équations par le pression externe $p[x, \delta(x)]$, le gradient de pression longitudinal est relevé dans le prolongement fictif du fluide parfait, le long de sa frontière, placée à la cote $y = Y(x)$ de la paroi. Dans le cas subsonique, le prolongement du fluide parfait jusqu'à la *surface de déplacement* $[Y(x) = \delta^*(x)]$ *peut suffire*, et une étude expérimentale détaillée [53] du recollement subsonique derrière une marche nous a montré que le champ de pression réel $\bar{p}(x, y)$, l'épaisseur de quantité de mouvement δ^{**}, et ce paramètre de forme H, vérifient indifféremment les deux équations globales :

$$\left[\begin{array}{l} \dfrac{d\delta^{**}}{dx} + \delta^{**}\cdot(H+2)\left[\dfrac{1}{u}\dfrac{du}{dx}\right]_{(x,\delta)} = \dfrac{C_f}{2} + \left(\dfrac{1}{\rho u^2}\right)_{(x,\delta)}\cdot\dfrac{d}{dx}\left\{\displaystyle\int_0^{\delta}\left[\bar{P}(x,y) - P(x,\delta)\right]dy\right\} \\[2ex] \dfrac{d\delta^{**}}{dx} + \delta^{**}\cdot(H+2)\left[\dfrac{1}{u}\dfrac{du}{dx}\right]_{(x,\delta^*)} = \dfrac{C_f}{2} \end{array}\right.$$

la vitesse de fluide parfait prolongée $u(x, \delta^*)$ étant calculée en admettant que $p(x,\delta^*) \simeq \bar{p}(x,0)$. En supersonique, nous avons montré [37] que le prolongement du fluide parfait doit être effectué jusqu'à la paroi $[Y(x) = 0]$, et que de cette manière on *acquiert la certitude d'éliminer dans tous les cas les comportements supercritiques qui seraient présents avec les mêmes équations en* conservant $Y = \delta(x)$. Dans ces cas difficiles où des sauts de pression supercritiques-subcritiques sont présents dans le fluide parfait en $Y = \delta(x)$, la distribution de pression continue $p(x, 0)$, obtenue dans le calcul couplé par prolongement du fluide parfait en $Y = 0$, *peut toutefois s'écarter encore de la pression effective à la paroi* $\bar{p}(x, 0)$. *La correction nécessaire* $[p(x,0) - \bar{p}(x,0)]$ peut alors être calculée à posteriori au moyen des équations de quantité de mouvement normales visqueuses et non visqueuses, ainsi simplifiées :

$$\left[\begin{array}{l} \dfrac{\partial p}{\partial y} = K\rho u^2 \qquad \dfrac{\partial \bar{p}}{\partial y} = K\bar{\rho}\bar{u}^2 \qquad K \simeq K(x) \simeq \dfrac{d}{dx}\left[\dfrac{v}{u}\right]_{(x,0)} \\[2ex] p(x,0) - \bar{p}(x,0) \simeq (\delta^* + \delta^{**})\cdot\left[\rho u^2\cdot\dfrac{d}{dx}\left(\dfrac{v}{u}\right)\right]_{(x,0)} \end{array}\right.$$

Nous avons pu [54] sur ces bases à peine plus complexes que les méthodes classiques de Lees-Reeves-Klineberg, traiter le problème *du décollement turbulent sur une rampe supersonique avec un résultat* semble-t-il *assez compétitif par rapport aux solutions* Navier-

Stokes actuelles (Fig. 9). L'équation de l'entraînement est utilisée pour équation intégrale auxiliaire. L'interaction, partout subcritique, est directement stabilisée par la condition $dp/dx = 0$ imposée à l'aval.

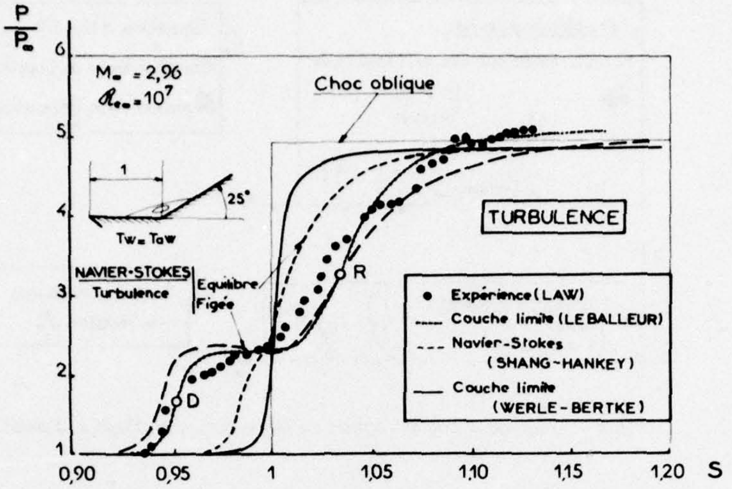

Fig. 9 – Interaction choc-couche limite turbulente (rampe supersonique).

Le prolongement du calcul de fluide parfait à l'intérieur de la couche dissipative demande un réexamen de la formulation du problème couplé, schématisé figure 8 pour l'option du "couplage à la paroi". Excepté en présence de couches dissipatives libres (sillages), la géométrie du domaine de fluide parfait est connue, et la difficulté associée au positionnement de la surface libre $y = \delta(x)$ est éliminée. Cette simplification a été mise à profit pour les calculs transsoniques de profils [55, 16]. Le problème de fluide parfait est inusuel dans la mesure où ses conditions aux limites ne sont ni de type direct $[\,v(x, o)$ connu$\,]$, ni de type inverse $[\,u(x, o)$ connu$\,]$. Les conditions de couplage sont a priori des relations complexes $\mathcal{R}$, *liant les variables visqueuses et non* visqueuses du domaine $0 < y < \delta$, équivalentes à leur raccord au loin de la paroi, par exemple en $y = \delta$. La relation $\mathcal{R}$ déterminante pour le pour le problème de fluide parfait assure le raccord des vitesses normales. Elle est habituellement condensée en introduisant une épaisseur de déplacement. Si on adopte pour celle-ci une définition conventionnelle, la condition de couplage à la paroi est déduite du raccordement en δ, des équations de continuité visqueuses et non-visqueuses, et de développement de Taylor des grandeurs non-visqueuses. Si $0 < Y(x) < \delta(x)$:

$$\left\|\begin{array}{ll} \delta^* . \left[\rho u\right]_{(x,Y)} & = \displaystyle\int_0^\delta \left[\rho u_{(x,Y)} - \bar{\rho}\,\bar{u}_{(x,y)}\right] . dy \\ \left[\dfrac{v}{u}\right]_{(x,Y)} & = \dfrac{d\delta^*}{dx} + (Y - \delta^*) . \left[\dfrac{1}{\rho u}\,\dfrac{d\rho u}{dx}\right]_{(x,Y)} + \cdots\cdot \end{array}\right.$$

On retrouve dans les deux premiers termes du développement les conditions classiques de glissement sur la surface de déplacement, ou de source équivalente à la paroi :

$$\left[\rho v\right]_{(x,0)} = \frac{d}{dx}\left[\rho u\,\delta^*\right]_{(x,0)} + \cdots\cdot$$

Le développement limité est consistant asymptotiquement ($R \to \infty$) avec la théorie du second ordre. Nous avons montré [37] qu'il l'est aussi avec la triple couche laminaire, ce qui paraît valider son emploi pour des interactions fortes. On doit enfin remarquer que la condition de source à la paroi précédente n'est approximative qu'en raison de la définition conventionnelle choisie pour δ^*.

Une définition plus générale prend en compte la variation suivant Oy de l'écoulement non visqueux :

$$\left|\begin{array}{l} \delta^* . \left[\rho u\right]_{(x,0)} = \displaystyle\lim_{\bar{y} \to \infty} \int_0^{\bar{y}} \left[\rho u_{(x,y)} - \bar{\rho}\bar{u}_{(x,y)}\right] . dy \\ \left[\dfrac{v}{u}\right]_{(x,0)} = \dfrac{d\delta^*}{dx} + \delta^* . \left[\dfrac{1}{\rho u}\,\dfrac{\partial \rho u}{\partial x}\right]_{(x,0)} \end{array}\right.$$

Cette relation est **rigoureuse**, ne fait appel qu'aux équations de continuité visqueuses et non visqueuses, à l'adhérence visqueuse $\overline{v}(x, o) = o$, et au raccordement :

$$o = \lim_{y \to \infty} \left[\rho u_{(x,y)} - \overline{\rho}\overline{u}_{(x,y)} \right] = \lim_{y \to \infty} \left[\rho v_{(x,y)} - \overline{\rho}\overline{v}_{(x,y)} \right]$$

Elle est applicable quelles que soient les équations dynamiques et thermiques du domaine visqueux, et même si le repère xOy n'est pas tangent à la paroi. Globalement, sachant que $d\delta^*/dx$ dépend essentiellement de $\left[\frac{du}{dx}\right]_{(x,o)}$, la condition aux limites de couplage à la paroi est du type :

$$\mathcal{R} \left[v_{(x,o)} \ , \left(\frac{du}{dx}\right)_{(x,o)} \right] = 0$$

On aurait pu attendre une relation symétrique en u et v, $\mathcal{R}\left[u_{(x,o)}, v_{(x,o)}\right]$. La relation dissymétrique réelle provient du changement d'échelle en y inhérent au phénomène physique de couche dissipative, indépendamment des équations utilisées pour la calculer.

3.2.1.5. Méthodes simplifiées

Signalons pour terminer l'existence de méthodes très simplifiées dans la prise en compte des effets visqueux, pour des écoulements où les techniques précédentes sont encore peu développées, comme les écoulements présentant des décollements généralisés. Les approximations sont généralements fondées sur les équations de Prandtl pour la prédiction des points de séparation, et sur des modélisations très spécifiques des décollements. On peut par exemple rechercher la frontière d'une eau morte isobare, ou encore modéliser le sillage d'un profil décroché comme un jet libre issu d'une répartition prédéterminée de sources $v(x, o)$, disposées sur les régions décollées du profil. On renvoit dans ce cas à quatre méthodes typiques [56, 57, 58, 59]. Outre leur manque de généralité, ces méthodes sont surtout insuffisantes au voisinage des points de séparation.

Remarquons enfin que des approximations de même nature sont souvent insérées dans les méthodes évoquées en 1.4. Dans le cas du profil transsonique on note par exemple l'absence de calcul du sillage [60, 61] l'ajustement empirique de la pression au voisinage du bord de fuite [60], la modélisation de δ^* pour des décollements légers [61], le traitement sommaire de l'interaction couche limite - onde de choc par étalement arbitraire de la compression [16, 55, 60, 61], le recours à des méthodes numériques non conservatives [55, 60, 61].

2. Progrès dans l'analyse "Fluide Parfait – Equations de Prandtl"

2.1. Inclusion des modèles asymptotiques ($R \to \infty$)

Remarquons tout d'abord que la consistance des méthodes de calcul avec ces modèles n'est pas indispensable, puisque dans les applications R est toujours fini. Elle fournit néanmoins un guide mathématique pour l'approximation et l'estimation de l'erreur, ainsi que pour la hiérarchisation des diverses échelles de longueur. Notons que si l'échelle δ ne pouvait être reliée à R^{-1}, il serait alors nécessaire pour définir les lois de similitudes de faire appel, comme l'a suggéré *Rom* [62], à deux nombres de Reynolds distincts, R et $(\delta . R)$. Les effets d'un changement d'échelle de la couche dissipative δ, et d'un changement de pression génératrice par exemple, ne seraient alors plus semblables. La même question pourrait se poser à propos des échelles de turbulence, si les conditions **initiales** étaient choisies hors de l'équilibre $\left[\delta \neq \mathcal{O}\left(\frac{1}{\text{Log} R}\right)\right]$.

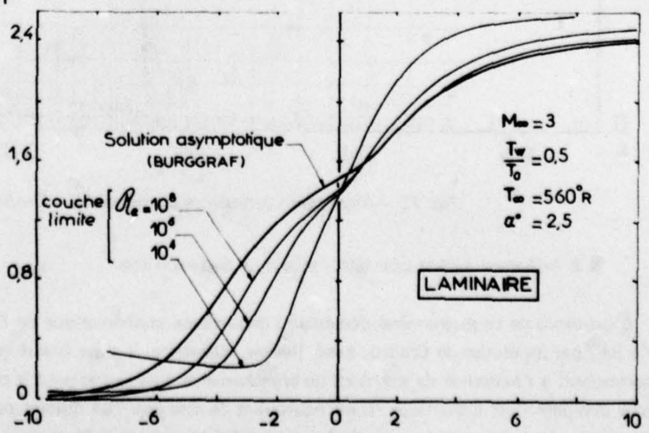

Fig. 10 – Rampe supersonique décollée – Comportement asymptotique (Vatsa - Werle).

En laminaire, un progrès longtemps controversé a été de voir que l'usage des équations de Prandtl avec un couplage fort (itération sur δ^*) suffit à sortir des limites de la théorie du second ordre, et à inclure des modèles asymptotiques plus complets, voir [9, 10]. Le plus notable est la triple couche, dont on peut vérifier que ses équations sont incluses dans celles de Prandtl [63], et pour laquelle le glissement sur la surface δ^* conventionnelle est consistant [37]. *Werlé, Vatsa, Burggraf* [63] se sont de plus assurés numériquement de la convergence uniforme des deux approches lorsque $R \to \infty$ (Fig. 10). Outre les problèmes de décollement supersonique, l'inclusion de la structure en triple couche est une garantie pour le bord de fuite laminaire [16], décollement naissant inclus. Pour le bord de fuite turbulent, il semble qu'une inconsistance [16] apparaisse à l'ordre $\delta^{3/2}$ (lorsque $\delta \to 0, R \to \infty$), voir section 1.1.

2.2. Adaptation aux écoulements complexes — Profil transsonique

Initialement réservées aux écoulements supersoniques par onde simple à décollement unique, les progrès des méthodes numériques (section 3) ont permis l'adaptation aux décollements multiples supersoniques [64] *ainsi qu'aux écoulements très généraux des méthodes de relaxation pour l'équation du potentiel.* La figure 11 rappelle la méthode proposée par *Melnik, Chow, Mead* [16] pour l'exemple typique du profil portant turbulent non décollé. Elle illustre la possibilité pratique de réunir sous une même modélisation des phénomènes divers (couche limite, bord de fuite, sillage . . .), et de résoudre le problème de fluide parfait ainsi perturbé sans qu'une connaissance initiale sur la solution ne soit nécessaire. Sur le profil, les effets visqueux sont pris en compte par une vitesse normale non nulle. Le sillage se manifeste par une coupure introduisant des sauts de vitesses normales et tangentielles, *traduisant respectivement les effets d'épaisseur et de courbure de la couche dissipative. On a enfin schématisé par des fonctions correctrices* F, G, H, *les modifications apportées par Melnik au voisinage du bord de fuite, modifications résultant d'une analyse asymptotique locale.* Nous avons montré dans le cas non portant [54] que ce type de méthode peut être enrichi d'un traitement des bulles de décollements, et d'une prise en compte "objective" de l'interaction couche limite - onde de choc, moyennant une adaptation locale des maillages à l'échelle de la couche limite, et l'usage d'un calcul non-visqueux conservatif (Fig. 12).

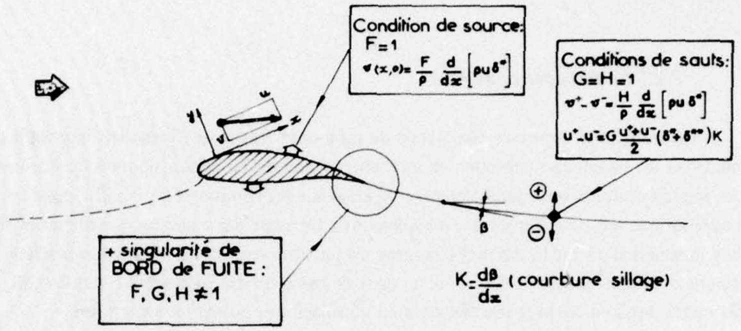

Fig. 11 — Conditions de couplage — Profil portant turbulent non décollé (Melnik - Chow - Mead).

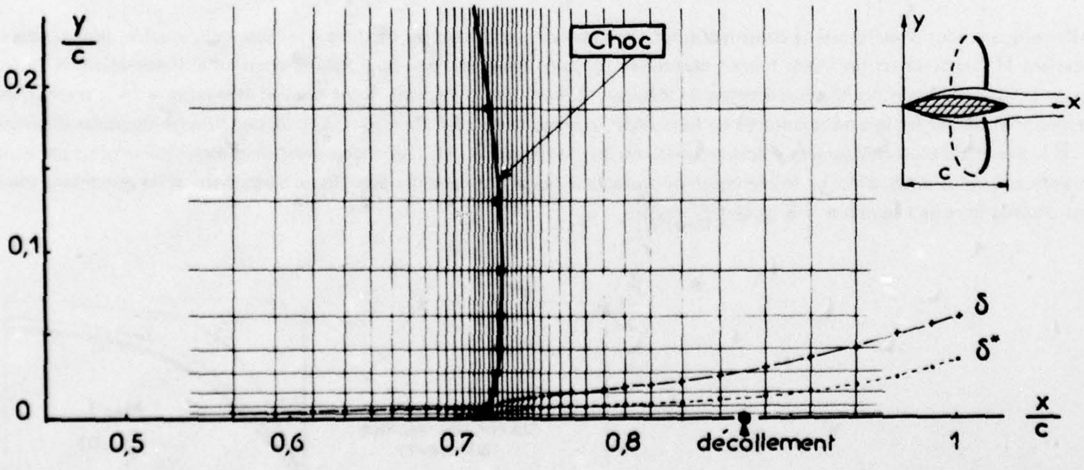

Fig. 12 — Interaction turbulente transsonique — Profil symétrique (petites perturbations).

2.3. Influence amont sans décollement en supersonique

L'existence de ce phénomène démontre l'importance mathématique de l'effet de couplage dans un calcul visqueux-non visqueux. Mis à jour par les études de Crocco, Lees, Reeves, Klineberg, il a été étudié en particulier par *Neiland, Garvine, Weinbaum* [34, 35], et correspond à l'existence de solutions de branchements divergentes pour le problème de conditions initiales, toutes les fois que la couche dissipative est subcritique. Il est équivalent de dire que l'on obtient paradoxalement un problème de conditions initiales mal posé par couplage d'équations hyperboliques et paraboliques, et qu'il doit être remplacé par un problème aux limites comportant une condition à l'aval (Fig. 6). On pourra se reporter à [37]. Indiquons qu'il s'agit d'un phénomème contenu dans des équations linéaires, qui résulte de la forme particulière de la relation de couplage $\mathcal{R}$ évoquée section 1.4. Posant $\theta = v/u$ et notant $\overline{M}$ le nombre de Mach visqueux, on obtient en intégrant les équations de Prandtl de $y=0$ à $y=\delta$ avec $\theta(x,0)=0$:

$$\theta(x,\delta) = B\,\frac{dp}{dx} + C \qquad B = \int_0^\delta \frac{1-\overline{M}^2}{\gamma p \overline{M}^2}\,dy \qquad C = \int_0^\delta \frac{1+(\gamma-1)\overline{M}^2}{\gamma p \overline{M}^2}\,\frac{\partial \overline{\tau}}{\partial y}\,dy$$

L'expression de C correspond au cas isoénergétique, et la singularité associée à $\overline{M}=0$ sera ici laissée de côté. De même, dans *une méthode intégrale, la condition aux limites imposée au fluide parfait s'écrit schématiquement, voir [37] :*

$$D_1 \cdot \theta_{(x,0)} = \delta^{**} \cdot D_2 \cdot \left[\frac{dp}{dx}\right]_{(x,0)} + D_3$$

où D_1, D_2, D_3 dépendent du nombre de Mach dans le fluide parfait $M(x,0)$ ainsi que de l'état local de la couche limite. L'annulation de D_1 correspond à la singularité de décollement, celle de D_2 aux points critiques de Crocco, Lees. L'élément important est le caractère quasi-linéaire entre θ et dp/dx de ces relations. Si le fluide parfait supersonique est une onde simple, il en résulte :

$$\sqrt{A} \cdot \frac{dp}{dx} = \frac{d\theta}{dx} \quad \text{(Fluide Parfait)} \qquad \sqrt{A} = \frac{1}{\gamma p M^2}\sqrt{M^2-1}$$

$$\theta = \frac{B}{\sqrt{A}} \cdot \frac{d\theta}{dx} + C \quad \text{(Eq. d'interaction)}$$

La solution linéarisée locale $\theta = C + k \cdot e^{\frac{\sqrt{A}}{B} x}$ explique les solutions de branchement divergentes lorsque $B>0$ (ou encore $D_1 . D_2 > 0$). Dans le cas d'un sillage supersonique où $\overline{M}(x,y)$ ne s'annule pas, l'intégrale B peut servir à caractériser le comportement subcritique ($B>0$) ou supercritique ($B<0$) et remplacer la définition de Crocco, Lees. Toutes les fois qu'une configuration est subcritique, la solution doit être stabilisée par une condition imposée à l'aval, ayant une **influence** décroissante **vers l'amont** (branchement). Si la région subcritique se poursuit à l'aval par une région supercritique, la condition sera celle de régularité au col (point critique) séparant les deux régions. Il s'agit de $\theta = C$ ou $\theta = D_3/D_1$ dans l'analyse ci-dessus. Si la région subcritique se prolonge à l'infini aval, la condition généralement choisie sera d'imposer le retour à la solution asymptotique d'interaction faible, c'est-à-dire $dp/dx = 0$ dans le cas de la rampe supersonique. Il est enfin important de noter que le signe de B est tributaire de l'épaisseur physique δ de la couche dissipative. Nous avons indiqué [37] que l'incertitude associée devait être évitée en s'attachant à la relation $\mathcal{R}$ effectivement appliquée au fluide parfait sur sa frontière. On redéfinit alors une nouvelle intégrale B qui diffère selon que la frontière est en δ , en δ^* , ou à la paroi. Dans ce dernier cas :

$$B = \lim_{\overline{y}\to\infty} \int_0^{\overline{y}} \frac{M(x,y) - \overline{M}(x,y)}{\gamma p M^2 \overline{M}^2}\,dy \qquad \left[\begin{array}{ll} M(x,y) : & \text{non-visqueux} \\ \overline{M}(x,y) : & \text{visqueux} \end{array}\right.$$

Cette expression garantit des interactions toujours subcritiques ($B>0$), le modèle de couplage devenant ainsi toujours elliptique, comme les équations de Navier-Stokes elles-mêmes.

2.4. Décollement – Singularité et influence amont

Une partie des difficultés associées au décollement provient des analyses asymptotiques. Pour l'interaction faible, la pression est imposée aux équations de Prandtl qui manifestent alors une singularité en racine carrée [6] au voisinage du point de frottement nul, $\left(\frac{\partial \tau}{\partial x}\right)_{y=0}$, $\frac{d\delta^*}{dx}$, $(v)_{y=\delta}$ ..... n'étant pas bornés. Dans le cas laminaire incompressible, la dérivation des équations locales fournit à la paroi :

$$\tau \cdot \frac{\partial \tau}{\partial x} = \nu \cdot \frac{\partial^4 u}{\partial y^4} \qquad \text{avec} \qquad \tau = \nu \cdot \frac{\partial u}{\partial y}$$

La singularité ne disparaît que si $\left(\frac{\partial^4 u}{\partial y^4}\right)_{y=0}$ s'annule au décollement, ce qui ne peut être le cas pour une distribution amont $p(x)$ quelconque. Une image de cette singularité est aussi présente dans les méthodes intégrales usuelles [37], la condition de régularité aux points correspondants étant de la forme :

$$\delta^{**} \cdot \frac{dp}{dx} = \text{cste} = -\frac{D_3}{D_2}$$

La singularité disparaît sitôt le couplage fort des équations de Prandtl au fluide parfait rétabli, puisque l'histoire amont $p(x)$ de la pression est influencée par la région décollée, *y compris en régime supersonique* (section 2.3), et que les conditions de singularité énoncées ci-dessus peuvent être satisfaites. A la limite $R \to \infty$, le modèle en triple couche fournit de cette façon des solutions décollées, mais le franchissement du "point de séparation" n'est pas réglé, puisque la triple couche toute entière se réduit à un point si $R \to \infty$. Cette difficulté asymptotique disparaît dans les calculs pratiques où R est fini, et où des couches limites insérant des bulles de décollement peuvent être résolues. La comparaison aux solutions Navier-Stokes est favorable (Fig. 13), et l'on peut en outre démontrer que les solutions régulières, Navier-Stokes ou bien Prandtl, décollent de la paroi sous l'angle β tel que :

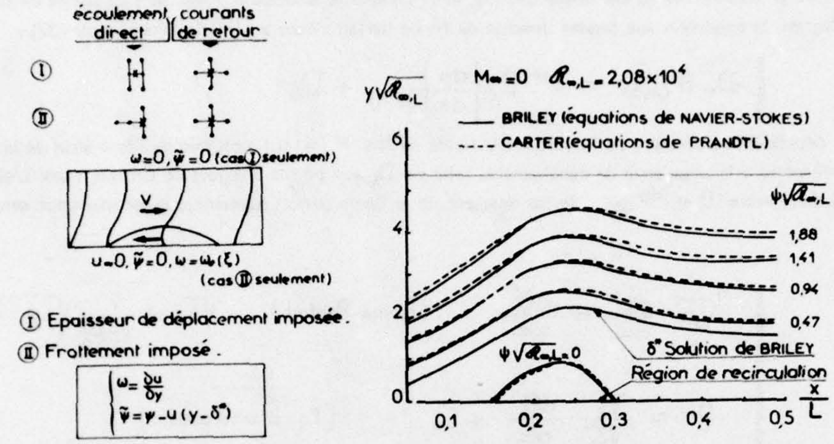

Fig. 13 – Décollement incompressible – Solution des équations de Prandtl (Carter).

$$\operatorname{tg} \beta = -\frac{3 \cdot \tau_x}{p_x} \qquad \text{avec} \quad \left[\begin{array}{ll} \tau_x = p_y & \text{Navier-Stokes} \\ \tau_x \neq p_y = 0 & \text{Prandtl} \end{array} \right.$$

Le problème couplé n'étant pas singulier, les difficultés numériques associées aux bulles décollées proviennent du souci de maintenir dissociés les calculs de fluide parfait et de couche limite. Trois solutions de couche limite ont été envisagées. La première résoud les équations de couche limite instationnaires [65] *pour une pression* $p(x)$ issue d'un calcul de fluide parfait stationnaire. *En principe, seul le respect* des conditions de compatibilité au point de décollement autorise un état stationnaire limite régulier, et la pression $p(x)$ doit être ajustée à cet effet. La seconde méthode consiste à développer des calculs classiques de couche limite stationnaire où $p(x)$ est donné (calculs directs). *Klineberg, Steger* [66] ont montré dans ce cas que le passage du point de décollement est numériquement hasardeux, même si la loi $p(x)$ imposée est effectivement celle qui, par une autre technique, sur le même maillage, avec les mêmes équations discrétisées, conduirait à une solution régulière. Il nous semble utile *dans l'exploitation* des calculs de couche limite classique au voisinage de $C_f = 0$ *de noter que l'obtention de ce point résulte plus souvent d'une divergence numérique que du* traitement de la singularité en racine carrée, et que de ce fait le décollement ne peut être "prédit" que si la divergence numérique renforce la décroissance de C_f. De plus, dans de nombreuses méthodes intégrales, la singularité et l'annulation de C_f ne coïncident pas rigoureusement. Une extension de ces calculs directs aux régions décollées a été suggérée par *Gay, Assassa* et *Pletcher, Dancey* [67]. Au lieu d'imposer $p(x)$, ils imposent la vitesse longitudinale externe $u(x)$, reliée à $p(x)$ par la relation de Bernouilli :

$$\frac{1}{\rho}\frac{dp}{dx} + \frac{1}{2}\left[u\frac{du}{dx} + v\frac{dv}{dx} \right]_{(x,\delta)} = 0$$

La pression $p(x)$ au voisinage du décollement peut ainsi être adaptée, puisque le terme $v\,\partial v/\partial x$, habituellement négligeable, deviendrait infini en cas de singularité. La troisième technique de calcul est dite *inverse*. La *régularité des solutions* est obtenue en faisant de $p(x)$ *un résultat du calcul, moyennant la donnée de* δ^* ou C_f par exemple [68, 66, 69]. Les méthodes précédentes [67] se rattachent *donc en fait à cette catégorie.* On renvoit à *Carter* [69] pour une analyse fine des changements de schémas numériques dans les régions de retour (influence aval), des itérations de relaxation, du maintien de la dominance diagonale des matrices dans le décollement, de la valeur de l'approximation "flare". Due à *Reyhner, Flüggelotz* [43], cette dernière consiste à négliger les termes convectifs $u\,\partial u/\partial x$ et $u\,\partial v/\partial x$ dans les zones de retour pour se ramener à un problème de conditions initiales. Voir aussi *Cebeci* [70]. La conclusion de Carter est de recommander la méthode à $\delta^*(x)$ fixé, celle-ci étant aisément introduite par *une transformation* de la fonction de courant ψ:

$$\tilde{\psi}(x,y) = \psi(x,y) - \bar{u}(x,y)\left[y - \delta^*(x)\right] \qquad \text{avec} \quad \tilde{\psi}(x,0) = \tilde{\psi}(x,\infty) = 0$$

Les méthodes de couche limite inverses traitent l'influence de l'aval convectée par les courants de retour, sauf dans l'approximation flare. La part essentielle de l'influence amont paraît dès lors contenue dans la condition aux limites imposée, $\delta^*(x)$, issue du couplage fort au fluide parfait. *L'effet de couplage semble ici de nouveau être* déterminant. Il y a en effet une forte présomption [44, 71, 70] pour que le calcul de couche limite direct à $p(x)$ fixé soit mal posé d'amont en aval dans les régions décollées, si l'approximation Flare ou bien si une méthode intégrale sont utilisées. L'examen d'une résolution intégrale instationnaire, à $p(x)$ fixé, nous a montré [37] que l'une des directions caractéristiques du système dans le plan (x,t) s'oriente vers l'amont dans les régions décollées. Il en résulte qu'une condition aval excédentaire doit être ajoutée lorsque le calcul n'inclut pas le recollement. S'il l'inclut, la condition est automatiquement remplacée par la condition de régularité des solutions au recollement, dont le rôle majeur est ainsi préservé.

2.5. Interaction couche limite - onde de choc

Les équations de Prandtl couplées n'éliminant aucune influence de l'aval sur l'amont (sections 2.3 et 2.4), le traitement de l'interaction couche limite - onde de choc est automatique à la double condition *que la discrétisation numérique soit à l'échelle des phénomènes, et* qu'elle préserve l'influence de l'aval. De plus, un progrès important dans la formulation des méthodes numériques récentes [44, 54, 64] permet de traiter des problèmes bien posés où les interactions peuvent être multiples et apparaissent d'elles-mêmes. Globalement, les *résultats quantitatifs paraissent fiables dans le cas laminaire* (Fig. 14). *Pour les méthodes intégrales turbulentes, l'amélioration de la for*mulation par prolongement du fluide parfait à la paroi apporte un progrès notable (Fig. 9 - 12), quantitativement et qualitativement (suppression des sauts de pression supercritiques). Pour les méthodes aux différences, outre les approximations de couplage et le traitement *des ondes de choc internes à la couche limite, les problèmes à faire progresser* touchent aux insuffisances des modélisations de la turbulence et de la transition, exactement comme dans le cas des équations de Navier-Stokes.

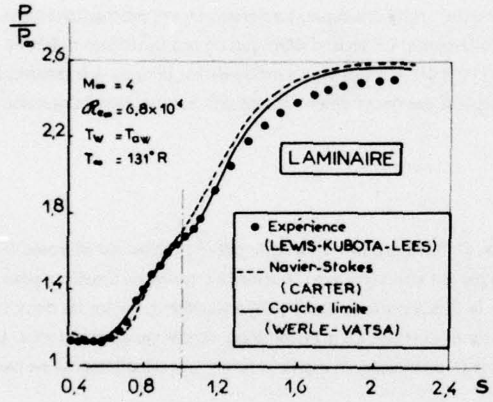

Fig. 14 — Interaction choc-couche limite laminaire : Rampe supersonique (Werle - Vatsa).

3. Progrès dans les méthodes numériques de couplage fort

3.1. Méthodes de tâtonnement en supersonique (Marching)

Le couplage des équations de Prandtl et d'Euler, aussi bien que la parabolisation des équations de Navier-Stokes, conduisent le plus souvent, en supersonique, à des problèmes de conditions initiales mal posés. Ils sont cependant faiblement mal posé, puisqu'une seule *condition stabilisatrice aval est généralement suffisante.* Rappelons ici que cette propriété a été largement exploitée dans les méthodes anciennes pour ignorer le problème aux limites et respecter la condition aval par tâtonnements successifs sur les conditions initiales. Celles-ci étaient connues à un paramètre de perturbation près, qui était traité comme une valeur propre. Son affinement progressif permettait d'intégrer de plus en plus loin vers l'aval le problème mal posé. Voir [27, 33, 43, 38]. La précision numérique nécessaire sur la valeur propre devenant souvent prohibitive, le domaine de calcul devait en pratique se réduire aux seules régions de fortes interaction visqueuse, supposées localisées à l'avance et traitées indépendamment l'une après l'autre. Dans le cas des méthodes intégrales où la condition aval était un point col (pt. critique), un premier progès applicable pour certains écoulements **simples** a été d'intégrer dans le plan de phase, en partant du col et en remontant vers l'amont (voir [41]). D'un point de vue pratique, le recours à ces techniques peut maintenant être évité.

3.2. Méthodes pseudo-instationnaires

Deux méthodes récentes de ce type doivent être notées. La première est suggérée par *Briley, Mc Donald* [65] pour les bulles de décollement en incompressible. Elle est fondée sur la résolution des équations instationnaires véritables de la couche limite. La méthode est pseudo-instationnaire car, à chaque pas de temps de couche limite, le fluide parfait est réajusté comme un écoulement stationnaire subissant l'effet de déplacement le plus récemment calculé. La technique n'est justifiée que par l'obtention de solutions stationnaires. Les résultats obtenus sur des maillages assez lâches paraissent encourageants, et sont peu altérés si les équations de couches limites sont remplacées par celles de Navier-Stokes. Les solutions de couche limite **non couplées** ont un comportement anormal dans la région décollée malgré l'approche instationnaire.

La seconde méthode est celle de *Werle, Vatsa* [44, 63, 64] pour les écoulements décollés supersoniques. *Le fluide parfait ne peut être* quelconque, son calcul étant réduit à une relation pression-déviation du type onde simple (Prandtl-Meyer, dièdre tangent . . .). La méthode résoud par différences finies les équations de Prandtl, couplées au fluide parfait prolongé jusqu'à la surface de déplacement. Par rapport aux méthodes supersoniques antérieures, l'apport fondamental de Werle, Vatsa *est d'abandonner les méthodes de tâtonnement*, et de résoudre directement un problème aux limites. Pour la rampe supersonique, la condition aux limites aval peut par exemple consister à égaler au dernier point $d\delta^*/dx$ à la pente de la rampe. Schématisant largement, le gradient de pression de la couche limite peut s'exprimer en fonction de $d^2\delta^*/dx^2$ *grâce à la relation de fluide parfait*, et donner :

$$\frac{\partial^2 u}{\partial y^2} + B_1(x,y) \cdot \frac{d^2\delta^*}{dx^2} = B_2(x,y)$$

Cette relation entre le profil de vitesse $u(x,y)$ et δ^* est rendue instationnaire, puis résolue par une méthode de direction alternée :

$$t^n \longrightarrow t^{n+\frac{1}{2}} \qquad \left(\frac{\partial^2 u}{\partial y^2}\right)^{n+\frac{1}{2}} + B_1^{n+\frac{1}{2}} \left[\left(\frac{d^2\delta^*}{dx^2}\right)^n - \frac{2}{\Delta t}\left(\delta^{*\,n+\frac{1}{2}} - \delta^{*\,n}\right)\right] = B_2^{n+\frac{1}{2}}$$

$$t^{n+\frac{1}{2}} \longrightarrow t^{n+1} \qquad \left(\frac{\partial^2 u}{\partial y^2}\right)^{n+\frac{1}{2}} + B_1^{n+\frac{1}{2}} \left[\left(\frac{d^2\delta^*}{dx^2}\right)^{n+1} - \frac{2}{\Delta t}\left(\delta^{*\,n+1} - \delta^{*\,n+\frac{1}{2}}\right)\right] = B_2^{n+\frac{1}{2}}$$

Le premier demi-pas de temps correspond à un calcul amont-aval de couche limite classique. La pression y est momentanément figée à celle du temps n et une procédure spéciale est requise pour passer les décollements. Le second demi-pas de temps diffuse d'amont en aval les variations de δ^*, donc de pression. La convergence est assez rapide (10 à 80 itérations). La méthode est la première technique supersonique opérationnelle d'un point de vue pratique, appliquée par exemple à des décollements *successifs sur une paroi sinusoïdale.*

3.3. Méthodes stationnaires itératives

L'idée est d'itérer sur les calculs stationnaires visqueux et non-visqueux. Dans l'itération directe, la pression $p(x)$ est imposée à la *couche limite qui calcule le déplacement* $\delta^*(x)$. Celle-ci appliquée au fluide parfait (calcul direct) fournit une nouvelle pression $p(x)$, etc . .. En cas d'usage d'une méthode de relaxation elle-même itérative pour le fluide parfait, *Lock* [55] a suggéré de mêler les deux itérations, et de calculer la couche limite, par exemple toutes les 10 itérations de relaxation. Le procédé n'est simple qu'en apparence. La pression doit être dérivée pour calculer la couche limite. La convergence n'est ni optimisée, ni même assurée. Les décollements ne peuvent être traités.

Brune, Rubbert, Nark [72] ont pour cette raison proposé de linéariser les calculs de fluide parfait et de couche limite au voisinage de l'itération n, et d'évaluer les matrices d'influence *correspondantes* $\mathcal{P}^n$ et $\mathcal{B}^n$. *Considérant les valeurs discrétisées* δ_i^{*n}, p_i^n *(fluide* parfait) et $\bar{\delta}_i^{*n}$, $\bar{p}_i^n$ (couche limite), on a :

$$\left[\begin{array}{ll} p_i - p_i^n = \mathcal{P}_{ij}^n \cdot (\delta_j^* - \delta_j^n) & \qquad \text{Fluide Parfait} \\ \bar{\delta}_i^* - \bar{\delta}_i^{*n} = \mathcal{B}_{ij}^n \cdot (\bar{p}_j - \bar{p}_j^n) & \qquad \text{Couche Limite} \end{array}\right.$$

Partant de valeurs δ_i^{*n}, $\bar{\delta}_i^{*n}$, p_i^n, $\bar{p}_i^n$ qui peuvent être distinctes pour le fluide parfait et la couche limite, on peut alors déterminer la solution exacte du problème couplé linéarisé δ_i^{*n+1}, p_i^{n+1}, qui s'exprime matriciellement par :

$$\left[\begin{array}{l} p^{n+1} = \bar{p}^{n+1} = p^n + \left(I - \mathcal{P}^n \cdot \mathcal{B}^n\right)^{-1} \cdot \left[\mathcal{P}^n \cdot (\bar{\delta}^{*n} - \delta^{*n}) + \mathcal{P}^n \cdot \mathcal{B}^n \cdot (p^n - \bar{p}^n)\right] \\ \delta^{*n+1} = \bar{\delta}^{*n+1} = \bar{\delta}^{*n} + \mathcal{B}^n \cdot \left[(p^n - \bar{p}^n) + (p^{n+1} - p^n)\right] \end{array}\right.$$

Deux nouveaux calculs de fluide parfait et de couche limite sont effectués avec pour conditions respectives δ^{*n+1} et $\bar{p}^{n+1}$. De *nouvelles matrices d'influences* $\mathcal{P}_{ij}^{n+1}$ et $\mathcal{B}_{ij}^{n+1}$ sont réestimées, etc . . . Si les effets de couplage sont faiblement non-linéaires, la convergence est rapide. Chaque itération est complexe.Elle demande l'inversion d'une matrice pleine ($I - \mathcal{P}^n \mathcal{B}^n$), et surtout l'estimation des matrices d'influences $\mathcal{P}^n$ et $\mathcal{B}^n$. Celle-ci requiert généralement la résolution par différences finies d'équations linéarisées de fluide parfait et de couche limite, en supplément des équations non-linéaires.

Une mise en œuvre plus simple est obtenue en perfectionnant l'itération directe évoquée plus haut. Si $U(x)$ et $\Theta(x)$ sont le module et la direction de la vitesse sur la frontière du fluide parfait, le problème à résoudre est une itération de point fixe s'écrivant après discrétisation :

$$\Theta_i^{n+1} = \mathcal{F}_i\left[\,\cdots\Theta_j\cdots\right]$$

L'opérateur $\mathcal{F}$ correspond à la succession d'un calcul de fluide parfait et de couche limite. La convergence de l'itération est liée aux valeurs propres de l'opérateur linéarisé vérifié par les petites perturbations θ_i :

$$\theta_i^{n+1} = F_{ij}\cdot\theta_j$$

Nous avons montré [54] par une analyse locale approchée du fluide parfait et de la couche limite, que les valeurs propres de F_{ij} *s'associent à des distributions* $\theta(x)$ *sinusoïdales, et qu'elles ont pour expression :*

$$\mu = \frac{-\lambda B}{\sqrt{1-M^2}}$$

λ : pulsation de $\theta(x)$
M : nombre de Mach local
B : fonction de la couche limite locale

La valeur $\mu(\lambda)$ de plus grand module correspond à la pulsation λ maximale que permettent le maillage en x ainsi que les schémas de discrétisation utilisés. On peut encore montrer que le caractère imaginaire de μ, en supersonique, autorise l'itération à propager vers l'amont les informations si $B>0$ (interaction subcritique). Il en résulte que la résolution directe d'un problème bien posé est possible, voir [54]. La connaissance du maximum de $\mu(\lambda)$ permet en outre de stabiliser le calcul en évaluant en tout point un coefficient de sous-relaxation ω_i^n :

$$\Theta^{n+1} = \Theta^n + \omega_i^n\cdot\left[\mathcal{F}_i\left(\cdots\Theta_j^n\cdots\right) - \Theta_i^n\right]$$

On peut montrer que $\omega_i \to 0$ si l'on se rapproche du point de décollement [54].

En cas de bulle décollée, le calcul de couche limite devient forcément inverse [$\Theta(x)$ connu, $U(x)$ calculé]. On peut alors lui associer un calcul de fluide parfait du type inverse [$U(x)$ connu, $\Theta(x)$ calculé] pour former une itération de point fixe sur $U(x)$, stabilisable par sous-relaxation. Cette technique a été utilisée par *Carter, Wornom* [45]. Le calcul inverse est bien adapté aux couches limites décollées car leur pression varie lentement avec Θ ($dU/d\Theta$ petit). La situation est opposée dans les régions attachées ($dU/d\Theta$ grand), de sorte que l'itération inverse y devient mal appropriée. *Klineberg, Steger* [42] ont pour cette raison traité les profils transsoniques par une itération mixte, directe dans les régions attachées, inverse dans les régions décollées ou proches de l'être. Cette méthode exige des calculs de fluide parfait à conditions aux limites mixtes, et soulève des difficultés numériques lorsqu'elle doit être généralisée à des écoulements présentant des régions directes et inverses répétées, voir [54].

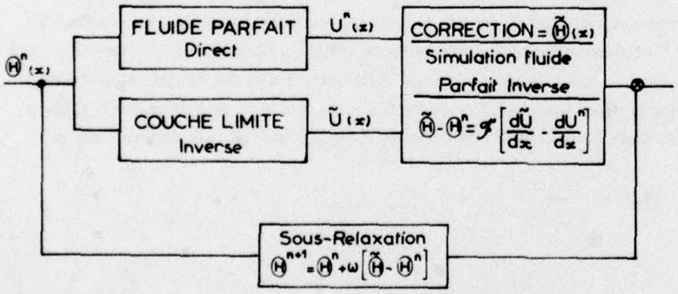

Fig. 15 – Itération de couplage "semi-inverse".

Nous avons proposé [54] de remplacer l'itération inverse des régions décollées par une itération semi-inverse (Fig. 15). Son principe est d'associer le calcul de couche limite inverse à un calcul de fluide parfait direct, commun aux régions attachées et décollées. Pratiquement, le problème *consiste à modifier itérativement la distribution* $\Theta(x)$ *pour amener à coïncidence les deux* estimations de la vitesse, $U(x)$ et $\tilde{U}(x)$, issues respectivement du fluide parfait et de la couche limite. Une analyse de même type a été appliquée par *Kuhn, Nielsen* [73] au profil transsonique symétrique, mais elle excluait l'interaction couche limite - onde de choc, et exigeait des tâtonnements manuels. Nous avons pu définir une procédure itérative automatique et stable pour *corriger* $\Theta^n(x)$. *La correction est obtenue à partir de l'erreur* $\left[\frac{dU}{dx} - \frac{d\tilde{U}}{dx}\right]^n$ en simulant localement un calcul de fluide parfait linéarisé inverse, voir [54]. La méthode a été appliquée en subsonique comme en supersonique où elle résoud un problème aux limites bien posé. Les commutations de l'itération directe à l'itération semi-inverse sont pilotées par l'état local de la couche limite, de sorte que les décollements peuvent être multiples et apparaissent d'eux-mêmes. De telles méthodes apparaissent comme le complément naturel des méthodes de relaxation transsoniques non-visqueuses.

CONCLUSIONS

Parallèlement aux méthodes de résolution numérique des équations de Navier-Stokes, il est possible de calculer les écoulements visqueux à grands nombres de Reynolds comme des problèmes de fluide parfait **perturbés**.

Une première possibilité est de résoudre des équations de Navier-Stokes tronquées où les équations d'Euler sont incluses. *On obtient alors des systèmes paraboliques dont le traitement est conditionné par leur caractère mal posé en subsonique*, sitôt qu'ils sont formulés comme des problèmes de conditions initiales. Cet effet est à l'origine de l'influence exercée par l'aval sur l'amont, influence persistant en régime supersonique grâce aux parties subsoniques des couches visqueuses. Toutes les fois que l'influence de l'aval est importante, la résolution d'un problème aux limites doit être envisagée. On peut alors introduire une itération analogue aux méthodes de relaxation, opérant par balayages successifs de l'amont vers l'aval. *L'avantage par rapport aux techniques totalement* elliptiques est de limiter l'itération au seul champ de pression, les autres variables étant calculées comme dans un problème de conditions initiales. Le stockage en mémoire du **seul** champ de pression présente un intérêt évident pour l'extension aux écoulements tridimensionnels. Les problèmes encore peu explorés dans cette approche sont ceux de la capture des ondes de choc, et du traitement des bulles de recirculation.

La seconde technique consiste à perturber un problème de fluide parfait seulement dans ses conditions aux limites qui, au lieu d'être connues à l'avance, résultent alors d'un couplage avec le calcul des phénomènes dissipatifs. Une première possibilité pour ce calcul est de recourir aux méthodes asymptotiques. Les analyses disponibles permettent d'aborder l'interaction couche limite-onde de choc ainsi que les écoulements de bord de fuite. L'apparition et le développement de certains types de décollements est possible, *à l'exception du cas turbulent, cette lacune étant certainement* la plus importante. En laminaire, ces analyses valident dans de nombreux cas l'utilisation des équations de Prandtl pour les nombres de Reynolds élevés. Une seconde possibilité de calcul consiste à traiter les régions de forte interaction visqueuse par une résolution locale des équations de Navier-Stokes, raccordée **au loin** à un calcul de fluide parfait. Le choix des conditions de raccordement, ainsi que l'étude des algorithmes permettant de les réaliser dans le cas stationnaire sont encore assez peu avancés. Les méthodes de couplage les *plus développées traitent la frontière du fluide parfait comme une surface libre positionnée* entre la paroi et la frontière externe physique des couches visqueuses. Le calcul dissipatif est restreint à ces seules régions et fait généralement appel à des équations simplifiées. Un progrès récent de ces méthodes a consisté à les rendre opérationnelles sur le plan pratique. On peut maintenant envisager une convergence automatique du processus itératif de couplage à tous nombres de Mach, régime transsonique inclus, pour des configurations réunissant des phénomènes divers tels que bords de fuite et interaction couche limite - onde de choc. *La solution apparaît d'elle-même sans qu'un prédicteur initial ne soit requis*, même en présence de multiples bulles de décollement dans les couches dissipatives. Ces progrès dans la définition d'algorithmes stables évitent les lissages arbitraires et résolvent des problèmes bien posés, respectant l'influence de l'aval sur l'amont permise par les équations simplifiées choisies. Un élément important est qu'une influence totale est déjà permise par le modèle simple des équations d'Euler **couplées** aux équations de Prandtl, même si ces dernières sont résolues par une **méthode intégrale**. *Les discontinuités de pression anormales associées aux couches limites supercritiques* peuvent maintenant être éliminées, et sont vraisemblablement en rapport avec la pénétration des ondes de choc à l'intérieur des couches turbulentes. Les profils transsoniques portants non-décollés sont de cette façon assez bien calculés, de même que le décollement et l'interaction couche limite-onde de choc en régime supersonique laminaire. En cas d'application de **méthodes aux différences**, le traitement des ondes de choc internes à la couche turbulente par adoption d'équations de Navier-Stokes tronquées est encore à développer. *Il est par ailleurs indispensable dans tous les cas de faire progresser* les modèles de turbulence, et notamment pour l'interaction couche limite-onde de choc, le décollement, la transition dans les décollements de bord d'attaque. En revanche, dans le cas laminaire, la résolution par différences finies des équations de Prandtl couplées au fluide parfait fournit des solutions fiables pour le décollement et l'interaction couche limite - onde de choc en supersonique. Il en est de même en subsonique pour les calculs inverses de couche limite décollée lorsque l'épaisseur de déplacement est connue.

REFERENCES

1 VAN DYKE M. – Perturbation methods in fluid mechanics. The parabolic Press (1975).

2 BAUM E., DENISON R. – Interacting supersonic laminar wake calculations by a finite difference method. AIAA J., vol. 5, No 7, pp. 1224-1230, (July 1967).

3 MELLOR G.L. – The large Reynolds number asymptotic theory of turbulent boundary layers. Intern. J. of Engineering Sci., Vol. 10, pp. 851-873 (1972).

4 MELNIK R.E., GROSSMAN B. – Analysis of the interaction of a weak normal shock wave with a turbulent boundary layer. AIAA paper No 74-598. Palo-Alto (June 17-19, 1974).

5 VIVIAND H. – *Application des méthodes asymptotiques à l'étude des couches visqueuses libres*. La Recherche Aérospatiale No 131 (juillet-août 1969).

6 GOLDSTEIN S. – On laminar boundary layer flow near a position of separation . Quart. J. Mech. Appl. Math. 1, 43-69 (1948).

7 MELNIK R.E., CHOW R. – Asymptotic theory of two-dimensional trailing-edge flows. NASA SP 347, Part 1, Langley (March 4-6, 1975).

8 CHOW R., MELNIK R.E. – Numerical solutions of the triple deck equations for laminar trailing edge stall. Grumman Rept. RE-526J (October 1976).

9 STEWARTSON K. – On the asymptotic theory of separated and unseparated fluid motions. SIAM J. Appl. Math., vol. 28, No 2, (March 1975).

10 STEWARTSON K.– Multistructured boundary layers on flat plates and related bodies. Advances in Appl. Mech., vol. 14, pp. 145-239 (1974).

11 GUIRAUD J.P. - Ecoulement décollé au voisinage du bord de fuite d'une aile mince tridimensionnelle. J. de Mécanique 13,3 p. 1-24 (1974).

12 BURGGRAF O.R. – Asymptotic theory of separation and reattachment of a laminar boundary layer on a compression ramp. AGARD CP-168, Göttingen (1975).

13 MESSITER A.F. – Laminar separation : a local asymptotic flow description for constant pressure downstream. AGARD CP-168 (1975).

14 SCHMITT R. – Décollement laminaire au voisinage du bord de fuite d'un profil mince. Note Technique ONERA No 1976-3 (1976). (ESA english translation TT-343).

15 MELNIK R.E., GROSSMAN B. – *Interaction of normal shock waves with turbulent boundary layers at transonic speeds.* Grumman Rept. RE-517J (March 1976).

16 MELNIK R.E., CHOW R., MEAD H.R. – Theory of viscous transonic flow over airfoils at high Reynolds number. AIAA paper 77-680, Albuquerque (June 27-29, 1977).

17 INGER G.R., MASON W.H. – Analytical theory of transonic normal shock-turbulent boundary layer interaction. AIAA J. vol. 14, No 9, pp. 1266-1272 (Sept. 1976).

18 BRUNE G.W., RUBBERT P.E., FORESTER C.K. – The analysis of flow fields with separation by numerical matching. AGARD CP-168 (1975).

19 SEGINER A., ROSE W.C. – A numerical solution of the flow field over a transonic airfoil including strong shock-induced flow separation. AIAA paper No 76-330, San Diego (July 14-16, 1976).

20 SEGINER A., ROSE W.C. – An approximate calculation of strong interaction on a transonic airfoil. AIAA paper No 77-210, Los Angeles (January 24-26, 1977).

21 MURPHY J.D., PRESLEY L.L., ROSE W.C. – On the calculation of supersonic separating and reattaching flows. AGARD CP-168 (1975).

22 BAUM E. – An interaction model of a supersonic laminar boundary layer on sharp and rounded backward facing steps. AIAA J., vol. 6, No 3, p. 440.

23 HIRSH R.S. – Calculation of supersonic three-dimensional free-mixing flows using the parabolic-elliptic Navier-Stokes equations. NASA SP-347, Langley (March 4-6, 1975).

24 PATANKAR S.V., SPALDING D.B. – A calculation procedure for heat, mass and momentum transfer in three-dimensional parabolic flows. Int. J. Heat Mass Transfer. Vol. 15, pp. 1787-1806 (1972).

25 OHRENBERGER J.T., BAUM E. – A theoretical model of the near wake of a slender body in supersonic flow. AIAA J., vol. 10, No 9, pp. 1165 (Sept. 1972).

26 SPALDING D.B. – Numerical computation of steady boundary layers-A survey. Computational methods and problems in aeronautical fluid dynamics. London and New York Academic Press (1976).

27 BAUM E., DENISON M.R. – Interacting supersonic laminar wake calculations by a finite difference method. AIAA J., vol. 5, No 7, p. 1224 (July 1967).

28 TASSA Y., ANDERSON B.H., RESHOTKO E. – Improved interactive calculation procedure for supersonic flows. Israel J. of Techn. vol. 14, p. 94 (1976) - (Proceed. XVIII Isr. Annu. Conf. Aviation and Astronautics, May 1976).

29 DAVIS R.T. – Numerical solution of the incompressible Navier-Stokes equations for two-dimensional flows at high Reynolds number. First Int. Conf. on Numerical Ship Hydrodynamics, Nat. Bureau of Standards (Oct. 20-22, 1975).

30 MAHGOUB H.E.H., BRADSHAW P. – *Calculation of turbulent shear layers with large normal pressure gradients* (submitted *to AIAA Journal*).

31 CROCCO L., LEES, L. – A mixing theory for the interaction between dissipative flows and nearly isentropic streams. J. Aero. Sci., vol. 19, No 10 (October 1952).

32 LEES L., REEVES B.L. – Supersonic separated and reattaching laminar flows. Pt I : General theory and application to adiabatic boundary layer-shock wave interaction. AIAA J., vol. 2, No 10 (1964).

33 KLINEBERG J.M. – *Theory of laminar viscous-inviscid interactions in supersonic flow.* Cal. Inst. Tech., Ph. D. Thesis (May 1968).

34 GARVINE R.W. – Upstream influence in viscous interaction problems. The Physics of Fluids. vol. 11, p. 1413 (July 1968).

35 WEINBAUM S., GARVINE R.W. – On the two-dimensional viscous counterpart of the one-dimensional sonic throat. J.F.M. vol. 39, pp 57-85 (1969).

36 KING MON TU, WEINBAUM G. – A non-asymptotic triple-deck model for supersonic boundary layer interaction. AIAA J. vol. 14, No 6, pp 767-775 (June 1976).

37 LE BALLEUR J.C. – *Couplage visqueux-non visqueux : analyse du problème incluant décollements et ondes de choc.* La Recherche Aérospatiale No 1977-6.

38 HANKEY W.L., HOLDEN M.S. – Two-dimensional shock wave-boundary layer interactions in high speed flows. AGARDograph AG-203 (June 1975).

39 MURPHY J.D. – A critical evaluation of analytic methods for predicting laminar boundary layer-shock wave interaction. NASA TN D-7044 (January 1971).

40 ROSE W.C. – Practical aspects of using Navier-Stokes codes for predicting separated flows. AIAA paper No 76-96, Washington (January 26-28, 1976).

41 CARRIERE P., SIRIEIX M., DELERY J. – Méthodes de calcul des écoulements turbulents décollés en supersonique. Progress in Aerospace Sci., vol. 16, No 4, pp. 385-429 (1975).

42 KLINEBERG J.M., STEGER J.L. – Calculation of separated flows at subsonic and transonic speeds. Proceed. of Intern. Conf. on Numerical Methods in Fluid Mech., Springer-Verlag, vol. 11, pp. 161-168 (1973).

43 REYHNER T.A., FLUGGE-LOTZ – The interaction of a shock-wave with a laminar boundary layer. Standford Univ. Dir. of Eng. Mech. (November 1966).

44 WERLE M.J., VATSA V.N. – *New method for supersonic boundary layer separations.* AIAA J., vol. 12, No 11 (November 1974).

45 CARTER J.E., WORNOM S.F. – Solutions for incompressible separated boundary layers including viscous-inviscid interaction. NASA SP-347, pp. 125-150 (1975).

46 ALZIARY DE ROQUEFORT T. – Contribution à l'étude de l'interaction et du décollement de la couche limite laminaire avec transfert de chaleur en régime supersonique. Thèse No 88. Université de Poitiers (1969).

47 NIELSEN J.N., LYNES L.L., GOODWIN F.K. – Calculation of laminar separation with free interaction by the method of integral relations. AFFDL TR-65-107 (June 1965).

48 CROCCO L. – Laminar separation. AGARD CP-168 (supplément), Göttingen, (1975) (ou TP ONERA 75-113).

49 ROSE W.C. – A method for analyzing the interaction of an oblique shock wave and a boundary layer. NASA SP-228, pp. 541-567 (1970).

50 DELERY J., LE BALLEUR J.C., SIRIEIX M. – Etude expérimentale de l'interaction choc-couche limite turbulente en écoulement supersonique. Communication au 13e Congrès IUTAM. Moscou (1972).

51 CHOW W.L., SPRING D.J. – Viscous interaction of flow redevelopment after flow reattachment with supersonic external streams. AIAA J., vol. 13, No 12, p. 1576 (Déc. 1975).

52 NAKAYAMA A., PATEL V.C., LANDWEBER L. – Flow interaction near the tail of a body of revolution. Part 2 : Iterative solution for flow within and exterior to boundary layer and wake. Trans. ASME, J. of Fluids engineering 98, serie I, No 3, (Sept. 1976).

53 LE BALLEUR J.C., MIRANDE J. – Etude expérimentale et théorique du recollement bidimensionnel turbulent incompressible. AGARD CP-168 (1975).

54 LE BALLEUR J.C. – Couplage visqueux-non visqueux : méthode numérique et application aux écoulements transsoniques et supersoniques. La Recherche Aérospatiale, No 1978-1.

55 LOCK R.C. – Calculation of viscous effects on aerofoils in compressible flows. RAE Tech. Memo. Aero. 1646 (Sept. 1975).

56 BHATELEY I.C., BRADLEY R.G. – A simplified mathematical model for the analysis of multi-element airfoils near stall. AGARD CP-102, Lisbonne (1972).

57 JACOB K., STEINBACH D. – A method for prediction of lift for multi-element airfoil systems with separation. AGARD CPP-143 (April 1974).

58 MASKEW B., DVORAK F.A. – Investigation of separation models for the prediction of $C_{\ell_{Max}}$. 33rd Annual Nat. Forum of American Helicopter Society, Washington (May 1977), preprint No 77.33-01.

59 BARWELL R.W. – Two inviscid computational simulations of separated flow about airfoils. AIAA paper No 76-379, San Diego (July 14-16, 1976).

60 BAVITZ P.C. – An analysis method for two-dimensional transonic viscous flow. NASA TN D-7718 (January 1975).

61 BAUER F., KORN D. – Computer simulation of transonic flow past airfoils with boundary layer correction. 2nd AIAA Comput. Fluid. Dyn. Conf., Hartford (June 1975).

62 ROM J. – Flows with strong interaction between the viscous and inviscid regions. SIAM J. Appl. Math., vol. 29 No 2 (Sept. 1975).

63 VATSA V.N., WERLE M.J. – *Quasi three-dimensional supersonic viscid-inviscid interactions including separation effects.* Univer. Cincinnati, Ohio, Tech. Rep. AFFDL-TR-75-138 (Sept. 1975).

64 WERLE M.J., POLAK A., VATSA V.N., BERTKE J.D. – Finite difference solutions for supersonic separated flows. AGARD CP-168, Göttingen (1975).

65 BRILEY W.R., McDONALD H. – Numerical prediction of incompressible separation bubbles. J.F.M., vol. 69, pt 4, pp. 631-656 (1975).

66 KLINEBERG J.M., STEGER J.L. – On laminar boundary layer separation. AIAA paper No 74-94, Washington (Jan.-Febr. 1974).

67 PLETCHER R.H., DANCEY C.L. – A direct method of calculating through separated regions in boundary layer flow. Trans. ASME. J. Fluids Engineering 94, serie I No 3 (Sept. 1976).

68 CATHERALL D., MANGLER K.W. – The integration of two-dimensional laminar boundary layer equations past the point of vanishing skin friction. J.F.M., vol. 26, part 1, (Sept. 1966).

69 CARTER J.E. – Inverse solutions for laminar boundary layer flows with separation and reattachment. NASA TR-R-447 (Nov. 1975).

70 CEBECI T., BRADSHAW P. – Momentum transfer in boundary layers. Mc Graw Hill/Hemisphere (1977).

71 WERLE M.J., BERTKE J.D. – A finite difference method for boundary layers with reverse flows. AIAA J., vol. 10, No 9, p. 1250 (Sept. 1972).

72 BRUNE G.W., RUBBERT P.E., NARK T.C. – A new approach to inviscid flow - boundary layer matching. AIAA paper No 74-601, Palo Alto (June 17-19, 1974).

73 KUHN G.D., NIELSEN J.N. – Prediction of turbulent separated boundary layers. AIAA J., vol. 12, No 7 (July 1974).

PHENOMENOLOGICAL ASPECTS OF QUASI-STATIONARY CONTROLLED AND UNCONTROLLED THREE-DIMENSIONAL FLOW SEPARATIONS

by

DAVID J. PEAKE*
NASA Ames Research Center
Moffett Field, California 94035, U.S.A.

SUMMARY

The extensive interest in three-dimensional flow separation is linked closely with wings of high leading-edge sweep and bodies of large fineness ratio operating at large angles of incidence or yaw, that are typical of many high-speed aircraft and missile layouts. Characteristically, these boundary-layer separations can lead to comparatively steady streamwise vortices, unlike the more familiar two-dimensional separations with their irregular mixing flows and buffeting. Customarily accompanying these strong viscous/inviscid interactions on hypersonic configurations is substantial heat transfer to the surface in zones of flow re-attachment.

This part of the lecture series will deal with quasi-steady three-dimensional separated flows about practical flight vehicles. The general character of the three-dimensional attached boundary layer, the concept of limiting streamlines, and the present understanding of the physics of three-dimensional separation and re-attachment will be offered. Specific examples will than be treated.

The advantages of swept, sharp edges that generate controlled (or fixed) three-dimensional flow separations on a vehicle — because of the qualitatively unchanging flowfield developed throughout the range of flight conditions — are promoted in preference to allowing uncontrolled (or unfixed) separations.

**Senior Research Associate; on leave of absence from NAE, Ottawa, Canada.*

1.0 INTRODUCTION

The earlier studies by Maskell and Küchemann on flow separation in three dimensions,[1,2,3,36] drew attention to the constructive role played by lines of separation. They proposed that these three-dimensional (3D) separation lines could be regarded as the skeleton around which the entire flow structure could be assembled.

When the separation lines can be fixed by salient edges (sharply-swept leading-edges, for instance, Fig. 1) we have an example of "controlled flow separation," Figure 2. Throughout the range of flight conditions, the flowfield is virtually invariant in form, being dominated by the viscous shear layers leaving the separation lines, to form well organized and comparatively steady vortex motions. These leading-edge vortices can, in turn, be controlled by additional active means, to induce more lift: first of all, to prevent vortex breakdown, by blowing in a spanwise direction along the axis of the vortex, as discussed by Cornish[4] and others[5,6] (Fig. 3); secondly, by blowing normal to the leading-edge, either to enhance the primary vortex,[7,8] or to control secondary separations.[9] Clearly, other examples of swept edges, such as strakes (Fig. 4.1) and vortex generators (Fig. 4.2), themselves provide controlled flow separations, but the generated vortex motions are used to promote mixing of high-energy air with recalcitrant viscous flows downstream of the flow separation device.

On the other hand, when the load-carrying, lifting and propulsion components are integrated into an aircraft or missile configuration, the resultant interfering pressure fields produce separations that are often unanticipated, are not fixed in location on the surface for all flight conditions, and so, in this sense, are "uncontrolled." Examples of these separated flows may be catalogued according to their causes:[10]

(a) flows over smooth walls in the presence of slowly varying circumferential and axial adverse pressure gradients. We include here, those flows about bodies whose longitudinal axis in part or in whole is swept with respect to the oncoming stream, such as upswept rear fuselages or pointed and bluff-nosed missiles at angles of attack;[11,12,13]

(b) flows about protuberances attached to a wall, where adverse pressure gradients are imposed suddenly. Bulbous wheel housings, cockpit canopies, pylons, boundary-layer diverters, and unfaired junctions of the wing and tail surfaces with the body are important examples;[11,14]

(c) flows about normal or inclined jets blowing from a wall. Control jets used for thrust vector control cause substantial three-dimensional separation of the local viscous flow in the region where the jet emerges from the vehicle surface.[15] In terms of upstream effect, the "solid blockage" caused by the jet is analogous with that of a protuberance;

(d) flows with shock waves present, sometimes associated with items (a) to (c). We shall pay particular attention to those separations produced in swept shock/boundary-layer interactions,[16,17,18] such as on the sidewall of rectangular supersonic inlets or upon swept-wing surfaces.

While the effect of these uncontrolled separations on drag may not always be significant or even apparent, high local heat transfer rates in re-attachment zones,[19] and the induced interaction effects of the vortex motions upon downstream control surfaces of a vehicle may be important.[20] In general, the uncontrolled flow separations have not been amenable to prediction, and are not well understood. The symmetry of the vortices and the scale of the separated flow domain, whether large such as in the case of the body vortices, or immersed within the depth of the oncoming boundary layer, as in the protuberance flow, will affect the magnitudes of locally-induced suction pressures, and hence, the non-linear increments in the body forces.

Compressibility alters the quantitative, but not the qualitative features of three-dimensional separated flows. It has been found by experiment that the effect of increasing Mach number is to reduce the scale of the rolled-up shear layers with respect to the oncoming boundary-layer thickness,[11 21] and to increase the critical angle for the development of flow asymmetry of the rolled-up shear layers from bodies at high angles of attack.[11]

The aerodynamic design of a lifting body, to be successful throughout a range of flight conditions, must ensure that the fluid flow is steady to minimize buffeting; that it should be of the same type throughout the flight envelope; and that there should be no unpleasant changes in force and moment characteristics. The goal to aim for is that flows should be dominated by free viscous vortices (with *no* large bubbles to produce unsteadiness) and that the primary lines of separation should remain fixed on the body throughout the flight range. This much wider than usual view of the aerodynamic design problem,[3] incorporating the philosophy of controlled flow separation, should be contrasted with the restricted outlook of allowing separation only at a trailing-edge.

As a base of understanding for these complex flows, we shall attempt a description of the component flowfields about simple shapes, whose geometry may be integrated into the design of an aircraft or missile. The slender delta wing, with subsonic leading-edges, a prime case of controlled or fixed flow separation, will be treated first-of-all. Subsequently, the uncontrolled or unfixed separations upon cone-cylinders, prolate spheroids, upswept fuselages and ahead of slender and bluff protuberances will be mentioned. Finally, the case of a swept-shock/turbulent boundary-layer interaction will be discussed, with potential for its control (and, perhaps, removal) by tangential air injection. The combination of some of these constituent flowfields into practical aerodynamic vehicles will be reviewed against examples of current design philosophy.

2.0 ATTACHMENT, SEPARATION AND RE-ATTACHMENT IN THREE-DIMENSIONAL FLOWS

2.1 Modelling

We generally accept that the non-linear Navier-Stokes equations model the motion of a viscous, compressible (laminar or turbulent) heat conducting fluid without chemical reactions, at points in space and time away from discontinuities in the flow such as shock waves. Unfortunately, full time-dependent solutions do not appear attainable in the near future, for to compute the various three-dimensional turbulence structures possessing a substantial range of length and time scales, computational techniques must be further refined. Current finite difference procedures employing numerical artifices such as damping from "artificial viscosity" inputs, for instance, appear inadequate because they introduce errors that may diverge in the development of the instantaneous flowfield. Rubesin[22] suggests that to define the three-dimensional turbulent boundary-layer flowfield about an aircraft, the smallest significant scale demands mesh spacing 10^{-5} of the boundary-layer thickness, to require the order of 10^{17} mesh points overall. He discusses that the corresponding allowable time step in any given marching procedure is one microsecond of real time. These requirements demand a computer storage capacity and speed of computation that are in excess of present-day or planned computer facilities. To overcome these difficulties, therefore, we must resort to modelling the turbulence structures in three-dimensional viscous flows with free shear layers springing up from 3D separation lines. An enlightened critique of computer simulation and accuracy limitations of numerical methods with regard to turbulence modelling is given in respective comments by Roache and Bradshaw in Reference 23, in response to the essay of Chapman et al.[24] Hence, for most practical examples under high Reynolds number conditions, we still try to blend an external or inviscid flow solution with an appropriate boundary-layer procedure, rather than attempting to exploit the conceptual simplicity of the more general Navier-Stokes equations. In laminar flow, numerical studies of the viscous/inviscid interactions about pointed[27] and blunt cones[30] have been attempted using approximations to the Navier-Stokes equations, and good comparison with experiment has been obtained, but at the expense of relatively long computation times.

In the classical aircraft example, the art of design has been to eliminate separation ahead of the trailing-edge, because increases in drag and flow unsteadiness are introduced with essentially two-dimensional (2D) separations on wings of high aspect ratio. With increases in speed, range and angle of attack, over which smaller aspect ratio lifting wings and bodies are required to operate, extensive regions of three-dimensional separated flow are predominant (Figs. 2 and 4.1) and we require new and suitable flow models. On wings or strakes, with sharp, swept leading-edges, 3D separation occurs, is fixed at the salient edges, and is essentially independent of the oncoming boundary-layer properties at the high Reynolds numbers of interest to us. The boundary-layer fluid departs from the surface to form rolled-up viscous shear layers whose scale is usually many times the local boundary-layer thickness. In the limit of infinite Reynolds numbers, or for practical purposes, at high enough Reynolds numbers, the coiled viscous shear layer may be modelled approximately by an inviscid flow vortex sheet. In other words, viscosity causes the separation, the location is determined by the edge geometry, after which the flow may be modelled by inviscid means. The coiled vortex sheet model of Mangler and Smith, and its extensions (see the list of papers in Ref. 10) have provided good qualitative prediction of pressure distributions on slender wings in conical flow with subsonic leading-edges, see Figure 5. A more recent, incompressible, advanced panel-type influence coefficient calculation method of Weber et al.,[25] is not restricted to conical flow. In this method, the wing, the rolled-up vortex sheets and the wake are represented by "piecewise" continuous quadratic doublet distributions, and the Kutta condition is imposed along both the leading and trailing-edges. Some results of these calculations[25] compare well with the low-speed delta-wing experiments of Marsden et al.,[26] and are displayed on Figure 6.[†]

On bodies, unfortunately, the separation location is not known *a priori*, and we must attempt to calculate its position via three-dimensional boundary-layer theory, using an initial attached inviscid flow pressure distribution. The inviscid rolled-up vortex sheet model may then be used on simple bodies such as pointed right-circular and elliptic cones, where the separation lines are along generators, and the co-ordinate geometry presents few difficulties.[12] More recently, McRae[27] has attempted to solve the laminar viscous flowfield about a pointed, right-circular cone at high angle of attack, utilizing a simplified set of the Navier-Stokes equations (incorporating the conically symmetric flow approximation) along with MacCormack's finite difference time-dependent scheme.[28] Using a body co-ordinate system, (R, θ, ϕ), a finite difference mesh was set up on the (θ, ϕ) spherical surface at a distance R from the cone apex. The calculation took place on this surface with viscous effects scaled by the Reynolds number based on the radius, R. The finite difference mesh was initialized with freestream values of the flow everywhere, except at the surface, where zero velocities were input. The numerical integration then proceeded in time, to the limit that produced a steady state solution. The outer boundary condition for the integration was the freestream, so that the bow shock wave was captured and allowed for in the use of the conservation form of the governing equations. Figure 7 illustrates the surface pressures and a crossflow velocity vector plot of a computed flowfield about a 10° half-angle cone in a nominally Mach 8 freestream at $\alpha/\theta_C = 2.4$, compared with the experimental data of Tracy with entirely laminar boundary-layer conditions, where a 3D separation was measured using surface flow visualization at $\phi = 150°$. The presence of a three-dimensional separation and rolled-up viscous shear layer is seen in McRae's calculated flowfield.

A new technique for calculating the entire flowfield about a spherically blunted circular cone at high angle of attack with 3D laminar separation has been reported by Lubard and Rakich.[30] The calculations are based on a single layer system of three-dimensional parabolic equations, that are approximations to the full steady Navier-Stokes equations, valid from the body surface to the bow shock wave. This system includes the circumferential shear stress terms and is capable of predicting the flow within the separation zone on the leeward side. The effects of viscous-inviscid interaction and entropy gradients due to both the curved bow shock and angle of attack effects are automatically included. Unseparated initial conditions are assumed at the sphere cone tangency plane and are provided by using an inviscid time dependent solution added to a viscous non-similar boundary-layer solution. The calculated results were compared with the experimental separated flow data of Cleary[31] for a 15° angle of attack at Mach 10.6 and at a Reynolds number based on the 23-inch slant length of the cone of about 2.3 million. Figure 8 shows the calculated crossflow plane vector velocity distribution in the region close to the leeward generator at 14.8 nose radii downstream from the nose. The three-dimensional separation occurs at 155°–160° in the cross-flow plane at this axial station. The remaining graphs on Figure 8 show the calculated surface pressure and heating distributions on the leeward surface that provide good agreement with experiment. Using the same approximate parabolic system of equations, Lubard and Rakich are now working to solve the flowfields about bodies other than bodies of revolution at angle of attack, to provide design information on vehicles such as the Space Shuttle.

[†] Compressibility corrections[79] extend the range of applicability of the method of Weber et al.[25] to high subsonic Mach numbers.

Notwithstanding the potential extensions of these useful laminar cone flow predictions,[27,30] our ability to assess the consequences in regions of high heat transfer at three-dimensional attachment points and along re-attachment lines is still unsatisfactory for a general configuration in turbulent flow.[19] For example, on Figure 9, we show the importance of contouring the apex of a 70° swept delta, in a Mach 6 flow, to reduce the leeward centre-line heating in the presence of laminar, transitional and turbulent boundary layers (freestream Stanton number, St_{∞}). On the sharp apex wing, the heating is some five times the value predicted on the lee-side meridian by laminar theory,[32,33] and that on the hyperbolic planform wing.

In general, then, we are unable yet to model the viscous flow encountered in 3D re-attachment and separation regions that will yield rational design procedures, although some promising avenues are opening in laminar flow. Fortunately, from the pioneering work of Sears,[34] Maskell,[1,35] Legendre,[37,38] Lighthill[39] and others, we do possess some understanding of the physical (mean flow) conditions close to attachment, separation and re-attachment, in three-dimensional flowfields.

2.2 Limiting Streamlines

If we consider the subject of three-dimensional viscous flows in its historical context, Sears in 1948, utilized the very important concept of "limiting streamlines" in a paper discussing the laminar boundary layer on a yawed cylinder.[34] Each streamline near the surface, in the inner collinear part of the boundary layer, is one of a continuous pattern, that originally approached the surface in the attachment region, and which subsequently departs from the surface at separation. No matter how small is the height of the streamline above the surface, the streamline will exist. If this height is allowed to approach a zero value, the streamline will be everywhere tangential to the vanishing fluid velocity as the surface is approached. (In the strictest sense, no streamlines can be drawn on the solid surface of a body, of course, for the no-slip condition at the surface would be violated.) The streamline is then identifiable as a limiting streamline, or, in other words, it possesses the same direction as a skin friction line or surface shear stress trajectory. The pattern of limiting streamlines may be alternatively viewed as a "sheath" surrounding the body, whose projections on to the surface are the skin friction lines. These limiting streamlines at the base of the boundary layer must not be confused with the streamlines of the external inviscid flow over the surface, and they will in general follow paths that are different in direction to the external streamlines. From continuity considerations, and provided the limiting streamline does not form a closed curve on the aforementioned sheath, it must join the sheath at some point of attachment, A, and depart from the sheath again at a subsequent separation point, S. The locus of such points, S, is called a three-dimensional separation line, on either side of which is a distinct set of limiting streamlines.

Sears, moreover, in his early paper, included a sketch[34] that showed apparent convergence of the two sets of limiting streamlines towards the separation line, although he did not call it by name; and later, Wild[40] substantiated Sears' physical interpretation of separation, in his investigation of the laminar boundary layer on yawed "infinite" wings. In subscribing to the Cornell University work, Eichelbrenner and Oudart[41,42] proposed that a three-dimensional separation line was the envelope of the limiting streamlines (conversely, from an attachment line, the limiting streamlines diverge) and this was also supported by Susan Brown[43] in a mathematical treatise. Lighthill,[39] on the other hand, disputed the term "envelope," in spite of flow visualization experiments seeming to support the previous authors. Coalescence of the limiting streamlines is an acceptable description, perhaps, to avoid argument.

It remained for Maskell,[1] however, to lay the ground rules for interpreting the physical composition of three-dimensional viscous flows — by demonstrating that the limiting streamlines provide a "three-dimensional skeleton structure of the viscous flow." If a flow visualization indicator is very thin on a wind-tunnel model, it has been shown[44] that the direction indicated by the streaks on the surface is very close to the direction of surface shear stress and the limiting direction of the velocity when the indicator is absent. Thus the type of oil-streak flow visualization techniques yield a powerful means of diagnosing and synthesizing the qualitative features of three-dimensional viscous flows.

Two types of separation were conceived by Maskell:[1] a bubble type (Fig. 10(a)) and a free shear layer type (Fig. 10(b)), but the latter appears to be the most common.* In fact, at all but (perhaps) very low Reynolds numbers, the shear layer displayed in Figure 10(a) is of the free shear-layer type rather than the bubble indicated. Fluid accumulating at a three-dimensional separation line, which in general is set obliquely to the direction of the external and essentially inviscid flowfield, leaves the separation line usually as a free shear layer (Fig. 10(b)) and rolls-up in the process of passing downstream. It is thought that the fluid departs from the region of the separation line, in a direction tangential to the surface.[10] The shear stress is finite *along* such a three-dimensional separation line on the surface, being locally zero only at a singular point, such as S on Figure 10(a). High local suction pressures are induced on the surface beneath the resulting vortices, Figure 5, close to which are noted inflexion points in the limiting streamline patterns. Examples here are the slender wing flow (the ONERA and RAE work being the most extensive — see the subject list in Ref. 12) and cones, the flows on long pointed and bluff-nosed slender and not-so slender bodies at incidence, those about upswept fuselages, and those about bluff protuberances.[12]

2.3 Attachment and Re-attachment

Flow attachment occurs at an upstream stagnation point that is situated upon a forward-facing surface of the vehicle, such as the nose. On a two-dimensional wing, the (singular) stagnation points along the

---

* We should note that Eichelbrenner,[45] in an article somewhat at variance with his previous publications,[41,42] considered only the three-dimensional bubble type of flow to be separated, because of its analogy with the corresponding two-dimensional flow case; that is, one that is inaccessible to the viscous flow coming from infinity upstream. Eichelbrenner[45] referred to Maskell's free shear-layer type as a "clash" situation and not a three-dimensional separation.

nose of the aerofoil section will also constitute the attachment line. In three-dimensional flows, on the other hand, when a flowfield has an inherent plane of symmetry as along the windward generator of a cone at incidence, there will be an "attachment line" in that plane, emanating from the attachment point at the nose. Along this latter attachment line, the pressures will not be equal to the stagnation pressure of the external stream. The mechanism of flow attachment at one point or at many points along an attachment line is still debated.[1,39]

Flow re-attachment occurs on the vehicle surface subsequent to a three-dimensional separation, where the attaching streamline may be one from the external flowfield, or one from the outer region of the upstream boundary layer. In the latter possibility, the stagnation pressure of the external flow will clearly not be recovered at the attachment point. Lighthill calls the point of attachment a nodal point,[39] and sketches a number of possible limiting streamline patterns adjacent to nodal points of attachment, as we see on Figure 11. From each kind of nodal point, an infinite number of limiting streamlines emerge, all having (except one) the same tangent, or otherwise, spirally. Spiral attachment would occur principally when either the surface or the external flow is rotating. However, the most frequent form is the "source flow" shown on the second of the sketches on Figure 11. This would be seen on the nose of an aircraft, for instance.

In Reference 10, Smith cites a potential list of interdependent properties for an attachment line to exist, two of which that are always found being:

1) that the attachment line is a limiting streamline, and
2) that two sets of limiting streamlines (whose origin in Lighthill's picture is the nodal point of attachment) run tangential to the attachment line initially, to eventually diverge from it.

Hence, two "independent" boundary layers develop on either side of the attachment line.

For convenience, we may regard the flow at the leading-edge of a swept wing, to attempt a description of the physics of the flow along an attachment line. There, a limiting streamline more-or-less parallel to the leading-edge divides the limiting streamline flow that passes above the wing from that which passes below the wing, Figure 12. Smith conjectures[10] that somewhere further away in the external flowfield at the edge of the attachment-line boundary-layer flow, there will be another streamline that also runs roughly parallel with the leading-edge, that divides the external flowfield into that which proceeds above the wing and that which passes below.

If we accept Lighthill's interpretation,[39] where is the nodal point of attachment situated that is the starting point for the attachment line? For an isolated swept wing, the apex at the intersection of the two swept halves is a stagnation point of the flow and the nodal attachment point.

When the wing is mounted on a fuselage, the effective protuberance pressure field of the wing section at the wing/fuselage junction can cause a horse-shoe shaped separation about the wing root, this separation being immersed within the depth of the fuselage boundary layer[11] — see Figure 12. We may postulate that a streamline in the outer region of the fuselage boundary layer will pass over the 3D rolled-up shear layer to form a nodal attachment point on the wing nose. Limiting streamlines emerging from the nodal point of attachment, one of which is the so-called attachment line, proceed along the leading-edge tangential or asymptotic to the attachment line to pass in a more chordwise direction over or beneath the wing. Around the nose and adjacent to the attachment line, the distance apart of these limiting streamlines is infinitesimal, such that they appear on flow visualization oil records as emerging tangentially from the attachment line. In other words, the attachment line appears to be the source or the envelope of the limiting streamlines in close proximity to it.

We note that this view is somewhat at variance with Maskell's interpretation of the conditions along an attachment line. He considered that an attachment line consisted of a number of attachment points such that when two limiting streamlines diverge from a given point on the attachment line, then that point is one at which a single attachment streamline joins the solid surface. Clearly, if there is a boundary-layer development along an attachment line, which measurements have demonstrated to be virtually constant in thickness on a swept wing of large aspect ratio,[46] then a large number of external streamlines cannot "attach" themselves to the surface along the attachment line. It would appear that the fluid within the boundary layer diverging or departing from the region of the attachment line is more-or-less balanced by the entrainment of irrotational fluid from outside the boundary layer. Maskell's concept can only be true at the limit of infinite Reynolds number.

2.4 Three-Dimensional Separation

Although there is usually little difficulty in recognizing so-called lines of 3D separation and attachment from the patterns of surface shear stress trajectories on a flight vehicle, there is a continuing debate regarding the fluid mechanics adjacent to them, stemming essentially from the respective postulates of Maskell[1] and Lighthill.[39] The discussion centers around the identification of limiting streamline patterns from surface oil flow visualization.

According to Maskell,[1] separation occurs at a point when two distinct limiting streamlines converge and meet there (Fig. 13.1) after which they combine and leave the surface as one separation streamline.

A 3D separation line is then composed of a large number of such "ordinary" points, being an envelope or cusp-locus of these points. Moreover, as we have seen previously, Maskell's view of the attachment line is this same picture but with the flow directions reversed on the limiting streamlines. Lighthill, in a later treatise,[39] considered these statements to be approximately valid, but disputed the envelope connotation. He argued that in the topography of the limiting streamlines, they must begin and end at (at least) one nodal point of attachment and one nodal point of separation. When two nodal points of attachment exist, Lighthill proposed that the limiting streamlines from each node must meet somewhere, and there must be a "saddle point." He sketched these as we see on Figure 13.2. Lighthill proceeded to define a separation line as one which issues from both sides of a saddle point of separation, and having embraced the body, disappears into a nodal point.

Let us look at these conceptual limiting streamline patterns about some flow components. The slender wing at incidence, shown on Figure 14, is a convenient first example. Lighthill suggests that the surface pattern is generated from two nodal points of attachment and a saddle point of separation which are coalesced at a sharp apex, but are distinct if the apex is rounded – see Figure 14.1. The limiting streamlines converging towards the 3D separation line S and diverging from the attachment line A are asymptotes rather than meeting at S or emanating from A.

Maskell's view, on the other hand, is shown on Figure 14.2. Clearly, for a sharp apex, it will not be possible to distinguish from flow visualization patterns which interpretation is philosophically correct, and for most practical purposes, it probably does not matter. The term "envelope" does seem to be a useful word to describe the merging of the limiting streamlines at the 3D separation line, and the mathematical interpretation is bound up with whether we want to look at solutions of the Navier-Stokes equations or boundary-layer equations;* and also whether it is possible for singular behaviour of the limiting flows to occur in practice?[10]

Does the limiting streamline pattern about a blunted slender body at incidence, where axial as well as transverse pressure gradients exist, provide additional help in diagnosing the approach to separation? An investigation of the subcritical flow about a 6:1 ellipsoid at high Reynolds number was reported in References 11 and 47, in which circumferential measurements of surface static pressure, surface impact pressure and oil-dot flow visualization were made, to identify the 3D viscous flow development. In contrast with the near conic viscous flowfield about the slender wing, the more general body flow exhibits substantial lengthwise effects, although the circumferential pressure gradients still dominate.

Figure 15 presents limiting streamlines on the ellipsoid at Mach 0.74, and at a Reynolds number of 44 million based on the 54-inch length of the body. The boundary layers were turbulent. The streamlines were deduced from oil-dot flow visualization records at angles of incidence from 10° to 25°, with only a few of them drawn for purposes of clarity. At the lowest angle of incidence shown, the flow is attached everywhere except for a bubble over a small region of the leeward afterbody, that is probably due to the effects of truncating the model for a sting mount through the model base. As we increase the angle of incidence, the circumferential adverse pressure gradient just past the $\phi = 90°$ position becomes more severe, causing a progressive thickening of the flow on the leeward side of the body; until at $\alpha = 25°$, there are two regions of coalesced limiting streamlines where we interpret that 3D separations are present. (This is not a very slender ellipsoid, but a corresponding situation would exist, of course, on a more slender ellipsoid at a reduced incidence.)

Figure 16 shows the calculated and the experimental isobar patterns (as well as some circumferential pressure distributions) on a distorted surface development at $\alpha = 25°$. A favourable circumferential pressure gradient is indicated by large open arrows and unfavourable gradients by shaded arrows. At this incidence, the circumferential pressure gradients completely swamp the axial gradients. From the calculated inviscid pressure distribution, we expect separation to occur somewhere on the lee-side of the minimum pressure line and the experimental pressure distribution reflects this. The separation lines taken from the oil-dot flow visualization records are shown here as chain-dotted lines. Figure 15 displays that the turbulent boundary layer separates, along S_1, over about the rear 60 percent of the body soon after it encounters the circumferential adverse pressure gradient. The flow with separation is symmetrical, with an attachment region along the leeward meridian, $\phi = 180°$, that is especially noticeable near the rear. We also see a secondary separation line S_2, extending well forward, outboard of this attachment.

The limiting streamlines can all be traced back to emanate from the attachment region on the nose and we cannot tell from the resolution provided by the oil streaks whether or not we have a system of nodal attachment and saddle separation points as Lighthill has conjectured.[39] The separation, attachment and re-attachment lines are fed from the upstream stagnation attachment region. There is a progressive thickening of the leeward flow with axial distance from the nose, with the limiting streamlines appearing asymptotic to the 3D separation lines as they approach the lines from either side. Just where the viscous vortices start can only be determined from profile measurements through the boundary layer. There is no theory available to predict them. At $\alpha = 25°$, substantial suction peaks in the circumferential wall static pressure distributions have developed along the body from $x/L = 0.25$, indicating roll-up of the viscous vortices from the primary separation lines, S_1.[11,47] There is fluid flow along the directions of S_1 and S_2 as well as along the (secondary) attachment line that exists between S_1 and S_2, so that the skin friction is finite everywhere. It is noteworthy that a similar ellipsoid at high incidence in Werlé's water tunnel,[77] with laminar boundary layers present, exhibits similar flow features to those just discussed in turbulent flow. Calculations of the laminar boundary layer (up to the primary 3D separation line) about an ellipsoid at incidence have recently been published by Geissler[56] with good qualitative accord with the results already discussed.

In this discussion on limiting streamlines, let us now look at the case of a bluff protuberance standing normal to a wall, where the streamwise adverse pressure gradient rather than the transverse gradient dominates the flow development. Even though in supersonic flow we have a bifurcated shock structure where the foot of the detached bow shock wave contacts the viscous flow ahead of the protuberance, the qualitative details of the limiting streamlines are virtually independent of Mach number.[11] For example, Figure 17 shows the limiting streamlines about a long circular cylinder standing normal to a wall in a Mach 2.5 stream,[48] where the Reynolds number based on the undisturbed boundary-layer thickness, $\delta_0 = 2.5$ cm, is $R_{\delta_0} = 4.8 \times 10^5$. The flow is from left-to-right. There is a saddle-point of separation S on the axis of symmetry about two diameters ahead of the cylinder wall, from which the 3D primary separation line emerges to pass around and downstream of the cylinder. Upstream and downstream limiting streamlines converge towards the 3D separation line to feed a viscous horse-shoe vortex springing from the separation within the depth of the undisturbed boundary layer. (We note that even though the scale of the separation relative to the undisturbed boundary-layer thickness is many times less than for the slender wing or slender body flows, the consequences are still severe.) A streamline in the outer boundary layer attaches at the nodal point A in the plane of symmetry just ahead of the cylinder junction with the wall,

---

* The boundary-layer equations, clearly, are not valid very close to separation, or attachment.

from which an attachment line emerges along the leading-edge and divergent limiting streamlines pass around and downstream of the cylinder. One limiting streamline passes from the attachment node to the saddle point of separation. Others fan out from the attachment point in the plane of symmetry to eventually proceed towards the 3D separation line. Superimposed on the limiting streamline pattern, we observe the bow shock wave B, and the rear leg (or Mach stem, M) of the bow shock bifurcation. The lower photo on Figure 17 illustrates the flattened horse-shoe vortex made apparent by means of the vapour screen technique.

More than one separation line may be formed ahead of the cylinder, depending upon the Reynolds number of the oncoming flow and the scale of the boundary layer relative to the cylinder dimensions. The picture on Figure 18 shows a case with three such zones, for example, after Sedney and Kitchens.[48]

We have seen that in all of the examples discussed, the limiting streamline that is characteristic of a 3D separation line, has one feature in common. It is a barrier across which the limiting streamlines on either side of it cannot pass. Whether we prefer to accept the subtle details of either Maskell's envelope approach[1] or Lighthill's asymptote arguments[39] on the flow conditions immediate to a separation or an attachment line, elements of both treatises would appear to exist. In general, flow visualization records do not allow us to distinguish which interpretation is absolute. More experiments are clearly necessary to diagnose the flow features adjacent to 3D separations and re-attachments.

3.0 EXAMPLES OF THREE-DIMENSIONAL SEPARATIONS ON PRACTICAL CONFIGURATIONS

3.1 Upswept Fuselages

Let us commence our illustrative examples by looking, first of all, at flows about upswept afterbodies. A typical complicated flow problem of this kind is shown on Figure 19.1. Here we can see from the tufts on the side of the upswept rear fuselage of a de Havilland of Canada Caribou aircraft that very large cross-flow angles are present, and separation is occurring along the lower rounded flanks of the fuselage. The cross-flow is exaggerated in this illustration by the large flap angle, but even under cruising conditions for this class of rear-loading aircraft, 3D separations are sometimes present.

In the context of this review, the separations from the rounded underside are uncontrolled in that depending on the aircraft pitch and yaw angles, the separation positions will move around the body and may cause handling problems. The flow separations can be fixed in location to alleviate handling deficiencies by fitting a strake to the fuselage side, Figure 19.2, or by using a sharp edge to the fuselage underside as we see on Figure 20, on the de Havilland of Canada Buffalo aircraft.

The next illustration, Figure 21, shows surface flow visualization on a research model tested in the NAE 5 × 5-ft. wind tunnel. The straight "beaver tail" shape, with elliptic cross-sections, is fairly typical of small aircraft of the twin-engine STOL type, but the upsweep angle, which was adjustable on this model, was set at a large upsweep angle of 20°. We note that even though primary and secondary separations are clearly present, the flow is symmetrical and well organized. We know virtually nothing, unfortunately, about turbulence fluctuation levels bordering 3D separations. Figure 22 indicates substantial increases in the amplitude of surface pressure fluctuations as the scale of the separations becomes greater.

The turbulent shear layers springing from the primary separation lines roll-up to form vortex motions, which we show on Figure 23, by pitot pressure isobars measured beneath another elliptical section afterbody. The analysis of this type of flow, which presents many difficulties, is further complicated by the presence of the wing downwash field and additional separations that may be present in the wing-root junction and from bulbous wheel housings, Figure 24. Thus, while we have a qualitative understanding of fuselage flows, we are still far from being able to predict the viscous-inviscid interactions about upswept bodies.

3.2 Pointed, Slender Missiles

On very long pointed slender bodies, we find that separation first occurs symmetrically with a pair of vortices trailing back along the body. Figure 25.1 illustrates such body separations on a blunted cone-cylinder-flare model. The symmetrical body vortices in low speed flow have been well documented by Grosche,[20] an illustration from which is given on Figure 25.2 (top); when a wing is added to the body, there is a substantial change in the position of the body vortices in the flowfield due to the larger induced effects of the controlled flow separations at the wing swept edges, see Figure 25.2 (bottom). These separations have an important effect on the static and dynamic flight stability of such vehicles. At small incidences, where the separation is steady and symmetrical with respect to the incidence plane, the resulting body vortices produce a nonlinear contribution to the normal force and pitching moment. If the fin system is not symmetrically orientated with respect to the incidence plane, a cross-coupling side force, yawing moment and rolling moment can arise even at small incidences. At larger incidences, the separations and body vortices become asymmetric (but still relatively steady in space) and large side forces, yawing moments and rolling moments are developed, especially on fin-stabilized vehicles. Figure 26, which gives the primary turbulent boundary-layer separation positions on the port and starboard side of a cone-cylinder and ogive-cylinder respectively, shows that the nose shape has an important influence on the initial asymmetry of the flow. For the 18° incidence case illustrated, the conical nose is at a relative incidence of about 3.1 and has generated substantial flow asymmetry, whereas the shorter ogival nose is only at a relative incidence of about 1.3 at the nose, where the initial separation is symmetrical. A ring of grit or a ring of vortex generators downstream of a bluff-nose can reduce yawing moments by factors of two or more.[62]

We may judge the occurrence of the onset of asymmetry by, say, the side force exceeding five percent of the normal force. This is illustrated on Figure 27. At subsonic speeds, where these asymmetric effects are most pronounced, we see that (following the trend indicated on Figure 26) as the semi-apex angle at the nose is increased, the onset of flow asymmetry is delayed. A longer afterbody, as one would expect, hastens the asymmetry, by providing a larger effective normalized incidence, α/θ_c. At higher Mach numbers (at M_∞ = 3.5, for the tests shown on Figure 27) when shock waves are present in the cross-flow, the separation positions remain symmetrical and the side forces disappear.

3.3 Slender Wings and Slender Bodies with Strakes

The most studied example of three-dimensional separation occurs along the leading-edges of lifting slender wings, as we discussed with the aid of Figure 5. The conical, inviscid flow theories, for example, that of Mangler and Smith,[10] have accounted for the vortex sheets springing from the leading-edges and coiling-up above the wing, but cannot include the effects of compressibility, nor the unloading that occurs at a subsonic trailing-edge. Polhamus[49,50] has attempted to remedy this with an overall theory, which assumes that, due to separation, the leading-edge suction force is rotated 90° into a direction normal to the wing chord plane thus given a nonlinear component to the normal force. While no theoretical proof of this method has been established, there is no doubt that it works. (In fact, Lamar has recently extended the Polhamus method to treat the vortex flow characteristics of wings with side edges.[51])

Figure 28 shows the overall normal force measured on a sharp-edged 70° delta wing under high Reynolds number conditions at Mach numbers of 0.7 and 1.6. The agreement of the subsonic measurements with the Polhamus theory is excellent up to a relative incidence of about unity. The departure from Smith's conical theory[10] is evident. We notice that there is a marked decrease in the nonlinear lift at supersonic speeds even though at Mach 1.6, the wing is still slender $\sqrt{M^2-1}\ s/L \simeq 0.43$. Other experimenters have noted that this is associated with a substantial flattening of the lee-side vortex structure.[33]

More complicated, but still conical cases have been treated by Levinsky and Wei[52] using essentially the same formulations as Mangler and Smith,[10] but accounting for a conical body. Some measurements that we have made using a 5° semi-apex angle cone with 75 percent strake wings are shown on the next illustration, Figure 29.1, in comparison with the Levinsky and Wei nonlinear theory. Up to relative incidences of about two, the experimental results for the subsonic and supersonic Mach numbers agree; but at higher relative incidences for the M_∞ = 1.8 case, conically mixed flow with internal shock waves occurs. The strakes provide a case of fixed or controlled flow separation to give a substantially different conical flowfield to that on the 5° cone alone.[53] But, while the Levinsky and Wei nonlinear theory accounts for the leading-edge separations, it cannot cope with the strong body separations in the wing body junctions.[11]

The flow about an ogive-cylinder with strakes at a sweepback angle of 78° at Mach 2 were studied by Fellows and Carter.[63] If we extrapolate the trend of Figure 27, the 17° semi-apex nose angle of the ogive in Reference 63 would have precluded flow asymmetry from body vortices up to angles of attack of about 50°. Vapour screen photos on Figure 29.2 depict a progressive and massive increase in scale of the strake symmetrical vortices (in relation to body geometry) above the lee-side of the body up to α/θ_c of greater than two.

One very important use of controlled flow separation in design is the low aspect ratio strake[54,55] mounted ahead of a wing of moderate sweep and aspect ratio such as the F-16 (Fig. 4.1) and the F-17 (Fig. 30). One significant advantage offered by the strakes is the induced lift provided by strake vortices to extend the maneuvering capabilities of the aircraft in transonic flow. With the aircraft at incidence, as we see on Figure 30, the fixed separations at the strake leading-edges form vortices that pass back over the main wing alongside the fuselage. Additional controlled separations are generated by the fuselage boundary-layer bleed diversion slots at the strake/fuselage intersection, the vortices from which roll up and also pass downstream on either side of the body. The flow over the wing is attached — up to the region of a strong normal shock/turbulent boundary-layer interaction proceeding to the tip. Küchemann[55] has proposed that the vortex avoids the necessity for the formation of the usual forward branch of the wing shock pattern by providing a "soft" boundary for the flow turning inboard over the leading-edge, instead of the "stiff" boundary given by the fuselage side.[10] (Note that the flow is from left-to-right and the nose is not in view in Figure 30.)

3.4 Hypersonic Configurations

The non-slender delta wing at incidence, with supersonic leading-edges, has received considerable attention by Whitehead et al.[32,33] and by Cross.[57] The lee-side flowfield (Fig. 31.1) is dominated by a swept-shock boundary-layer interaction that causes a three-dimensional separation of most of the top-wing boundary layer. The swept shock is inside the bow shock wave envelope, being positioned very close to a freestream Mach cone from the wing apex. In contrast to the subsonic leading-edge delta-wing flow that is dominated by leading-edge separation, (Fig. 31.2), the supersonic leading-edge flow is characterized by a Prandtl-Meyer expansion. Along the attachment line of the lee-side meridian, intense heating is measured.[33] If a body is attached beneath the delta wing, the flowfield becomes complex in detail on the underside. Figure 32 shows flow separation and attachment lines on the under-surface of a half-cone delta wing at 15° incidence at Mach 12.6. Boundary-layer conditions are laminar. The transmitted shock from the cone produces separation on the delta wing, and there is also a junction-type separation. The high local heat transfers at the flow attachment lines on the same configuration are shown in the next graph, Figure 33, as well as the heat transfer minima at the separation lines.

As we saw on Figure 9, the contouring of the leading-edge of a planar 70° swept delta wing at Mach 6 alleviated the heating on the lee-meridian. Can the philosophy of controlled flow separation be used to reduce the peak heating on Space Shuttle shapes? Figure 34 shows surface oil flow on an Orbiter vehicle[58] at 30° incidence at a Mach number close to 20. The three-dimensional separation from the wing fillet passes back across the top surface of the wing (analogous to the strake flow discussed with reference to Fig. 30) although it is now associated with a swept shock wave. Another 3D separation, beginning about the cockpit housing, and continuing downstream is also evident, with an attachment region existing on the fuselage side and on the leeward meridian. Unfortunately, no circumferential heat transfer measurements were taken in Reference 58 to improve the identification of the attachment line regions.

The potential for altering the lee-surface geometry to achieve reduced lee-side heating[59] is shown on Figure 35 for several shuttle configurations at Mach 6 and 8. The idea was to use relatively sharp edges to fix or control the 3D separations and encourage the coiling-up of the viscous shear layers to leave the proximity of the fuselage.

On the left of Figure 35, the initial slope of the side profile was increased and then broken sharply. We see that the heating data resulting from this modification show a substantial reduction along 50 percent of the leeward meridian. Additional verification of the potential for reduced lee-side heating by controlled flow separation is discussed by Shultze and McGee[60] and by Connor.[61] The configuration of the former authors with relatively large initial slope angle and sharp break in contour generated significantly lower lee-surface heating than did the shape chosen by Connor, who used less sharp contour changes.

3.5 Swept Interactions

The three-dimensional interaction between a turbulent boundary layer, developing along a surface and a perpendicular, glancing oblique shock wave (sometimes called a "skewed" shock wave) – see Figure 37 – is a phenomenon of considerable importance in the design of swept wings, wing/body and tail/body junctions, quasi-2D and half-cone inlets. Figure 36, for example, shows a half-cone inlet of a typical fighter aircraft operating near design at Mach 1.6, with the shock from the half-cone causing a massive 3D separation of the fuselage boundary layer.

Despite several previous investigations,[64-67] Green noted[68] that there was little quantitative understanding of interactions between swept shock waves and turbulent boundary layers, although Stalker[64] and Stanbrook[65] introduced some qualitative features in their early work, while later investigations by McCabe[66] and Lowrie[67] provided some insight into the crossflows developing in the interaction. Much of the existing analysis has been developed for so-called "infinite" swept flows, and so is of a quasi two-dimensional nature; while most experiments have been conducted using the nozzle boundary layers in relatively small supersonic wind tunnels. At a given mainstream Mach number, the flow deflection angle for so-called "incipient separation" has usually been determined as when the limiting streamlines become parallel to the projection of the shock wave (in the external stream) on to the wall, and Korkegi[69] has made a simple correlation of incipient separation data from References 66 and 67.

In some experiments[16,17] in the NAE 5 × 5-inch blowdown (pilot) wind tunnel, the mean flow features including wall static pressure, surface impact pressure and limiting streamline direction, and pitot and stagnation temperature profiles, were gathered through swept interactions at mainstream Mach numbers of 2 and 4, up to and beyond flow deflection angles through the shock wave that produced three-dimensional separation, see Figure 37. The Reynolds number based upon the mainstream conditions and the undisturbed boundary-layer thickness, δ_0, of 0.2-inch, was 2×10^5. The wall conditions were essentially those of zero heat transfer. (Similar boundary-layer experiments were conducted by Oskam[18] at Princeton University.)

Subsequently, for the Mach 2 flow, a small convergent/divergent tangential wall jet nozzle was installed in the test wall (Fig. 38) upstream of the interaction region, to investigate whether a strong three-dimensional shock-induced separation could be controlled or destroyed by a Mach number 3 supersonic wall jet. (The planning of the 3D experiment followed the criteria established by Peake[70] for supersonic blowing boundary-layer control in a two-dimensional shock/boundary-layer interaction.) The direction of the jet efflux could be oriented at various angles with respect to the line of separation, as we see on the diagrammatic sketch of Figure 37.

Figure 39 shows the effects of a wedge deflection angle of 16° in a Mach 4 airstream where there is a substantial 3D separation generated way ahead of the shock wave in the external flow (as we see on the wall pressure plot and the Schlieren/oil dot flow visualization picture). The pitot pressure profiles through the interaction, measured by a 3-tube yawmeter that nulled into the direction of the local velocity, are shown on the top graph of Figure 40. The profile measurement stations situated relative to the calculated shock are shown at the intersection of the pitot profiles with the abscissa. The profiles are sufficiently close together to allow a construction of the forward oblique leg of the shock bifurcation at the foot of the wedge shock. Downstream of the 3D separation line position, the presence of the shear layers with heat transfer is indicated by rapid changes and troughs on the temperature plots. From these distributions, we may postulate that the deficit troughs correspond with the core flow of a flattened vortex structure of the rolled-up shear layer from the 3D separation line, much like the corner flow model proposed by Cooper and Hankey in Reference 71 and witnessed via electron beam flow visualization by Henderson and Bertram.[72] The axis of the vortex would appear to be just ahead of the line of the calculated shock (the origin of which is the wedge apex) where the "overshoot" towards 0° on the yaw profile (that is, parallel to the mainstream at infinity) is at its maximum. The substantial swings in the total temperature distributions. Figure 41.1, that are found in distinct contrast to the expected form in unseparated flow, Figure 41.2, would appear to be a useful indicator of a 3D separated flowfield.

Can such an undesirable 3D separation be diminished or destroyed by blowing boundary-layer control, for we know that on swept wings, especially in transonic flow, the viscous vortex from a 3D separation can sometimes burst over the wing, leading to unpleasant difficulties in airplane control; while in the quasi-2D supersonic intake, once 3D separations are present on the sidewalls, they appear to promote high fluctuation and distortion levels at the compressor face further downstream. But perhaps the most significant aspect of 3D separated flows in the hypersonic régime, is the high heat transfer to the surface in the region of flow re-attachment, which poses severe problems of skin cooling, as we have seen already. The particular losses caused by the pitot pressure deficit in the rolled-up viscous vortex, and the associated skin friction increases in re-attachment zones, have not been quantified to the author's knowledge.

On Figure 42, we demonstrate the invigoration of the 3D wedge-generated separation by a Mach 3 supersonic wall jet. This illustration provides a selection of wall static pressure distributions along and just off the tunnel centre-line for various angular settings of the jet efflux with respect to the tunnel centre-line. The positive sign of θ_j indicates a jet direction towards the wedge surface, and this angular setting yields no control, and large peaks and troughs in the static pressure distribution(s) corresponding with free vortical shear layer(s) rolling up from the three-dimensional separation line(s). On the other hand, the jet rotation angle of -25° produces a relatively smooth pressure rise. The wall jet has produced a local expanding flow around the wedge leading-edge (due to the 25°-11.5° expansion angle) to alleviate the originally induced large shock pressure rise. In the present, constrained geometrical conditions, it is not clear, unfortunately, whether the advised direction of blowing would carry over to controlling a 3D shock-induced separation on, say, a swept wing or body flow with internal shock waves.[74]

4.0 CONCLUDING REMARKS

In this brief review, we have illustrated some of the diverse kinds of fixed and unfixed three-dimensional separations that can, and do, occur on aircraft and missiles. It is evident that the concept of controlled flow separation in three-dimensions provides the designer with substantial rewards in having a qualitatively non-varying flowfield at his disposal. However, we must always be aware of the consequences on flight vehicle drag, which are not readily predictable. At the outset, we have no quantitative yardstick to determine the scale of the device to "fix" separation, and to say how "sharp" should a sharp edge be? We do not understand what determines the scale of the resulting vortical flows from 3D separations, and when they will be close to the surface and when they will not. What precise influence does body shape and vehicle relative incidence have on the scale of separation? Substantial research effort is required to reveal the answers to these questions, as all practical configurations produce three-dimensional interactions and vortical flows.

As of now, we see that, in general, even if the inviscid interfering flowfields can be calculated, the growth, separation and roll-up of three-dimensional turbulent boundary layers cannot yet be adequately predicted.

5.0 REFERENCES

1. Maskell, E.C. — *Flow Separation in Three Dimensions.* RAE Aero. Rept. 2565, November 1955.

2. Küchemann, D. — *Flow with Separations.* Unpublished RAE Tech. Memo., December 1955.

3. Maskell, E.C.; Küchemann, D. — *Controlled Separation in Aerodynamic Design.* Unpublished RAE Tech. Memo., March 1956.

4. Cornish, J.J., III — *High Lift Applications of Spanwise Blowing.* ICAS Paper 70-09, September 1970.

5. Bradley, R.G.; Wray, W.O. — *A Conceptual Study of Leading-Edge-Vortex Enhancement by Blowing.* Jour. Aircraft, Vol. 11, No. 1, January 1974, pp. 33-38.

6. Campbell, J.F. — *Augmentation of Vortex Lift by Spanwise Blowing.* AIAA 75-993, August 1975.

7. Barsby, J.E. — *Calculations of the Effect of Blowing from the Leading-Edges of a Slender Delta Wing.* RAE Tech. Rept. 71077, ARC R and M 3692, 1971.

8. Spillman, J.; Goodridge, M. — *Flow Characteristics about a Delta Wing at 15° Incidence with and without Leading-Edge Blowing.* Coll. of Aero., Cranfield, Rept. Aero. 9, 1972.

9. Alexander, A.J. — *Experiments on a Delta Wing using Leading-Edge Blowing to Remove the Secondary Separation.* Coll. of Aero., Cranfield, Rept. 161, 1963.

10. Smith, J.H.B. — *A Review of Separations in Steady, Three-Dimensional Flow.* AGARD CP-168, May 1975.

11. Peake, D.J.; Rainbird, W.J.; Atraghji, E.G. — *Three-Dimensional Flow Separations on Aircraft and Missiles.* AIAA Jour., Vol. 10, No. 5, May 1972, pp. 567-580.

12. Rainbird, W.J.; Crabbe, R.S.; Peake, D.J.; Meyer, R.F. — *Some Examples of Separation in Three-Dimensional Flows.* CASI Jour., Vol. 12, No. 10, December 1966, pp. 409-423.

13. Peake, D.J. — *Three-Dimensional Flow Separations on Upswept Rear Fuselages.* CASI Jour., Vol. 15, No. 10, December 1969, pp. 399-408.

14. Sedney, R.; Kitchens, C.W. — *The Structure of Three-Dimensional Separated Flows in Obstacle, Boundary-Layer Interactions.* AGARD CP-168, May 1975.

15. Hsia, H.T-S.; Seifert, H.S. — *Shocks Induced by Secondary Fluid Injection.* AIAA 64-111, January 1964.

16. Peake, D.J. — *The Three-Dimensional Interaction of a Swept Shock Wave with a Turbulent Boundary Layer and the Effects of Air Injection on Separation.* Ph.D. Thesis, Carleton University, Ottawa, Canada, March 1975. NRC, Aeronautical Report LR-592, National Research Council Canada, Ottawa, Ontario, July 1976.

17. Peake, D.J.
Rainbird, W.J.
The Three-Dimensional Separation of a Turbulent Boundary Layer by a Skewed Shock Wave; and its Control by the Use of Tangential Air Injection.
AGARD CP-168, May 1975.

18. Oskam, B.
Vas, I.E.
Bogdonoff, S.M.
An Exploratory Study of a Three-Dimensional Shock Wave Boundary Layer Interaction at Mach 3.
AGARD CP-168, May 1965.

19. Korkegi, R.H.
Survey of Viscous Interactions Associated with High Mach Number Flight.
AIAA Jour., Vol. 9, No. 5, May 1971., pp. 771-784.

20. Grosche, F.R.
Wind Tunnel Investigation of the Vortex System Near an Inclined Body of Revolution with and without Wings.
AGARD CP-71, September 1970.

21. Rao, D.M.
Whitehead, A.H.
Lee-Side Vortices on Delta Wings at Hypersonic Speeds.
AIAA Jour., Vol. 10, No. 11, November 1972, pp. 1458-1465.

22. Rubesin, M.
Subgrid or Reynolds Stress Modelling for Three-Dimensional Turbulence Computations.
NASA SP-347, Part I, March 1975, pp. 317-339.

23. Roache, P.J.
Bradshaw, P.
Letters in Response to Reference 24, Astronautics and Aeronautics, Vol. 13, No. 9, September 1975, pp. 4-6.

24. Chapman, D.R.
Mark, H.
Pirtle, M.W.
Computers Versus Wind Tunnels for Aerodynamic Flow Simulations.
Astronautics and Aeronautics, Vol. 13, No. 4, April 1975, pp. 22-29; 35.

25. Weber, J.A.
Brune, G.W.
Johnson, F.T.
Lu, P.
Rubbert, P.E.
A Three-Dimensional Solution of Flows over Wings with Leading-Edge Vortex Separation.
AIAA 75-866, June 1975.

26. Marsden, D.J.
Simpson, R.W.
Rainbird, W.J.
The Flow over Delta Wings at Low Speeds with Leading-Edge Separation.
Coll. of Aero., Cranfield, Rept. 114, February 1958.

27. McRae, D.S.
A Numerical Study of Supersonic Viscous Cone Flow at High Angle of Attack.
AIAA 76-97, 1976.

28. MacCormack, R.W.
The Effect of Viscosity in Hypervelocity Impact Cratering.
AIAA 66-354, 1969, pp. 1-7.

29. Tracy, R.R.
Hypersonic Flow Over a Yawed Circular Cone.
GALCIT Memo. No. 69, Graduate Aeronautical Labs., California Institute of Technology, Pasadena, California, 1963.

30. Lubard, S.C.
Rakich, J.V.
Calculation of the Flow on a Blunted Cone at High Angle of Attack.
AIAA 75-149, January 1975.

31. Cleary, J.W.
Effects of Angle of Attack and Bluntness on Laminar Heating Rate Distribution on a 15° Cone at Mach Number of 10.6.
NASA TND-5450, October 1969.

32. Whitehead, A.H.
Bertram, M.H.
Alleviation of Vortex-Induced Heating to the Lee Side of Slender Wings in Hypersonic Flow.
AIAA Jour., Vol. 9, No. 9, September 1971, pp. 1870-1872.

33. Whitehead, A.H.
Hefner, J.N.
Rao, D.M.
Lee-Surface Vortex Effects Over Configurations in Hypersonic Flow.
AIAA 72-77, January 1972.

34. Sears, W.R.
Collected Papers of W.R. Sears Through 1973.
Ed. by N.H. Kemp, March 1974, pp. 61, 94, 162, 167.

35. Maskell, E.C.
On the Principles of Aerodynamic Design.
Prog. in Aero. Sci., Vol. 1, No. 1, 1961, pp. 1-7.

36. Küchemann, D.
Aerodynamic Design.
Aero. Jour., Vol. 73, No. 698, February 1969, pp. 101-110.

37. Legendre, R.
Lignes de Courant d'un Ecoulement Continu.
Rech. Aérosp., No. 105, 1965, pp. 3-9.

38. Legendre, R.
La Condition de Joukowski en Ecoulement Tridimensionnel.
Rech. Aérosp., No. 5, 1972, pp. 241-8.

39. Lighthill, M.J.
Attachment and Separation in Three-Dimensional Flow.
Section II.2.6 of "Laminar Boundary Layers," Ed. by L. Rosenhead, Oxford Univ. Press, 1963, pp. 72-82.

40. Wild, J.M.
The Boundary Layer of Yawed Infinite Wings.
Jour. Aero. Sci., Vol. 16, No. 1, January 1949.

41. Eichelbrenner, E.A.
Oudart, A.
Observations on a Criterion of Three-Dimensional Laminar Boundary-Layer Separation.
Rech. Aéron., No. 40, July-August 1954, pp. 3-5. Also: NRC (Canada) TT-962, 1961.

42. Eichelbrenner, E. A.
Oudart, A.
Three-Dimensional Laminar Boundary-Layer Separation.
Rech. Aéron., No. 47, 1955, pp. 11-14. Also: NRC (Canada) TT-963, 1961.

43. Brown, S.
Singularities Associated with Separating Boundary Layers.
Roy. Soc. of London Phil. Trans., Series A, Vol. 257, 1965, pp. 409-444.

44. Maltby, R.L.
Flow Visualization in Wind Tunnels using Indicators.
AGARDograph 70, April 1962.

45. Eichelbrenner, E.A.
Three-Dimensional Boundary Layers.
Annual Review of Fluid Mechanics, Vol. 5, 1973, pp. 339-360.

46. Cumpsty, N.A.
Head, M.R.
The Calculation of the Three-Dimensional Turbulent Boundary Layer; Part 3, Comparison of Attachment-Line Calculations with Experiment.
Aero. Quart. Vol. XX, 1969, pp. 99-113.

47. Atraghji, E.G.
Surface Visualization, Surface Pressure and Surface Preston Tube Pitot Pressure Measurements over a 6:1 Ellipsoid at Incidence, at Mach 0.3 and 0.74.
NRC (Canada) NAE Data Report 5X5/0032, 1968.

48. Sedney, R.
Kitchens, C.W.
The Structure of Three-Dimensional Separated Flows in Obstacle, Boundary-Layer Interactions.
AGARD CP-168, May 1975.

49. Polhamus, E.C.
A Concept of the Vortex Lift of Sharp-Edge Delta Wings Based on a Leading-Edge Suction Analogy.
NASA TND-3767, December 1966.

50. Polhamus, E.C.
Applications of the Leading-Edge Suction Analogy of Vortex Lift to the Drag due to Lift of Sharp-Edge Delta Wings.
NASA TND-4739, August 1968.

51. Lamar, J.E.
Prediction of Vortex Flow Characteristics of Wings at Subsonic and Supersonic Speeds.
AIAA 75-259, January 1975.

52. Levinsky, E. S.
Wei, M.H.Y.
Non-Linear Lift and Pressure Distribution on Slender Conical Bodies with Strakes at Low Speeds.
NASA CR-1202, 1968.

53. Rainbird, W.J.
The External Flow Field about Yawed Circular Cones.
AGARD CP-30, May 1968.

54. Ray, E.J.
McKinney, L.W.
Carmichael, J.G.
Maneuver and Buffet Characteristics of Fighter Aircraft.
AGARD CP-102, 1972.

55. Küchemann, D.
On the Possibility of Designing Wings that Combine Vortex Flows with Classical Aerofoil Flows.
Unpublished RAE Tech. Memo, 1971.

56. Geissler, W.
Calculation of the Three-Dimensional Laminar Boundary Layer Around Bodies of Revolution at Incidence and with Separation.
AGARD CP-168, May 1975.

57. Cross, E.J.
Experimental and Analytical Investigation of the Expansion Flow Field over a Delta Wing at Hypersonic Speeds.
ARL 68-0027, February 1968.

58. Stone, D.R.
Mulfinger, R.
Hypersonic Stability and Control Characteristics of the Rockwell International 139-B Space Shuttle Orbiter.
NASA TMX-71968, July 1974.

59. Hefner, J.F.
Lee-Surface Heating and Flow Phenomena on Space Shuttle Orbiters at Large Angles of Attack and Hypersonic Speeds.
NASA TND-7088, November 1972.

60. Schultze, H.D.
McGee, K.W.
Heat Transfer Tests of the LMSC Delta-Body Orbiter and Stage-and-One-Half Ascent Configuration.
DMS-DR-1143, Chrysler Corporation, June 1971.

61. Conner, L.E.
Heat Transfer Tests of the Lockheed Space Shuttle Orbiter Configuration Conducted at the Langley Research Center Mach 8 Variable Density Tunnel
TM 54/20-241, Lockheed Missiles and Space Co., December 1969.

62. Clark, W.H.
Peoples, J.R.
Briggs, M.M.
Occurrence and Inhibition of Large Yawing Moments during High Incidence Flight of Slender Missile Configurations.
AIAA 72-968, September 1972.

63. Fellows, K.A.
Carter, E.C.
Results and Analysis of Pressure Measurements on Two Isolated Slender Wings and Slender Wing-Body Combinations at Supersonic Speeds. Part 1 — Analysis.
ARC CP 1131, 1970.

64. Stalker, R.J.
Sweepback Effects in Turbulent Boundary-Layer/Shock Wave Interaction.
Jour. Aero. Sci., Vol. 27, No. 5, May 1960, pp. 348-356.

65. Stanbrook, A.
An Experimental Study of the Glancing Interaction Between a Shock Wave and a Turbulent Boundary Layer.
ARC CP 555, 1961.

66. McCabe, A.
The Three-Dimensional Interaction of a Shock Wave with a Turbulent Boundary Layer.
Ph.D. Thesis, University of Manchester, October 1963; Aero. Quart., Vol. XVII, August 1966, pp. 231-252.

67. Lowrie, B.W.
Cross-Flows Produced by the Interaction of a Swept Shock Wave with a Turbulent Boundary Layer.
Ph.D. Thesis, University of Cambridge, December 1965.

68. Green, J.E.
Interaction Between Shock Waves and Turbulent Boundary Layers.
RAE TR 69098, May 1969; Progress in Aerospace Sciences, Vol. 11, Pergamon Press at Oxford, 1970, pp. 235-340.

69. Korkegi, R.H.
A Simple Correlation of Incipient Turbulent Boundary-Layer Separation due to a Skewed Shock Wave.
AIAA Jour., Vol. 11, No. 11, November 1973, pp. 1578-1579.

70. Peake, D.J.
The Use of Air Injection to Prevent Separation of the Turbulent Boundary Layer in Supersonic Flow.
NGTE R256, November 1963; ARC CP 890, 1966; M. Sc. Thesis, University of Bristol, 1962.

71. Cooper, J.R.
Hankey, W.L.
Flowfield Measurements in an Asymmetric Axial Corner at M = 12.5.
AIAA Jour., Vol. 12, No. 10, October 1974, pp. 1353-1357.

72. Bertram, M.H.
Henderson, A.
Some Recent Research with Viscous Interacting Flow in Hypersonic Streams.
ARL 75-0212, 1969, pp. 1-30.

73. Culley, M.
Annual Report of Dept. of Supply.
Aeronautical Research Labs., Melbourne, Australia, 1966-67.

74. Rainbird, W.J.
Turbulent Boundary-Layer Growth and Separation on a Yawed Cone.
AIAA Jour., Vol. 16, No. 12, December 1968, pp. 2410-2416.

75.
Private Communication from ARA, Great Britain, 1966.

76. Küchemann, D.
The Aerodynamic Design of Aircraft — An Introduction, Part 5.
RAE Tech. Memo. Aero. 1622, February 1975.

77. Werlé, H.
Aperçu sur les Possibilités Expérimentales du Tunnel Hydrodynamique à Visualisation de l'O.N.E.R.A.
ONERA Tech. Note 48, 1958.

78. Beeman, E.R.
Private Communication, Northrop Corporation, March 1977.

79. Brune, G.W.
Rubbert, P.E.
Boundary-Value Problem of Configurations with Compressible Free Vortex Flow.
AIAA Jour., Vol. 15, No. 10, October 1977, pp. 1521-1523.

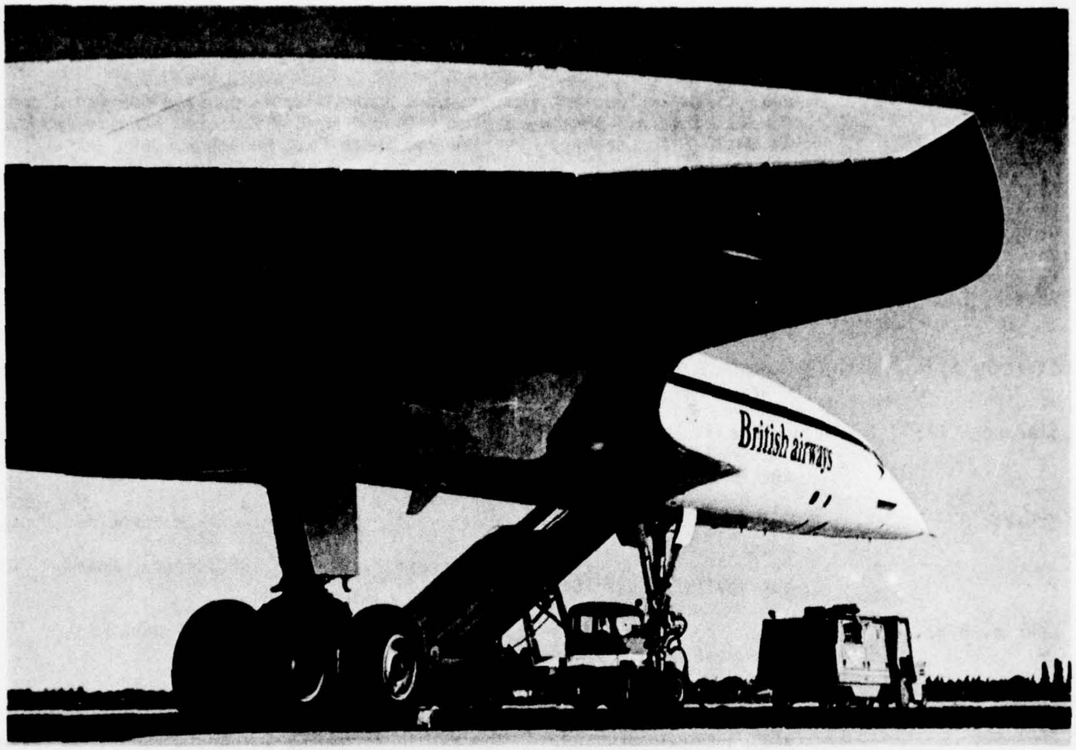

FIG. 1: SHARP SWEPT LEADING-EDGE OF "CONCORDE"

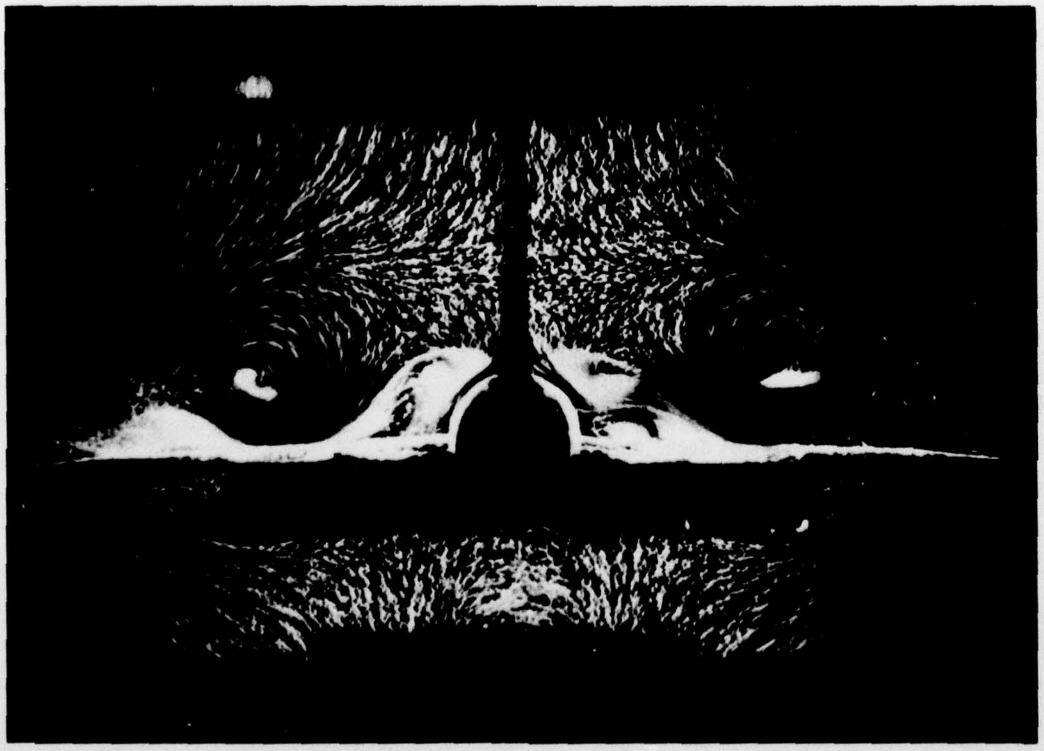

FIG. 2: VORTICES FROM SHARP SWEPT LEADING-EDGES

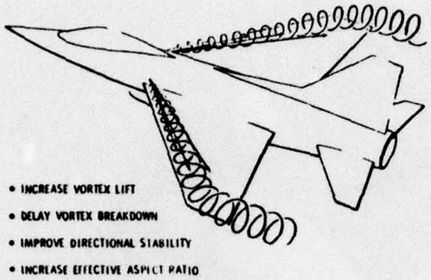

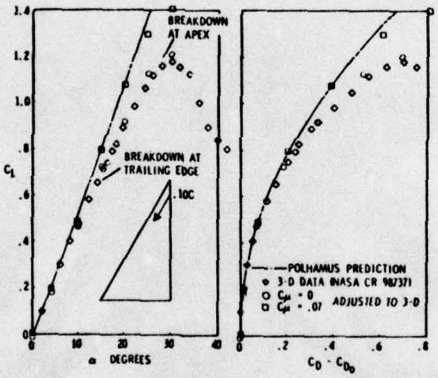

Comparison with theory—delta wing.

FIG. 3: SPANWISE BLOWING ALONG LEADING-EDGE[5]

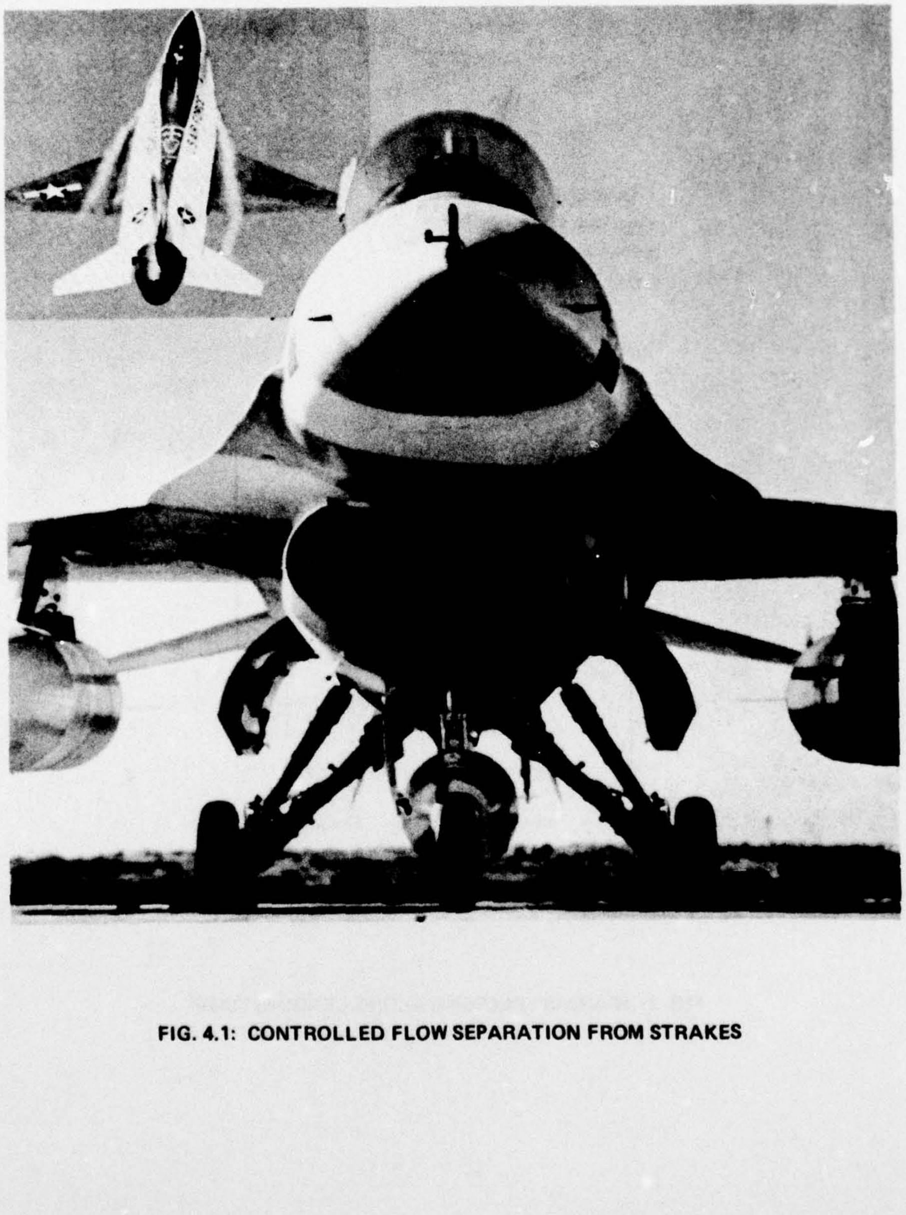

FIG. 4.1: CONTROLLED FLOW SEPARATION FROM STRAKES

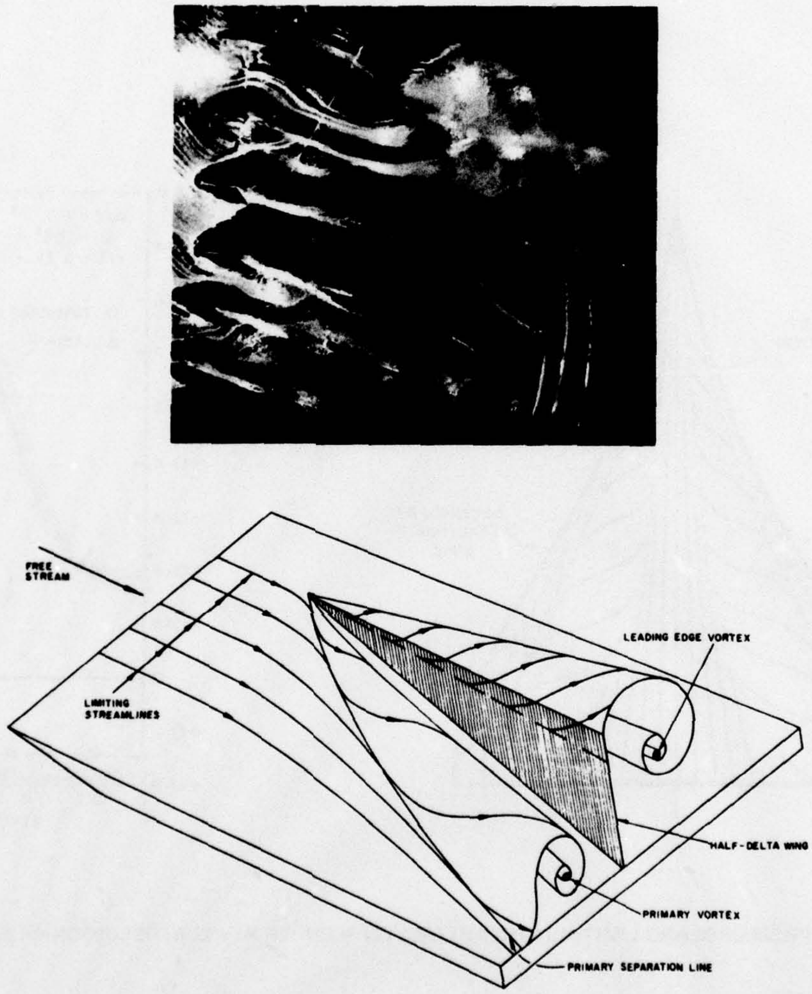

FIG. 4.2: CONTROLLED SEPARATION FROM SWEPT EDGES OF VORTEX GENERATORS ON FUSELAGE[75]

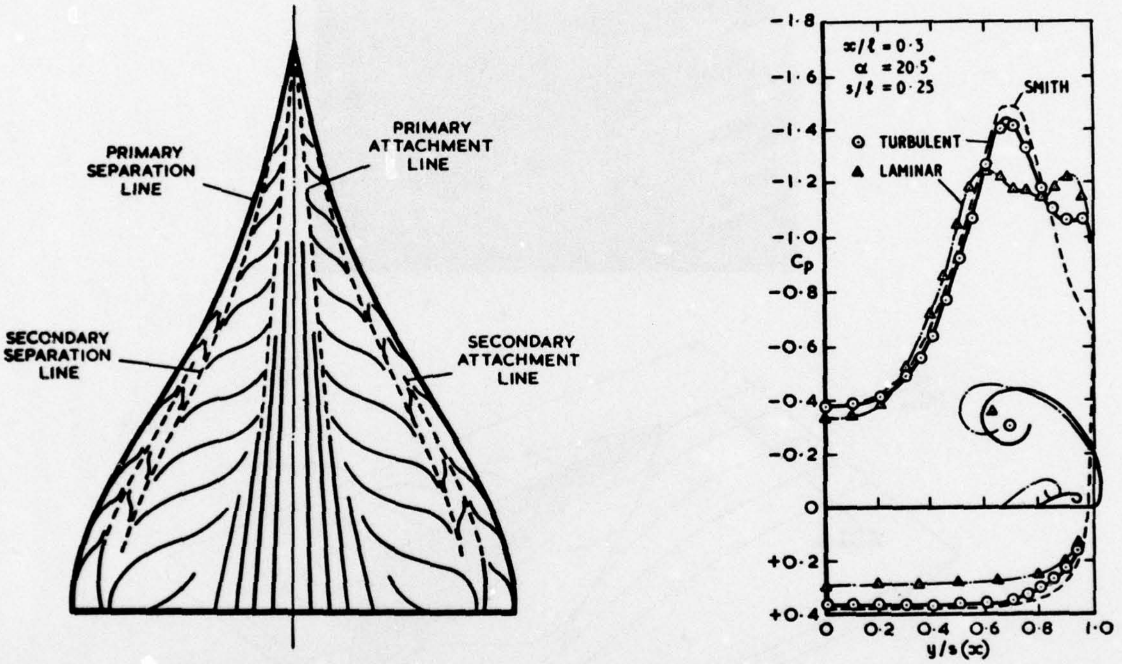

FIG. 5: SURFACE PRESSURES AND LIMITING STREAMLINES ON SLENDER WINGS WITH SUBSONIC LEADING-EDGES[76]

AD-A050 762 ADVISORY GROUP FOR AEROSPACE RESEARCH AND DEVELOPMENT--ETC F/G 20/4
THREE DIMENSIONAL AND UNSTEADY SEPARATION AT HIGH REYNOLDS NUMB--ETC(U)
FEB 78
UNCLASSIFIED AGARD-LS-94 NL

2 OF 4
AD
A050762

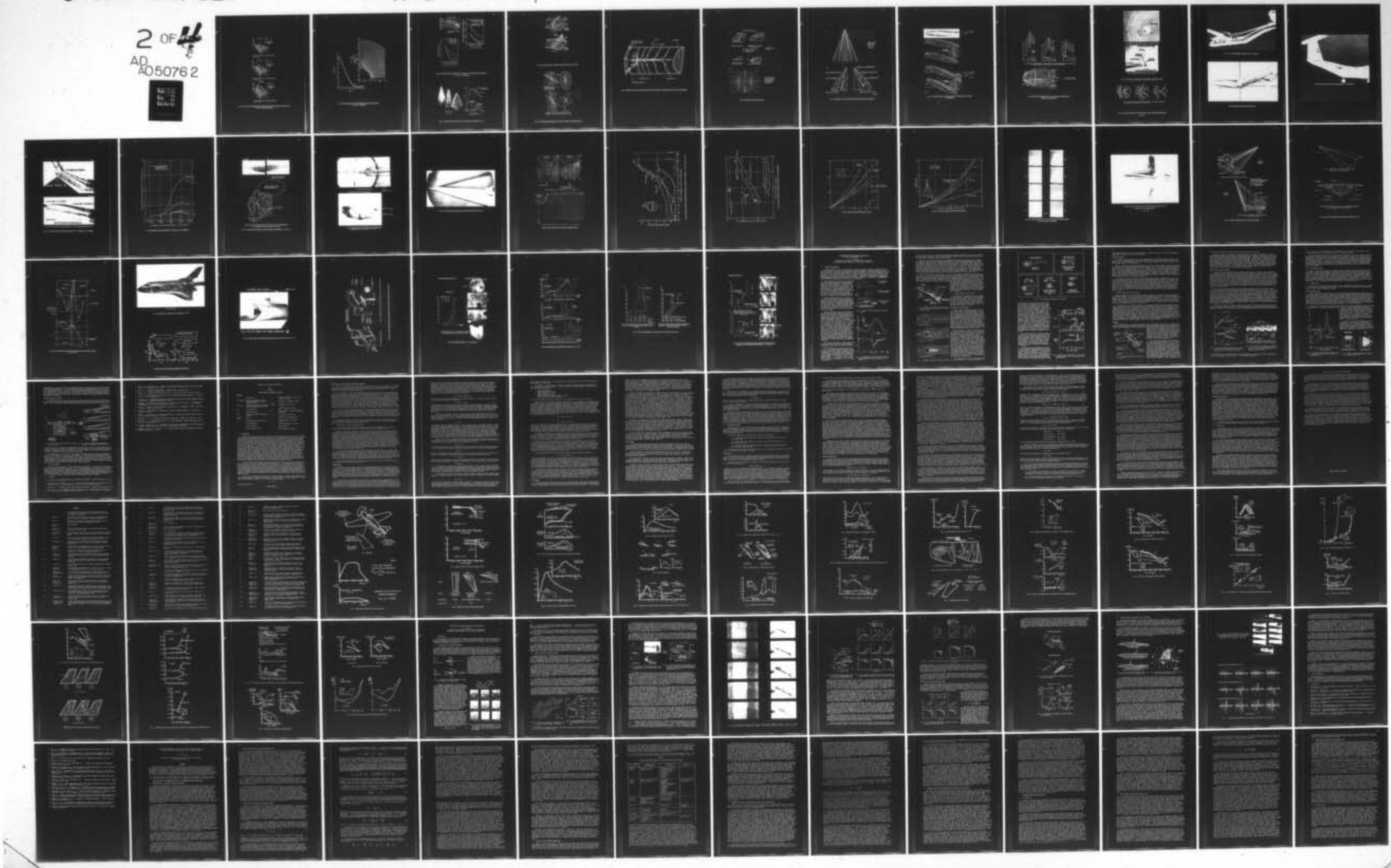

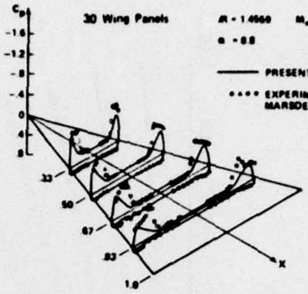

Surface Pressure Distribution of Delta Wing With 30 Wing Panels at α = 8.8°

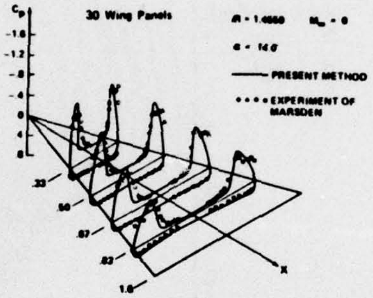

Surface Pressure Distribution of Delta Wing With 30 Wing Panels at α = 14.0°

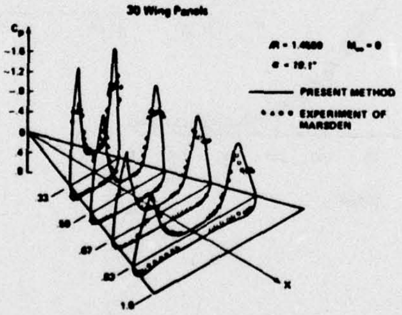

Surface Pressure Distribution of Delta Wing With 30 Wing Panels at α = 19.1°

FIG. 6: CALCULATED PRESSURES ON SLENDER WING WITH CONTROLLED[25] SEPARATION AT ALL THREE SHARP EDGES

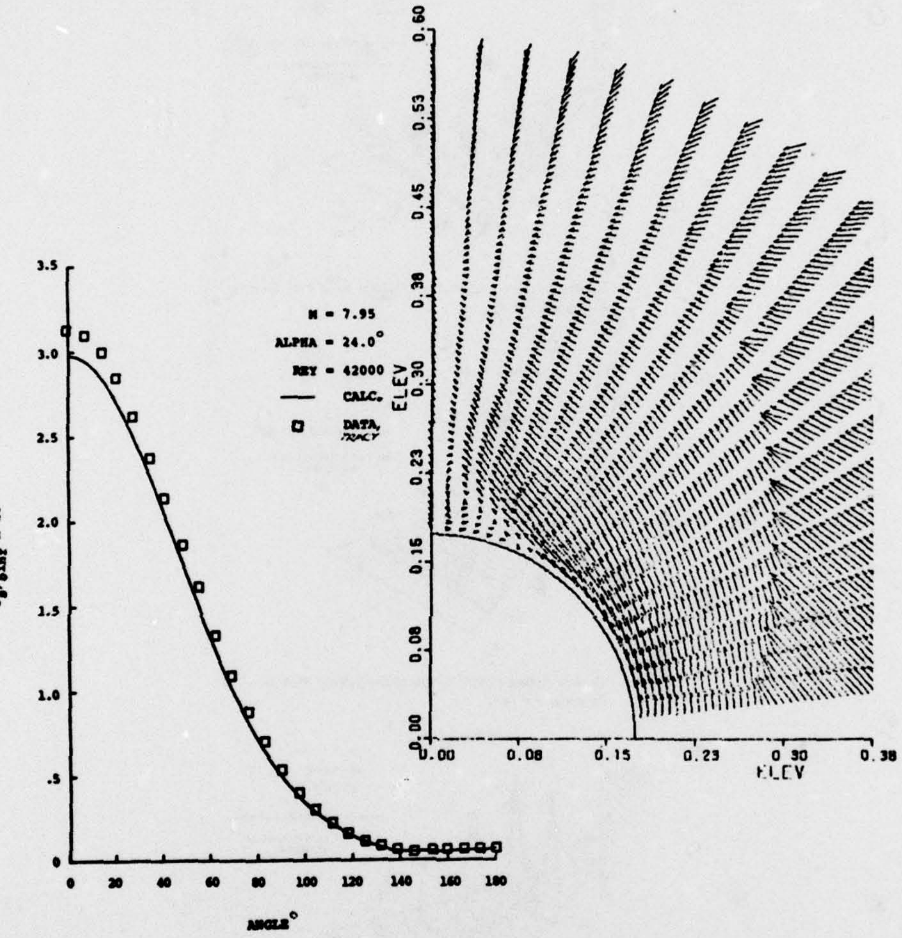

FIG. 7: SIMPLIFIED NAVIER-STOKES POINTED CONE FLOW SOLUTION[27]: $\theta_c = 10°$, M = 8, LAMINAR

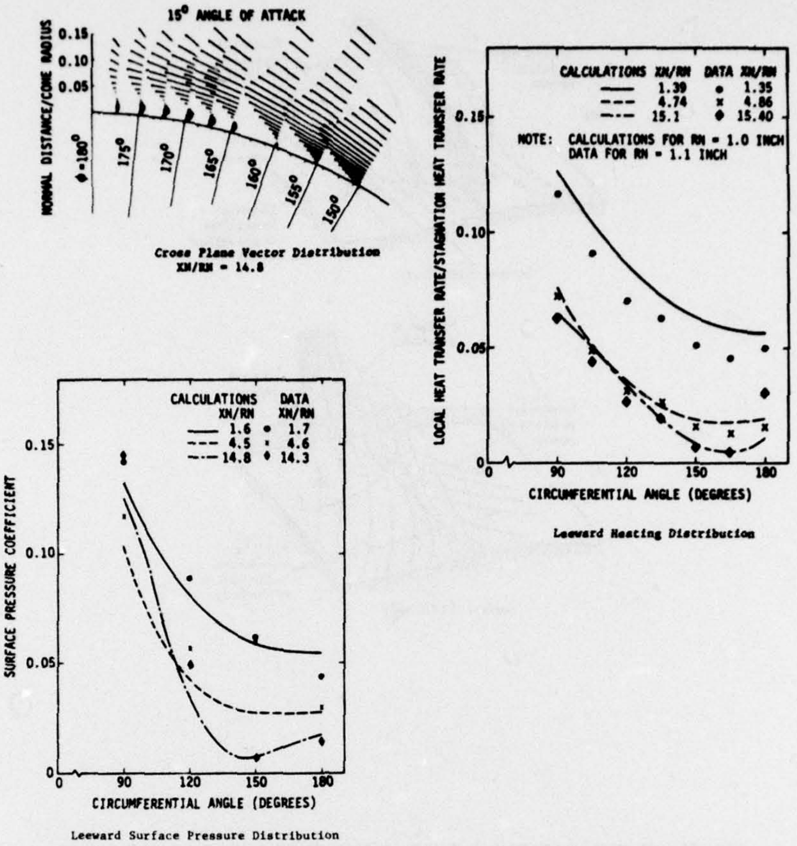

Cross Plane Vector Distribution
XN/RN = 14.8

Leeward Heating Distribution

Leeward Surface Pressure Distribution

FIG. 8: BLUNTED CONE SOLUTION USING "PARABOLIC" NAVIER-STOKES EQUATIONS[30]:
$\theta_c = 15°$, M = 10.6, LAMINAR

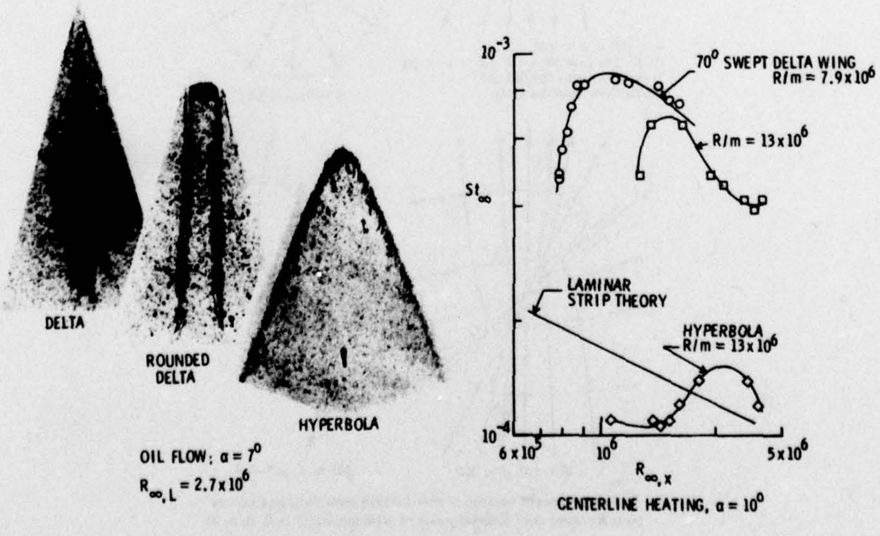

FIG. 9: LEE SURFACE FLOW OVER DELTA AND CONTOURED WINGS AT M = 6[33]

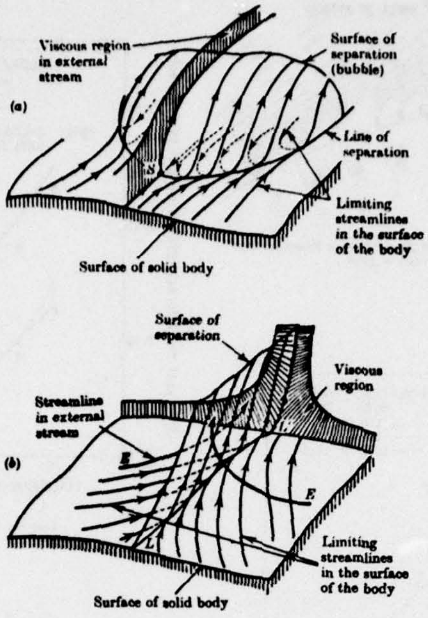

FIG. 10: 3D SEPARATIONS:[1] BUBBLE AND FREE SHEAR LAYER TYPES

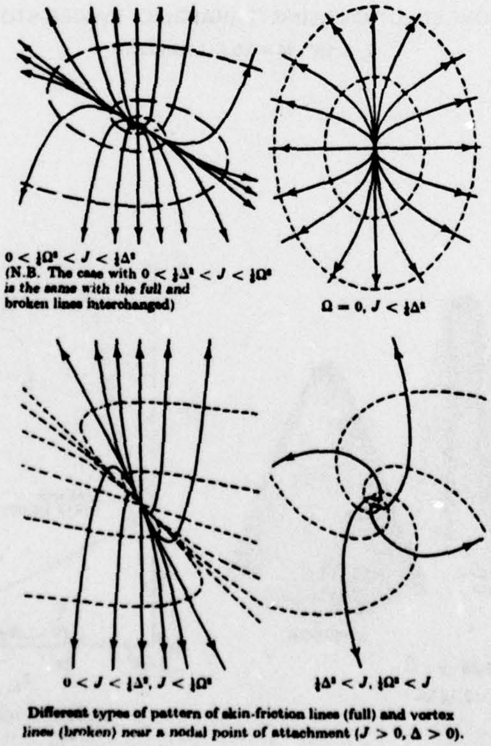

$0 < \frac{1}{4}\Omega^2 < J < \frac{1}{4}\Delta^2$
(N.B. The case with $0 < \frac{1}{4}\Delta^2 < J < \frac{1}{4}\Omega^2$ *is the same with the full and* broken lines interchanged)

$\Omega = 0, J < \frac{1}{4}\Delta^2$

$0 < J < \frac{1}{4}\Delta^2, J < \frac{1}{4}\Omega^2$

$\frac{1}{4}\Delta^2 < J, \frac{1}{4}\Omega^2 < J$

Different types of pattern of skin-friction lines (full) and vortex *lines (broken) near a nodal point of attachment* ($J > 0, \Delta > 0$).

FIG. 11: LIMITING STREAMLINES (FULL) ABOUT A NODAL ATTACHMENT POINT[39]

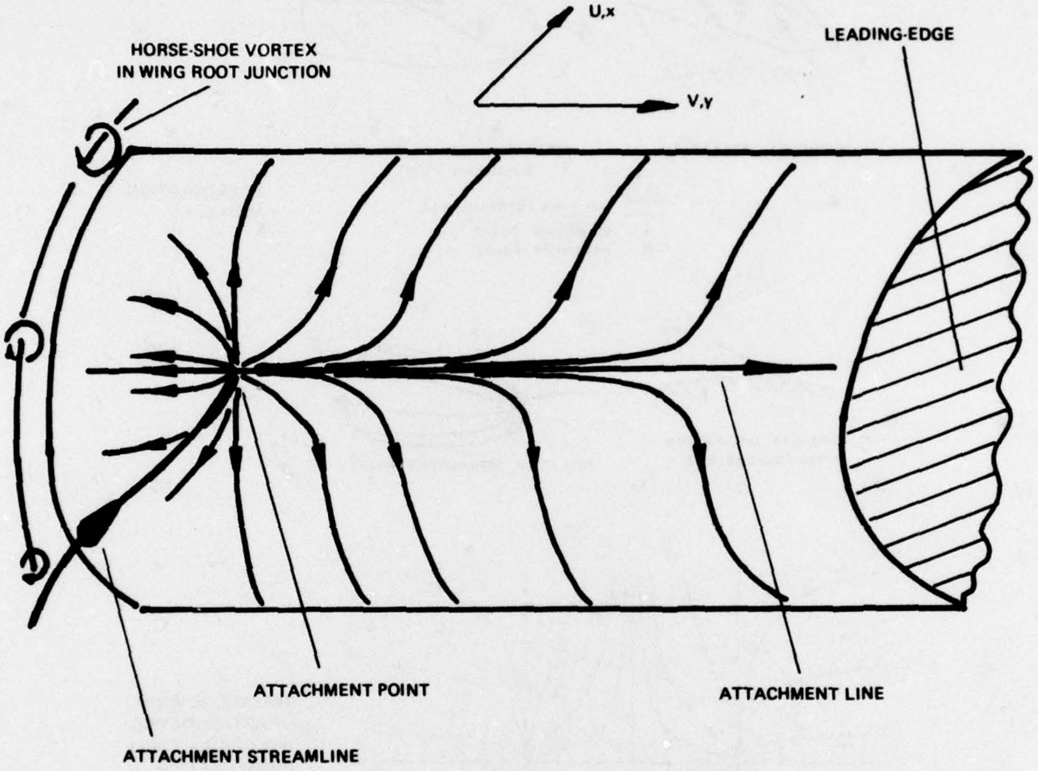

FIG. 12: POSSIBLE LIMITING STREAMLINE PATTERN ABOUT NODAL ATTACHMENT POINT ON WING LEADING-EDGE

13.1

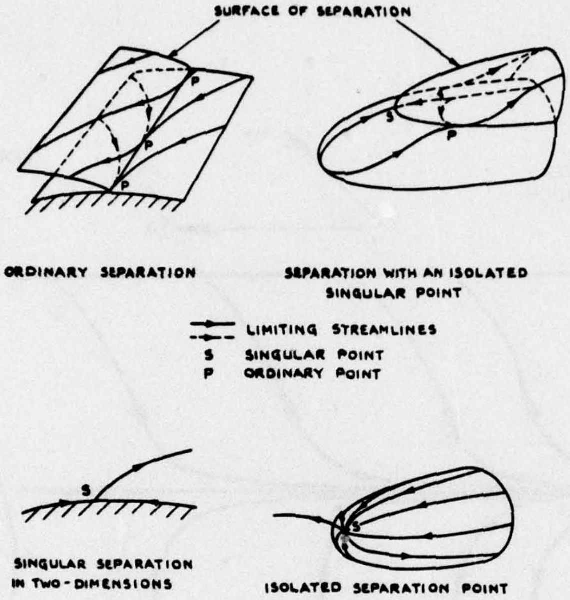

3D SEPARATION, MASKELL[1]

13.2

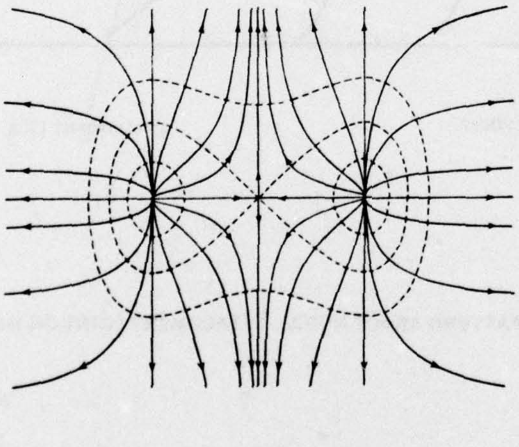

TWO NODAL POINTS OF ATTACHMENT & ONE SADDLE POINT OF SEPARATION, LIGHTHILL[39]

FIG. 13: POSTULATES OF 3D SEPARATION

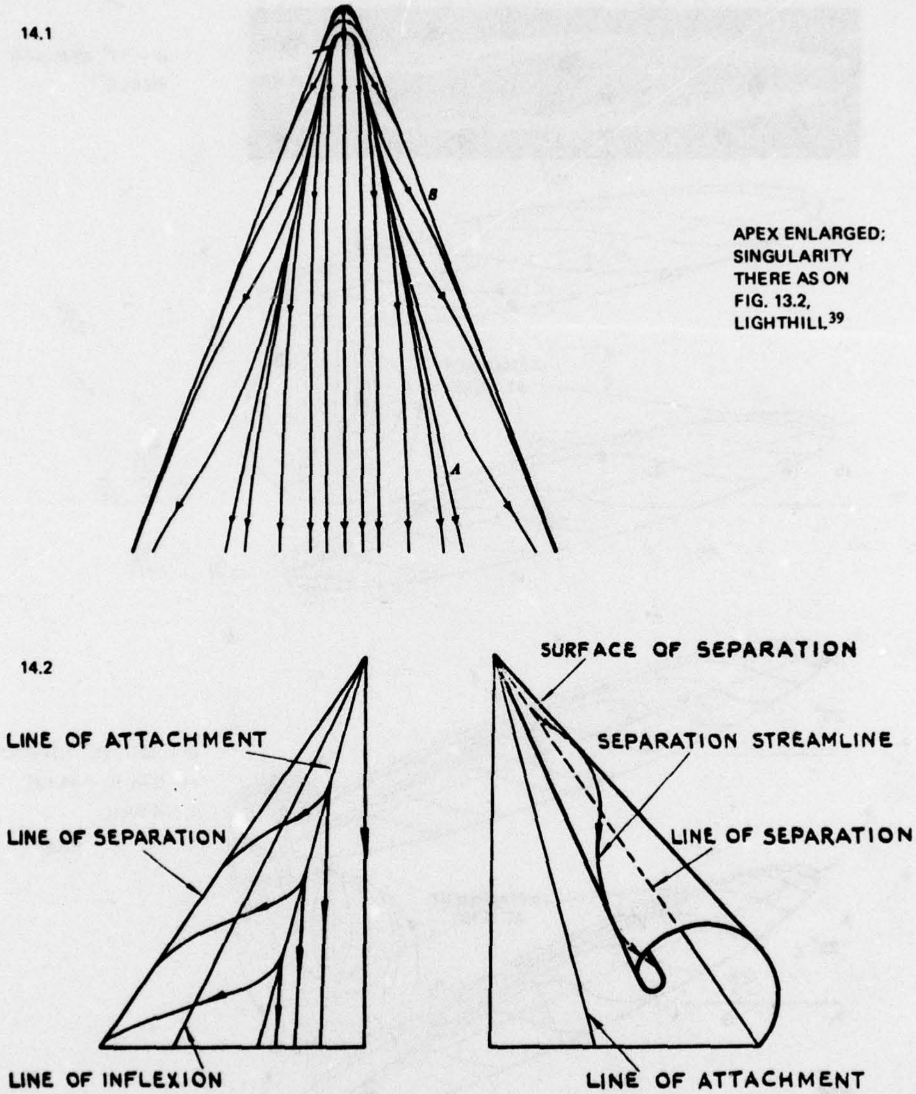

APEX ENLARGED;
SINGULARITY
THERE AS ON
FIG. 13.2,
LIGHTHILL[39]

MASKELL[1]

FIG. 14: CONCEPTUAL LEE-SIDE FLOW ABOUT SLENDER WING AT INCIDENCE

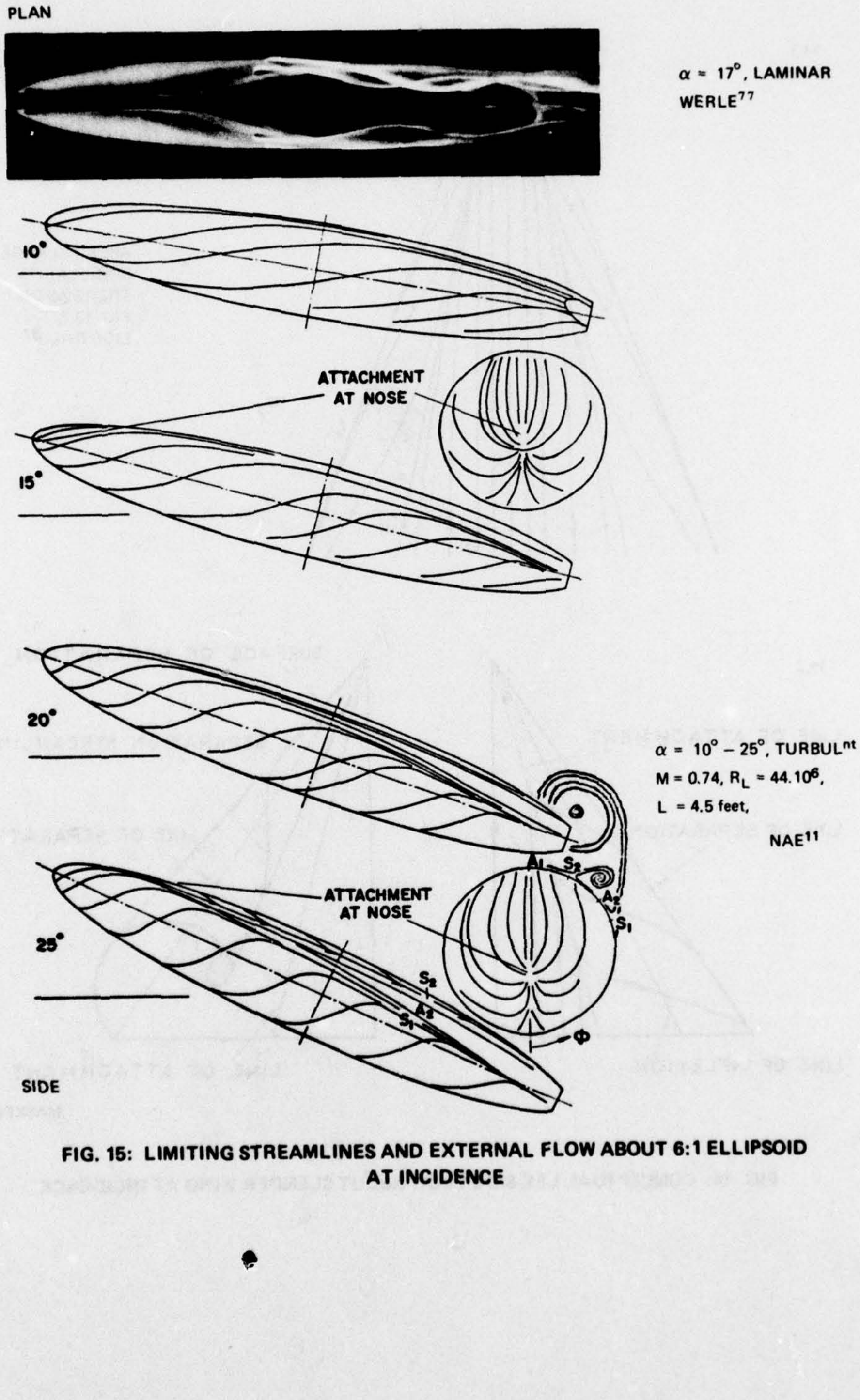

$\alpha = 17^\circ$, LAMINAR
WERLE[77]

$\alpha = 10^\circ - 25^\circ$, TURBUL^{nt}
$M = 0.74$, $R_L = 44.10^6$,
$L = 4.5$ feet,
NAE[11]

FIG. 15: LIMITING STREAMLINES AND EXTERNAL FLOW ABOUT 6:1 ELLIPSOID AT INCIDENCE

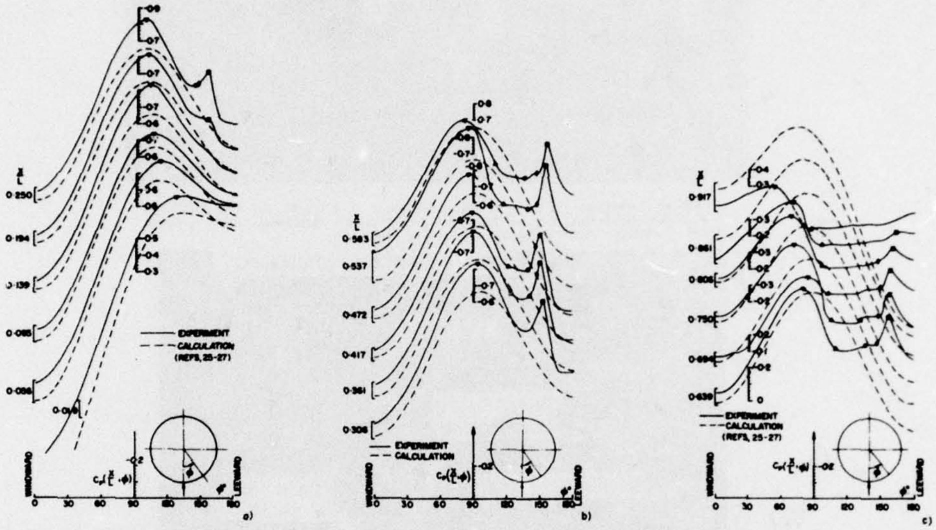

Circumferential **pressures on 6:1 ellipsoid at $\alpha = 25°$, $M_\infty = 0.74$, and $R_L = 44 \times 10^6$. ∇—minimum pressure, Δ—primary separation, ○—secondary** ***attachment*, ◊—secondary separation, □—suction peak from primary vortex.**

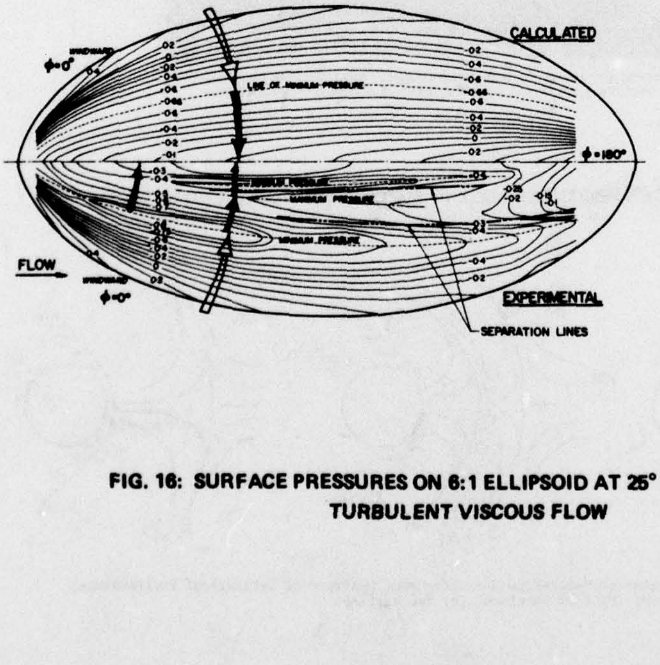

Isobars on 6:1 ellipsoid at $\alpha = 25°$, $M_\infty = 0.74$, and $R_L = 44 \times 10^6$.

FIG. 16: SURFACE PRESSURES ON 6:1 ELLIPSOID AT 25° INCIDENCE WITH TURBULENT VISCOUS FLOW

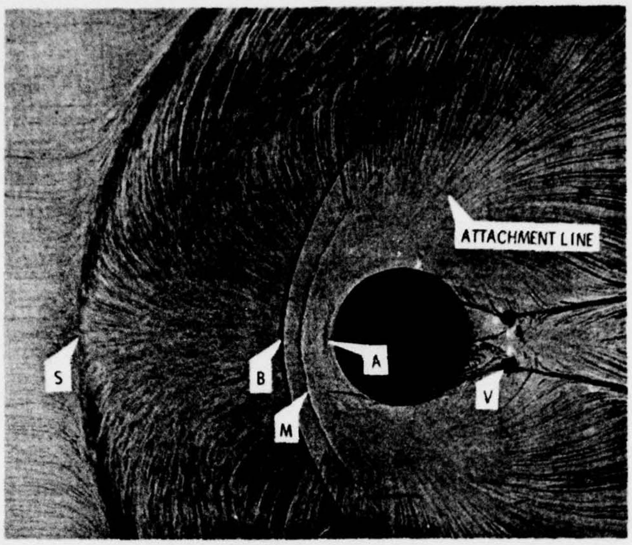

Plan-View Shadowgraph for Large Protuberance, Model 2D, $M = 2.50$, $R/\ell = 19.3 \times 10^6/\mathrm{m}$. S - Primary Separation, B - Bow Shock, M - Mach Stem, A - Attachment Line, V - Vortex Core. Attachment Line Indicated Originates at Point A.

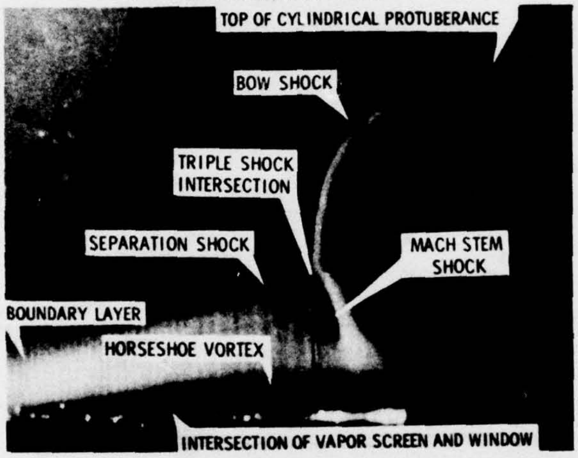

Vapor Screen Photograph for Large Protuberance, Model 2D, with Light Sheet in Symmetry Plane and Camera at 30° to Sheet, $M = 2.50$, $R/\ell = 9.3 \times 10^6/\mathrm{m}$.

FIG. 17: CYLINDER PROTUBERANCE IN SUPERSONIC TURBULENT FLOW[48]

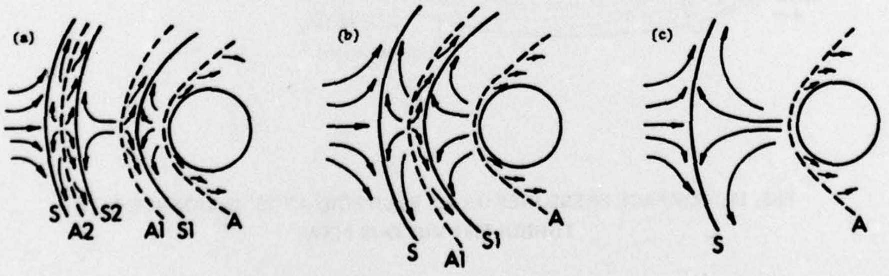

Plan-View Sketches of Separation and Attachment Upstream of Cylindrical Protuberance; (a) Six Vortices; (b) Four Vortices; (c) Two Vortices.

FIG. 18: MULTI-3D TURBULENT SEPARATIONS[48] ABOUT CYLINDER PROTUBERANCE AT M = 2.5

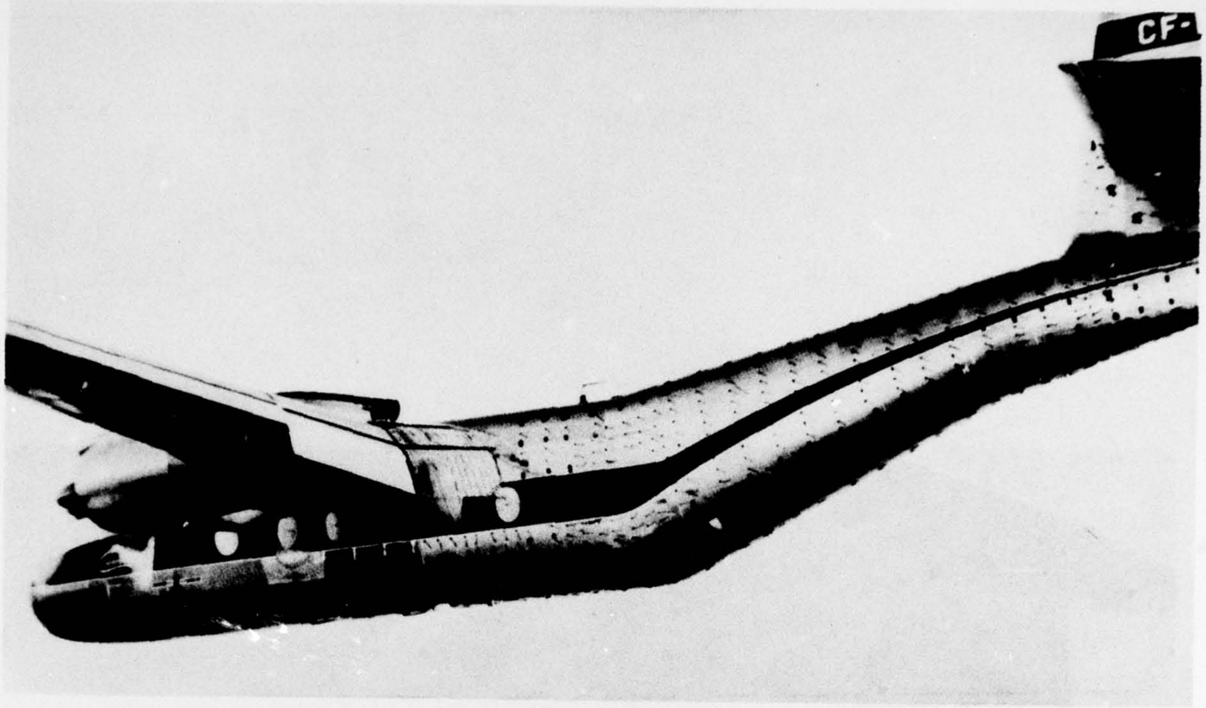

FIG. 19.1: TUFTS ON UPSWEPT FUSELAGE OF D.H. "CARIBOU"

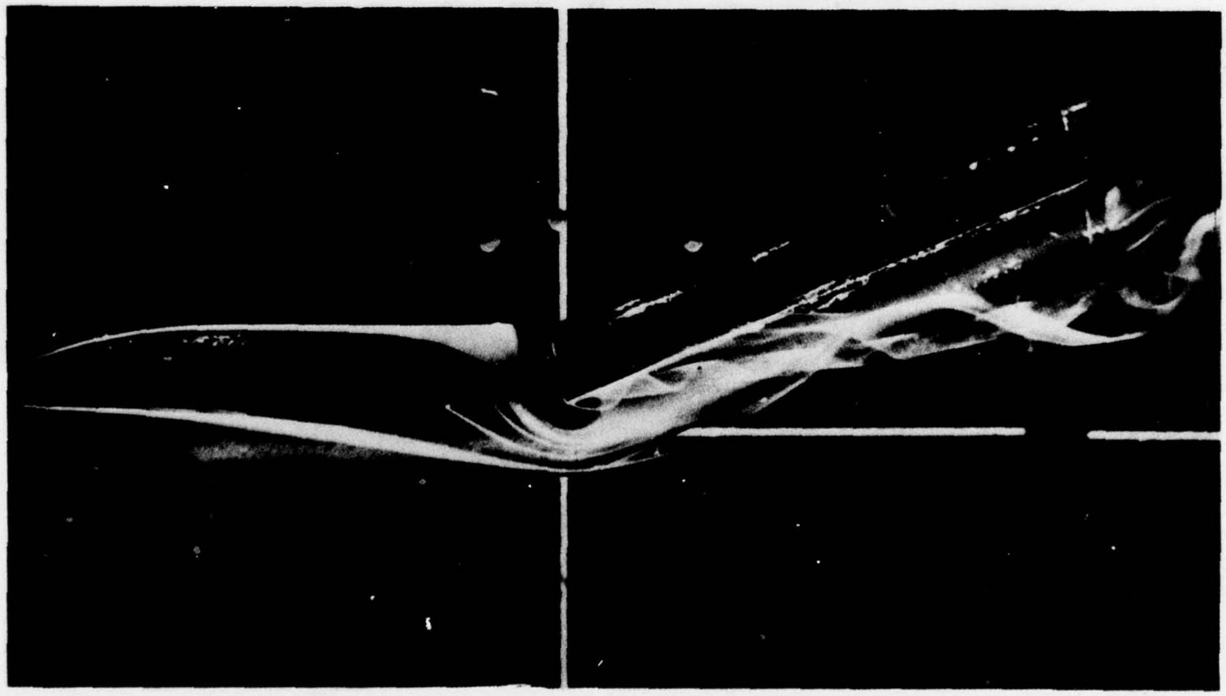

FIG. 19.2: UPSWEPT FUSELAGE WITH STRAKES

FIG. 20: SHARP EDGES ON FUSELAGE UNDERSIDE OF D.H. "BUFFALO"

FLANK

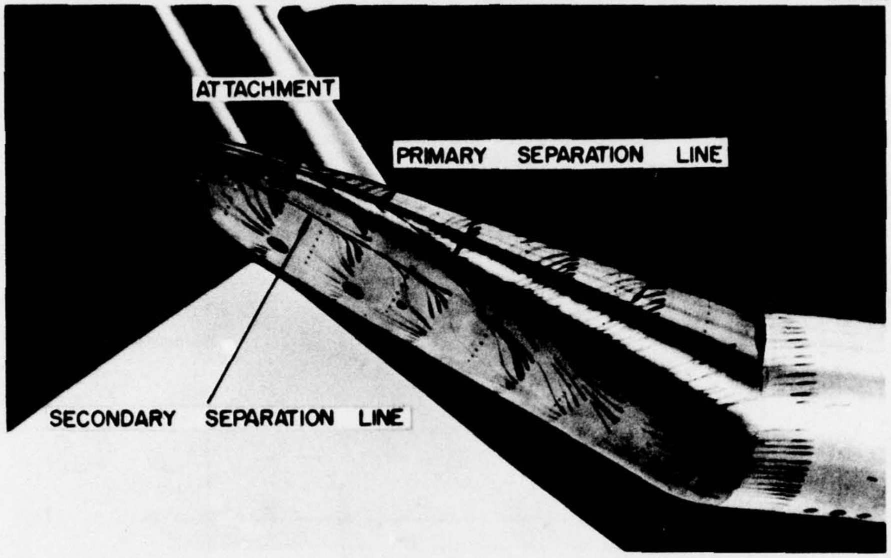

UNDERSIDE

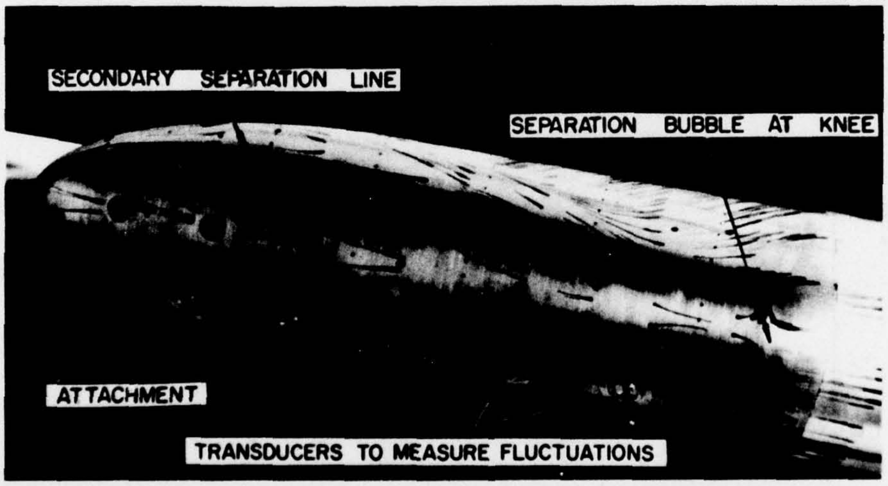

$M = 0.73$; $R = 10 \times 10^6$ PER FT; AFTERBODY LENGTH = 17.2 IN; TURBULENT BOUNDARY LAYERS

FIG. 21: LIMITING STREAMLINES ON NAE "BEAVER TAIL" AFTERBODY AT 20° UPSWEEP

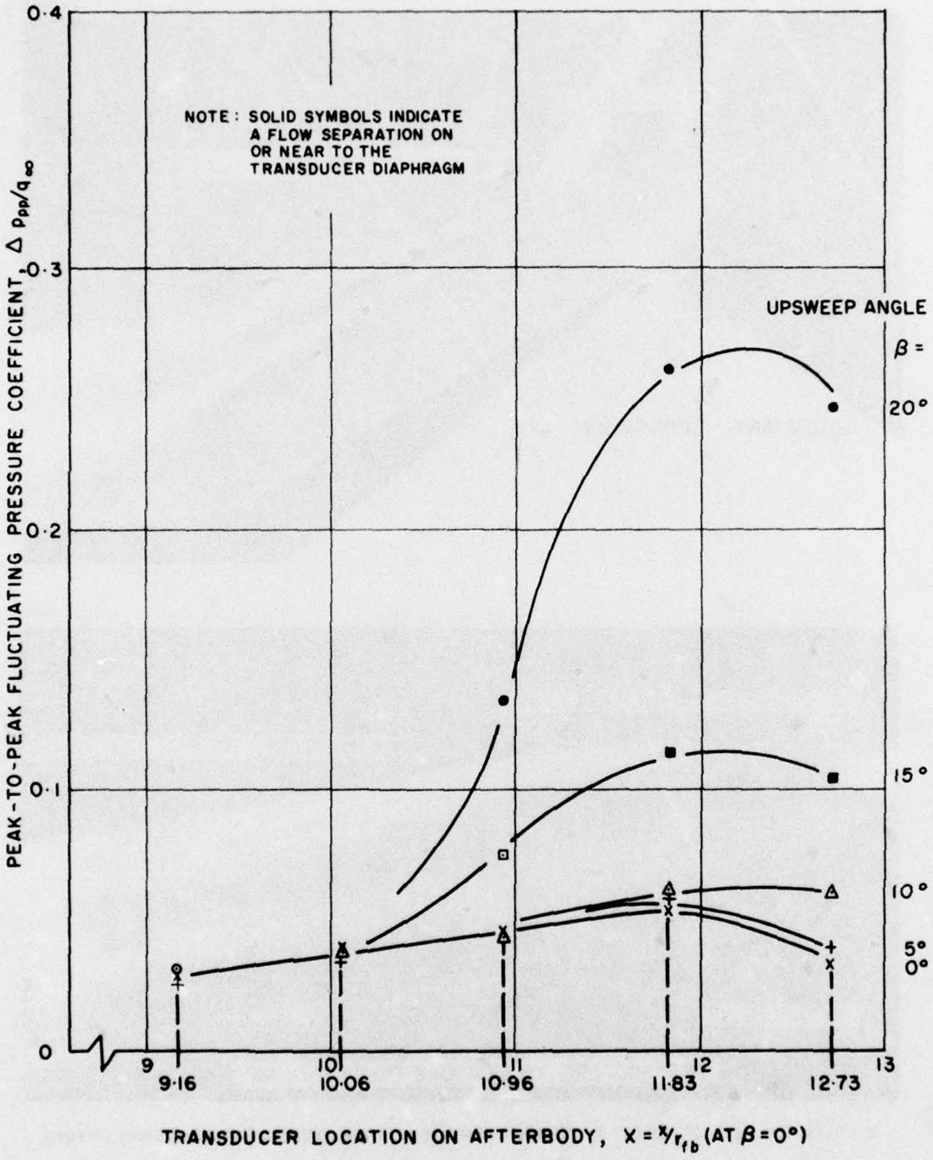

FIG. 22: PRESSURE FLUCTUATIONS ON NAE "BEAVER TAIL" AFTERBODY

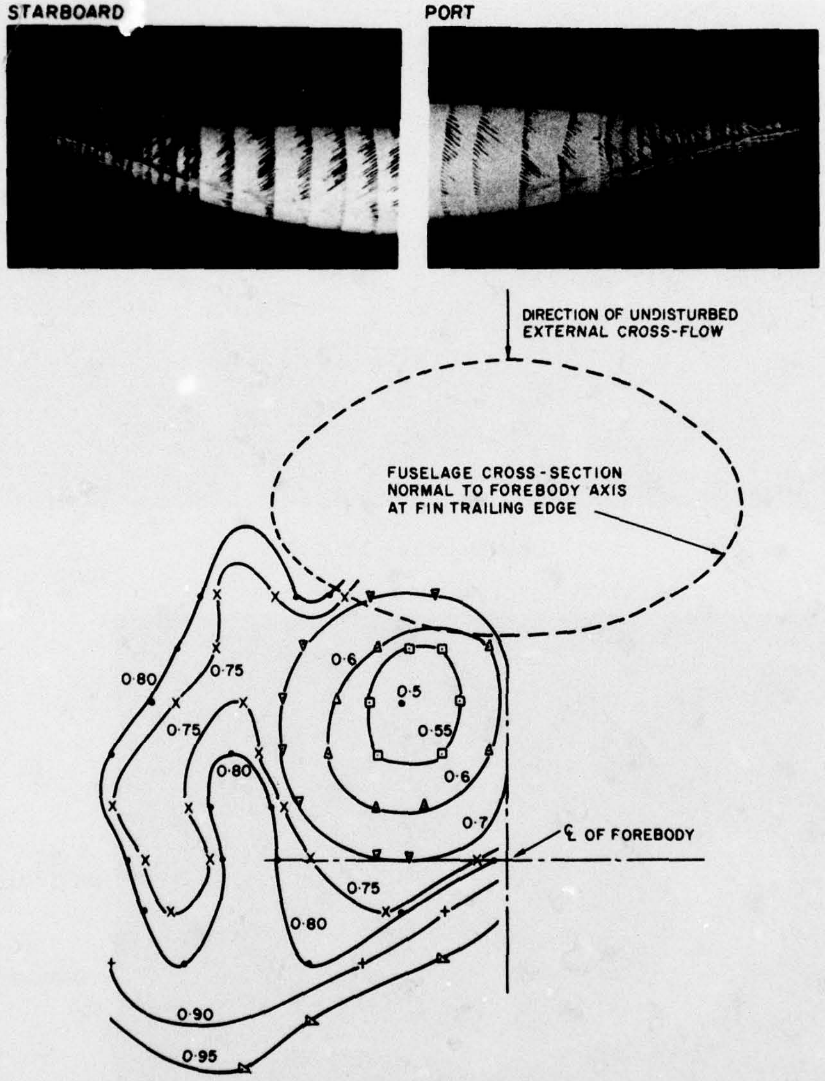

CONTOURS OF PITOT PRESSURE COEFFICIENT, C_{p_0}, JUST DOWNSTREAM OF AFTERBODY TIP (VIEW LOOKING UPSTREAM)

FIG. 23: TURBULENT VORTEX WAKE FROM 9° UPSWEPT AFTERBODY, $\alpha = -15°$, M = 0.3

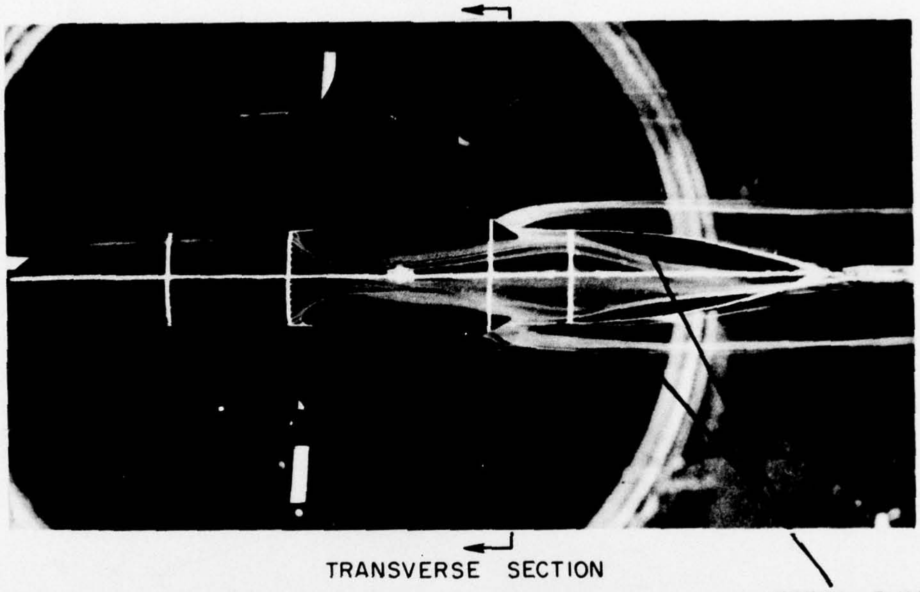

TRANSVERSE SECTION SHOWN ABOVE

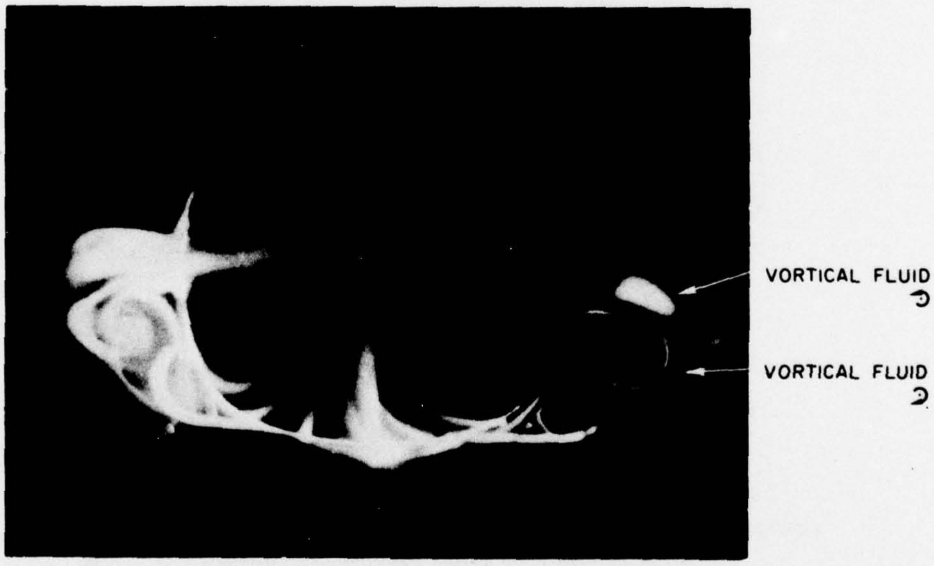

FIG. 24: WING ROOT/UNDERCARRIAGE POD INTERFERENCE: LAMINAR FLOW, $L = 0.87$ FOOT, $R_L = 1.7 \times 10^4$

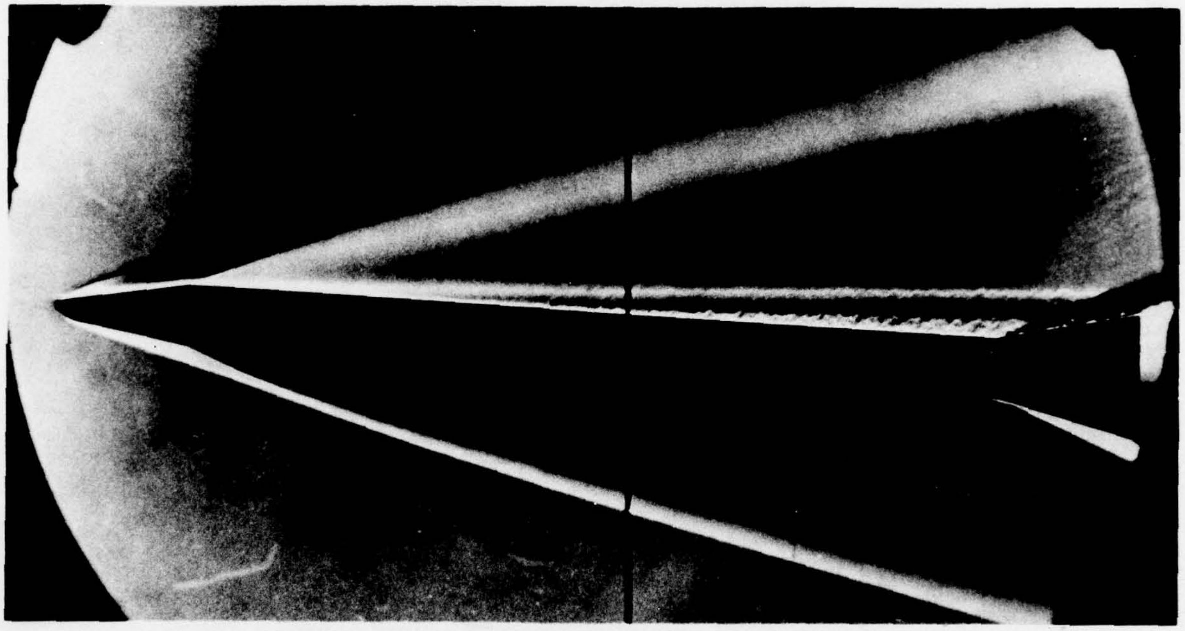

FIG. 25.1: BODY SEPARATIONS ON BLUNTED CONE-CYLINDER-FLARE AT M = 4

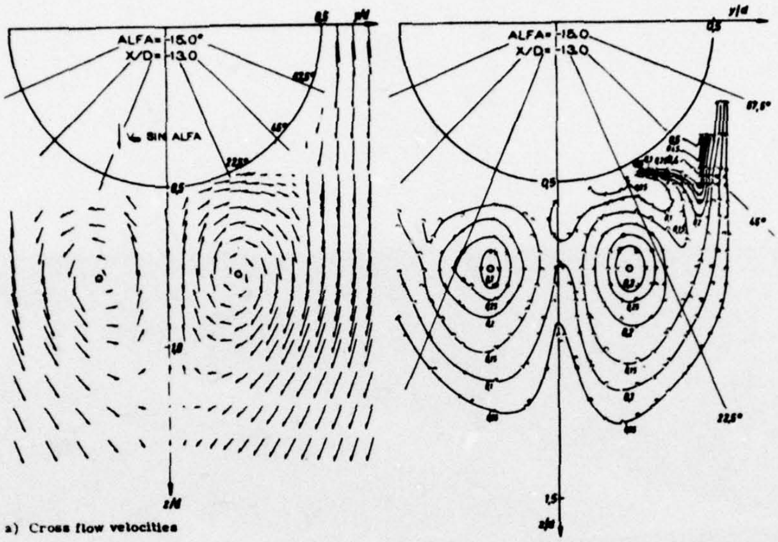

a) Cross flow velocities

b) Isobars of total pressure loss, $(p_{t\infty} - p_t)/q_\infty$ = const

Flow field at the plane x/d = - 13 ; angle of attack α = - 15° ; wingless body.

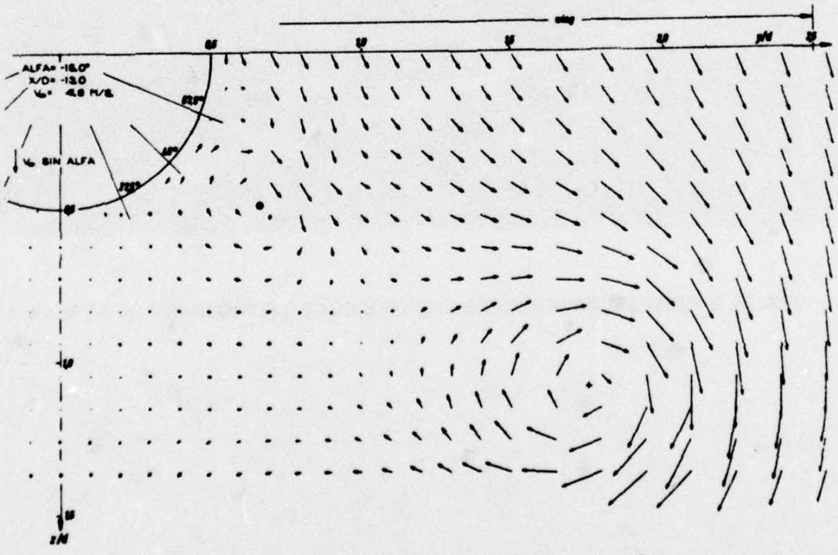

Cross flow velocities at the plane x/d = - 13 ; angle of attack α = - 15° ; with delta wing.

FIG. 25.2: BODY VORTICES IN TURBULENT, LOW SPEED FLOW[20]

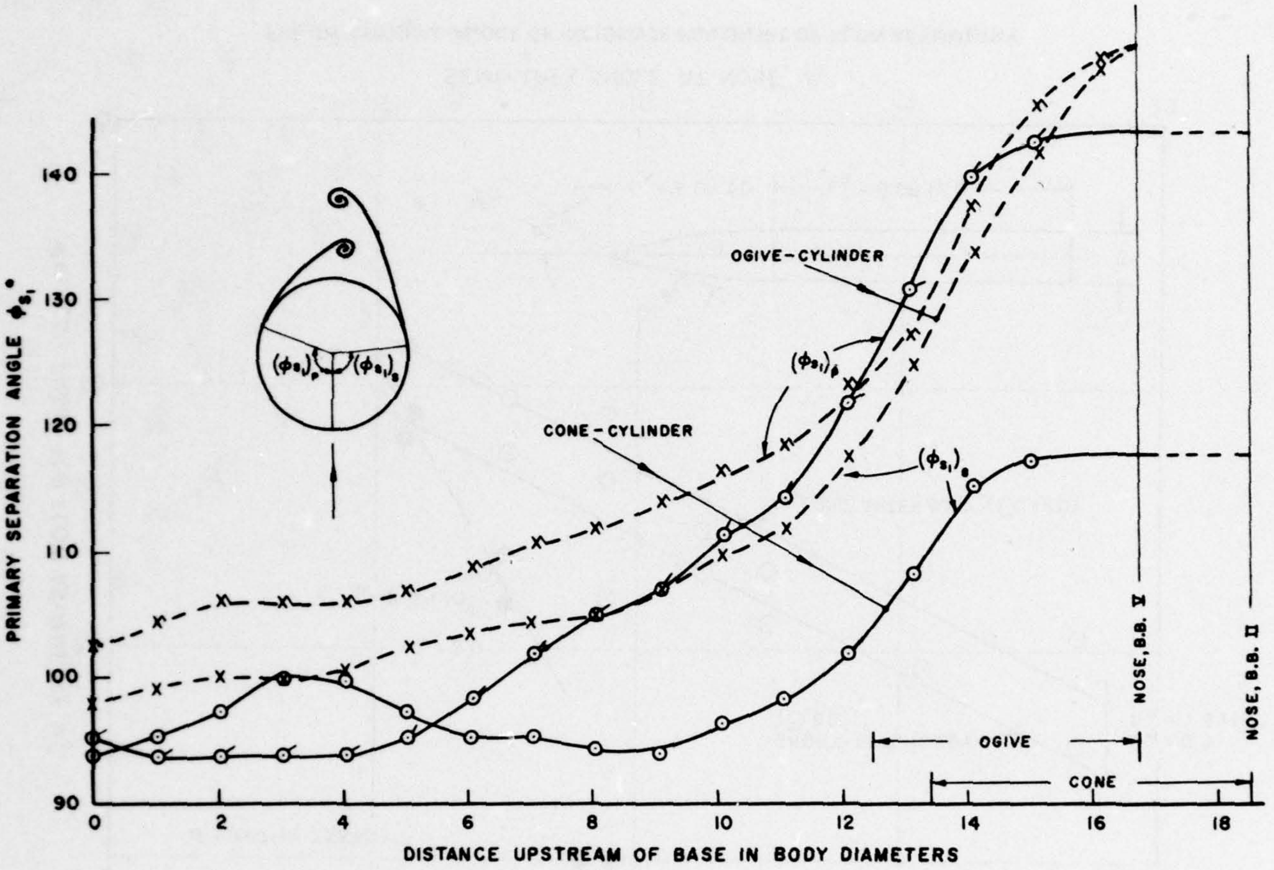

FIG. 26: ASYMMETRIC PRIMARY SEPARATION ON CONE– AND OGIVE–CYLINDERS, $\alpha = 18°$, $M \doteq 0.6$, $R_L \doteq 3.5 \times 10^7$

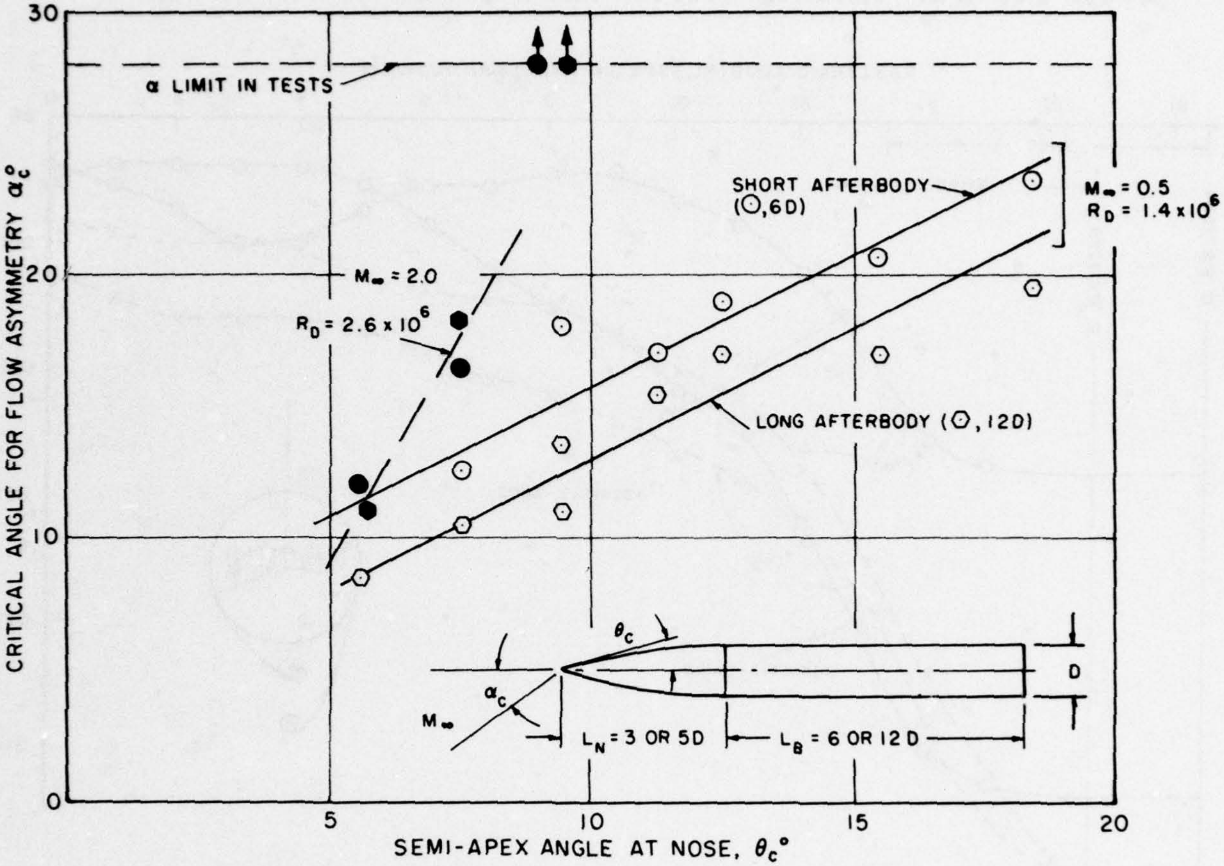

FIG. 27: CRITICAL ANGLE OF INCIDENCE FOR ONSET OF FLOW ASYMMETRY

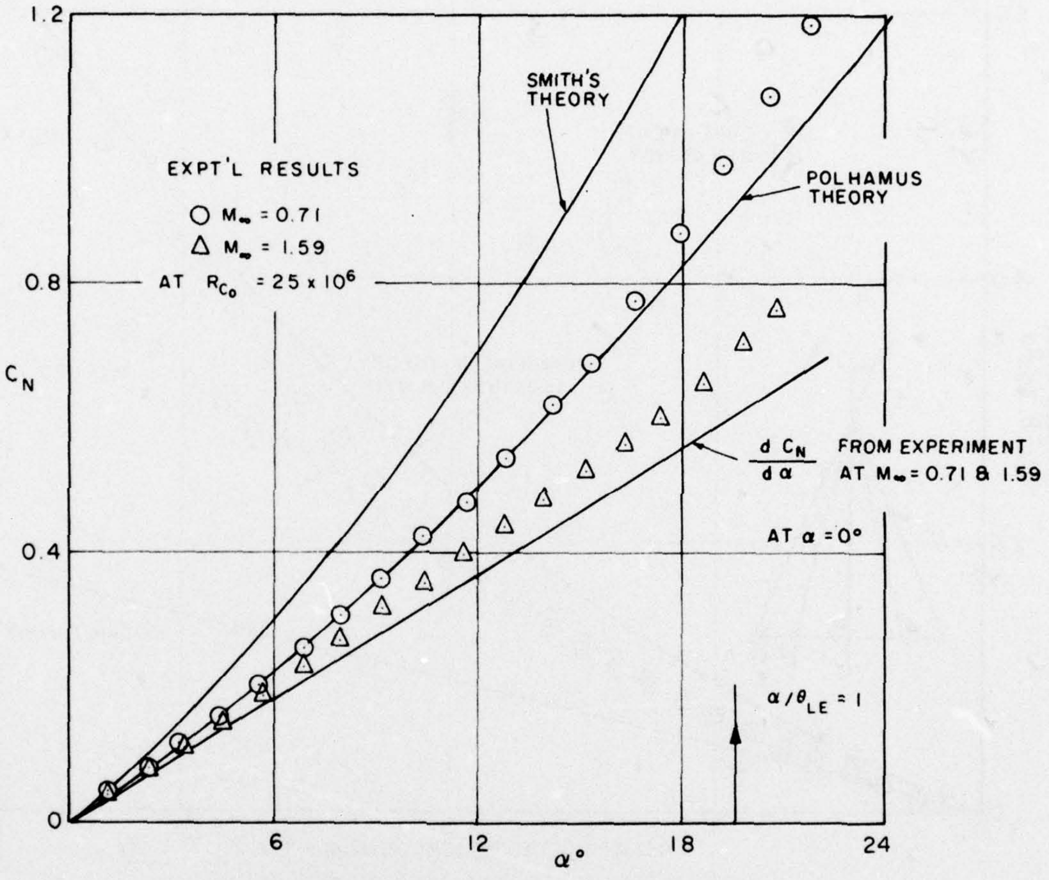

FIG. 28: OVERALL NORMAL FORCE ON 70° DELTA

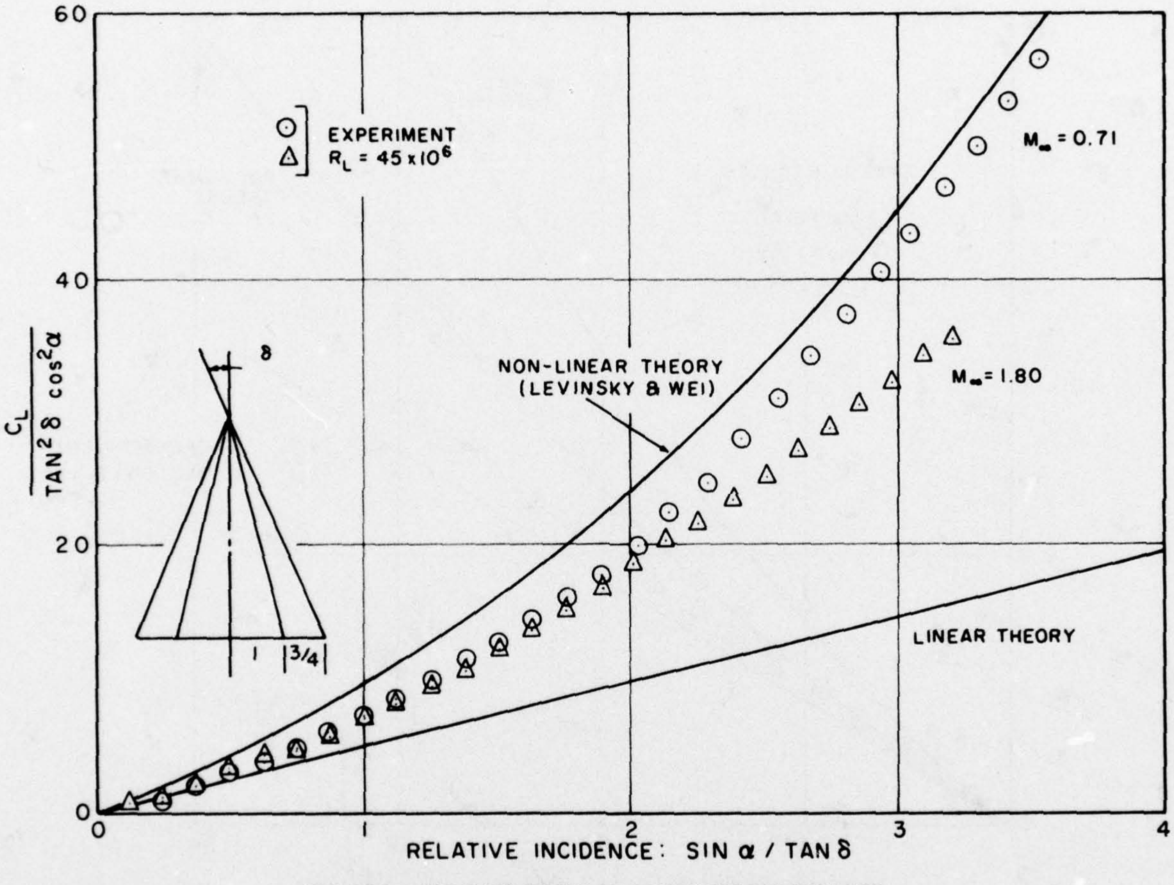

FIG. 29.1: LIFT ON 5° CIRCULAR CONE WITH 75% STRAKES

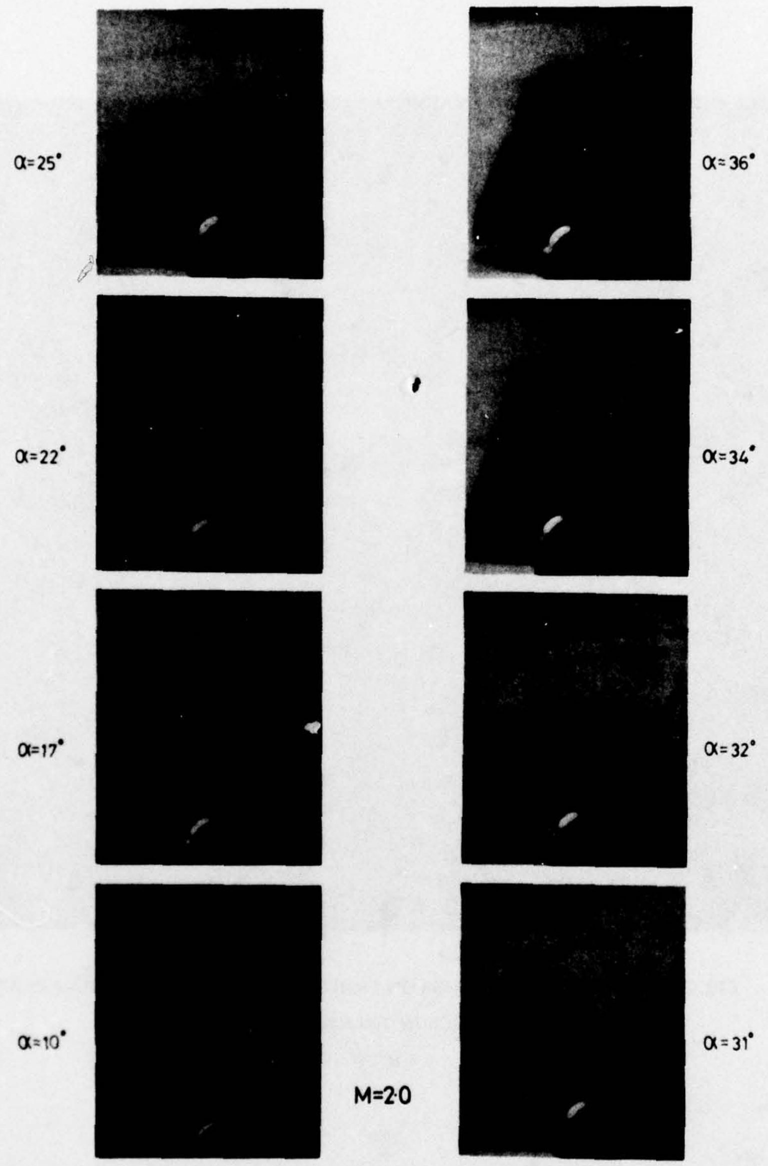

FIG. 29.2: VAPOUR SCREEN PHOTOS OF VORTICES ABOVE 78° SWEPT WINGS ATTACHED TO OGIVE-CYLINDER[63]

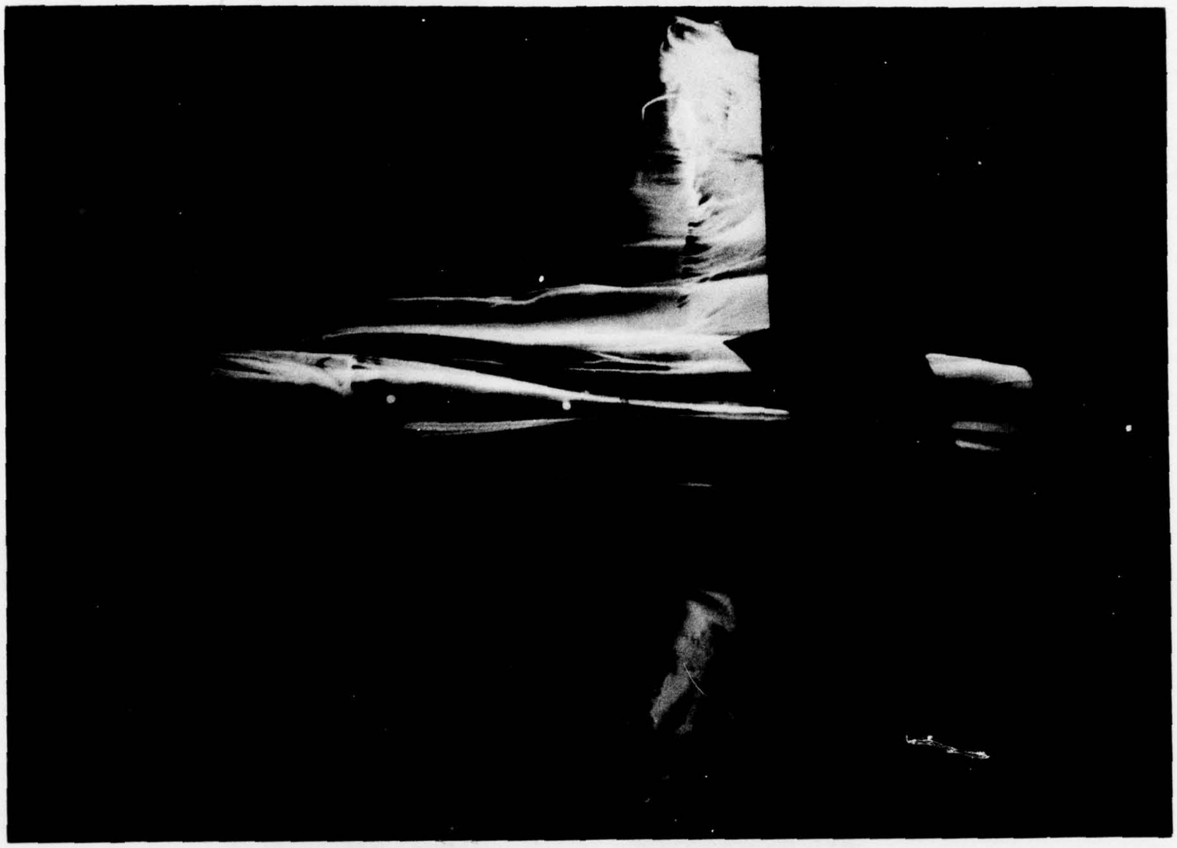

FIG. 30: LIMITING STREAMLINES ON FIGHTER AIRCRAFT WITH STRAKES AT INCIDENCE IN TRANSONIC FLOW[78]

$\alpha = 8^\circ$, $M \doteq 0.9$

31.1

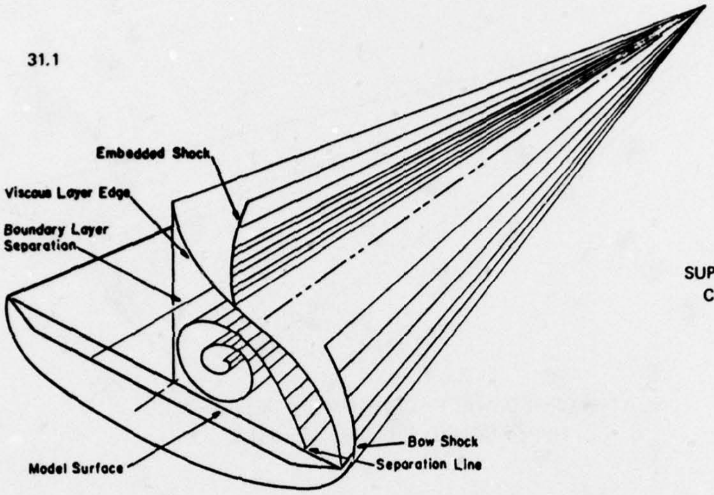

L.E.
SUPERSONIC:
CROSS[57]

DOMINANT FEATURES OF LEE SIDE FLOW FIELD/75° DELTA WING

31.2

L.E.
SUBSONIC:
NAE[11]

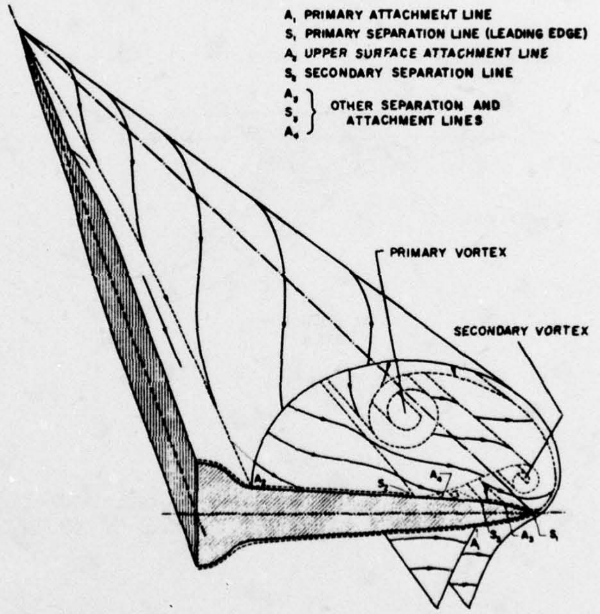

INTERPRETATION OF FLOW ABOUT 70-DEGREE DELTA WING
AT 16.5 DEGREES INCIDENCE

FIG. 31: LEE-SIDE FLOWS OVER DELTA WINGS AT INCIDENCE

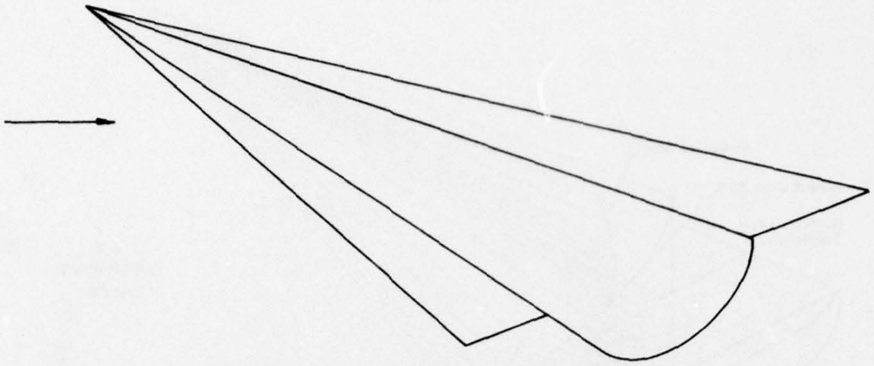

FLAT-TOPPED HALF-CONE-AND-DELTA-WING
HYPERSONIC LIFTING VEHICLE

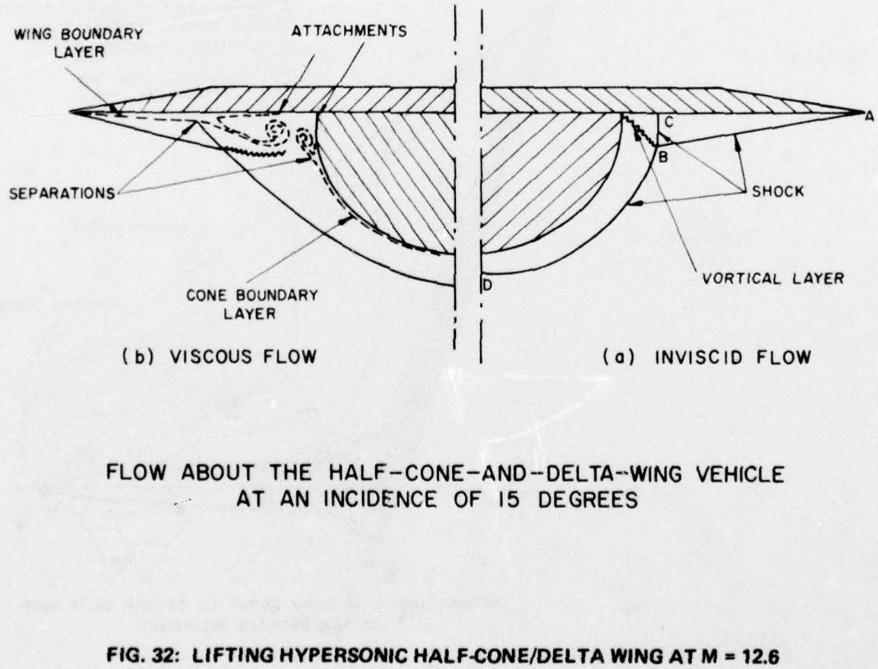

FLOW ABOUT THE HALF-CONE-AND-DELTA-WING VEHICLE
AT AN INCIDENCE OF 15 DEGREES

FIG. 32: LIFTING HYPERSONIC HALF-CONE/DELTA WING AT M = 12.6

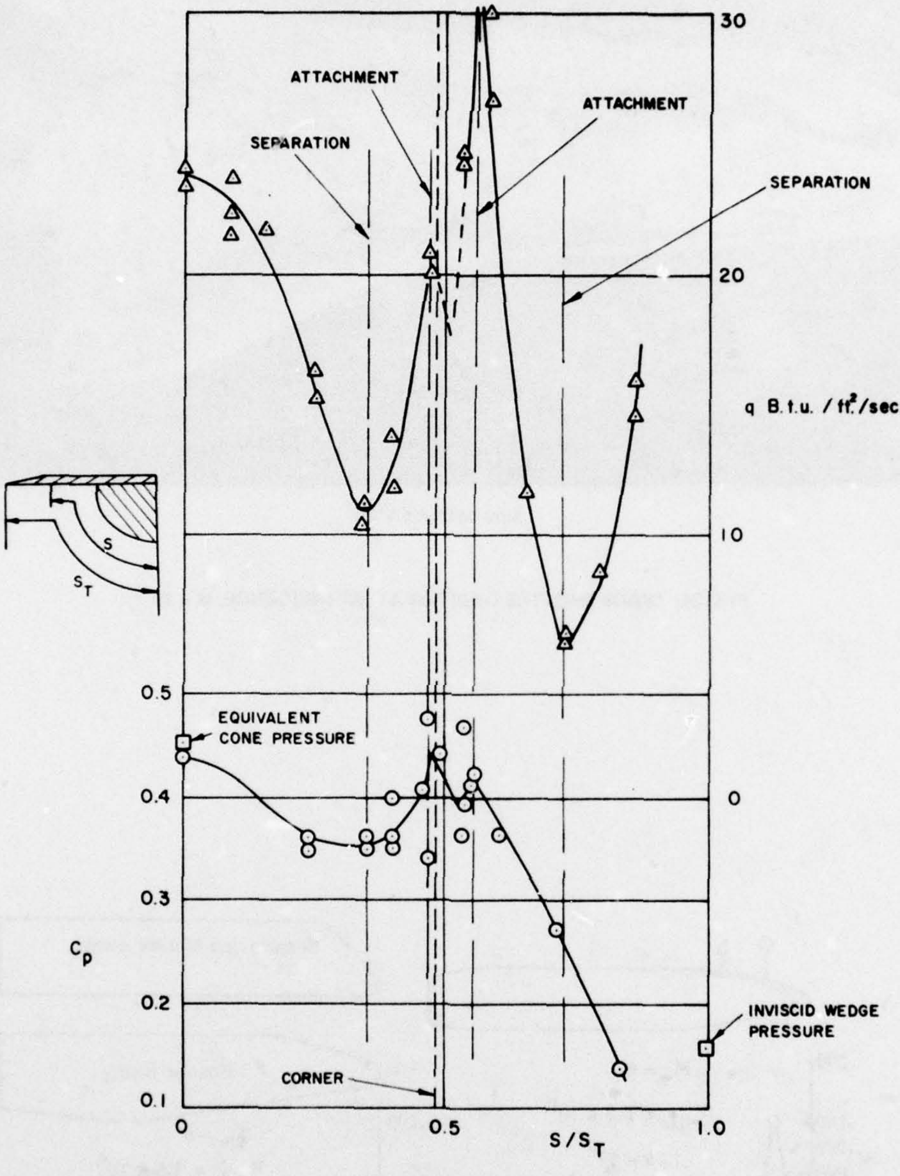

FIG. 33: HEAT TRANSFER AND SURFACE PRESSURES ON HALF-CONE/DELTA WING, $\alpha = 15°$, M = 12.6

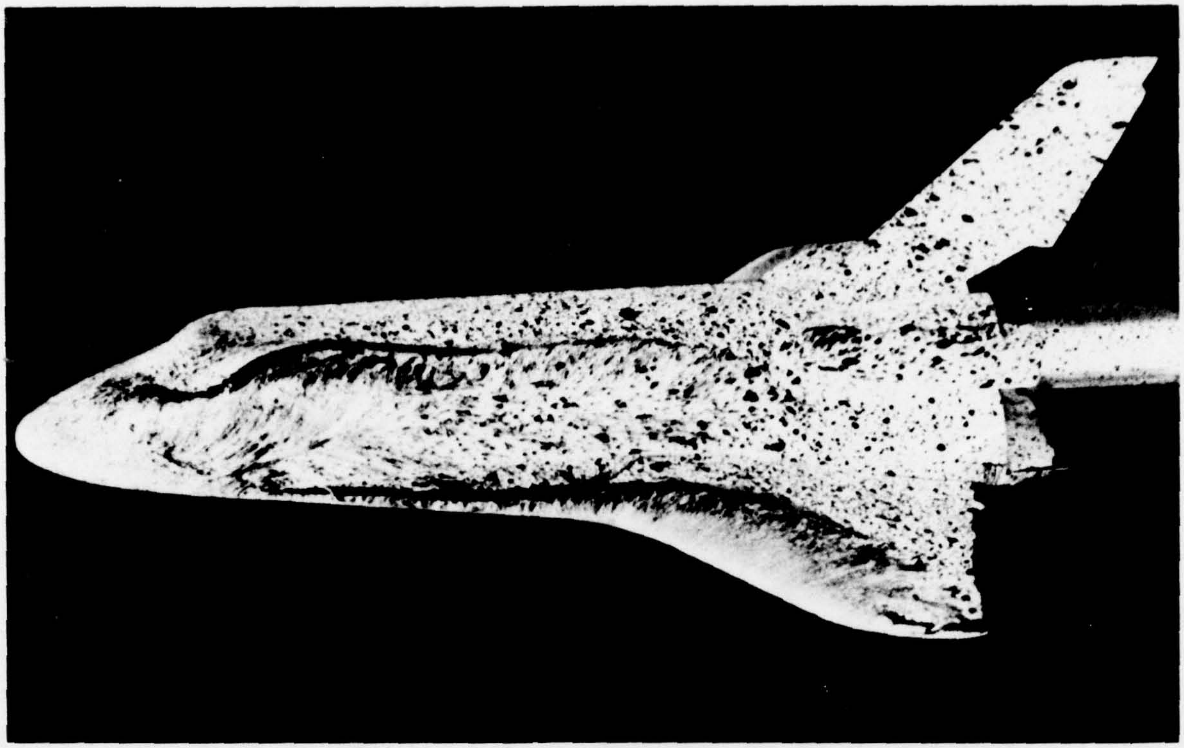

SIDE OBLIQUE VIEW

FIG. 34: SPACE SHUTTLE ORBITER AT 30° INCIDENCE, M ≐ 20[58]

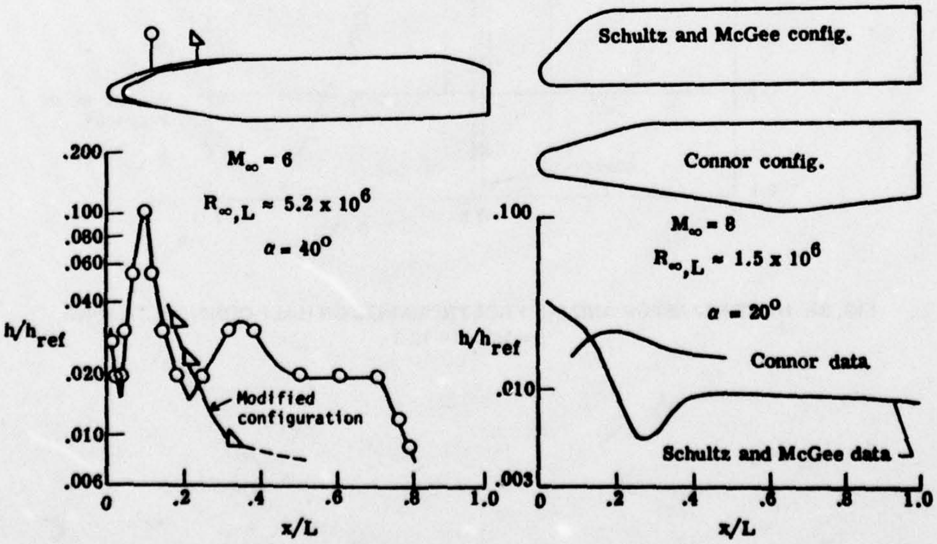

FIG. 35: EFFECT OF LEE-SURFACE GEOMETRY ON HEATING[59]

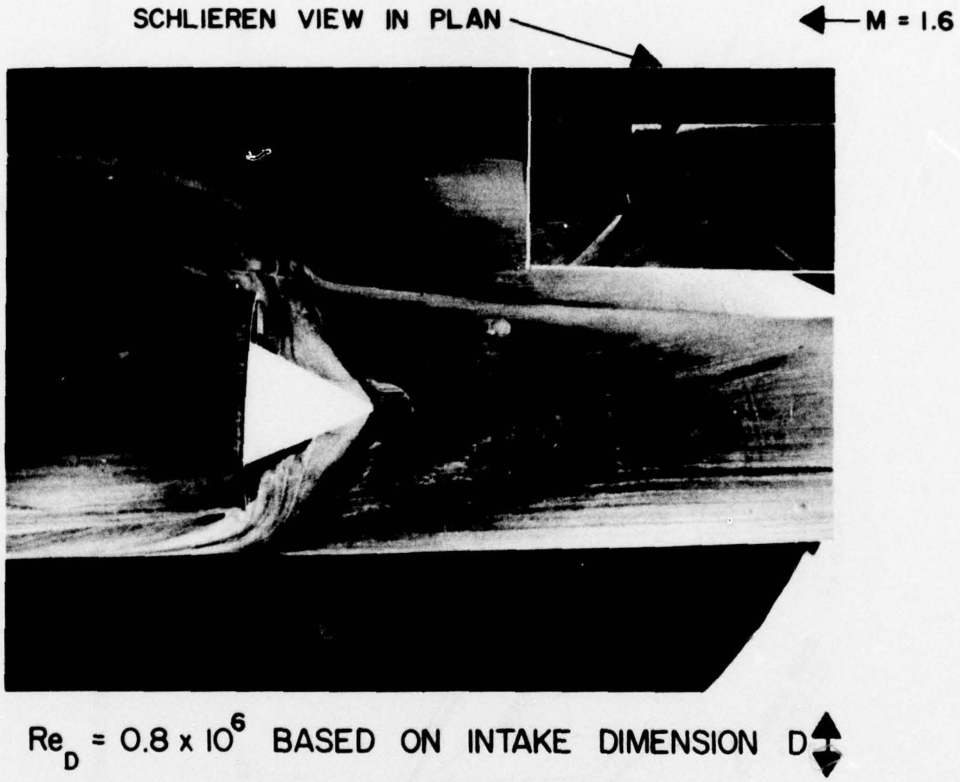

$Re_D = 0.8 \times 10^6$ BASED ON INTAKE DIMENSION D

FIG. 36: SWEPT-SHOCK INDUCED 3D SEPARATION ABOUT HALF-CONE INTAKE AT M = 1.6[73]

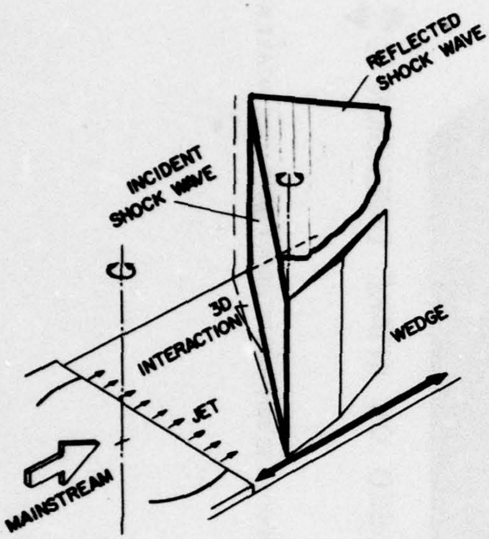

FIG. 37 FLOW CONFIGURATION

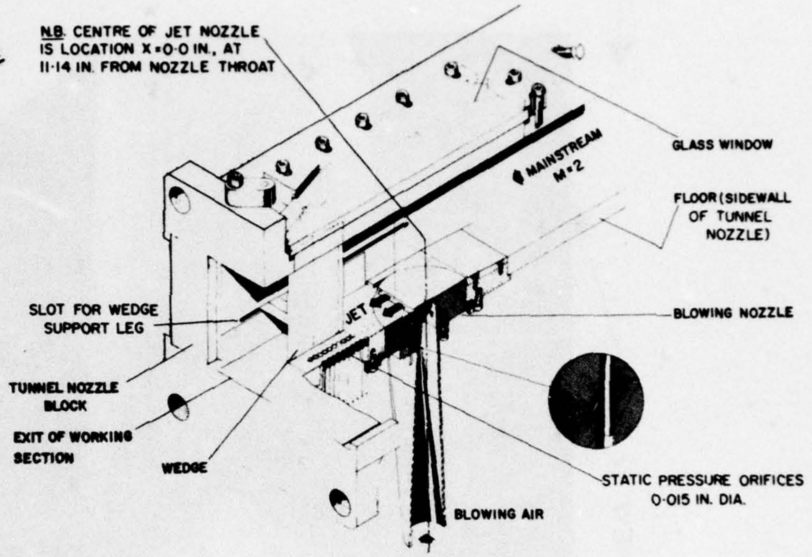

FIG. 38 TYPICAL ASSEMBLY OF WORKING SECTION OF 5 x 5 IN. WIND TUNNEL FOR BLC

FIGS 37 & 38: SWEPT SHOCK/TURBULENT BOUNDARY-LAYER INTERACTION WITH AIR INJECTION

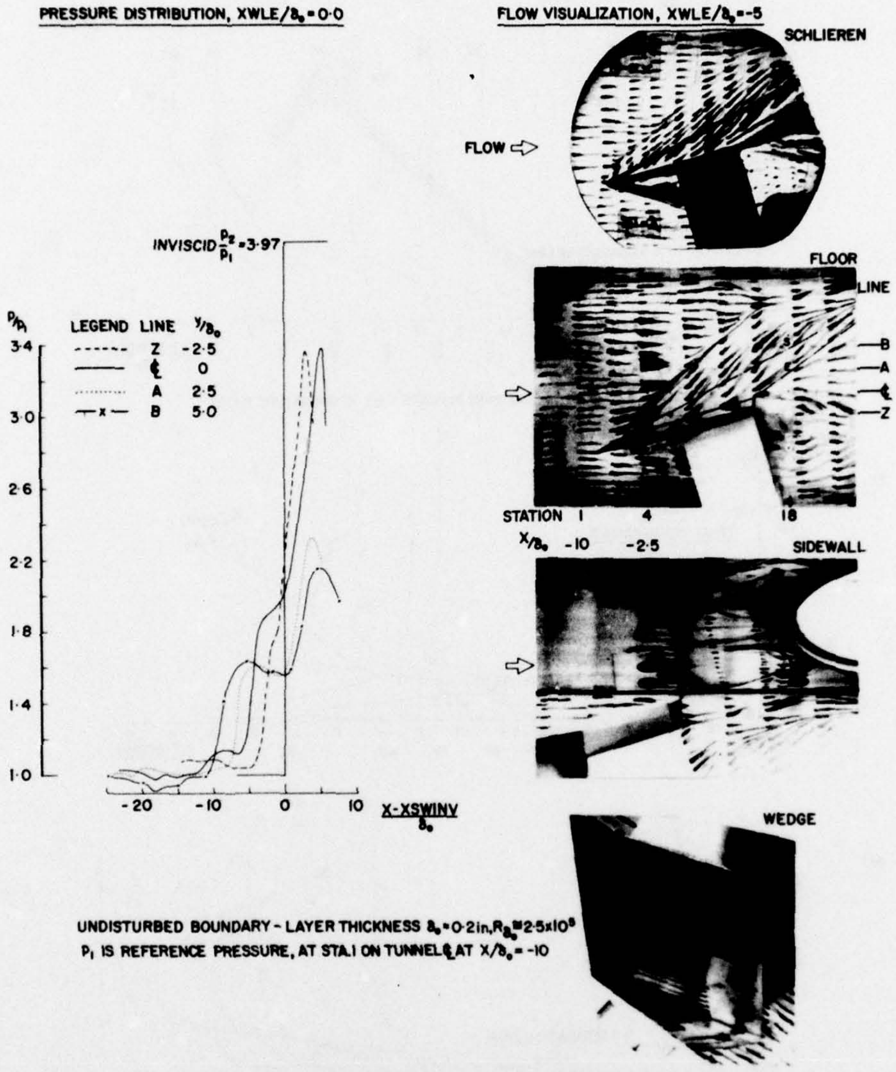

UNDISTURBED BOUNDARY-LAYER THICKNESS $\delta_0 = 0{\cdot}2$ in, $R_{\delta_0} \approx 2{\cdot}5 \times 10^5$

p_1 IS REFERENCE PRESSURE, AT STA.1 ON TUNNEL ℄ AT $X/\delta_0 = -10$

FIG. 39: 3D SEPARATION WITH $\delta_w = 16°$ AT MACH 4

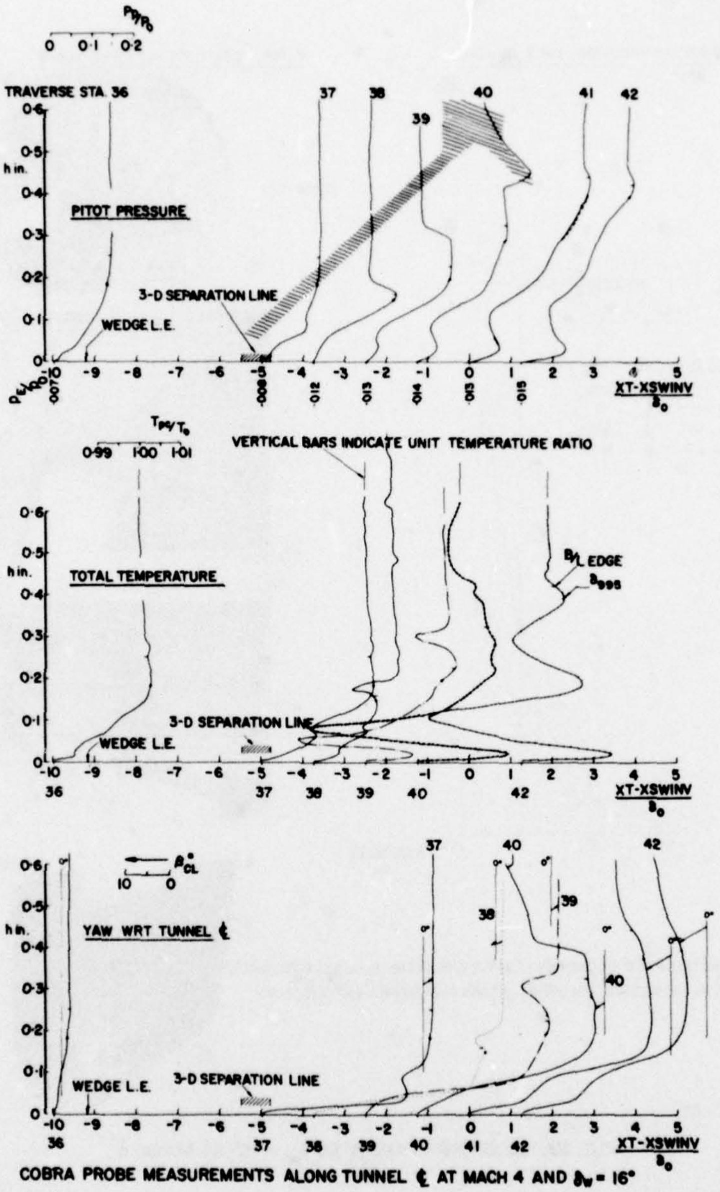

COBRA PROBE MEASUREMENTS ALONG TUNNEL ℄ AT MACH 4 AND $\delta_w = 16°$

FIG. 40: 3D BOUNDARY-LAYER PROFILES ALONG ℄, M = 4, δ_w = 16°

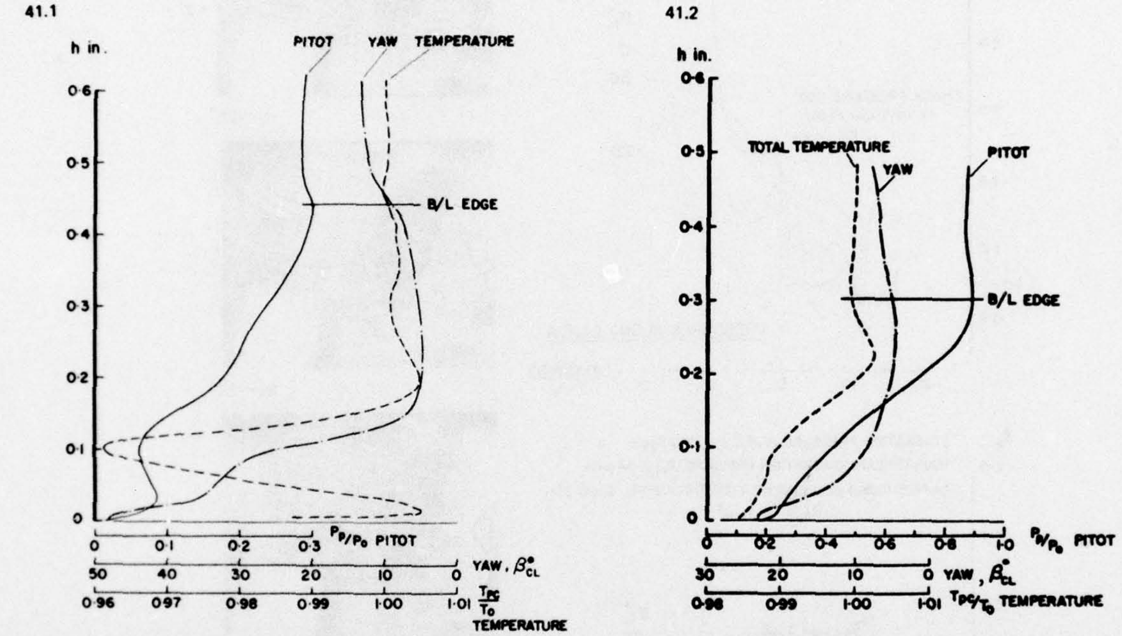

PITOT, TOTAL TEMPERATURE AND YAW ANGLE DISTRIBUTIONS FOR STATION 41 NEAR INVISCID SHOCK WAVE LOCATION; FOR $\delta_w = 16°$ AT MACH 4.

PITOT, TOTAL TEMPERATURE AND YAW ANGLE DISTRIBUTIONS FOR STATION 11 NEAR INVISCID SHOCK WAVE LOCATION; FOR $\delta_w = 8°$ AT MACH 2

FIG. 41: STAGNATION TEMPERATURE CHANGES IN FLOW WITH 3D SEPARATION

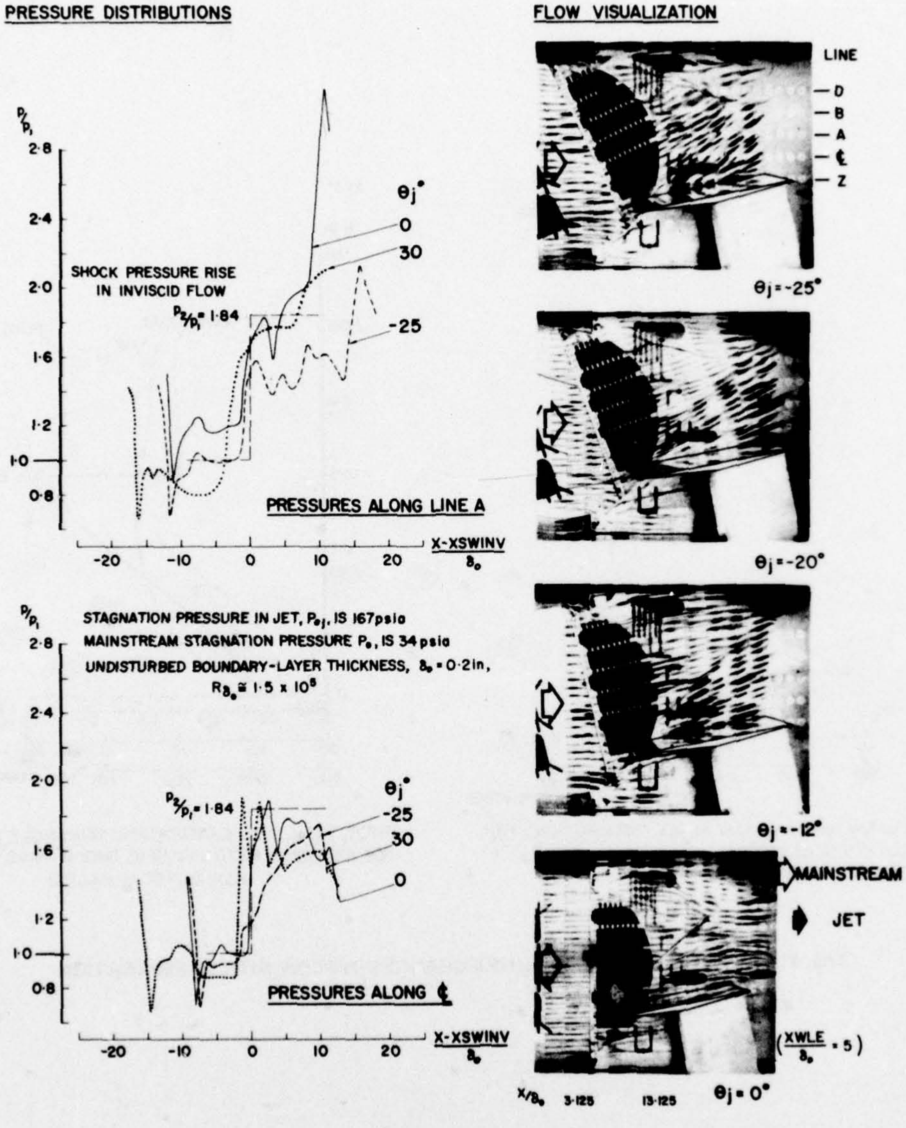

STAGNATION PRESSURE IN JET, P_{oj}, IS 167psia
MAINSTREAM STAGNATION PRESSURE P_o, IS 34psia
UNDISTURBED BOUNDARY-LAYER THICKNESS, $\delta_o = 0·2$in,
$R_{\delta_o} \cong 1·5 \times 10^5$

FIG. 42: EFFECT OF BLOWING DIRECTION ON SWEPT SHOCK/TURBULENT BOUNDARY-LAYER INTERACTION AT MACH 2: $\delta_w = 11.5°$, $M_1 = 3$

INTRODUCTION TO UNSTEADY ASPECTS OF SEPARATION IN SUBSONIC AND TRANSONIC FLOW

W. J. McCroskey
Aeromechanics Laboratory—U.S. Army Aviation R&D Command
Ames Research Center, Moffett Field, California 94035, U.S.A.

1.0 GENERAL CONSIDERATIONS

Unsteady separation occurs in a wide range of fluid flows that are of practical importance (Ref. 1). In many applications, the ideal flow environment of a device is nominally steady, but the onset of separation is very often accompanied by some degree of irregular unsteadiness. Undesirable unsteady effects can also arise either due to self-induced motions of a body in a moving stream, or due to fluctuations or nonuniformities in the surrounding fluid. On the other hand, some devices may be required to execute time-dependent motion in order to perform their basic functions. In general, the combination of unsteadiness and flow separation produces fluctuating forces, vibrations, aeroelastic instabilities, or combinations thereof that are as undesirable as they are difficult to predict.

The fluctuating fluid dynamic forces associated with unsteady separation can be almost completely stochastic, highly organized, or a combination of random and periodic components. An example of the first type, buffeting on an aircraft wing, is illustrated in Fig. 1. A highly organized flow is the well-known periodic vortex shedding from a wire or cable. Retreating blade stall flutter on a helicopter rotor (Fig. 2 adapted from Ref. 2) exhibits significant amounts of both random and periodic fluctuations. These and other representative examples will be addressed in the following lectures.

It should be emphasized that this entire subject remains open to much additional fundamental research, since the general fluid dynamic problem of unsteady separation at high Reynolds number remains unsolved. At present, no completely reliable prediction techniques exist. Instead, the design engineer must draw from a combination of approximate theories, empirical correlations of data, and finite difference programs based on uncertain physical modeling of turbulence.

What are some of the factors that distinguish quasi-steady and unsteady separated flow behavior in practical situations? From dimensional analysis, we would expect large-scale unsteady effects to be important—for example, with regard to overall performance—when some time scale of the physical motion is comparable to the basic fluid dynamic time scale; that is, when $\omega L/U$ or L/Ut are of the order of 1 or greater. Here the quantities ω, L, and U are the characteristic frequency, length, and velocity, respectively, of the motion, and t denotes time.* Even at much lower reduced frequencies, however, fluctuating fluid dynamic forces may develop which are out of phase with the body motion; these forces can then lead to flow-induced instabilities, such as flutter, that are important to aeroelasticians and structural engineers. Although this "negative aerodynamic damping," whereby the body extracts energy from the flow, can also occur in purely inviscid flows, the phenomenon is often enhanced considerably by separation. Furthermore, certain types of flutter occur only when separation is present.

There are also instances of uniform body motion in which separated viscous shear layers develop hydrodynamic instabilities with distinct periodicity

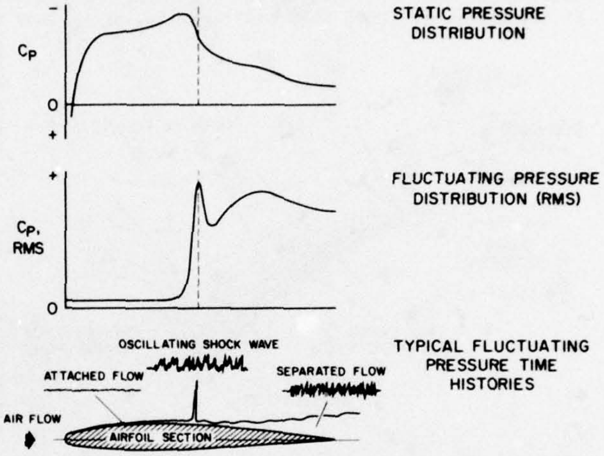

Fig. 1. Sketch of transonic buffet on a lifting airfoil.

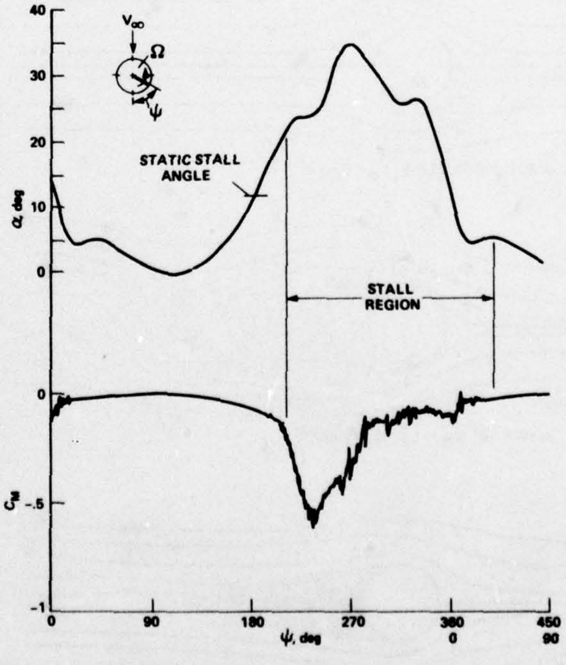

Fig. 2. Blade-element angle of attack and pitching moment response on a model helicopter rotor (Ref. 2).

---

*For slender-body oscillations, the quantity $k = \omega L/U_\infty$ is called the reduced frequency, and the relevant characteristic length is normally a streamwise dimension. On the other hand, the characteristic frequency associated with vortex shedding from arbitrary bodies has traditionally been called the Strouhal number, $S = fL/U$, where $f = \omega/2\pi$ is the cycle frequency, L is usually a dimension perpendicular to the flow, and generally $U = U_\infty$ if there is a mean flow.

in the near wake. These, in turn, may induce large-scale unsteady fluctuations in the entire flow field. Such self-induced, nonlinear, viscous-inviscid interactions usually produce fluctuating pressures and airloads that have no counterpart in purely steady flows.

Another distinction is the rather subtle but fundamental difference in the application of boundary layer theory to quasi-steady and unsteady flow problems. The classical steady boundary layer equations are incomplete approximations to the Navier-Stokes equations, but at high Reynolds numbers they provide considerable insight and practical information to design engineers. In particular, good estimates of separation and of the onset of stall in real flows are often obtained from boundary layer calculations of the point where the surface shear stress vanishes; that is, where $\tau_w = \mu\, \partial u/\partial y = 0$. This point delineates the onset of reversed flow near the wall. It also happens to be a singular point for the steady two-dimensional boundary layer equations, although not for the Navier-Stokes equations. Even though classical boundary layer theory breaks down here, this mathematically-singular behavior is a useful engineering tool, since it often correlates well with the onset of significant changes in the entire flow field.

However, the flow-reversal point, where $\tau_w = 0$, has no such special significance in unsteady flow (Refs. 1, 3 - 5), nor is it a singular point, in general. Within the past 5 years, a number of flow fields have been analyzed and calculated using boundary-layer techniques downstream of the unsteady flow-reversal point. The qualitative features of these results are indicated schematically in Fig. 3 from Ref. 5. The major questions that have arisen are these: (1) does a singularity exist somewhere else in the flow, and if so, where; (2) does this elusive singularity have practical significance analogous to that of the well-known separation singularity in steady flows; and (3) to what extent can meaningful and valid estimates of separation-like behavior of real flows be made in unsteady flows, using the classical boundary layer approach? This whole subject is one of active current research, with a great deal remaining to be learned about the physical significance of unsteady boundary layer calculations.

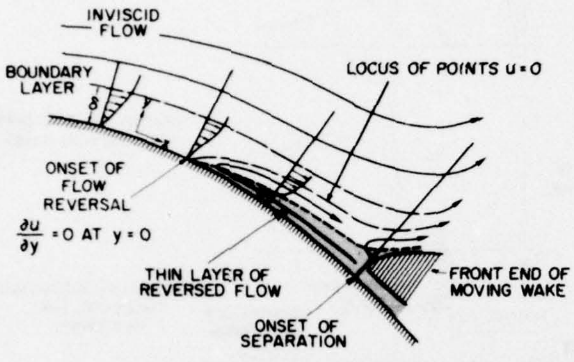

Fig. 3. The model of Sears and Telionis (Ref. 5) for upstream-moving separation of an unsteady boundary layer.

2.0 EXTERNAL FLOWS PAST BLUFF BODIES

The characteristic unsteady feature of nominally uniform flow past a bluff body is the strong tendency for the free shear layers to develop into alternate vortices in the wake, over a wide range of flow conditions. The rigid circular cylinder provides the most familiar example of periodic vortex shedding and the associated fluctuating forces that are induced on the body by the vortices in the wake.

Stationary Circular Cylinders

Figure 4 shows one ideal and two real flow patterns for this case. Although the geometry is appealingly simple, there is no discrete point, such as a corner, from which the flow naturally tends to separate. Consequently, the separation phenomenon and free shear-layer development in the wake are sensitive to Reynolds number and, unlike thin airfoils, there is no regime that can be described by potential flow theory. Only at $Re \lesssim 1$ does the flow even approximately resemble the sketch in Fig. 4(a), and both unsteady effects and viscous separation are interactively important for $Re \gtrsim 50$. On the other hand, the splitter plate illustrated in Fig. 4(c) destroys the organized vortex shedding by effectively uncoupling the periodic separation from the two sides of the cylinder.

Figure 5 from Ref. 1 summarizes the primary flow-field characteristics on the basic cylinder without a splitter plate for various flow regimes, at Mach numbers below the onset of shock waves. Figure 6, also from Ref. 1, indicates the wide ranges of time-averaged drag, fluctuating lift, and Strouhal number that can occur. Unsteady effects are almost always important for $Re \gtrsim 50$, although the alternate vortex shedding with dominant periodicity is most pronounced for $100 \lesssim Re \lesssim 200{,}000$. This encompasses the vortex-street and subcritical regimes, where the flow near the surface of the cylinder is laminar up to and past the point of separation; transition to turbulence occurs in the wake, if at all. The mean drag coefficient and Strouhal number are well defined, although considerable scatter occurs in the fluctuating lift or side-force data, as shown in Fig. 6. Not shown is the unsteady drag, which fluctuates with an amplitude of the order of 0.05 to 0.10 and a frequency twice that of the lift fluctuations, which are synchronized with each pair of shed vortices.

Major changes occur at a critical Reynolds number that is of the order of 2×10^5, where transition

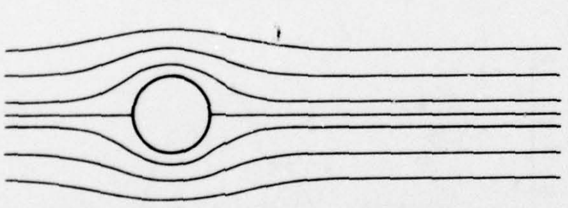

a. POTENTIAL FLOW $C_D = C_L = 0$

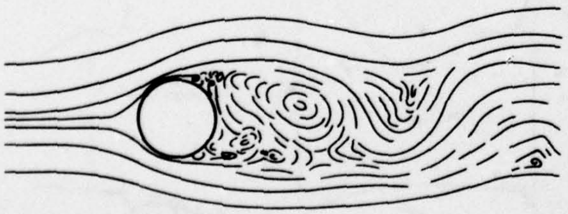

b. $Re \approx 10^4$ $C_D \approx 1.1$, $C_L \approx 0.4e^{i\omega t}$

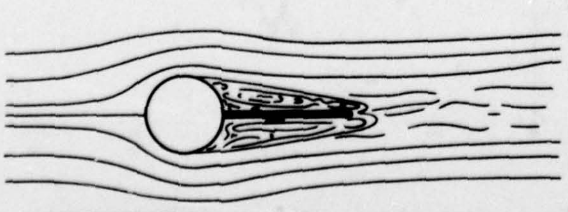

c. SPLITTER PLATE $C_D \approx 0.6$, $C_L \approx 0$

Fig. 4. Sketches of flow past a circular cylinder.

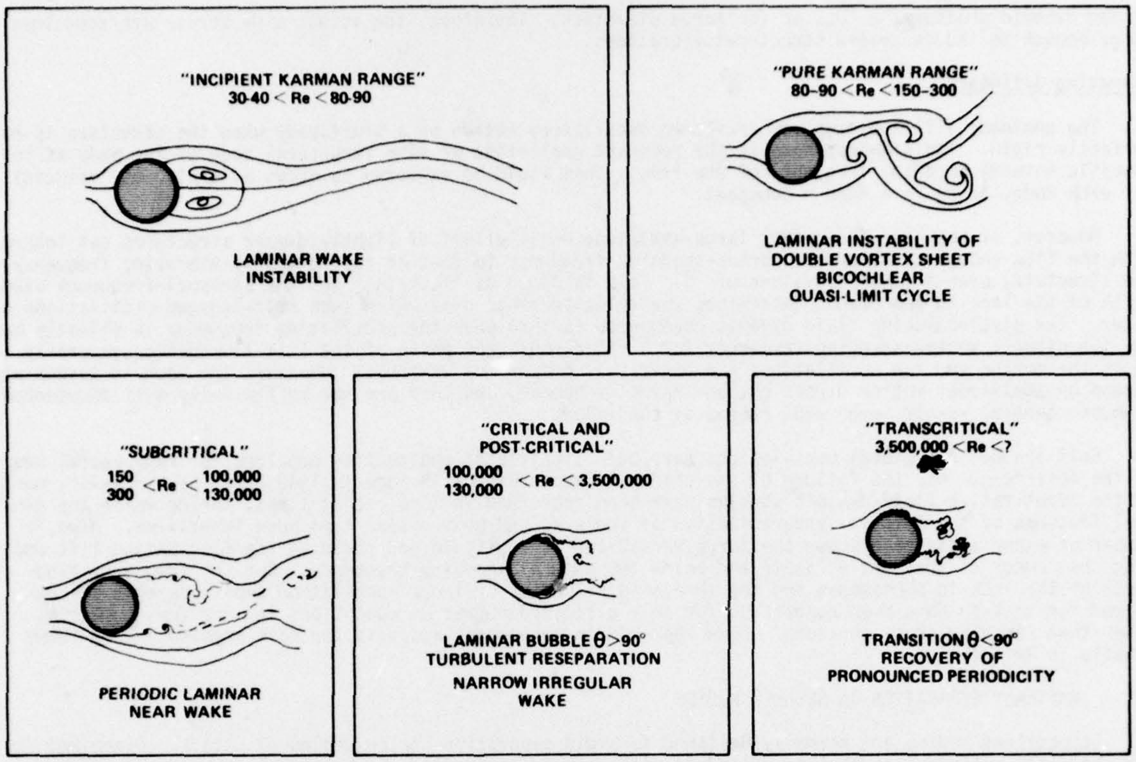

Fig. 5. Fluid dynamic flow regimes for a cylinder.

occurs so quickly in the laminar free-shear layer that turbulent reattachment occurs on the surface of the cylinder. The boundary layer then reseparates as a turbulent free-shear layer a short distance farther around the perimeter. The flow on the rear half of the cylinder changes dramatically as a result of this longer run of thin boundary-layer flow (cf. Fig. 5), and the redistribution of pressure causes the well-known large decrease in the mean drag coefficient shown in Fig. 6. The dominant periodicity ceases and the Strouhal number is usually ill-defined, although significant fluctuations continue. These fluctuations are wide-band, but not completely random. Therefore, a wide range of Strouhal numbers have been reported for this regime; this is indicated by the cross-hatched regions in Fig. 6. The flow in this low supercritical regime is highly sensitive to freestream turbulence, surface roughness, and three-dimensional disturbances. Both the mean and the fluctuating forces diminish considerably, but the details of the flow are not well understood nor adequately documented in this regime.

For smooth cylinders and at Reynolds numbers of the order of 3×10^6 and above, transition to turbulence occurs ahead of, and thereby supersedes, the laminar separation bubble. When this occurs, pronounced periodicity in the fluctuating lift reappears, implying a return to some form of periodic vortex shedding. This regime is usually called "transcritical," although the supercritical and transcritical labels are sometimes interchanged in the literature.

Although it has not been established whether there is a Reynolds number above which S, C_D, and C_L remain constant, a predominant Strouhal number becomes rather well defined at $S \approx 0.3$ for $Re \gtrsim 10^7$ and C_D increases approximately twofold above its minimum value at $Re \approx 6 \times 10^5$. The fluctuating lift coefficient is much lower than in the subcritical regime. However, this high-Reynolds number regime is only attained at relatively high values of free-

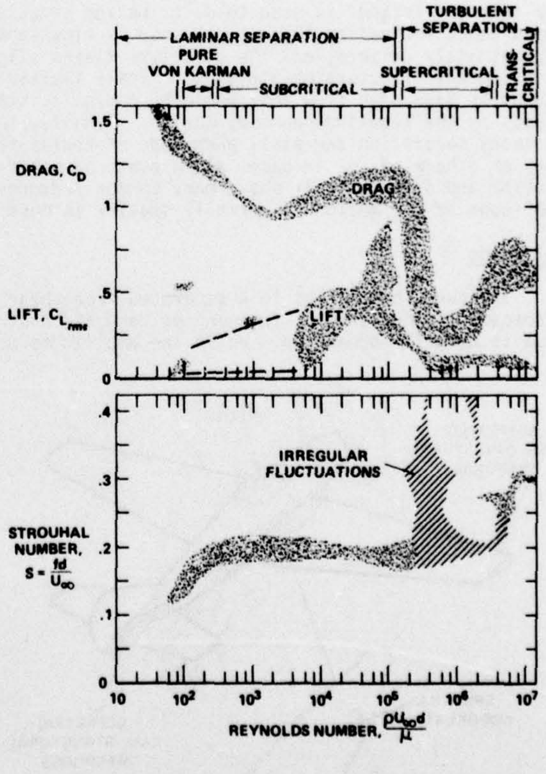

Fig. 6. Mean drag, fluctuating lift, and Strouhal shedding frequency for rigid circular cylinders (Ref. 1).

stream dynamic pressure, $\frac{1}{2}\rho U_\infty^2$, or for large diameters. Therefore, the actual side forces are sometimes large enough to induce severe structural vibrations.

Vibrating Cylinders

The unsteady lift and drag can excite an oscillatory motion of a bluff body when the structure is not perfectly rigid. The simplest case is the resonant excitation of some structural mode of the body at the specific natural shedding frequency of the flow. This would be expected to occur at a discrete velocity for each mode, since $S = fd/U \approx$ constant.

However, it has been found that large-amplitude oscillations of lightly damped structures can interact with the flow enough to alter the vortex-shedding frequency to that of the naturally-vibrating frequency of the structure, over a range of values of S. This is known as "lock-in," and the Strouhal-frequency bandwidth of the lock-in phenomenon determines the velocity range over which such self-induced oscillations can occur. The distinguishing fluid dynamic phenomenon is that when the oscillating frequency is slightly below the natural vortex-shedding frequency for a rigid body, the phase of the lift fluctuation generally leads the motion and the oscillations are negatively damped, or unstable. However, the lock-in forces also depend on amplitude, motion direction, and Reynolds number, and they are not sufficiently well documented to quote general results over wide ranges of condition.

Self-induced structural oscillations have been significant engineering problems for many years; one of the most famous was the failure of the original Tacoma Narrows Bridge in 1940 (Ref. 6). However, most of the quantitative fluid-dynamic studies have been performed in more recent times, during which the general features of the lock-in synchronization of the wake and body motion have been identified. Also, a number of experiments have shown the large variations in amplitude and phase of the fluctuating lift and drag that occur at frequencies above and below the natural shedding frequency. But the frequency bandwidth of the lock-in phenomenon and the threshold values of cylinder oscillation amplitude that are required for lock-in have been quantified for only a limited number of conditions and for few geometries other than circular cross sections. Some approximate methods of analysis for this problem are reviewed briefly in Ref. 1.

3.0 UNSTEADY SEPARATION ON SLENDER BODIES

Streamlined bodies are normally designed to avoid separation at low angles of attack. Organized vortex shedding, analogous to that on cylinders with laminar separation, may occur at low Reynolds numbers. However, most streamlined configurations operate at high Reynolds numbers, $10^6 < Re < 10^8$, so that turbulent boundary layers prevail. At high flight speeds, shock waves are likely to cause the turbulent boundary layer to separate, whereas stall may occur at lower speeds and at high angles of attack. In any case, turbulence in free shear layers and wakes tends to disorganize the flow, to produce fluctuating fluid dynamic forces, and to compound the analytical difficulties.

For slender bodies at high Reynolds numbers, the unsteady separated external flow problems can be roughly classified into three main categories, which are very much associated with the motion of the body. The term "buffeting" is used to describe the structural response of aircraft or missile components to the aerodynamic excitation that is produced by flow separation. In this case, the overall body motion is approximately uniform, and the structure flexes slightly and irregularly under the influence of the separation-induced fluctuating airloads. "Stall flutter" refers to oscillations of an elastic body that are caused by separated flow that would be nominally steady in the absence of the body, but which is made unsteady by the flow-induced body motion. Finally, the term "dynamic stall" is often used to describe the unsteady separation and stall phenomena on bodies that are forced to execute time-dependent motion, oscillatory or otherwise, or in cases where gusts or other flow-field disturbances induce transitory stall. Stall flutter and dynamic stall share many common features; the primary fluid dynamic difference is that the amplitude of the motion is normally smaller in most cases of stall flutter.

Buffeting

The turbulent eddies in a separated free-shear layer produce velocity and pressure fluctuations that encompass a wide range of frequencies, and the distribution of turbulent energy across the frequency spectrum is normally broadband. While the amplitudes of these fluctuations are generally much smaller than typical mean values, they are usually 10 to 100 times larger than those of attached boundary layers, as indicated in Fig. 1. Consequently, the separated pressure fluctuations may become greater than the threshold levels that are required to excite normal modes of vibration of an aircraft structure. This resonant aerodynamic excitation of structural vibrations is characterized by the level, scale, and degree of correlation of the pressure fluctuations.

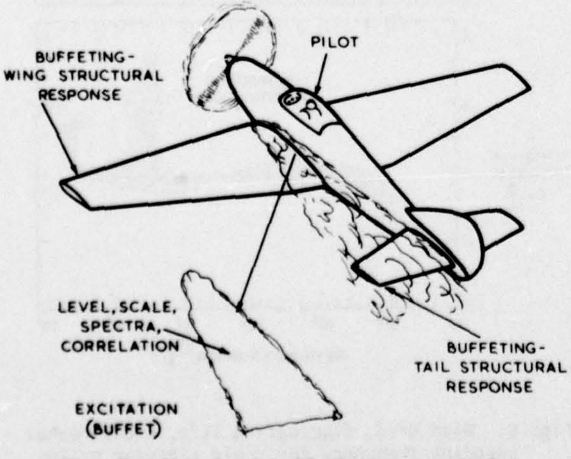

Fig. 7. Sketch of buffeting on an airplane (Ref. 7).

The earliest investigations of buffeting dealt with often-catastrophic vibrations of aircraft tails operating in the separated wake of the main wing, or of the wing-fuselage junction, as indicated in Fig. 7 from Ref. 7. An analogous bluff-body problem would be the vibrations induced by the impact of the external wake of one tube on another in a multiple-tube, cross-flow-type heat exchanger. Buffeting may also occur on the wing itself, of course, and this is the more common problem today. Wing buffeting of modern aircraft and missiles generally occurs at the extremes of the operational flight envelope, either near $C_{L_{max}}$ during landing or maneuvers, or near the onset of transonic drag divergence in cruise. Maneuver limitations and drag divergence invariably involve separation induced by shock waves.

Although the onset of flow separation and buffeting can be estimated by a combination of boundary layer methods and potential flow theory, no reliable theoretical or numerical technique exists for predicting the fluctuating pressures in turbulent separated shear flows. Consequently, the design engineer must rely on correlations of experimental data and on tests of models in wind tunnels for estimates of aerodynamic characteristics, structural vibrations, and fatigue loads. The fluid dynamic characteristics are often inferred or measured directly on conventional rigid models or surfaces. However, it has not been established to what extent the statistical characteristics of the aerodynamic exciting forces are essentially independent of the motion of the body surface. These questions of experimental techniques and philosophy will be covered in detail in the following lecture, as well as classifications and detailed discussions of wing flows with buffeting. In subsequent lectures, the fundamental fluid dynamic aspects of unsteady shock wave-boundary layer interactions will be addressed.

Dynamic Stall and Stall Flutter

A certain degree of unsteadiness always accompanies the flow over an airfoil or other streamlined lifting surface at high incidence, but the stall of a profile undergoing unsteady motion is even more complex than static stall. If the angle of attack oscillates around the static stall angle, the fluid dynamic forces and moments exhibit large amounts of hysteresis. The maximum values of C_L, C_D, and C_M can greatly exceed their static counterparts, and a condition of negative aerodynamic damping in pitch often develops during part of the cycle. This is illustrated by the dotted shading in Fig. 8* from Ref. 8. The aerodynamic pitch damping is given by $-\oint C_M \, d\alpha$. If the average value over the cycle is negative, the airfoil extracts energy from the air stream, and the pitch oscillations will tend to increase in amplitude, unless restrained. This, of course, is the condition for flutter, and unsteady separation hysteresis permits it to occur in a single degree of freedom of oscillatory body motion. Normally in unseparated flows, flutter only occurs when the body motion includes multiple degrees of freedom; for example, combined bending and torsion of an aircraft wing.

A great deal has been learned about the basic phenomena of dynamic stall within the last decade, especially in connection with the retreating-blade stall problem of helicopter rotors (Refs. 1, 9). On an airfoil whose incidence is increasing rapidly, the onset of stall can be delayed to incidences considerably in excess of the static stall angle. If the airfoil attains a sufficiently high incidence to penetrate deep into stall by virtue of large-amplitude motion, the breakdown of the flow field begins with the formation of a strong vortex-like disturbance that is shed from the leading-edge region. This vortex moves downstream over the upper surface of the profile, as shown in Fig. 9. Its passage distorts the chordwise pressure distribution and produces transient forces and moments that are fundamentally different from their static counterparts and that can not be reproduced by neglecting the unsteady motion of the airfoil. Another feature of the unsteady stall case is that large negative values of pitching moment caused by the rearward shift of the aerodynamic center of pressure, that is, "moment stall," occur before the maximum in lift or normal force, or "lift stall."

The details of dynamic stall depend strongly on the frequency of oscillation, the amplitude and mean angle of the motion, and in some cases, on the airfoil geometry. The effect of Mach number seems fairly important, although the extent to which the vortex shedding phenomenon is suppressed by shock wave-boundary

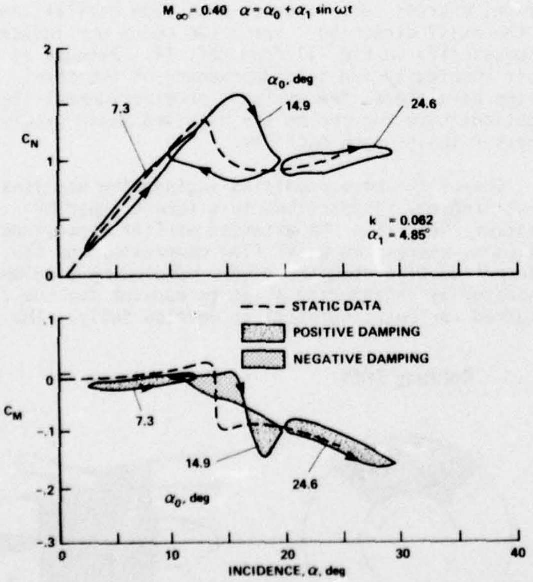

Fig. 8. Force and moment coefficients on an oscillating airfoil at several mean angles (Ref. 8). Pitch axis at $X/c = 0.25$, $Re = 4.8 \times 10^6$.

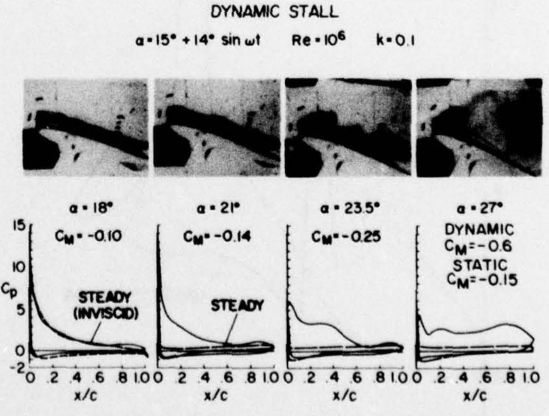

Fig. 9. Flow visualization and pressure measurements of the vortex-shedding phase of dynamic stall on an oscillating airfoil (Ref. 1). Pitch axis at $X/c = 0.25$.

---

*In this and all subsequent figures, the reduced frequency has the definition that has evolved from potential-flow theory: $k = \omega c/2U_\infty$, where c is the chord of the airfoil.

layer interaction has not been established. The dependence on Reynolds number is rather weak. The role of these parameters will be discussed in more detail in a subsequent lecture.

The related phenomenon of stall flutter also involves oscillations in pitch, but as mentioned earlier, the amplitude of the oscillation is usually smaller than in the case of dynamic stall. When this is true, the large-scale, organized vortex-shedding phenomenon just described is absent or much less prominent. Nevertheless, the hysteresis in C_M vs. α, which is necessary to produce the negative aerodynamic damping that initiates stall flutter, still has its origins in the phase of the nonlinear separation and reattachment of the boundary layer. Consequently, the frequency of the oscillation, which is approximately the torsional natural frequency of the structure, is a predominant parameter. The airfoil geometry and the freestream Mach number largely determine the boundary layer separation characteristics, and, therefore, they are also important.

Flutter of Control Surfaces

Finally, control surface flutter is an important practical problem, especially aileron buzz at transonic speeds. Under certain combinations of Mach and Reynolds numbers, the spectrum of the fluctuating pressures in the separated zone behind the shock wave in Fig. 1 contain one or more predominant frequencies. If the airfoil section includes a hinged flap, the resultant periodic hinge moments may produce an oscillatory flap motion, which in turn interacts with the flow field near and behind the shock wave to sustain a limit-cycle flutter motion. As in the related problem of transonic buffet, a satisfactory analytical or numerical treatment of this problem is not yet available, but considerable basic research is in progress on the model problem of forced small-amplitude oscillation of the flap of an airfoil in transonic flow (Refs. 1, 10). This problem will be discussed further in a subsequent lecture.

4.0 INTERNAL FLOWS

Separated flows in ducts with variable geometry and in turbomachinery exhibit many features in common with the external flows discussed above. However, there are important differences which are described briefly in the following representative examples.

Axial-Flow Compressors

The qualitative features of dynamic stall and stall flutter have been observed in compressors and their nonrotating analogs, cascades. However, the interference between adjacent blades and three-dimensional and rotational effects has a strong influence on the quantitative details of the stall behavior (Refs. 11, 12). In particular, the hysteresis loops of forces and moments are considerably more complicated than those of isolated airfoils, as indicated in Fig. 10 from Ref. 13. Furthermore, in this experiment the maximum normal force was observed to increase approximately linearly with the nondimensional pitch rate, but the rate of increase of C_N in this correlation was much less than in the isolated airfoil case. More detailed measurements will be required to determine to what extent stall on rotating components can be understood in terms of the semi-empirical analyses and concepts of dynamic stall on airfoils and wings.

Although they lie outside the scope of this lecture series, the global unsteady stall problems of surge and rotating stall in turbomachines may be mentioned in passing. As their names suggest, rotating stall is a large-scale separation phenomenon that propagates circumferentially in a direction opposite to the rotor motion, whereas surge induces mass flow oscillations in the axial direction. These two modes are indicated schematically in Fig. 11 from Ref. 14. Because of their complexity and interdependence on the total system parameters, few analyses or experimental investigations have focused on the detailed fluid dynamic behavior inside such machines.

One of the more promising engineering analyses of these problems is described in a recent paper by Greitzer (Ref. 15). He extended earlier linearized analyses, wherein an axial flow compressor and its adjacent ducting downstream were modeled by a Helmholtz resonator by introducing a lag to account for the time required for rotating stall to develop fully. The

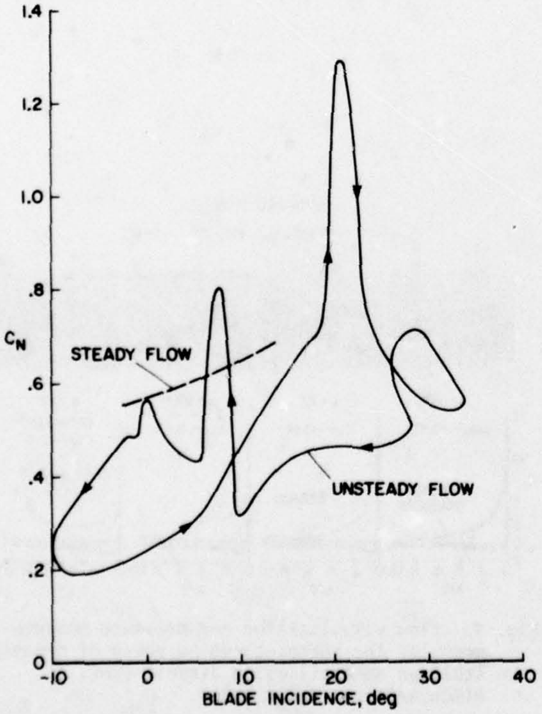

Fig. 10. Normal force coefficient for dynamic stall on a compressor rotor blade due to inlet distortions (Ref. 13).

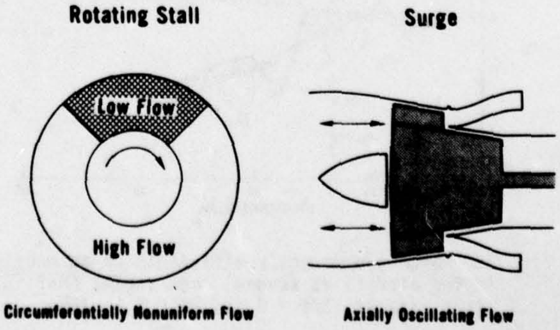

Fig. 11. Sketch of two possible modes of compressor instability (Ref. 14).

nondimensional time constant of this lag in compressor response was found to be proportional to the Helmholtz resonator frequency, ω_H. Greitzer stressed the importance of a parameter B; it is the inverse of the reduced frequency based on ω_H, the equivalent duct length encompassing the compressor disc, and the mean circumferential velocity of the rotor. He found that for a given compressor, the mode of the instability that would occur at the stall line, that is, surge or rotating stall, would depend on whether B were greater or less than a critical value, corresponding to the onset of limit cycle behavior of pressure rise versus axial velocity.

Transitory Stall in Diffusers

A different type of stall occurs in diffusers that are operating close to their maximum pressure recovery. Basic flow regimes were identified some years ago (Ref. 16) for low speed flows, as indicated in Fig. 12. Some of the transonic modes that were classifed more recently in Ref. 17 are sketched in Fig. 13.

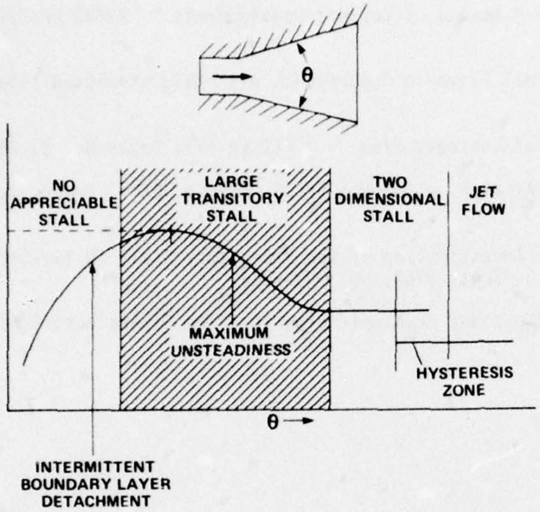

Fig. 12. Flow regimes in two-dimensional low-speed diffusers (Ref. 16).

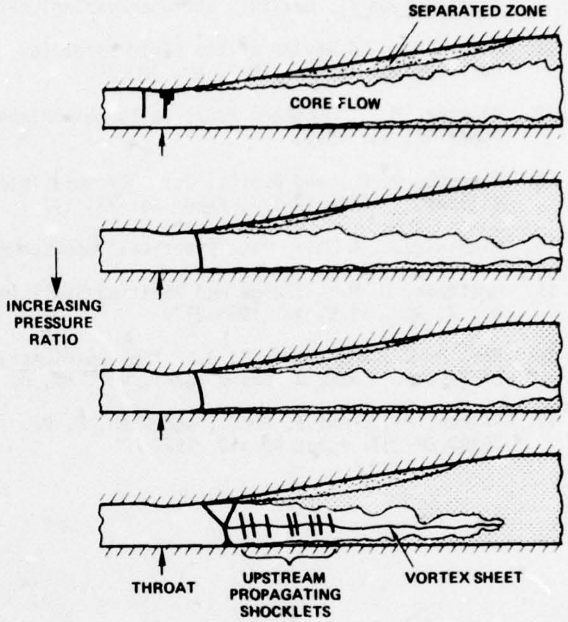

Fig. 13. Typical instantaneous flow patterns in transonic and supersonic diffusers (Ref. 17).

In these transitory stall regimes, large amplitude fluctuations can occur more or less periodically as the separated fluid washes in and out of the downstream end of the diffuser, or as the stalled region grows and collapses in the lateral direction. As shown in Fig. 13, the unsteadiness in the supercritical modes was caused by the unsteady shock wave-boundary layer interactions.

The frequency of the transitory stall in low-speed two-dimensional configurations has been found to be given very approximately by $f L \sin\theta/U_0 = 0.0055$, where L is the length, U_0 is the average entrance velocity, and θ is the total included angle of the diffuser. For the maximum amplitudes of the fluctuations, typical values of θ are in the range 15° - 30°, which would mean $\omega L/U_0 \approx 0.1$. It has not yet been established whether this represents a truly unsteady problem, insofar as the overall performance is concerned. However, for the large-amplitude oscillating airfoils, this range of reduced frequencies represents a regime wherein unsteady effects grow rapidly with increasing frequency.

5.0 CONCLUDING REMARKS

Almost any flow that separates will have some degree of unsteadiness. In some cases, the fluctuations will be almost complete stochastic; in others it will be highly organized; and in others, it will be a combination of random and periodic components. In this introductory lecture, some of the peculiar unsteady phenomena have been reviewed and several broad classes of flow problems have been discussed briefly. It should be emphasized again that a great deal remains to be learned about unsteady separated flows, especially at high Reynolds numbers. A considerable amount of research is under way in an effort to understand the basic fluid dynamic mechanisms better and to develop new engineering prediction methods.

6.0 REFERENCES

1. McCroskey, W. J.: "Some Current Research in Unsteady Fluid Dynamics." ASME J. Fluids Engr., vol. 99, no. 1, Mar. 1977, pp. 8 - 38.

2. McCroskey, W. J., and Fisher, R. K., Jr.: "Detailed Aerodynamic Measurements on a Model Rotor in the Blade Stall Regime." J. Am. Helicopter Soc., vol. 17, no. 1, Jan. 1972, pp. 20 - 30.

3. Telionis, D. P.: "Unsteady Boundary Layers, Separated and Attached." AGARD CP-227, Paper No. 16, 1977.

4. Williams, J. C., III: "Incompressible Boundary Layer Separation." Annual Review of Fluid Mechanics, vol. 9, Palo Alto: Annual Reviews, 1977, pp. 113 - 144.

5. Sears, W. R., and Telionis, D. P.: "Boundary Layer Separation in Unsteady Flow." SIAM J. Appl. Math., vol. 28, no. 1, Jan. 1975, pp. 215 - 235.

6. Fung, Y. C.: The Theory of Aeroelasticity. New York, Dover: 1969, pp. 62 - 63.

7. Mabey, D. G.: "Beyond the Buffet Boundary." Aero. J., vol. 77, no. 748, Apr. 1973, pp. 201 - 215.

8. Liiva, J.: "Unsteady Aerodynamic and Stall Effects on Helicopter Rotor Blade Sections." J. Aircraft, vol. 6, no. 1, Jan. 1969, pp. 46 - 51.

9. Philippe, J. J.: "Le Déchrochage Dynamique: Un Exemple d'Interaction Forte entre Ecoulements Visqueux et Non-Visqueux." AGARD CP-227, Paper No. 21, 1977.

10. Tijdeman, H.: "On the Motion of Shock Waves on an Airfoil with Oscillating Flap." IUTAM Symposium Transsonicum II, Berlin: Springer-Verlag, 1976, pp. 49 - 56,

11. Sisto, F.: "A Review of the Fluid Mechanics of Aeroelasticity in Turbomachines." ASME J. Fluids Engr., vol. 99, no. 1, Mar. 1977, pp. 40 - 44.

12. Platzer, M.: "Unsteady Flows in Turbomachines—A Review of Current Developments." AGARD CP-227, Paper No. 33, 1977.

13. Peacock, R. E., and Øverli, J.: "Dynamic Internal Flows in Compressors with Maldistributed Inlet Conditions." AGARD CP-177, Paper No. 17, 1975.

14. Mikolajczak, A. A.: "The Practical Importance of Unsteady Flow." AGARD CP-177, Paper No. 1, 1975.

15. Greitzer, E. M.: "Surge and Rotating Stall in Axial Flow Compressors." ASME J. Engr. Power, vol. 98, no. 2, Apr. 1976, pp. 190 - 217.

16. Fox, R. W., and Kline, S. J.: "An Experimental Investigation of the Transitory Stall in Two-Dimensional Diffusers." ASME J. Basic Engr., vol. 84, no. 3, Sept. 1962, pp. 303 - 312.

17. Sajben, M., Kroutil, F. C., and Chen, C. P.: "Unsteady Transonic Flow in a Two-Dimensional Diffuser." AGARD CP-227, Paper No. 13, 1977.

PREDICTION OF THE SEVERITY OF BUFFETING

by

D G MABEY

ROYAL AIRCRAFT ESTABLISHMENT, BEDFORD

NOTATION

c	wing chord (m)	p	pressure fluctuation in a band Δf at frequency f (N/m^2)
$C_B = C_B(M,)$	buffeting coefficient - wing root strain signal/kinetic pressure (arbitrary units)	$\bar{p}$	rms pressure fluctuations (N/m^2)
$C_B{}' = C_B{}''$	dimensionless buffeting coefficients defined in Equations (3) and (4)	$\overline{p^2}/q^2$	$= \int_{\log n=-\infty}^{\log n=\infty} nF(n)d(\log n)$
C_L	lift coefficient	q	kinetic pressure $\frac{1}{2}\rho V^2$ (N/m^2)
f	frequency (hz(c/s)	R	Reynolds number - based on aerodynamic mean chord
F(n)	contribution to $\overline{p^2}/q^2$ in frequency band Δn	V	free stream velocity (m/s)
$\sqrt{nF(n)}$	$p/q(\varepsilon)^{1/2}$	x	distance from leading-edge (m)
K	transformation factor Equation (3)	α	angle of incidence or angle of attack (°)
L	typical dimension	ε	analyser bandwidth ratio $(\Delta f/f)$
l	bubble length (m)	Λ	sweep angle (°)
n	frequency parameter fL/V	ρ	free stream density (kg/m^3)

1.0 INTRODUCTION

We must first establish what we mean by buffeting. Buffeting is defined as the structural response to the aerodynamic excitation produced by separated flows. In the example sketched in Figure 1, there is a large area of separated flow on the wing. This provides the excitation which at a given point may be characterised by the rms level, the frequency spectrum (we shall see that the spectrum is often fairly flat at low frequencies), the degree of correlation in space and time, and the length scale. The pressure fluctuations excite a response of the structural modes which we call buffeting. The aircraft structure acts as a selective filter for the excitation so that spectra of buffeting always contain pronounced peaks at structural frequencies. In the example sketched in Figure 1 both the wing and the tailplane are excited. Rigid body modes may also be excited, such as "wing rocking", "wing dropping" or "nose slicing", but these are at much lower frequencies and can be regarded as aircraft handling problems, of great importance but outside the scope of this chapter. Buffet onset is often defined as the first appearance of a significant area of separated flow, although aerodynamicists often argue about how large the area must become before it is significant. (This is one of the uncertainties inherent in the theoretical methods for the prediction of buffet onset now being developed. These methods are briefly discussed in the Appendix). The onset of buffeting in flight is even more difficult to specify, for much of our present data are based on pilot impressions, which may be inaccurate if the pilot sits on or close to a node of the predominant modes being excited. Most pilots expect wing buffeting to provide a warning of more serious phenomena such as stall, pitch up or wing-drop, and are unhappy with aircraft which do not provide such a warning, unless an automatic visual or audio warning system is fitted.

The term buffeting was apparently first introduced into aeronautical literature when a structural failure occurred to the tail of a Junkers monoplane in 1930 (Ref 1). This failure was attributed by the British accident investigation to buffeting of the tailplane excited by flow separations on the wing. The flow separations on the wing were caused by an encounter with a severe gust and the German investigation attributed the accident directly to the structural failure of the wing caused by the gust (Ref 2). This incident emphasises again that buffeting often occurs in critical flight situations, when limit loads are being approached or when the aircraft is approaching lateral or longitudinal stability boundaries. (These early reports even include some discussion of the importance of correctly representing the aircraft geometry on the model and of the problems posed by testing at low Reynolds numbers. These issues are still important today).

A consistent, dimensionless representation of excitation spectra is required when comparing measurements made at different flow densities and velocities. We shall adopt the notation suggested by T B Owen (Ref 3) and represented in Figure 2. Here we have a frequency parameter

$$n = fL/V \ ,$$

and an excitation level

$$p/q\sqrt{\varepsilon} = \sqrt{nF(n)} \ .$$

Buffeting Criteria for Fighter and Transport Aircraft

Figure 3 illustrates how buffeting criteria, expressed in terms of C_L - M boundaries, can influence the choice of wing loading for fighter and transport type aircraft. The boundaries presented for onset, light, moderate and heavy buffeting are based on some unpublished RAE measurements (Ref 4). (These boundaries are derived by a method outlined later).

A typical fighter aircraft (with a wing leading-edge of sweep angle 42^o) will cruise well below the buffet onset boundary, but will frequently perform 5g manoeuvres which take it well beyond the buffet boundary to the moderate buffeting, or even to the heavy buffeting contour. For a fighter aircraft the moderate buffeting limit is sometimes taken as the highest level at which guns or missiles can be aimed successfully, whereas the heavy buffeting limit is that at which the aircraft becomes useless as a weapon platform, but is still controllable. For a fighter, frequent buffeting loads can seriously influence the fatigue life of the structure, for they are considerably larger than the loads caused by turbulence. The influence of the buffeting loads on the fatigue life of the new generation of advanced combat aircraft will need careful consideration. These aircraft can manoeuvre at higher lift coefficients and kinetic pressures than previous aircraft, without encountering rigid body modes such as wing dropping or nose slicing, because the separations are well controlled. However the pilot could be largely unaware of high frequency responses occurring in structural modes which could strongly influence the life of the airframe.

In contrast a typical transport aircraft (with the wing leading-edge of sweep angle 27^o) may cruise at about 0.1 in C_L below the buffet onset boundary. On infrequent occasions the aircraft may encounter a strong gust which carries the aircraft beyond the buffet boundary, right up to the moderate buffeting level. (The gust of 12.5 m/s selected in this example would have a wavelength of about 33 m (Ref 5). The steady load achieved during the excursion into buffeting is probably more serious than the buffeting loads, which may be little larger than those associated with the atmospheric turbulence encountered during every flight.

Buffeting on fighter and transport aircraft only determines the extent of the penetration beyond the buffet boundary if there are no other handling limitations, such as wing rocking, wing dropping, pitch-up or stalling. We will return to this point later.

2.0 CLASSIFICATION OF WING FLOWS AND BUFFETING

A broad classification of wings with separated flows that excite buffeting will be useful as a framework for our discussion, even if the classification suggested is incomplete (Fig 4).

Wings with low angles of sweep are characterised beyond the buffet boundary at subsonic speeds by leading-edge or trailing-edge separations. These separations form bubbles on the wing which usually excite heavy buffeting. At transonic speeds the presence of strong shock waves nearly parallel with the leading-edge add to the difficulties of predicting the flow, so that we give this flow a prediction rating of 10. (These prediction ratings are arbitrary and not used in any calculations; an increase in prediction rating represents increased difficulty of prediction). Swept wings are characterised by a combination of mixed flows (Ref 6) which are difficult to predict. The separated flows on a swept wing at transonic speeds may include shock waves (which vary in intensity across the span), bubbles (from the leading-edge or the trailing-edge) and vortices. Thus a small increase in Mach number may dramatically alter the position of a shock wave or the reattachment point of a bubble. Similarly an increase in unit Reynolds number or a change of the roughness band used to fix transition on the model in wind tunnel tests may completely alter the character of the shock wave/boundary layer interaction (References 7 and 8). These difficulties seem to justify a prediction rating for swept wings of 100; an even higher rating would be appropriate for a variable geometry wing.

Slender wings with sharp leading-edges are characterised by a simple vortex type of flow, which prevails over the complete speed range from subsonic to supersonic speeds. This unified type of flow is a powerful argument for the application for supersonic aircraft (Ref 9). The vortices, which produce significant non-linear lift, have a well defined, small scale structure and we shall see that they do not produce severe buffeting unless vortex breakdown occurs at high angles of attack outside the normal flight envelope. In addition the vortices on slender wings with sharp leading-edges are relatively insensitive to wide variations in Reynolds number. Hence slender wings are given a prediction rating of 1.

These prediction ratings are, of course, arbitrary, but they reflect real differences between the flows, which are now considered in greater detail.

Unswept Wings

The character of the excitation caused by leading-edge separation bubbles on unswept wings may be inferred (Ref 10) from the simplified model for a bubble suggested by Norbury and Crabtree in Reference 11 (Fig 5). In the constant-pressure region of the bubble, we would expect the excitationcaused by low frequency fluctuations in the separation point to be relatively small, whereas in the reattachment region, where the rate of pressure recovery is high, the excitation should be much higher. Thus the excitation might be expected to reach a maximum in the middle of the reattachment region. These inferences from the mean static pressure distributions are broadly confirmed by the measurements, although the excitation attenuates both upstream and downstream of the reattachment region owing to the influence of the shear layer.

The spectrum of surface pressure fluctuations for a boundary layer approaching separation in an adverse pressure gradient may be divided into high-frequency and low-frequency components (Ref 12). The high-frequency pressure fluctuations are similar to those found under a boundary layer in zero pressure gradient (Ref 13) and are generated in the small scale inner region of the boundary layer associated with the law of the wall. The low-frequency pressure fluctuations are generated in the large-scale outer region associated with the law of the wake, and increase in intensity as the outer region of the boundary layer thickens. Between separation and reattachment, measurements suggest that the low-frequency pressure fluctuations continue to increase steadily as the separated boundary layer thickens, until a point is reached where the mixing layer turns towards the surface and the mean pressure starts to increase. (Bradshaw has shown that the flow in the reattachment region is dominated by a rapid reduction in eddy size as the shear layer is divided into two halves. The lower half of the shear layer moves upstream from reattachment; the upper half moves downstream (Ref 14). It seems reasonable that this sudden reduction in eddy size should be accompanied by a sudden reduction in excitation at low frequencies). Somewhere close to the reattachment point, the measurements for a wide range of bubble flows show a maximum value of the rms pressure fluctuation coefficient of

$$\bar{p}/q \text{ between } 0.10 \text{ and } 0.04 \quad .$$

The spectra also shows a marked similarity if the frequent parameter n is based on the bubble length l, for a peak pressure fluctuation is found when

$$n = fl/V = 0.5 \text{ to } 0.8 \quad . \qquad (1)$$

This probably implies a feed-back process between conditions at the reattachment and separation points. Equation (1) will be inappropriate when there is a strong, coherent disturbance in the wake (eg a Kármán vortex street) or if there are acoustic resonances (as there may be in cavities). The measured pressure fluctuations always cover a broad band of low frequencies, rather than a single discrete frequency as given by Equation (1), probably because the velocity of the eddies in the shear layer varies with the eddy size.

Leading-edge bubbles may be important for aircraft with sharp leading-edges, for which we have some good excitation measurements (Fig 6). Leading-edge bubbles were formed on the centre section of the Bristol 188 aircraft (Ref 15) and on a Venom aircraft with a sharp leading-edge (Ref 16). Figure 6 shows that the rms excitation at two points on the Bristol 188 increases gradually from separation (x/l = 0), reaches a maximum of

$$\bar{p}/q = 0.10$$

just upstream of the reattachment point (x/l = 1.0), and then decreases. The frequency parameter n based on the bubble length has a maximum at about n = 0.7 and correlates the spectra quite well at x/c = 0.85, where most of the measurements are taken in the region of rapid pressure recovery (x/l = 0.94). The peak level is about $\sqrt{nF(n)} = 0.006$. (The parameter n does not work so well at x/c = 0.50, where some of the measurements are taken in the constant steady pressure region (x/l = 0.56)). Measurements of pressure fluctuations on a Venom aircraft also conform to the general pattern shown in Figure 6(a) and show no significant variation in the rms pressure fluctuations or the spectra over the Mach number range from M = 0.3 to 0.6. Only a small Reynolds number effect on the low-speed pressure fluctuations was measured between the aircraft and a model (Ref 16). Some pressure fluctuation measurements on aerofoils with round leading edges (Ref 17) suggest similar rms levels and a peak frequency parameter of about 0.8 to 1.0.

Equation (1) helps us to discriminate between the excitation frequencies associated with long and short bubbles because of the large change in the bubble length between the two flows. A long bubble covers a significant area of the aerofoil chord and, from Reference 18, because

$$l/c = O(1)$$

the pressure fluctuations will be at comparatively low frequencies which can excite the structural modes; eg for a long bubble on a wing with a chord of 3 m moving at 70 m/s, the excitation frequency would be

$$O\ (12\ \text{Hz}) \quad .$$

(Typical wing fundamental bending frequencies are 10 Hz for a small aeroplane and 2 Hz for a large aeroplane). A short bubble only influences a small area of the wing, but, in addition, because

$$l/c = O(0.01)$$

these pressure fluctuations will be at such high frequencies that they are unlikely to excite structural modes; eg for a short bubble on a wing with 3 m chord moving at 70 m/s, the excitation frequency would be

$$O\ (1200\ \text{Hz}) \quad .$$

Flight tests on the Venom with a sharp leading-edge (Ref 16), and the canard control of the XB-70 (Ref 19), showed that buffet onset corresponded with the formation of a long bubble. The buffeting then increased steadily as the bubble extended downstream, until the reattachment point approached the trailing-edge and the trailing-edge pressure diverged. This point corresponded with heavy buffeting. Hence the local pressure fluctuations within a long bubble must be quite strongly correlated.

The character of the excitation caused by a spoiler of height h (Fig 6(b)) closely resembles that caused by a leading-edge bubble. The excitation increases steadily from separation and reaches a maximum of

$$\bar{p}/q = 0.05$$

just upstream of reattachment. The peak frequency parameter n for the spoiler is about 0.9 in the experiments of Fricke, rather than 0.7 for the leading-edge bubble. The experiments of Fricke (Ref 20), in air, and of Greshilov (Ref 21), in water, give peak frequency parameters of about 0.9 and 0.8 although the bubble lengths are respectively 16 h and 5.5 h. The coincidence of the frequency parameters based on bubble length confirms that this is a useful parameter for comparing the spectra of the pressure fluctuations generated by bubble flows.

The character of the rms pressure fluctuations and spectra caused by bubbles is largely independent of the origin of the bubble (Ref 10). Thus, in particular, the maximum pressure fluctuations occur just upstream of reattachment for:

- leading-edge bubbles,
- bubbles downstream of spoilers,
- bubbles downstream of steps,
- bubbles upstream of steps,
- bubbles downstream of sudden expansion in pipes,
- bubbles within shallow cavities (Fig 7).

Thus the data correlations presented in Reference 10 have application to a wide class of flows.

The prediction of the onset and severity of buffeting is of crucial importance at transonic speeds. In this speed range, the mixed subsonic/supersonic flows and the different regimes of shock/boundary layer interaction can modify the model for bubble flows described here, at least near the shock. However, downstream of the shock, an approximately constant average pressure is often observed in the separated flow region, followed by a rapid rise to reattachment. Coe's investigation (Ref 22) of the loads on launch vehicles included some measurements at subsonic and transonic speeds of the mean and fluctuating static pressures caused by a separation bubble downstream of a step in a body of revolution (Fig 8). Both the mean and fluctuating pressure distributions aft of the step correspond very well in general character with the low-speed pressure distributions over the complete speed range from $M = 0.60$ to 1.19, although the maximum fluctuating pressure falls steadily from

$$\tilde{p}/q = 0.06 \text{ at } M = 0.80$$

to

$$\tilde{p}/q = 0.03 \text{ at } M = 1.19 \quad .$$

This fall in the pressure fluctuations is probably due to the improved stability of the mean bubble flow because of the reduction of upstream influence from the reattachment region as the region of supersonic flow expands. (The base-pressure fluctuations on a body of revolution also fall from subsonic to supersonic speeds and a similar explanation may be applicable (Ref 23)). The mean pressure distribution suggests that the length of the bubble does not change significantly from $M = 0.60$ to 1.19 so that, within this speed range, there is probably no major change in the internal structure of the bubble.

The apparent universality of the pressure fluctuations caused by bubble flows at subsonic speeds is also well illustrated in Figure 8 which includes the pressure fluctuations measured (Ref 24) behind a two-dimensional step at $M = 0.33$ as well as those measured (Ref 22) behind a step on a body of revolution at $M = 0.80$. The similarity at subsonic speeds between both the rms pressure fluctuations and the spectra for the two different experimental configurations and Reynolds numbers is good.

Recently some interesting measurements of the excitation on a two-dimensional lifting aerofoil at transonic speeds were made by Moss and Mundell and reported in Reference 25 (Fig 9). The condition selected for this aerofoil ($M = 0.82$, $\alpha = 6.7^{\circ}$) is just beyond buffet onset. Although the trailing-edge pressure has not yet diverged, there is a short separation bubble on the aerofoil (with a length of about $l = 0.1\ c$) immediately downstream of the shockwave. The position of the bubble was inferred from the shape of the mean pressure distribution, because it could not be seen in oil flow tests. (The interpretation of oil flow tests on two-dimensional aerofoils is often difficult because there are no telltale inflexions in the streak lines as there are on swept wings).

The excitation measurements along the chord are presented from two frequency parameters

$$n = fc/V = 0.08 \text{ and } 0.8 \quad .$$

At a frequency parameter of $n = 0.08$, a typical value for wing structural modes, there is a large local increase in excitation in the vicinity of the shock wave. This local excitation decreases rapidly downstream of the shock wave but then shows a small local maximum in the vicinity of the reattachment region, before decreasing again. This variation in low-frequency excitation must be caused by the coupling of the shock wave motion (at separation) with the development of the bubble and with conditions at reattachment. In contrast, at a frequency parameter of $n = 0.8$, a typical value for wing panel modes, the excitation increases progressively downstream from the shock position, reaches a maximum close to the reattachment line and then falls rapidly as in the other bubble flows discussed in this section.

To find how the excitation develops, the angle of attack may be increased at constant Mach number. The separation bubble then extends rapidly towards the trailing-edge and the trailing-edge pressure diverges, while the shock wave starts to move upstream slowly. Thus the area of the aerofoil influenced by both the low frequency and high frequency excitation increases, and a progressive increase in buffeting would be expected. It should be noted that as the bubble extends rapidly in length from about $l = 0.1\ c$ to $l = 0.5\ c$, the predominant bubble frequency parameter will fall from $n = 8$ to $n = 1.6$, so that there should be a large increase in excitation in a frequency range centred on this lower value.

Swept Wings

Figure 10 shows the complex separated flow on a typical model with swept wings at a Mach number of 0.80 at low Reynolds number. These sketches illustrate some of the features which make buffet prediction difficult for swept wings and justify the prediction rating of 100 allotted in Figure 4. At buffet onset there are at least three shockwaves on the wing and a small shock induced separation bubble (with a length of perhaps 0.05 c) immediately downstream of the strongest shock wave, which runs roughly parallel with the leading-edge. At moderate buffeting there are complex shock patterns on the wing, areas of separated flow and areas with attached flow having a strong spanwise velocity component. (Great care is always necessary to achieve an optimum transition fix for the boundary layer under high lift conditions like this at transonic speeds if large scale effects are to be avoided. The essential aim in the model test is to achieve the full scale boundary layer shape parameter, H, at the shock-wave/boundary-layer interaction. This aim can often be achieved by comparing the results of modern boundary layer calculation methods at model and full scale Reynolds numbers).

Pressure fluctuations are presented for a single point P on the wing; Figure 11 shows the variation of rms pressure fluctuations with the angle of attack. An attempt is made to explain this variation, but it is speculative because of the difficulty of discriminating between local events at P and what is happening simultaneously elsewhere on the wing. A local Mach number of 1.0 is reached at a small angle of attack at a point on the wing near the leading-edge and close to the tip. A local region of supersonic flow then develops as the angle of attack increases. This supersonic region is terminated by a shock wave, which oscillates upstream and downstream. The pressure fluctuations at P first increase slowly with the angle of attack (point A, $\alpha = 1.8^{\circ}$) because of the combined effect of the shock oscillation and the pressure fluctuations caused by an attached boundary layer growing under an increasingly adverse pressure gradient (Ref 12). As the terminal shock wave approaches and passes the transducer position (point B, $\alpha = 5.0^{\circ}$) the pressure fluctuations increase rapidly; the major part of this increase must come from the shock wave oscillation. Shortly after point B the boundary layer separates at the terminal shock, and the terminal shock then starts to move forward and buffeting is detected by the wing-root strain gauges. (Thus the wing-root strain gauges give a measure of the integrated excitation on the wing). When the terminal shock moves upstream of the pressure transducer the local pressure fluctuations fall rapidly to a minimum at about $\alpha = 6^{\circ}$ because the point P is no longer influenced directly by the shock oscillation. The pressure fluctuations then increase to a maximum (point C, $\alpha = 7.2^{\circ}$), when the reattachment line crosses the pressure transducer, just as on the aerofoil (Fig 9). The local pressure fluctuations then decrease as the bubble extends downstream, although the wing buffeting, which is the response to the total excitation on the wing, continues to increase steadily from moderate to heavy.

The spectra of the pressure fluctuations provide additional information. Figure 12 shows that at point A, well below the buffet onset, the increase in pressure fluctuations is above the frequency range of wing modes. At the point B, with the terminal shock oscillating across the transducer, the peak pressure fluctuations become larger and move to lower frequencies, within the range of wing modes. At the point C, this peak is lower, because the shock is upstream of the transducer. However we notice at point C that there is an increase in pressure fluctuations at high frequencies ($n > 0.5$). This may be associated with the separation bubble downstream of the shock. By analogy with the low-speed results, we might expect to find a second peak in the spectra at $n = 5$ to 10 with this short length of bubble ($l \simeq 0.1$ c) but the present measurements did not extend much beyond $n = 1.0$.

This is obviously only a simplified account of the development of the excitation, using data from a single point on a wing. A complete description of the excitation all over a wing (including rms levels, spectra and correlations) is difficult to achieve. Extensive computing facilities are also needed to utilize this data to predict buffeting (3.0). Hence few measurements of excitation are currently available for swept wings at transonic speeds. However, we can learn a great deal about the wing behaviour from buffeting measurements, and these are discussed later.

Slender Wings

The fluctuating normal force measurements of Earnshaw and Lawford (Ref 26) (Fig 13) show that slender wings with sharp leading-edges can operate up to quite high angles of attack (and hence achieve reasonably high lift coefficients) without experiencing strong excitation. Although these tests were made at low Reynolds number ($R = 0.2 \times 10^6$ to 0.4×10^6), the flow characteristics of wings with sharp leading-edges are insensitive to wide changes in Reynolds number, primarily because the separation lines are fixed.

Recent measurements on the Concorde by BAC/Aerospatiale confirm that the level of excitation is light and almost identical with that measured on a 1/30 scale model (Ref 27) (Fig 14). Hence we may be confident that Reynolds number effects on the excitation of slender wing configurations with sharp leading-edges are insignificant.

The excitation is also light on slender wings with round leading-edges. However on slender wings with round leading-edges, large scale effects have been observed, particularly at subsonic speeds. A well documented example is the scale effects on the development of the leading-edge separations observed on the FD2 research aircraft (see References 28 and 29, and Figure 12 in Reference 30).

Although the level of excitation on slender wings is small, the level of buffeting attained is of interest because a slender-wing aircraft must fly above the buffet boundary on every take-off and landing, and thus acquire a large number of loading cycles during its operational life. The buffeting on rigid models of slender wings can be detected by sensitive semiconductor strain gauges (Ref 31). Measurements on two different rigid models conformed to the same pattern. Buffeting increases after the formation of the vortices and then reaches a plateau (Fig 15). This plateau is obtained because, although the area influenced by the vortices is increasing, the vortices are moving away from the wing. A sudden further increase in buffeting occurs when the vortex breakdown point moves across the trailing-edge, but it is unlikely that a slender wing aircraft would be required to operate in this region. An unusual feature of these buffeting measurements was that the third symmetric mode predominated, rather than the fundamental (as discussed later). Thus these measurements could not be used with confidence to predict the level of buffeting, quite apart from uncertainties about the appropriate damping coefficient. The solution found to this problem was to test an aero-elastic model for a rather similar configuration.

The buffeting on this aeroelastic model was readily detected by wire strain gauges (Ref 31), even though the tests were restricted to low equivalent airspeeds because of the danger of overloading and destroying a valuable aeroelastic model. (Most aeroelastic models are designed for flutter testing under zero lift conditions). The buffeting on the aeroelastic model was also predominantly in the second and third structural modes, confirming the results for the rigid models. This response is probably caused by the excitation being localized to a comparatively small area under the vortices, rather than being distributed across the span as for unswept and swept wings. The level of buffeting extrapolated to full scale from this model was estimated to be small but just measurable. This prediction has recently been confirmed in flight.

In flight most of the buffeting is in the second and third structural modes. At the low values of EAS at which the aircraft flies above the buffet boundary there is little aerodynamic damping in these modes so that we may reasonably assume constant damping. The wing-tip acceleration A will then vary with V^2 at a constant angle of attack. Hence the curve of

$$A/V^2 \text{ versus } \alpha$$

derived from the flight measurements at constant weight closely resembles that measured on the model (Fig 15) at constant kinetic pressure.

The level of buffeting has also been calculated by Mitchell (Ref 32), using as the excitation the pressure fluctuations measured at 14 points on the 1/30 scale model (Ref 27). Mitchell had to make rather sweeping assumptions about the correlations of the pressure fluctuations, and also to assume values of total damping appropriate to the motion, but he succeeded in predicting almost exactly the buffeting levels recently measured in flight.

Many readers will be disappointed that the correlation of the pressure fluctuations in these vortex flows has not been discussed. This primarily because there are so few correlation measurements available. The most complete set available to the author are those for a model of the BAC 221, a slender wing research aircraft. Figure 16 shows a typical example, with vortex breakdown about halfway between the apex of the wing and the trailing-edge (Ref 27). The contours of excitation have a maximum value underneath the point at which the vortex bursts. Using this point as reference we can then observe the correlation of the pressure fluctuations at the frequency selected. The clear impression given by all the contours of correlation is of a definite wave pattern. It is possible to show, by time delay techniques, that the contours are caused by the convection downstream of a fixed wave pattern associated with the vortex burst.

3.0 - EXPERIMENTAL METHODS

Although the onset of flow separations (the buffet boundary) can be predicted by a combination of boundary layer methods and potential flow theory, adequate theoretical methods are not yet available to predict the aerodynamic excitation after separation. Hence the prediction of the severity of aircraft buffeting will continue to depend on model tests in wind tunnels, and recent improvements in these tests are of considerable interest.

Three types of model tests to predict aircraft buffeting are discussed:

(1) Ordinary wind tunnel models used to measure the unsteady wing-root strain in the first bending mode,

(2) Ordinary wind tunnel models used to measure the unsteady pressure across the appropriate surface, and

(3) Aeroelastic models (ie models designed with representative stiffness and inertia) used to measure unsteady responses.

The importance of using wind tunnels with low levels of flow unsteadiness is emphasised. Alternative methods of determining buffet onset are discussed.

Buffet Onset

In Reference 33 Huston et al suggested a method for predicting the onset of buffeting and flight buffeting loads from measurements of unsteady wing-root strain made on ordinary wind tunnel models with unswept and swept wings. Thus buffeting tests could be made simultaneously with routine force measurements. The similarity relations suggested are shown in Figure 17.

The method assumes that the reduced frequencies of the wing fundamental mode are about the same for the model and the aircraft, ie

$$fc_{model}/fc_{aircraft} \simeq 1 \ .$$

In practice a variation in reduced frequency parameter from 0.7 to 1.6 seems to be acceptable, at least for measurements of buffet onset (Ref 29), probably because the buffet excitation spectra are always comparatively smooth (eg Figure 12, Curves B and C). The measurement of unsteady wing-root strain is generally accepted as the most consistent and reliable method of assessing buffet onset from model tests (References 29, 34 and 35) and many tunnel/flight comparisons of buffet onset are available (References 29 and 35). There is generally a fair correlation between the tunnel and flight buffet onset boundaries over an extreme range of wing planforms and thickness distributions. Tunnel results obtained by this method are usually somewhat pessimistic, particularly at subsonic speeds, but are extremely useful for project studies and comparative tests. Reference 36 includes numerous examples of such comparisons.

Some recent buffet onset measurements (Ref 37) on a large half model are of particular interest, because the model achieved full scale Reynolds numbers. On this 42° swept wing scale effects were small and Fig 18 shows an excellent comparison between the tunnel and flight buffet onset boundaries.

The improvements in wing buffeting caused by the postponement or alleviation of flow separations can sometimes be associated with changes in the mean forces and pressures on the wing, particularly for low angles of sweepback where the buffeting is generally heavy. (For moderate or highly swept wings this is a much more difficult process. The term "kinkology" has been applied for these methods of determining improvements in buffet. Reference 38 includes some interesting examples). Thus Figure 19 shows that the slats which delay heavy buffeting on the 35°swept wing (Ref 39) also improve $C_{L_{max}}$ from about 1.0 to 1.3. The slat also delays the divergence of the trailing-edge static pressure at a typical wing station ($2y/b = 0.50$).

When dynamic wing buffeting tests are made in wind tunnels with low levels of flow unsteadiness the onset of buffeting is normally well defined. However if the flow unsteadiness at the wing fundamental frequency exceeds the levels specified in Reference 40, interpretation of the wing-root strain measurements may be difficult, and incorrect answers can be obtained. When the wing-root strain measurements are ambiguous a critical assessment of the overall forces may identify buffet onset. The examples which follow represent a bad failure of the dynamic method in some early tests in an unsteady tunnel ($\sqrt{nF(n)} = 0.008$), and are not typical of what is readily achieved in a tunnel with low unsteadiness.

Figure 20 shows a comparison of the buffet onset boundary for a typical wing with low sweepback with two criteria for the onset of flow separations (Ref 29). The breaks in the C_D vs $C_L{}^2$ curves correspond quite well with the onset of flow separations derived from surface flow visualisation. This boundary also compares fairly well with the buffet boundary at subsonic speeds ($M < 0.80$) but at transonic speeds the buffet boundary is manifestly too high. In contrast the breaks in the C_L vs α curves occur at such a high C_L over the complete Mach number range that they give too high a level for buffet onset. This observation is in accordance with the experiments of Ray and Taylor on a large number of wings (Ref 34). On a three-dimensional wing the initial onset of separation and loss of lift on one area of the wing may be associated with a compensating increase in lift on another area of the wing, so that there may be no breaks in the C_L vs α curves at buffet onset. Although Bore has obtained some success with particular wings in using breaks in the C_L vs α curves to obtain buffet onset boundaries (Ref 41), this method is not generally recommended.

Figure 21 shows the same buffet boundary compared with the trailing-edge pressure divergence boundaries. We see that every spanwise position on the wing gives a different divergence boundary, but that the boundary for $2y/b = 0.82$ gives reasonably good agreement with the onset of flow separations at high subsonic and transonic speeds as Pearcey suggested (Ref 42). This station is recommended because many swept wings are designed so that the flow first separates at about $2y/b = 0.80$. Indeed at transonic speeds the combination of wing taper, leading-edge sweep and thickness distribution will often ensure the onset of flow separations in this area, unless flow separations can be deferred by modifications to the wing planform, the wing section or the wing twist distribution. For this wing the flow separations extend rapidly downstream from the leading-edge (at subsonic speeds) or from the terminal shock wave (at transonic speeds) and hence trailing-edge pressure divergence correlates reasonably well with buffet onset. The leading-edge separations on highly swept wings at transonic speeds generally extend rapidly to the trailing-edge so that trailing-edge pressure measurements can assist the interpretation of buffeting measurements on these wings (Ref 43). If the flow separations extend slowly downstream from the leading-edge, we have seen that trailing-edge pressure divergence will occur significantly later than buffet onset. (References 16 and 19).

Observation of the wing tip vortices can help to define the buffet onset boundary, if the initial flow separations are close to the wing tip. This technique has been rarely exploited, but during buffet tests in the RAE 3ft × 3ft tunnel (Ref 29) close agreement was obtained on several models between the angle of attack at buffet onset derived from measurements of unsteady wing-root strain and the angle of attack at which the cores of the wing tip vortices disappeared from the schlieren image. When the wing flow is attached, the boundary layer near the wing tip is concentrated into the core of the wing tip vortex, and is clearly visible in a schlieren system with a horizontal knife-edge. However, if there is a separation on the outboard wing section, the vortex core rapidly diffuses and it is difficult to distinguish on the schlieren system. The change between these types of flow is well defined on the schlieren but not very well reproduced on photographs. The critical angle of attack is repeatable to $\pm 1^\circ$ and small asymmetries between the onset of separation on port and starboard wings can be identified.

Severity of Buffeting

We must now return to the scaling of the buffeting loads from the model to the aircraft, which presents serious difficulties (Fig 17). Huston assumed that any differences between the mode shapes of the rigid model and the flexible aircraft would be insignificant and this is probably a fair assumption. He also assumed that it would be fairly easy to establish the total damping coefficient appropriate to the model and flight experiments but experience proves this hope is not well founded. Huston showed that for a given Mach number and angle of attack, if

$$\text{Wing-root strain} \propto \text{air density}$$

then the damping of the motion was predominantly structural and constant. Structural damping (generally denoted by g/2 % critical) seems to predominate on nearly all steel wind tunnel models (References 44 and 45) and remains constant from zero lift to heavy buffeting conditions. In contrast, if

$$\text{Wing-root strain} \propto (\text{air density})^{1/2}$$

Huston showed that the damping of the motion was predominantly aerodynamic. Huston suggested that this law would be followed in flight if the aerodynamic damping (generally denoted by γ % critical) was unaltered by the onset of flow separations. However until recently there were few reliable flight experiments, and no conclusive tests on aeroelastic models in wind tunnels to verify this law. The measurements of Jones (Ref 46) originally suggested that in flight at constant density and velocity, but with varying angle of attack, the basic assumption of a constant damping coefficient equal to the attached flow value was in error. Thus Figure 22(a) shows the variation of total apparent damping coefficient with normal force coefficient for a small fighter aircraft (Ref 46). At buffet onset the total apparent damping coefficient appeared to increase rapidly from its attached flow value, 3% critical, to 16% critical and then fall again to about 4% of critical in the region of moderate buffeting. No convincing explanation of this phenomena was given and it was not known whether this behaviour was peculiar to this aircraft, or typical of most swept wing aircraft. A recent reappraisal of the estimates by Butler and Jones (Ref 47) suggests that at buffet onset the total apparent damping increases because of modal interference at low amplitudes. In this situation, the simple single degree of freedom analysis is inappropriate and misleading estimates can be obtained. In contrast, at moderate buffeting the fundamental bending mode generally predominates and realistic values of total damping are again obtained. This hypothesis explains the surprising variation in the previous estimates (Ref 46), which have been widely quoted. Fig 22 includes new estimates based on the original and additional measurements using refined techniques (Ref 47). The total damping estimates now only vary a little with normal force coefficients. This hypothesis could explain previous variations in apparent damping observed in other flight and tunnel tests, which have been analysed in a similar fashion.

A similar variation of total damping with lift coefficient has been derived at least once before (Ref 48) during wind tunnel buffeting tests of a rigid model over a limited Mach number range from M = 0.93 to 1.00. Figure 22(b) shows that the structural damping of this model was low and the same for all configurations tested (g/2 = 0.4% of critical damping). For the clean wing the total damping of the fundamental mode remained about 2% from low lift until well beyond buffet onset, then increased slowly to about 3% and then decreased again. (This variation is rather larger than we would expect for a rigid model, although Wornom and Davies observed a variation from 3% to 1.5% which could be related with the lift on the model (Ref 44). In contrast, for the same wing structure and frequency, but with the aerodynamics altered by the addition of bodies and fences, the damping started at low lift coefficients at the same level as the clean wing (2%) but then increased rapidly to 6% at buffet onset (C_L = 0.7). The damping reached a maximum of 8.5% at C_L = 0.08 and then fell to about 4% at C_L = 0.9 to 1.0. The author of the original report thought that this change in damping was caused by the change in the flow produced by the wing modifications and not by any peculiar variation of structural damping. Figure 22(c) shows a similar variation of total damping for another improved configuration of the same wing at a Mach number of 0.98. Once again, a large increase in the total damping seems to occur before buffet onset. If variations of damping coefficient of this kind are going to occur in flight or tunnel experiments it will be impossible to utilize the simple relations for the severity of buffeting previously suggested (Fig 17).

Recently, Jones showed (Ref 49) that the non-dimensional aerodynamic excitation parameter appropriate to a flexible mode of vibration could be derived from measurements of buffeting response and total damping ratio. Subsequently this non-dimensional buffet excitation parameter in the first wing bending mode was derived from measurements made on wings of different materials, to give variations in response and damping, but under nominally identical free stream conditions (Ref 50). To test the scaling relationships implicit in the use of this non-dimensional buffet excitation parameter the flow required to excite the wing buffeting had to be relatively unaffected by a wide variation in Reynolds number and preferably unaltered in general character by a Mach number variation from subsonic to supersonic speeds. These conditions were satisfied by the choice of a slender wing with a well-ordered vortex flow (Ref 9), and accordingly a half-model of a delta wing, with a sharp leading-edge swept back 65°, was used. On this simple configuration a variation in the relative proportions of aerodynamic and structural damping at constant Reynolds number was obtained by testing two nominally identical wings, one of mild steel, and the other of magnesium alloy. These materials were selected because they had the same ratio of Young's modulus E, to density ρ_m. (Aluminium alloy also has the same value of E/ρ_m as steel and magnesium). Hence their natural frequencies were virtually identical and their mode shapes similar. Both wings could be tested over a wide range of free stream air density, ρ, at constant Mach number, giving the same values of the ratio ρ/ρ_m for different combinations of ρ and ρ_m.

The idea of using geometrically similar models of steel and magnesium was suggested by a previous buffeting investigation (Ref 51). However the results of that investigation were inconclusive, possibly because the aerodynamic characteristics of the wing planform and section selected were sensitive to changes in Mach number and Reynolds number. (In that investigation the kinetic pressure q was varied by changing the Mach number at constant tunnel total pressure, and no tests were included at constant Mach number over a range of Reynolds number).

The results of the present investigation on the 65° delta wing configuration show that on the steel wing small variations in total damping ratio with free stream density can be detected. On the magnesium wing significantly larger variations in total damping ratio with free stream density are observed (Fig 23). When the total damping ratios are combined with the responses (given by the wing-root strain) a measure of the buffet excitation (or forcing function) is derived, and this is almost the same for both wings and independent of Reynolds number (Fig 24). The measurements extend well into the vortex breakdown region, and thus represents a useful extension of our knowledge of slender wing buffeting. (Earlier measurements of slender wing buffeting were limited by a load restriction on the aeroelastic model (Ref 31). Fig 24 also includes the buffet excitation parameter measured by Butler and Spavins[37] on a typical fighter aircraft.

The wider implication of these tests is that it should be possible always to predict the buffet forcing function from tests of ordinary wind-tunnel models, as long as the total damping ratio is derived accurately. (Aluminium alloy also has the same value of E/ρ_m as steel and magnesium). However if predictions for buffeting in flight are required, the total damping ratio measured during the model tests must be separated into the aerodynamic and structural components. This condition is somewhat restrictive, and implies that a wide free stream density variation (say 2/1) should be included for several Mach numbers of the model test programme.

Alternatively we may by-pass the uncertainties associated with the damping in flight and use the buffeting measurements on rigid wind tunnel models with constant damping to derive dimensionless buffeting coefficients which can then be compared directly with the buffet penetration achieved in flight (Ref 30) on aircraft for which we do not know the damping coefficients. Many assumptions are implicit in this method, but it works reasonably well. The basic hypothesis is that the tunnel unsteadiness (which must be known) can be used as a given level of aerodynamic excitation to calibrate the model response at the wing fundamental frequency, and hence to derive buffeting coefficients from the buffeting measurements. These buffeting coefficients are a measure of the generalised force in the wing fundamental mode due to any distribution of pressure fluctuations on the wing. Past experience with nine aircraft models suggests that levels of buffeting coefficient obtained in this way can be identified appropriate to the maximum flight penetration of buffeting for both transport and fighter type aircraft. The method is illustrated by a typical example (Ref 29), (the same model as discussed in Figures 20 and 21).

Figure 25 shows the curve of unsteady wing-root strain signal at the wing fundamental frequency, f_1, plotted against angle of attack. If these signals are divided by the appropriate kinetic pressure $q = \frac{1}{2}\rho V^2$, we have, if the flow is insensitive to changes in Reynolds number.

$$\text{Wing-root strain signal}/q = C_B(M, \alpha) \qquad (2)$$

where $C_B(M, \alpha)$ is a dimensional function of Mach number M and is independent of q at a given M and angle of attack, if the total damping of the wing fundamental mode is constant (Ref 45). Before the onset of flow separations on the model, most of the curves in Reference 29 and numerous tests in other wind tunnels (Ref 34) show that $C_B(M, \alpha)$ is constant and equal to $C_B(M, \alpha = 0)$. This is the portion of the model response caused by the tunnel unsteadiness $\sqrt{nF(n)}$ at the appropriate Mach number and the same frequency f_1. We now scale all the measurements so that the level $C_B'(M, \alpha = 0)$ represents the tunnel unsteadiness and the model response to that unsteadiness. Thus

$$C_B'(M, \alpha = 0) = \sqrt{nF(n)} = 1/K \cdot C_B(M, \alpha = 0) \qquad (3)$$

where K is a constant scaling factor. The subsequent increase in $C_B'(M, \alpha)$ as the angle of attack increases gives a measure of the integrated pressure fluctuations arising from the wing buffet pressures and of the model response to this excitation. Having used the tunnel unsteadiness $\sqrt{nF(n)}$ to establish a datum buffeting scale, this signal must now be subtracted to give the true buffeting level in the absence of tunnel unsteadiness. If the tunnel unsteadiness does not exceed the criteria in Reference 40 there should be no correlation between the tunnel unsteadiness and the wing buffeting and so we can calculate a corrected buffeting coefficient

$$C_B''(M, \alpha) = \sqrt{C_B'(M, \alpha)^2 - C_B'(M, \alpha = 0)^2}. \qquad (4)$$

The angle of attack at which $C_B''(M, \alpha)$ first differs from zero is buffet onset. Contours of buffeting coefficients are then readily obtained as a function of Mach number and angle of attack or lift coefficient. For the seven fighter aircraft models heavy buffeting corresponds with

$$C_B'' = 0.012 \text{ to } 0.016$$

For fighter aircraft there is considerable scatter from the flight buffet onset boundary to the $C_B'' = 0.004$ contour. Hence for fighter aircraft the following buffeting criteria are suggested:

Buffet onset	$C_B'' = 0$
Light buffeting	$C_B'' = 0.004$
Moderate buffeting	$C_B'' = 0.008$
Heavy buffeting	$C_B'' = 0.016$.

For the two transport aircraft models the buffeting limit corresponds with $C_B'' = 0.006$.

Figure 26 illustrates a test of this hypothesis for a fighter aircraft. The model was similar to the one considered in Figure 25 but the tunnel unsteadiness was much lower ($\sqrt{nF(n)} = 0.002$) and the Reynolds number much higher ($R \simeq 4 \times 10^6$). Buffet onset in the new flight tests (carefully derived from wing-tip accelerometers) agrees well with the light buffeting contour

$$C_B'' = 0.004$$

and the maximum flight penetration corresponds with the heavy buffeting contour

$$C_B'' = 0.016 .$$

Figure 27 shows sketches based on typical oil flow photographs taken on this model at Mach numbers of 0.70 and 0.90 at the light, moderate and heavy buffeting levels, and we note the progressive development of the areas of separated flow as the buffeting coefficient increases.

The correlations established between buffeting contours and maximum flight penetration are somewhat surprising because it might reasonably be expected that the severity of buffeting in flight would be based on the dimensional level of vibration (either estimated by the pilot or measured by an accelerometer), rather than a dimensionless buffeting coefficient. There are two alternative explanations for the correlations established. Either

(1) the severity of wing buffeting is not really the limiting factor so that pilots of fighter or strike aircraft tend to fly right up to a handling boundary, such as pitch-up, stalling or wing dropping. This handling boundary might coincide with the heavy buffeting contour. Or

(2) the pilot may instinctively include in his assessment of buffeting a 'q' factor, as he tends to do in the application of steady loads to the aircraft.

If he does introduce a 'q' factor, pilot-defined boundaries for light, moderate and heavy buffeting at constant altitude would tend to be uniformly spaced above the buffet onset boundary where Mach number effects are small, and would correspond with constant values of pressure-fluctuation coefficients measured in the tunnel and hence of buffeting coefficients, C_B' (see Figure 14 in Reference 16 for the Venom aircraft with a sharp leading-edge).

The pilots of transport aircraft generally sit further from the nodal points of the wing fundamental mode than do pilots of fighter or strike aircraft and would not wish to approach a handling boundary, even if sufficient thrust were available. Thus for transport aircraft the maximum penetration coefficient $C_B' = 0.006$ seems more reasonable than the value of 0.016 for fighter aircraft. This limit for maximum flight buffet penetration for transport aircraft of $C_B' = 0.006$ is based on measurements for only two models at low Reynolds numbers and may need to be revised as additional tunnel/flight comparisons become available for this class of aircraft.

The heavy buffeting contour can be given a general physical significance because the buffeting coefficient ought to be of the same magnitude as the fluctuating normal force coefficient if the flow over most of the wing is separated and the excitation is well correlated across the wing. The measurements of Polentz on aerofoils (Ref 52) show a maximum normal force coefficient at low frequencies of about 0.010 to 0.020 which brackets the heavy buffeting contour of 0.016. Similarly Figure 13 shows that the maximum fluctuating normal force coefficient at a particular low frequency parameter $n = 0.05$ for a family of slender wings varies from about $\sqrt{nG(n)} = 0.008$ to 0.010 for $\Lambda = 45^{\circ}$ to $\sqrt{nG(n)} = 0.014$ to 0.019 for $\Lambda = 70^{\circ}$. These high values of normal force coefficient are obtained when vortex breakdown occurs on the wings irrespective of the details of the vortex flow (Ref 26).

Aircraft such as the Harrier, in which the spanwise development of flow separations is carefully controlled, achieve appreciably higher heavy buffeting coefficients than previous aircraft. This fact could have important implications for the structural loading of such aircraft (Ref 53, Section 3.1.3).

One application of this method utilized buffeting measurements made by Hanson on an aeroelastic model of a variable geometry fighter aircraft; the original report repays careful study (Ref 54). The aeroelastic model was tested in Freon 12 in the NASA Langley Transonic Dynamics Tunnel. The model was flown on wires and achieved an almost exact duplication of the aircraft modes and dampings for the different wing sweep angles. As expected, the response measured by the wing-root strain bridge was predominantly in the wing fundamental mode, at about 16 Hz model scale (Figure 8a of Reference 54), and the damping was predominantly aerodynamic. (The advantage of using correctly scaled aeroelastic models for buffeting tests is that the response in modes other than the wing fundamental bending can be measured accurately. Thus in Hanson's tests the tail response and fuselage vertical bending were measured. Hence the buffet excitation parameter (Refs 49 and 50) can also be derived for these widely differing modes).

Figure 28 shows the buffeting coefficients C_B' derived from these wing-root strain measurements and the tunnel flow unsteadiness level (Figure 1b of Reference 54). Different transformation factors, K, are required for the port and starboard wings, and for every Mach number, because the damping of the fundamental mode is predominantly aerodynamic and varies with kinetic pressure q. These values of K reduce the buffeting measurements to single, well defined curves of C_B' vs C_N. The angles of attack selected for the onset, light and moderate buffeting contours correspond with $C_B' = 0$, 0.004 and 0.008 respectively, as derived from tests on ordinary sting-supported wind tunnel models tested in air.

Figure 29 shows a comparison of the buffeting contours derived from the model tests and the buffet onset and maximum penetration achieved in flight. In the tunnel tests the maximum penetration was not limited by wing buffeting, but instead either by a limiting tail deflection (the aeroelastic model must fly trimmed) or by a roll instability which the "pilot" could not control. Similarly in flight no manoeuvres were aborted due to the severity of buffeting, but only due to the attainment of the "g" and "α" limits mentioned in the report. For $\Lambda = 26^{\circ}$ and 50° the flight buffet onset boundary agrees fairly well with the buffet onset contour $C_B' = 0$ derived from the tunnel tests. For $\Lambda = 70^{\circ}$ the flight buffet onset boundary is between the buffet onset contour $C_B' = 0$ and the light buffeting contour $C_B' = 0.004$. Above buffet onset the flight and tunnel contours look similar and support the broad conclusion that maximum flight penetration would have corresponded fairly well with the heavy buffeting contour $C_B' = 0.016$, if this could have been achieved on the aeroelastic model. Even with the severe restrictions applied to the aeroelastic model by the tail deflection and the roll instability, maximum levels of $C_B' = 0.010$ and 0.013 were achieved for $\Lambda = 26^{\circ}$ and 70° respectively.

These results from an aeroelastic model flown on wires may reasonably be viewed as a severe, and yet fairly satisfactory, test of the hypothesis originally advanced in Reference 30 on the basis of tests on ordinary wind tunnel models supported by stings. It should be noted that buffeting tests on an ordinary sting-supported model of the aircraft would not have been limited by tail loads or a roll instability, and could probably have been made at higher Reynolds numbers. (The test Reynolds numbers quoted on page 10 of Reference 54 are in fact Reynolds numbers/ft so that the model Reynolds numbers are comparatively low, although this did not spoil the buffeting measurements).

It is interesting to note that in both the flight and tunnel tests reported in Reference 54 rapid increases in angle of attack excited less severe buffeting than slow increases in angle of attack. This effect has been noticed previously in flight tests of other combat aircraft. Although part of the delay can be attributed to the finite time taken by the structure to respond to the aerodynamic excitation (as discussed by Zbrozek and Jones in Reference 5), there is some evidence that there may well be, in addition, a transient effect on the development of the flow separations, if the rate of change of the angle of attack is high.

Buffeting measurements have also been made on a model of composite construction which represents the static bending and torsional stiffnesses of an aircraft project, but not the inertia distribution (Ref 55). Although this composite model was not a full aeroelastic model, having unrepresentative frequency parameters, it was more representative of the aircraft than the solid aluminium model tested for comparison. The composite model provided useful advance warning of a "torsional buzz" phenomenon subsequently observed in flight, which lies in the "no mans-land" between buffeting and flutter, and which did not occur on the solid model. There is still some doubt as to precisely how the pressure fluctuations on the wing couple with the torsional vibration, which is only observed with a leading-edge sweep angle of 27.2° in a small region about a Mach number of about 0.70 and an incidence of 9° (Ref 55, Fig 17). In some unpublished tests on an ordinary, steel wind tunnel model with almost the same geometry a large discrete excitation was observed in the same region at the same frequency parameter, although there was no structural mode on the model at that frequency.

Recent research on ordinary wind tunnel models has confirmed that in general the wing bending does not influence the measured oscillatory pressures when the flow is separated. (This may be seen directly from Figs 16 to 19 of Ref 56 or inferred from the buffeting measurements of Ref 50). The unsteady pressures measured on ordinary wind tunnel models provide a useful indication of any unusual discrete excitation in the spectrum (as occurs with the circular cylinder). These pressures may, in principle, be integrated to give the total excitation (Ref 57). However the aircraft response can only be calculated with some additional assumption about the total damping in the mode. Hence most future predictions of the severity of buffeting will continue to be made from accelerometer or wing-root strain measurements, using either the buffet excitation parameter (Ref 49) or buffeting coefficients (Ref 30).

Alleviation of Buffeting

The measurement of unsteady wing-root bending moments has been widely used for comparative tests to assess the alterations in wing buffeting produced by changes in wing design. Figure 30 shows three typical examples. The first part shows how the addition of a slat to the leading-edge of a 35° swept wing of constant chord delays the build up of buffeting to much higher wing angles of attack (Ref 39). Measurements are only given for a Mach number of 0.65 because it is difficult to design a leading-edge profile which gives a satisfactory compromise over a wide speed range from $M = 0.50$ to 0.90. Hence a variable geometry leading-edge, as proposed in the "RAEVAM" principle, may yet be used to optimize wing buffeting characteristics. The second part shows how the addition of a slat to a 1/20 scale model of the Phantom aircraft raised the buffet onset boundary; a somewhat smaller improvement was obtained in flight (Ref 35) (Fig 21). The third part shows how the buffet onset boundary of a wing with its quarter chord line swept 45° was improved (Ref 48). The addition of carefully streamlined bodies to retard the downstream movement of the terminal shock raised the lift coefficient for buffet onset by about 0.2 for Mach numbers of 0.6 to 0.8 and by about 0.40 at a Mach number of 0.90. The addition of small boundary layer fences to the noses of these bodies produced a further increase in buffet onset lift coefficient of about 0.2 at subsonic speeds (where there were probably shock and/or vortex type separations close to the leading-edge) but no further increase at $M = 0.90$ (where the separation were probably shock-induced further downstream on the wing).

An interesting flight investigation on the F-104 aircraft of the alleviation of buffeting achieved by the deflection of leading-edge and trailing-edge flaps is described in Reference 58.

4.0 CONCLUSIONS

The main themes relate to Figure 4, and can be reiterated as follows: (1) For bubble flows, which occur in many different situations, the largest excitation is found just upstream of the reattachment point; (2) For slender wings with sharp leading-edges the buffeting is light, but just measurable, exactly as predicted from wind tunnel tests 8 to 10 years in advance of flight; and (3) For swept wings the complex nature of the flows and wing performance assessment are best examined by buffeting measurements on rigid models, despite their limitations. In the future these buffeting measurements will be supplemented by extensive measurements of the excitation of the type presented in Reference 59 (which should be read in conjunction with Reference 35).

For older aircraft with swept wings we frequently find significant differences between wind tunnel predictions and flight measurements of the buffet onset boundary. Figure 31 shows a typical example (Ref 35). There are large differences between the buffet onset boundaries for the clean wing and the wing with slats at subsonic speeds, but only relatively small errors at transonic speeds. In contrast there is now evidence (References 60 and 61) from modern aircraft with swept wings that our simulation is in error even at transonic speeds. Our inability to produce the correct flows is probably due to our failure to reproduce sufficiently high Reynolds numbers. Hence if we are to guarantee the buffeting limits of future aircraft with advanced wing designs (not merely buffet onset but also maximum penetration), new high Reynolds number facilities, suitable for buffeting tests, will have to be provided. Buffeting tests will place constraints on these facilities in terms of levels of flow unsteadiness (Ref 40) and in terms of running times.

If ground based high Reynolds number facilities suitable for buffeting tests are provided, the aerodynamicist will no longer be able to attribute discrepancies between tunnel predictions and flight performance to the inadequate simulation of Reynolds number. We shall then see a demand for far more searching flight tests in order to establish if the separations obtained in the wind tunnel are being duplicated in flight. The experiments of Jones (Ref 46) and Hollingsworth (Ref 35) may be cited as typical of the most detailed research of this type so far achieved in flight, but even these tests were not sufficiently detailed. They revealed differences between the developments of the separations on the model and in flight, but not the origin of these differences, or how the differences could be removed. If we are to explain these differences we shall have to measure the static pressure distributions over the wings, the development of the boundary layer upstream of separation and downstream of reattachment, as well as the fluctuating pressures and the wing response.

These flight experiments will be difficult and might even justify the allocation of special aircraft. A few really detailed comparisons of the separated flows obtained on wind tunnel models and on aircraft will probably make the most significant single contribution to the achievement of safe flight beyond the buffet boundary, and to our understanding of the relevant problems of Fluid Mechanics.

APPENDIX - THE FUTURE OF BUFFETING RESEARCH

Although we may be able to predict the buffet onset boundary, boundary-layer theory is generally invalid beyond separation. Hence above the buffet boundary we shall still have to rely on model tests in wind tunnels for the prediction of steady and fluctuating pressures. Some deficiencies are already apparent in the simulation for existing aircraft in our present transonic tunnels (Ref 60). These deficiencies may be more serious with advanced wing designs, unless the Reynolds number available can be increased (Ref 61).

The buffeting coefficients selected from tests on conventional models in type A flow situations, at low Reynolds number (1×10^6 to 4×10^6) as appropriate for maximum penetration in flight, may well include a scale effect on the development of the separations (Ref 62). With advanced wing designs, in type B flow situations, the character of the scale effects may be different from those on conventional wings, requiring different buffeting coefficients from those previously established. This justifies the inclusion of comparative buffeting tests on advanced and conventional wing designs over a wide range of Reynolds numbers.

Rigid models will be used exclusively for buffeting tests in these new facilities, because of the difficulty of constructing sufficiently strong aeroelastic models for prolonged tests under lifting conditions. Even with rigid models static aeroelastic distortion may require the model wing to differ from the aircraft shape by up to 0.4° twist (Ref 63). At present buffeting tests of aeroelastic models of swept wings under lifting conditions are confined almost exclusively to the NASA Langley Transonic Dynamics Tunnel (with a working section of 16ft × 16ft) which can be operated with air or Freon 12. Although operation with Freon 12 allows the aerodynamic damping to be more readily simulated, there is some evidence that its inadequate simulation of the specific heat ratio may produce incorrect data at high lift at transonic speeds (Ref 64). However, one buffeting test in this tunnel, using Freon 12, has given a good prediction for the wing-root strain on a dynamic model of a variable geometry aircraft (Ref 54).

Kilgore et al have shown that the problems caused by static aeroelastic distortion should be less severe in cryogenic transonic tunnels (Ref 65). In cryogenic tunnels the kinetic pressure may be held constant while the Reynolds number is increased at constant Mach number by reducing the free stream static temperature. This appears an attractive concept for obtaining high Reynolds numbers at transonic speeds.

The use of sound absorbing walls in the working section of wind tunnels can significantly reduce dynamic interference on models (Ref 66). This concept is advantageous for buffeting measurements, as shown by comparative tests (Ref 67) in a modified, temporary, working section for the RAE 3ft × 3ft tunnel. Fig 32 shows that buffet onset is more clearly defined with the sound absorbing walls than with the hard walls used in conventional working sections. This effect is relatively small in the closed working sections (Fig 32a), both of which have a low level of flow unsteadiness. However, the effect is large in the slotted working sections (Fig 32b) because the slotted working section with hard walls has a much higher level of flow unsteadiness. This concept may well be exploited in the design of the working sections in the new generation of transonic tunnels.

REFERENCES

1 - *Technical Report on the Accidents Investigation Sub-Committee on the Accident to the Aeroplane G-AAZK at Meopham, Kent on 21 July 1930.* RM 1360, January 1931.

2 Blenk, H. *Ueber neuere englische Arbeiten zur Frage des Leitwerkschüttelns* ZEM 24, 1933, 21-24, also English translation NACA TM 669.

3 Owen, T.B. *Techniques of Pressure Fluctuation Measurements Employed in the RAE Low Speed Wind Tunnels,* AGARD Report 172, 1958.

4 Mabey, D.G.; Moss, G. RAE unpublished.

5 Zbrozek, J.K.; Jones, J.G. *Transient Buffet Loads on Wings,* Journal of Sound and Vibration, Vol.5, No.2, pp.197-214, 1967.

6 Rogers, E.W.E.; Hall, I.M. *An Introduction to the Flow about Plane Swept-Back Wings at Transonic Speeds.* Journal of Royal Aeronautical Society, Vol.64, pp.449-464, 1960.

7 Green, J.E. *Some Aspects of Viscous-Inviscid Interactions at Transonic Speeds, and their Dependence on Reynolds Number,* AGARD CP 83, 1971.

8 Blackwell, J.A. *Preliminary Study of the Effects of Reynolds Number and Boundary Layer Transition Location on Shock Induced Separation,* NASA TN D 5003, 1969.

9 Küchemann, D; Weber, J. *An Analysis of Some Performance Aspects of Various Types of Aircraft Designed to Fly over Different Ranges at Different Speeds.*

10 Mabey, D.G. *Analysis and Correlation of Data on Pressure Fluctuations in Separated Flow.* AIAA Journal, August/September 1972.

11 Norbury, J.F.; Crabtree, L.F. *A Simplified Model of the Incompressible Flow past Two-Dimensional Aerofoils with a Long Bubble Type of Separation,* RAE TN Aero 2352, June 1955.

12 Bradshaw, P. *'Inactive' Motion and Pressure Fluctuations in Turbulent Boundary Layers,* NPL Aero Report 1172, October 1965, (Also published as ARC 27338).

13 Lilley, G.M. *On Wall Pressure Fluctuations in Turbulent Boundary Layers,* ARC 24241, November 1962.

14 Bradshaw, P.; Wong, F.Y.G. *The Reattachment and Relaxation of a Turbulent Shear Layer.* Journal of Fluid Mechanics Vol.52, part p 1, pp 113-135, 1972.

15 Lawford, J.A,; Beauchamp, A.R. *Low Speed Wind Tunnel Measurements of Pressure Fluctuations on the Wing of a Twin Jet Aircraft (Bristol 188),* ARC R&M 3551, 1968.

16 Rose, R.; Nicholas, O.P. *Flight and Tunnel Measurements of Pressure Flvctuations on the Upper Surface of the Wing of a Venom Aircraft with a Sharp Leading-Edge.* ARC CP 1032, November 1967.

17 Heller, H.H.; Bliss, D.B.; Widnall, S.E. *Incipient Stall Detection through Unsteady-Pressure Monitoring on Aircraft Wings,* Journal of Aircraft, Vol.9, No.2, pp.186-188, February 1972.

18 Crabtree, L.F. *The Formation of Regions of Separated Flow on Wing Surfaces, Pt II Laminar Separation Bubbles and the Mechanism of the Leading-edge Stall,* RAE Report Aero 2578, July 1957, also in Pt 2 of ARC R&M 3122, 1959.

19 Jenkins, J.M. et al *Flight Measurements of Canard Loads, Canard Buffeting and Wing Tip Hinge Moments on the XB70 Aircraft Including Comparisons with Predictions.* NASA TN D5359, August 1969.

20 Fricke, F.R.; Stevenson, D.C. *Pressure Fluctuations in a Separated Flow Region.* Journal of the Acoustical Society of America, Vol.44, No.5, pp 1189-1201, November 1968.

21 Greshilov, E.M.; Evutshenko, A.V.; Lyamshev, L.M. *Spectral Characteristics of the Wall Pressure Fluctuations Associated with Boundary Layer Separation Behind a Projection on a Smooth Wall,* Soviet Physics - Acoustics. Vol.15, No.1, pp 29-34, July-September 1969.

22	Coe, C.F.	*The Effects of Some Variations in Launch Vehicle Nose Shape on Steady and Fluctuating Pressures at Transonic Speeds.* NASA TM X646, March 1962.
23	Mabey, D.G.	*Some Measurements of Base Pressure Fluctuations at Subsonic and Supersonic Speeds.* RAE TR 70 148, August 1970, (also published as ARC CP 1204, 1972).
24	Mohsen, A.M.	*Experimental Investigation of the Wall Pressure Fluctuations in Subsonic Separated Flows.* Boeing Co. Report D6-17094, AD669214, January 1967.
25	Moss, G.F. Mundell, A.R.G.	RAE - unpublished.
26	Earnshaw, P.B. Lawford, J.A.	*Low Speed Wind Tunnel Experiments on a Series of Sharp-Edge Delta Wings.* R&M 3424, August 1964.
27	Keating, R.F.A.	RAE - unpublished.
28	Dee, F.W. Nicholas, O.P.	*Flight Determination of Wing Flow Patterns and Buffet Boundaries for the Fairey Delta Aircraft at Mach Numbers between 0.4 and 1.3 and Comparison with Wind Tunnel Tests.* R&M 3482, 1964.
29	Mabey, D.G.	*Comparison of Seven Wing Buffet Boundaries Measured in Wind Tunnels and In Flight.* ARC CP 840.
30	Mabey, D.G.	*An Hypothesis for the Prediction of Flight Penetration of Wing Buffeting from Dynamic Tests on Wind Tunnel Models.* ARC CP 1171, 1971.
31	Mabey, D.G.	*Measurements of Buffeting on Slender Wing Models.* ARC CP No.954, 1967.
32	Mitchell, C.G.B.	*Calculations on the Buffeting on a Slender Wing Aircraft at Low Speeds.* Proceedings of the Symposium on Structural Dynamics, Loughborough University, March 1970.
33	Huston, W.B.	*A Study of the Correlation between Flight and Wind Tunnel Buffet Loads.* AGARD Report 121, April 1957. (Also published as ARC 20704).
34	Ray, E.G. Taylor, R.T.	*Buffet and Static Aerodynamic Characteristics of a Systematic Series of Wings Determined from a Subsonic Wind Tunnel Study.* NASA TN D 5805, 1970.
35	Hollingsworth, E.G. Cohen, M.	*Comparison of Wind Tunnel and Flight Test Techniques for Determining Transonic Buffet Characteristics on the McDonnell Douglas F-4 Airplane.* AIAA Paper No.70-584. 1970.
36	Anon	*The Effects of Buffeting and other Transonic Phenomena on Manoeuvring Combat Aircraft.* AGARD AR-82, July 1975.
37	Butler, G.F. Spavins, G.	*Preliminary Investigation of a Technique for Predicting Buffet Loads in Flight from Wind-Tunnel Measurements on Models of Conventional Construction.* AGARD CP 204.
38	John, H.	*Critical Review of Methods to Predict the Buffet Capability of Aircraft.* AGARD Report R623, September 1974.
39	Moss, G.F. Haines, A.R. Jordan, R.	*The Effect of Leading-Edge Geometry on High Speed Stalling.* AGARD CP 102, November 1972. (Also published as RAE TR 72099).
40	Mabey, D.G.	*Flow Unsteadiness and Model Vibration in Wind Tunnels at Subsonic and Transonic Speeds.* ARC CP 1155, 1971.
41	Bore, C.L.	*Post Stall Aerodynamics of the "Harrier" GRI.* AGARD CP 102, November 1972.
42	Pearcey, H.H.	*Simple Methods for the Prediction of Wing Buffeting Results from Bubble Type Separations.* NPL Aero Report 1024, June 1962.
43	Mayes, J.F. Lores, M.E. Barnard, H.R.	*Transonic Buffet Characteristics of a 60 Degree Swept Wing with Design Variation.* AIAA Paper 69-793 (1969) also Journal Aircraft I, pp 523-530 (1970).
44	Davis, D.D. Wornom, D.E.	*Buffet Tests of an Attack Airplane Model with Emphasis on Data from Wind Tunnel Tests.* NACA RML57 H13, February 1958.
45	Mabey, D.G.	*Measurements of Wing Buffeting on a Scimitar Model.* ARC CP 954, 1966.

46 Jones, J.G. *The Dynamic Analysis of Buffeting and Related Phenomena.* AGARD CP 102, November 1972.

47 Butler, G.F.; Jones, J.G. RAE - unpublished. Note in preparation.

48 Cornette, E.S. *Wind Tunnel Investigation of the Effects of Wing Bodies, Fences, Flaps and Fuselage Addition on Wing Buffet Response of a Transonic Transport Model.* NASA TN D 637.

49 Jones, J.G. *Aircraft Dynamic Response Associated with Fluctuating Flow Fields.* AGARD Lecture Series 74, Aircraft Stalling and Buffeting, February 1975.

50 Mabey, D.G.; Butler, G.F. *Measurements of Buffeting on Two 65° Delta Wings of Different Materials*, RAE TR 76-009, also AGARD Paper 6, Symposium on Air Frame Response to Transonic Flow, April 1977.

51 Rainey, A.G.; Byrdsong, T.A. *An Examination of Buffeting Analysis based on Experiments with Wings of Varying Stiffness.* NASA TN D 3 (1959).

52 Polentz, P.P.; Page, W.A.; Levy, L.L. *The Unsteady Normal Force Characteristics of Selected NACA Profiles at High Subsonic Mach Numbers.* NACA RM A 55 002, May 1955.

53 Stapleton, S.F.; Pegram, B.V. *Comments on some Wind Tunnel and Flight Experience of the Post-Buffet Behaviour of the Harrier Aircraft.* Paper 20A1, AGARD CP-187, April 1976.

54 Hanson, P.W. *Evaluation of an Aeroelastic Model Technique for Predicting Aircraft Buffeting Loads.* NASA TN D 7066, February 1973.

55 Moss, G.F.; Pierce, D. *The Dynamic Response of Wings in Torsion at High Subsonic Speeds.* Paper 4, AGARD Symposium on Airframe Response to Unsteady Flow, April 1977.

56 Coe, C.F.; Riddle, D.W.; Hwang, C. *Separated Flow Unsteady Pressures and Forces on Elastically Responding Structures.* Paper I, AGARD Symposium on Airframe Response to Unsteady Flow, April 1977.

57 Becker, J.; Dau, K. *Evaluation of Vibration Levels at the Pilot Seat Caused by Wing Flow Separation.* Paper 5 AGARD Symposium on Airframe Response to Separated Flow, April 1977.

58 Friend, E.L.; Sefic, W.V. *Flight Measurements of Buffet Characteristics of the F-104 Airplane for Selected Wing-Flap Deflections.* NASA TN D 6943, August 1972.

59 Lemley, C.E.; Mullans, R.E. *Buffeting Pressures on a Swept Wing in Transonic Flight - Comparison of Model and Full-Scale Measurements.* AIAA Paper 73-311, March 1973.

60 Cahill, J.F. *Simulation of Full Scale Flight Aerodynamic Characteristics by Tests in Existing Transonic Wind Tunnels.* AGARD CP 83-71.

61 Haines, A.B. *Possibilities for Scale Effect on Swept Wings at High Subsonic Speeds: Recent Evidence from Pressure Plotting Tests.* Paper 14 AGARD CP 83, 1971.

62 Pearcey, H.H.; Osborne, J.; Haines, A.B. *Interaction Between Local Effects at the Shock and Rear Separations - a Source of Significant Scale Effects in Wind Tunnel Tests on Aerofoils and Wings.* NPL Aero 1071 (ARC 30477) September 1968.

63 Evans, J.Y.G.; Taylor, C.R. *Some Factors Relevant to the Simulation of Full Scale Flows in Model Tests and to the Specification of New High Reynolds Number Transonic Tunnels.* AGARD CP 83, 1971.

64 Treon, S.L.; Hofstetler, W.R.; Abbott, F.T. *On the Use of Freon-12 for Increasing Reynolds Number in Wind Tunnel Testing of Three-Dimensional Aircraft Models at Subcritical and Supercritical Mach Numbers.* AGARD CP 83, 1971.

65 Kilgore, R.A.; Adcock, J.B.; Ray, E.J. *Flight Simulation Characteristics of the Langley High Reynolds Number Cryogenic Transonic Tunnel.* AIAA Paper 74-80, February 1974.

66 Mabey, D.G. *The Use of Sound Absorbing Walls to Reduce Dynamic Interference in Wind Tunnels.* RAE TR 76-157, November 1976.

67 Mabey, D.G. *The Reduction of Dynamic Interference by Sound Absorbing Walls in the RAE 3ft Tunnel.* RAE TR 77-120, August 1977.

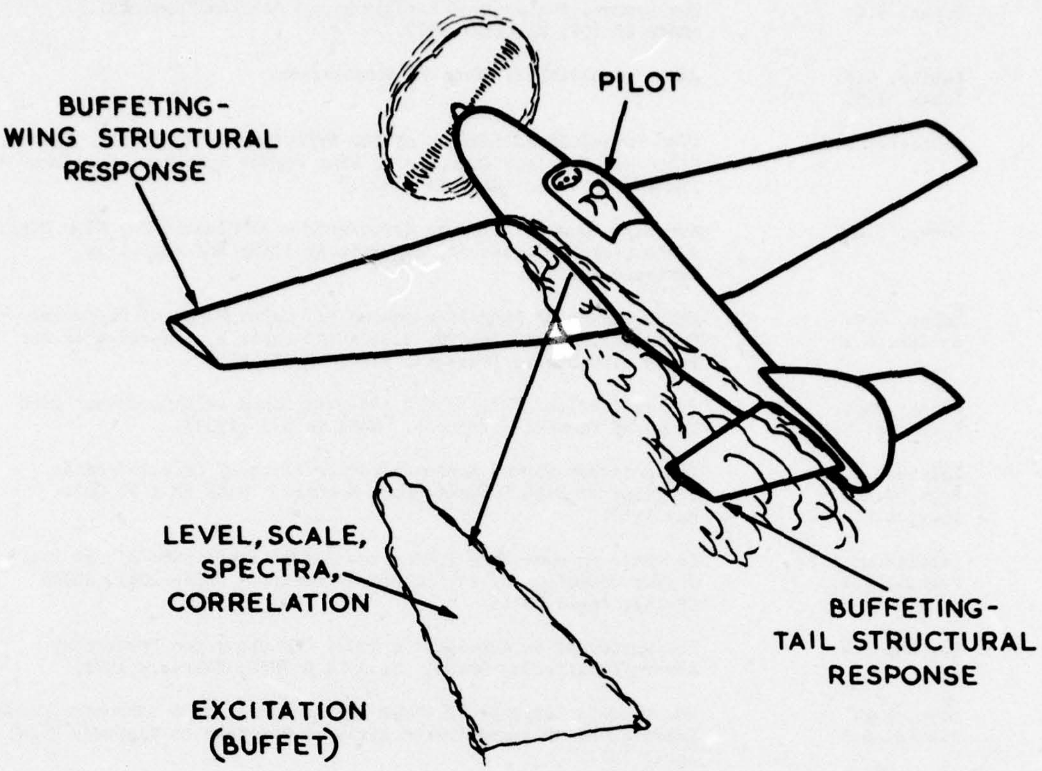

Fig.1 Buffeting

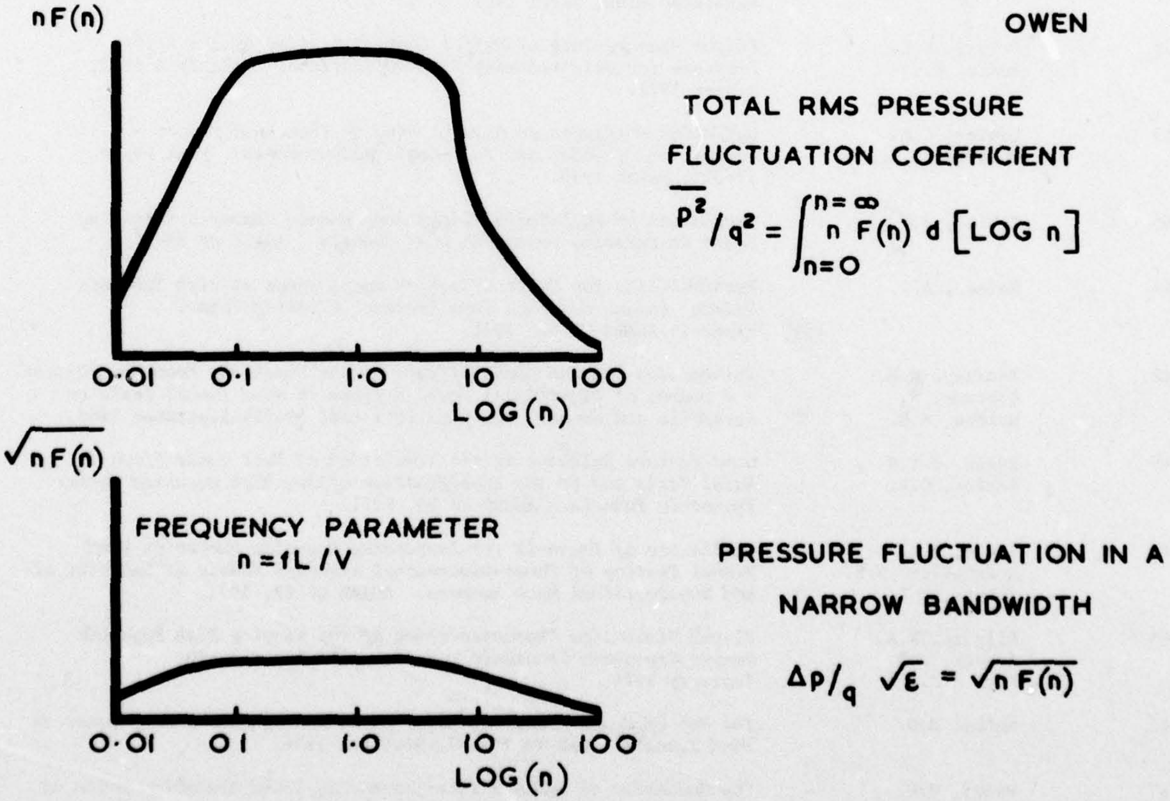

Fig.2 Dimensionless representation of excitation spectra

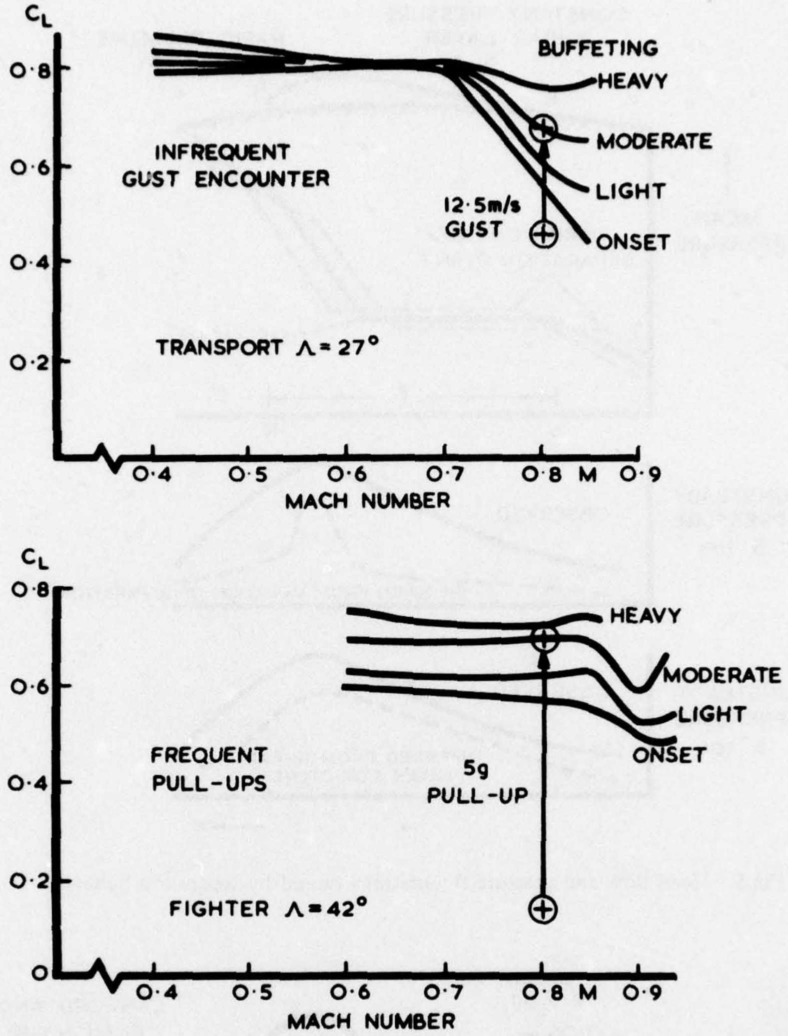

Fig.3 Buffeting criteria for transport and fighter aircraft

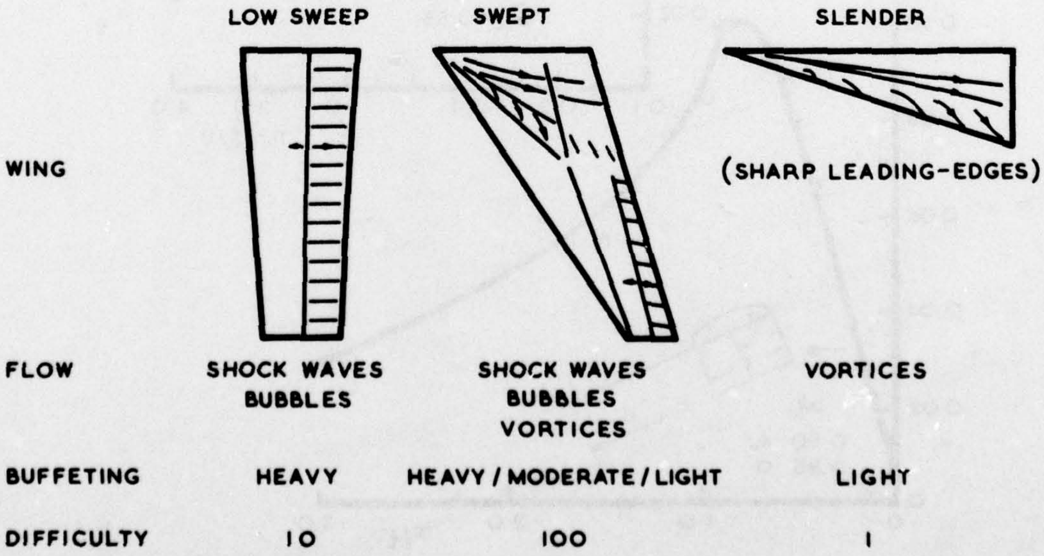

Fig.4 Classification of flows and associated buffeting

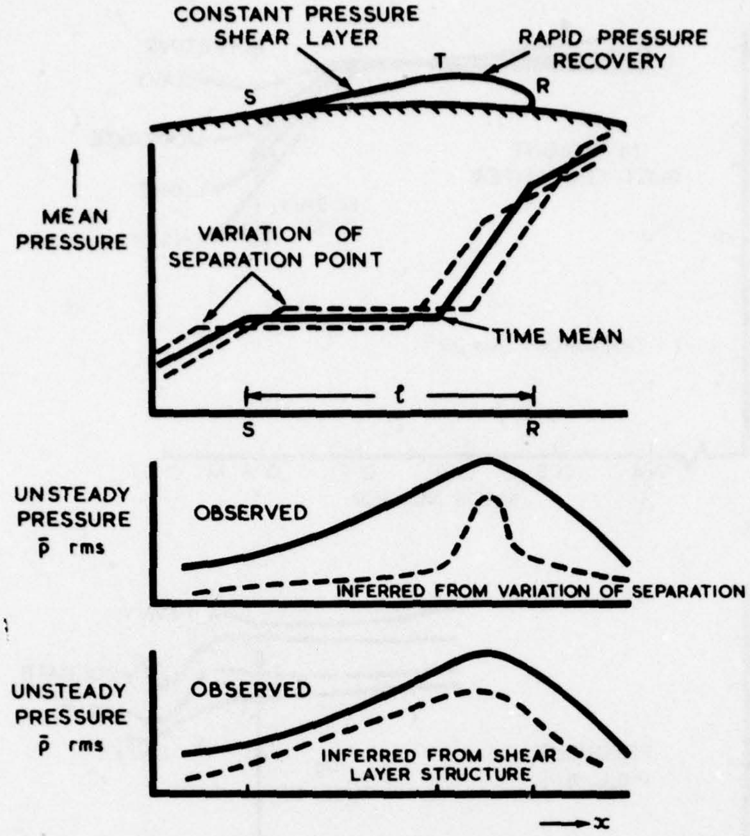

Fig.5 Mean flow and pressure fluctuations caused by separation bubbles

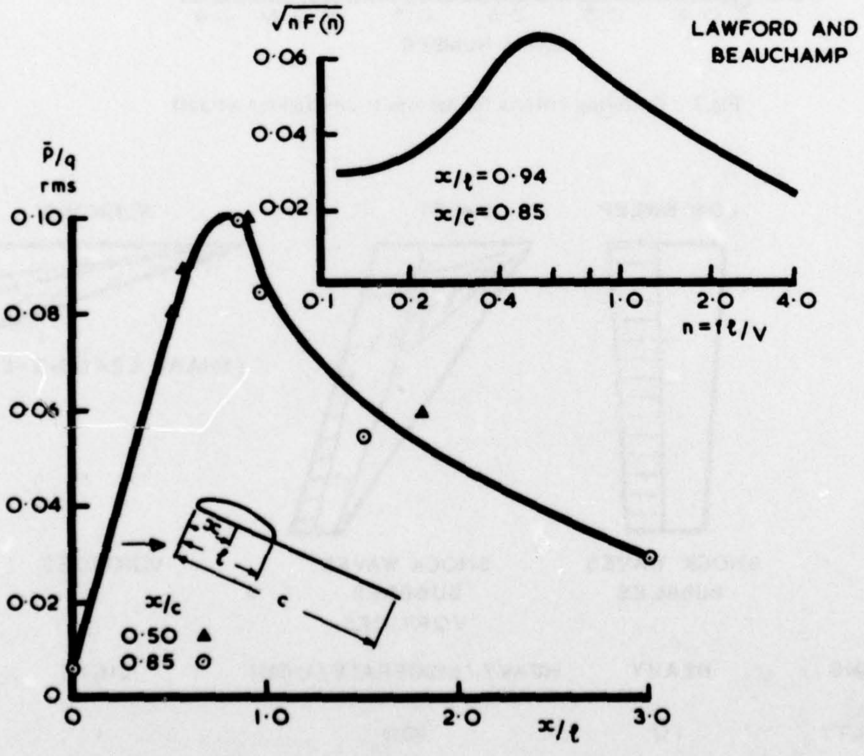

Fig.6a Excitation caused by leading-edge bubble, M = 0.14

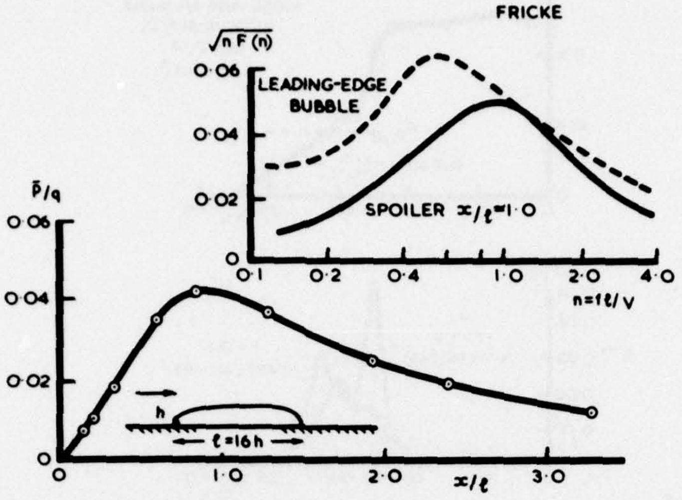

Fig.6b Excitation caused by a spoiler, M = 0.12

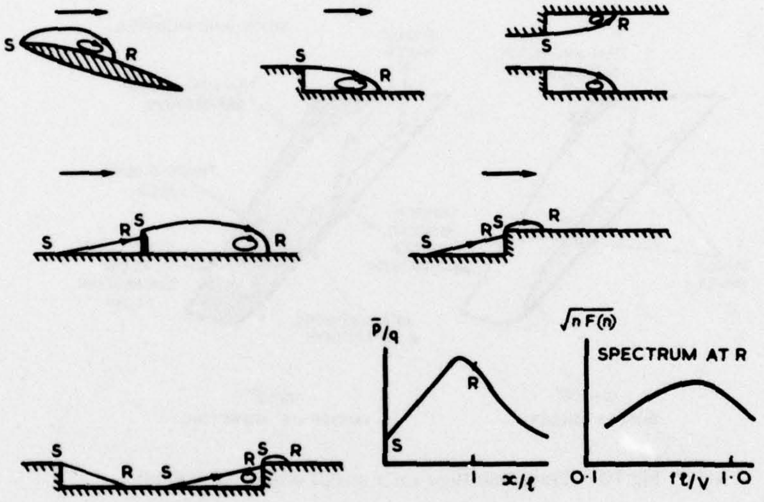

Fig.7 Types of bubble flow

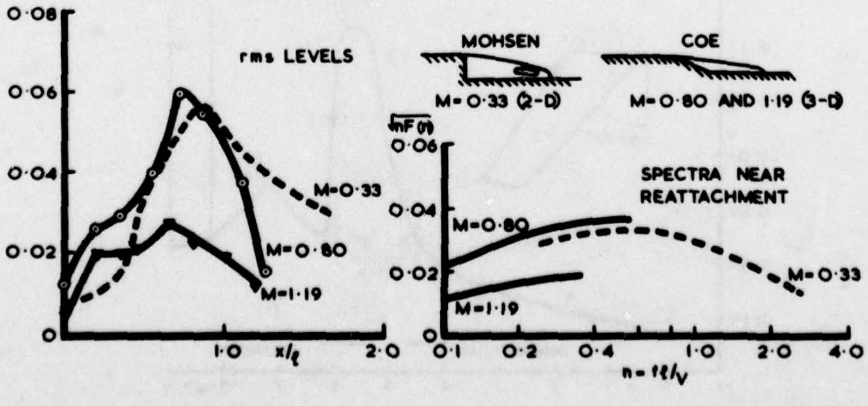

Fig.8 Comparison of excitation caused by the flow down a step at M = 0.33, 0.80 and 1.19

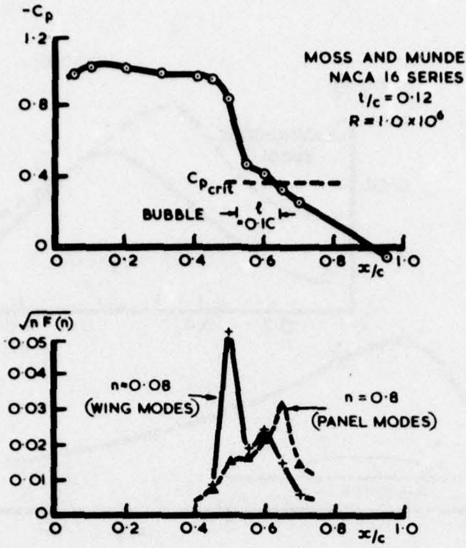

Fig.9 Excitation on an aerofoil near buffet onset, M = 0.82 α = 6.7°

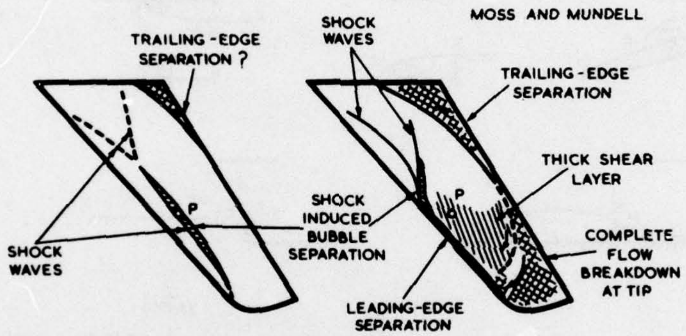

α=5·9°
BUFFET ONSET

α=8°
MODERATE BUFFETING

Fig.10 Transonic flow on a swept wing, M = 0.80

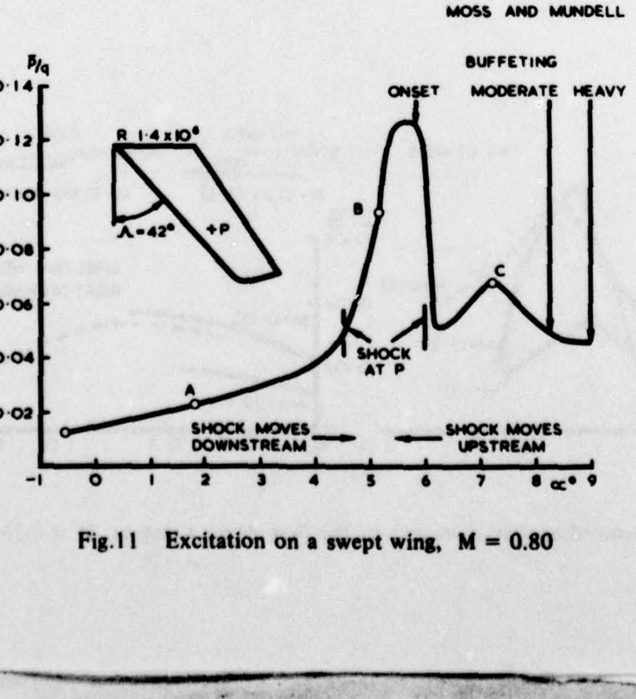

Fig.11 Excitation on a swept wing, M = 0.80

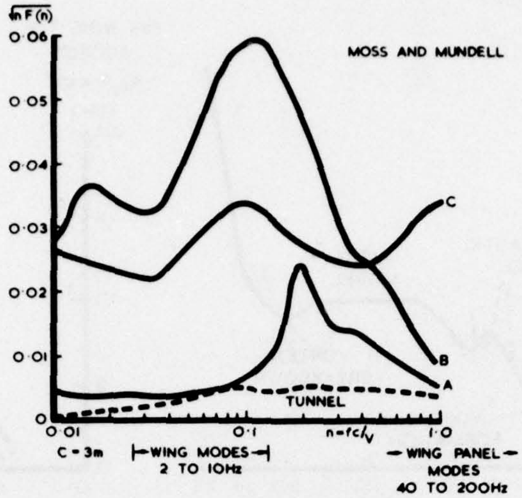

Fig.12 Spectra of excitation on a swept wing, M = 0.80

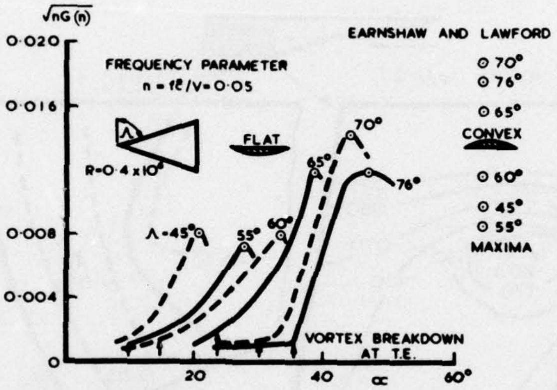

Fig.13 Variation of fluctuating normal force coefficient with incidence for delta wings M = 0.08

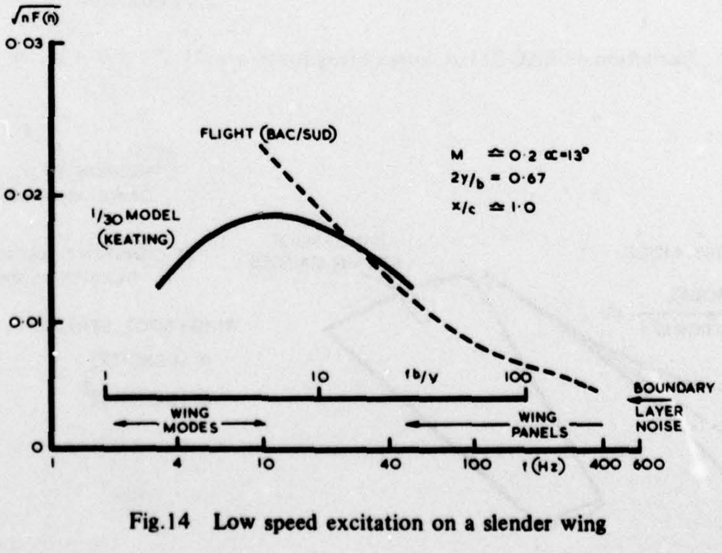

Fig.14 Low speed excitation on a slender wing

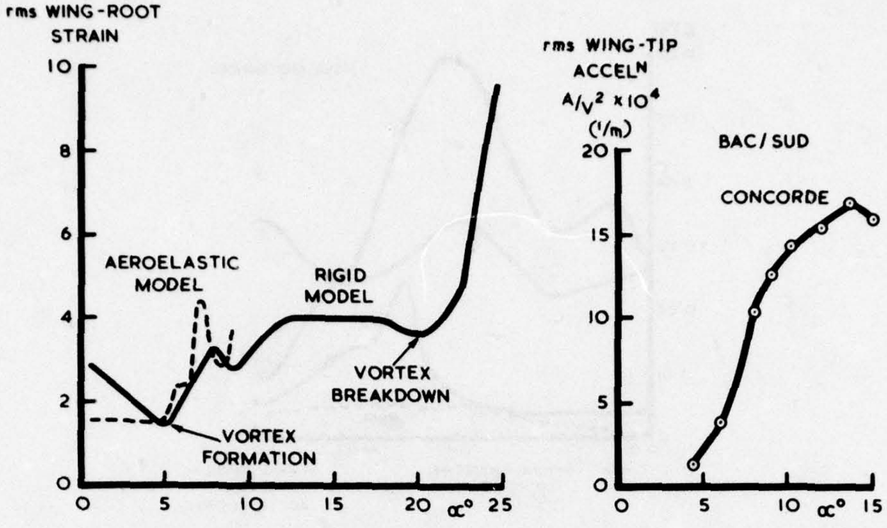

Fig.15 Light buffeting on slender wings, M = 0.2

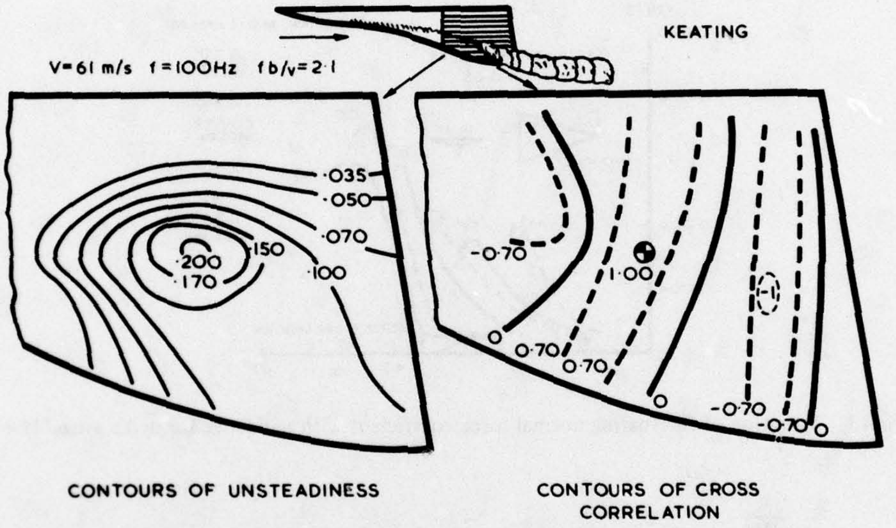

CONTOURS OF UNSTEADINESS

CONTOURS OF CROSS CORRELATION

Fig.16 Excitation on BAC 221 at vortex breakdown $\alpha = 21.5°$, $\beta = -3°$, M = 0.2

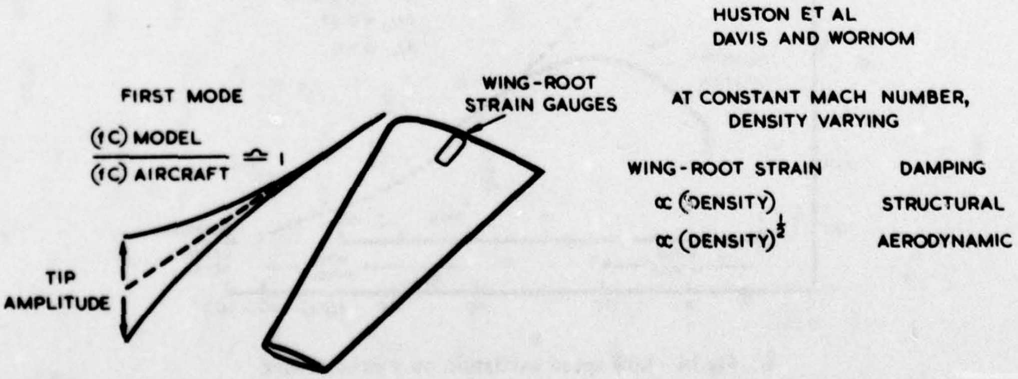

Fig.17 Similarity relations for buffeting

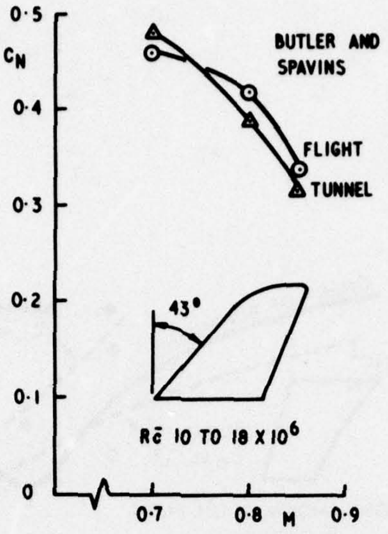

Fig.18 Flight/tunnel comparison for buffet onset on a small fighter aircraft

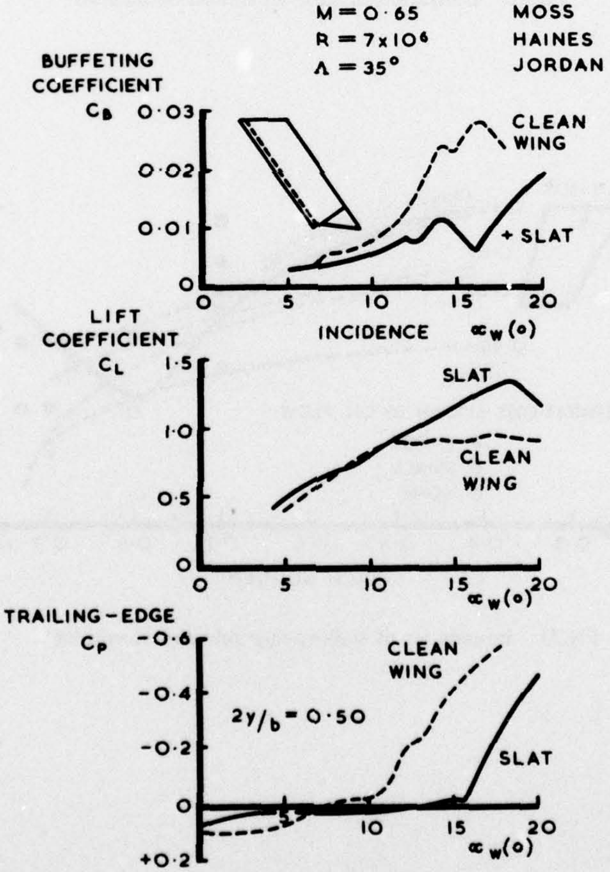

Fig.19 Influence of leading-edge slats on buffeting, forces and trailing-edge pressures

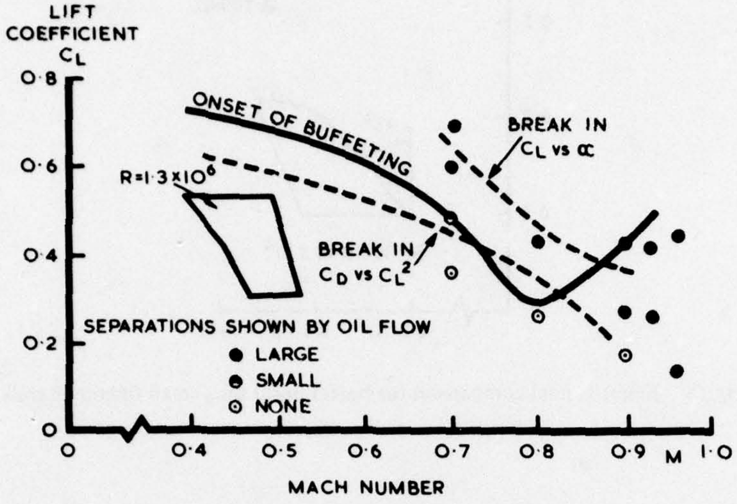

Fig.20 Derivation of flow separation boundaries

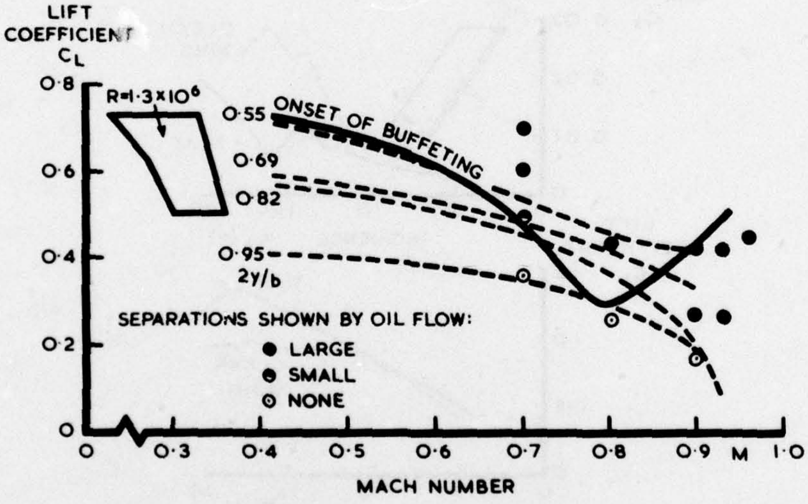

Fig.21 Boundaries of trailing-edge pressure divergence

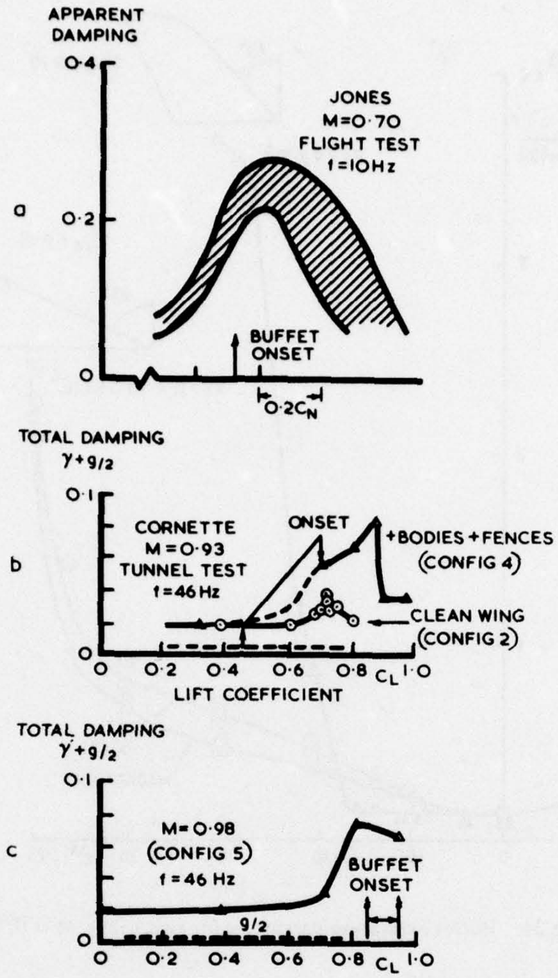

Fig.22 Variation of total damping with lift coefficient

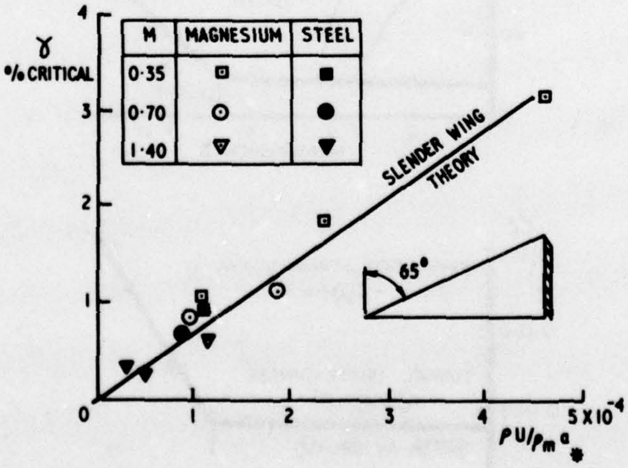

Fig.23 First bending mode – variation of aerodynamic damping with density and velocity

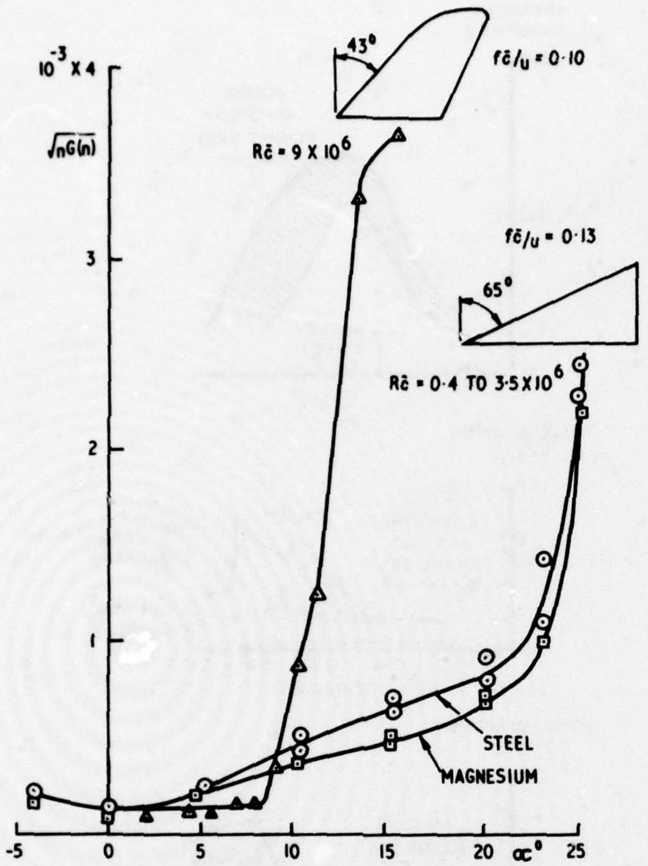

Fig.24 Buffet excitation parameter for two wings M = 0.70

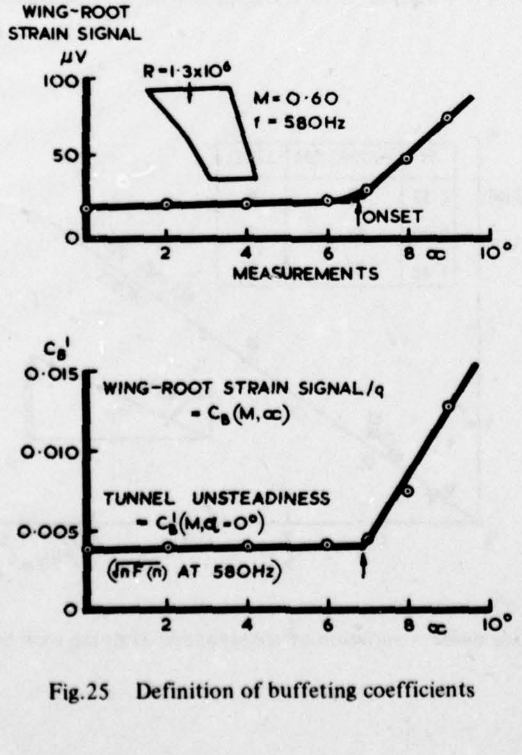

Fig.25 Definition of buffeting coefficients

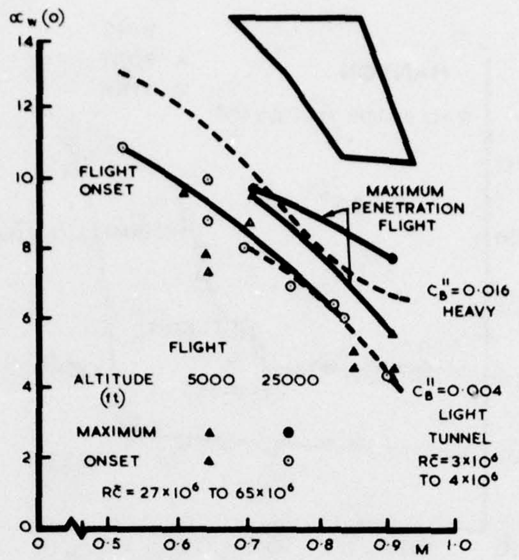

Fig.26 Aircraft buffeting penetration boundaries and model buffeting contours

a $M = 0·70$ $R = 4 \times 10^6$

b $M = 0·90$ $R = 4 \times 10^6$

Fig.27a
Fig.27b | Surface flow patterns at different levels of buffeting

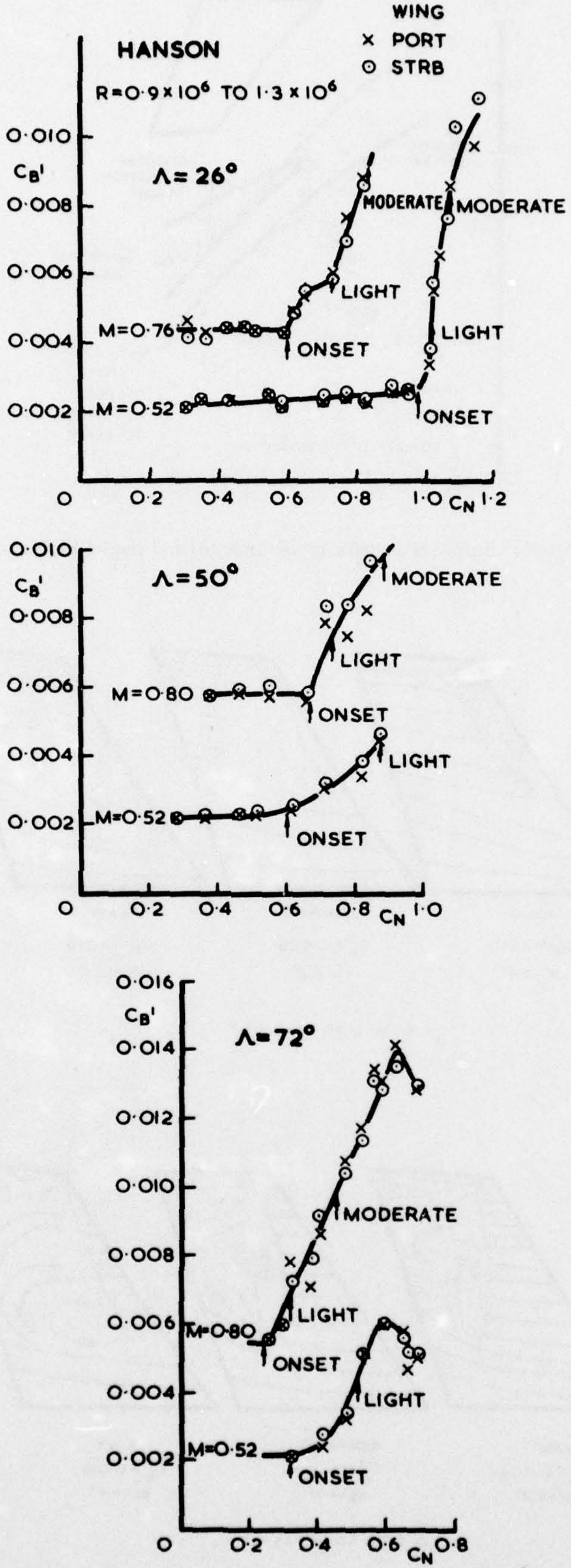

Fig.28 Buffeting coefficient versus normal force coefficient for a variable geometry aeroelastic model

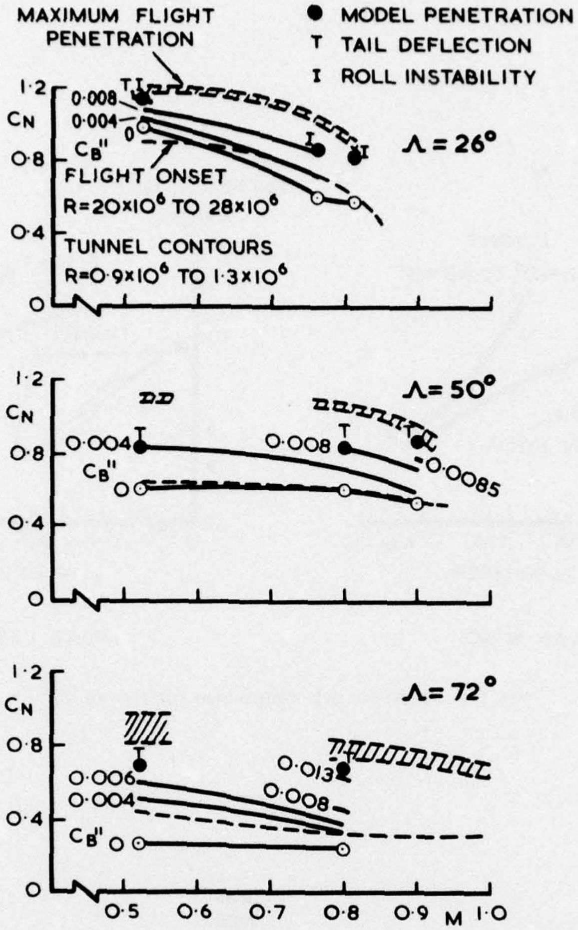

Fig.29 Variable geometry aircraft buffeting penetration boundaries and model buffeting contours

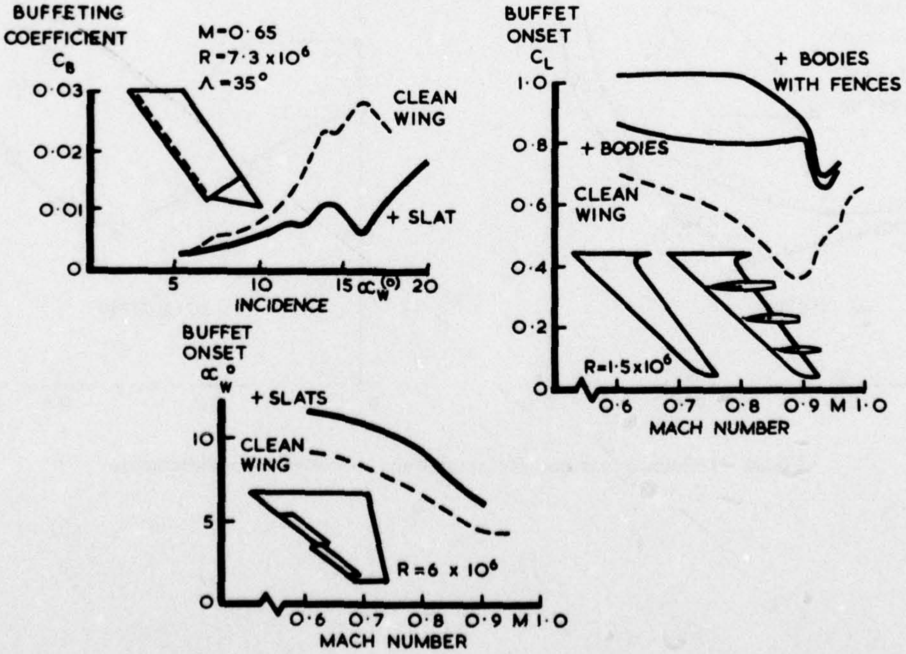

Fig.30 Alleviation of buffeting by wing modifications

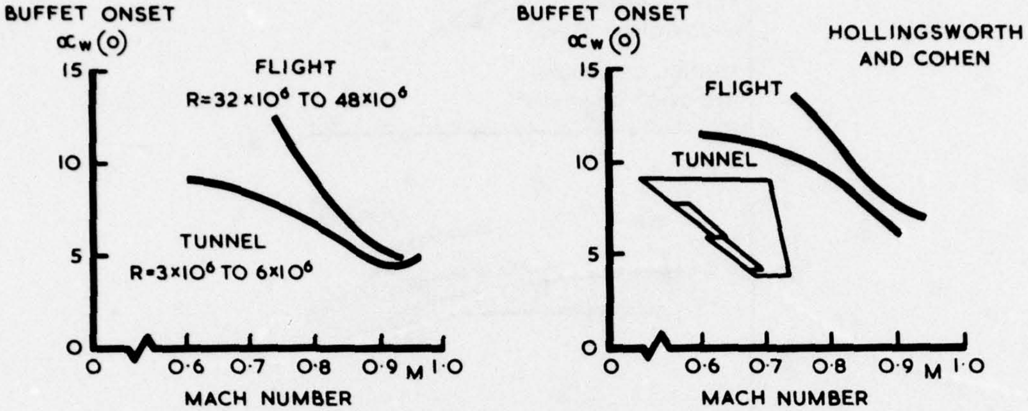

CLEAN WING

SLATS EXTENDED

Fig.31 Flight/tunnel comparison for F-4 aircraft

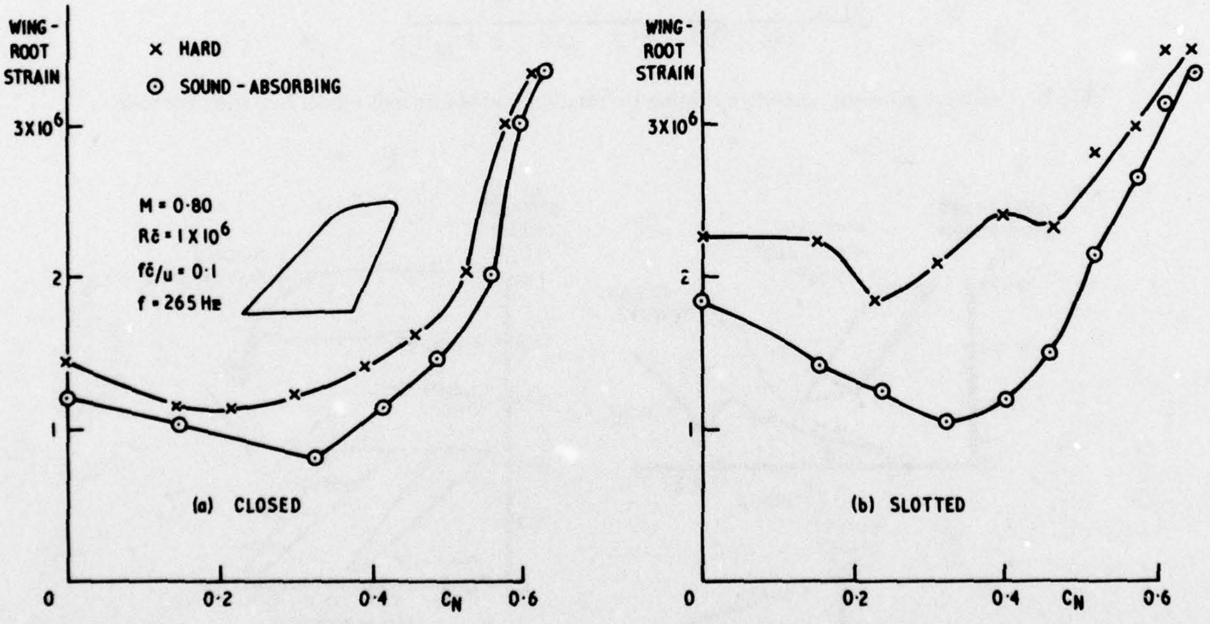

Fig.32 Influence of sound-absorbing walls on buffeting measurements

SOME UNSTEADY SEPARATION PROBLEMS FOR SLENDER BODIES

W. J. McCroskey
Aeromechanics Laboratory—U.S. Army Aviation R&D Command
Ames Research Center, Moffett Field, California 94035, U.S.A.

1.0 INTRODUCTION

The development of reliable prediction techniques for engineering purposes requires a fundamental and detailed understanding of the unsteady flow fields on wings and rotating blades. Some of the peculiar features of unsteady separated flows that are not simple analogs or extensions of quasi-steady flows are discussed in more detail in this section.

2.0 THE UNSTEADY KUTTA-JOUKOWSKI CONDITION

In developing the potential theory of flow over airfoils and lifting surfaces, the role of viscous processes in determining the circulation of the lifting sections always has to be taken into account. In most cases, these complicated processes are summed up in the well-known Kutta-Joukowski trailing-edge condition. For steady flows over profiles with sharp trailing edges, the concept is most often expressed as selecting, from an unlimited number of possibilities, the single solution that keeps the velocity finite at the trailing edge. Both the velocity and pressure are, therefore, continuous at that point.

However, in unsteady flow the situation is not so clear, either physically or mathematically. Figure 1 contrasts the classical interpretation of trailing-edge conditions with a hypothetical interpretation of what really happens (Ref. 1). The classical interpretation of the trailing-edge hypothesis of Kutta and Joukowski has been called into question when the trailing edge is not sharp, when boundary layer separation is present near the trailing edge, or when the near wake is highly deformed. While these effects are not completely resolved even in steady flows, the unsteady aspects have created additional concerns, especially for airfoils with high-frequency lift fluctuations, that is, for $k >> 1$.

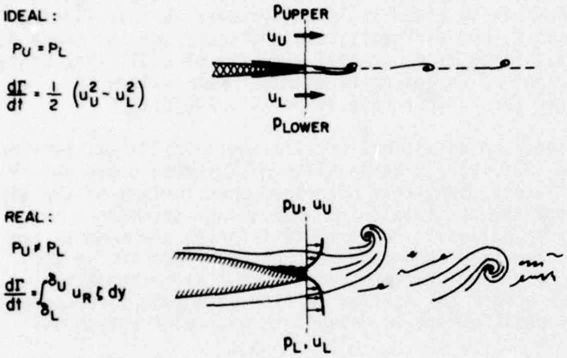

Fig. 1. Sketches of the Kutta-Joukowsky trailing edge condition in unsteady flow.

A theoretical consequence of the classical Kutta-Joukowski condition, and one that is embodied in all of the unsteady potential theories that have been developed to date, is that the pressure difference across the airfoil approaches zero at the trailing edge. However, even in the absence of stall or large amounts of separation, pressure measurements at high frequency have been found to deviate from the theoretical predictions in the trailing edge region. Usually, discrepancies tend to show up more as phase lags of the absolute pressure than in a significant Δp near the trailing edge, a finding that is consistent with an incomplete analysis of this problem by Brown and Daniels (Ref. 2). However, the magnitude of the pressure fluctuations can be in error, as well. It has also been found that the wake tends to distort itself into a regular vortex pattern, as shown in Fig. 2 from Ref. 3, rather than remaining approximately planar, as assumed in linear potential flow theory.

Thoughtful discussions of the flow around blunt trailing edges have been published recently by Gostelow (Ref. 4) and Sears (Ref. 5), the latter reference dealing particularly with unsteady trailing-edge separation. The potential flow would be singular in blunt trailing-edge regions were it not for the adjustments provided by the boundary layer and the wake. Even with separation, the relationship shown in the lower half of Fig. 1 is still valid. That is, the connection between the rate of change of circulation and the flux of vorticity out of the boundary layer and into the wake is

$$\frac{d\Gamma}{dt} = \int_{\delta_L}^{\delta_U} u_r \zeta \, dy \qquad (1)$$

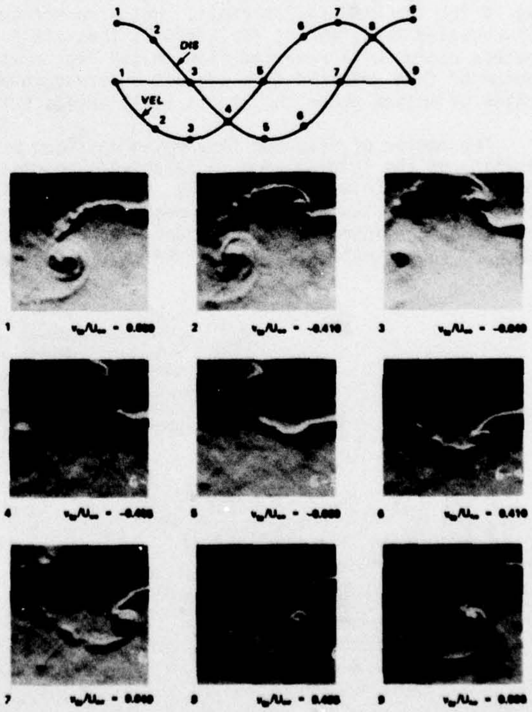

Fig. 2. Flow near the trailing edge of an airfoil oscillating at high frequency (Ref. 3). Airfoil pitch axis at $X/c = 0.30$; trailing edge displacement = $0.04\ c \cos \omega t$; $\omega c/2U_\infty = 8.0$, Re = 34300.

where Γ is the instantaneous bound circulation of the airfoil, u_r is the local velocity of the flow within the boundary layer relative to the moving separation point, ζ is the local vorticity, and δ is the boundary-layer thickness.

This application of Kelvin's theorem was further developed by Sears (Ref. 5) in the unsteady case for both sharp and blunt trailing edges. He also showed how the circulation criterion of Eq. (1) is related to the version of the Kutta-Joukowski condition that equates, approximately, the pressures above and below the trailing edge.

Without developing actual solutions, Sears proposed dual models for calculating the flow field, forces, and moments. A vortex-sheet model in the spirit of classical thin airfoil theory suffices for the lift, moment, and pressure and vortex-strength distributions, but the circulation for this model has to be determined from a second model, wherein boundary layer calculations are performed around the actual contour. Thus the flow of each model depends on the other, and the two would have to be calculated iteratively.

Unfortunately, neither definitive experiments nor analyses have yet clarified the nature of the unsteady trailing edge flow on airfoils, with or without moderate amounts of separation. However, the correct theoretical modeling of the generalized trailing edge condition is important in understanding the mechanisms involved in certain classes of bird and insect flight, in determining the acoustic radiation from trailing edges of wings and rotating blades, in analyzing the potential flow in turbomachines with closely spaced blades, and as a prelude to analyzing trailing-edge stall on oscillating airfoils by approximate methods.

3.0 DYNAMIC STALL ON OSCILLATING AIRFOILS

Major changes occur in flow fields when the thin viscous layer near the surface of a body erupts into the phenomenon called stall. Unsteady effects can fundamentally alter the stall process for oscillating airfoils, helicopter blades, marine propellers, compressors, and diffusers; and unsteady stall on these devices is extremely difficult to predict accurately. In this section, several examples of stall that contain peculiar time-dependent features are discussed in the light of recent developments. The reviews by McCroskey (Ref. 6) and Philippe (Ref. 7) may be consulted for further details of this subject.

A conceptual description of how dynamic stall proceeds on an airfoil oscillating in pitch was provided a few years ago by Ham and Garelick (Ref. 8) and by Ham (Ref. 9). A vortex-like disturbance grows out of the boundary layer in the leading-edge region and then passes downstream over the upper surface of the airfoil. Figure 9 of Paper 6 and Fig. 3 of this section show the progression of this vortex-shedding phenomenon and how it affects the chordwise pressure distribution.* The transient forces and moments are fundamentally different from their static counterparts, and they cannot be reproduced by neglecting the unsteady motion of the airfoil. A characteristic feature of the unsteady case is that large negative increases in the pitching moment, or "moment stall," occur before the maximum in lift or normal force, that is, "lift stall." Also, the beginning of the series of stall events is delayed to angles of attack well above the static stall angle.

The dynamic stall process involves a series of distinct events, which are indicated schematically in Fig. 4 for the NACA 0012 airfoil. Hot wire anemometry, flow visualizations, and pressure measurements (Ref. 10) revealed that, except for airfoils that stall by the mechanism of leading-edge bubble bursting, the process begins with reversed flow on the rear portion of the profile, as indicated by Fig. 4(a). This long tongue of thin reversed flow was not observed under quasi-static conditions, and it only appeared for angles of attack above the static stall angle, but before the onset of dynamic stall.

The region of reversed flow moved upstream with increasing incidence. When it reached the general vicinity of the leading edge, a relatively concentrated, vortex-like disturbance began to form within the boundary layer (Fig. 4(b), and Fig. 9(b) of Paper 6. The subsequent growth and initial rearward movement of this vortex signaled the onset of moment stall for $k \gtrsim 0.05$. The lift, drag, and nose-down pitching moment continued to increase due to the induced pressure field associated with the vortex, which moved rearward at approximately 40% of the free-stream velocity.

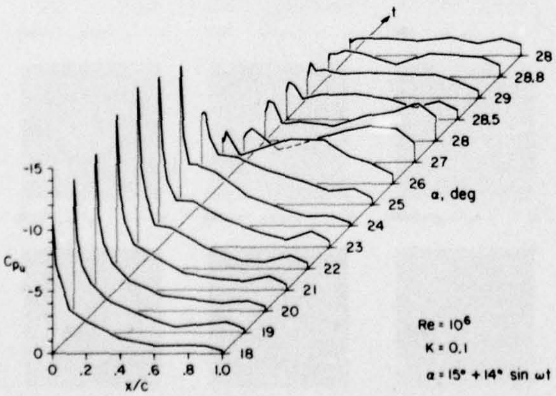

Fig. 3. Pressure distributions on the upper surface of an airfoil during dynamic stall (Ref. 6).

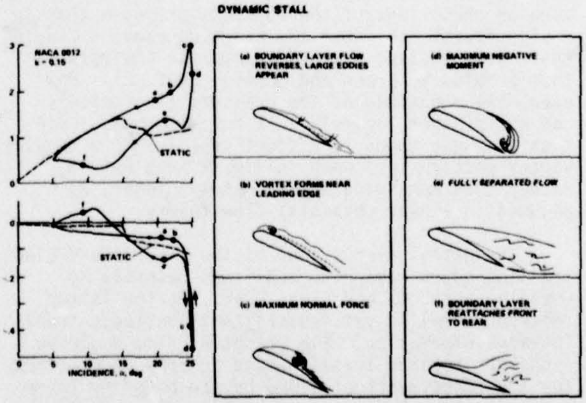

Fig. 4. The important dynamic stall events on an oscillating airfoil at $Re = 2.5 \times 10^6$ (Ref. 10).

---

*In this and all subsequent figures in this section, the motion is sinusoidal pitch oscillation about an axis at $X/c = 0.25$, and $k \equiv \omega c/2U_\infty$.

The maximum value of C_L was obtained when the vortex disturbance was centered at $X/c \approx 0.6$ (Fig. 4(c)), and the maximum negative value of C_M was obtained as the vortex approached the trailing edge (Fig. 4(d)). The approach to a fully-separated flow that resembled the flow field on a statically-stalled airfoil (Fig. 4(e)) was accompanied by smaller aerodynamic forces and moments, and this flow picture persisted during the downstroke for several chord-lengths of travel of the freestream flow. Finally, at an incidence well below the static stall angle, the flow began to reattach in the leading edge region. The reattachment process (Fig. 4(f)) moved rearward at about 1/3 U_∞.

The general features described above were observed over a wide range of unsteady flow conditions and airfoil geometries. However, the details of the boundary layer flow reversal were found to depend on the leading edge geometry. Figure 5 shows the variations that were tested. Figure 6 illustrates the movement with time of the point along the airfoil where the boundary layer flow near the surface reversed its direction. For the large-amplitude conditions shown, this occurred while the airfoil was still pitching up, but after the static stall angle had been exceeded.

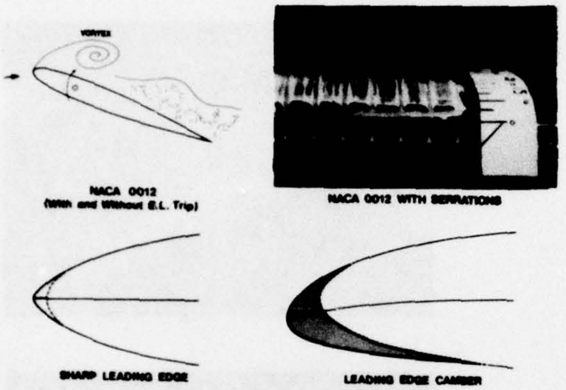

Fig. 5. Variations in leading-edge geometry used in experiments on oscillating airfoils (Refs. 10, 13).

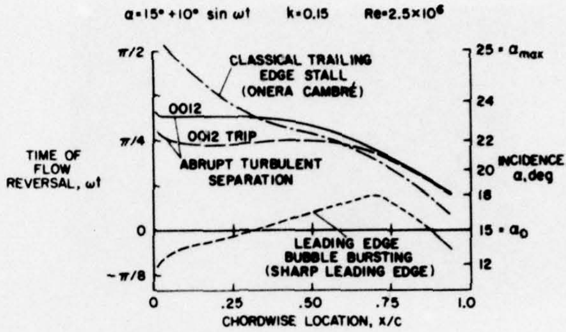

Fig. 6. The time of the onset of unsteady flow reversal as a function of chordwise position on oscillating airfoils that stall by different mechanisms (Ref. 10).

The cambered profile at positive incidence exhibited more or less classical trailing-edge stall, developing from a rear-to-front progression of boundary-layer flow reversal that was more gradual than on the 0012 airfoil. On the other hand, the cambered airfoil at negative incidence stalled following the bursting of a leading-edge separation bubble. In this case, the separated zone moved downstream and enlarged with increasing time. The same was true of an airfoil with a small leading-edge radius, $r_0/c = 0.004$. The most striking case was the standard NACA 0012 profile, which generally exhibits leading-edge static stall characteristics. In this case, it was found both statically and dynamically that the leading-edge stall was caused by an abrupt breakdown of the turbulent flow on the forward portion of the airfoil, rather than by bubble bursting, as is commonly presumed. Nevertheless, the vortex-shedding phenomenon was common to all of the airfoils tested under unsteady conditions.

The general phenomena described above for the airfoils that exhibited trailing-edge stall have been observed over a wide range of Reynolds numbers, from approximately 3000 to over 3×10^6. However, two aspects of dynamic stall have shown a dependence on Reynolds number. The first is an increase in the angle of attack for the onset of dynamic stall with increasing Reynolds number, similar to the dependence of the static stall angle on Re. The second effect is the appearance of a trailing-edge vortex bubble at low Reynolds number, approximately concurrent with the leading edge vortex, that seems to help suppress the large negative pitching moments indicated in Fig. 4 (Ref. 11). Figure 7 shows this phenomenon in sequences of flow visualizations at two widely different values of Reynolds number (Refs. 10, 12). These scenes have been chosen with approximately equal values of $U_\infty \Delta t/c$ between photographs. At low Reynolds number, with laminar flow everywhere, the rear vortex is comparable in size to the leading edge vortex, although the strength of the latter seems greater. At the high Reynolds number, the turbulent boundary layer is thick on the rear of the airfoil. A necking down or reduction in streamtube area occurs over the middle of the airfoil, as in the laminar case, but the rear vortex is not apparent in either the flow visualizations or in the pressure distribution (Ref. 13). Despite the qualitative similarity in the two examples, however, the evolution of the aerodynamic forces and moments is quite different (Refs. 11, 13).

Experiments of Philippe and Sagner (Ref. 14) and Liiva et al. (Ref. 15) have shown the general influence of the mean angle of attack on dynamic-stall behavior, with other parameters held fixed. In Fig. 8, the case of $\alpha_0 = 7.3°$ essentially follows the predictions of potential-flow theory, and at this reduced frequency the unsteady effects are relatively small. When $\alpha_0 = 24.6°$, the airfoil is always fully stalled, but the hysteresis is not significantly greater than in the low-incidence case. The most interesting case is for $\alpha_0 = 14.9°$, which is approximately the static stall angle. As the airfoil oscillates in and out of stall, the hyseresis loops are much larger, and the aerodynamic pitch damping changes sign twice during each cycle of oscillation. For the conditions shown, the net damping is slightly negative, which means that the airfoil extracts energy from the airstream and that the oscillation would tend to increase in amplitude, if unrestrained. This, of course, is the condition for flutter.

An important parameter affecting dynamic stall is obviously the reduced frequency of the oscillation. Figure 9, adapted from Ref. 13, shows the variation in the lift, drag, and pitching moment as k was increased. A small amount of hysteresis was observed even at $k = \omega c/2U_\infty = 0.004$, but the vortex-shedding phenomenon did not develop fully into the state described above until $k \approx 0.05$. Its influence on the maximum values of the force and moment coefficients was very large for $k \gtrsim 0.05$, and negative aerodynamic

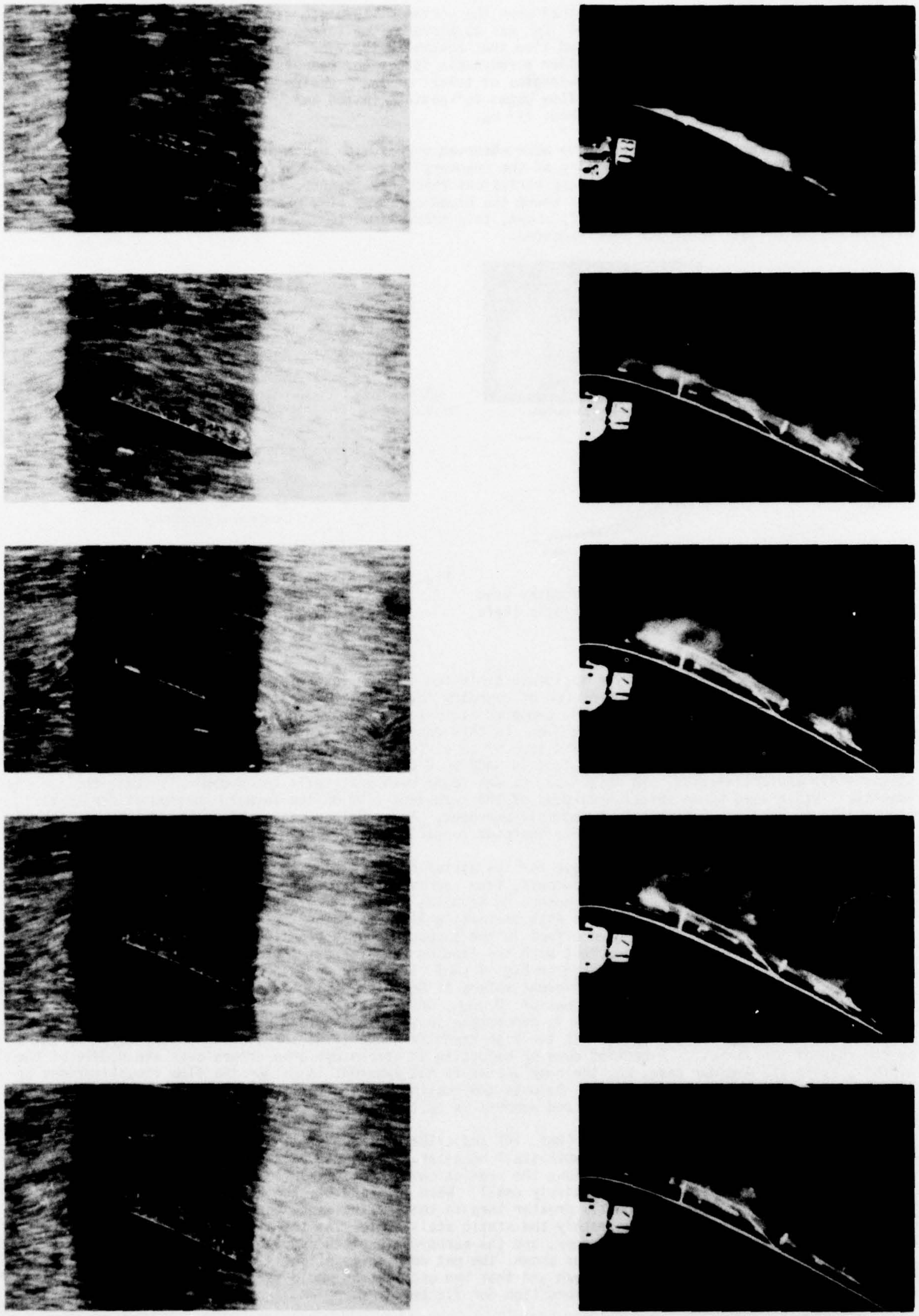

Fig. 7. *Flow visualization of the early stages of dynamic stall on NACA 0012 airfoils.* Left: $\alpha = 10^\circ + 10^\circ \sin \omega t$, $Re = 10^4$, $k = 0.25$ (Ref. 12). Right: $\alpha = 15^\circ + 10^\circ \sin \omega t$, $Re = 1.5 \times 10^6$, $k = 0.15$ (Ref. 10).

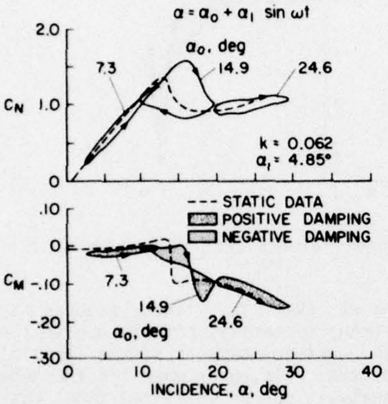

Fig. 8. The effect of mean angle on dynamic force and moment coefficients. Re = 4.8 × 10^6, M = 0.40 (Ref. 15).

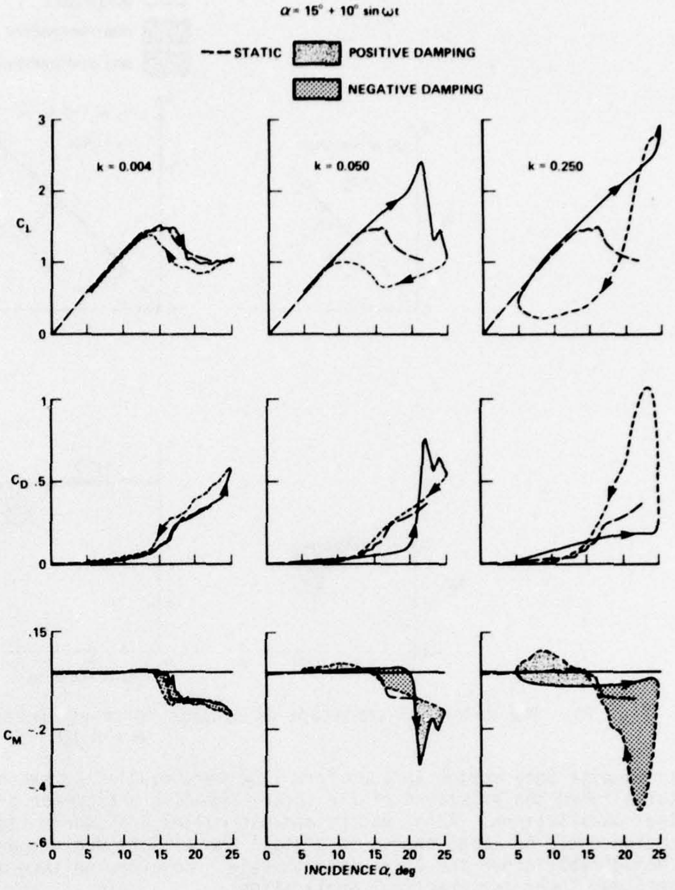

Fig. 9. The effect of reduced frequency on dynamic force and moment coefficients (Ref. 13). Re = 2.5 × 10^6, M = 0.09.

damping in pitch occurred for $0.04 \lesssim k \lesssim 0.12$. Above $k \approx 0.15$, the strength of the vortex appeared to be approximately independent of reduced frequency, and it traveled over the upper surface of the airfoil at approximately $0.4\ U_\infty$. On the other hand, as k increased, the airfoil completed a larger fraction of a cycle of oscillation during the vortex passage. Therefore, the various dynamic stall events shown in Fig. 4 occurred at different phases during the cycle for different values of k. As a result, the hysteresis loops of C_L, C_D, C_M versus α were quite different in quantitative detail, even though polars of C_M vs. C_L were found to be approximately independent of reduced frequency for $k \gtrsim 0.05$ (Ref. 10).

The influence of the amplitude of the unsteady motion is illustrated in Fig. 10. For this comparison, α_0 is approximately the static stall angle, and the reduced frequency was varied so as to maintain a constant value of the maximum pitch rate parameter, that is, $(\dot{\alpha}c/U_\infty)_{max} = 2\alpha_1 k$ = constant. For the cases of $\alpha_1 = 10°$ and 14°, the vortex shedding phenomenon begins while $\dot{\alpha} > 0$, that is, before $\alpha = \alpha_{max}$. The subsequent flow-field development is very similar in the two cases, although the different stall events occur at different phases of the motion. Therefore, the curves of C_L, C_D, and C_M vs. α are quantitatively different. However, when $\alpha_1 = 6°$, dynamic stall does not begin until after $\alpha = \alpha_{max}$, when $\dot{\alpha} < 0$. As a result, the vortex-shedding phenomenon is less pronounced. This is not unexpected, and in the limit of very small amplitude, it would essentially disappear.

Figure 11 shows some effects of increasing Mach number on dynamic stall. As in the previous figure, the data are taken from the extensive program of Liiva et al. (Ref. 15). Here progressively smaller mean angles were selected because of the decrease in the static-stall angle with increasing Mach number. The similarity of the static-stall characteristics at M = 0.2 and 0.4 suggests that transonic shock-wave formation does not play a role in either case, but the static M = 0.6 data show clear evidence of shock-induced separation and stall. The dynamic data at M = 0.6 suggest that the formation of shock waves somehow inhibits the development of the vortex shedding process, although some vestiges of the phenomenon remain. New experiments, similar to the ones that have been done at low speeds, are needed to resolve this question further.

Brief mention should be made of unsteady motions other than airfoil pitch oscillations. The vertical displacement, or "plunging" data of Liiva et al. (Ref. 15) for small-amplitude motion indicated the same qualitative features of dynamic stall that have been described above. Some important quantitative differences have been reported (Ref. 16), but they will probably not change the current engineering practice of treating pitch and plunge oscillations as though they were equivalent.

Airfoils at fixed incidence in a stream that oscillates in speed have recently been examined by Saxena, Fejer, and Morkovin (Ref. 17), and the lift, drag, pitching-moment, and boundary-layer changes due to

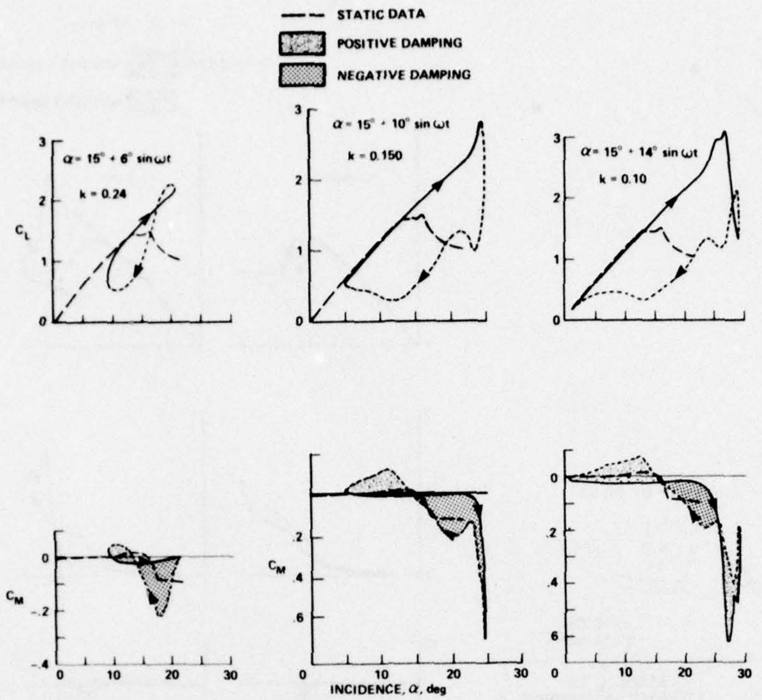

Fig. 10. The effect of amplitude on dynamic force and moment coefficients (Ref. 13). Re = 2.5 × 10^6, M = 0.09.

streamwise body motion in a uniform flow were studied by Rabont et al. (Ref. 18). These studies have established the existence of the vortex-shedding phenomenon and strong hysteresis effects due to longitudinal oscillations. Also, Rabont and his colleagues showed that the unsteady effects of the translational motion could be large enough to unstall the airfoil during part of the cycle, even when the incidence was considerably above the static-stall angle. However, neither an analysis nor an empirical model has yet been developed for practical applications.

Pierce, Kunz, and Malone (Ref. 19) combined airfoil pitch oscillations at one frequency with freestream velocity oscillations at another. They indicated that although the freestream perturbations altered the instantaneous pitching moment behavior, the overall effect on aeroelastic stability was surprisingly insignificant. Since this is the only study of this kind that has been performed, it is not yet clear how universal this conclusion may be.

Applications to Helicopter Rotor Blades

The basic studies described in the preceding section provide first approximations to the real flows on helicopter blades, and to some extent, on propellers and compressor blades. The very low aspect ratio of typical marine propellers make rotational and tip effects especially important. On the other hand, the primary three-dimensional effect in the helicopter case is probably due to the rotor blade's periodic spanwise component of velocity, $V_\infty \cos \Omega t$. Figure 12 shows the velocity components arising from the combined rotational and translational motion of a blade element.

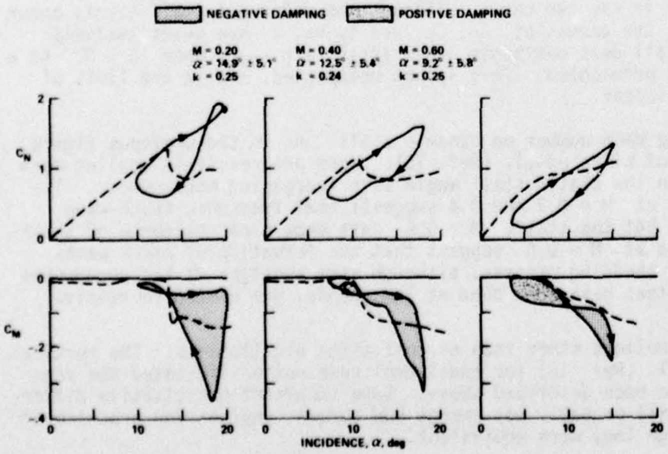

Fig. 11. The effect of Mach number on dynamic force and moment coefficients (Ref. 15).

Figure 13 shows the variations in chordwise velocity, angle of attack, normal force coefficient, and pitching-moment coefficient measured on a model rotor at two values of rotor thrust coefficient (Ref. 20). The rotor blade azimuthal position is $\psi = \Omega t$. In addition, the local blade element sweep angle is given approximately by

$$\Lambda = \tan^{-1}\left[\frac{V_\infty \cos \Omega t}{\Omega r + V_\infty \sin \Omega t}\right] \qquad (2)$$

Detailed analysis of the pressure data obtained on the model rotor blades indicated that the initial stages of retreating-blade stall development, which occur for $180° < \psi < 270°$ where the spanwise flow is radially inward, are essentially two-dimensional and are well approximated by airfoils oscillating sinusoidally in pitch, provided the large-amplitude variations in α (Fig. 13) were matched approximately. The vortex-shedding phenomenon appeared at $\psi \approx 210°$, followed by large transient overshoots in C_N and C_M that initiated stall flutter at the torsional natural frequency of the blades.

However, these and other model rotor data indicate that three-dimensional effects produce significantly larger lift in the fully stalled regime, 270° < ψ < 360°, where the cross flow is radially outward. Also, helicopter rotors having more blades or operating at lower flight speeds may experience severe interactions between the boundary-layer flow on one blade and the trailing tip vortex laid down by a preceding blade (Refs. 21, 22). Stall precipitated by such blade-vortex encounters would be expected to be more three-dimensional and higher in frequency than the case portrayed in Fig. 13. At the moment, estimates of helicopter blade loads based on unsteady two-dimensional airfoil data should be viewed with a certain amount of caution.

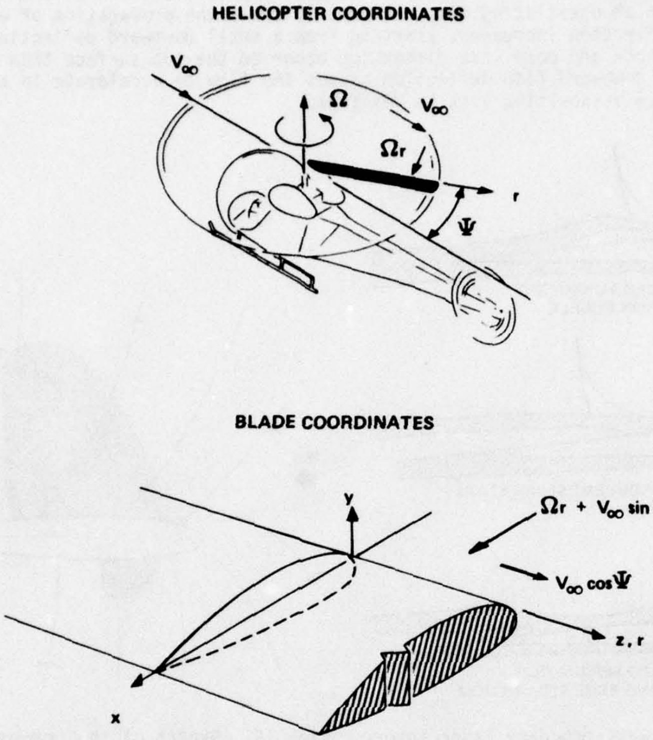
HELICOPTER COORDINATES

BLADE COORDINATES

Fig. 12. Sketch of coordinates and nomenclature for helicopter rotor blades.

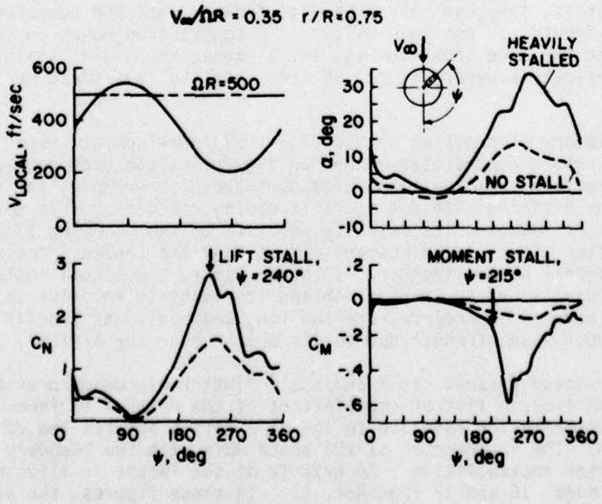

Fig. 13. Aerodynamic environment of a model helicopter rotor (Ref. 20).

4.0 UNSTEADY SHOCK WAVE—BOUNDARY LAYER INTERACTION

Shock waves that terminate in the vicinity of boundary layers are seldom steady. This is particularly true of normal shock waves that occur on transonic wings and control surfaces, as discussed in connection with Fig. 1 of Paper 6. Three of the more common types of shock wave-boundary layer interactions are depicted in Fig. 14. In some cases, the interactions are observed to oscillate periodically with relatively large amplitudes, and these fluctuations can cause severe buffeting, flutter, or control-surface buzz.

Even in the absence of boundary-layer separation, mixed subsonic and supersonic flow fields become rather complicated when unsteadiness is introduced. These complications can be examined for the model problem of an airfoil with an oscillating flap. Figure 15 shows the propagation of expansion and compression waves as the flap deflection increases, starting from a small downward deflection and a fully-developed flow field. A stronger shock and more wave distortion occur on the top surface than on the bottom for the conditions depicted. The downward flap deflection causes the flow to accelerate to a higher local Mach number on the upper surface as positive lift is developed.

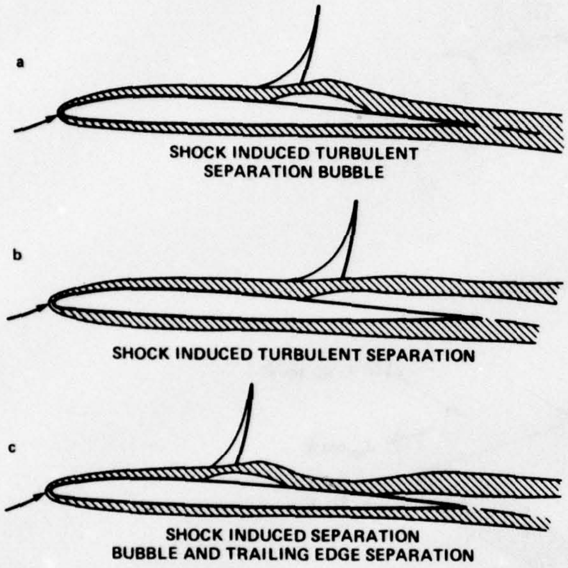

Fig. 14. Sketch of shock wave-boundary layer interaction on an airfoil in transonic flow.

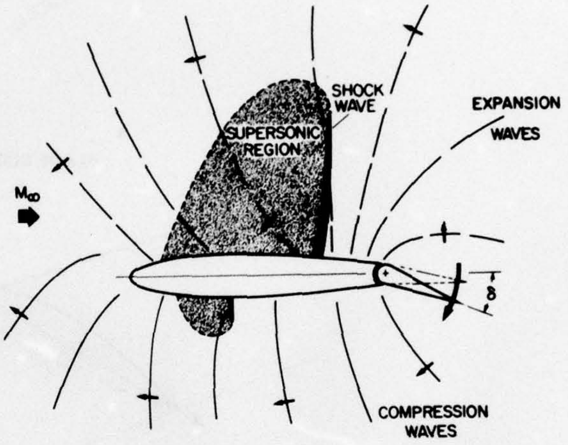

Fig. 15. Sketch of the transonic flow field on an airfoil with an oscillating flap.

It is important to note that signals from the oscillating flap only reach the leading edge via the so-called receding waves, which must detour around the shock wave. Because their propagation is perpendicular to the wave fronts and because they move at the local sonic speed, these waves can only propagate forward into the supersonic zone from points along the sonic line where they arrive at some inclination relative to the flow. That is, they can only propagate forward when the component of the local Mach number perpendicular to the wave fronts is less than unity. The compression waves on the lower surface arrive at the leading edge earlier in the case shown in Fig. 14, because they travel against lower local Mach numbers. On both top and bottom surfaces, however, it can be seen that the flow field development lags the flap deflection.

The effects of oscillatory flap motion on the flow-field development, especially the shock wave motion and strength, depend in a rather complicated manner on the freestream Mach number and on the amplitude and frequency of the flap deflection. As the flap moves downward, for example, the receding expansion waves reach the upper shock after a finite time and start it moving rearward. This motion reduces the pressure jump across the shock wave by reducing its velocity relative to the oncoming flow, a "dynamic effect." This effect is in competition with a "displacement effect," or the tendency for a shock wave in a more rearward position on an airfoil to be stronger. In other words, the actual instantaneous shock strength depends on both the shock wave's change in position and its velocity relative to the airfoil. The essential unsteady features of this problem, therefore, are the long and nonlinear transit time of the upstream-moving waves and the change in shock-wave strength due to its motion over the airfoil.

As in the case of low-speed dynamic stall and stall flutter discussed previously, the unsteady shock-wave motion can lead to limit-cycle flutter oscillations of the control surface. This occurs when the phase of the unsteady pressure distribution relative to the flap motion permits the control surface to extract energy from the air stream. The interaction of the shock wave with the boundary layer introduces additional mechanisms for flutter instabilities. An example of the latter is illustrated by the intermediate Mach number case shown in Figs. 16 and 17 from Ref. 23. In these figures, the airfoil is fixed and the freestream flow is nominally steady. The flow at $M = 0.72$ is characterized by a weak shock wave and trailing edge separation, both of which fluctuate only slightly and irregularly. The flow at $M = 0.78$ fluctuates somewhat more, but it could still be classified as quasi-steady in an overall sense. However, at $M = 0.75$ the flow is highly unsteady; it is characterized by distinctly periodic shock-wave motion and oscillations in boundary-layer separation between the trailing-edge and shock-induced types sketched in Fig. 14. The reduced frequency of the oscillatory flow field was $k = \omega c/2U_\infty \approx 0.4$, and the amplitude of the fluctuating pressure coefficient was found to be of the same order as the average C_p on the airfoil.

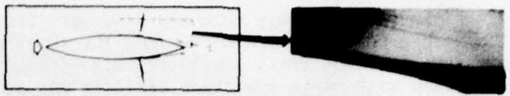

(a) STEADY FLOW, TRAILING EDGE SEPARATION

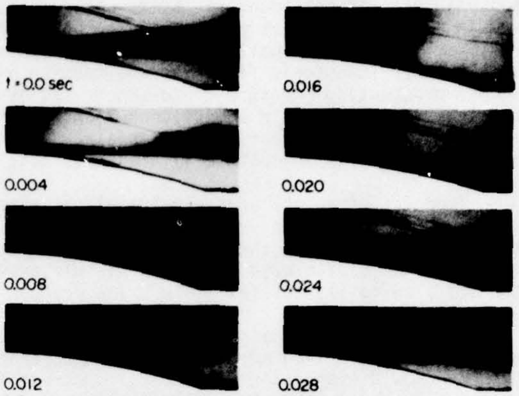

(b) UNSTEADY FLOW, OSCILLATORY SEPARATION

(c) STEADY FLOW, SHOCK-INDUCED SEPARATION

Fig. 16. Flow visualization of three types of shock wave-boundary layer interaction on a stationary circular-arc airfoil (Ref. 23). Case a, M_∞ = 0.72; case b, M_∞ = 0.75; case c, M_∞ = 0.78.

STEADY FLOW, TRAILING-EDGE SEPARATION, $M_\infty = 0.720$

UNSTEADY FLOW, OSCILLATORY SEPARATION, $M_\infty = 0.754$

STEADY FLOW, SHOCK-INDUCED SEPARATION, $M_\infty = 0.783$

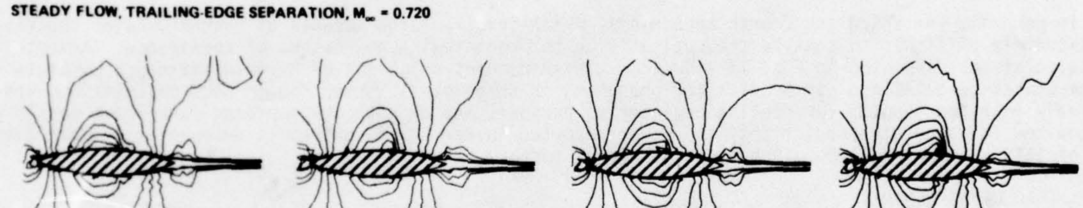

Fig. 17. Calculated Mach contours for the transonic flow shown in Fig. 16 (Ref. 23).

Finke (Ref. 24) has recently described four similar examples and has given an informative discussion of possible unsteady flow mechanisms for shock wave oscillations. The first two of these are thought to be responsible for small-amplitude, high-frequency oscillations, that is, k $\gtrsim$ 1, and the latter two are associated with large-amplitude oscillations at lower frequencies.

Type 1. *If a small pressure disturbance appears during the interaction, it propagates upstream in the* subsonic part of the boundary layer. This disturbance will result in flow changes in the boundary layer and in an upstream shift of the separation point. For laminar shock wave-boundary layer interaction, the familiar lambda-shock pattern usually develops. The upstream-propagated disturbances will cause changes in the outer supersonic flow, thereby causing a change in the strength of the first shock wave and a downstream-propagating pressure disturbance. It is the latter which gives rise to the unsteady oscillation of the interacting inviscid and viscous flow. For small angles of attack, comparisons between experiments and a small-disturbance stability analysis are generally favorable, indicating that this mechanism can be more or less understood theoretically. What is less certain is when the theory is applicable.

Type 2. Often the upstream-traveling, shock-induced disturbances tend to accumulate at a certain point *just outside the boundary layer. However, the pressure rise can be transmitted upstream around the* supersonic zone and through the outer subsonic region, as discussed earlier in connection with Fig. 15. After reaching the leading-edge region, these disturbances create new upstream flow conditions which tend to return the aft flow to its initial state. The process then repeats itself.

Type 3. At large angles of attack in which the upper-surface separated region extends from the shock wave past the trailing edge, Fig. 14(b) for example, the frequency tends to be lower and the amplitude larger. Now disturbances also travel upstream in the subsonic region on the lower side of the profile and, by the arguments set forth earlier concerning the speed of upstream propagation against different local Mach numbers, significant phase differences can be expected in the unsteady pressures on the top and bottom surfaces. Associated with the oscillating pressure field will be fluctuating lift, and hence oscillations *in circulation around the profile. The oscillating bound circulation* will be accompanied in turn by oscillations of the circulation in the wake, but with the opposite sign.

Type 4. Oscillating trailing edge and wake conditions can manifest themselves in another way, in the lateral direction. If the boundary layer at the rear portion of the wing separates, unsteady pressure disturbances are produced in the outer subsonic flow which propagate downstream and upstream. The shock wave travels into regions of smaller Mach numbers, and the angle between the edge of the separated boundary layer and the freestream direction is reduced. Then negative pressure disturbances in the outer flow downstream of the shock wave are produced and the shock wave is forced to move downstream again. The lateral oscillation of the wake is particularly intense for the biconvex circular-arc airfoil; for example, see Figs. 16 and 17.

In general, the third and fourth mechanisms, which involve large amounts of boundary-layer separation, are extremely difficult to analyze theoretically or to predict with any degree of confidence. Nevertheless, the calculations displayed in Fig. 17 show that time-dependent solutions of Reynolds-averaged compressible Navier-Stokes calculations can predict the phenomena in some detail. Even though such calculations are presently much too lengthy for routine engineering purposes and even though improved turbulence models will be required for accurate predictions, the study reported in Ref. 23 is extremely encouraging. More discussion of this approach will be given in a subsequent lecture.

5.0 CONCLUDING REMARKS

Three important classes of unsteady external flows over thin profiles have been described in detail; all three are inadequately understood and in each case satisfactory engineering prediction methods are lacking. They are presently receiving considerable attention, however, and improvements are being realized rapidly. The ability to predict and suppress unsteady separation on oscillating control surfaces, wings, and rotating blades will undoubtably lead to significantly improved aerodynamic devices.

6.0 REFERENCES

1. McCroskey, W. J.: "Some Current Research in Unsteady Fluid Dynamics." ASME J. Fluids Engr., vol. 99, no. 1, Mar. 1977, pp. 8 - 38.

2. Brown, S. N., and Daniels, P. G.: "On the Viscous Flow about the Trailing Edge of a Rapidly Oscillating Plate." J. Fluid Mech., vol. 67, Part 4, Feb. 1975, pp. 743 - 761.

3. Kadlec, R. A., Davis, S. S.: "Visualization of Quasi-Periodic Unsteady Flow." AIAA/ASME 19th Structures, Structural Dynamics and Materials Conf., Apr. 1978.

4. Gostelow, J. P.: "Trailing Edge Flows over Turbomachine Blades and the Kutta-Joukowsky Condition." ASME Paper 75-GT-94, Mar. 1975.

5. Sears, W. R.: "Unsteady Motion of Airfoils with Boundary Layer Separation." AIAA J., vol. 14, no. 2, Feb. 1976, pp. 216 - 220.

6. McCroskey, W. J.: "Recent Developments in Dynamic Stall." Symposium on Unsteady Aerodynamics, Kinney, R. B., ed., Tucson: Univ. Arizona, 1975, pp. 1 - 33.

7. Philippe, J. J.: "Le Déchrochage Dynamique: un Exemple d'Interaction Forte entre Ecoulements Visqueux et Non-Visqueux." AGARD CP-227, Paper No. 21, 1977.

8. Ham, N. D., and Garelick, M. S.: "Dynamic Stall Considerations in Helicopter Rotors." J. Am. Helicopter Soc., vol. 13, no. 2, Apr. 1968, pp. 49 - 55.

9. Ham, N. D.: "Aerodynamic Loading on a Two-Dimensional Airfoil during Dynamic Stall." AIAA J., vol. 16, no. 10, Oct. 1968, pp. 1927 - 1934.

10. Carr, L. W., McAlister, K. W., and McCroskey, W. J.: "Analysis of the Development of Dynamic Stall Based on Oscillating Airfoil Experiments." NASA TN-D 8382, Jan. 1977; also AIAA J., vol. 14, no. 1, Jan. 1976, pp. 57 - 63.

11. Mehta, U. B.: "Dynamic Stall of an Oscillating Airfoil." AGARD CP-227, Paper No. 23, 1977.

12. Werlé, H., private communication, 1976.

13. McAlister, K. W., Carr, L. W., and McCroskey, W. J.: "Dynamic Stall Experiments on the NASA 0012 Airfoil." NASA TP-1100, 1977.

14. Philippe, J. J., and Sagner, M.: "Calcul et Mesure des Forces Aérodynamiques sur un Profil Oscillant, avec et sans Déchrochage." AGARD CP-111, Paper No. 11, 1972.

15. Liiva, J. et al.: "Two-Dimensional Tests of Airfoils Oscillating near Stall." U.S. Army Aviation Material Lab., Fort Eustis, Va., Tech. Report 68-13, Apr. 1978; also J. Aircraft, vol. 6, no. 1, Jan. 1969, pp. 46 - 51.

16. Fukushima, T., and Dadone, L. U.: "Comparison of Dynamic Stall Phenomena for Pitching and Vertical Translation Motions." NASA CR-2793, Feb. 1977.

17. Saxena, L. S., Fejer, A. A., and Morkovin, M. V.: "Features of Unsteady Flows over Airfoils." AGARD CP-227, Paper No. 22, 1977.

18. Rabont, J., et al.: "Recollement Dynamique sur un Profil d'Aile en Mouvement de Tamis: Influence des Parametres d'Oscillation." AGARD CP-227, Paper No. 29, 1977.

19. Pierce, G. A., Kunz, D. L., and Malone, J. B.: "The Effect of Varying Freestream Velocity on Dynamic Stall Characteristics." Proc. 32nd Annual Forum Am. Helicopter Soc., May 1976, Preprint No. 1036.

20. McCroskey, W. J., and Fisher, R. K., Jr.: "Detailed Aerodynamic Measurements on a Model Rotor in the Blade Stall Regime." J. Am. Helicopter Soc., vol. 17, no. 1, Jan. 1972, pp. 20 - 30.

21. Ward, J. F.: "Helicopter Rotor Periodic Differential Pressures and Structural Response Measured in Transient and Steady-State Maneuvers." J. Am. Helicopter Soc., vol. 16, no. 1, Jan. 1971, pp. 16 - 25.

22. Byham, G. M., and Beddoes, T. S.: "The Importance of Unsteady Aerodynamics in Rotor Calculations." AGARD CP-227, Paper No. 33, 1977.

23. Levy, L. L., Jr.: "An Experimental and Computational Investigation of the Steady and Unsteady Transonic Flow Field about an Airfoil in a Solid-Wall Test Channel." AIAA Paper 77-678, Jun. 1977.

24. Finke, K., "Unsteady Shock Wave Boundary Layer Interaction on Profiles in Transonic Flow." AGARD CP-168, Paper No. 28, 1975.

INVISCID FLUID MODELS, BASED ON ROLLED-UP VORTEX SHEETS, FOR THREE-DIMENSIONAL SEPARATION AT HIGH REYNOLDS NUMBER

by

J. H. B. Smith

Aerodynamics Department, Royal Aircraft Establishment,
Farnborough, Hants. UK

SUMMARY

The text falls into two parts. In the first, the inviscid fluid models which have been used to represent flows with three-dimensional separations of vortex type are introduced and described. Their strengths and weaknesses are discussed and suggestions are made for improvements. A selection of results for a wide range of problems is presented. In the second, the difficulties which arise in trying to extend these models to represent separation from highly swept separation lines on smooth bodies are discussed and a view is given of the present position and developments in the immediate future.

The material is to be presented as two lectures in the AGARD-VKI Lecture Series 94 "Three-dimensional and unsteady separation at high Reynolds numbers" in February 1978.

1 CASES IN WHICH THE SEPARATION LINE IS DETERMINED BY THE BODY SHAPE

1.1 Introduction - the delta wing at incidence

By way of introduction, a description is given of a flow for which we have reasonably good inviscid models of the striking effects of flow separation. Consider a flat-plate delta wing whose aspect ratio is small, say about one, at an angle of incidence between about 5^o and 40^o to a subsonic stream at a high Reynolds number. A pair of vortices sits above the upper surface of the wing, just inboard of the leading edges. These sweep the flow on the upper surface of the wing outboard towards the leading edges. The flow on the lower surface is also directed outboard close to the leading edge, so that the flow leaves both surfaces at the leading edge to form a shear layer. At the leading edge, the shear layer is formed by the amalgamation of the two three-dimensional boundary layers on the wing. These merge and the layer develops subsequently under the influence of the essentially inviscid flow outside it. The shear layer is convected upwards and wrapped round the outside of the vortex by the mean velocity field. Thus the size and strength of the vortex grow in the downstream direction from a notional zero at the apex of the wing.

On the upper surface of the wing, surface oil-flow pictures show the herring-bone pattern associated with an attachment line. At high incidence there is just one of these along the centre line, at lower incidences there is a pair, with the flow between them almost parallel to the centre line. A sketch of this pattern is shown in Fig 1, for a wing with curved leading edges. Outboard of the attachment lines the air in the boundary layer is swept further outboard. Initially, as the suction peak under the vortex is approached, this flow is assisted by a favourable pressure gradient, but once the suction peak is passed the pressure gradient becomes adverse. In these circumstances a laminar boundary layer separates almost at once; a turbulent one holds on a little longer; but in both cases a secondary separation occurs. This usually shows in the surface oil-flow as a line where pigment accumulates, but sometimes the oil which collects there washes the pigment away, leaving the model surface visible. This separation line, like the primary separation line at the leading edge, is highly swept, and the separation again takes the form of a vortex. The sense of rotation of this secondary vortex is opposite to that of the primary, and the inboard trend of the surface oil-flow beneath it can usually be seen. There is evidence that the presence of this secondary vortex affects the remainder of the flow (see, eg, Ref 1). In particular it appears to change the surface pressure distribution in different ways, depending on whether the boundary layer is laminar or turbulent at the secondary separation line. Modelling the secondary separation is a topic for section 2, where separation from smooth surfaces is considered. For the present we simply bear it in mind as an unrepresented feature of the real flow.

Another unrepresented feature of the real flow is the occurrence of vortex breakdown at sufficiently large angles of incidence. This appears as an increase in the diameter and turbulence level of the core of the vortex, usually as a response to a rise in the ambient pressure. The underlying mechanism is still in some doubt[2]. There is some recent Japanese work[3] in which breakdown appears to have been predicted successfully through a viscous calculation, while in recent Russian work[4] it apparently emerges from an inviscid model. We shall not be dealing with the phenomenon.

At the trailing edge of the wing, the flow separates in the usual way to form a wake, as sketched in Fig 2. Rather surprisingly, most of the circulation shed from the trailing edge is also of the opposite sense to that in the primary vortex. The wake tends to be swept outboard by the substantial mean lateral velocities induced by the primary vortex above it. Several vortices may be formed and the flow downstream of the trailing edge is complex. If a model of the flow is to represent the upstream effects of the wake, it needs to represent the trailing edge separation properly, as well as the leading-edge separation.

1.2 Inviscid modelling of the delta wing flow

If we imagine the Reynolds number of this flow to increase, we shall find the boundary layers and shear layers becoming thinner. Instead of losing track of the shear layer from the leading edge where it meets the vortex, we shall be able to distinguish a thin shear layer rolling up into a spiral form, with more and more turns becoming apparent as the Reynolds number rises. This is the situation depicted in Fig 2. More details of the vortex structure are given in Ref 5. A viscous core will always remain at finite Reynolds number, but this is very small. If we proceed to the limit of infinite Reynolds number, the vortex becomes a spiral vortex sheet embedded in an irrotational, potential flow. This is the usual limit employed in the first approximation of aerodynamics, in which the thickness of the boundary layer and wake is ignored. Just as in classical wing aerodynamics the wake leaving the trailing edge is represented by a vortex sheet, implying the Kutta condition of finite velocity and continuous pressure at the sharp trailing edge, so, in this model of leading-edge separation, the shear layer leaving the leading-edge is represented by a vortex sheet, implying a Kutta condition of finite velocity at the sharp leading-edge. In both cases the potential flow becomes uniquely defined when the separation line is specified. The difference is the practical one that the properties of the classical wing can be obtained adequately without knowing the shape of the trailing-edge vortex sheet, while the properties of the slender wing depend on the shape taken up by the leading-edge vortex sheet. The difference arises simply from the proximity of the leading-edge vortex sheet to the wing.

The same model of the flow can be reached by choosing to represent the actual vorticity distribution present in the vortex at a finite Reynolds number by a spiral vortex sheet. However, the motivation is then less clear. Whichever approach is used, it is this picture of the vortex and its feeding shear layer as a single, infinitely rolled-up, vortex sheet which forms the basis for the inviscid treatment of separation from highly-swept separation lines.

Many attempts have been made to determine the form of the inner part of such a spiral. If the shape is basically circular, there is general agreement[6,7] about the existence of an asymptotic solution. However, it is likely that the spiral is generally somewhat elliptical in form, being flattened by its closeness to the wing surface[8]. A solution of this kind has been proposed by Maskell[9], but no fully documented solution exists and it is not even clear that the asymptotic problem is well posed[10]. There are also strong effects of compressibility[11,12] on the structure of the inner parts of conical vortices and of viscosity[13] very close to their axes. It seems likely that if the details of the flow in the inner region are required, they can best be obtained by patching an appropriate solution for the inner part of the vortex into an adequately described outer flow field. The kind of calculations with which we shall be concerned here provide little information about the behaviour of the inner part of the spiral.

1.3 Description of various particular models

The first of these models to be discussed preserves the identity of the outer part of the spiral vortex sheet, but introduces a simplified representation of the inner part. This is easiest to visualize in terms of the slender-body approximation, though the treatment has recently been applied at Boeing[14,15] in the context of subsonic lifting-surface theory. In slender-body theory we deal with solutions of quasi-two-dimensional problems of incompressible potential flow in planes at right angles to the free-stream direction. From now on, we shall be discussing irrotational flows in which vorticity is condensed into vortex sheets and line vortices. We shall use the same word 'vorticity' to refer to the strength of a vortex sheet, ie, a vector equal in magnitude to the jump in the tangential component of the velocity across the sheet, with a direction normal to this jump and tangential to the sheet. This appears to be common usage and need cause no confusion.

In slender-body theory, the only component of vorticity which enters the calculation of the induced velocity field is the streamwise, or trailing, component. The vorticity can then therefore be treated as a scalar, equal to the jump in the component of velocity in the cross-flow plane tangential to the vortex sheet. The condition that the pressure is continuous across the sheet is satisfied by relating this jump, Δv_t , to the jump in the streamwise component of velocity, Δu , by

$$U\Delta u + v_{t_m} \Delta v_t = 0 \quad . \qquad (1)$$

Here U is the undisturbed speed and v_{t_m} is the mean, or convective, tangential velocity on the sheet in the cross-flow plane. We note in passing that this equation is nonlinear in the disturbance velocities. This nonlinearity arises because, in the slender-body approximation to Bernoulli's equation the quadratic terms in the cross-flow plane are of the same order as the linear term in the streamwise disturbance.

The simplification in the representation of the inner part of the spiral vortex sheet is best thought of in the cross-flow plane. All the vorticity on the inner part of the sheet is condensed into a line vortex, at a point to be determined. Since the strength of this vortex will not, in general, be the same in different cross-flow planes and its connection with the wing has been broken, Kelvin's theorem is violated and some inconsistency is to be expected. This inconsistency takes the form of a local force sustained by the fluid. Because the circulation, Γ, round the line vortex changes with the streamwise coordinate, x, there is a jump in the value of u on any path surrounding the vortex:

$$\Delta u = \Delta \frac{\partial \Phi}{\partial x} = \frac{\partial}{\partial x} \Delta \Phi = \frac{d\Gamma}{dx} \neq 0 \quad . \tag{2}$$

To make Φ and u single-valued, a cut must be introduced connecting the free end of the outer part of the vortex sheet to the line vortex, so forbidding the description of paths round the vortex. Wherever the cut is placed, equation (1) is violated across it, because $\Delta u \neq 0$ and $\Delta v_t = 0$. The resulting difference in pressure is the same along the whole length of the cut in the cross-flow plane, so that the force acting on it in the cross-flow plane is independent of its shape. This force in the fluid is proportional to $d\Gamma/dx$ and to the distance from the end of the outer part of the sheet to the line vortex. We now choose to balance this force by a force on the line vortex, ie the line vortex is deliberately inclined to the local flow direction. Fig 3 shows the resulting configuration. The equation expressing this condition of zero total force on the vortex and the cut can be shown[31] to take the form:

$$(Z_v - Z_E)\frac{d\Gamma}{dx} + \Gamma \frac{dZ_v}{dx} = \Gamma\, \overline{\lim_{Z \to Z_v} \frac{d}{dZ}\left(\frac{W}{U} - \frac{\Gamma}{2\pi i U}\ln(Z - Z_v)\right)} \quad . \tag{3}$$

Here the cross-flow plane is described by the complex variable Z, taking the values Z_v and Z_E at the line vortex and the free end of the sheet, W is the complex velocity potential, the form of the right-hand side arises from a consideration of the velocity induced at the line vortex, and the over-bar denotes the complex conjugate.

Equation (3) is two real equations, which it is helpful to regard as determining the inclination of the vortex, dZ_v/dx. The strength, Γ, of the vortex can be regarded as determined by the Kutta condition at the leading edge, where $Z = s$:

$$\lim_{Z \to s} \frac{dW}{dZ} \quad \text{is finite} \; . \tag{4}$$

The conditions to be satisfied on the outer part of the vortex sheet are that it should be a stream surface of the three-dimensional flow and that the pressure should be continuous across it. The first of these yields a relationship between the component of velocity, v_n, in the cross-flow plane and normal to the section of the sheet and the rate of growth of the sheet in the streamwise direction. Various forms are useful, but a particularly simple one is:

$$\frac{v_n}{U} = -\frac{\partial r}{\partial x} \sin \phi \quad . \tag{5}$$

Here we have supposed that the shape of the sheet is described by specifying the polar coordinate r as a function of x and the polar angle θ, where $Z = re^{i\theta}$, (see Fig 3). The angle ϕ is the angle between the tangent and the radius vector, all in the cross-flow plane. The condition of pressure continuity is equation (1), but it is useful to remove the explicit dependence on u. The analysis of Refs 16 and 86 leads to

$$\frac{\partial \Delta \Phi}{\partial x} = \Delta v_t \left(\frac{\partial r}{\partial x} \cos \phi - \frac{v_{t_m}}{U}\right) \quad . \tag{6}$$

Here $\Delta\Phi$, the jump in potential across the sheet, is also a function of x and θ.

If we suppose that the shape of the sheet and its strength are given numerically by N values of r and N values of $\Delta\Phi$ at specified values of θ, we can see that the rates of change of these $2N$ unknowns are determined in principle by applying equations (5) and (6) at N points on the sheet. If the whole configuration, wing shape, vortex position, sheet shape and sheet strength are known at some value of x, the equations (3) to (6) determine the derivatives of these quantities in the streamwise direction. A numerical marching solution is then possible[16,17] and we shall describe results obtained in this way later.

Alternatively, if we suppose the solution is conical, a supposition which is obviously consistent with the slender-body approximation for flow past a plane delta wing, we have

$$\frac{d\Gamma}{dx} = \frac{\Gamma}{x}\, , \quad \frac{dZ_v}{dx} = \frac{Z_v}{x}\, , \quad \frac{\partial r}{\partial x} = \frac{r}{x}\, , \quad \frac{\partial \Delta\Phi}{\partial x} = \frac{\Delta\Phi}{x} \quad . \tag{7}$$

When these expressions for the derivatives are introduced into (3), (5) and (6), a set of nonlinear and strongly coupled equations emerges, to which solutions can be found by numerical methods[8,18-21]. Equations of the same form emerge if self-similar solutions[22] are sought in which (7) is replaced by relations involving general powers of x. Such a conical or self-similar solution can provide the initial values for the solution of the system of differential equations (3) to (6).

We shall later describe some of the illuminating results obtained from this model. Meanwhile, before the consideration of other inviscid models, two difficulties with this one should be pointed out. The first arises from the enforced rotational symmetry of the inner part of the vortex. As mentioned earlier, calculations[8] using the model show that the inner part of the vortex has a measure of ellipticity. This ellipticity is likely to be large when the vortex is close to a boundary. Failure to represent it may be responsible for some of the difficulties which have been found with the model for vortices close to the wing surface[23,24]. Before further attempts are made on problems of this kind, a model incorporating an elliptic core region needs to be developed. The second difficulty concerns the self-induced velocity of the line vortex. Within the slender-body approximation there is no problem; the vortex is regarded as being straight. However, if we move away from this approximation, the curvature of the line vortex cannot be ignored, since it leads formally to an infinite local contribution to the self-induced velocity. The correct treatment is to evaluate the local contribution to the self-induced velocity by a more complete model. Returning to a vortex of finite diameter, related to the dimensions of the outer part of the sheet, we find that the local contribution to the self-induced velocity is finite, depending strongly on the ratio of its diameter to its radius of curvature and rather weakly on the distribution of vorticity inside it. Details appear in Ref 25. Plausible distributions of vorticity can be derived from the solutions mentioned above for the inner parts of vortices.

The second inviscid model of flow separated from a sharp edge can be thought of as a special case of the first. If the vortex sheet is omitted altogether, the entire circulation of the leading-edge vortex is condensed into a single line vortex and a far simpler model results. This was finally formulated by Brown and Michael[24], as a result of earlier work by Legendre[27,28], Adams[29] and Edwards[30]. Brown and Michael visualized the cut, which now connects the line vortex to the leading edge, as a planar vortex sheet composed entirely of transverse, or bound, vorticity. Viewed in this way, it provides continuity between the vortex lines in the wing and the line vortex representing the leading-edge vortex, but at the expense of kinks in the vortex lines. The mathematical consequences, at least in the context of slender-body theory, are the same as those derived above. The governing equations for non-conical flow[31] are simply (3) and (4) above, with

$$Z_E = s , \tag{8}$$

corresponding to the elimination of the vortex sheet. The original equations given by Brown and Michael for conical flow follow with the substitutions (7). The simplicity of this model has led to its wide application, both within the confines of slender-body theory and beyond. Generally speaking, computational difficulties are not serious, but it should not be assumed that a solution always exists (see, eg, Barsby[32]) nor that it is unique (see, eg, Levinsky and Wei[19]).

The third model is rather different and has the great advantage of being readily extended from the slender-body approximation to fully three-dimensional incompressible flow. If we think again of the infinitely rolled-up spiral vortex sheet springing from the wing leading edge, we can imagine drawn on the sheet lines along which the jump in velocity potential across the sheet is the same. These lines of constant $\Delta\Phi$ are also streamlines of the mean flow in the sheet, ie, they bisect the angle between the two streamlines on the inside and outside of the sheet at each point. Each such line will start at a point on the leading edge and follow a helical path on the sheet, turning about the axis of the vortex as it proceeds downstream, but not getting very much closer to or further from this axis. These lines divide the sheet up into ribbons. The circulation about each ribbon is the same along the whole of its length and each ribbon springs from the leading edge. If the ribbon is reasonably narrow, the direction of the vorticity in it is nearly the same across the width of the ribbon, being parallel to the edges at the edges. Hence we can concentrate the vorticity lying in the ribbon into a line vortex along its middle line. This leads us to a model consisting of a set of line vortices which spring from the leading-edge and follow helical paths round the axis of the leading-edge vortex as they are convected downstream.

Each line vortex is of constant strength, so it must follow a streamline of the three-dimensional steady flow. Its strength must be based on the Kutta condition at the leading edge. In several practical calculation procedures[33-35] for three-dimensional incompressible flow, the wing is represented by a vortex lattice, so that the Kutta condition is replaced by a requirement for the continuity of the vortices between the wing representation and the sheet representation, just as for the Kutta condition at the trailing edge. The use of the vortex lattice approach makes for conceptual simplicity and great flexibility, but also raises questions about the sensitivity of the results to the details of the lattice and the positioning of the control points. One apparent difficulty can be disposed of, however. The use of curved line vortices invites questions about their infinite self-induced velocity. Again, we return to a better model to resolve the question. This time the better model is the vortex sheet, which produces no local self-induced velocity. The infinite local contribution to the self-induced velocity of the curved line vortex should therefore be omitted in this case.

The first use of the model was by Sacks et al[36], in the slender-body approximation. A different approach is then needed to obtain the circulation of the shed vortex from the Kutta condition at the leading edge. Within this approach it is possible to handle dozens of vortices, representing a fine subdivision of the original vortex sheet. Unfortunately, the increase in the number of vortices results in the emergence of instability, leading to a chaotic distribution of vortices in place of the orderly spiral shape which we imagined. A useful device to delay the onset of instability without loss of accuracy has recently been demonstrated by Fink and Soh[37]. They redistribute the circulation amongst the vortices after every step in the marching process in the downstream direction, in such a way that the vortices remain equally spaced along the curve which represents the sheet. Another useful technique for delaying the onset of instability was used by Moore[38]. Unlike the other workers with this model, he treats the vortex nearest the centre of the spiral differently, regarding it as representing a core of the rolled-up vortex. He tests the angle which the next two vortices subtend at the core vortex and, when this angle exceeds 90°, he amalgamates the penultimate vortex with the core vortex. This has the effect of shortening the length of the sheet which is represented. The basis for it is that at least four vortices are needed to provide even a nominal representation of a turn of the spiral.

These more elaborate techniques have been developed for the slender-body approximation or for time-dependent planar flows. The published work in fully three-dimensional flows has not required them because the number of free vortices has remained fairly small. Vortex amalgamation has however been used in three-dimensional wake roll-up calculations.

A conceptual difficulty arises over the treatment of the vortex ribbon closest to the apex of a delta wing. One edge of this ribbon originates at the apex and, in our ideal picture, runs along the axis of the vortex. The other edge follows a helix around this axis. The ribbon between these edges forms the whole inner part of the spiral vortex sheet and representing it by a single spiralling vortex appears a rather drastic approximation. Computations[39,40] show that this first vortex does not lie at all close to the axis of the spiral sheet, confirming the difficulty. Increasing the number of vortices would probably improve the situation. A more elegant way of improving it would be to modify the model so that the first vortex actually starts from the wing apex with zero strength and grows, as in the Brown and Michael[26] model, until the second vortex is shed from the edge. The first vortex would then be freed to follow a streamline and the second one allowed to grow in strength until the third one is shed, and so on. Such a treatment would provide a core around which the other vortices could gyrate in a more stable manner, and with which amalgamation could take place downstream. This modification could be regarded as representing each ribbon of vortex sheet by a pair of vortices along its edges.

The final group of models are to some extent less representative of the physics of the flow in that some assumption is made about the form of the shed vorticity. The simplest of these assumptions is that the shed vorticity is so close to the plane of the wing that its effects can be calculated as if it were actually in that plane. Surprisingly, such a simple treatment, guided by a little empiricism, does produce a model from which conclusions can be drawn. Moreover, the model, due to Küchemann[41], has been extended to supersonic speeds in two slightly different ways[42,43]. In passing, it is worth noting that the shed vorticity does lie appreciably closer to the wing, for the same incidence, at supersonic speeds than at subsonic speeds.

The next, and historically the first[44], idea is to localize the vorticity shed from the side edges or streamwise tips of a wing on sheets which lie at right angles to the wing and extend upwards some way towards the free stream direction. These sheets have an obvious resemblance to end-plates, though, of course, they should be force-free. Little work has been done with this model, perhaps because tip separation is not very important on wings of high aspect ratio, while rectangular wings of low aspect ratio on guided missiles are usually so thin that leading-edge separation complicates the flow. Perhaps now that attempts to calculate the boundary layer on the upper surface of a finite wing are encountering problems because the external flow comes round the tip from the lower surface, this kind of model will be re-examined.

Finally, in the model due to Gersten[45], vorticity is shed at a fixed angle of one-half the angle of incidence from every point of the wing. Although this sounds very crude, it is clearly possible for vorticity to be represented at the points in the flow field at which it is present in real flows. The model proved relatively easy to integrate with existing subsonic lifting surface theories and good results were obtained for overall lift and pitching moment. It could also readily be extended to unsteady flow, again yielding good agreement with experimental results for overall forces and moments.

1.4 The use of the models summarized

Table 1 lists a great deal of the work that has been done with these various models. Completeness has not been sought, though almost all work on the first three models has been quoted, and an attempt has been made to include both the earliest and latest references in each area. The models are listed down the left-hand side in the order in which they have been described. At the bottom comes the leading-edge suction analogy[46,47].

This is not really a model of separated flow, but it is a remarkably successful way of prediciting lift, drag, pitching moment and roll damping of plane wings. Across the top are three flow regimes, distinguished by the different forms taken by the continuity equation for small disturbance, potential flow: Laplace's equation for incompressible and subsonic flow, the two-dimensional form of Laplace's equation for the slender-body approximation, and the wave equation for supersonic flow.

It is clear that very little has been done specifically for supersonic flow. This clearly reflects the difficulty of applying any but the simplest of models. There is also an obvious dominance of papers using the slender-body approximation. The great simplicity to which this approximation leads has made it possible to treat a great variety of boundary conditions, representing many different physical problems. Effects of thickness[48,60] and camber[16,32,58,59] separately and together[62], effects of yaw[20,49] and roll[17,61], effects of pitching and plunging oscillations[50,55,56] and effects of gusts and sudden changes of incidence[57] have all been treated. Combinations of wings and bodies[19] and of wings and foreplanes[67] have been studied and a wing design problem has been attempted[53]. All this work is subject to the serious limitations of the slender-body approximation. In particular, because the theory allows no signals to propagate upstream, loadings calculated for subsonic flow do not fall off correctly as the trailing edge is approached. Overall forces and moments are therefore incorrectly predicted at subsonic speeds. At supersonic speeds, nonlinear effects of leading-edge separation fall off rapidly as the Mach number normal to the leading edge rises towards one, so once again slender-body estimates are not very useful. Comparisons with experiment designed to test the validity of the separated flow models must therefore usually be based on measurements[78] made on the forward part of a wing at subsonic speeds. Measurements at transonic speeds can also provide useful evidence, but little work has been done in this area.

Table 1

Work with inviscid models of separation from sharp edges

Model \ Regime	Incompressible and subsonic	Slender-body theory	Supersonic
Vortex sheet	Weber et al[14] Johnson et al[15]	Mangler and Smith[18] Smith[8,22,48] Levinsky and Wei[19] Barsby[21,23,32] Pullin[20] Jones[17,49] Cooper[50] Clark[16]	
Single line vortex	Nangia and Hancock[51] Matoi et al[52]	Legendre[27,28] Adams[29] Edwards[30] Brown and Michael[26] Smith[31,53,54] Randall[55] Lowson[56] Dore[57] Jobe[58] Squire[59] Portnoy and Russell[60] Hanin and Mishne[61] Clark et al[62]	Nenni and Tung[63] Nikolskii[64]
Multiple line vortices	Belotserkovskii[33] Rehbach[34,39,65] Maskew[66] Kandil et al[35,40] Aparinov et al[4]	Sacks et al[36] Finkleman[67] Fink and Soh[37]	
Planar		Küchemann[41]	Squire[42] Carafoli[43]
End-plate	Küchemann[41] Ermolenko[68]	Betz[44] Bollay[69]	
Distributed vorticity	Gersten[45,70] Garner and Lehrian[71,72]	Garner and Lehrian[71] Nikolitsch[73]	
Leading-edge suction analogy	Polhamus[46,47] Boyden[74] Bradley et al[75] Lamar[76]		Davenport[77]

What then do such comparisons tell us about the validity of the models? The present context does not permit a balanced presentation of the experimental evidence, so what follows can only be a personal verdict. The vortex sheet model appears to give reasonably reliable predictions of the shape, position and strength of the leading-edge vortex for the classical case of the flat-plate delta wing at moderate to large incidence. The lift on the forward part of the wing is also well predicted. The prediction of the pressure distribution over the forward part of the wing is good, except for the form of the suction peak when the secondary separation is laminar. Small discrepancies in the lateral position of the vortex can be attributed with some confidence to the absence of any representation of secondary separation, a defect shared by all the models. There is less experimental information available for the other problems to which the model has been applied, but nothing suggests any marked loss of accuracy. These conclusions relate to calculations using a vortex sheet which extends for a quarter of a turn or more about the central line vortex.

If there is no sheet, this model reduces to the second, the single line vortex model. For the flat-plate delta wing, this gives a significant over-estimate of vortex strength and lift, probably because the vorticity is concentrated away from the leading edge, where it could have exerted a stronger influence on the Kutta condition. The height of the vortex is well predicted, but its lateral position is further outboard than that predicted by the sheet model, which is itself a little outboard of the true position. There is some evidence[23,32], based on comparison with the sheet model, that the single vortex model becomes rather more accurate for weak vortices.

The multivortex model gives very similar results to the vortex sheet model when a large number of vortices are employed (Sacks et al[36] used as many as 96), so long as the somewhat chaotic distribution of the individual vortices is unimportant. With a small number of vortices, the flow near the apex of a delta wing is not well represented, so pitching moment is more in error than lift. Overall lift is given accurately by Rehbach[65] and by Kandil et al[35] for low speed flow. The general location of the shed vorticity is also well predicted, though it appears to extend rather further inboard in the calculations than is found experimentally.

The planar model is really only of continuing interest because it can be applied to estimate the lift and pressure distribution at supersonic speeds. The end-plate model successfully predicts the lift and pitching moment of rectangular wings and predicts (or assumes) an appropriate location for the shed vorticity. The distributed vorticity model gives overall lift and pitching moment quite accurately and also gives a good indication of the spanwise loading on rectangular wings. None of these simple models appears to have much future application as modern computing power makes the more representative multivortex and vortex sheet models possible to apply outside the bounds of slender-body theory. The leading-edge suction analogy is, as remarked above, very successful as a means of predicting overall forces and moments. By its nature, it cannot provide information about the leading-edge vortex, nor generate a pressure distribution.

1.5 Examples of results obtained with the vortex-sheet model

Now let us look at some results to see what sort of information the more elaborate models can provide. As before, we start with the vortex-sheet model, and most of the examples involve the slender-body approximation.

Fig 4 shows a comparison of calculated and measured surface pressure distributions on a flat-plate delta wing at low speeds. The measurements by Hummel and Redeker[79], are at four different lengthwise stations along the wing and show that the flow is markedly non-conical. The calculations for separated flow are shown by the broken line. With the slender-body approximation, the model is conical; so the same pressure distribution is predicted at all stations, in terms of the conical similarity variable, spanwise distance y divided by local semi-span $s(x)$. On both the upper and lower surfaces very good agreement is achieved near the apex of the wing, the only significant discrepancy occurring near the leading-edge on the upper surface. Here secondary separation modifies the experimental distribution. The appreciable pressure rise achieved outboard of the peak suction shows that the secondary boundary layer was turbulent at separation. The chain-dotted curve is the theory for attached flow, which is clearly irrelevant in these conditions. The measurements suggest that the vortex sheet model is good, but would be improved if a representation of secondary separation could be incorporated. They also confirm the remarks above about the shortcomings of slender-body theory at low speeds. Fig 5 is another comparison between the same theory and experiments. Now it is the pattern of bound vortices which is displayed. These are the vortex lines which represent the total vorticity in the boundary layers on the upper and lower surfaces of the wing. Taken together with the vorticity shed from the leading and trailing edges of the wing, these vortices would induce the complete disturbance field of a thin wing. Again we see that theory and experiment agree closely near the apex of the wing. The deterioration towards the trailing edge is rather less marked than in the previous figure, suggesting that the direction of the disturbance velocity is predicted better than its magnitude. It is noteworthy that the configurations of both calculated and measured bound vortices are consistent with the earlier comment that most of the circulation shed from the trailing edge is in the opposite sense to that shed from the leading edge.

We now see in Fig 6 the effect of removing the slender-body assumption. The calculations here are the ones carried out at Boeing[14] and referred to earlier. The model is essentially the same vortex sheet model as on the two last figures, but here it is implemented by a subsonic panel method, so that the upstream influence of the trailing edge is represented. The experimental measurements are by Marsden, Simpson and Rainbird[80]. The form of the suction peak on the upper surface is rather different from that in Fig 4, at least near the apex, because the secondary boundary layer is laminar at separation, resulting in a much smaller pressure rise before secondary separation occurs. It is clear that the general form of the pressure distribution is now being predicted successfully over the whole wing. The need to represent the secondary separation is clearly greater when it is laminar. The wake modelling in these particular calculations is incomplete, but further developments have been reported since[15]. It is of some interest that the calculated shape of the vortex sheet is almost conical and very little different from that found with slender-body assumptions; it is its strength which falls off towards the trailing edge.

We now leave the simple flat-plate delta and return to calculations using slender-body assumptions, still with the vortex-sheet model. Fig 7 illustrates the way in which increasing thickness, associated here with increasing edge angle, reduces the lift. The configurations are rhombic cones of apex angle 2γ and edge angle δ, at incidence α. The experimental results were obtained by Kirkpatrick[81], using a split-model technique to measure the normal force on the forward part of a wind-tunnel model at low speeds. Note that the normal force coefficient has been divided by the incidence to give a sensitive presentation of the results. The bottom curve is the calculation for attached flow, valid here as a limiting value for zero incidence. The lift-slope falls off along it from the flat-plate value of 2π on the left. Each of the other curves, for increasing values of the incidence from the bottom to the top, has a set of experimental values associated with it. We see that the discrepancy between theory[48] and experiment increases as the thickness increases across the picture. This is consistent with an early observation[82] that secondary separation becomes more pronounced on thicker wedges. The theoretical work correctly predicts that the nonlinear lift is more affected by the increase in thickness than is the linear lift.

Turning now from conical thickness to conical camber, we see in Fig 8 a presentation of the effect of leading-edge separation on the lifting efficiency of delta wings[32]. The wings have cross-sections in the form of circular arcs, with camber p, as sketched. The ordinate is the lift-dependent drag factor

$$K = \pi A C_D / C_L^2 . \tag{9}$$

(Since this is an inviscid calculation, using slender-body theory for a thin wing, all the drag is vortex drag.) For attached flow past an essentially planar wing K has a lower bound of 1. The curves shown are for the indicated values of the lift coefficient C_L. Looking at the curve for $C_L = 0.1$, we see it terminates on the right at a point at which the flow is attached along the leading edge, ie the leading-edge droop is sufficient to suppress the separation. To the left of this, there is less droop and a vortex forms above the wing. K falls initially, showing an increase in aerodynamic efficiency as the flow separates. Experimental results[83] confirm that slender wings are more efficient if they are cambered to produce attached flow at an incidence below their intended operating points. For the large lift coefficients, Fig 8 shows that increases in camber up to the attachment condition are beneficial. This is probably because of the marked non-planarity of the wing at the larger values of p and it might not be found if the camber were confined to the leading-edge region.

Fig 9 is the last one illustrating a conical flow, again for the vortex-sheet model with slender-body assumptions. We have returned to the flat-plate wing, but it is now at a fixed angle of incidence, equal to half its apex angle, with varying angles of yaw or sideslip[49]. The upper half shows the calculated shapes of the vortex sheet on the leeward or retreating leading edge. As the yaw angle increases the vortex is swept outboard and lifts away from the wing. Note that for b greater than one, the edge is geometrically a trailing edge, but the local flow is unaware of any sudden change. The sheet on the windward, or advancing, edge is shown below at twice the scale of the upper half of Fig 9. Increasing yaw has much less effect on the form of the windward vortex. The same problem was treated by Pullin[20]; Jones[49] managed to cover a larger range of yaw angle.

We turn now to some non-conical configurations, still calculated by slender-body theory using the vortex-sheet model. The first of these, sketched in Fig 10, is a flat-plate wing with a curved leading edge . For x less than one, the leading edge is straight, so the flow is the same as on a delta wing. The leading edge then curves, becoming streamwise for x greater than two. The figure shows the vorticity in the vortex sheet, as a function of an angular coordinate, Θ along the sheet, in various cross-flow planes indicated by the values of x. The sign has been chosen so that the vorticity appears positive for the delta portion of the planform. Note how, as the leading-edge curves back towards the stream direction, the sheet vorticity falls, particularly at the leading edge. At $x = 2$, the vorticity being shed is of the opposite sign to that further along the sheet and in the core vortex. This shows that the vortex is locally stronger than would be needed to satisfy the Kutta condition. This negative vorticity is convected along the sheet, appearing further round at $x = 2.5$ and $x = 3$. Meanwhile, the vorticity shed from the edge becomes positive again. These results show the mechanism for the reduction in overall circulation predicted for such a wing by the single-vortex model[31]. The vortex-sheet shapes associated with the results of Fig 10 are smooth: the negative vorticity is apparently convected round the vortex in the same way as the positive vorticity.

Fig 11 shows the vorticity in the vortex sheet for another non-conical configuration. This is the delta wing with lengthwise camber whose centre section is sketched[16]. For x less than one, the local incidence is constant, and the distribution is that for a plane delta wing, as in the previous figure. As x increases, the local incidence falls. Some distance upstream of the station $x = 2$ where the local incidence vanishes, the shedding rate at the leading edge becomes negative and numerically very large. Clearly, the vortex is again stronger than is needed to satisfy the Kutta condition, and in this case the relation persists and intensifies instead of reverting to the conventional behaviour. Fig 11 suggests that the negative vorticity is accumulating near the leading edge instead of spreading round the sheet. The associated sheet shapes show that a large distortion builds up near the base of the sheet, suggesting that a distinct, counter-rotating vortex is forming. Ref 16 presents experimental evidence to show that such counter-rotating vortices are formed upstream of the station at which the local incidence vanishes. This is not a behaviour that can be predicted by the single-vortex model, which fails in these circumstances[55].

The last illustration of the predictions of the vortex sheet model is Fig 12, taken from calculations[50] by slender-body theory of the effect of small oscillations about a mean incidence. In this case the mean incidence is equal to half the apex angle of the delta wing and the oscillations are sinusoidal in heave. The figure shows how the phase angles of the various flow parameters change as the frequency increases. The non-dimensional frequency parameter is based on the distance x downstream of the apex. Since it is a heaving oscillation the effective incidence is always 90° in advance of the wing position. The circulation in the core lags behind the effective incidence, since it takes time for the vorticity shed from the leading edge to be convected into the core. Since the Kutta condition must be satisfied in each plane at each instant, the defect in core circulation must be compensated by an excess of sheet strength near the leading edge, so that the shedding rate must lead the effective incidence, as we see it does. The overall circulation reflects these two behaviours, lying between the curves for the core and the shedding rate, but closer to the former, because the bulk of the circulation is in the core. The scale of the effect can be grasped by noting that, if the wing moves forward a distance x in a quarter of the period of the oscillation, then at a distance x from the apex there are leads and lags of about 30°.

1.6 Examples of results obtained with the multivortex model

We come now to results obtained with the multivortex model. Fig 13 brings out the essential equivalence between the results of the multivortex model and the vortex sheet model. In this case both have been applied within the slender-body approximation. The figure is taken from Fink and Soh[37]. Their results are shown by the solid lines, comparable results[8] for the vortex sheet model being shown by broken lines. Above are vortex sheet shapes, below are pressure distributions on the wing, in each case for an angle of incidence equal to half the apex angle of the delta wing. It is clear that the absence of a representation of the core leads to some distortion of the sheet shape in the multivortex model, but the difference is aesthetic rather than practical. The extent of the leading-edge vortex and the surface pressure distributions are predicted almost identically.

In these calculations by slender-body theory, Fink and Soh were able to handle 70 vortices. For a fully three-dimensional calculation this would certainly be expensive and might be unmanageable. Fig 14 shows some results obtained by Rehbach[39] using nine vortices shed from points equally spaced along the leading edge of a delta wing in incompressible flow. The upper part shows cross-sections at 50%, 75% and 100% of the length from the apex. There is remarkably little change in the shape. This agrees with the observation above about the results obtained at Boeing[14] with the vortex-sheet model in incompressible flow: the vortex sheet was found to be almost conical. On the other hand, the Boeing results showed a vortex sheet shape which was almost the same as that found using slender-body theory, while the lower part of Fig 14 shows a large difference between Rehbach's multivortex configuration in the plane of the trailing edge and the slender-body vortex sheet configuration[8]. The lower part of Fig 14 is not in itself surprising, since we should expect to see differences between the slender-body theory and the full three-dimentional theory at the trailing edge. Moreover, the differences are in the direction we should expect from observation, which shows the vortex core turning closer to the free-stream direction near the trailing edge, ie, moving inboard and upwards relative to the wing semi-span. However the calculated changes in the vortex position, shown in the upper half of the picture, are small and in the opposite direction. It may be that we cannot expect to obtain details of this kind from a representation involving so few vortices, particularly if there is no distinct representation of the core.

Fig 15 is taken from Aparinov et al[4], who use essentially the same multivortex representation as Belotserkovskii[33] and Rehbach[34,39,65]. There appear to be only eight vortices shed from the leading edge, so it is doubtful whether the details emerge accurately. However, the overall picture is interesting, particularly for what it shows downstream of the trailing edge. The entire vortex configuration rises towards the free-stream direction, the vortex cores become more nearly parallel, and beneath the coiled sheets the individual vortices leaving the trailing edge are swept sharply outboard. The kink in the cross-section of the wake suggests that vorticity of the reversed sense is about to roll up into a distinct vortex, as sketched in Fig 2.

The first applications of the multivortex model were to side-edge, rather than leading-edge separation. Fig 16 shows calculations by Maskew[66] for a fully three-dimensional model of side-edge separation on two rectangular wings of aspect ratio one quarter, which had been tested by Wickens[84]. The upper part of the figure shows the configuration calculated for the plane wing, first from the side, then from above. Below are the same two views for the wing bent downwards at midchord. In each case the incidence of the forward part of the wing is 20°. For the lower configuration the rear of the wing is at a local incidence of 40°. The calculated vortex lines show a remarkably smooth evolution. This may be helped by the large angles of incidence which keep them well clear of the wings. In addition to the directly calculated vortex lines, the figure also shows the loci of the centroids of the individual vortices, calculated in cross-flow planes, as broken lines, and the cores of the vortices found by Wickens, as chain-dotted lines. These agree very closely in the side view at the top of the figure. For the bent wing, a second vortex core appeared in the experiment and Maskew has divided his vortices into two groups to represent these two cores. As the side view in the lower part of the figure shows, this is only qualitatively satisfactory.

In Fig 17 we return to quantitative comparisons with measured quantities. Rehbach[65] reported difficulty in obtaining good comparisons with measured pressure distributions using the multivortex model in its fully three-dimensional form. Fig 17 shows the loading calculated for a delta wing by Kandil et al[40], using what appears to be essentially the same model. The agreement with the measurements[80] is satisfactory enough when we observe from the form of the measured suction peak that it is for a laminar secondary separation. A turbulent secondary separation would have produced a higher peak, with a larger pressure recovery towards the leading edge. In their own paper[40] Kandil et al present a comparison with a load distribution measured on a wing with a turbulent secondary separation. The comparison is good, but the aspect ratio of the wing, the incidence and the measuring station are different from those used in the calculation. The results in Fig 17 were obtained with 12 vortices shed from the leading edge, so adequate load predictions can apparently be obtained without extremely detailed modelling.

Finally, in Fig 18 we revert to the slender-body approximation. Here the multi-vortex model has been applied to a wing and canard combination[67], sketched at the top of the figure. The results below show how the nonlinear part of the normal force builds up from the front to the rear of the canard and the wing. For the canard, the curve is almost parabolic as it would be if the flow were exactly conical and the normal force grew as the square of the local span. For the wing, however, the nonlinear part of the normal force is negative near the apex, because of the downwash induced by the vortices from the canard. Halfway back along the wing its local span becomes equal to the span of the canard and the normal force begins to increase. However, even at the trailing edge, the wing has not caught up with the canard. Finkleman[67] suggests this is a good reason to blunt the apex of the wing, as on the Viggen.

2 SEPARATION FROM SMOOTH SURFACES

2.1 Introduction

Section 1 demonstrated a considerable measure of success for inviscid models of three-dimensional flows separating from highly swept sharp edges. When separation takes place at a highly swept separation line on a smooth surface, we can again expect to find a shear layer leaving the surface and rolling up into a vortex. Again, we can expect that the vorticity shed will be approximately parallel to the free-stream direction. It is therefore reasonable to believe that the separated flow, except perhaps in the immediate neighbourhood of the separation line, can be represented by an inviscid model of the same type as was successful in describing the separated flow from a sharp edge. This leaves open the question of modelling the separation process, in particular, of determing the separation line.

Separation from highly swept separation lines on smooth surfaces is an important phenomenon on the forebodies of aircraft which are required to manoeuvre rapidly, on missiles and stores at high angles of incidence, on the rounded leading edges of Concorde, on the upper surfaces of slender wings beneath the primary vortices, on up-swept aft fuselages and, presumably, on the well-rounded leading edges of the Space Shuttle at landing conditions.

The classical aerodynamic approximation scheme is based on calculating the inviscid flow past the body, with a vortex sheet shed from the trailing edge; then using this inviscid flow as the external flow in a calculation of the development of the boundary layer and wake; and then using the displacement thickness of these layers to modify the shape of the body and inviscid wake as a basis for a further inviscid calculation. The methods which were discussed in section 1 are modifications to this classical aerodynamic scheme in which wakes are permitted to be shed from any sharp edge. Such modifications may be complicated in practice, but they are essentially simple in conception. They are also essentially limited in scope. In particular, if the boundary layer calculation breaks down, predicting separation upstream of the sharp edge, the classical approximation is strictly helpless. It is not even possible to conclude that separation would take place where it is predicted, because the external flow under which the boundary layer has developed contains no representation of the separation. Only if we have a smooth sequence of solutions, depending on a parameter such as the incidence, in which attached flows are found for $\alpha < \alpha_0$, while separation is predicted for $\alpha = \alpha_0$, can we say that we have a valid prediction of the separation line at $\alpha = \alpha_0$.

Now it is clear that there are methods of calculating three-dimensional boundary layers which do provide plausible indications of separation at highly-swept separation lines, whether or not these correspond quantitatively to real flows. Some of these are described in a recent review paper[85]. There is therefore a strong case for bringing together such boundary layer methods with the best inviscid models of separated flow. We can imagine, for instance, attempting an iterative calculation in the following way. A separation line is assumed well downstream of its likely position and a suitable inviscid model of the flow incorporating that separation line is calculated. A boundary layer starting at the front stagnation point is calculated using the calculated inviscid flow. We may suppose this separates upstream of the assumed separation line. A new separation line is now chosen between the assumed and calculated separation lines, and incorporated into the inviscid flow model. This new inviscid flow forms the basis for a new boundary layer calculation, and so on. This process may converge: if it does we appear to have a calculation of a consistent model of the separated flow.

This is all very generalized. To see where some of the difficulties lie let us consider what is probably the simplest possible case, the circular cone at incidence. As before we suppose the Reynolds number is large enough for the boundary layer to be thin, and we suppose the Mach number is not so high that entropy variations are significant. If the free-stream is supersonic and the bow shock is attached, the first inviscid approximation to the flow is conical. For subsonic flows past slender cones at large angles of incidence the inviscid flow over much of the surface is nearly conical. The displacement effect of the thin boundary layer will not affect the conicality of the flow significantly. None of this applies very close to the actual apex of the cone: the local Reynolds number is always small there and the boundary layer thickness is not small compared with the local diameter of the cross-section of the cone. Fortunately real flows establish a conical behaviour within a short distance of the apex.

The flow attaches to the surface along the windward generator of the cone, where the pressure is highest. From there it expands round the sides of the cone. If the angle of incidence is less than the semi-apex-angle of the cone, the boundary layer remains attached round to the leeward generator and the flow field is well described by the first inviscid approximation. The limiting streamlines on the developed surface of the cone are sketched in Fig 19. At appreciably larger angles of incidence, the limiting streamlines on the surface of the cone which run outward from the windward generator encounter an apparent barrier, which they approach but cannot cross. This is a separation line, which looks like an envelope of the limiting streamlines. On the cone it lies along a generator if the boundary layer is laminar and very closely along another generator if the boundary layer is turbulent. The limiting streamlines on the leeward side of the separation line originate at another attachment line, or pair of attachment lines, on the leeward side of the cone. Shear layers leave the surface at the separation line at a small angle and roll up around vortices which closely resemble those found above delta wings.

2.2 Vortex sheet model for conical flow

Now suppose we wish to represent these shear layers and the vortices by spiral vortex sheets, as for the delta wings. The first conclusion we come to is that the vortex sheet must leave the surface of the cone tangentially. This follows from the observation that, for a spiral vortex sheet model, the fluid on both sides of the separation line has come from the free-stream without undergoing any dissipative process, and so its total pressure is the same. Its static pressure is also the same, since this is continuous across the sheet. Consequently the magnitude of the velocity is the same on both sides of the separation line. If the vortex sheet is not tangential to the wall, it forms two concave corners with the wall. Since the sheet is a stream surface this means the velocity is directed along the separation line on both sides of it. This can happen in two ways: if the velocity vector is the same on both sides of the separation line, the strength of the sheet is zero; if the velocity vector is equal in magnitude but opposite in direction, there is no mean velocity and no vorticity can be convected away from the surface. Hence, if vorticity is being shed, the sheet must be tangential to the wall. This is a general result[86], not special to conical flow.

Since the sheet is tangential to the wall, it serves to distinguish between the two sides of the separation line. We can call the side on which the sheet lies against the wall the downstream side and the other side, the upstream side. This agrees with physical intuition. We then see that, at the separation line, the inviscid flow on the downstream side must be parallel to the separation line. This condition is a replacement for the Kutta condition which holds at a sharp edge. On the upstream side of the separation line the surface streamlines of the inviscid model are of course tangential to the wall, but are inclined to the separation line. These inviscid streamlines are sketched in the third configuration in Fig 19.

We can now construct an inviscid vortex sheet model in the same way as for the slender sharp-edged delta wing. The inner part of the infinitely rolled-up spiral sheet is replaced by a line vortex and a cut joining it to the free end of the outer part of the sheet. This depends on the two coordinates and the strength of the line vortex. These three quantities can be regarded as determined by the vanishing of the two components of the force on the vortex and cut in the cross-flow plane and by the replacement for the Kutta condition deduced above. If the outer part of the sheet is determined by N values of a geometrical parameter and N values of the sheet strength, satisfying the two sheet boundary conditions at N points along it will provide 2N equations to determine the remaining unknowns. It appears therefore that, once the separation line is specified, we obtain a well-posed inviscid problem. As for the sharp-edged delta wing, this means that we can expect, in general, a finite number of solutions. There may be none, or several, and there is no existence or uniqueness theorem known.

Apart from that fundamental difficulty, several practical difficulties remain. The vortex sheet, together with its image in the circular cross-section of the cone, form a sheet with a cusp, on which the strength of the sheet is opposite in sign on the two branches. It is quite easy to show that the usual formula for the induced velocity:

$$v - iw = \frac{1}{2\pi i}\int \frac{\gamma(\sigma)d\sigma}{Z - Z(\sigma)} \tag{10}$$

yields a finite value at the cusp itself. No Cauchy principal value is required there, essentially because the singular contributions from the two branches cancel. However, is this finite velocity the fluid velocity outside the cusp, inside the cusp, or neither? I believe it is the velocity outside, but have not obtained a completely satisfactory proof.

Now consider the calculation of the velocity induced on one branch of the cusp by the vorticity on the other. This means dealing with the integration in equation (10) for the case when $Z(\sigma)$ becomes very nearly, but not quite, equal to Z on the path of integration. Experience with this type of numerical problem shows that it is substantially more difficult than the Cauchy principal value which arises when $Z(\sigma)$ actually becomes equal to Z. The best approach is probably to use a local approximation to the sheet shape $Z(\sigma)$ and strength $\gamma(\sigma)$ which lead to an expression for $v - iw$ in closed form. A circular arc, as used in Ref 18, is one possibility.

We shall see later that the vortex sheet initially curves away from the body surface. Subsequently it rolls up, and so must acquire a point of inflexion. It is therefore not advisable to describe its shape by a polar coordinate system based on the line vortex, either in a transformed plane[8] or in the physical plane[16]. An intrinsic representation seems more promising, for example defining the sheet by values of its slope at fixed intervals of arc length[21,23]. Finally, the vortices shed from circular cones will lie close to the surface for a considerable range of angles of incidence. The cores will therefore be flattened, and an improved core model may well be needed. However, there is no doubt that all these difficulties can and will be resolved.

How can an inviscid calculation of this kind, with assumed straight separation lines, be complemented by a boundary layer calculation? If the boundary layer is laminar and the external flow is conical, it is a well-known result of Moore[87] that the boundary layer growth is quasi-conical. Certain properties of the boundary layer turn out to be constant along conical rays: in particular the inclination of the limiting streamlines is constant along each conical ray. Hence if a limiting streamline is tangential to a conical ray, limiting streamlines will touch the ray all along its length. The ray is then an attachment or separation line. Hence a conical flow model with separation along a generator is consistent with laminar boundary layer theory. If the boundary layer is turbulent, the form of the separation line depends on the turbulence model used. The method of Mowlem and Smith[88], for instance, would lead to a straight separation line in conical flow. More usually, as in the recent work of Bontoux and Roux[89], we must expect the azimuthal position of the separation line to change as the local Reynolds number increases along the length of the cone. However, the extent of this variation, as calculated by Bontoux and Roux[89], is small for a factor of ten in the Reynolds number, provided this is already fairly large. Hence, over the major part of the length of a cone with a fully turbulent boundary layer, the separation line will again lie close to a generator, so that a consistent model again emerges. If transition occurs at some significant fraction of the length, as sketched in the fourth part of Fig 19, a non-conical inviscid treatment is needed.

Self-consistency is, of course, only a part of the story. The question is whether an iteration between the inviscid calculation and the boundary layer calculation will converge. There is one example, with a laminar boundary layer, in which convergence was achieved. This is an attempt by Nutter[24] to compute a conical vortex-sheet model of secondary separation on the upper surface of a delta wing. Fig 20 shows a sketch, in the cross-flow plane, of the model used. Both primary and secondary vortices are represented by finite sheets, cuts and line vortices, all within slender-body theory. After considerable difficulty, inviscid solutions for specified positions of the secondary separation line were obtained. The method of Cooke[90] for a laminar boundary layer in a conical external field was then used to calculate the quasi-conical boundary layer growth outboard from the attachment line, which, for the incidence chosen, lies on the centre-line of the wing. For all physically realistic positions of the assumed secondary separation line, the boundary layer separated upstream, ie inboard, of it. However, by allowing the assumed secondary separation line to move further inboard, a solution was obtained in which the calculated and assumed positions of the secondary separation line came together. In this solution, separation took place virtually at a pressure minimum, that is to say the separation was smooth, with no adverse gradient upstream of it (for further discussion of smooth separation, see section 2.5). Unfortunately, this pressure minimum was not the suction peak under the primary vortex, but a rather insignificant pressure minimum well inboard of the primary vortex. From the point of view of modelling secondary separation therefore the work was a failure, but as a demonstration of the possibility of consistent inviscid and boundary layer calculations the work is significant. It has not yet been written up.

2.3 Vortex-sheet model for non-conical flow

What happens when we get away from conical bodies and conical flows? The next simplest case is perhaps the ogive-cylinder. If the incidence is high enough, the flow will separate along lines which run right forward to the apex of the ogive. If slender-body theory held exactly, the flow very close to the apex would be the same as on the cone which touches the ogive at the apex. We could calculate the separated flow on this cone and so obtain an initial solution for a downstream marching process. Using slender-body assumptions we could certainly carry the inviscid calculation downstream in this way, using Clark's technique[16], for instance. We could also carry the boundary layer calculation downstream, since the boundary layer equations are hyperbolic. Some rule for extending the separation line downstream is required and a possible algorithm is sketched in Fig 21. This shows the body surface in the plane of the sketch and we suppose the complete flow has been calculated up to the plane $x = x_n$, with separation line Σ. To advance to the plane $x = x_{n+1}$, guess a point S_1 in which Σ might meet the new plane, but bias the guess further round the body than seems likely. Then, with separation assumed at S_1, find the inviscid flow in the plane $x = x_{n+1}$ and use this to advance the boundary layer calculation to $x = x_{n+1}$. Suppose this boundary layer calculation extends Σ, regarded as a limiting streamline, to a point $\bar{S}_1$ in the plane $x = x_{n+1}$. Since the choice of S_1 was biased in the downstream direction, $\bar{S}_1$ will almost certainly be upstream of S_1, as indicated in the sketch, and a point S_2 can be chosen between S_1 and $\bar{S}_1$. Now assume separation takes place at S_2 and repeat the process. It seems likely that eventually a point S_m will lead to a point $\bar{S}_m$ which is close enough to S_m to be used as the next point on Σ.

When the incidence is lower, separation starts some way back along the surface of the ogive-cylinder. How the separation line starts is not clear, but oil-flow pictures have been obtained, eg by Boersen[91], which show a clear pattern of skin-friction lines, with no trace of any singular behaviour at the starting point of the separation line. The sort of pattern which might arise on an ogive-cylinder is sketched in side view in Fig 22. The separation line, S, appears to be formed from an ordinary limiting streamline as other limiting streamlines run into it. An attachment line, A, also grows from an ordinary limiting streamline. There seems to be no reason why an infinitely rolled-up vortex sheet model should not be capable of representing such a separation, right from its inception, but I have no idea of what form it would take. How rapidly, for instance, would the overall circulation grow? This seems to be a problem ripe for solution.

If the body is not sufficiently slender for slender-body theory to be a reliable guide, so that significant upstream influence is felt, the situation is more complicated. We can again imagine calculating an inviscid separated flow, using a vortex-sheet representation, from an assumed separation line, perhaps by the technique of Refs 14 and 15. From this we could calculate the boundary layer development, including a separation line. However it is now far from obvious how the assumed separation line should be modified in order to obtain a better estimate for the true separation line. Modelling becomes more difficult if the separation line starts with no sweep back, in the leeward plane of symmetry. A vortex-sheet model may however still be applicable, as suggested in Ref 85, but there is as yet nothing more definite to be said on the subject.

2.4 Simpler models

Two of the other models described in section 1 have been applied to separation from smooth bodies: the single line vortex model and the multivortex model. These have been applied to calculate the properties of bodies of revolution at incidence, within the framework of slender-body theory, by a number of workers from Bryson[92] onwards. Bryson used the single line vortex model, applying it particularly to circular cones and to the unsteady planar flow past circular cylinders. Among other results, he finds that the equations have no solutions for cones at small angles of incidence. Angelucci[93] uses the multivortex model for bodies of revolution and obtains encouraging agreement with experiment when an observed position of the separation line is introduced. There is unfortunately an error in the expression for the attached flow in his later extension[94] to bodies of more general cross-section. Wardlaw[95] treats the asymmetric flow past a body of revolution at high incidence, in which something resembling a vortex street is formed. He represents each of the vortices by a single line vortex, with the pair closest to the body being 'fed' through cuts. A considerable degree of empiricism is required.

The single line vortex model and the multivortex model are formulated in the same way for smooth surfaces as for sharp edges, except for the form of the Kutta condition. This condition is usually taken to be that the velocity component in the cross-flow plane and tangential to the body surface should vanish. This is often referred to as 'the stagnation of the cross-flow', which is not strictly accurate, since a component of the cross-flow normal to the wall exists in general. Enforcing this condition means that for a body of revolution, the velocity vector at the separation line lies along a meridian of the body. For an ogive-cylinder, the azimuthal position of the separation

AD-A050 762   ADVISORY GROUP FOR AEROSPACE RESEARCH AND DEVELOPMENT--ETC   F/G 20/4
THREE DIMENSIONAL AND UNSTEADY SEPARATION AT HIGH REYNOLDS NUMB--ETC(U)
FEB 78

UNCLASSIFIED   AGARD-LS-94   NL

3 OF 4
AD
A050762

~~END~~
DATE
FILMED
4 -78
DDC

CONT.

line changes along the body length, so this condition is not appropriate. Even for a cone, on which the separation line is a meridian, the following argument suggests we can do better.

Returning to the vortex sheet model, we recall that the velocity vector on the downstream side of the separation line must be tangential to the separation line, simply because this is the only direction in which the fluid can move. To describe the kinematics, we use the cylindrical polar coordinate system of section 1, with x along the body axis and the body surface described by $r = f(x, \theta)$. The separation line on the body surface can be described by $\theta = g(x)$ and $r = f(x, g(x))$. The direction ratios of the separation line are then:

$$1 : f_x + f_\theta g' : fg' \quad .$$

If this is a streamline,

$$U = \frac{v_r}{f_x + f_\theta g'} = \frac{v_\theta}{fg'} \quad , \tag{11}$$

where streamwise disturbances are neglected, the incidence is small and v_r and v_θ are the radial and circumferential components of the velocity in the cross-flow plane. If v_{t_d} is the component of velocity in the cross-flow plane tangential to the body on the downstream side of the separation line, we can write

$$v_{t_d} = v_r \cos\phi + v_\theta \sin\phi \quad , \tag{12}$$

where ϕ is the angle between the tangent and the radius vector, as in Fig 3. (Note that $\tan\phi = r\,d\theta/dr = f/f_\theta$.) Using (11) and (12), since the downstream side of the separation line is a streamline, we have:

$$v_{t_d} = U(f_x \cos\phi + fg' \operatorname{cosec}\phi) \quad . \tag{13}$$

The jump Δv_t in tangential velocity across the sheet is twice the difference between v_{t_d} and the mean tangential velocity, v_{t_m} :

$$\begin{aligned} \Delta v_t &= 2\left(v_{t_d} - v_{t_m}\right) \\ &= 2\left(Uf_x \cos\phi + Ufg' \operatorname{cosec}\phi - v_{t_m}\right) \quad , \end{aligned}$$

by (13). This result can be introduced into equation (6), representing the continuity of pressure across the sheet, to give

$$U\frac{d\Gamma}{dx} = 2\left(v_{t_m} - Uf_x \cos\phi - Ufg' \operatorname{cosec}\phi\right)\left(v_{t_m} - Uf_x \cos\phi\right) \quad , \tag{14}$$

where Γ , the overall circulation, has been written for $\Delta\Phi$. Equation (14) only involves quantities which appear in the discrete vortex models: the circulation Γ , the mean velocity v_{t_m} at the separation line, and the geometry. It can therefore be applied as a Kutta condition in such models.

To see what it means, let us take two simple examples. First, a body of revolution with the separation line along a meridian, so that $\phi = \pi/2$ and $g' = 0$. Then

$$v_{t_m} = \pm\sqrt{\frac{U}{2}\frac{d\Gamma}{dx}} \quad .$$

With the positive direction of v_t towards the downstream side of the separation line, it is clear that the positive sign is required, to convect the vorticity from the separation line to the vortex. Even for this case, the tangential component of velocity does not vanish as long as the circulation is increasing. Secondly, for the secondary separation on the upper surface of a flat delta wing in conical flow, g' and ϕ are both zero, so that,

$$v_{t_m} = Uf_x + \sqrt{\frac{U}{2}\frac{d\Gamma}{dx}} .$$

The first term on the right is the tangential velocity needed to turn free-stream along the separation line and the second term provides the extra velocity needed to convect the vorticity off the wing. Further consideration suggests it is always the larger root of (14), regarded as an equation for v_{t_m}, that is physically realistic.

The way in which $d\Gamma/dx$ in (14) is obtained depends on the model. For the single line vortex model, (14) is a differential equation for Γ. This must be solved simultaneously with the two differential equations obtained by equating to zero the two transverse components of the force on the combination of the vortex and cut. This procedure leads to a modification to Bryson's model[92] for the flow past a body of revolution. For a multivortex model, like that of Angelucci[93], in which vortices of finite strength are introduced at discrete points along the separation line, it is necessary to decide first where the Kutta condition is to be applied. It seems reasonable to satisfy it at stations midway between the stations at which the vortices are introduced. v_{t_m} can be found from the flow field at such a station midway between $x = x_n$ and $x = x_{n+1}$ and equation (14) then gives a value for $d\Gamma/dx$, from which the strength, Γ_n, of the next vortex to be introduced follows from

$$\Gamma_n = (x_n - x_{n-1}) \left.\frac{d\Gamma}{dx}\right|_{x = \frac{1}{2}(x_n + x_{n-1})} . \tag{15}$$

The problem discussed above, of how a vortex sheet might begin at some distance back from the apex of an ogive-cylinder, still arises for the simpler models. Bryson's original equations[92] predict an exponential variation in the strength of the vortex when it is close to the body. He avoids the difficulty by introducing the vortex with a small circulation at a small distance from the surface, but this is mathematically unsatisfactory.

It is difficult to see how the simpler models could be used successfully with a boundary layer calculation to produce a complete solution, since the nature of the flow field near the separation line is not properly described. Omitting the vortex sheet immediately downstream of the separation line must have a marked effect on the pressure gradient upstream of it. The future of the simpler models probably lies in problems for which the separation line is known from experiment, or problems in which the desired results are not very sensitive to the assumed position of the separation line. Sensitivity tests seem not to be generally available, so it is perhaps worth quoting from some unpublished work by Jepps[96]. He found that a shift of 8° in the circumferential position of the separation line approximately doubled the nonlinear lift at incidences above 15° in his inviscid calculations for an ogive-cylinder, using a single-line-vortex model.

2.5 The flow near the separation line

To conclude, I shall describe some recent work[86] of my own on the behaviour of a vortex sheet leaving a smooth wall, and discuss its implications for modelling separation in three-dimensional flow. My work used the framework of slender-body theory, but a generalization avoiding these assumptions has been provided by F.T. Smith[97]. It is possible to show by a local analysis that, if the distance, z, from the wall of a point on the vortex sheet is related to its distance y from the separation line (see Fig 23) by an asymptotic relation

$$z \sim \mu y^n , \tag{16}$$

then the only possible values of n are 3/2, 5/2, 7/2... If $n = 3/2$, so that the curvature of the sheet is infinite at the separation line, an adverse pressure gradient occurs upstream of the separation line. This adverse gradient becomes infinite at the separation line itself. On the other hand, if $n = 5/2$, so that the curvature of the sheet is equal to that of the body, the pressure gradient is finite, but not locally determined, at the separation line. It is conventional to refer to this latter situation as 'smooth' separation. These results, obtained for the vortex-sheet model of separation from a highly swept separation line, are closely analogous to the predictions of the Kirchhoff model for two-dimensional, free-streamline flow past a circular cylinder. In that case, it emerges that for almost all positions of the 'separation' line, the curvature is locally infinite and the pressure gradient is infinite. For just one position, smooth separation occurs. We can conjecture therefore that in general smooth separation will only occur for a finite number of positions of the separation line in three-dimensional flow.

The significance of smooth separation in two-dimensional flow arises from the work of Sychev[98]. He predicted the existence of an asymptotic solution of the Navier-Stokes equations for the neighbourhood of two-dimensional, free-streamline separation, valid for large Reynolds numbers. This solution showed separation occurring close to the position of smooth separation, the distance from the position of smooth separation being of order $Re^{-1/16}$. These predictions have been confirmed by numerical calculations by F.T. Smith[99], who has also extended the theory to three-dimensional flow[97].

Now laminar boundary layer theory is essentially an infinite Reynolds number approximation, in the sense that, for instance, the prediction of separation in a given external field is independent of Reynolds number. Suppose, then, that we obtained convergence in an iteration process between the inviscid separated flow calculation and the laminar boundary layer calculation, the sort of process frequently referred to above. It seems highly probable, if the calculations are accurate, that the calculated separation will be smooth, corresponding to the limit of infinite Reynolds number in Sychev's solution. The experience of Nutter[24] described in section 2.2 supports this view. On the other hand, by comparing the shape of the vortex sheet in the inviscid calculation with equation (16) with $n = 3/2$, we can find the coefficient μ as a function of the assumed position of the separation line and so pick out the position (or positions) which correspond to smooth separation with $\mu = 0$. It seems therefore that iterating with the laminar boundary layer calculation would produce no extra information.

What we want, of course, is not the infinite Reynolds number limit, but the position of separation at finite Reynolds numbers. It appears[97] that this can be found, for large Reynolds number, by matching the behaviour of μ, as a function of separation line position, in the inviscid solution to the behaviour of the corresponding quantity in the asymptotic analysis of Sychev[98] and F.T. Smith[99], which depends on Reynolds number. If this can be done, and we are trying to do it at RAE, then a mathematically consistent account of laminar separation from smooth surfaces at highly swept separation lines and high Reynolds numbers will have been achieved.

Whether such an account will have any physical significance remains to be seen. It certainly cannot be assumed that the simultaneous assumptions of laminar flow and large Reynolds number will lead to sensible predictions. No really convincing support emerges from the two-dimensional flow past a circular cylinder, since actual separation takes place a long way downstream of the position of smooth separation for the Kirchhoff model for the largest Reynolds numbers at which the separation is laminar. (See, for example, p 168 of Ref 100.) However, the Kirchhoff model, with its wake at free-stream pressure, is not in itself a satisfactory model of the two-dimensional flow. The vortex-sheet model has shown itself to be much more realistic in its predictions of the behaviour of sharp-edged wings, so there are grounds for hope.

For the more practical case in which the boundary layer is turbulent much less can be said. Presumably for any particular algebraic model of turbulence, an analysis like that of Sychev[98] and F.T. Smith[99] could be carried out. Whether it could be done for a more realistic model of turbulence I cannot judge. If it could be carried through it might provide a basis for preferring one turbulence model to another, at least for the prediction of separation. Otherwise, we fall back on the idea of iterating between the inviscid and the boundary layer calculations.

2.6 Conclusions

To represent flow separating from highly-swept sharp edges, a number of well-developed models exist, whose capabilities and short-comings are reasonably well known and understood. Progress in tackling problems of practical concern should therefore be proportional to the effort expended, at least up to several times the present rate of progress. A few perplexing difficulties remain, but these tend to be peripheral to the subject.

For flow separating from smooth bodies the situation is quite different. The central problem is to predict the separation line and for this there is no single entirely satisfactory calculation. There are a number of hopeful signs: separation predicted approximately using a measured external flow or a calculated attached external flow[85], convergence achieved in an iteration between an inviscid separated flow model and a boundary layer calculation[24], and a mathematical treatment of the laminar viscous-inviscid interaction problem at high Reynolds number[97-99]. There are also still substantial difficulties with the inviscid modelling of separation originating downstream of the apex of the body.

REFERENCES

No.	Author	Title, etc
1	J.H.B. Smith	How the state of the boundary layer may affect the flow over slender wings. Euromech 14, Stockholm, 1969. RAE Technical Memorandum Aero 1157 (1969)
2	M.G. Hall	Vortex breakdown. Annual Review of Fluid Mechanics 4, pp 195-218, Annual Reviews Inc. (1972)
3	Y. Hayashi T. Nakaya	Flow field in a vortex with breakdown above sharp-edged delta wings. Jap. Nat. Aerosp. Lab TR-423 (1975)
4	V.A. Aparinov S.M. Belotserkovskii M.I. Nisht O.N. Sokolova	On the mathematical simulation in an ideal fluid of stalled flow past a wing and the destruction of the vortex sheet. Dok. Ak. Nauk SSSR 227, pp 820-823 (1976)
5	E.C. Maskell	Some recent developments in the study of edge vortices. 3rd ICAS Congress, Stockholm, 1962. Proceedings pp 737-750, Spartan Books (1964)
6	K.W. Mangler J. Weber	The flow field near the centre of a rolled-up vortex sheet. J. Fluid Mech. 30, pp 177-196 (1967)
7	J.P. Guiraud R.Kh Zeytonnian	A double-scale investigation of the asymptotic structure of rolled-up vortex sheets. J. Fluid Mech. 79, pp 93-112 (1977)
8	J.H.B. Smith	Improved calculations of leading-edge separation from slender delta wings. Proc. R. Soc. Lond. A 306, pp 67-90, 1968, also RAE Technical Report 66070 (1966)
9	E.C. Maskell	On the asymptotic structure of a conical leading-edge vortex. IUTAM Symp. on Vortex Motions, Ann Arbor, 1964, see Prog. in Aero. Sci. 7, pp 35-51, Pergamon Press (1966)
10	D.W. Moore	The rolling-up of a semi-infinite vortex sheet. Proc. R. Soc. Lond. A 345, pp 417-430 (1975)
11	S.N. Brown	The compressible inviscid leading-edge vortex. J. Fluid Mech. 22, pp 17-32 (1965)
12	S.N. Brown K.W. Mangler	An asymptotic solution for the centre of a rolled-up conical vortex sheet in compressible flow. Aero. Quart. 18, pp 354-366 (1967)
13	K. Stewartson M.G. Hall	The inner viscous solution for the core of a leading-edge vortex. J. Fluid Mech. 15, pp 306-318 (1963)
14	J.A. Weber G.W. Brune F.T. Johnson P. Lu P.E. Rubbert	Three-dimensional solution of flows over wings with leading-edge vortex separation. AIAA Journal 14, pp 519-525, 1976 also NASA CR 132709 and 132710 (1975)
15	F.T. Johnson P. Lu G.W. Brune J.A. Weber P.E. Rubbert	An improved method for the prediction of completely three-dimensional aerodynamic load distributions on configurations with leading-edge separation. AIAA paper 76-417 (1976)
16	R.W. Clark	Non-conical flow past slender wings with leading-edge vortex sheets. Euromech 41, Norwich, 1973. RAE Technical Report 76037 (1976)
17	I.P. Jones	Leading-edge vortex flows. Thesis, University of East Anglia (1974)
18	K.W. Mangler J.H.B. Smith	A theory of the flow past a slender delta wing with leading-edge separation. Proc. R. Soc. Lond. A 251, pp 200-217, 1959 RAE Report Aero 2593 (1957)

REFERENCES (continued)

No.	Author	Title, etc
19	E.S. Levinsky M.H.Y. Wei	Nonlinear lift and pressure distribution on slender conical bodies with strakes at low speeds. NASA CR 1202 (1968)
20	D.I. Pullin	Calculations of the steady conical flow past a yawed slender delta wing with leading-edge separation. Imp. Coll., Lond., Aero Report 72-17 (1972)
21	J.E. Barsby	Calculations of the effects of blowing from the leading edges of a cambered delta wing. ARC 36252 (1975)
22	J.H.B. Smith	Similar solutions for slender wings with leading-edge separation. 13th Int. Cong. Th. Appl. Mech., Moscow (1972)
23	J.E. Barsby	Separated flow past a slender delta wing at low incidence. Aero. Quart. 24, pp 120-128 (1973)
24	J. Nutter	Unpublished work on modelling secondary separation. University of East Anglia
25	S.E. Widnall	The structure and dynamics of vortex filaments. Annual Review of Fluid Mechanics 7, pp 141-165, Annual Reviews Inc. (1975)
26	C.E. Brown W.H. Michael	Effect of leading-edge separation on the lift of a delta wing. J. Aero. Sci. 21, pp 690-694 and 706, 1954 NACA TN 3430 (1955)
27	R. Legendre	Écoulement au voisinage de la pointe avant d'une aile à forte flèche aux incidences moyennes. 8th Int. Cong. Th. Appl. Mech., Istanbul, 1952, Rech. Aero. 30, 1952 and 31 (1953)
28	R. Legendre	Écoulement au voisinage de la pointe avant d'une aile à forte flèche aux incidences moyennes. Rech. Aero. 35 (1953)
29	Mac C. Adams	Leading-edge separation from delta wings at supersonic speeds. J. Aero. Sci. 20, p 430 (1953)
30	R.H. Edwards	Leading-edge separation from delta wings. J. Aero. Sci. 21, pp 134-135 (1954)
31	J.H.B. Smith	A theory of the separated flow from the curved leading edge of a slender wing. RAE TN Aero 2535, ARC R & M 3116 (1957)
32	J.E. Barsby	Flow past conically-cambered slender delta wings with leading-edge separation. RAE Technical Report 72179, ARC R & M 3748 (1972)
33	S.M. Belotserkovskii	Calculation of the flow around wings of arbitrary planform over a wide range of angles of attack. Izv. Ak. Nauk SSSR Mekh. Zhid. i Gaza, 3, pp 32-44, 1968 RAE Library Trans. 1433 (1970)
34	C. Rehbach	Étude numerique de l'influence de la forme de l'extremité d'une aile sur l'enroulement de la nappe tourbillonaire. Rech. Aero. 1971-6, pp 367-8 (1971)
35	O.A. Kandil D.T. Mook A.H. Nayfeh	Nonlinear prediction of the aerodynamic loads on lifting surfaces. J. of Aircraft 13, pp 22-28 (1976)
36	A.H. Sacks R.E. Lundberg C.W. Hanson	A theoretical investigation of the aerodynamics of slender wing-body combinations exhibiting leading-edge separation. NASA CR-719 (1967)
37	P.T. Fink W.K. Soh	Calculation of vortex sheets in unsteady flow and applications in ship hydrodynamics. Univ. of New South Wales, School of Mech. Engg. Nav/Arch 74/1 (1974)

REFERENCES (contined)

No.	Author	Title, etc
38	D.W. Moore	A numerical study of the roll-up of a finite vortex sheet. J. Fluid Mech. 63, pp 225-235 (1974)
39	C. Rehbach	Étude numérique de nappes turbillonaires issues d'une ligne de decollement pres du bord d'attaque. Rech. Aero. 1973-6, pp 325-330 (1973)
40	O.A. Kandil D.T. Mook A.H. Nayfeh	A numerical technique for computing subsonic flow past three-dimensional canard-wing configurations with edge separations. AIAA Paper 77-1 (1977)
41	D. Küchemann	A nonlinear lifting surface theory for wings of small aspect ratio with edge separations. RAE Report Aero 2540, ARC 17769 (1955)
42	L.C. Squire	The estimation of the nonlinear lift of delta wings at supersonic speeds. J.R. Aero. Soc. 67, pp 476-480 (1963)
43	E. Carafoli	Wing theory in supersonic flow. pp 446-462, Pergamon (1969)
44	A. Betz	Division J. of Aerodynamic Theory in Applied Airfoil Theory, Vol IV, ed. W.F. Durand, Springer (1935)
45	K. Gersten	Nonlinear theory for rectangular wings in incompressible flow. Z. Flugwiss, 5, pp 276-280 (1957)
46	E.C. Polhamus	A concept of the vortex lift of sharp-edged delta wings, based on a leading-edge suction analogy. NASA TN D-3767 (1966)
47	E.C. Polhamus	Charts for predicting the subsonic vortex lift characteristics of arrow, delta and diamond wings. NASA TN D-6243 (1971)
48	J.H.B. Smith	Calculation of the flow over thick conical slender wings with leading-edge separation. RAE Technical Report 71057, ARC R & M 3694 (1971)
49	I.P. Jones	Flow separation from yawed delta wings. Computers and Fluids 3, pp 155-177 (1975)
50	R.K. Cooper	Oscillatory slender wings with leading-edge vortex sheets. ARC 35922 (1975)
51	R.K. Nangia G.J. Hancock	A theoretical investigation for delta wings with leading-edge separation at low speeds. ARC CP 1086 (1968)
52	T.K. Matoi E.E. Covert S.E. Widnall	A three-dimensional lifting-surface theory with leading-edge vortices. ONR-CR-215-230-2 (1975)
53	J.H.B. Smith	Attempted design of a slender wing with leading-edge separation. RAE Technical Report 71079 (1971)
54	J.H.B. Smith	The isolated vortex model of leading-edge separation revised for small incidence. RAE Technical Report 73160 (1974)
55	D.G. Randall	Oscillating slender wings with leading-edge separation. Aero. Quart. 17, pp 311-331 (1966) RAE Report Structures 284 and 286 (1963)
56	M.V. Lowson	The separated flows on slender wings in unsteady motion. Southampton Univ. Dept. of Aeronautics Rep. ARC 25118 (1963)
57	B.D. Dore	Nonlinear theory for slender wings in sudden plunging motion. NPL Aero. Rep. 1128, ARC 26488 (1964)

REFERENCES (continued)

No.	Author	Title, etc
58	C.E. Jobe	An aerodynamic theory of slender wings with leading-edge separation. Thesis, Ohio State Univ. (1966)
59	L.C. Squire	Camber effects on the nonlinear lift of slender wings with sharp leading edges. ARC CP 924 (1966)
60	H. Portnoy S.C. Russell	The effect of small conical thickness distributions on the separated flow past slender delta wings. ARC CP 1189 (1971)
61	M. Hanin D. Mishne	Flow about a rolling slender wing with leading-edge separation. Israel J. Tech. <u>11</u>, pp 131-136 (1973)
62	R.W. Clark J.H.B. Smith C.W. Thompson	Some series-expansion solutions for slender wings with leading-edge separation. RAE Technical Report 75004, ARC R & M 3785 (1975)
63	J.P. Nenni C. Tung	A second-order slender wing theory for wings with leading-edge separation in supersonic flow. NASA CR 1860 (1971)
64	A.A. Nikolskii	A nonlinear law of similarity for the separated flow of an ideal gas around a rectangular wing at supersonic speed. 13th Int. Cong. Th. Appl. Mech., Moscow, 1972 TsAI Uchenye Zapiski <u>3</u>, pp 10-17 (1972)
65	C. Rehbach	Numerical investigation of leading-edge vortex for low aspect ratio thin wings. AIAAJ <u>14</u>, pp 253-255 (1976)
66	B. Maskew	Calculation of potential flow aerodynamic characteristics of combined lifting surfaces with relaxed wakes. Euromech 41, Norwich, HSA (Brough) Note YAD 3192 (1973)
67	D. Finkleman	Nonlinear vortex interactions on wing-canard configurations. J. of Aircraft <u>9</u>, pp 399-406 (1972)
68	S.D. Ermolenko	On the nonlinear theory of wings of small aspect ratio. Izv. Vys. Uch. Zav. Av. Tekh. <u>2</u>, pp 9-18 (1966) RAE Library Trans. 1218
69	W. Bollay	A nonlinear wing theory and its application to rectangular wings of small aspect ratio. ZAMM <u>19</u>, pp 21-35 (1939)
70	K. Gersten	Calculation of nonlinear aerodynamic stability derivatives of aeroplanes. AGARD Report 342 (1961)
71	H.C. Garner D.E. Lehrian	Nonlinear theory of steady forces on wings with leading-edge flow separation. NPL Aero. Rep. 1059, ARC R & M 3375 (1963)
72	H.C. Garner D.E. Lehrian	Pitching derivatives for a gothic wing oscillating about a mean incidence. NPL Aero. Note 1010, ARC CP 695 (1963)
73	D. Nikolitsch	Über die Anwendung der nichtlinearen Tragflächentheorie von K. Gersten auf den Fall der Schallanströmung Bölkow Ber. FM 389 (1967)
74	P.P. Boyden	Theoretical and experimental studies of the effects of leading-edge vortex flow on the roll-damping of slender wings. J. of Aircraft <u>8</u>, pp 543-547 (1971)
75	R.G. Bradley C.W. Smith I.C. Bhateley	Vortex-lift predictions for complex planforms. J. of Aircraft <u>10</u>, pp 379-381 (1973)
76	J.E. Lamar	Vortex flow characteristics of wings. J. of Aircraft <u>13</u>, pp 490-494 (1976)
77	E.E. Davenport	Aerodynamics characteristics of three slender sharp-edge 74° swept wings at subsonic, transonic and supersonic Mach numbers. NASA TN D-7631 (1974)
78	W. Stahl K. Hartmann W. Schneider	Force and pressure measurements on a slender delta wing at transonic speeds and varying Reynolds numbers. DFVLR Rep. 70 A01 (1970)

REFERENCES (continued)

No.	Author	Title, etc
79	D. Hummel G. Redeker	Experimentelle Bestimmung der gebundenen Wirbellinien sowie des Strömungsverlaufs in der Umgebung der Hinterkante eines schlanken Deltaflügels. Ab. Braunsch. Wiss. Ges. 22, p 273 (1972)
80	D.J. Marsden R.W. Simpson W.J. Rainbird	The flow over delta wings at low speeds with leading-edge separation. CoA, Cranfield, Rep. 114 (1957)
81	D.L.I. Kirkpatrick	Investigation of the normal force characteristics of slender delta wings with various rhombic cross-sections in subsonic conical flows. RAE Technical Report 65291 (1965)
82	N. Rott	Diffraction of a weak shock with vortex generation. J. Fluid Mech. 1, pp 111-128 (1956)
83	P.J. Butterworth	Further low-speed wind-tunnel tests on cambered wings of mild gothic planform and aspect ratio 1.4. RAE Technical Report 77018 (1977)
84	R.H. Wickens	The vortex wake and aerodynamic load distribution of slender rectangular wings. Can. Aero. Sp. J. 13, pp 247-260 (1967)
85	J.H.B. Smith	*A review of separation in steady, three-dimensional flow.* In Flow Separation, AGARD-CP-168 (1975)
86	J.H.B. Smith	Behaviour of a vortex sheet separating from a smooth surface. RAE Technical Report 77058 (1977)
87	F.K. Moore	Laminar boundary layer on a circular cone in supersonic flow at a small angle of attack. NACA TN 2521 (1951)
88	A.R. Mowlem R.A. Smith	Analysis of compressible turbulent flow over a yawed cone. AIAAJ. 12, pp 1171-1172 (1974)
89	P. Bontoux B. Roux	Compressible turbulent boundary layer on a yawed cone. AIAAJ. 14, pp 545-546 (1976)
90	J.C. Cooke	The laminar boundary layer on an inclined cone. RAE Technical Report 65178; ARC R & M 3530; AGARDograph 97, Part II, pp 909-931 (1965)
91	S.J. Boersen	Reynolds number effects on pressure and normal force distribution along conically pointed circular cylinders at a free-stream Mach number of 2.3. NLR Technical Report 75124 (1975)
92	A.E. Bryson	Symmetric vortex separation on circular cylinders and cones. J. Appl. Mech. (ASME Trans.) 26, pp 643-646 (1959)
93	S.B. Angelucci	A multivortex method for axisymmetric bodies at angle of attack. J. of Aircraft 8, pp 959-966 (1971)
94	S.B. Angelucci	Multivortex model for bodies of arbitrary cross-sectional shapes. AIAA Paper 73-104 (1973)
95	A.B. Wardlaw	Prediction of yawing force at high angle of attack. AIAAJ. 12, pp 1142-1144 (1974)
96	S.A. Jepps	A theoretical investigation of the subsonic flow past an ogive-cylinder body. BAC (Warton) Maths Services Note 226 (1977)
97	F.T. Smith	Three-dimensional viscous and inviscid separation from a smooth non-slender body. RAE Technical Report in draft.
98	V.V. Sychev	On laminar separation. Izv. Ak. Nauk, Mekh. Zhid. i Gaza, 3, pp 47-59, 1972, Translated in Fluid Dynamics, Plenum Pub. Corp. pp 407-417, March-April 1974

REFERENCES (concluded)

No.	Author	Title, etc
99	F.T. Smith	The laminar separation of an incompressible fluid streaming past a smooth surface. Proc. R. Soc. Lond., A 356, pp 443-463 (1977)
100	B. Thwaites (ed.)	Incompressible Aerodynamics. OUP (1960)

The references quoted are not necessarily available.

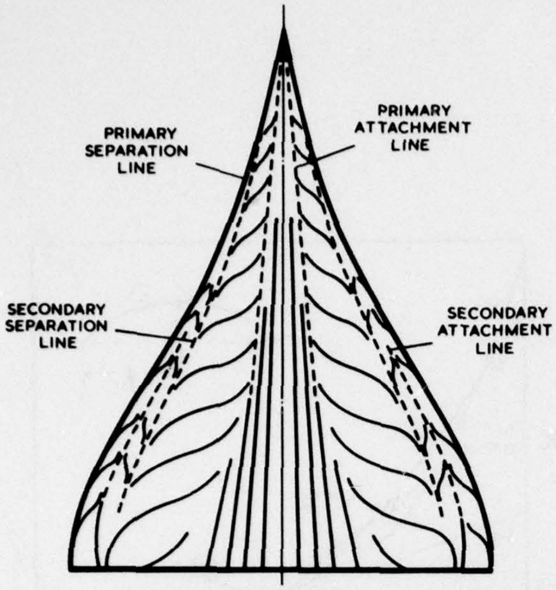

Fig 1 Streamline pattern on the upper surface of a slender wing at low speeds. $\alpha = 15^0$

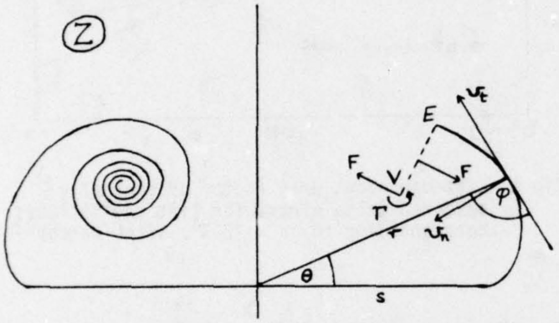

Fig 3 Simplification of representation of inner part of vortex sheet

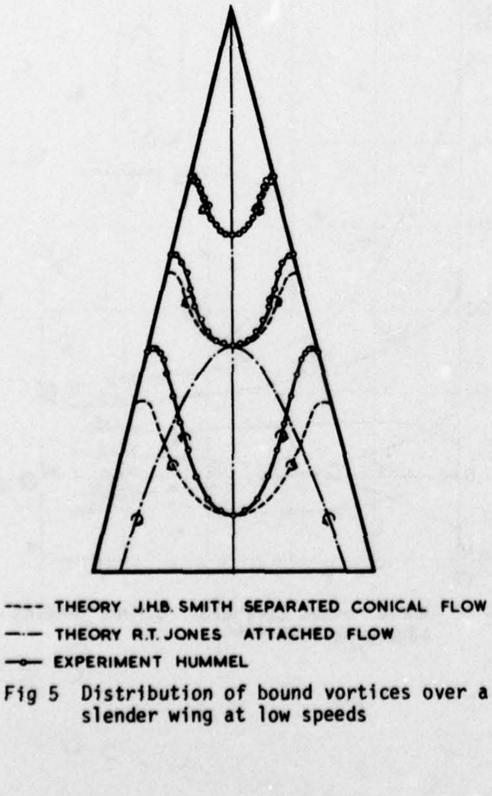

Fig 5 Distribution of bound vortices over a slender wing at low speeds

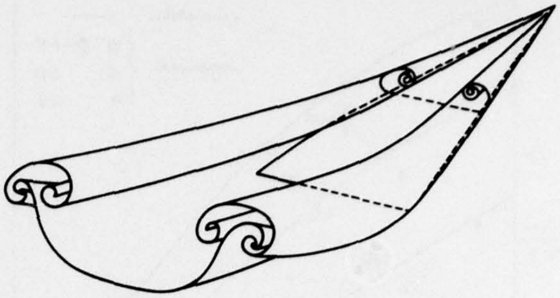

Fig 2 Model of the flow past a lifting slender wing. After R.L. Maltby

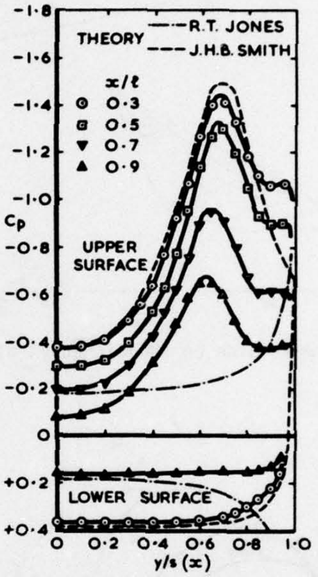

Fig 4 Pressure distributions over a thin delta wing at low speeds. $s/\ell = 0.25$; $\alpha = 20.5^0$. After D. Hummel & G. Redeker (1972)

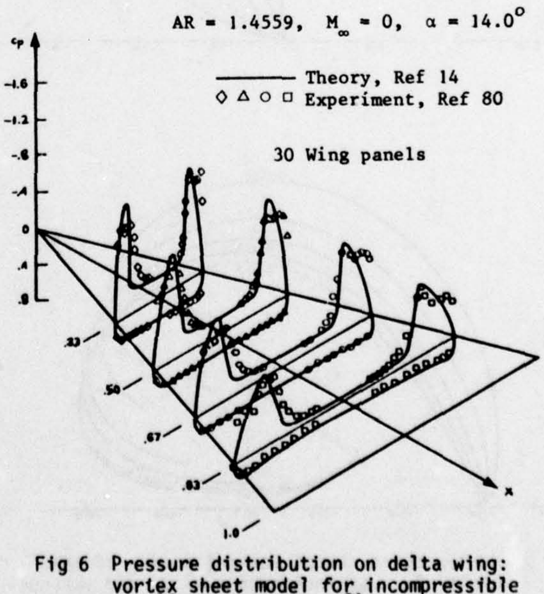

Fig 6 Pressure distribution on delta wing: vortex sheet model for incompressible flow[14] and experiment[80]

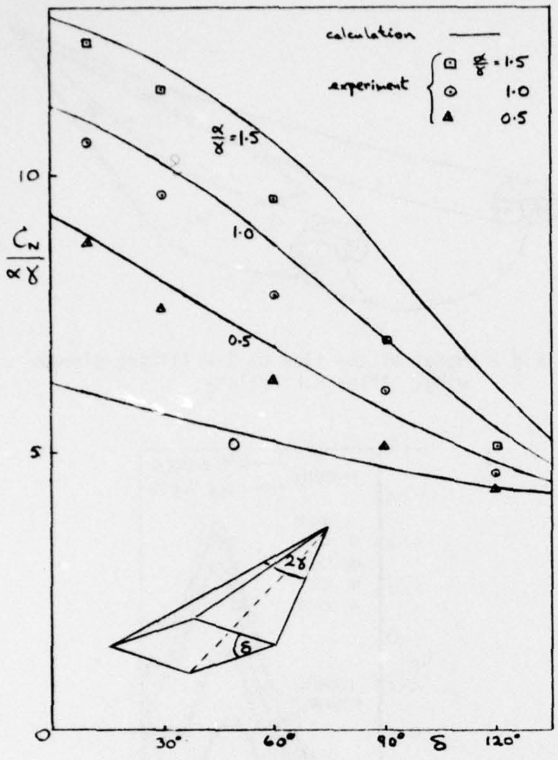

Fig 7 Normal force on rhombic cones at incidence

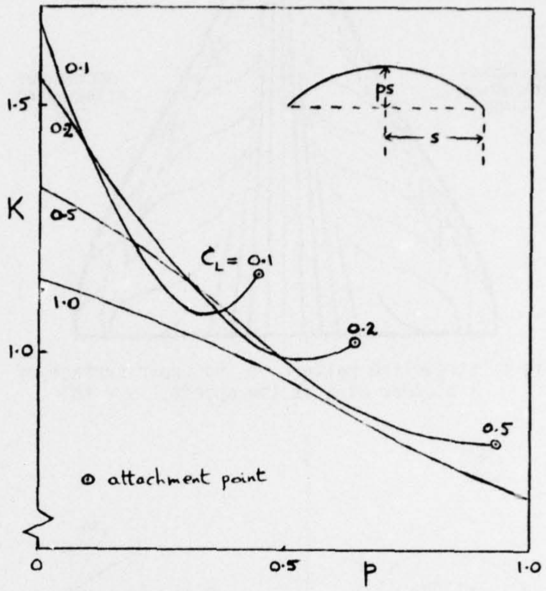

Fig 8 Lift-dependent drag factor of conically-cambered delta wings, for lift coefficients corresponding to $\Lambda = 72.5^0$, after Barsby[32]

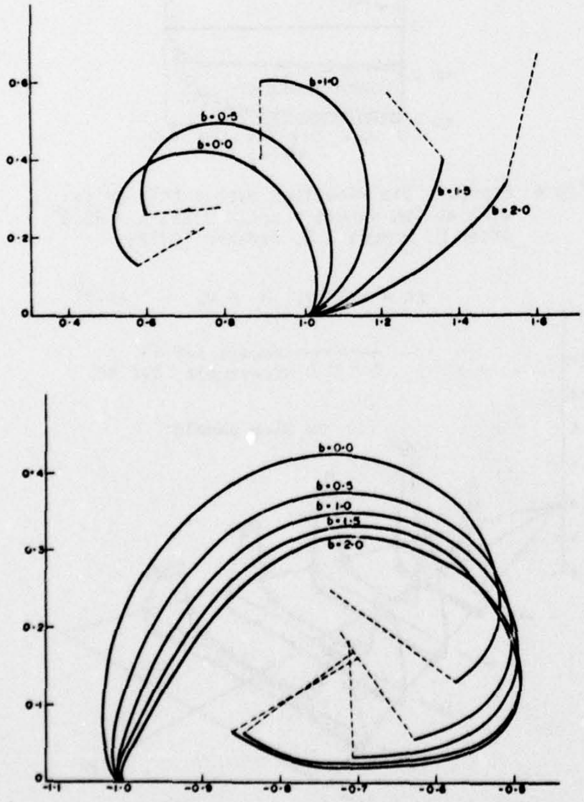

Fig 9 Vortex sheet shapes for delta wing of apex angle 2γ , at incidence α = γ and various yaw angles β = bγ . Leeward above, windward below (Jones[49])

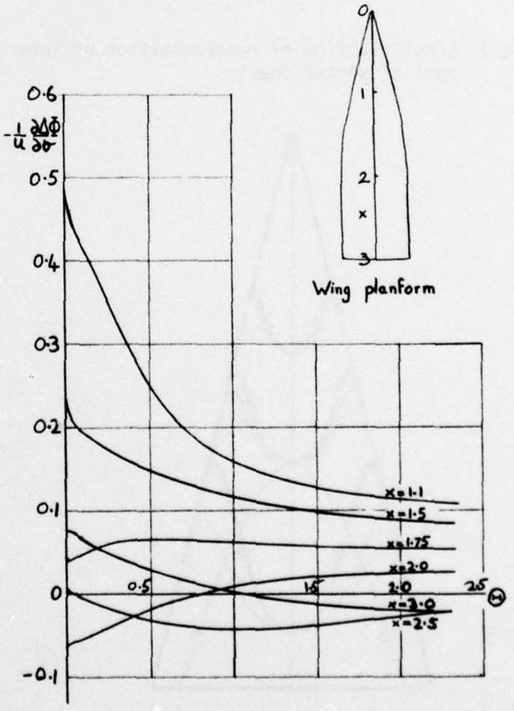

Fig 10 Vortex sheet strength. Curved leading edge wing (Clark[16])

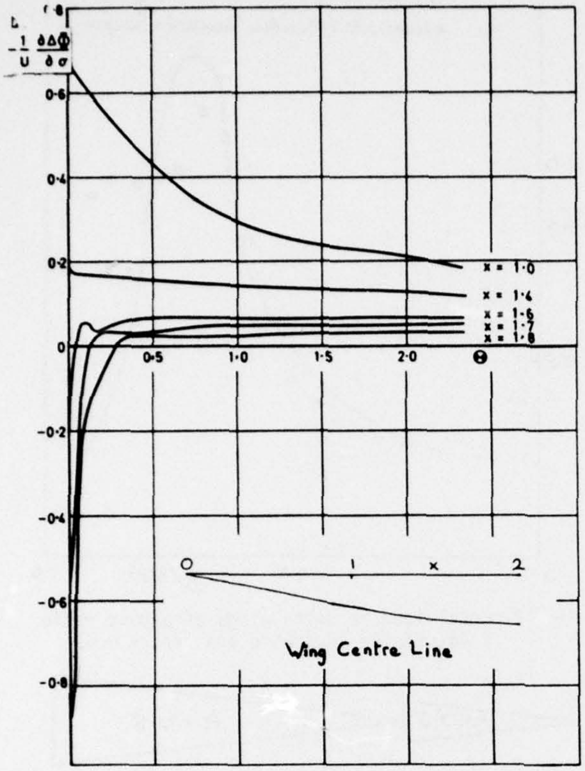

Fig 11 Vortex sheet strength. Cambered delta wing (Clark[16])

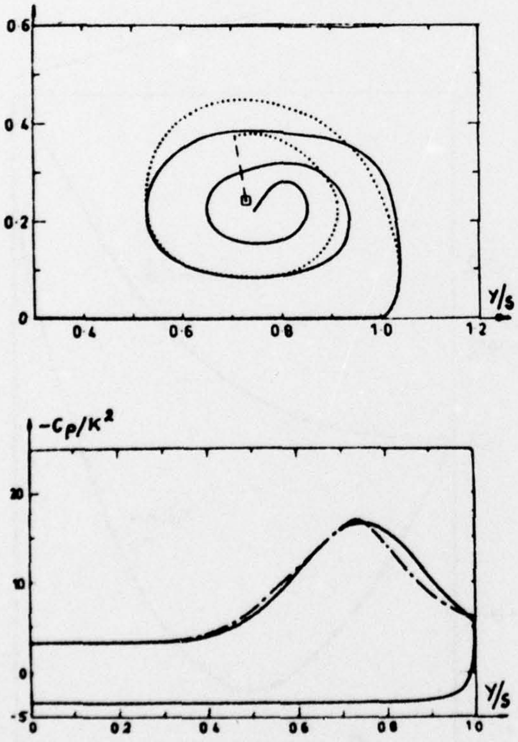

Fig 13 Multivortex[37] and vortex sheet[8] results for a delta wing - sheet shapes above, pressure distributions below

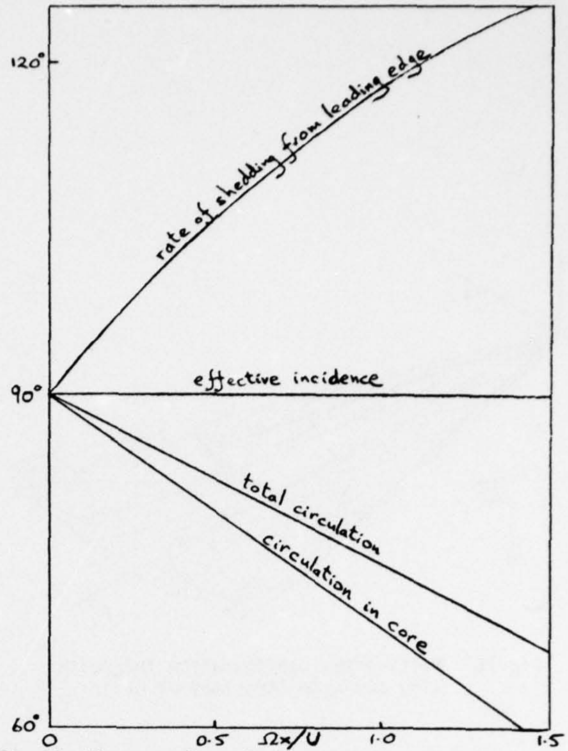

Fig 12 Phase angles of the disturbances for a delta wing in a small heaving oscillation about a mean incidence of half its apex angle at an angular frequency Ω (Cooper[50])

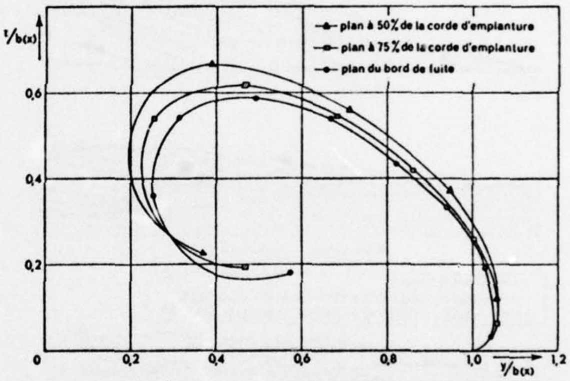

Vérification de la conicité de l'écoulement.

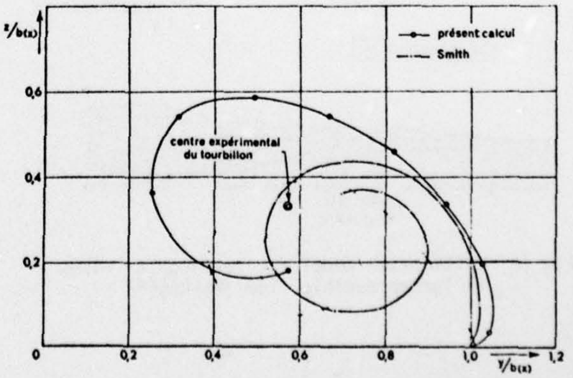

Trace de la nappe dans le plan transversal du bord de fuite pour α = 1.

Fig 14 Sheet shapes from multivortex model for incompressible flow past a delta wing (Rehbach[39])

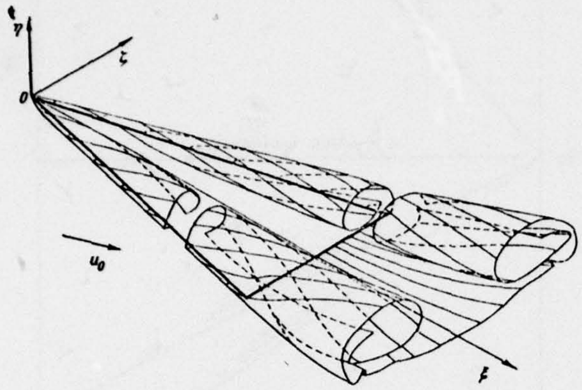

Fig 15 Multivortex configuration for delta wing and wake (Aparinov *et al*4)

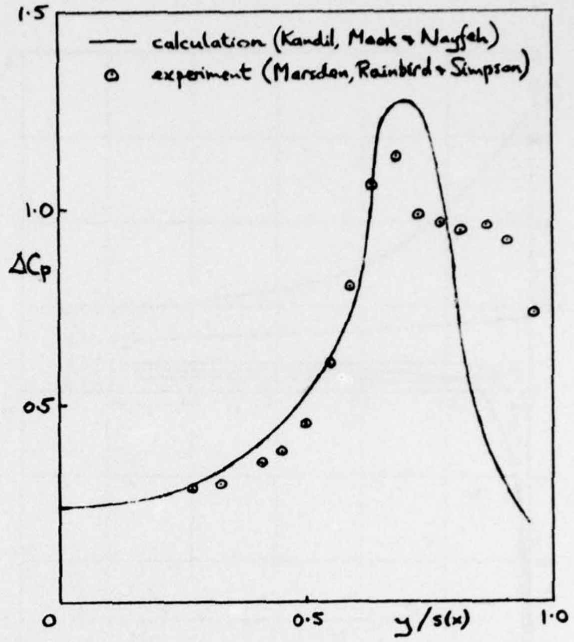

Fig 17 Local load on delta wings of aspect ratio 1.46, at 14° incidence and x/c = 0.67

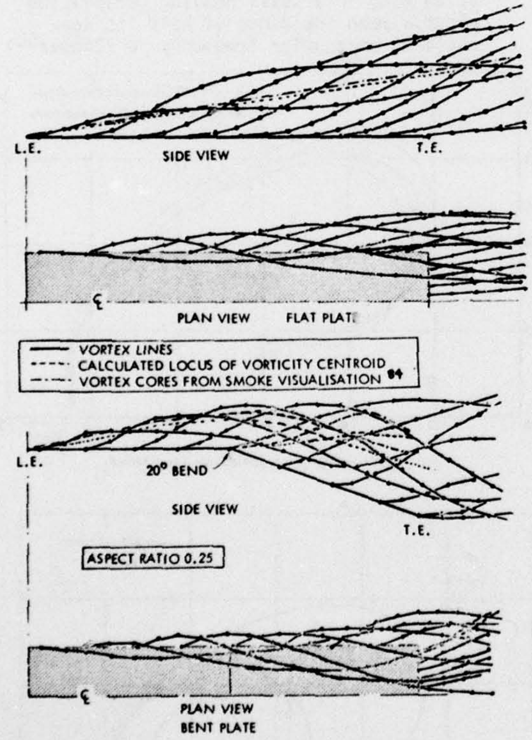

Fig 16 Multivortex model for rectangular wings in incompressible flow (Maskew66)

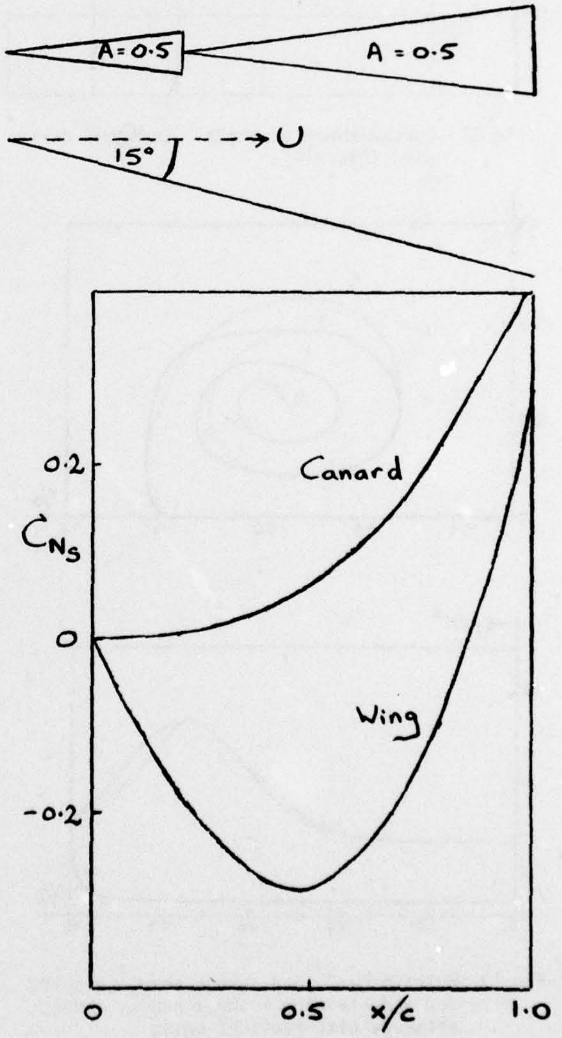

Fig 18 Distribution of nonlinear normal force on wing and canard surfaces (Finkleman67)

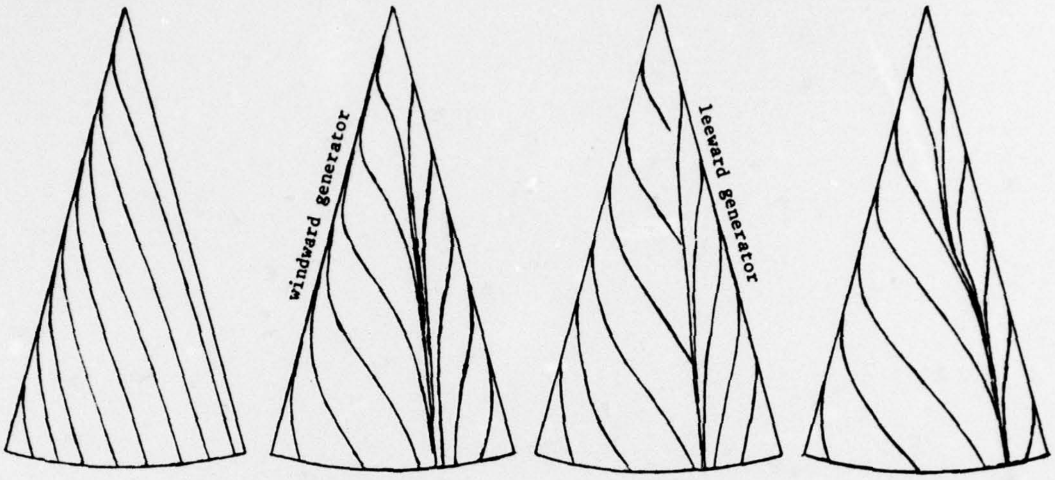

attached flow
limiting streamlines

laminar separation
limiting streamlines

laminar separation
inviscid streamlines

laminar-turbulent separation
limiting streamlines

Fig 19 Streamlines on the developed surface of a slender cone at incidence (diagrammatic)

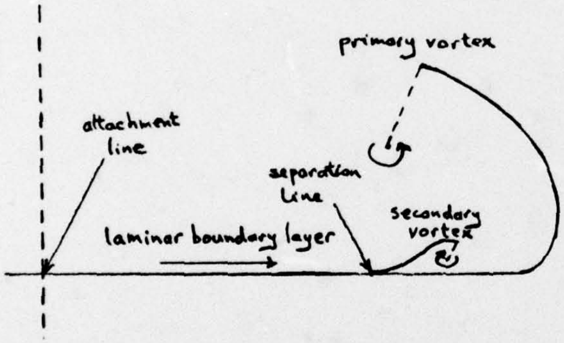

Fig 20 Model for secondary separation calculation[24]

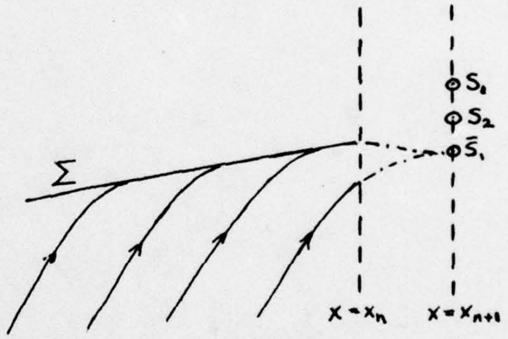

Fig 21 Proposed procedure for constructing separation line

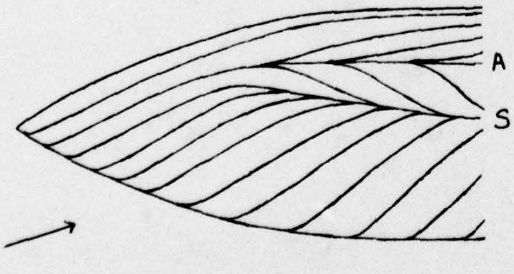

Fig 22 Side view of possible skin-friction lines on ogive-cylinder

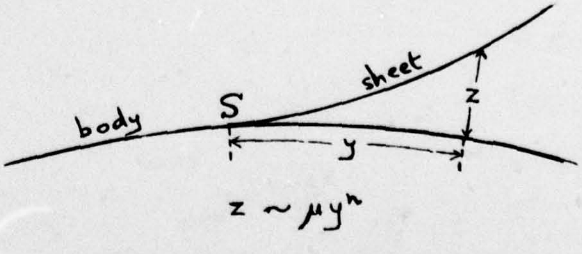

Fig 23 Section through vortex sheet leaving smooth wall

STRUCTURE OF TURBULENCE IN COMPLEX FLOWS

P.Bradshaw
Imperial College
London, SW7 2BY

A "complex" turbulent flow is one in which the turbulence structure is significantly different from that in classical textbook shear layers such as the plane boundary layer and mixing layer (Refs. 1-3). The two commonest causes of complexity in this sense are interaction between the shear layer and another turbulence field - perhaps another shear layer - and distortion of a single shear layer by an externally-imposed strain rate in addition to the mean shear. Unsteadiness and three-dimensionality do not constitute complexities in themselves but allow more opportunities for interaction or distortion to occur. In nearly all cases the turbulent flow is dominated by a shear layer because it is, as a rule, only in shear layers that large Reynolds-stress gradients can arise. However if the flow is strongly distorted the shear layer may not obey Prandtl's thin-shear-layer ("boundary layer") approximation that terms of order δ/ℓ are negligible, and some attention will be given below to higher-order approximations. It will be found that such approximations are best treated on the same empirical level as turbulence modelling, and that is why they are discussed in the present section.

First, the effects of unsteadiness or three-dimensionality on turbulence and turbulence "models" (empirical equations for Reynolds stress) will be discussed. We then outline the response of shear layers to extra rates of strain and present the concept of the "fairly thin shear layer", in which terms that are neglected in the shin-shear layer equations are retained but approximated. Finally the special problems of separated flow are briefly reviewed.

1.0 Effect of Unsteadiness on Turbulence Structure

It is assumed herein that a satisfactory form of statistical average for an unsteady flow has been chosen already: it can be a phase average in a periodic flow, an ensemble average in any flow, or even something less accessible to experiment like a spanwise average in a two-dimensional flow. Denoting the chosen average by an overbar, the exact transport equation for the Reynolds shear stress $-\rho\overline{uv}$ in two-dimensional unsteady flow at high local Reynolds number is (Ref. 4)

$$\frac{\partial(-\overline{uv})}{\partial t} + U\frac{\partial(-\overline{uv})}{\partial x} + V\frac{\partial(-\overline{uv})}{\partial y} = \overline{v^2}\frac{\partial U}{\partial y} - \overline{\frac{p'}{\rho}\left(\frac{\partial u}{\partial y} + \frac{\partial v}{\partial x}\right)} + \frac{\partial}{\partial y}\left(\frac{\overline{p'u}}{\rho} + \overline{uv^2}\right) \qquad (1)$$

This is exactly the same as in steady flow with the addition of the time-dependent terms.

Now the whole left-hand side, written $D(-\overline{uv})/Dt$ for short, is the time derivative of $\overline{uv}$, following the ensemble-average movement of a fluid element. It is sometimes called the "substantial" derivative of $-\overline{uv}$. The fluid element has no way of sensing the ratio of spatial derivatives to time derivative in the left-hand side: therefore this ratio is immaterial to the behaviour of the right-hand side: therefore a steady-flow turbulence model can be used to close the equation, providing that $D\overline{uv}/Dt$ in the unsteady flow does not exceed the values for which the turbulence model is satisfactory in steady flow. For example, if the most rapid streamwise change which the turbulence model can cope with in a boundary layer is a doubling of $-\overline{uv}$ in a distance of 10δ, $|D\overline{uv}/Dt| \ngtr U_e\,\overline{uv}/(10\delta)$ where U_e is the free-stream velocity. If $D\overline{uv}/Dt$ is wholly a time derivative and $\overline{uv}$ changes by 100 percent in a cycle (as in the boundary layer on an infinite plate below an oscillating free stream) the time constant or circular frequency of the flow must not exceed $U_e/(10\delta)$ where U_e is the (maximum) free stream velocity. Note that separate bounds on streamwise wavelength and on frequency in a space-dependent unsteady flow are not required according to this analysis; an upper limit on the frequency seen by a moving fluid element can be derived separately from steady-flow considerations. Let us suppose, for instance, that the steady-flow turbulence model cannot simulate the response to spatial changes with a wavelength less than 8δ, whatever their magnitude. Then the moving-axis frequency $\omega - kU$ must not exceed $2\pi U_e/(8\delta)$; here k is the wave number, $2\pi/(\text{wavelength})$.

Providing that these limits on $D\overline{uv}/Dt$ and on moving-axis frequency are not exceeded, the steady-flow turbulence model can be used without change and with confidence. The limits quoted above are merely examples, order-of magnitude estimates for a good transport-equation turbulence model. An eddy-viscosity model might have rather more restrictive quantitative limits, but the transposition of steady-flow limits to unsteady flow via the above discussion of the exact Reynolds-stress transport equation is valid whether the turbulence model uses that equation explicitly or not. It need hardly be said that steady-flow limits on $D\overline{uv}/Dt$ and moving-axis frequency have not been well defined. There may be specialized unsteady-flow problems, for example high-frequency problems, which would warrant an effort to develop a special turbulence model but I am not aware that any such work has been done; on the other hand several authors (Refs.5-7) have considered turbulence models for steady flow over wavy surfaces which pose much the same modelling problems as oscillating flows. Ref.8 discusses turbulence generated by internal waves.

2.0 Effect of Mean-Flow Three-Dimensionality on Turbulence Structure.

It has been implicitly assumed in nearly all calculation methods for 3D flow, and has been explicitly argued by several people including the present author, that since turbulence is always (instantaneously) three-dimensional it should not be greatly affected by mild three-dimensionality of the mean flow. It is of course to be expected that symmetry results like $\overline{uw} = 0$(where y is normal to the surface) will disappear, but structure parameters like $\overline{v^2}/(\overline{u^2} + \overline{w^2})$ should not, it is argued, be greatly affected.

Measurements in a three-dimensional separating boundary layer at NLR, Amsterdam (Refs. 9,10) revealed quite large discrepancies in existing calculation methods. Specifically the resistance of the boundary layer to separation was over-predicted by the calculations. Comparisons of all available calculation methods at the "Trondheim Trials" (Ref.11) showed the same effect. In terms of an eddy-viscosity model, the experiments showed a very much smaller eddy viscosity in the cross-stream plane, $-\overline{vw}/(\partial W/\partial y)$, than in the longitudinal plane, $-\overline{uv}/(\partial U/\partial y)$. A similar behaviour was discernible in the data of Johnston (Ref.12) for the rapidly-separating flow up a swept, forward-facing step. It is to be expected that as the direction of the resultant shear velocity gradient (Fig.1) changes with x the direction of the resultant shear stress will lag behind it instead of coinciding with the direction of the resultant velocity gradient as predicted by an eddy-viscosity model. This is just a consequence of the presence of D/Dt terms ("history effect") in the Reynolds-stress transport equations (see Section 1.0), and is generally observed in 3D boundary layers in moderate pressure gradients. However in the inner part of Johnston's flow the direction of the resultant shear stress rotated in the opposite sense to the direction of the resultant velocity gradient, and a tendency towards the same effect is apparently responsible for the disagreement between the NLR data and the calculation methods. In the NLR measurements, the angle between the resultant shear stress and the x direction - the initial flow direction, namely

$$\gamma_\tau \equiv \tan^{-1} \frac{\overline{vw}}{\overline{uv}} \tag{2}$$

was of the same sign as

$$\gamma_g \equiv \tan^{-1} \frac{\partial W/\partial y}{\partial U/\partial y} \tag{3}$$

but smaller, by an amount greater than could be explained by history effects. (The ratio of the two *tangents is of course the ratio of the two components of eddy viscosity mentioned above).*

A very plausible explanation has been given by Rotta (Ref.13). In a calculation method based on the transport equations for $-\overline{uv}$ and $-\overline{vw}$, namely

$$\frac{D(-\overline{uv})}{Dt} \equiv \left(U\frac{\partial}{\partial x} + V\frac{\partial}{\partial y} + W\frac{\partial}{\partial z}\right)(-\overline{uv}) = \overline{v^2}\,\frac{\partial U}{\partial y} - \overline{p'\left(\frac{\partial u}{\partial y} + \frac{\partial v}{\partial x}\right)} + \frac{\partial}{\partial y}\left(\overline{p'u} + \overline{uv^2}\right) \tag{4}$$

$$\frac{D(-\overline{vw})}{Dt} = \overline{v^2}\,\frac{\partial W}{\partial y}\,\overline{p'\left\{\frac{\partial w}{\partial y} + \frac{\partial v}{\partial z}\right\}} + \frac{\partial}{\partial y}\left(\overline{p'w} + \overline{wv^2}\right) \tag{5}$$

the most important part of the process of empirical closure ("modelling") is the choice of an empirical expression for the pressure-strain terms, $\overline{p'(\partial u/\partial y + \partial v/\partial x)}$ and its equivalent in the $\overline{vw}$ equation. The exact Poisson equation for the pressure fluctuation, derivable from the Navier Stokes equation (Ref.4) is

$$-\frac{1}{\rho}\nabla^2 p' = \frac{\partial U}{\partial y}\frac{\partial v}{\partial x} + \frac{\partial W}{\partial y}\frac{\partial v}{\partial z} + \ldots \tag{6}$$

where the additional terms are further terms containing mean velocity gradients (which are small in boundary layers) and also terms containing only turbulence quantities (which are not small). It is therefore generally agreed that the empirical expressions for the pressure-strain term should contain the mean velocity gradient. Largely because of the development of 3D calculation methods from 2D prototypes, it is explicitly or implicitly assumed that $\overline{p'(\partial u/\partial y + \partial v/\partial x)}$ depends on $\partial U/\partial y$ but not on $\partial W/\partial y$, while $\overline{p'(\partial w/\partial y + \partial v/\partial x)}$ depends on $\partial W/\partial y$ but not on $\partial U/\partial y$. Rotta has pointed out that this assumption is correct only if the turbulence is statistically symmetrical about the direction of the resultant mean velocity gradient, γ_g as defined in Eq.(3). This is unlikely to be the case if $\gamma_g \neq \gamma_\tau$, for instance. Rotta's suggested improvement violates the principle of translational invariance, and it is better, at least for expository purposes, to consider the general assumption that the relative contributions of the two velocity gradients to the two pressure-strain terms depends on γ_g and γ_τ. Suppose that we write the part of $\overline{p'(\partial u/\partial y + \partial v/\partial x)}$ *that depends on the mean velocity gradients as* $\overline{p'_A(\partial u/\partial y + \partial v/\partial x)}$, the remaining, turbulence-dependent, part being represented by suffix T, and define $\overline{p'_A(\partial w/\partial y + \partial v/\partial z)}$ similarly. Then define

$$\gamma_p \equiv \tan^{-1} \frac{\overline{p'_A\,(\partial w/\partial y + \partial v/\partial z)}}{\overline{p'_A\,(\partial u/\partial y + \partial v/\partial x)}} \tag{7}$$

Rotta's argument is that γ_p is not the same as γ_g, but that $\gamma_p - \gamma_g$ depends on $\gamma_g - \gamma_\tau$. Note that according to the principle of rotational invariance only relative angles matter. Rotta's suggestion also implies a change *in the magnitude of the resultant pressure-strain term, the fractional change being a function of* $\gamma_g - \gamma_\tau$ also, but we will neglect this here for simplicity of exposition. If we require the magnitude to be the same as in a quasi-two-dimensional flow (with $\gamma_p = \gamma_g = \gamma_\tau$) then we can write

$$\overline{p'_A\left(\frac{\partial u}{\partial y} + \frac{\partial v}{\partial x}\right)} = K_{ss}\,\overline{v^2}\left[\left(\frac{\partial U}{\partial y}\right)^2 + \left(\frac{\partial W}{\partial y}\right)^2\right]^{\frac{1}{2}} \cos\gamma_p \equiv K_{ss}\,\overline{v^2}\,\frac{\partial U}{\partial y}\,\frac{\cos\gamma_p}{\cos\gamma_g} \tag{8}$$

$$\overline{p'_A\left(\frac{\partial w}{\partial y} + \frac{\partial v}{\partial z}\right)} = K_{ss}\,\overline{v^2}\,\frac{\partial W}{\partial y}\,\frac{\sin\gamma_p}{\sin\gamma_g} \tag{9}$$

where K_{ss} is the same (positive) constant as in two-dimensional flow. If we assume that the direction of the vector formed by the turbulence-dependent part of the pressure-strain term is the same as that of the resultant shear stress (that is, these turbulent "scrambling" terms are assumed to reduce the magnitude of the shear stress without affecting its direction), and if we neglect the mean and turbulent transport terms (the first and last in Eqs.(4) and (5)), we get the eddy-viscosity ratio as

$$\frac{\tan\gamma_\tau}{\tan\gamma_g} = \frac{-\overline{vw}/(\partial W/\partial y)}{-\overline{uv}/(\partial U/\partial y)} \approx \frac{1 - K_{ss}\,\sin\gamma_p/\sin\gamma_g}{1 - K_{ss}\,\cos\gamma_p/\cos\gamma_g} \tag{10}$$

which is less than unity of $\gamma_p > \gamma_g$. We note that the eddy-viscosity ratio depends on the direction of the axes! If we choose the x axis along the direction of the resultant velocity gradient so that $\gamma_g = 0$ the ratio becomes infinite if $\gamma_p = \gamma_g$, because $\partial W/\partial y = 0$ but $\overline{vw} = 0$ in these axes. N. Pontikos and the author are currently conducting experiments (in computer and in wind tunnel) to explore the behaviour of γ_p. It seems most likely that γ_p depends on $\partial\gamma_g/\partial x$ or $\partial\gamma_\tau/\partial x$ rather than on local conditions.

The conclusion which the non-specialist can draw from this rather mathematical argument is that quasi-two-dimensional assumptions such as isotropy of eddy viscosity should not be made unthinkingly in 2D flows.

The discussion has concentrated on aerofoil-type boundary layers. "Slender" shear layers, like the flow near a wing-body junction or a wing tip, may hold further surprises. Certainly the existing turbulence models are suspect; one of the most advanced, that of Naot et al. (Ref.14) predicts the wrong sign for the effect of $\partial W/\partial y$ discussed above.

3.0 Extra Rates of Strain

It is well known that longitudinal curvature of the mean streamlines can have a large effect on turbulent flow (Ref 15). The effect is much the same whether the streamline curvature arises from surface curvature or from bodily rotation of the flow system. Lateral divergence, such as occurs on a cone or a cylinder-flare combination, also produces large effects. The tendency for the skin-friction coefficient in a retarded supersonic boundary layer to rise and the shape parameter H to fall - contrary to what happens in low speed flow - seems to imply a large effect of pressure gradient on turbulence structure (Ref.16), although recent work (Ref.17) suggests that the effect is reproduced automatically by the more advanced turbulence models.

It is convenient to group these phenomena together as the effect of "extra rates of strain" - extra, that is, to the basic mean shear that drives the shear layer. (The surprising effects of an extra component of mean shear in a 3D boundary layer deserve separate treatment and received it in the last section). Such extra strain rates ($\partial V/\partial x$ for curvature, $\partial W/\partial z$ for lateral divergence, $-\text{div}\,\underline{U}$ for bulk compression) appear as extra terms in the Reynolds-stress transport equations. However the effects on the turbulence structure are much larger than the size of these explicit extra terms would suggest, and the implication is that the extra strain rates strongly affect the existing terms in the transport equations even though the existing terms do not contain the extra strain rates explicitly.

The mechanism by which the extra strain rates act is not always clear. In the case of streamline curvature, one can show qualitatively that small disturbances will be amplified if the angular momentum decreases outward from the centre of curvature (as in the case of the boundary layer on a concave surface) and conversely. The effects of lateral divergence and bulk compression can both be explained, again qualitatively and not altogether convincingly, by arguing that the z component vorticity of the large eddies will be increased if the cross section of a fluid element in the x y plane decreases as it moves downstream, leading to increased entrainment and mixing. Quantitatively, a "rule of thumb" is that the effect of a small extra strain rate e on the apparent eddy viscosity is to multiply it by a factor of order

$$1 + \frac{10\,e}{\partial U/\partial y}$$

although the ratio of the explicit extra terms in the Reynolds-stress transport equations to the main terms is only of order $e/(\partial U/\partial y)$. More refined, but still linear, allowances are discussed in Ref.15.

Large extra strain rates can have an overwhelming effect on turbulence. The best demonstration of this is still the flow-visualization work of Johnston et al. (Ref.18) in a rotating duct flow where turbulence was virtually suppressed on the "stable" side and large quasi-steady streamwise vortex rolls ("convection cells") appeared on the unstable side. The analogy between streamline curvature (centrifugal or Coriolis "force") and buoyancy is quantitatively helpful if the extra strain rates are small and at least qualitatively helpful if they are large. The rapidly-rotating core of an aircraft trailing vortex or of an atmospheric tornado seems to be so strongly stabilized by rotation that radial motion almost disappears and high longitudinal velocities can occur in the core without generating restraining Reynolds stresses. Strong acceleration can cause reverse transition in a supersonic boundary layer even if the pressure rise is quite small, about $75\,\tau_w$ according to Narasimha and Viswarath (Ref.19). At low speeds, where $75\,\tau_w$ is roughly a quarter of $\frac{1}{2}\rho U_e^2$, so small a pressure rise would be very unlikely to cause reverse transition.

Unsteadiness and three dimensionality provide more opportunities for extra strain rates to occur. The lateral divergence $\partial W/\partial z$ in a three-dimensional boundary layer is likely to be non-zero nearly everywhere, for instance, and highly-skewed flows may develop concentrated longitudinal vortices in which the stabilizing effects of streamline curvature may be apparent. A similar stabilizing effect could occur in the strong transverse vortex that forms in the boundary layer of an aerofoil oscillating in pitch (Paper 8), or in transverse shed vortices.

4.0 "Fairly thin" shear layers (Fig.2)

The derivation of the laminar boundary-layer (thin-shear-layer) equations from the Navier-Stokes equations by neglecting terms of order $(\delta/\ell)^2$ - strictly, $(d\delta/\partial x)^2$ - is well known. In turbulent flow, terms of order δ/ℓ times the main terms - notably $\partial\overline{u^2}/\partial x$ - are commonly neglected. The usual textbook derivation applies to a boundary layer on a flat surface, or some other plane shear layer, where $\partial p/\partial y$ is of order $\rho U_e^2\,\delta/\ell^2$. On a surface of radius of curvature R in the stream direction, $\partial p/\partial y$ is of order $\rho U_e^2/R$ and therefore generally of order $\rho U_e^2/\ell$; that is, it is larger by a factor of order ℓ/δ than on a flat surface. The ratio of the normal velocity gradient in the free stream, $\partial U/\partial y \approx -U/R$, to a typical velocity-gradient within the shear layer is of order δ/R, i.e. δ/ℓ. Thus as long as the radius of longitudinal curvature of the shear layer is of order ℓ, we can consistently neglect terms like $\partial u^2/\partial x$ and assume $\partial p/\partial y = 0$.

Now in a turbulent jet δ/ℓ is roughly 0.2 and neglect of terms of order δ/ℓ is shaky. Again, streamline radii of curvature an order of magnitude smaller than ℓ are found in the near wakes of aerofoils, in free shear layers over bluff bodies, and in duct elbows. Large values of $d\delta/dx$ occur near separation. Although it is easy to show that viscous or turbulent stress gradients are usually significant only in fairly thin shear layers, a compromise between the neglect of terms of order δ/ℓ and the retention of all terms in the Navier Stokes equations is needed.

Second-order boundary layer theory has been developed rigorously only for laminar flows and is of limited use. A more general stratagem is to approximate, rather than neglect, terms of order δ/ℓ. It happens that this stratagem merges almost imperceptibly with the approximate processes of turbulence modelling and finite-difference solution, which is why it is most conveniently discussed here. For instance the term $\partial \overline{u^2}/\partial x$ in the x-component momentum equation could be taken as - say - a constant times $\partial(-\overline{uv})/\partial x$, and $\partial(-\overline{uv})/\partial x$ at given x approximated as $\left[(-\overline{uv})_x - (-\overline{uv})_{x-\Delta x}\right]$ in preparation for a step forward to $x+\Delta x$. Again $\partial p/\partial y$ can in simple cases be approximated as $\rho U^2/R$, where R is the known radius of curvature of the surface. Thus at given y

$$\frac{\partial p}{\partial x} = \frac{\partial p_w}{\partial x} + \frac{\partial}{\partial x}\left[\frac{1}{R}\int \rho U^2\, dy\right] = \frac{\partial p_w}{\partial x} - \frac{1}{R^2}\frac{dR}{dx}\int \rho U^2\, dy + \frac{1}{R}\int \frac{\partial}{\partial x}(\rho U^2)\, dy \tag{11}$$

Nominally this converts the x-component momentum equation into an integro-differential equation, but it is easy to see that the system of equations as a whole remains parabolic because the approximation for $\partial p/\partial y$ contains no derivative itself. The finite-difference evaluation of the integrals would be straightforward, and if the numerical method is iterative (necessary in order to improve on an "upstream" value for U in $U\partial U/\partial x$) the derivative inside the integral can be evaluated to the same accuracy as $U\partial U/\partial x$ itself.

It has been found in practice, by the present author and doubtless by many other workers, that small terms which change the type of a differential equation do not necessarily cause inaccuracy or catastrophic failure of a numerical solution. For example the addition of small diffusive terms to hyperbolic equations, making them parabolic, does not necessarily degrade the accuracy or stability of the method of characteristics. Again, small elliptic terms may not invalidate a marching solution; $\mu\partial^2U/\partial x^2$ could be retained in the laminar boundary layer equations providing that the finite-difference representation did not involve values of U further downstream than the position reached by the calculation. Clearly the retention of type-changing terms needs caution; in most cases the numerical method will either continue to work accurately or fail catastrophically (and therefore noticeably) but an intermediate stage of large but non-obvious inaccuracy may occur.

Even if type-changing terms are large it may be possible to take advantage of the similarity between single-sweep marching solution of parabolic (or hyperbolic) equations and multiple-sweep line-relaxation solutions of elliptic equations. For example (Ref.20) the normal-component momentum equation - in slightly simplified form -

$$U\frac{\partial V}{\partial x} + V\frac{\partial V}{\partial y} = -\frac{1}{\rho}\frac{\partial p}{\partial y} - \frac{\partial \overline{uv}}{\partial x} - \frac{\partial \overline{v^2}}{\partial y} \tag{12}$$

can be solved together with the equations for x-component momentum, continuity and Reynolds stress by a multiple-sweep marching method. Starting from a guess of the pressure field p(x,y), the x-momentum, continuity and Reynolds stress equations are solved at each x step in the usual way, after which Eq.(12), with U, V and the Reynolds stresses known, can be solved at once to give a new profile p(y) for that x. After the sweep is finished the new p(x,y) is used for a second sweep, and so on. Patankar, Pratap and Spalding (Ref.21) have used a slightly different procedure for three-dimensional internal flows; in this, the momentum equations and Reynolds-stress equations are solved first and the pressure is then adjusted, with consequent quasi-inviscid adjustments of the velocity components, to satisfy the continuity equation. It is not clear whether this procedure is made necessary by the three-dimensionality or by the specification of $V = 0$, rather than $p = p_e$, at the upper boundary. The sequence in which Eq.(12) is solved last - and is then trivial - is easier to fit into an existing thin-shear-layer program and is also most convenient for the viscous-inviscid matching procedure in which $p\ (y=\delta)$ comes from, and $V(y=\delta)$ goes to an inviscid calculation method for the flow outside $y = \delta$. It is immediately applicable to three-dimensional "boundary sheets" with $p(y=\delta) = p(x,z)$; in principle it could also be used in unsteady flow but this has not yet been considered. These schemes rely on upstream influence proceeding only via the pressure; if U becomes negative so that information can be convected upstream, $U(x+\Delta x)$ is needed before U(x) can be calculated, and in this case U(x,y) as well as p(x,y) must be stored from sweep to sweep. Multiple-sweep methods for these "recirculating" flows are discussed in Section 6.3, for the special case where $\gamma p/\partial y$ is negligible.

The availability of adequate and efficient numerical methods for "fairly thin" shear layers, in which the boundary-layer equations are inaccurate and the full Navier-Stokes equations unnecessary, should aid the development of turbulence models for such cases.

5.0 Special Problems of Separated Flow

Flow-visualization studies quickly show that a separated-flow region is always unsteady and three-dimensional. Typical fluctuation frequencies can be orders of magnitude less than in the downstream-going flow; the wavelengths are of the same order as in the main flow but velocities are much less. Consequently a perturbation entering the recirculating flow region may be returned to the main flow at a much later time. Unless a vortex street or other feedback mechanism is present, even these very slow fluctuations count as "turbulence". They can contribute to Reynolds stresses in the recirculating region itself and, on re-entrainment into the free shear layer, can disturb the turbulence structure of the latter. The main effect of the very slow fluctuations is likely to be a bodily displacement of the shear layer, but this too must be counted as turbulence in the sense of Reynolds averaging, because a fluctuating displacement appears as an increase in mean spreading rate and therefore necessarily an increase in Reynolds stress. It is clear that a proper description of the flow would require several levels of time averaging to distinguish the different frequency ranges; however the ranges are not completely distinct.

Our preoccupation with mean values can even lead to confusion in interpreting flow-visualization patterns. Brederode (Ref.22) found that the direction of rotation of the corner vortices in the recirculating-flow region behind a backward-facing step, as shown by surface oil-flow visualization, changed sense when the boundary layer on the top of the step was tripped. Further investigation with surface injection showed that in all cases the sense of rotation fluctuated irregularly with time, so the direction of rotation of the final mean pattern was determined by the small difference of two large quantities.

The most important single property of a recirculating-flow region is the "residence time" (Ref.23). This is the average time for which a marked particle introduced into the recirculating-flow region will remain there. It is of the order of the volume of the recirculating-flow region divided by the rate of entrainment from that region into the free shear layer that bounds it. It happens also to be of the same order as the "spin-up" time required to establish the recirculating flow.

In three-dimensional separated flow - including most nominally two-dimensional flows - the recirculating flow is usually strongly ventilated at its spanwise extremities because of the presence of streamwise vorticity (Fig.3) and the size of the recirculating region will depend on the ratio of this ventilation rate to the entrainment through the main part of the free shear layer.

In unsteady separated flow the near-equality of the residence time and the spin-up time causes the growth in volume and the growth in angular momentum to take place at roughly the same rate if the spin up is controlled by the shear stress in the free shear layer. In many unsteady separated flows the main source of vorticity is convection from upstream rather than shear transfer from the shear layer and in these cases high rotation rates can be attained very rapidly.

Virtually nothing is known of the behaviour of turbulence in recirculating flows. The above description suggests that it is highly complicated and that only in very undemanding cases will one be able to represent it by simple eddy-viscosity models or even the present vintage of Reynolds-stress transport models.

REFERENCES

1.	Bradshaw, P.	Variations on a Theme of Prandtl. AGARD Conf. Proc.93 "Turbulent Shear Flow", p.C-1, 1971.
2.	Bradshaw, P.	Complex Turbulent Flows. J.Fluid Engg., Vol.97, p.146, 1975.
3.	Bradshaw, P.	Complex Turbulent Flow. Theoretical and Applied Mechanics (W.T.Koiter, Ed.) North-Holland, 1972, p.103.
4.	Bradshaw, P. (Ed.)	Turbulence (Topics in Applied Physics, Vol.12), Springer-Verlag, 1976.
5.	Townsend, A.A.	Flow in a deep turbulent boundary layer over a surface distorted by water waves. J.Fluid Mech., Vol.55, p.719, 1972.
6.	Davis, R.E.	On prediction of the turbulent flow over a wavy boundary. J.Fluid Mech., Vol.52, p.287, 1972.
7.	Davis, R.E.	Perturbed turbulent flow, eddy viscosity and the generation of Reynolds stresses. J.Fluid Mech., Vol.63, p.673, 1974.
8.	Geller, M.A., Tanaka, H. and Fritts, D.C.	Production of turbulence in the vicinity of critical levels for internal gravity waves. J.Atmos.Sci., Vol.32, p.2125, 1975.
9.	Berg, B.v.d., Elsenaar, A., Lindhout, J.P.F. and Wesseling,P.	Measurement in an incompressible three-dimensional turbulent boundary layer, under infinite swept-wing conditions, and comparison with theory. J.Fluid Mech., Vol.70, p.127, 1975.
10.	Berg,B.v.d.	Investigations of three-dimensional incompressible turbulent boundary layers. NLR, Amsterdam, TR 76001 U, 1976.
11.	East, L.F.	Computation of three-dimensional turbulent boundary layers. FFA, Sweden, TN AE-1211, 1975.
12.	Johnston, J.P.	Measurements in a three-dimensional turbulent boundary layer induced by a swept forward-facing step. J.Fluid Mech., Vol.42, p.823, 1970.
13.	Rotta, J.C.	A family of turbulence models for three-dimensional thin shear layers. DLR, Göttingen, IB-251-76A25 (paper presented at Penn.State University Symposium on Turbulent Shear Flow, 1977).
14.	Naot, D., Shavit, A. and Wolfshtein, M.	Fully developed turbulent flow in a square channel. Wärme-und Stoffubertragung, Vol.7, p.155, 1974.
15.	Bradshaw, P.	Effect of streamline curvature on turbulent flow. AGARDograph 169, 1973.
16.	Bradshaw, P.	The effect of mean compression or dilatation on the turbulence structure of supersonic boundary layers. J.Fluid Mech., Vol.63, p.449, 1974.
17.	Rubesin, M.W. et al.	A critique of some recent second-order turbulence closure models for compressible boundary layers. AIAA paper 77-128, 1977.
18.	Johnston, J.P., Halleen, R.M. and Lezius, D.K.	Effects of spanwise rotation on the structure of two-dimensional fully developed turbulent channel flow. J.Fluid Mech., Vol.56, p.533, 1972.
19.	Narasimha, R. and Viswarath, P.R.	Reverse transition at an expansion corner in supersonic flow, AIAA J., Vol.13, p.693, 1975.
20.	Mahgoub, H.E.H. and Bradshaw, P.	Calculation of turbulent shear layers with large normal pressure gradients. Submitted to AIAA J. 1977
21.	Patankar, S.V., Pratap, V.S. and Spalding, D.B.	Prediction of turbulent flow in curved pipes. J.Fluid Mech., Vol.67, p.583, 1975.

22. Brederode, V.A.S.L. de — Three-dimensional effects in nominally two-dimensional turbulent flows. PhD thesis, Imperial College, 1975.

23. Humphries, W. and Vincent, J.H. — Experiments to investigate turbulent transport processes in the near wakes of disks in turbulent air flow. J.Fluid Mech., Vol.75, p.737, 1976. (*see also* Vol.73, p.453).

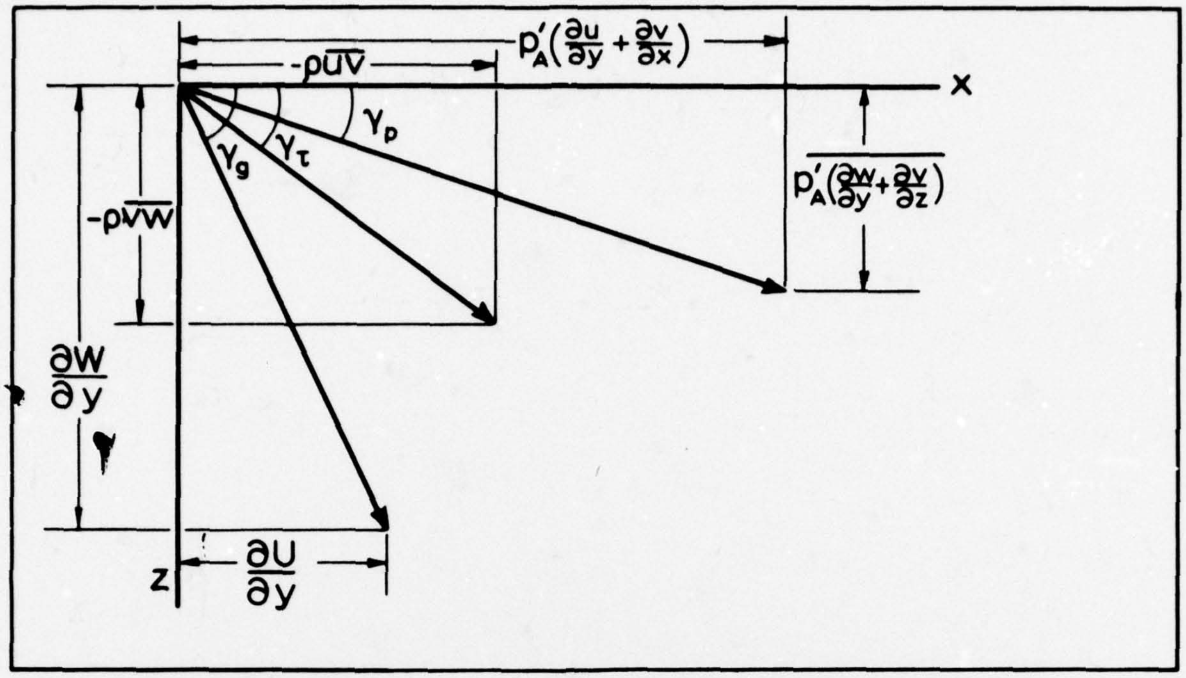

Fig. 1 DEFINITIONS OF 'VELOCITY GRADIENT VECTOR', 'SHEAR STRESS VECTOR' AND 'PRESSURE STRAIN VECTOR' IN 3D BOUNDARY LAYER.

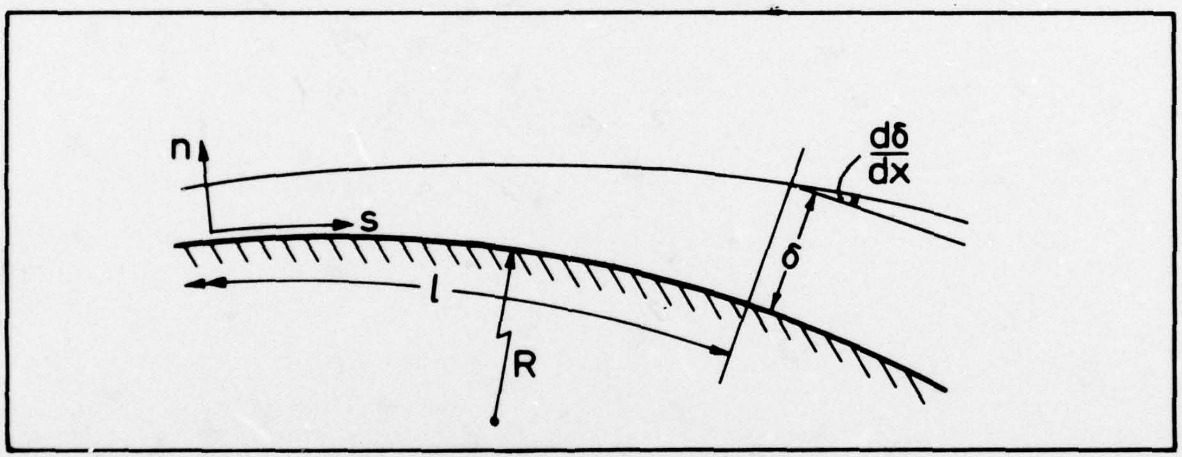

Fig. 2 'FAIRLY THIN SHEAR LAYER' : $d\delta/dx <\!\!< 1$ or $\delta/R <\!\!< 1$

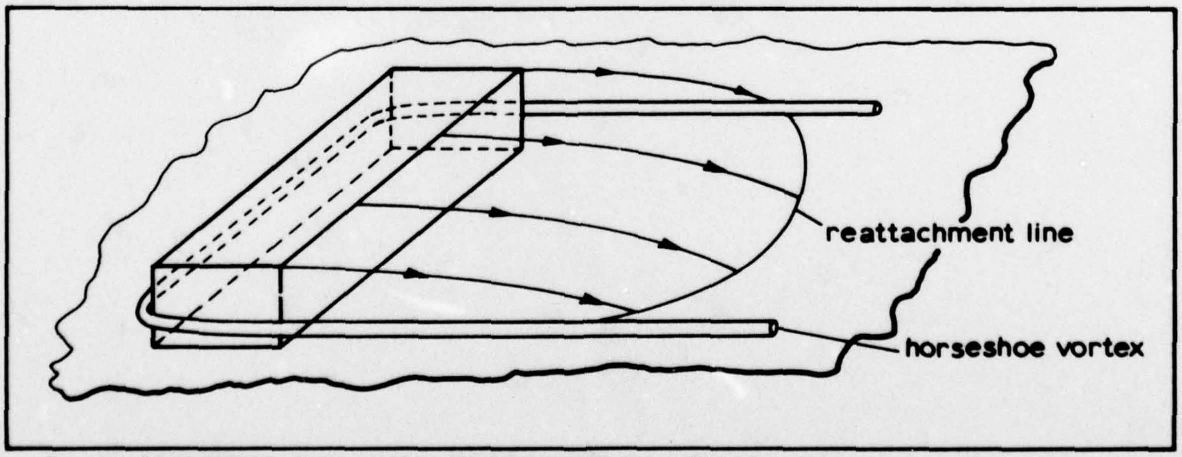

Fig. 3 SEPARATED FLOW OVER 3D OBSTACLE ON A PLATE

PREDICTION OF SEPARATION USING BOUNDARY LAYER THEORY

P.Bradshaw
Imperial College
London, SW7 2BY

As was well pointed out by Townsend (Ref.1) an experimental surface pressure distribution for a separating flow almost always shows an abrupt decrease in adverse pressure gradient at the separation point - because of the sudden increase in $d\delta^*/dx$ - so that the position of separation can be found quite accurately by inspection. Carrying out a boundary layer calculation for such a flow, taking the pressure distribution as known, is therefore of no practical value. Especially in separating flow, practical problems involve the matching of a shear-layer* calculation to that of an inviscid† outer‡ flow. One part of this process is the solution of equations for the shear layer (e.g. boundary layer and wake) with a pressure distribution at the shear-layer edge derived from the inviscid solution. This is the problem addressed in this Section. Calculation of the boundary layer up to a short distance from separation is straightforward in principle, and we therefore consider first the presence or otherwise of a singularity at separation, followed by a discussion of calculation methods for reversed flow. Global Navier-Stokes solutions will not be considered but attention will be given to cases where the thin-shear-layer approximation is not accurate enough.

1.0 The Singularity at Separation

"Separation" is commonly used to mean either "vanishing surface shear stress" or "departure of the shear layer as a whole from a solid surface". In steady two-dimensional flow the two phenomena usually occur together, although if "departure" means "recession to a distance >> δ" then some shallow separation bubbles have points of zero shear stress but no "departure". Below we use "separation" to imply "departure", and refer to the point of zero shear stress only as such.

In unsteady flow, surface shear stress can change sign without separation occurring, for example on an oscillating plate in still air. In three-dimensional flow the shear layer can depart from the surface without the magnitude of the surface shear stress falling to zero; usually, however, there is a change of sign of the component of surface shear stress normal to the line on which the plane of the departing shear layer intersects the surface (Fig.1). A simple example is the radial jet that departs from the equator of a sphere rotating in still air; the meridional component of surface shear stress has opposite signs in the two hemispheres.

Occasionally, as in the case of the rotating sphere, the thin-shear-layer approximation may be applicable to the whole of the departed viscous region, except near the line of departure itself. More often the departed viscous region will consist of a recirculating-flow region bounded by a free shear layer on one side and the solid surface on the other (Fig.2) and although the thin-shear-layer (TSL) approximation may be good enough for the shear layer it will not do for the recirculation zone. In virtually all cases except very shallow separation bubbles, the TSL approximation will be inadequate near the line of departure because the streamline curvature becomes large.

In practice one is interested in calculating both the line of departure and the line of zero surface shear stress, and the status of the thin shear layer equations near the latter line needs examination. A great deal of discussion has centred on the presence of a singularity in the solution at the line of zero shear stress. For a clear and thorough review which has yet to be superseded, see Ref.2. The simplest way to demonstrate what happens, due to Curle (Ref.3) is to take the three-dimensional unsteady thin shear layer equation for the U component velocity

$$\frac{\partial U}{\partial t} + U\frac{\partial U}{\partial x} + V\frac{\partial U}{\partial y} + W\frac{\partial U}{\partial z} = -\frac{1}{\rho}\frac{\partial p}{\partial x} + \nu\frac{\partial^2 U}{\partial y^2} - \frac{\partial}{\partial y}(\overline{uv}) \tag{1}$$

and differentiate with respect to y. Using the continuity equation

$$\frac{\partial U}{\partial x} + \frac{\partial V}{\partial y} + \frac{\partial W}{\partial z} = 0 \tag{2}$$

to merge two terms we get

$$\frac{\partial}{\partial t}U_y + UU_{xy} + VU_{yy} + W_yU_z + WU_{yz} - U_yW_z = \nu U_{yyy} - (\overline{uv})_{yy} \tag{3}$$

where $u_y = \partial U/\partial y$, etc. Differentiating again and writing the equation at $y = 0$, where U, V, W and all gradients with respect to x and z (and therefore, using Eq.(2), $\partial V/\partial y$) are zero, we get

$$\frac{\partial}{\partial t}\frac{\partial^2 U}{\partial y^2} + \frac{\partial}{\partial x}\left\{\frac{1}{2}\left(\frac{\partial U}{\partial y}\right)^2\right\} - \frac{\partial U}{\partial y}\frac{\partial}{\partial t}\left(\frac{\partial W}{\partial y}\right) + 2\frac{\partial W}{\partial y}\frac{\partial}{\partial z}\left(\frac{\partial U}{\partial y}\right) = \nu\frac{\partial^4 U}{\partial y^4} - \frac{\partial^3\overline{uv}}{\partial y^3} \tag{4}$$

where all terms are evaluated at $y = 0$. Now consideration of the wall boundary condition on the motion shows that for small $y, u = y\,a(t)$ and - using the fluctuating continuity equation - $v = y^2\,b(t)$, plus higher order terms in both cases. Therefore $\overline{uv} = c\,y^3$ + higher order terms and $\partial^3\,\overline{uv}/\partial y^3 = 6c$. There is still uncertainty about whether the constant c is zero even in constant-pressure flow but it certainly cannot be <u>assumed</u> zero at present.

---

* A shear layer is a region whose y-wise extent δ is much smaller than its x-wise extent ℓ and in which the dominant rate of strain component is $\partial U/\partial y$. A <u>thin</u> shear layer is one in which quantities of order δ/ℓ are small enough to be neglected. The shear-layer family includes boundary layers, duct flows, wakes, jets etc; I cannot bring myself to call a free shear layer a boundary layer!

† "Inviscid" is an abbreviation for" having negligible viscous-stress terms and turbulent-stress terms, because of the absence of large rates of strain (not because of the absence of viscosity"

‡"Outer" simply means "outside the shear layer"; most of what is said below can be applied to internal-flow problems also.

(i) Two-dimensional steady flow.

$$\frac{\partial}{\partial x}\left\{\tfrac{1}{2}\left(\frac{\partial U}{\partial y}\right)^2\right\} \equiv \frac{\partial}{\partial x}\left(\tfrac{1}{2}\frac{\tau_w{}^2}{\mu^2}\right) = \nu\frac{\partial^4 U}{\partial y^4} - 6c \tag{5}$$

Unless the right-hand side is zero, we get

$$\tfrac{1}{2}\frac{\tau_w{}^2}{\mu^2} = A\,(x - x_s) \tag{6}$$

where A is the non-zero value of the right-hand side near the separation point $x = x_s$. The above analysis holds for a solid surface, $V_w = 0$; however similar results are obtained when V_w is a specified function of x (Ref.4). Thus $\tau_w \sim (x - x_s)^{\frac{1}{2}}$, so the surface shear stress goes to zero as $(x - x_s)^{\frac{1}{2}}$ on one side of separation and is imaginary on the other. There is no obvious reason why the right-hand side should be exactly zero, and it is worth noting that retaining the full viscous term $\nu\nabla^2 U$ in Eq.(1) merely leads to a term in $\partial^3 p/\partial x^3$ in the two-dimensional version of Eq.(4) (because of the relation $\mu(\partial^2 U/\partial y^2)_w = \partial p/\partial x$), which does nothing to reduce the right-hand side to zero in general, because $\partial^4 U/\partial y^4 - 6c$ depends on the history of the pressure gradient rather than its local behaviour. Evidently only an interaction between the boundary layer velocity field and the pressure - such as relaxation of the boundary layer approximation $\partial p/\partial y = 0$ - can relieve the singularity. However the change of τ_w is rapid rather than large. Consider laminar flow and estimate $\partial^4 U/\partial y^4$ as U_e/δ^4 to an order of magnitude. Then

$$\frac{\delta}{U_e}\,\frac{\tau_w}{\mu} \simeq \left[\frac{2\nu}{U_e\delta^2}\,(x - x_s)\right]^{\frac{1}{2}} \tag{7}$$

Now δ is rather larger than $(2\nu\, x/U_e)^{\frac{1}{2}}$ where x is measured from the leading edge, so a generous estimate for τ_w is

$$\frac{\delta}{U_e}\,\frac{\tau_w}{\mu} \simeq \left(\frac{x - x_s}{x}\right)^{\frac{1}{2}} \tag{8}$$

The upstream influence allowed by the Navier Stokes equations but ignored by the boundary layer equations will extend for a distance of order not greater than δ. Thus a rough but generous estimate of the maximum difference between a singular boundary layer solution and the regular Navier Stokes solution is obtained by putting $x - x_s = \delta$ in Eq.(8). Since in constant-pressure flow $(\delta/U_e)\ \tau_w/\mu$ is of order unity this shows that the maximum error in τ_w caused by the singularity is of order $(\delta/x)^{\frac{1}{2}}$ times the constant-pressure value of τ_w. That is, the singularity is rather weak. From this it follows that only a small adjustment to the boundary layer calculation - essentially, a small departure from the specified pressure - is needed to suppress the effects of the singularity. One might even be able to march right over the point of zero wall shear stress in a numerical calculation, using a step length of the order of the boundary layer thickness. This is indeed often done in calculations of a flat-plate wake where the Blasius profile is assumed to apply up to the trailing edge $x = x_T$ and some crude approximation is made to obtain $U(x = x_T + \Delta x,\ y = 0)$; for example if the y spacing of the finite-difference net is Δy one can write the momentum equation on the centre line

$$U\,\frac{\partial U}{\partial x} = \frac{1}{\rho}\,\frac{\partial \tau}{\partial y} \tag{9a}$$

as

$$\frac{\tfrac{1}{2}\,U^2(x = x_T + \Delta x)}{\Delta x} = \frac{\tau_w}{\rho\Delta y} \tag{9b}$$

I would not like to recommend a general procedure for marching over the singularity at a point of zero shear stress (flow reversal) on a flat surface, nor do I wish to imply that one could or should always do this. However the idea of the singularity at separation as something catastrophic needs to be corrected, and several authors who have studied the behaviour of the boundary layer equations find that conventional solution techniques fail only very close to the singular points. The weakness of the singularity is also demonstrated by the success of inverse boundary-layer calculations in which δ^* or τ_w, rather than p, is specified as a function of x. If an implicit calculation method is used it is almost trivially easy to iterate at given x to get the required value of δ^* or τ_w: taking $\partial p/\partial x = (p(x)-p(x-\Delta x))/\Delta x$ one guesses p(x), solves the direct problem with the coefficients - like U in $U\partial U/\partial x$ - evaluated at $x - \Delta x$, compares the value of δ^* with that required, adjusts p, updates the coefficients and recalculates U(x) and so on. The adjustment of p can be carried out by Newton's method, $\partial\delta^*/\partial p$ being obtained numerically from two consecutive iterates. A more refined technique, in which p is formally treated as an unknown, is Cebeci's "Mechul function" approach (Ref.6). Note that inverse techniques do not in themselves overcome the second difficulty of boundary-layer calculations for separated flows, the absence of upstream influence.

The reason why freeing p and fixing δ^* removes the singularity is that, although there is no upstream influence in the differential equations, the solution of the finite-difference equations at x is allowed to adjust the pressure gradient in the finite-difference interval $(x - \Delta x, x)$ so as to preserve a smooth δ^* contour. If a singularity in $(\partial U/\partial y)_w$ occurred there would also be a singularity in δ^* because of the rapid change of profile shape very near the surface. It is not very helpful to ask "how does $(\partial^4 U/\partial y^4)_w$ adjust itself to zero at the point of zero shear stress?" The equations simply yield $(\partial^4 U/\partial y^4)_w = 0$ when $(\partial U/\partial y)_w$ passes smoothly through zero; in general of course $(\partial^4 U/\partial y^4)_w$ varies as $(x - x_s)$. It is possible in principle to remove the singularity by freeing p and fixing almost any property of the solution, such as the velocity at some specified distance from the surface. There is absolutely no connection between the presence of the singularity in shear stress and the rapid growth of δ or δ^* at separation; the singularity is a local effect. In practice of course it is the interaction between the shear layer and the external flow that adjusts p to avoid the singularity but there is no reason why that interaction should be strong. The other common form of inverse calculation, with τ_w specified, is conceptionally straightforward; the singularity disappears from τ_w and does not appear elsewhere.

In turbulent flow the region affected by the singularity will be confined to the viscous sublayer. In view of our ignorance of the behaviour of the sublayer, especially near separation, refined treatment of the singularity would be premature.

(ii) Three-dimensional steady flow.

Choose the axes so that $(\partial U/\partial y)_w$ passes through zero along a line in the z direction (Fig.1). Then on this line $(\partial U/\partial y)_w$ and $\partial/\partial z\ (\partial U/\partial y)_w$ are zero and Eq.(4) reduces to exactly the same form as in two dimensions irrespective of the behaviour of $\partial W/\partial y$ if it is regular. The two-dimensional analysis holds in entirety; unless p or some other boundary condition is freed, there will be a singularity (Ref.7). If both $(\partial U/\partial y)_w$ and $(\partial W/\partial y)_w$ go to zero at the same point (isolated point of zero shear stress) the z-derivative terms in Eq.(4) will not necessarily be zero if a singularity occurs, but they will be zero if it does not occur. That is, these terms do not affect the formation of a singularity. Since an isolated point of zero shear stress is almost certain to be associated with a massive separation, as in an atmospheric tornado, the thin-shear-layer equations would not be applicable to the problem anyway.

(iii) *Unsteady two-dimensional flow.*

There is great controversy about this case. Inspection of Eq.(4), with the W terms neglected, again shows the $\partial U/\partial y$ will approach zero as $(x_s - x)^{\frac{1}{2}}$ unless the other terms cancel. (Note again that $(\partial^2 U/\partial y^2)_w = (1/\mu)\partial p/\partial x$ and therefore its time derivative, *the first term in Eq.(4), is determined by the external* conditions and is not in general zero). An exception, of course, is the semi-infinite oscillating plate on which $\partial U/\partial y$ goes to zero at all x simultaneously. The controversy is partly but not wholly attributable to confusion between "separation" (i.e. departure of the shear layer from the surface) and the occurrence of zero shear stress, and between "separation", as just defined, and the appearance of a singularity. (a) There is no doubt that in unsteady flow the point of zero shear stress and the point of separation can be distinct. (b) The prediction of large $d\delta/dx$ (or order unity) by the boundary layer equations is a sign that those equations are inadequate because $d\delta/dx \ll 1$ is assumed in their derivation: however this is a physical inadequacy which does not necessarily imply the gross mathematical inadequacy represented by the singular behaviour of τ_w.

Two rather detailed reviews of unsteady boundary layers have been published recently, and disagree considerably. Sears and Telionis (Ref.8) do not discuss the detailed behaviour of Eq.(1) or Eq.(4) near *the point of zero τ_w but state that their numerical calculations show no difficulties at separation.* Riley (Ref.9) discusses mathematical behaviour in more detail and quotes the work of Buckmaster (Ref.10) whose asymptotic analysis shows that the singularity at the point of zero shear stress is smoothed out although the possibility of its reappearance in the reversed-flow region cannot be ruled out. The above analysis differs from both these view points, which appear to contradict the findings of Brown and Stewartson (Ref.2) without saying so explicitly.

(iv) Two-dimensional steady compressible flow.

Differentiation of the equivalent of Eq.(1) for laminar flow yields

$$\rho \frac{\partial}{\partial x}\left\{\left(\frac{\partial U}{\partial y}\right)^2_w\right\} = \left[\frac{\partial^3}{\partial y^3}\left(\mu \frac{\partial U}{\partial y}\right)\right]_w = \left[3\frac{\partial^2 \mu}{\partial y^2}\frac{\partial^2 U}{\partial y^2} + \frac{\partial \mu}{\partial y}\frac{\partial^3 U}{\partial y^3} + \mu\frac{\partial^4 U}{\partial y^4}\right]_w \tag{10}$$

and the right-hand side contains derivatives of μ as well as of U. Now μ is controlled by the enthalpy equation which is in turn coupled to the momentum equation via U, and in particular via the dissipation term $\mu(\partial U/\partial y)^2$; it is therefore probable *that a singularity in $\partial U/\partial y$ will lead to a singularity in enthalpy* h or in $\partial h/\partial y$, and possible that the two equations will in fact interact so as to avoid the singularity. The enthalpy equation for a gas with constant c_p is

$$\rho c_p\left(U\frac{\partial T}{\partial x} + V\frac{\partial T}{\partial y}\right) = U\frac{dp}{dx} + \mu\left(\frac{\partial U}{\partial y}\right)^2 + \frac{\partial}{\partial y}\left(k\frac{\partial T}{\partial y}\right) \tag{11}$$

At the separation point $(U = V = \partial U/\partial y = 0)$ this gives

$$\frac{\partial}{\partial y}\left(k\frac{\partial T}{\partial y}\right)_w = 0 \tag{12a}$$

or

$$\left(\frac{\partial T}{\partial y}\frac{\partial k}{\partial y} + k\frac{\partial^2 T}{\partial y^2}\right)_w = 0 \tag{12b}$$

If the heat transfer through the surface is zero, $(\partial T/\partial y)_w$ is zero and so, from Eq.(12b) is $\partial^2 T/\partial y^2$; therefore if μ is a function of T only, the right-hand side of Eq.(11) reduces to $(\mu\partial^4 U/\partial y^4)_w$ as in incompressible flow, and the singularity is still present. If the heat transfer is non-zero the coupling can suppress the singularity. Stewartson (Ref.11) has reached a firmer but more restricted conclusion, that heat transfer almost certainly does preclude the appearance of the singularity in the case of a gas with $\mu \propto T$ and $Pr = 1$, by analysing a power-series expansion of the solution. The situation in unsteady or three-dimensional flow is not clear but it seems likely that the velocity and temperature fields will again interact to avoid the singularity.

Buckmaster (Ref.10) says "reasonable men may differ in their opinion as to whether this singular behaviour occurs in practice" (that is, in the Navier Stokes equations). In fact there is no positive reason to suppose that the solution of the Navier Stokes equation is singular except perhaps at discontinuities in surface slope. The above analysis suggests that even the singularity in the boundary layer equations is quite weak.

2.0 Upstream Influence

Here we follow the usual meaning of "upstream", namely the direction opposite to the main direction of motion: the latter is normally the positive x direction. According to the Navier Stokes equations, conditions at a point P (x_o, y_o) can influence the flow at $x < x_o$ by

(i) pressure disturbances, propagating at the speed of sound (assumed infinite in incompressible flow)
(ii) convected disturbances, moving along the streamlines at the velocity of the fluid
(iii) viscous diffusion, at a typical velocity of order $Re_x^{-1/2}$ times the flow speed, or turbulent diffusion at a typical velocity of order 0.01 to 0.1 times the flow speed.

Viscous diffusion in the negative x direction is very weak at high Reynolds numbers and can almost always be neglected (in principle it could aid in the avoidance of the singularity at the point of zero shear stress but is probably not essential even there; Stewartson's triple deck analysis of separation (Ref.12) uses the thin-shear-layer approximation in the "lower deck" next to the surface and thus neglects x-wise diffusion). Longitudinal turbulent diffusion of momentum is also weak. Pressure disturbances can carry upstream influence either through the shear layer itself or via the inviscid external flow (or via a recirculating-flow region below a separated shear layer). When the shear layer is thin and slowly growing, the upstream influence transmitted in the shear layer itself is negligible compared with that transmitted via the potential flow and down into the shear layer further upstream. According to the thin shear layer approximation it is zero. To represent upstream propagation of pressure disturbances in the shear layer we have to allow the pressure within the shear layer to vary independently of the free-stream pressure, i.e. to allow $\partial p/\partial y$ to be non-zero. This is why the inclusion of (x-wise) upstream influence requires inclusion of the y-component momentum equation. Note that highly-curved but slowly-growing shear layers may have significant $\partial p/\partial y$ but negligible upstream influence (in such cases the y-component momentum equation reduces to $\partial p/\partial y \approx \rho U^2/R$ where R is the radius of curvature of the surface or the known axis of the shear layer, and this leaves the equations parabolic). Self-consistent sets of approximate equations including the y-component momentum equation will be discussed below.

The one form of upstream influence within the shear layer that can virtually never be ignored is convection by a reversed-flow region. If it is present, the boundary layer equations cannot be solved uniquely by marching downstream (Ref.13) even if the reversed-flow region is followed by a unidirectional thin shear layer so that downstream boundary conditions are not required. In shallow "separation" bubbles, $\partial p/\partial y$ may be negligible and longitudinal diffusion small so that the thin shear layer approximation suffices even though the streamline angles reach 90 deg. at the extremities of the closed streamlines (Fig.2).

Many authors have developed iterative schemes for solving the thin-shear-layer equations for separation bubbles. The first and simplest scheme, that of Reyhner and Flügge-Lotz (Ref.14), sets U to zero in $U\partial U/\partial x$ whenever it is predicted to be negative, thus removing the convective upstream influence. This scheme will be discussed below; it is currently used only as a first approximation. Most of the later schemes have been developed for laminar flow but could be extended to turbulent flow by inserting a suitable turbulence model: the prospects for such models are discussed in Paper 10.

The essential feature of any reversed-flow calculation method is the simulation of convective upstream influence by allowing conditions at $x + \Delta x$ to influence the solution at x. That is, the finite-difference "molecule" used in the reversed-flow region must extend downstream of the station being calculated (Fig.4): a central-difference molecule could be used in principle but properties at $x - \Delta x$ would be irrelevant and their use can destabilize the solution if the mesh Reynolds number $U\Delta x/\nu$ exceeds about 2. The use of one-sided "upwind" differences* like those implied by Fig.4 gives only first-order accuracy in $\partial U/\partial x$; that is, the finite-difference approximation to $U\partial U/\partial x$ at x in the reversed-flow region is

$$U\frac{\partial U}{\partial x} = \frac{U}{\Delta x}\left[U(x+\Delta x) - U(x)\right] + U\frac{\Delta x}{2}\frac{\partial^2 U}{\partial x^2} + \cdots \qquad (13)$$

where the position at which the unsubscripted U and $\partial^2 U/\partial x^2$ are evaluated is immaterial to the argument. The term in $\partial^2 U/\partial x^2$ can be grouped with the viscous term $\nu\partial^2 U/\partial y^2$ and $U\Delta x/2$ is often called a "pseudoviscosity". If $V\partial U/\partial y$ is also evaluated by an upwind - y-component - difference formula an error of order $(V\Delta y/2)\partial^2 U/\partial y^2$ appears. In a conventional boundary layer with a typical ratio of Δx to Δy the two pseudoviscosity terms would be of the same order. In a conventional boundary layer $\partial U/\partial y$ would normally be evaluated from a central-difference formula because V is usually too small for instability problems to arise, but in reversed flow regions V may be large enough to exceed the stability limit of the central-difference scheme, $V\Delta y/\nu \approx 2$. If so, the central-difference scheme will be unsuitable and the pseudoviscosity term $V\Delta y\partial^2 U/\partial y^2$ in the upwind-difference scheme may be appreciable. So far, however, central-difference schemes for y derivatives have been used, without apparent trouble, in reversed-flow regions. Patankar and Spalding (Ref.15) describe a "high-lateral-flux" modification to their program for conventional boundary layers, which is implemented if V/U is large and which introduces an upwind difference for $\partial U/\partial y$: similar action could be taken in reversed-flow regions.

It is important to distinguish between the use of upwind differences and the use of downwind (upstream) marching. Logically, if the thin-shear-layer equations are used we should march in the direction of local U, discarding profile data more than one x step behind the current x station. However exactly the same results can be obtained, with the same finite-difference molecule, by successive downstream sweeps, using stored profile data from the previous sweep and starting with a rough approximation to the solution. That is, on the n'th sweep we evaluate $\partial U/\partial x$ in a reversed-flow region as

$$\partial U/\partial x \approx \left[U^{n-1}(x+\Delta x) - U^{n}(x)\right]/\Delta x \qquad (14)$$

with $U^{n-1}(x+\Delta x)$ known, and solve for $U^n(x)$, whereas in the single sweep of upstream marching we evaluate $\partial U/\partial x$ as

$$\partial U/\partial x \approx \left[U(x+\Delta x) - U(x)\right]/\Delta x \qquad (15)$$

* "upwind" means "against the local stream direction"; "upstream" means "against the main stream direction"

with U (x+Δx) known, and solve for U(x). Clearly if the successive downstream sweeps converge so that profiles at the n'th and (n-1)'th sweeps are the same, Eqs.(14) and (15) are the same. Successive downstream marching requires more computing time and, because of the need to store U at all mesh points within the reversed-flow region, more computer storage. However it is easier to incorporate in a solution for the main downstream-going flow because iteration is needed to match the results from the upstream sweep in the reversed region to the results from the downstream sweep in the main part of the flow.

Klemp and Acrivos (Ref.16) have obtained solutions for a steady laminar separation bubble by matching downwind sweeps at the boundary between the downstream-going and reversed regions of the flow (the "zero-U line"). The position of the zero-U line was guessed, one sweep performed in each region, and the boundary position y = Γ(x) adjusted to improve the matching of ∂U/∂y (equivalent to τ in a laminar flow; U is of course set to zero on y = Γ(x) for both sweeps). Klemp and Acrivos used

$$\Gamma^{n+1}(x) = \Gamma^{n}(x)\left[1 + r\,\frac{\tau(x,\Gamma^{-}) - \tau(x,\Gamma^{+})}{\tau(x,\Gamma^{+})}\right] \qquad (16)$$

where r is an under-relaxation factor set at about 0.3: thus if τ or ∂U/∂y is too large at the upper boundary of the reversed flow region, the boundary is moved outwards to reduce ∂U/∂y in the reversed flow region. This is not the only possible strategy for matching, but apparently no further work has been done on the matching of sweeps in opposite directions.

The earliest technique used to permit downstream matching in a reversed-flow region is the FLARE (Flugge-Lotz and Reyhner) scheme (Ref.14) of setting U∂U/∂x to zero whenever U is negative. This of course removes upstream influence from the equations, and the x-component momentum equation becomes

$$V\,\frac{\partial U}{\partial y} = -\,\frac{1}{\rho}\,\frac{dp}{dx} + \nu\,\frac{\partial^{2} U}{\partial y^{2}} \qquad (17)$$

which, if V is regarded as known, is an ordinary differential equation for U. If V happened to be negligible, this equation would give the Couette-flow solution of a parabolic U profile. Matching at the zero-U line is automatic, to within ordinary finite-difference errors, because Eq.(17) is correct there. Note that the decision whether or not to neglect convective terms is based on the sign of the finite-difference form of U used for the coefficient in U∂U/∂x; if that finite-difference form is the sum of two or more velocities at different mesh points the individual signs are not considered. It follows that the zero-U line does not have to be defined explicitly in the way that it is in Klemp and Acrivos' method. Carter (Ref.17) states that if reversed-flow values of U are less than roughly 5 percent of the main stream velocity, the FLARE approximation is adequate. Carter's paper is a useful review of past work on inverse methods.

Several more recent workers have used repeated sweeps of downstream marching, changing the sense of the finite-difference molecule in the reversed-flow region to retain "upwind" differences. One of the latest versions of this approach is the DUIT scheme due to Williams (Ref.18); an implementation of this for the "box" molecule is described by Cebeci and Bradshaw (Ref.6). It seems to be immaterial whether "primitive" variables (the velocity and pressure) or the stream function and vorticity are used. However Carter, using an upwind-difference expression for vorticity, had to resort to central differences for the x-wise gradients of his stream function; the reason appears to be that stream function is not strictly a convected quantity. These schemes frequently use FLARE to provide a first approximation.

We recall that the above schemes are often used in an inverse manner (specified δ^* or τ_w rather than p) to relax the singularities at point of zero shear stress. Furthermore the whole shear-layer calculation has to be iteratively matched, in a real problem, with the inviscid-flow solution. The need for this "outer iteration" means that the "inner iteration" required in the shear layer calculation can be carried on at the same rate, and in the same loop, and is therefore "free of charge".

The above schemes were developed for steady, two-dimensional flow. The extension to steady three-dimensional flow describable by the boundary-sheet equations (with the inequality ∂/∂x, ∂/∂z << ∂/∂y) is straightforward in principle. In attached three-dimensional flow, difficulties are encountered in obtaining the solution in the yz plane, at given x, if W changes sign. These difficulties are quite closely analogous to those found in the xy plane in recirculating two-dimensional flow. The brute-force solution is to solve as if the equations were elliptic in the yz plane, analogous to a Navier-Stokes field solution for recirculating two-dimensional flow. However Cebeci (see Ref.19) has recently used a scheme which, at each x, marches in the predominant direction of W (say the positive z direction, root-to-tip on a swept wing) and changes the sense of z-wise differencing when W changes sign. Providing that the x step, Δx, is smaller than (U/W)Δz (the appropriate form of the Courant condition for the xz plane, z-wise viscous diffusion being neglected) the procedure is stable. Only one z-wise sweep is needed at each x; this is not an iterative procedure but an x-wise development from a "known" solution at the initial x. Clearly it is much faster than an elliptic solution in the yz plane at each x, and combining it with one of the iterative schemes for recirculating-flow described above would be fairly economical. The calculation would consist of three nested loops (Fig.5): the innermost loop is the z wise march, calculating U(y) and W(y) at each z, the sense of z-wise differencing depending on the sign of W; the next loop is the streamwise march, with the sense of x-wise differencing depending on the sign of U; and the outer loop is the iteration which improves the initial guess at the solution for U and W as functions of x, y and z.

The strongly three-dimensional separation that occur at highly-swept leading edges or on the leeward side of conical bodies have been discussed in Paper 9. Providing that the vortex sheet leaves the body at a sufficient angle to be well outside the boundary layer this approach is quite acceptable. There are, however, occasions when rolled-up vortex sheets remain merged with the boundary layer. Examples include wing-body junctions and the flow over a cone at an angle of incidence slightly larger than its own semi-angle. It is a nice point whether such flows should be counted as separated; in any case they must be treated by using the "slender-shear-layer" equations in which y-wise gradients and z-wise gradients are of equal order while x-wise derivatives are of order δ/ℓ times these. The behaviour of the pressure in in the y z plane may be critical. The solution of these equations involves an elliptic problem in the y z plane combined with an x-wise marching scheme and is straightforward in principle providing that the boundary conditions can be specified explicitly or derived from iteration with a boundary layer solution over the rest of the body surface.

One of the first successful solutions for unsteady "separated" flow was that of Phillips and Ackerberg (Ref.20). The flow treated was actually that over an oscillating, semi-infinite plate so the surface shear stress changed sign but the shear layer did not leave the surface. The solution involved marching in the positive-x direction, once for each time step. The inviscid unsteady-flow equations are hyperbolic, so the behaviour of the convective terms in the unsteady thin-shear-layer equations is hyperbolic also. Thus Phillips and Ackerberg had to ensure that the time step was less than $\Delta x/u$ and that the spatial differencing followed the usual "upwind" rules. A guessed solution is required at $t = 0$ for all x, y; if the motion starts at $t = 0$ the solution is null. Phillips and Ackerberg's flow was a rather specialized one, and they were able to use the Rayleigh solution for an oscillating infinite plate as the downstream boundary condition at $x > t/U$ where U is a typical downstream-going flow velocity. Similar but more complicated expedients may be usable in more general flows.

REFERENCES

1. Townsend, A.A. The behaviour of a turbulent boundary layer near separation. J.Fluid Mech., Vol.12, p.536, 1962.

2. Brown, S.N. and Stewartson, K. Laminar separation. Ann.Rev.Fluid Mech., Vol.1, p.45, 1969.

3. Curle, S.N. The Laminar Boundary Layer Equations. University Press, Oxford, 1962.

4. Terrill, R.M. Laminar boundary layer flow near separation with and without suction. Phil.Trans.Roy.Soc., Vol.A253, p.1022, 1960.

5. Werle, M.J. and Davis, R.T. Incompressible laminar boundary layers on a parabola at angle of attack. J. Appl.Mech. Vol.E39, p.7, 1972.

6. Cebeci, T. and Bradshaw, P. Momentum Transfer in Boundary Layers. McGraw Hill/Hemisphere, 1977.

7. Brown, S.N. Phil.Trans. Roy.Soc., Vol.A257, p.409, 1965.

8. Sears, W.R. and Telionis, D.P. Boundary layer separation in unsteady flow. SIAM J.Appl.Math., Vol.28, p.215, 1975.

9. Riley, N. Unsteady laminar boundary layers. SIAM Rev., Vol.17, p.274, 1975.

10. Buckmaster, J. The unsteady equilibrium of the singularity at separation. J.Engg.Math., Vol.7, p.223, 1973.

11. Stewartson, K. The behaviour of a laminar compressible boundary layer near a point of zero skin-friction. J.Fluid Mech., Vol.12, p.117, 1962.

12. Stewartson, K. Multistructured boundary layers on flat plates and related bodies. Adv.Appl.Mech., Vol. 14, p.145, 1974.

13. Catherall, D. and Mangler, K.W. The integration of the two-dimensional laminar boundary layer equations past the point of vanishing skin friction. J.Fluid Mech., Vol.26, p.163, 1966.

14. Reyhner, T.A. and Flugge-Lotz, I. The interaction of a shock wave with a laminar boundary layer. Int.J. Non-Linear Mech., Vol.3, p.173, 1968.

15. Patankar, S.V. and Spalding, D.B. Heat and Mass Transfer in Boundary Layers. Inbrtext, New York, 1970.

16. Klemp, J.B. and Acrivos, A. A method for integrating the boundary-layer equations through a region of reversed flow. J.Fluid.Mech., Vol.53, p.177, 1972.

17. Carter, J.E. Inverse solutions for laminar boundary layer flows with separation and reattachment. NASA TR R-447, 1975.

18. Williams, P.G. A reverse flow computation in the theory of self-induced separation. Lecture Notes in Physics, Vol. 35, Springer-Verlag 1975, p.445.

19. Bradshaw, P., Cebeci, T and Whitelaw, J.H. Engineering calculation methods for turbulent flows, lecture series, Cal.State Univ., Long Beach. 1977 (also Imperial College Aero Tech. Note 77-102, 1977)

20 Phillips, J.H. and Ackerberg, R.C. A numerical method for integrating the unsteady boundary layer equations when there are regions of back flow. J.Fluid Mech., Vol.58, p.561, 1973.

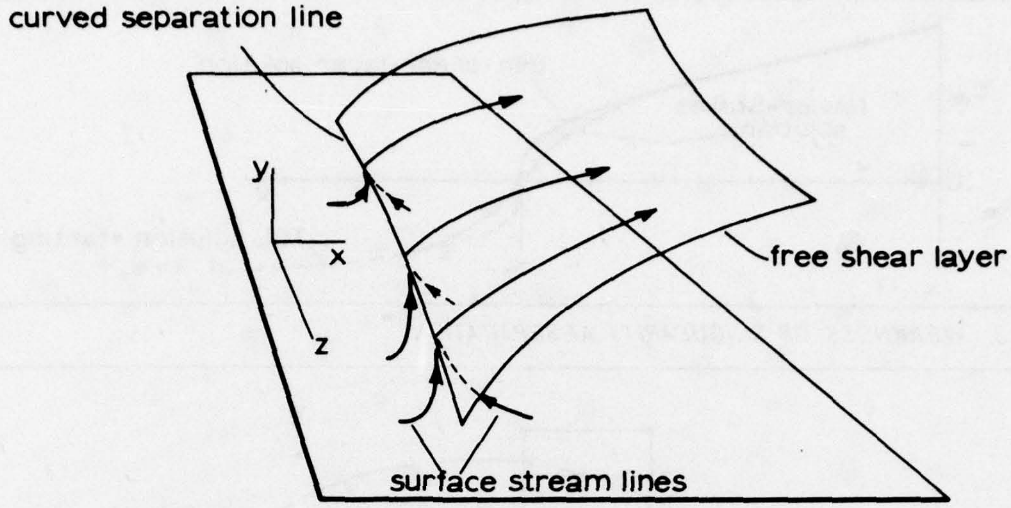

(a) Separation from swept wing

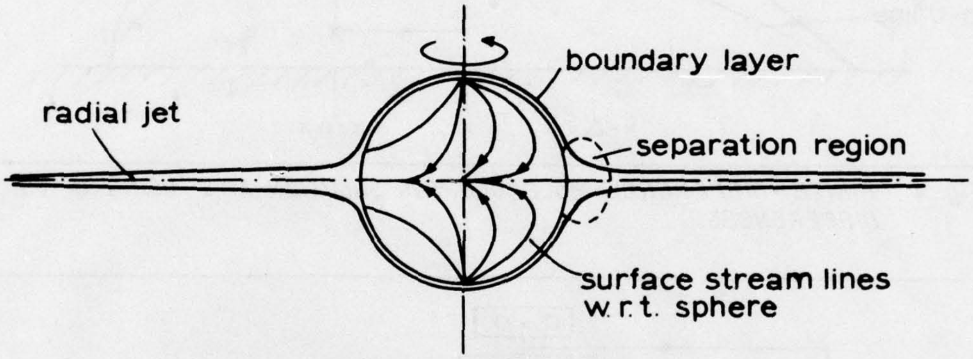

(b) Separation from rotating sphere

Fig.1 SURFACE STREAMLINES IN 3D

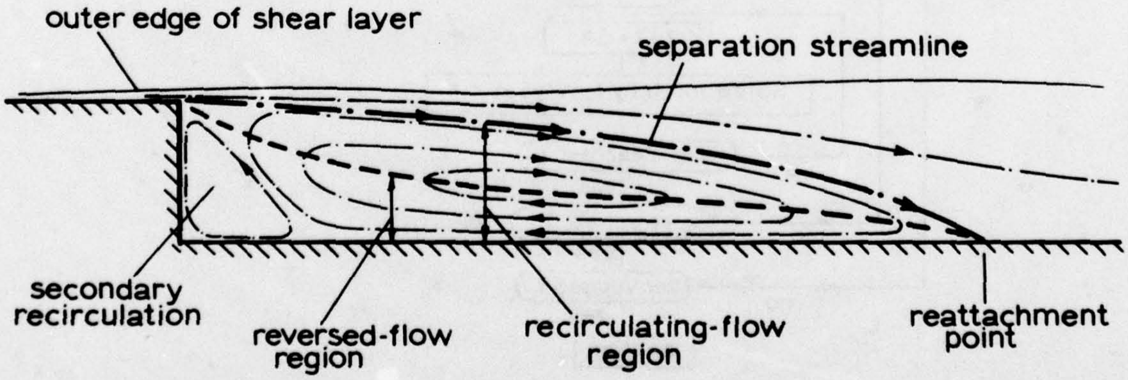

Fig. 2 NOMENCLATURE FOR SEPARATED REGION
(approx. to scale for turbulent flow behind a step)

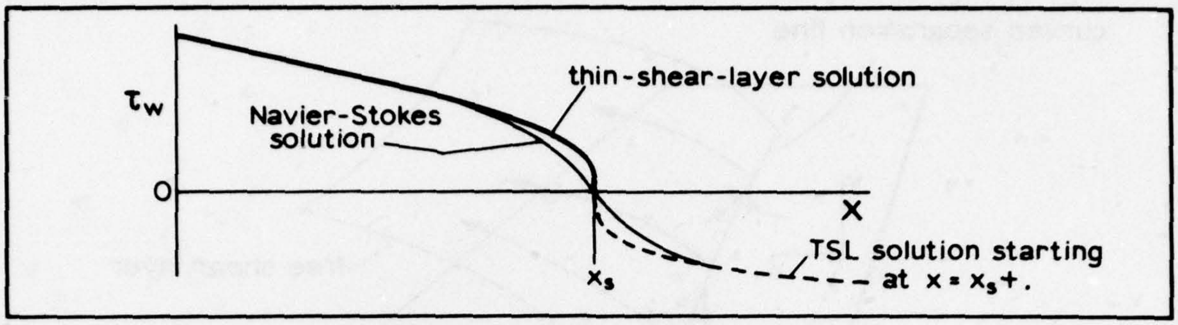

Fig. 3 WEAKNESS OF SINGULARITY AT SEPARATION.

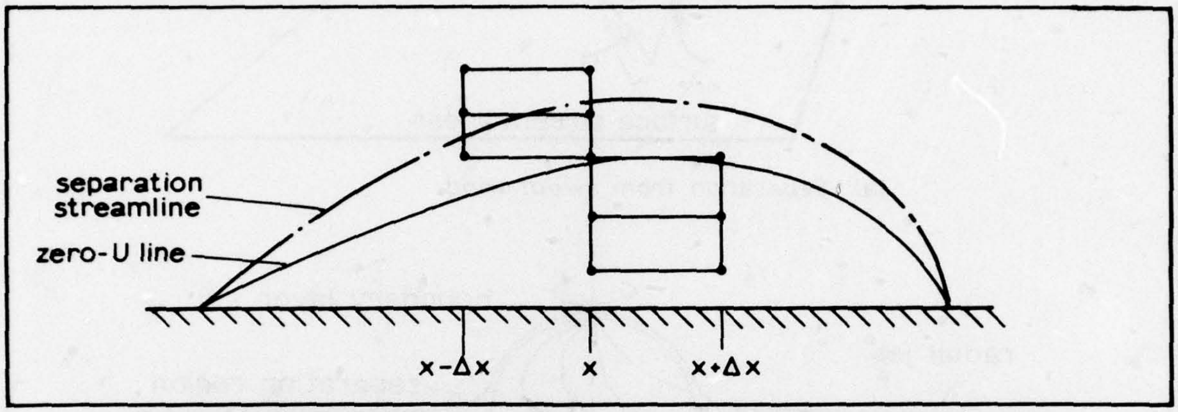

Fig. 4 FINITE-DIFFERENCE MOLECULE FOR SOLUTION AT x USING 'UPWIND' DIFFERENCES.

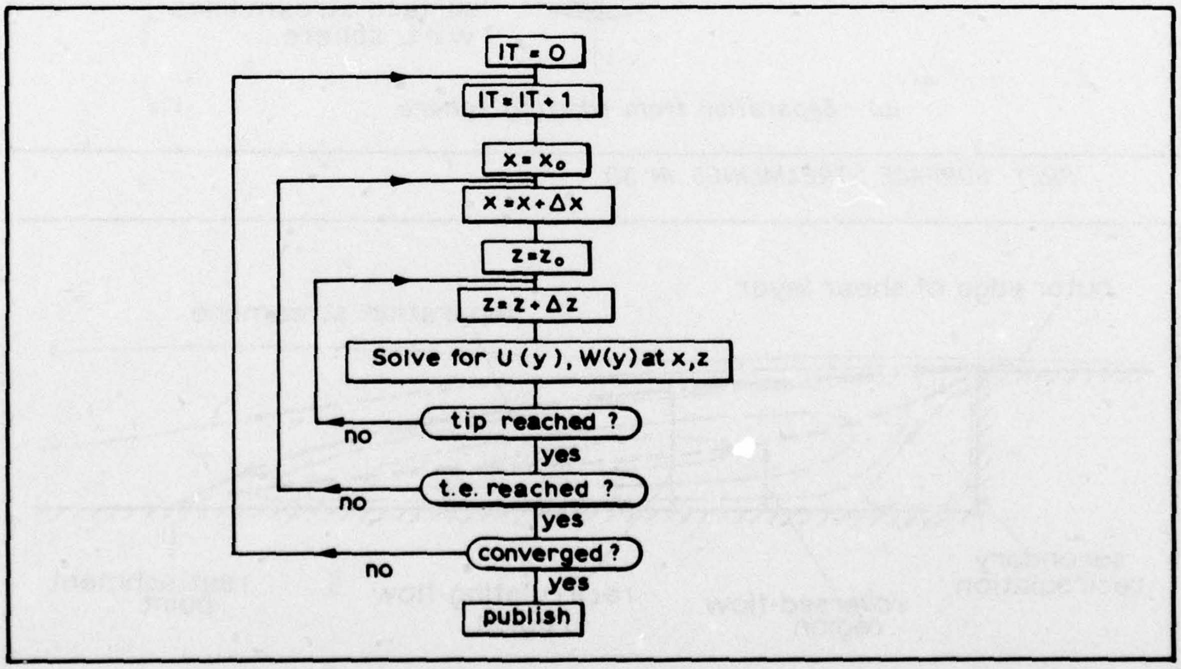

Fig. 5 FLOWCHART FOR 3D SEPARATED FLOW CALCULATION USING REPEATED DOWNSTREAM MARCHING WITH 'UPWIND' DIFFERENCES

PREDICTION OF UNSTEADY SEPARATED FLOWS ON OSCILLATING AIRFOILS

W. J. McCroskey
Aeromechanics Laboratory—U.S. Army Aviation R&D Command
Ames Research Center, Moffett Field, California 94035, U.S.A.

1.0 INTRODUCTION

The calculation of any high Reynolds number flow with large amounts of separation presents a formidable challenge to the modern fluid dynamicist. The general features of unsteady separated flows on oscillating airfoils have been described in detail in Papers 6 and 8; some of these are indicated schematically in Fig. 1. We turn our attention now to a number of special techniques that have been suggested for predicting the engineering quantities of interest, such as the instantaneous values of lift, drag, and pitching moment. It should be emphasized again that all of these methods are still being developed, refined, and improved, even in two spatial dimensions. Furthermore, all except the laminar Navier Stokes calculations invoke some sort of simplifying assumptions and approximations, and their limitations and validity remain to be established.

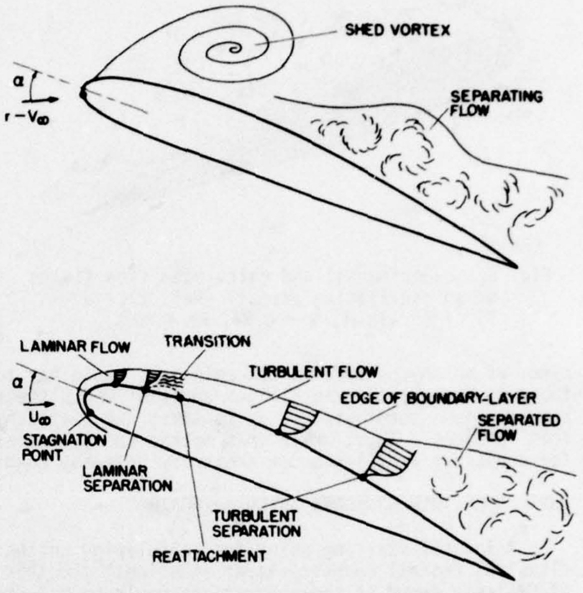

Fig. 1. Sketch of the flow fields around airfoils at high incidence.

2.0 THE DISCRETE POTENTIAL VORTEX APPROACH

One of the most promising analytical approaches to the problem of strong dynamic stall with fully developed vortex shedding takes its cue from the discrete vortex model that has been applied to bluff-body separation (Fig. 2). In the simpler case of a cylinder in the low subcritical Reynolds number regime (Paper 6, Section 2), alternate or staggered rows of potential vortices produce the essential features of the actual forces on the cylinder, but the vortex spacing and frequency have to be specified empirically.

The initial vortex-shedding phenomenon on a thin flat plate was first modeled by a series of emitted vortices by Ham (Ref. 1), as shown on the right in Fig. 2. Each vortex moves under the influence of all the others, and the result is a tendency for the individual filaments to coalesce into a structure that resembles the experimentally-observed features of dynamic stall.

As in the case of the cylinder, assumptions have to be made regarding the geometry and strength of the vortex emissions. In fact, the crux of this general approach lies in choosing the strength to be assigned to each vortex and in the mechanism for relating the birth of the vortices to the boundary-layer separation characteristics on the body. Ham started the process at an arbitrarily-assumed incidence, and adjusted the strength of the vortex emissions to insure stagnation points at the two edges of the plate.

This approach has been extended and refined at Société Bertin in France (Refs. 2, 3) for an airfoil with finite thickness and leading-edge radius. The vortices are emitted from the point of boundary-layer separation in the leading-edge region, and the circulation of the vortex filaments grows according to the flux of vorticity from the boundary layer. This has been simplified to

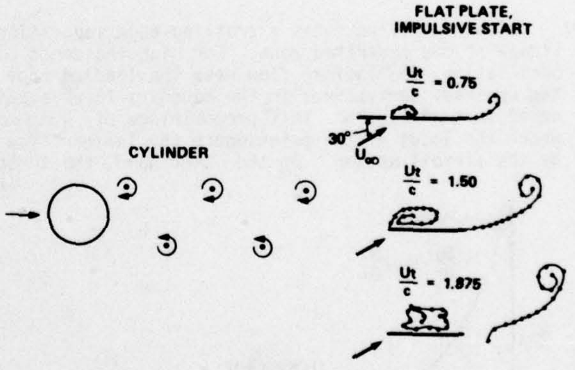

Fig. 2. Sketch of the discrete vortex model applied to a cylinder in a uniform free stream and to a flat plate following an impulsive start.

$$\frac{\Delta\gamma}{\Delta t} = -\frac{1}{2}\left(U^2 - U_r^2\right) \tag{1}$$

where U is the velocity at the edge of the boundary layer at the separation point and U_r is the maximum reverse velocity induced by the free vortices above the airfoil. The flow fields resulting from the combination of the body and the free vortices is calculated by an adaptation of the numerical potential-flow technique of Giesing (Ref. 4).

Figure 3 shows a comparison between the calculated and measured flow-field development, indicating both the complexity of the flow and the degree to which the overall features are reproduced. Normal force hysteresis loops are compared in Fig. 4. The theoretical case starts from potential flow at $\alpha = 15°$; the curve fails to close because steady-state oscillatory viscous motion is not achieved at the end of the first cycle. Nevertheless, the results are encouraging.

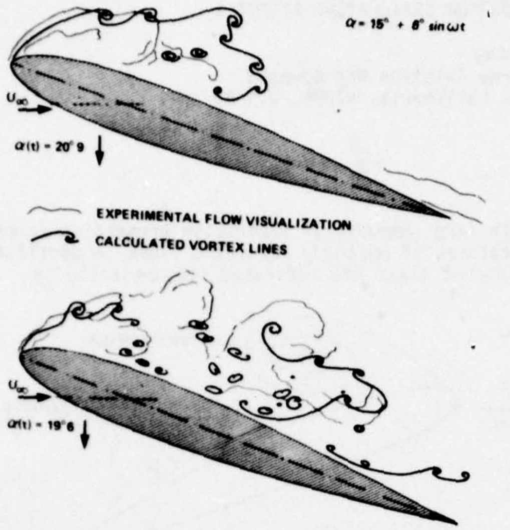

Fig. 3. Experimental and calculated flow fields on an oscillating airfoil (Ref. 2). $\alpha = 15° + 6° \sin \omega t$, $k = 0.24$, $Re = 10^6$.

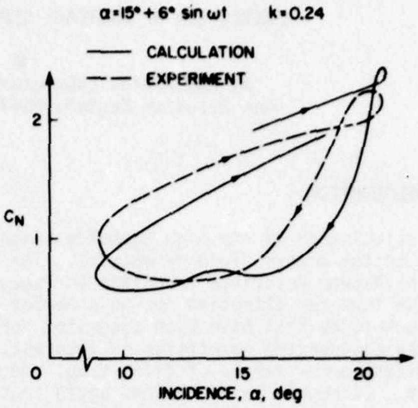

Fig. 4. Experimental and calculated normal force hysteresis for the conditions of Fig. 3.

Although somewhat complex, the numerical implementation of this approach does not seem to be a major limitation. Instead, the main drawback at this time is that crucial assumptions still have to be made in order to perform the calculations. The incidence, or time, at which the free-vortex emissions begin has to be specified. In addition, the results have been found to be sensitive to (1) the angle at which the vortex sheet leaves the surface; (2) the time at which the emissions terminate, so as to start the reattachment process; and (3) the viscous diffusion of the free vortices. Thus, while this method seems promising, it has not yet been developed to a reliable state for arbitrary profiles under arbitrary unsteady conditions.

3.0 THE THIN BOUNDARY LAYER APPROACH

A logical starting point for calculating unsteady separated flow is to analyze, with the aid of the classical Prandtl boundary-layer equations, the thin viscous layer on an oscillating airfoil. The inclusion of unsteady terms in these equations could be expected to alter the separation characteristics, so that some indication of unsteady stall behavior might be calculated, even though this approach is incapable of treating the problem in its entirety. Any one of several unsteady boundary-layer methods should suffice (Refs. 5, 6).

Figure 5 illustrates a trailing-edge separation flow for which boundary-layer theory might apply upstream of the separated zone. For high-incidence conditions at low or moderate reduced frequencies of oscillation, the laminar flow near the leading edge is exposed to severe spatial pressure gradients, and the unsteady derivatives in the boundary-layer equations are relatively unimportant, as indicated in the upper part of Fig. 5. This predominance of $u\,\partial u/\partial x$ over $\partial u/\partial t$ is manifested in Fig. 6 from Ref. 7, where the locus of the point where the laminar flow reverses, that is, where $C_f = 0$, is hardly affected by the airfoil motion. On the other hand, the turbulent flow reversal occurs in a region where temporal

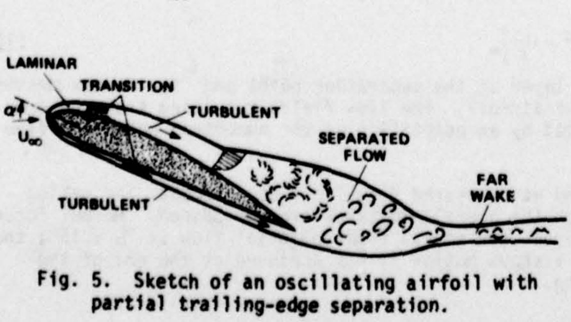

Fig. 5. Sketch of an oscillating airfoil with partial trailing-edge separation.

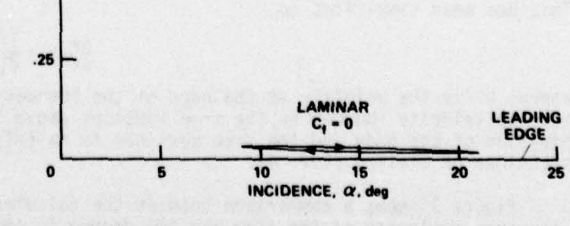

Fig. 6. Calculations of the loci of laminar and turbulent flow reversal on an oscillating airfoil (Ref. 7). Arrows indicate increasing time.

and spatial gradients are comparable in magnitude, again indicated in Fig. 5. As a result, the locus of turbulent $C_f = 0$ shows a large amount of hysteresis, in agreement with experimental observations. Figure 7, from Ref. 8, shows another example wherein unsteady effects delay the onset of turbulent flow reversal on an airfoil whose incidence increases linearly with time.

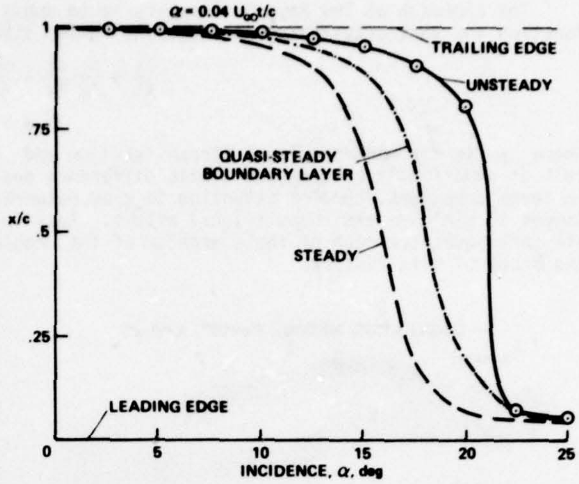

Fig. 7. Calculations of the loci of turbulent flow reversal on a linearly-pitching airfoil (Ref. 8).

Although calculations of the types shown in Figs. 6 and 7 provide a qualitative explanation of the delay in the onset of dynamic stall, they have limited quantitative utility. Furthermore, they give few clues to the mechanisms responsible for the vortex-shedding phenomenon that is such a prominent feature of strong dynamic stall. Part of this is simply the inherent limitations of classical boundary layer theory insofar as a coupled interaction between viscous and inviscid regions is concerned. Also, part is probably due to the fact that the point of boundary layer flow reversal, as calculated by the standard methods, does not have the special significance in the unsteady case that it does in steady flows. This difference between flow reversal and catastrophic separation has been addressed in previous lectures of this series, and so the point will not be dwelt upon here. A great deal more basic research remains to be done to define useful separation criteria based on boundary layer theory for the unsteady cases of practical importance.

4.0 THE STRONG INTERACTION APPROACH

A more realistic representation of the flow field sketched in Fig. 5 would result if the boundary-layer concepts were to be retained wherever possible, while allowing a strong coupling to exist between the viscous flow in the separated zone and the surrounding inviscid flow. Crimi and Reeves (Ref. 9) have made an ambitious analysis of this sort. However, they paid more attention to the details of bursting of the leading-edge bubble, shown in Fig. 5 as the mechanism for transition, rather than to the effects of trailing-edge separation. Partly as a result of this and partly because of some deficiencies that are described below, the method has not yet gained widespread acceptance.

Crimi and Reeves modeled the inviscid flow with an extension of unsteady thin-airfoil theory, representing the airfoil and the separated flow with distributed source and vortex singularities. Finite difference calculations of the unsteady boundary layer equations were performed for the attached flow, using an eddy-viscosity model for the turbulent flow. In the absence of boundary-layer separation, no interaction between the viscous and inviscid flow was considered.

For the airfoil considered, laminar separation occurred near the leading edge. The ensuing free-shear layer was analyzed with an integral method that had been developed earlier for supersonic wake flows (Refs. 10, 11). Because this method included the analysis of the leading edge separation bubble, the first step was to determine whether the turbulent flow following transition within the bubble would, in fact, overcome the adverse pressure gradient and reattach within the bounds of the inviscid pressure distribution. That is, would the bubble close without bursting? If not, then the separated zone was allowed to grow according to a prescribed mass-conservation law and to interact with the inviscid flow. In this case, the viscous and inviscid regions were iterated until mutually-consistent solutions were obtained.

Despite the many approximations and assumptions that had to be made in the analysis, all of the essential flow elements seem to have been included, although the application to trailing-edge stall was not attempted. Crimi and Reeves (Ref. 9) and Crimi (Refs. 12, 13) applied the method to a variety of unsteady airfoil and helicopter problems, with varying degrees of success. One of the main faults was that the basic prediction of whether the leading-edge bubble would burst, even under static conditions, did not seem to depend in the proper manner on Reynolds number and leading-edge geometry. Attempts by the present author to apply the method to the prediction of the static and dynamic stall characteristics of several helicopter-type airfoils which are thought or known to stall by the bubble-bursting mechanism have not correlated well with experiments.

A recent improvement of the bubble analysis (Ref. 14) seems to show better agreement with experiments on unstalled airfoils, but the reliable prediction of leading-edge stall remains to be demonstrated.* Furthermore, the viscous part of the analysis does not account for the feature of a thin layer of reversed flow near the wall before catastrophic separation begins in the unsteady case, as discussed in Paper 6, Section 1; Paper 8, Section 3; and Section 3 of this Paper. Therefore, its application to dynamic stall should be viewed with caution at this time. Nevertheless, the general approach of matching various viscous and inviscid regions, with simplifying approximations in each, remains an attractive alternative to the Navier-Stokes calculations described below.

5.0 SOLUTIONS TO THE NAVIER-STOKES EQUATIONS

The inherent limitations of potential theory and boundary-layer theory can, of course, be overcome by the use of the full Navier-Stokes equations. Unless special techniques or approximations are employed, however, this approach is limited to laminar flows at Reynolds numbers much lower than realistic for most practical applications. Nevertheless, recent calculations (Refs. 15 - 18) have shed new light on the basic mechanisms of stall under unsteady conditions at $2000 \le Re \le 10{,}000$.

---

*The same statements apply to other bubble-bursting prediction methods, as well.

The approach at low Reynolds numbers is to apply implicit finite difference techniques to the stream-function and vorticity-transport equations in two dimensions,

$$\frac{\partial \zeta}{\partial t} + \frac{\partial \psi}{\partial y}\frac{\partial \zeta}{\partial x} - \frac{\partial \psi}{\partial x}\frac{\partial \zeta}{\partial y} = \frac{1}{Re}\nabla^2 \zeta \qquad (2)$$

$$\nabla^2 \psi = -\zeta \qquad (3)$$

where ψ is the nondimensional stream function and ζ is the nondimensional vorticity. The formidable task of numerically solving the finite difference analogs of these equations requires large amounts of time on large computers, careful attention to grid networks and boundary conditions, and special numerical techniques to minimize the computational effort. Each investigator (Refs. 15 - 18) has his special and elaborate techniques for each of these aspects of the problem, and further discussion of these methods is beyond the scope of this lecture.

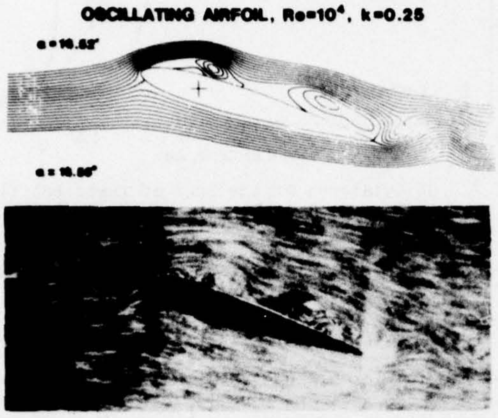

Fig. 8. Navier-Stokes calculaticns (Ref. 15) and flow visualization (Ref. 19) of the flow field of an oscillating airfoil. Conditions cited in Fig. 9.

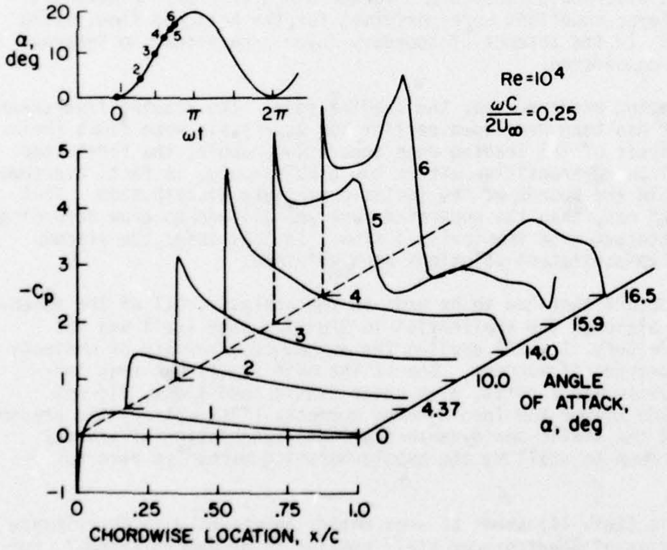

Fig. 9. Calculations of the upper-surface pressure distribution before and during dynamic stall (Ref. 15).

Mehta's results (Ref. 15) may be cited as representative of the state of the art for this approach. Figure 8 shows streamlines calculated using a second-order scheme for an oscillating airfoil at $Re = 10^4$, compared with flow visualizations obtained by H. Werlé of ONERA (Ref. 19) for identical flow conditions. The latter were obtained as trajectories of air bubbles in a water tunnel, and the experimental flow pattern shows the same structure of separation bubbles and vortices that were calculated. Figure 9 shows the variation of $\alpha(t)$ after a uniform state had been developed at $\alpha = 0$, as well as the calculated pressure distribution during the early stages of the oscillatory motion. The suction peaks over the middle of the airfoil shown in curves 5 and 6 are direct manifestations of the two main separation bubbles and vortices shown in Fig. 8.

These calculations have produced impressive results that show the forward vortex development to be qualitatively similar to the experimental results obtained at high Reynolds numbers, described in Papers 6 and 8 Nevertheless, the calculated force and moment behavior at $Re = 10^4$ is considerably different, quantitatively, from the behavior at $Re = 10^6$ and higher. This is not surprising, in view of the turbulent state of the boundary layer, separated region, and far wake at high Reynolds number and the absence of the multiple-vortex pattern that occurs at low Reynolds number. These differences point out the limitations of the low Reynolds number, or purely laminar, calculations, apart from any questions of the practicality of the computer codes.

The next logical question, then, is what about high Reynolds number calculations of the so-called Reynolds-averaged Navier-Stokes equations with some sort of turbulence modeling? So far, this approach has been applied to several simpler problems, such as the transonic shock wave-boundary layer interactions described in Paper 8, Section 4, but not to the dynamic stall problem on an oscillating airfoil. Mr. MacCormack will address these issues in more detail in the following lecture, but the prospects for success for the latter seem less than favorable at the moment. The viscous region of the dynamic stall flow field is quite large, and this may require a relatively fine computational grid over a much larger portion of the flow field than is now feasible. Much more difficult, however, is the question of how to model the turbulence in such a complex situation. Considerable new basic research, both theoretical and experimental, will be required to answer this question adequately.

6.0 EMPIRICAL CORRELATIONS OF EXISTING DATA

Despite the lack of a thorough understanding of dynamic stall and the shortcomings of the various theoretical approaches, several empirical methods exist for estimating the unsteady airloads on oscillating airfoils. These methods seek to correlate force and moment data obtained from relatively simple wind tunnel tests in formulations that show the effects of the numerous relevant parameters, such as airfoil shape, Mach number, amplitude and frequency of sinusoidal oscillations, mean angle, and type of motion.

Common to all the available literature relevant to dynamic stall is the observation that unsteady effects increase with increasing pitch rate, that is, rate of change of airfoil incidence. It is also evident that the dynamic stall events require finite times to develop. Therefore, some form of the nondimensional parameters $\dot{\alpha}c/U_\infty$ and $U_\infty \Delta t/c$ appears in all of the empirical methods. Another common aspect is that the empirical correlations are used as corrections to steady airfoil data, so that the geometrical and Reynolds number effects are only accounted for insofar as they determine the static section characteristics.

The highlights of several methods currently in use by the helicopter industry are outlined below. More detailed accounts of each can be found in the references cited and in two recent review articles (Refs. 20, 21).

Boeing-Vertol Gamma Function Method (Refs. 22, 23)

The onset of dynamic stall is assumed to occur at $\alpha_{DS} = \alpha_{SS} + \Delta\alpha_D$, where α_{SS} is the static stall angle and $\Delta\alpha_D = \gamma\sqrt{\dot{\alpha}c/U_\infty}$. The quantity γ, which is the essential empirical function, depends on airfoil geometry and Mach number and is different for lift and moment stall. The gamma functions were generated from a large amount of data generated in a Boeing transonic wind tunnel test of various airfoils oscillating sinusoidally in pitch. The force and moment coefficients are constructed from static data using an equivalent angle of attack that accounts for unsteady potential-flow effects, α_{eq}, and a reference angle, $\alpha_r = \alpha - \gamma\sqrt{|\dot{\alpha}c/U_\infty|}\,\mathrm{sign}(\dot{\alpha})$, as follows:

$$\left.\begin{aligned} C_L &= [\alpha_{eq}/\alpha_r]\, C_L \text{ (at } \alpha_r) \\ C_D &= C_D \text{ (at } \alpha_r) \end{aligned}\right\} \alpha_r \text{ based on } \gamma_{\text{lift}} \qquad C_M = [0.25 - X_{c.p.}]\, C_L \tag{4}$$

The location of the aerodynamic center of pressure, $X_{c.p.}$, is specified empirically in the current version of the method (Ref. 24). This formulation permits a dynamic overshoot of C_L above its maximum static value, but not of C_D. Also, it should be noted that α_{DS} is always less than α_{max}.

UTRC α, A, B METHOD (Refs. 25, 26)

A table-lookup correlation method, which has recently been synthesized into a more streamlined format, was developed at United Technologies Research Center to determine C_L and C_M from three independent parameters of the airfoil motion. The choice of the parameters was inspired by thin-airfoil potential theory; they are the instantaneous incidence $\alpha(t)$, the angular velocity parameter $A = \dot{\alpha}c/2U_\infty$, and the angular acceleration parameter $B = \ddot{\alpha}c^2/4U_\infty^2$. The data base for the empirical correlations came from experiments on an NACA 0012 airfoil oscillating in pitch at $M \lesssim 0.3$, including both sinusoidal and nonsinusoidal motion. None of the data attained the extreme values that have been observed to accompany the fully-developed vortex shedding phenomenon.

MIT Method (Ref. 27)

This method is basically an empirical representation of the forces and moments due to the vortex-shedding phenomenon for ramp changes in angle of attack. The actual angle of dynamic stall must be specified separately; the value $\alpha_{DS} = \alpha_{SS} + 3°$ has normally been used. For $\alpha_{SS} < \alpha < \alpha_{DS}$, the data below static stall are extrapolated. Starting at $\alpha = \alpha_{DS}$, C_L and C_M are assumed to increase linearly with time, over a specified time interval, from inviscid to peak values that depend on $\dot{\alpha}c/U_\infty$ at the instant of dynamic stall. If this is attained before $\alpha = \alpha_{max}$, then C_L and C_M remain constant until α_{max}. They decay exponentially* with preassigned time constants thereafter, until the static-stall values are attained. These new values are retained until $\alpha = \alpha_{SS}$ on the downstroke, when the unstalled static section characteristics are resumed.

Lockheed Method (Refs. 28, 29)

This combined analytical and empirical modeling of dynamic stall incorporates phase lag time constants and pitch-rate-dependent stall angle delay increments into a ficticious effective angle of attack. This effective angle is used to construct C_L and C_M from static airfoil characteristics and a linear combination of a number of separate dynamic stall elements. Some of these elements are assumed to be analogous flow phenomena that have been treated elsewhere in the literature, such as leading edge jets, the lag in circulation build-up on a pitching airfoil in potential flow, separation over moving walls, fluctuating pressure propagation in turbulent boundary layers, and the vortex lift due to leading-edge vortices on delta wings. Other elements are modeled directly from dynamic-stall measurements on oscillating airfoils. In this sense, the method has more degrees of freedom than any of the others, and information from many sources has been utilized.

At low frequency, the phase lag of the effective incidence is linearly proportional to $\omega c/U_\infty$. The latest version (Ref. 29) includes increments of C_L and C_M due to the vortex shedding phenomenon, that are proportional to $\sin^2\alpha$. Compressibility corrections are developed from various applications of the Prandtl-Glauert rule. It may be mentioned that this is the only method which distinguishes between pitching and plunging motion.

Time-Delay Methods (Refs. 30, 31)

The basic idea of this approach is that each dynamic stall event is governed by a separate, universal nondimensional time constant of the form $\tau = U_\infty \Delta t/c$, regardless of the time-history of the motion. The construction of the force and moment characteristics can be explained with the aid of Fig. 10, which is adapted from Ref. 31. If t_0 is the time at which the angle of attack passes through α_{SS}, then moment stall begins at time $t_1 = t_0 + \tau_1 c/U_\infty$ and $C_{L_{max}}$ occurs at $t_2 = t_0 + \tau_2 c/U_\infty$. For $t_0 < t < t_1$ (line segments 1 in the figure), the values of C_L and C_M are taken from unsteady potential theory. For $t_1 < t < t_2$, C_L continues this trend, but the aerodynamic center of pressure moves rearward along the locus of the static curve of $X_{c.p.}$ vs α. Therefore, $-C_M$ increases along line segment 2 according to the relation $C_M = (0.25 - X_{c.p.})\, C_L$ during this time interval.

---

*A linear decay over a time interval $\Delta\omega t \approx 0.2$ has also been used.

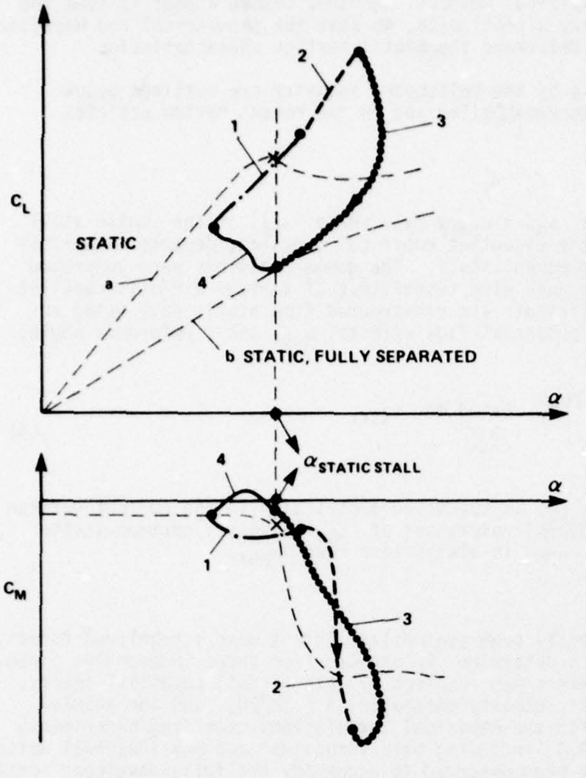

Fig. 10. Sketch of the principal phases of the dynamic stall calculations by the Time-Delay Method.

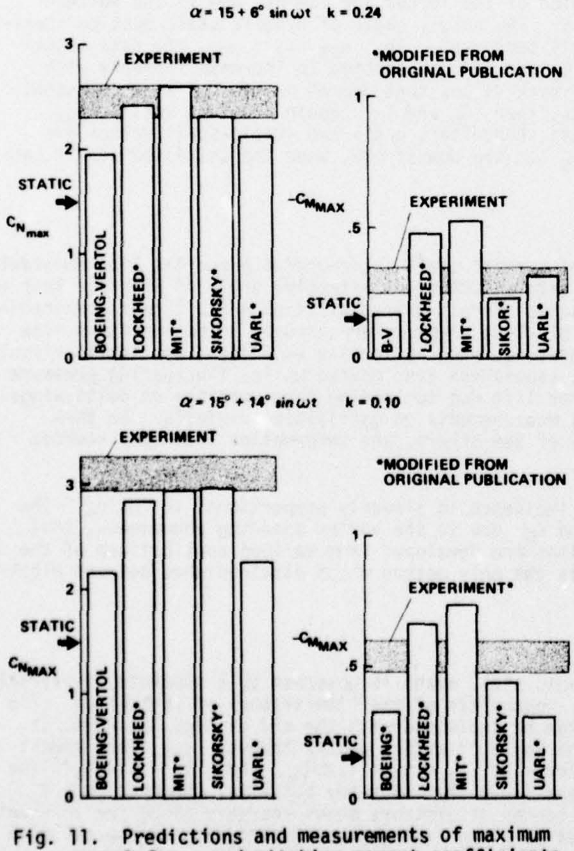

Fig. 11. Predictions and measurements of maximum normal-force and pitching-moment coefficients for an oscillating airfoil; revision of Ref. 20.

After lift stall at $t = t_2$, C_L decreases by an empirical exponential law with respect to time, whereas C_M is calculated from the same relation as before. Line segments 3 terminate at $\alpha = \alpha_{SS}$ and at a value of C_L that corresponds to a fully-separated approximation, indicated in the figure. The return to minimum incidence, line segments 4, is governed by still other exponential functions.

In Ref. 30, the time constants $\tau_1 = 2$ and $\tau_2 = 6$ were chosen based on the NACA 0012 studies at UTRC that supplied the data for the α, A, B Method. These values have since been modified to 2.5 and 5.0, respectively (Ref. 32). The large Boeing-Vertol data base was used in Ref. 31 to set $\tau_1 = 2.44$ and $\tau_2 = 5.41$. The method makes no provision for compressibility phenomena other than in the static characteristics for $C_L(\alpha)$ and $X_{c.p.}(\alpha)$, nor for the contribution of the vortex-shedding phenomenon to C_L, and hence to C_M.

Discussion of the Methods

All of the methods described above provide estimates of the effects of unsteady incidence changes, but each has shortcomings. Each method manages to reproduce reasonably well most of the data sets that were used in their development, but almost no comparisons have been made between any given method and independent sets of data.

One notable exception was reported in Ref. 20. With the assistance of the originators and their colleagues, the writer was able to compare the results of the aforementioned methods to an experiment in which the amplitude of sinusoidal pitching motion was varied from 6° to 14°, while the maximum pitch rate parameter was held constant at $(\dot{\alpha}c/U_\infty) \approx 0.050$, the mean angle was kept constant at approximately the static-stall angle, $Re = 2.5 \times 10^6$, and $M = 0.09$ (Ref. 33). Four quantities were compared for each of three amplitudes: the phase angle, ωt, at the onset of moment stall; the phase angle and maximum value of the normal force coefficient, C_N; and the value of $-C_{M_{max}}$.

The phase angles for the onset of moment stall were predicted almost to within the experimental uncertainty by the Time-Delay Methods. But lift stall occurred earlier than predicted. The latest version of the Lockheed Method predicted both phase angles correctly for the intermediate condition $\alpha_1 = 10°$, but the values were significantly too large for $\alpha_1 = 14°$ and too small for $\alpha_1 = 6°$. The other methods predicted all phase angles substantially smaller than the experimental values.

Figure 11 shows the maximum values of C_N and $-C_M$ for the minimum and maximum amplitude cases. It should be mentioned that the experimental values of C_M in Ref. 33 were significantly less than had been reported earlier in Ref. 34. The latter had been plotted in Ref. 20, whereas the values from Ref. 33 are shown in Fig. 11.

The Boeing-Vertol Method and the UTRC α, A, B Method are seen to consistently underpredict the force and moment coefficients. The Sikorsky version (Ref. 30) of the Time-Delay Method tended to predict lift stall later than the experiment, thereby partially compensating for the failure to include the excess normal force overshoot due to the vortex shedding phenomenon; since τ_2 in the Westlands version (Ref. 31) is approximately the same as Sikorsky's latest value, $C_{N_{max}}$ would be expected to be almost the same as Sikorsky predicts. Since $C_{N_{max}}$ is somewhat low and C_M is derived from C_N, so is $-C_{M_{max}}$ below the experimental uncertainty band. The MIT and Lockheed Methods overemphasize the importance of vortex shedding on C_M.

On the whole, the predictions seem reasonably satisfactory, although the need for further improvements is indicated. Further comparisons of this type for a wide variety of airfoil shapes and over a range of higher Mach numbers would certainly be desirable.

7.0 CONCLUDING REMARKS

As indicated at the beginning of this section, the calculation of the flow around an airfoil undergoing dynamic stall is a formidable task. The calculation has not yet been accomplished at high Reynolds numbers, although several approximate analytical methods have been proposed. The most promising of those methods seems to be either a combination of the discrete potential vortex and thin boundary layer approaches, or a significantly improved version of the strong viscous-inviscid interaction approach. The former may prove to be superior for low-speed, high-amplitude flows, but the latter seems likely to be more suitable for airfoils that operate under supercritical transonic flow conditions and for cases that do not penetrate deeply into stall.

At the present time, the engineer who is faced with the need to predict the aerodynamic forces and moments on oscillating airfoils would be better advised to turn to one of the empirical correlation techniques described in Section 6.0, or perhaps to utilize more than one method and average the results. In any event, these methods permit the essential features of dynamic stall to be described, even though further improvements are highly desirable. Future efforts will probably see more use made of the two-dimensional theoretical analyses, while experiments can be expected to play the major role in assessing the importance of the three-dimensional effects that are likely to be encountered in practice.

8.0 REFERENCES

1. Ham, N. D.: "Aerodynamic Loading on a Two-Dimensional Airfoil during Dynamic Stall." AIAA J., vol. 6, no. 10, Oct. 1968, pp. 1927 - 1934.

2. Baudu, N., Sagner, M., and Souquet, J.: "Modelisation du Décrochage Dynamique d'un Profil Oscillant." AAAF 10th Colloque d'Aérodynamique Appliquée, Lille, France, Nov. 1973.

3. Philippe, J. J., and Sagner, M.: "Calcul et Mesure des Forces Aérodynamique sur un Profil Oscillant, avec et sans Déchrochage." AGARD CP-111, Paper No. 11, 1972.

4. Giesing, J. P.: "Nonlinear Two-Dimensional Potential Flow with Lift." J. Aircraft, vol. 5, no. 2, Mar.-Apr. 1968, pp. 135 - 143.

5. McCroskey, W. J.: "Some Current Research in Unsteady Fluid Dynamics." ASME J. Fluids Engr., vol. 99, no. 1, Mar. 1977, pp. 8 - 38.

6. Telionis, D. P.: "Unsteady Boundary Layers, Separated and Attached." AGARD CP-227, Paper No. 16, 1977.

7. McCroskey, W. J., and Philippe, J. J.: "Unsteady Viscous Flow on Oscillating Airfoils." AIAA J., vol. 13, no. 1, Jan. 1975, pp. 71 - 79.

8. Scruggs, R. M., Nash, J. F., and Singleton, R. E.: "Analysis of Dynamic Stall Using Unsteady Boundary Layer Theory." NASA CR-2467, Oct. 1974.

9. Crimi, P., and Reeves, B. L.: "A Method for Analyzing Dynamic Stall of Helicopter Rotor Blades." NASA CR-2009, May 1972; also AIAA Paper 72-37, Jan. 1972.

10. Reeves, B. L., and Lees, L.: "Theory of Laminar Near Wake of Blunt Bodies in Hypersonic Flow." AIAA J., vol. 3, no. 11, Nov. 1965, pp. 2061 - 2074.

11. Hunter, L. G., and Reeves, B. L.: "Results of a Strong-Interaction, Wake-Like Model of Supersonic Separated and Reattaching Turbulent Flows." AIAA Paper 71-128, Jan. 1971.

12. Crimi, P.: "Dynamic Stall." AGARDograph No. 172, 1973.

13. Crimi, P.: "Investigation of Nonlinear Inviscid and Viscous Effects in the Analysis of Dynamic Stall." NASA CR-2335, Feb. 1974.

14. Crimi, P., and Reeves, B. L.: Analysis of Leading-Edge Separation Bubbles on Airfoils." AIAA J., vol. 14, no. 11, Nov. 1976, pp. 1548 - 1555.

15. Mehta, U. B.: "Dynamic Stall of an Oscillating Airfoil." AGARD CP-227, Paper No. 23, 1977.

16. Wu, J. C., Sankar, N. L., and Sampath, S.: "A Numerical Study of Unsteady Viscous Flows Around Airfoils." AGARD CP-227, Paper No. 24, 1977.

17. Kinney, R. B.: "Two-Dimensional Viscous Flow Past an Airfoil in an Unsteady Airstream." AGARD CP-227, Paper No. 26, 1977.

18. Thompson, J. F. et al.: "Numerical Solution of the Unsteady Navier-Stokes Equations for Arbitrary Bodies Using Boundary-Fitted Curvilinear Coordinates." *Symposium on Unsteady Aerodynamics*, Kinney, R. B., ed., Tucson: Univ. Arizona, 1975, pp. 453 - 485.

19. Werlé, H.: private communication, 1976.

20. McCroskey, W. J.: "Recent Developments in Dynamic Stall." *Symposium on Unsteady Aerodynamics*, Kinney, R. B., ed., Tucson: Univ. Arizona, 1975, pp. 1 - 33.

21. Philippe, J. J.: "Le Déchrochage Dynamique; un Exemple d'Interaction Forte entre Ecoulements Visqueux et Non-Visqueux." AGARD CP-227, Paper No. 21, 1977.

22. Harris, F. D., Tarzanin, F. J., Jr. and Fisher, R. K., Jr.: "Rotor High Speed Performance; Theory vs. Test." J. Am. Helicopter Soc., vol. 15, No. 3, Jul. 1970, pp. 35 - 44.

23. Gormont, R. E.: "A Mathematical Model of Unsteady Aerodynamics and Radial Flow for Application to Helicopter Rotors." U.S. Army AMRDL TR-72-67, Eustis Directorate, 1973.

24. Dadone, L. U.: private communication, 1975.

25. Carta, F. O., et al.: "Unsteady Normal Investigation of Airfoil Dynamics Stall and Its Influence on Helicopter Control Loads." U.S. Army AMRDL TR-72-51, Eustis Directorate, Sep. 1972.

26. Bielawa, R. L.: "Synthesized Unsteady Airfoil Data With Applications to Stall Flutter Calculations." Proc. 31st Annual Forum Am. Helicopter Soc., May 1975, Preprint No. 935.

27. Johnson, W.: "The Effect of Dynamic Stall on the Response and Airloading of Helicopter Rotor Blades." J. Am. Helicopter Soc., vol. 14, no. 2, Apr. 1969, pp. 68 - 79.

28. Ericsson, L. E., and Reding, J. P.: "Dynamic Stall Analysis in the Light of Recent Numerical and Experimental Results." J. of Aircraft, vol. 13, no. 4, Apr. 1976, pp. 248 - 255.

29. Ericsson, L. E., and Reding, J. P.: "Quasi-Steady and Transient Dynamic Stall Characteristics." AGARD CP-204, Paper No. 24, 1976.

30. Carlson, R. G., et al.: "Dynamic Stall Modeling and Correlation with Experimental Data on Airfoils and Rotors." NASA SP-352, Rotorcraft Dynamics, Feb. 1974, Paper No. 2.

31. Beddoes, T. S.: "A Synthesis of Unsteady Aerodynamics Stall Effects, Including Hysteresis," Proc. First European Rotorcraft and Powered Lift Aircraft Forum, Univ. Southampton, England, Sep. 1975, Paper No. 17.

32. R. H. Blackwell: private communication, 1975.

33. McAlister, K. W., Carr, L.W., and McCroskey, W. J.: "Dynamic Stall Experiments on the NASA 0012 Airfoil." NASA TP-1100, 1977.

34. Martin, J. M. et al.: "An Experimental Analysis of Dynamic Stall on an Oscillating Airfoil." J. Am. Helicopter Soc., vol. 19, no. 1, Jan. 1974, pp. 26 - 32.

STATUS AND FUTURE PROSPECTS OF USING NUMERICAL METHODS TO STUDY COMPLEX FLOWS AT HIGH REYNOLDS NUMBERS

Robert W. MacCormack
Ames Research Center, NASA, Moffett Field, California 94035, U.S.A.

SUMMARY

The Navier-Stokes equations adequately describe aerodynamic flows at standard atmospheric temperatures and pressures. If we could efficiently solve these equations there would be no need for experimental tests to design flight vehicles or other aerodynamic devices. Although we have made much progress toward their solution, including complex unsteady two-dimensional and steady three-dimensional separated flows and have recently made some dramatic improvements in developing numerical methods, the calculation of flow fields past complete aircraft configurations at flight Reynolds numbers are far beyond our reach, perhaps as long as a decade away. They await substantial progress in devising accurate and efficient numerical methods, in understanding and modeling the physics of turbulence, and in developing reliable and powerful computer hardware.

1. INTRODUCTION

The unsteady compressible form of the Navier-Stokes equations is a coupled nonlinear parabolic system of partial differential equations that describes viscous fluid flow at standard atmospheric conditions. Reynolds number is a measure of the ratio of the inertial forces to the viscous forces of the fluid. The viscous terms that cause the system to be parabolic are of the order of the reciprocal of the Reynolds number. At high Reynolds number the system is almost everywhere hyperbolic; the viscous terms are negligible except in thin layers near body surfaces. Because of the disparity in magnitude at high Reynolds number between the inertial and viscous terms and also because of their resulting length scales, such systems are difficult to solve numerically and are termed stiff.

Much success has been achieved by efficiently solving subsets of the Navier-Stokes equations. Two examples are (1) the Euler equations for flows for which viscous effects are negligible and (2) the boundary-layer equations for attached flows near surfaces with mild pressure gradients and little interaction with the exterior inviscid flow. For complex flows with separation and strong viscous-inviscid interaction these subsets are inadequate and a larger set, though not necessarily the complete set of Navier-Stokes equations, is required.

An excellent survey of numerical methods for solving the unsteady compressible Navier-Stokes equations was presented by Peyret and Viviand in 1975 (Ref. 1). The present paper presents some recent developments relating to the use of numerical methods to study complex flows at high Reynolds number. Numerical results for separated unsteady two-dimensional and steady three-dimensional flows will be presented. Techniques for accounting for the effects of turbulence will be discussed. An excellent study of turbulence modeling for compressible flows has been presented by Marvin in 1977 (Ref. 2). Finally, future prospects for calculating flow fields past complete aircraft configurations at flight Reynolds numbers will be assessed.

2. THE NAVIER-STOKES EQUATIONS

2.1 Differential Equations

The time-dependent compressible Navier-Stokes equations in two dimensions may be written in conservation form as

$$\frac{\partial U}{\partial t} + \frac{\partial F}{\partial x} + \frac{\partial G}{\partial y} = 0 \qquad (1)$$

where

$$U = \begin{bmatrix} \rho \\ \rho u \\ \rho v \\ e \end{bmatrix}, \quad F = \begin{bmatrix} \rho u \\ \rho u^2 + \sigma_x \\ \rho u v + \tau_{xy} \\ (e + \sigma_x)u + \tau_{yx}v - \kappa \frac{\partial \varepsilon}{\partial x} \end{bmatrix}, \quad G = \begin{bmatrix} \rho v \\ \rho u v + \tau_{yx} \\ \rho v^2 + \sigma_y \\ (e + \sigma_y)v + \tau_{xy}u - \kappa \frac{\partial \varepsilon}{\partial y} \end{bmatrix}$$

$$\sigma_x = p - \lambda\left(\frac{\partial u}{\partial x} + \frac{\partial v}{\partial y}\right) - 2\mu\frac{\partial u}{\partial x}, \qquad \tau_{xy} = \tau_{yx} = -\mu\left(\frac{\partial u}{\partial y} + \frac{\partial v}{\partial x}\right)$$

$$\text{and} \quad \sigma_y = p - \lambda\left(\frac{\partial u}{\partial x} + \frac{\partial v}{\partial y}\right) - 2\mu\frac{\partial v}{\partial y}$$

in terms of density ρ, x, and y velocity components u and v, viscosity coefficients λ and μ, total energy per unit volume e, specific internal energy ε, and coefficient of heat conductivity κ. Finally, the pressure p is related to ε and ρ by an equation of state, $p(\varepsilon,\rho)$, where

$$\varepsilon = \frac{e}{\rho} - \frac{u^2 + v^2}{2}$$

2.2 Integral Equations

Using the Divergence Theorem we can write Eq. (1) in integral form by integrating it over an arbitrary volume V enclosed by surface S

$$\frac{\partial \bar{U}}{\partial t} + \int_S \vec{H} \cdot \vec{n} \, ds = 0 \tag{2}$$

where

$$\bar{U} = \int_V U \, dv$$

$$\vec{H} = F\vec{i}_x + G\vec{i}_y$$

and $\vec{n}$ is the local unit outer normal to S.

3. COMPUTATIONAL MESH FOR INVISCID-VISCOUS INTERACTING FLOWS

For computational efficiency the number of mesh points must be kept to the minimum required to spacially resolve all significant features of the flow. A typical computational mesh for calculating inviscid-viscous interacting flows such as that sketched in Fig. 1 for a shock wave boundary-layer interaction is shown in Fig. 2. It consists of a fine boundary-layer type mesh near the body surface for resolving the flow where viscous effects are important and a coarse outer mesh where the flow is essentially inviscid. A mesh about a more general body surface is shown in Fig. 3. Additional efficiency can be gained by stretching the fine or coarse mesh away from the body to reduce the number of mesh points in regions requiring less resolution.

In the fine viscous layer mesh, about 20 mesh points are typically positioned across the layer. Along the layer the spacing is much coarser, usually of the order of the boundary-layer thickness itself. Such a mesh cannot give adequate support to every term of the Navier-Stokes equations. Finite difference quotients can accurately approximate the transverse direction terms; however, not all the remaining terms, and particularly not all the pure longitudinal diffusion terms, will be resolved. The set of terms of the Navier-Stokes equations that is resolved, however, is larger than that usually retained by boundary-layer theory and contains all the terms of the Euler equations. In general, for laminar or "sheet like" flows the unresolved terms have been found by comparison of computational and experimental results to be negligible. Some results will be presented later. For flow regions that need all terms resolved, the mesh point spacing in the longitudinal direction must be severely reduced. The outer mesh region, in which the mesh spacing is relatively coarse in each direction, can at most support the subset consisting of the Euler equations.

Because of computer speed and memory limitations, the computational mesh cannot be made fine enough to resolve all significant eddy length scales of high Reynolds number turbulent flow. Turbulent flows will have to be modeled; mesh size and smaller turbulence effects must be accounted for by closure models.

4. TURBULENCE MODELING

A turbulent flow fluctuates rapidly about the mean flow solution, which also may itself be varying in time. Because the instantaneous solution is impossible to determine with present or foreseeable computational resources and because mean flow quantities such as lift, drag, and heat transfer are of primary interest, solutions of the Reynolds or "time-averaged" Navier-Stokes equations are sought. These equations are obtained by expanding each dependent variable into two parts, a mean part and a fluctuating part. For example, $\rho = \bar{\rho} + \rho'$, where $\bar{\rho} = \frac{1}{T}\int_0^T \rho \, dt$ and T is long relative to turbulent eddy time scales, but short relative to mean flow time scales. Each dependent variable is replaced by its expanded form and a new set results that closely resembles the original set with the exceptions that the mean flow variables take the place of the original flow variables and there are some new terms called Reynolds stress and turbulent heat transfer terms. A particularly convenient time-averaged set has been devised by Rubesin and Rose (Ref. 3) using time-mass-averaged variables. For example, using this approach the x-momentum equation of Eq. (1) becomes

$$\frac{\partial \bar{\rho}\tilde{u}}{\partial t} + \frac{\partial}{\partial x}\left(\bar{\rho}\tilde{u}\tilde{u} + \bar{\sigma}_x + \overline{\rho u'u'}\right) + \frac{\partial}{\partial y}\left(\bar{\rho}\tilde{u}\tilde{v} + \bar{\tau}_{xy} + \overline{\rho u'v'}\right) = 0$$

where $\tilde{u} = \overline{\rho u}/\bar{\rho}$, $\tilde{v} = \overline{\rho v}/\bar{\rho}$ and the terms $\overline{\rho u'u'}$ and $\overline{\rho u'v'}$ are Reynolds stresses.

The time averaging procedure loses information on the instantaneous solution and increases the number of unknowns to include the Reynolds stress and heat transfer terms. Because the number of equations remains the same during the procedure, relationships for the additional unknowns must be determined. This is called the turbulence closure problem. Two types of relationships, algebraic and differential, have been devised to close the system.

4.1 Algebraic Turbulence Models

Several models have been devised which directly relate the Reynolds stress and turbulent heat transfer terms to the mean flow conditions using simple algebraic relations. Bousinesq's eddy viscosity concept is used to relate the terms to the product of an eddy viscosity coefficient $\hat{\mu}$ or a turbulent heat transfer coefficient $\hat{\kappa}$, and spacial derivatives of the mean flow velocities or temperatures. For example

$$\overline{\rho u'v'} = \hat{\mu}\left(\frac{\partial \bar{u}}{\partial x} + \frac{\partial \bar{v}}{\partial y}\right)$$

The turbulent mixing coefficients $\hat{\mu}$ and $\hat{\kappa}$ are also determined from mean flow conditions. A widely used procedure for this has been developed by Cebeci and Smith (Ref. 4). Their model consists of two layers, one near the wall including the laminar sublayer and the other covering the outer part of the boundary layer. The mixing coefficients are evaluated in the inner layer using Prandtl's mixing-length hypothesis with van Driest's wall damping factor; in the outer layer Clauser's formulation is used.

In general, the algebraic closure model has performed well for calculating compressible attached turbulent boundary layers in zero to mild pressure gradients. For strong adverse pressure gradients, strong enough to cause flow separation, the model has been deficient. Calculations show that this model, which assumes that the turbulent Reynolds terms instantaneously adjust to local flow conditions, over-predicts turbulent mixing in regions with pressure gradients strong enough to cause flow separation. The excess mixing transfers higher momentum fluid deep into the boundary layer thus retarding separation.

Shang and Hankey (Ref. 5) modified the simple algebraic model by adding a relaxation length, usually of the order of a few boundary-layer thicknesses. Instead of an instantaneous adjustment to turbulent equilibrium, the algebraic model with relaxation assumes the flow reaches equilibrium after the mean flow travels a given distance and thus delays turbulence change. The flow separation predictions of Shang and Hankey agreed closely with experiment. Other studies showed, however, that although the separation region for a given choice of relaxation length was better predicted, the model underpredicts turbulent mixing in regions of flow reattachment and in general overpredicts the length of separated regions.

4.2 Differential Turbulence Models

Several models have been devised which relate the Reynolds terms to the mean flow variables plus quantities determined by solving additional flow equations. The models vary from the one-equation model, which determines turbulent kinetic energy, $k = 1/2(\overline{\rho u'u'} + \overline{\rho v'v'})$, and the two-equation model, which adds a length scale equation, to the complete Reynolds stress model which contains 12 equations. The equations describe changes in turbulence in terms of convection, diffusion, production, and dissipation. They contain constants which are determined and adjusted from experimental data and theoretical analysis.

Considerable experience has been obtained with Rubesin's one-equation model (Ref. 6) and two-equation models such as those of Saffman and Wilcox (Ref. 7). In general, the differential models, which contain more turbulence physics, provide more flexibility and thereby better predictions of turbulent flows. Unfortunately, they are at present far from being universal; adjustments depending on flow conditions are still required.

5. NUMERICAL METHODS

5.1 Basic Concepts

Many numerical methods have been devised for solving the compressible Navier-Stokes equations. As noted earlier, a good review was presented by Peyret and Viviand in 1975 (Ref. 1). Since that time some new and dramatic advances have been made in the development of numerical methods for calculating complex flows, including shock wave induced separation, at high Reynolds numbers. These advances have each successfully dealt with the numerical stiffness problem associated with high Reynolds number solutions. Before we examine them, some basic concepts will be reviewed.

Let us begin our discussion with a model linear scalar parabolic equation representative of the Navier-Stokes equations

$$\frac{\partial v}{\partial t} = -c\,\frac{\partial v}{\partial y} + \nu\,\frac{\partial^2 v}{\partial y^2}$$

The first term on the right-hand side represents a hyperbolic convection-like term with characteristic velocity c. The second term represents a viscous diffusion term with viscosity ν. In the high Reynolds number limit, $\nu/c \to 0$, this equation is hyperbolic in character everywhere except in thin viscous regions. The model equation can be solved numerically by first discretizing time and space into Δt and Δy increments. The solution at time $t = (n + 1)\Delta t$ can then be determined from the known solution at $t = n\Delta t$ by solving an algebraic finite difference equation that approximates the model equation.

5.1.1 Explicit and Implicit Finite-Difference Equations

If the difference equation approximates the spacial derivatives by differences using only solution values known at $t = n\Delta t$, the difference equation is called explicit. On the other hand, if the approximations to the spacial derivatives are expressed in terms of the to be solved for solution at $t = (n+1)\Delta t$, the difference equation is called implicit. For example, a simple explicit difference equation (upwind, $c > 0$) approximating the model equation is

$$v_j^{n+1} = v_j^n - \frac{c\Delta t}{\Delta y}\left(v_j^n - v_{j-1}^n\right) + \frac{\nu\Delta t}{\Delta y^2}\left(v_{j+1}^n - 2v_j^n + v_{j-1}^n\right)$$

and an implicit one (Crank-Nicolson) is

$$v_j^{n+1} = v_j^n - \frac{c\Delta t}{4\Delta y}\left(v_{j+1}^{n+1} - v_{j-1}^{n+1} + v_{j+1}^n - v_{j-1}^n\right) + \frac{\nu\Delta t}{2\Delta y^2}\left(v_{j+1}^{n+1} - 2v_j^{n+1} + v_{j-1}^{n+1} + v_{j+1}^n - 2v_j^n + v_{j-1}^n\right)$$

The implicit equation can be rewritten as

$$b_j v_{j-1}^{n+1} + a_j v_j^{n+1} + c_j v_{j+1}^{n+1} = f_j$$

and solved for by inverting a tridiagonal matrix.

5.1.2 Splitting

Instead of approximating every term of the model equation in a single difference equation, as shown above, the difference approximation can be split or factored into a sequence of simpler difference equations. For example, we could construct the following sequence of two equations to approximate the model equation:

$$v_j^* = v_j^n - \frac{c\Delta t}{\Delta y}(v_j^n - v_{j-1}^n)$$

$$v_j^{n+1} = v_j^* + \frac{\nu\Delta t}{2\Delta y^2}(v_{j+1}^{n+1} - 2v_j^{n+1} + v_{j-1}^{n+1} + v_{j+1}^* - 2v_j^* + v_{j-1}^*)$$

The first equation approximates only the convection term of the model equation and uses a simple explicit upwind difference. The second equation accounts for the diffusion term using an implicit Crank-Nicolson approximation.

5.1.3 Characteristic Equations

Consider the model equation with $\nu = 0$

$$\frac{\partial v}{\partial t} + c\,\frac{\partial v}{\partial y} = 0$$

Using characteristics theory to transform this partial differential equation into a simple ordinary differential equation, we obtain

$$\frac{dv}{d\xi} = 0$$

where the total derivative

$$\frac{d}{d\xi} = \frac{\partial}{\partial t} + c\,\frac{\partial}{\partial y}$$

Thus, the solution v is constant along characteristic paths having slope $1/c$ in the y-t plane. In Fig. 4 the characteristic path passing through the point $y = y_j$ and $t = (n + 1)\Delta t$ intersects the known solution line $t = n\Delta t$ at $y = y_\alpha$. Thus

$$v_j^{n+1} = v_\alpha^n$$

v_α^n can be determined by interpolation. For example

$$v_\alpha^n = \frac{(y_{k+1} - y_\alpha)v_k^n + (y_\alpha - y_k)v_{k+1}^n}{y_{k+1} - y_k}$$

where

$$y_k \le y_\alpha \le y_{k+1}$$

5.1.4 Numerical Accuracy

The first requirement of an accurate finite difference approximation is that in each flow region all the physically significant terms of the governing equations are resolved. Though not necessary or sufficient, a good rule of thumb is to approximate each physically significant term to the same order of accuracy and to choose time and space increments so that the coefficients of the terms appearing in the difference equations are of the same order of magnitude. We illustrate this rule by first examining the difference equations of Sec. 5.1.1.

The coefficients of the explicit upwind difference equation are 1, $c\Delta t/\Delta y$, and $\nu\Delta t/\Delta y^2$. The second coefficient is called the CFL (Courant, Friedrichs, and Lewy) number. For the numerical stability of this explicit method, this number cannot exceed 1. Violation of the CFL condition causes a rapid error growth which quickly renders the numerical solution meaningless. If the second and third coefficients are of the same order of magnitude

$$\frac{c\Delta t}{\Delta y} \approx \frac{\nu\Delta t}{\Delta y^2}$$

or

$$\frac{c\Delta y}{\nu} \approx 1$$

This last number is the mesh Reynolds number. A mesh Reynolds number of the order of 1 is necessary so that the convection difference term neither dominates nor is dominated by the diffusion difference term. For flow regions in which convection and diffusion are each physically significant, the mesh increments can be chosen ($\Delta y \approx \nu/c$ and $\Delta t \approx \Delta y/c$) so that each coefficient is near 1, satisfying the second part of the rule. Expanding the convection and diffusion difference terms by Taylor series we obtain

$$c \, \frac{v_j - v_{j-1}}{\Delta y} = c \, \frac{\partial v}{\partial y} - \frac{c\Delta y}{2} \frac{\partial^2 v}{\partial y^2} + \theta(\Delta y^2)$$

and

$$\nu \, \frac{v_{j+1} - 2v_j + v_{j-1}}{\Delta y^2} = \nu \, \frac{\partial^2 v}{\partial y^2} + \theta(\Delta y^2)$$

As shown above the convection term is approximated only to first order in Δy but the diffusion term is second order accurate, a violation of the rule. Because $c\Delta y \approx \nu$, the error in the convection approximation is of the same order as the diffusion term itself and hence is an inadequate approximation.

The coefficients of the implicit Crank-Nicolson approximation are 1, $c\Delta t/4\Delta y$, and $\nu\Delta t/2\Delta y^2$. Unlike the explicit method, this method is stable for any CFL number but, as we will see in the next section, if the second coefficient exceeds 1, inaccuracies will occur, although the numerical solution will remain stable. Again, if convection and diffusion are both physically significant, the third coefficient should be chosen so that the mesh Reynolds number is of the order of 1. By Taylor series expansion it can be shown that all terms are second-order accurate.

Finally, let us also consider the characteristic equation of Sec. 5.1.3 for solving the hyperbolic part of the model equation ($\nu = 0$)

$$v_j^{n+1} = v_\alpha^n$$

This can be rewritten as

$$v_j^{n+1} = v_j^n - \frac{c\Delta t}{y_j - y_\alpha} (v_j^n - v_\alpha^n)$$

where $c\Delta t/(y_j - y_\alpha)$, the corresponding CFL number, is exactly 1. The accuracy is limited only by the interpolation procedure for obtaining v_α^n.

5.1.5 Numerical Efficiency

In solving unsteady flow problems, the relative numerical efficiencies of competing methods of the same order of accuracy can be measured by the machine computation time required to calculate a given flow from time $t = 0$ to $t = T$. Numerical efficiency is therefore directly proportional to the time step size Δt and inversely proportional to the machine time required by one time step of the method. The methods presented earlier, typical of explicit and implicit methods, require about the same order of magnitude of computation time. Implicit methods generally require more time, by a factor of about 2, than explicit methods. Therefore, numerical efficiency strongly depends on time step size. We will now examine the allowable time-step sizes of these methods for solving the model equation in the high Reynolds number limit ($\nu = 0$).

The time step size of an explicit method is limited by stability conditions to CFL numbers less than 1. Its numerical efficiency is therefore proportional to

$$\Delta t \leq \frac{\Delta y}{c}$$

On the other hand, implicit methods, in general not subject to stability conditions, are frequently limited by accuracy conditions to CFL-like limits. This can be illustrated by considering the solution to the initial value problem

$$\frac{\partial v}{\partial t} + c \, \frac{\partial v}{\partial y} = 0$$

and at time $t = 0$ the solution is ramp-like as shown in Fig. 5. The length of the ramp is $\lambda = 4\Delta y$. For $t > 0$ the wave profile propagates to the right with speed c. For accuracy, the time step cannot be so large that the wave moves more than one wave length, $c\Delta t/\lambda \leq 1$. Otherwise there is a region of the flow that lies ahead of the wave before and behind the wave after the time step. Mesh points within this region should see a zero spacial gradient at each time as shown in Fig. 6 and thus have no accurate numerical way to change in value. Figure 7 shows the results of using the Crank-Nicolson method with "implicit CFL numbers" of 1, $\Delta t = \lambda/c$, for which the numerical solution shows agreement with the exact solution and of 2, $\Delta t = 2\lambda/c$, which shows poor agreement. The numerical efficiency of an implicit method is proportional to

$$\Delta t \leq \frac{\lambda}{c}$$

where λ is the smallest wave length to be resolved. For unsteady flows containing significant features of length $\theta(\Delta y)$, implicit methods offer no advantage. On the other hand for low Reynolds number flows, which are diffusion dominated and contain only smooth flow features, or for flows that after initial transients characterized by small wave length phenomena, are past and the flow is approaching a steady state, the ratio λ/c is high and implicit methods are significantly more efficient than explicit methods.

Finally, let us again consider the characteristic approximation. The characteristic method, technically an explicit method, is like the implicit method not limited by any time step condition. As shown earlier, it automatically adjusts its computational length scale for any time step so that its "CFL *number*" is exactly 1. Figure 8 shows the results of applying the characteristic method of Sec. 5.1.3 to solve the initial value problem presented earlier with $\Delta t = \lambda/c$ and $\Delta t = 2\lambda/c$. For these integral time steps the numerical results are exact. In general, they will have error of the order of the interpolation procedure. The machine computation time per step is about the same as for the implicit method. Its numerical efficiency is high for all wave lengths.

5.2 Explicit Methods

Several explicit numerical methods have been developed and used (Refs. 8-11) for solving the Navier-Stokes equations at high Reynolds numbers. Solutions obtained at Reynolds numbers as high as 20×10^6 compare accurately with experiment but required hours of computing time on machines like the CDC 7600. One widely used method will be presented to serve as a reference point for the developments to be described later. The method, originally presented by MacCormack in 1971 (Ref. 9), is briefly described in the following for two-dimensional unsteady flow. Its extension to three-dimensional flow is straightforward.

If the solution $U^n_{i,j}$ is known at time $t = n\Delta t$ at each mesh point (i,j), the solution at time $t = (n + 1)\Delta t$ is calculated by

$$U^{n+1}_{i,j} = \mathcal{L}(\Delta)U^n_{i,j}$$

where $\mathcal{L}(\Delta t)$ is a symmetric sequence of time-split, one-dimensional difference operators $\mathcal{L}_x(\Delta t_x)$ and $\mathcal{L}_y(\Delta t_y)$. For example,

$$U^{n+1}_{i,j} = \mathcal{L}_x\left(\frac{\Delta t}{2}\right)\mathcal{L}_y(\Delta t)\mathcal{L}_x\left(\frac{\Delta t}{2}\right)U^n_{i,j}$$

In this sequence the $\mathcal{L}_x$ operator is called twice, each time advancing the solution in time by $\Delta t/2$ by accounting only for the effect on the solution of the x-derivative in Eq. (1). Similarly, the $\mathcal{L}_y$ operator advances the solution by Δt once by accounting only for the effect of the y-derivative on the solution. The $\mathcal{L}_y$ operator solves the time-split differential "equation"

$$\frac{\partial U}{\partial t} + \frac{\partial G}{\partial y} = 0$$

by first predicting a new value $U^{(p)}_{i,j}$ from the current solution value $U_{i,j}$

$$U^{(p)}_{i,j} = U_{i,j} - \frac{\Delta t}{\Delta y}\left(G_{i,j} - G_{i,j-1}\right)$$

and then correcting the predicted value,

$$U^{(c)}_{i,j} = \frac{1}{2}\left\{U_{i,j} + U^{(p)}_{i,j} - \frac{\Delta t}{\Delta y}\left[G^{(p)}_{i,j+1} - G^{(p)}_{i,j}\right]\right\}$$

The corrected value then becomes the current value for the next split difference operator in the sequence. The operator $\mathcal{L}_x$ is similarly defined.

The operators $\mathcal{L}_x(\Delta t_x)$ and $\mathcal{L}_y(\Delta t_y)$ are stable if

$$\Delta t_x \le \frac{\Delta x}{|u| + c + (1/\rho)\{(2\gamma\mu/Pr\Delta x) + [(-\lambda\mu)^{1/2}/\Delta y]\}}$$

and

$$\Delta t_y \le \frac{\Delta y}{|v| + c + (1/\rho)\{[(-\lambda\mu)^{1/2}/\Delta x] + (2\gamma\mu/Pr\Delta y)\}}$$

where c is the speed of sound, γ is the ratio of specific heats of the gas, and Pr is the Prandtl number.

For calculating an inviscid-viscous interacting flow on the two-mesh system shown in Fig. 2, typical operator sequences are (1) for all (i,j) in the coarse mesh

$$U^{n+1}_{i,j} = \mathcal{L}_x\left(\frac{\Delta t}{2}\right)\mathcal{L}_y(\Delta t)\mathcal{L}_x\left(\frac{\Delta t}{2}\right)U^n_{i,j}$$

where $\Delta t \le \min_{i,j}\{2 \max \Delta t_x, \max \Delta t_y\}$, and (2) for all (i,j) in the fine mesh

$$U^{n+1}_{i,j} = \left[\mathcal{L}_y\left(\frac{\Delta t}{2m}\right)\mathcal{L}_x\left(\frac{\Delta t}{m}\right)\mathcal{L}_y\left(\frac{\Delta t}{2m}\right)\right]^m U^n_{i,j}$$

where m is the smallest integer such that $(\Delta t/m) \le \min_{i,j}\{\max \Delta t_x, 2 \max \Delta t_y\}$.

For high Reynolds number calculations, the viscous region becomes very thin, requiring Δy near the wall to be very small. This causes Δt_y of the $\mathcal{L}_y$ operator also to be small and the integer m to be large. Values for m often exceed 100, requiring a great amount of calculation time in the fine mesh.

Deiwert (Ref. 12) has extended the above explicit method to solve the Navier-Stokes equations in integral form, Eqs. (2), on a mesh consisting of arbitrarily shaped quadrilaterals. He has applied the method to solve for high Reynolds number turbulent transonic flows past arbitrarily shaped blunt nosed lifting airfoils at angle of attack. His results, using an algebraic eddy viscosity model, for flow at a Reynolds number of 21×10^6 past a Garabedian-Korn airfoil are shown in Fig. 9; the agreement with experiment is exceptionally good. The simple turbulence model performed well for the mild pressure gradient flow.

5.3 Implicit Methods

Encouraged by the advantages in numerical efficiency, noniterative or one step implicit methods have been developed in recent years. In 1973, Lindemuth and Killeen (Ref. 13) developed an alternating direction implicit method for solving the two-dimensional equations of magnetohydrodynamics. Briley and McDonald (Ref. 14), also in 1973, presented an efficient implicit method for solving the three-dimensional compressible Navier-Stokes equations with applications to low Mach number viscous flows. Later, in 1975, they extended their method to efficiently treat steady supersonic viscous or inviscid flows (Ref. 15). In 1976, Beam and Warming (Ref. 16), following an approach similar to that of Briley and McDonald, developed an implicit method in conservation-law form capable of treating flows with shock waves. The Beam and Warming method has been applied to solve inviscid flows (Ref. 17) and unsteady shock separated viscous flows (Ref. 18). Their approach is briefly presented in the following.

If the solution is known at time $t = n\Delta t$ at each mesh point (i,j), the solution at time $t = (n+1)\Delta t$ is calculated to second-order accuracy in time by

$$U^{n+1}_{i,j} = U^n_{i,j} - \frac{\Delta t}{2}\left(\frac{\partial F^{n+1}_{i,j}}{\partial x} + \frac{\partial G^{n+1}_{i,j}}{\partial y} + \frac{\partial F^n_{i,j}}{\partial x} + \frac{\partial G^n_{i,j}}{\partial y}\right)$$

Linearizing $F^{n+1}_{i,j}$ and $G^{n+1}_{i,j}$ by Taylor series expansion we obtain

$$F^{n+1}_{i,j} = F^n_{i,j} + A^n_{i,j}(U^{n+1}_{i,j} - U^n_{i,j}) + \theta(\Delta t^2)$$

$$G^{n+1}_{i,j} = G^n_{i,j} + B^n_{i,j}(U^{n+1}_{i,j} - U^n_{i,j}) + \theta(\Delta t^2)$$

where A and B are 4×4 matrices for two-dimensional flow and 5×5 matrices for three-dimensional flow and represent the Jacobians of F and G with respect to U. By substitution we obtain

$$\left[I + \frac{\Delta t}{2}\left(\frac{\partial}{\partial x}A^n_{i,j} + \frac{\partial}{\partial y}B^n_{i,j}\right)\right]U^{n+1}_{i,j} = \left[I + \frac{\Delta t}{2}\left(\frac{\partial}{\partial x}A^n_{i,j} + \frac{\partial}{\partial y}B^n_{i,j}\right)\right]U^n_{i,j} - \Delta t\left(\frac{\partial F^n_{i,j}}{\partial x} + \frac{\partial G^n_{i,j}}{\partial y}\right)$$

where I is the identity matrix and the differential operator

$$\left(\frac{\partial}{\partial x}A + \frac{\partial}{\partial y}B\right)U \quad \text{denotes} \quad \frac{\partial AU}{\partial x} + \frac{\partial BU}{\partial y}$$

We can rewrite this equation as

$$\mathcal{L}^*(\Delta t)U^{n+1}_{i,j} = \mathcal{L}^*(\Delta t)U^n_{i,j} + \beta^n_{i,j}$$

or

$$\mathcal{L}^*(\Delta t)\Delta U^n_{i,j} = \beta^n_{i,j}$$

where

$$\mathcal{L}^*(\Delta t) = I + \frac{\Delta t}{2}\left(\frac{\partial}{\partial x}A^n_{i,j} + \frac{\partial}{\partial y}B^n_{i,j}\right)$$

$$\Delta U^n_{i,j} = U^{n+1}_{i,j} - U^n_{i,j}$$

and

$$\beta^n_{i,j} = -\Delta t\left(\frac{\partial F^n_{i,j}}{\partial x} + \frac{\partial G^n_{i,j}}{\partial y}\right)$$

To complete the numerical approximation, the differential operators ∂/∂_x and ∂/∂_y must be replaced by difference operators. Beam and Warming have several ways of doing this, including first, second, and fourth-order accurate approximations, each using only three grid points. In application, second-order central difference approximations have been used. Finally, because inversion of the matrix equation implied by $\mathcal{L}^*(\Delta t)\Delta U^n_{i,j} = \beta^n_{i,j}$ is difficult, the operator $\mathcal{L}^*(\Delta t)$ is factored or split so that only block tridiagonal matrices need to be inverted. This procedure is attributed to Peaceman and Rachford (Ref. 19), Douglas (Ref. 20), and Douglas and Gunn (Ref. 21). The equation, still second-order accurate, becomes

$$\mathcal{L}^*_x(\Delta t)\mathcal{L}^*_y(\Delta t)\Delta U^n_{i,j} = \beta^n_{i,j}$$

where

$$\mathcal{L}^*_x(\Delta t) = I + \frac{\Delta t}{2}\frac{\partial}{\partial x} A^n_{i,j}$$

and

$$\mathcal{L}^*_y(\Delta t) = I + \frac{\Delta t}{2}\frac{\partial}{\partial y} B^n_{i,j}$$

The factored method is solved in two steps, each inverting a block tridiagonal matrix

1. $\mathcal{L}^*_x(\Delta t)\Delta U^*_{i,j} = \beta^n_{i,j}$
2. $\mathcal{L}^*_y(\Delta t)\Delta U^n_{i,j} = \Delta U^*_{i,j}$

The new solution is

$$U^{n+1}_{i,j} = U^n_{i,j} + \Delta U^n_{i,j}$$

The method can be extended to three dimensions in a straightforward manner. Steger (Ref. 18) has used the method with general coordinate transformation and grid generation techniques to calculate inviscid and viscous flows past arbitrarily-shaped airfoils at low and transonic Mach numbers. The time step sizes were chosen for accuracy considerations and not, as in the explicit method, for stability conditions; hence, solutions were obtained with much less computer time.

5.4 Hybrid Methods

In the last few years several methods have been developed which attempt to combine the best features of explicit, implicit, and characteristic approximations. The basic approach is to split the governing stiff set of equations into parts, none of which is stiff by itself. Appropriate numerical methods are chosen for each part. The methods chosen from mathematical, physical, and numerical considerations are combined to form a sequence of numerical operators which is used to obtain the complete solution. The approach is optimum in that as new and better numerical methods evolve they can be used to replace less efficient component operators of the sequence. The approach has drastically reduced the computation time required to obtain complex two- and three-dimensional unsteady viscous flow solutions.

Three hybrid methods — Li in 1976 and 1977 (Refs. 22, 23), Shang in 1977 (Ref. 24), and MacCormack in 1976 (Ref. 25) — have been developed and applied to solve shock-boundary layer interactions. Each uses the basic framework of the explicit method outlined in Sec. 5.2 and replaces the operator $\mathcal{L}_y$ in the sequence for the fine mesh region, with more efficient operators. As noted earlier this operator for high Reynolds number calculations and consequently small mesh spacings required very small time steps. The time step limit of this operator outside the fine mesh region, as well as the $\mathcal{L}_x$ operator in all regions, was one or two orders of magnitude larger.

Li and Shang independently replaced the explicit operator $\mathcal{L}_y$ in the sequence for the fine mesh with an implicit operator $\mathcal{L}^*_y$. The "equation"

$$\frac{\partial U}{\partial t} + \frac{\partial G}{\partial y} = 0$$

is first linearized and then numerically solved implicitly for each time step using either a Crank-Nicolson approximation or a Laasonen approximation. The Crank-Nicolson method is second-order accurate in both time and space but can exhibit erratic behavior under certain known conditions. The Laasonen method is first-order accurate in time, second-order in space, and generally behaves well under all conditions. For the test problems considered and with the time step size no longer controlled by the $\mathcal{L}_y$ operator in the fine mesh, the hybrid methods of Li and Shang reduced the required computation time by an order of magnitude. Shang has used his method for calculating unsteady three-dimensional viscous flows with arbitrary geometries.

MacCormack replaced the explicit operator $\mathcal{L}_y$ in the sequence for the fine mesh by two operators, $\mathcal{L}_{y_H}$ for solving the hyperbolic part using characteristic approximations and $\mathcal{L}^*_{y_p}$ for solving the parabolic or viscous part using an implicit approximation. This method is briefly described in the following.

The operator $\mathcal{L}_{y_H}$ solves the split conservation law "equation"

$$\frac{\partial U}{\partial t} + \frac{\partial G_H}{\partial y} = 0 \quad \text{where} \quad G_H = \begin{bmatrix} \rho\underline{v} \\ \rho u\underline{v} \\ \rho v\underline{v} + \underline{p} \\ (e + \underline{p})\underline{v} \end{bmatrix}$$

The convection velocity v and pressure p have been underlined for later reference. Characteristic relations, as shown in Fig. 10, are used at each time step to calculate provisional values, $p^*_{i,j}$ and $v^*_{i,j}$, at each mesh point. These values are used to obtain time-averaged convection and pressure gradients at $t = (n + 1/2)\Delta t$, which are used in turn to define the underlined variables above in a conservation-law form finite difference approximation to solve Eq. (3). With the exception of the determination of the underlined variables, the conservation-law form finite difference approximation is the same as that of the explicit operator $\mathcal{L}_y$; however, time steps that are orders of magnitude larger are now possible.

The operator $\mathcal{L}^*_{y_p}$ solves the "equation"

$$\frac{\partial U}{\partial t} + \frac{\partial G_p}{\partial y} = 0$$

where

$$G_p = G - G_H$$

The operator is implicit, using Crank-Nicolson or Laasonen approximations, and is in conservation-law form. Because G_p does not contain the hyperbolic terms, no linearization is required and simple scalar, instead of block tridiagonal, procedures are used.

Several shock wave boundary-layer interaction problems were calculated using the former explicit method of Sec. 5.2 and the present hybrid method. For each calculation the flow was at Mach 2, and a shock wave incident on a flat plate increased the pressure by a factor of 1.4. Molecular viscosity was calculated using Sutherland's formula, and turbulent eddy viscosity was calculated using a simple algebraic Cebeci-Smith turbulence model. Figure 11 compares the results of both methods, experiment (Ref. 26), and boundary-layer theory (Ref. 27) (using Crocco's method), for a separated laminar boundary layer at a Reynolds number of 2.9×10^5. The results of the two methods agree well. The computing times of the former and present methods for a wide range of Reynolds numbers are compared in Fig. 12. For each case the mesh was 32×32, with 16 points in the fine mesh; the calculation was run 128 time steps to convergence. The present method reduced the required computation time by one and two orders of magnitude. The present method has been applied with similar success to solve the Navier-Stokes equations in integral form, Eq. (2), for flows with arbitrary geometries. Hung and MacCormack (Ref. 28) have extended the method to solve three-dimensional viscous flows.

6. COMPUTATIONAL RESULTS

6.1 Two-Dimensional Unsteady Flow

A joint experimental and computational study to examine turbulent transonic flows is being conducted at Ames Research Center. McDevitt, Levy, and Deiwert (Ref. 29) experimentally investigated the flow past a symmetric circular arc airfoil, of thickness 18% the chord length, for a range of Mach and Reynolds numbers. An unexpected phenomenon occurred: For fixed Reynolds number, as the Mach number was increased the flow, at first steady, became unsteady with strong oscillations; then, as the Mach number was increased further, the oscillations stopped and the flow returned to the steady state. The boundaries of the three regions are shown in Fig. 13. The shaded area in Fig. 13, labeled "hysteresis," represents a steady flow region if approached in Mach number from below and an unsteady flow region if approached in Mach number from above. On examination of shadowgraph movies it was observed that for the low Mach number steady-flow region, the turbulent boundary layer separated at the trailing edge of the airfoil; for the high Mach number steady-flow region, the flow was separated at the shock wave and covered the last 30% of the airfoil surface; and for the middle Mach number unsteady-flow region, the separation point oscillated between the trailing edge and the shock wave. Three test cases, shown also in Fig. 13, were selected for computations by Levy (Ref. 30), one in each region. For his application, Levy modified Deiwert's computer program, employed the hybrid explicit-implicit-characteristics method of Sec. 5.4, and used an algebraic eddy viscosity model to account for the effects of turbulence. His results are shown and compared with experiment in Fig. 14. The bars on the experimental results and the shaded region about the computational results represent the maximum and minimum values of the unsteady fluctuations and not uncertainty in the measured mean values. Levy's surface pressure distributions exhibit the same steady-unsteady-steady phenomenon found experimentally. They agree well with experiment where the boundary layer is attached or, as in Fig. 14(a), slightly separated at the trailing edge, but disagree significantly where the boundary layer is well separated, as in Fig. 14(c), between the shock located at $x/c = 0.65$ and the trailing edge. This disagreement is attributed to inadequate turbulence modeling. For the unsteady case, Levy determined that both the wave form and frequency of the airfoil surface pressure oscillations agreed reasonably well with experiment. Incorporation of differential turbulence models is under way.

6.2 Three-dimensional Flow

Hung and MacCormack (Ref. 28), also using an explicit-implicit-characteristics hybrid method they devised for three dimensions, have calculated the supersonic viscous flow past a compression corner with a sidewall (Fig. 15). The flow shows strong three-dimensional effects, including shock-shock and shock-boundary-layer interactions. Their computational domain and mesh are shown in Figs. 16 and 17. The velocity profiles and deflection angles across the sidewall boundary layer are shown in Fig. 18. The separation and reattachment lines on the compression surface that bound a "wine glass" region of separated flow at the corner are shown in Fig. 19. Note the two-dimensional result obtained by Hung and MacCormack earlier (Ref. 31).

6.3 Comparison of Turbulence Models

Viegas and Coakley (Ref. 32), also using a hybrid explicit-implicit-characteristic method, have computed the interaction of a normal shock wave with a turbulent boundary layer within an axisymmetric channel. Their results, using an algebraic, algebraic with relaxation, and the Rubesin one-equation differential turbulence models, are compared with the experimental results of Mateer (Ref. 33) in Fig. 20. For this flow, ranging in Reynolds number from 9×10^6 to 4×10^8, surface pressure was predicted well with all models. However, for skin friction only the results using the Rubesin model agree with experiment. The relaxation model offered no improvement over the simple algebraic model for this flow.

7. FUTURE PROSPECTS

During the past two decades rapid progress has been made in computer hardware development. Computer technology has increased computing speeds by a factor of 10 approximately every 5 years. This has resulted in a reduction of the computation cost of a given problem by a factor of 10 about every 7 years. During the next decade it appears that this trend will continue and that computers more than two orders of magnitude faster than present machines and with memories as large as 32 million words can be built for fluid dynamics applications.

The availability of powerful computers has spurred on the development of numerical methods for solving the Navier-Stokes equations. During the past decade, dramatic progress in computational fluid dynamics has reduced the time required to solve a given problem on a given computer by one and two orders of magnitude. During the next decade we can expect that this trend will continue and that numerical methods an order of magnitude faster will be devised.

Finally we can expect the availability of fast computers and methods to spur on the development of the third essential element — the understanding and modeling of the physics of turbulence. Where today we can calculate some complex unsteady two- and three-dimensional flows about simple but arbitrary geometries at high Reynolds numbers, a decade from now we will, perhaps, be routinely calculating, for design purposes and in computation times measured only in minutes, flows past complete aircraft configurations at flight Reynolds numbers.

REFERENCES

1. Peyret, R. and Viviand, H.: Computation of Viscous Compressible Flows Based on the Navier-Stokes Equations. AGARDograph No. 212., Sept. 1975.

2. Marvin, J. G.: Turbulence Modeling for Compressible Flows. NASA TM X-73,188, Jan. 1977.

3. Rubesin, M. W. and Rose, W. C.: The Turbulent Mean-Flow Reynolds-Stress and Heat Flux Equations in Mass-Averaged Dependent Variables. NASA TM X-62,248, March 1973.

4. Cebeci, T. and Smith, A. M. O.: Analysis of Turbulent Boundary Layers. Academic Press, 1974.

5. Shang, J. S. and Hankey, W. L.: Numerical Solution of the Navier-Stokes Equations for Supersonic Turbulent Flow Over a Compression Corner. AIAA paper 74-4, Jan. 1974.

6. Rubesin, M. W.: A One-Equation Model of Turbulence for Use with the Compressible Navier-Stokes Equations. NASA TM X-73,128, April 1976.

7. Saffman, P. G. and Wilcox, D. C.: Turbulence Model Predictions for Turbulent Boundary Layers. AIAA Journal, Vol. 12, No. 4, 1974.

8. Skoglund, V. J., Cole, J. K., and Staiano, E. F.: Numerical Techniques for Viscous Compressible Flows with Shock Waves. Proceed. 1968 Heat Transfer and Fluid Mech. Inst., Stanford University Press, 1968, pp. 15-173.

9. MacCormack, R. W.: Numerical Solution of the Interaction of a Shock Wave with a Laminar Boundary Layer. Lecture Notes in Physics, Vol. 8, Springer-Verlag, 1971, pp. 151-163.

10. Carter, J. E.: Numerical Solutions of the Navier-Stokes Equations for the Supersonic Laminar Flow Over a Two-Dimensional Compression Corner. NASA TR R-385, July 1972.

11. Viviand, H. and Ghazzi, W.: Numerical Solution of the Compressible Navier-Stokes Equations at High Reynolds Numbers with Application to the Blunt Body Problem. Lecture Notes in Physics, Vol. 59, 1976, pp. 434-439.

12. Deiwert, G. S.: Recent Computation of Viscous Effects in Transonic Flow. Proceedings of the Fifth International Conference on Numerical Methods in Fluid Dynamics, Springer-Verlag, New York, 1976.

13. Lindemuth, I. and Killeen, J.: Alternating Direction Implicit Techniques for Two-Dimensional Magnetohydrodynamic Calculations. J. Comp. Phys., Vol. 13, 1973, pp. 181-208.

14. Briley, W. R. and McDonald, H.: Solution of the Three-Dimensional Compressible Navier-Stokes Equations by an Implicit Technique. Proceedings of the Fourth International Conference on Numerical Methods in Fluid Dynamics, Springer-Verlag, New York, 1976.

15. McDonald, H. and Briley, W. R.: Three-Dimensional Supersonic Flow of a Viscous or Inviscid Flow. J. Comp. Phys., Vol. 19, 1975, pp. 150-178.

16. Beam, R. M. and Warming, R. F.: An Implicit Finite-Difference Algorithm for Hyperbolic Systems in Conservation Law Form. J. Comput. Phys., Vol. 22, 1976, pp. 87-110.

17. Beam, R. M. and Warming, R. F.: An Implicit Factored Scheme for the Compressible Navier-Stokes Equations. Proceedings of the AIAA 3rd Computational Fluid Dynamics Conference, Albuquerque, New Mex., June 1977.

18. Steger, J. L.: Implicit Finite Difference Simulation of Flow About Arbitrary Geometries with Application to Airfoils. AIAA paper 77-665, June 1977.

19. Peaceman, D. W. and Rachford, H. H.: The Numerical Solution of Parabolic and Elliptic Differential Equations. J. Soc. Indust. Appl. Math., Vol. 3, 1955, pp. 28-41.

20. Douglas, J.: On the Numerical Integration of $u_{xx} + u_{yy} = u_t$ by Implicit Methods. J. Soc. Indust. Appl. Math., Vol. 3, 1955, pp. 42-65.

21. Douglas, J. and Gunn, J. E.: A General Formulation of Alternating Direction Methods. Numer. Math., Vol. 6, 1964, pp. 428-453.

22. Li, C. P.: A Mixed Explicit-Implicit Splitting Method for the Compressible Navier-Stokes Equations. Proceedings of the Fifth International Conference on Numerical Methods in Fluid Dynamics, Springer-Verlag, New York, 1976.

23. Li, C. P.: A Numerical Study of Laminar Separated Flows Induced by Shock-Wave/Boundary Layer Interaction. AIAA paper 77-168, Jan. 1977.

24. Shang, J. S.: An Implicit-Explicit Method for Solving the Navier-Stokes Equations. Proceedings of the AIAA 3rd Computational Fluid Dynamics Conference, Albuquerque, New Mex., June 1977.

25. MacCormack, R. W.: An Efficient Numerical Method for Solving the Time-Dependent Compressible Navier-Stokes Equations at High Reynolds Number. Computing in Applied Mechanics, AMD Vol. 18, The American Society of Mechanical Engineers, 1976.

26. Hakkinen, R. J., Greber, I., Trilling, L., and Abarbanel, S. S.: The Interaction of an Oblique Shock Wave with a Laminar Boundary Layer. NASA Memo 2-18-59W, 1959.

27. Van Driest, E. R.: Investigation of Laminar Boundary Layer in Compressible Fluids Using the Crocco Method. NASA TN-2597, 1952.

28. Hung, C. M. and MacCormack, R. W.: Numerical Solution of Supersonic Laminar Flow Over a Three-Dimensional Compression Corner. AIAA paper 77-694, June 1977.

29. McDevitt, J. B., Levy, L. L., Jr., and Deiwert, G. S.: Transonic Flow About a Thick Circular-Arc Airfoil. AIAA Journal, Vol. 14, No. 5, May 1976, pp. 606-613.

30. Levy, L. L., Jr.: An Experimental and Computational Investigation of the Steady and Unsteady Transonic Flow Fields About an Airfoil in a Solid-Wall Test Channel. AIAA paper 77-678, July 1977.

31. Hung, C. M. and MacCormack, R. W.: Numerical Solutions of Supersonic and Hypersonic Laminar Compression Corner Flows. AIAA Journal, Vol. 14, No. 4, April 1976, pp. 475-481.

32. Viegas, J. R. and Coakley, T. J.: Numerical Investigation of Turbulence Models for Shock Separated Boundary-Layer Flows. AIAA paper 77-44, Jan. 1977.

33. Mateer, G. G., Brosh, A., and Viegas, J. R.: A Normal Shock-Wave Turbulent Boundary Layer Interaction at Transonic Speeds. AIAA paper 76-161, Jan. 1976.

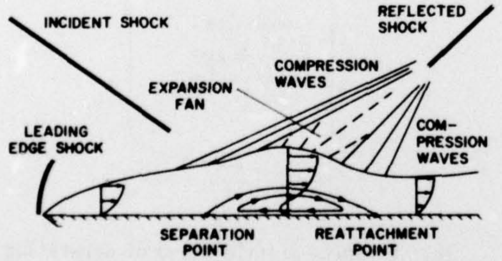

Fig. 1. Shock wave boundary-layer interaction.

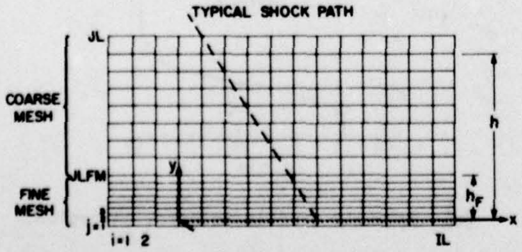

Fig. 2. Computational mesh for inviscid-viscous interaction flows.

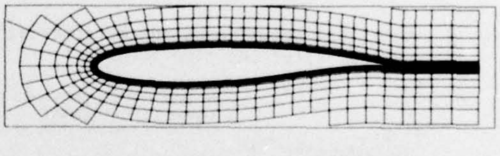

Fig. 3. Computational mesh for viscous flow about an airfoil.

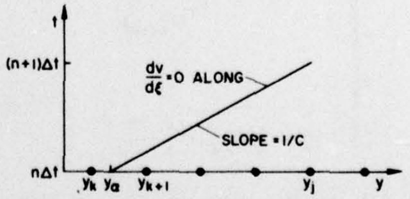

Fig. 4. Characteristic path through $[y_j, (n + 1)\Delta t]$.

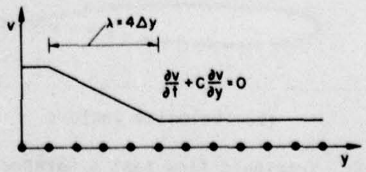

Fig. 5. Initial value problem (t = 0).

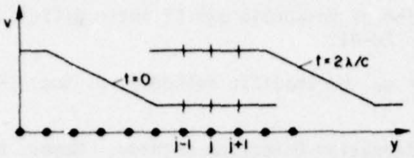

Fig. 6. Exact solution at t = 0 and t = 2λ/c.

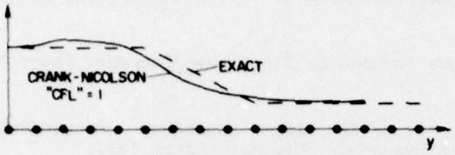

(a) Δt = λ/c

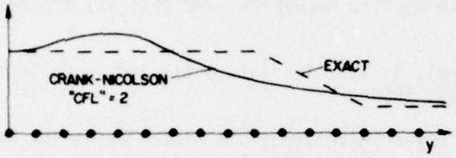

(b) Δt = 2λ/c

Fig. 7. Numerical solutions using implicit method after one time step.

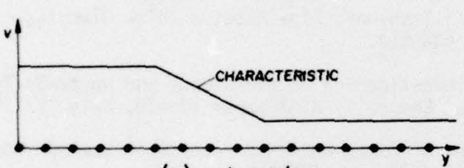

(a) Δt = λ/c

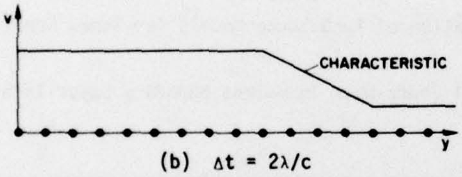

(b) Δt = 2λ/c

Fig. 8. Numerical solution using characteristic method after one time step.

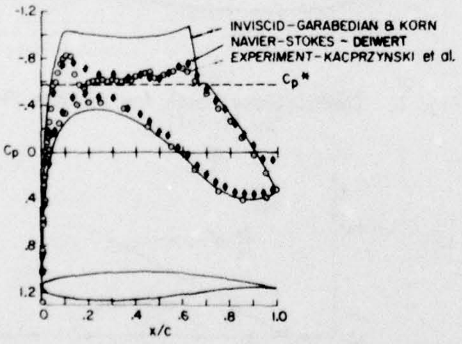

(a) Surface pressure distribution.

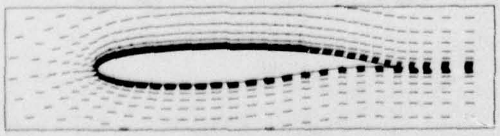

(b) Velocity vectors.

Fig. 9. Transonic flow past a Garabedian-Korn shockless airfoil: M = 0.755, Re = 21×10⁶, and α = 0.12.

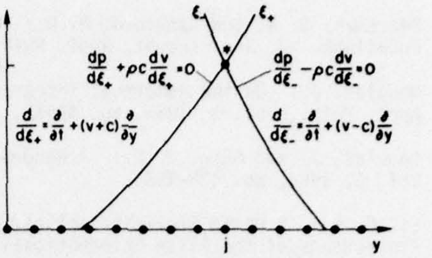

Fig. 10. Characteristic solution.

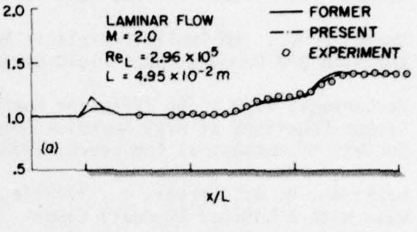

(a) Surface pressure.

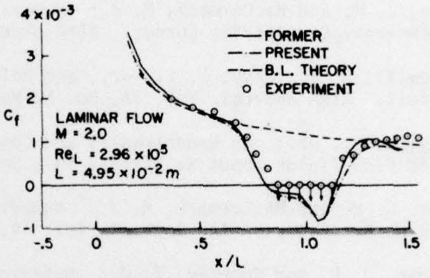

(b) Skin friction.

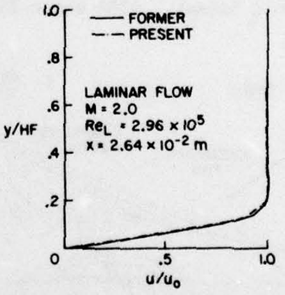

(c) Velocity profile ahead of separation.

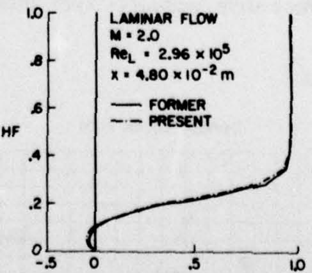

(d) Velocity profile interaction region.

Fig. 11. Comparison of results of former and present methods for calculating laminar separated flow.

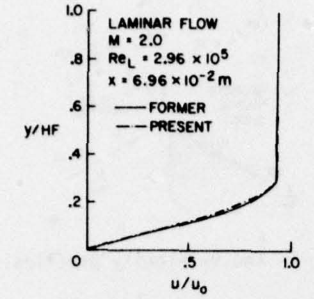

(e) Velocity profile aft of reattachment.

Fig. 11. Concluded.

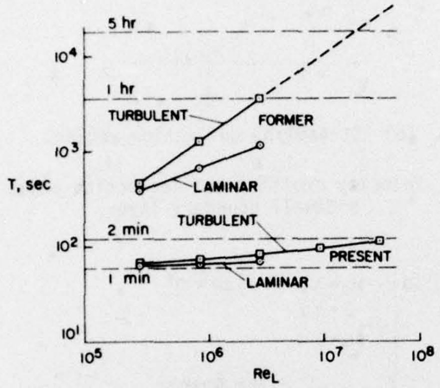

Fig. 12. Comparison of computing times for former and present methods on the CDC 7600 vs Reynolds number for several shock boundary-layer interaction calculations.

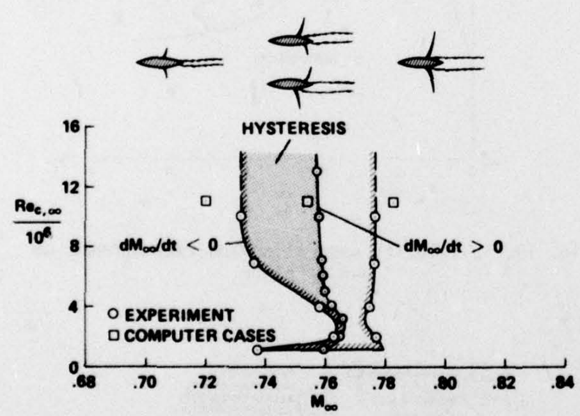

Fig. 13. Experimental flow domains for the 18% thick circular arc airfoil.

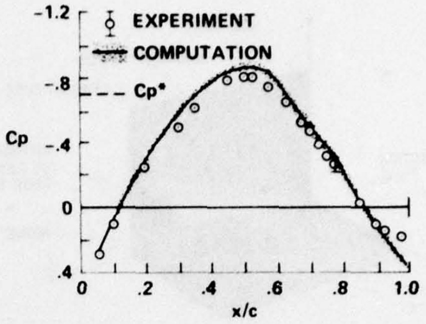

(a) $M_\infty = 0.720$

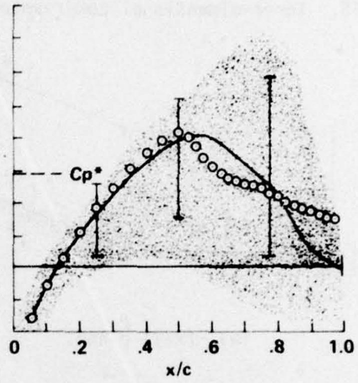

(b) $M_\infty = 0.754$

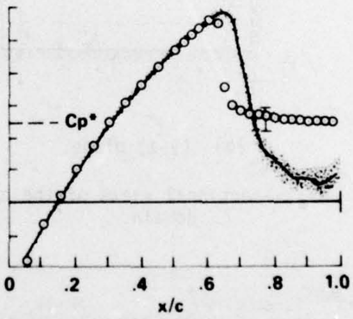

(c) $M_\infty = 0.783$

Fig. 14. Computed and experimental pressure distributions on the circular arc airfoil, $Re_{c,\infty} = 11 \times 10^6$.

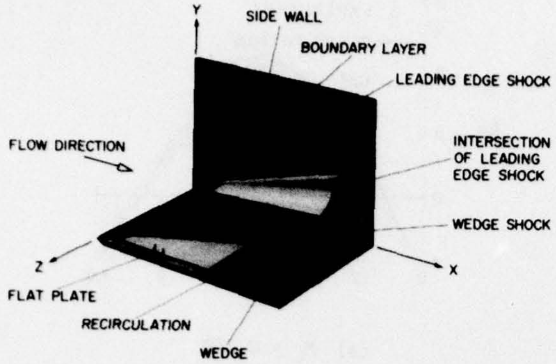

Fig. 15. Three-dimensional compression corner.

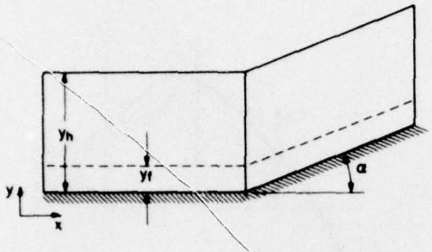

(a) (x-y) plane.

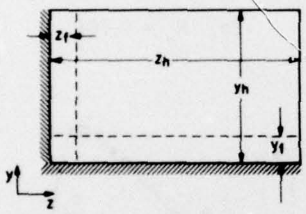

(b) (y-z) plane.

Fig. 16. Cross-sectional views of the computational domain.

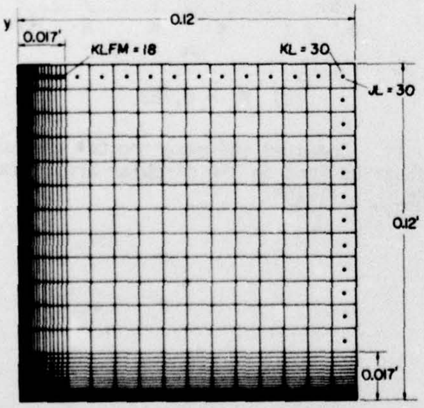

Fig. 17. Details of "mesh" cells in (y-z) plane.

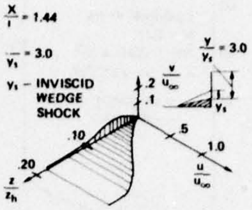

(a) u- and v-velocity profiles.

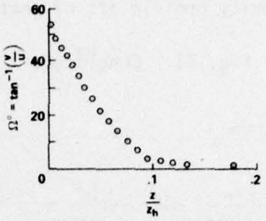

(b) Streamline deflection angles.

Fig. 18. Velocity profiles and deflection angle across sidewall boundary layer.

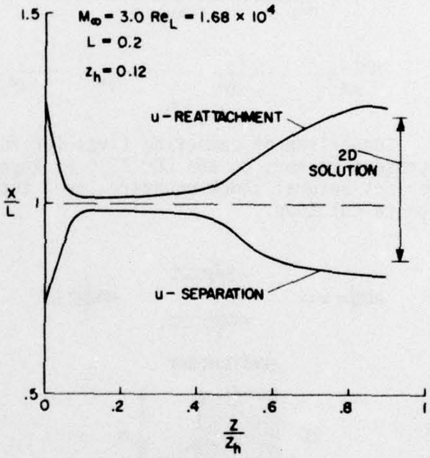

Fig. 19. u-velocity separation and reattachment on y = 0 plane.

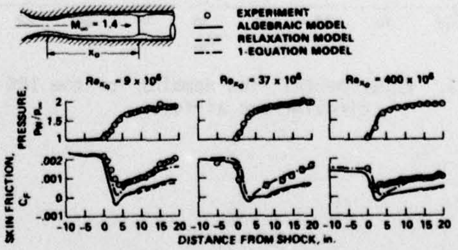

Fig. 20. Improvements in turbulence modeling for a flow having a normal shock wave interacting with a turbulent boundary layer.

REPORT DOCUMENTATION PAGE

1. Recipient's Reference	2. Originator's Reference	3. Further Reference	4. Security Classification of Document
	AGARD-LS-94 ✓	ISBN 92-835-0210-8	UNCLASSIFIED

5. Originator
Advisory Group for Aerospace Research and Development ✓
North Atlantic Treaty Organization
7 rue Ancelle, 92200 Neuilly sur Seine, France

6. Title
THREE DIMENSIONAL AND UNSTEADY SEPARATION AT HIGH REYNOLDS NUMBERS

7. Presented at
the Von Kármán Institute, Rhode-Saint-Genese, Belgium, on 20–24 February.

8. Author(s)	9. Date
Various	February 1978

10. Author's Address	11. Pages
Various	250

12. Distribution Statement
This document is distributed in accordance with AGARD policies and regulations, which are outlined on the Outside Back Covers of all AGARD publications.

13. Keywords/Descriptors

Boundary layer separation
Unsteady flow
Three dimensional flow
Fluid flow
Turbulent flow
Mathematical prediction
Numerical analysis

14. Abstract

These articles cover ~~This Lecture Series will be devoted to~~ two major aspects of the topic: the physics of flow separation and reattachment, with particular reference to turbulent flows, and a consideration of some practically important types of separated flows which occur in aeronautics. Under both headings articles are ~~lectures will be~~ included on the most recent experimental work, computational techniques and prediction methods, and an attempt is made to assess progress and to identify those areas in which further work should be done. Although attention is not ~~will not be~~ confined to incompressible flows, ~~it is intended that~~ only passing reference is ~~should be~~ made to shock-wave boundary layer interaction.

The material in this publication was assembled to support a Lecture Series under the sponsorship of the Fluid Dynamics Panel and the Consultant and Exchange Programme of AGARD.

AGARD Lecture Series No.94
Advisory Group for Aerospace Research and Development, NATO
THREE DIMENSIONAL AND UNSTEADY SEPARATION AT HIGH REYNOLDS NUMBERS
Published February 1978
250 pages

This Lecture Series will be devoted to two major aspects of the topic: the physics of flow separation and reattachment, with particular reference to turbulent flows, and a consideration of some practically important types of separated flows which occur in aeronautics. Under both headings lectures will be included on the most recent experimental work, computational techniques and prediction methods, and an attempt made

P.T.O.

AGARD-LS-94

Boundary layer separation
Unsteady flow
Three dimensional flow
Fluid flow
Turbulent flow
Mathematical prediction
Numerical analysis

AGARD Lecture Series No.94
Advisory Group for Aerospace Research and Development, NATO
THREE DIMENSIONAL AND UNSTEADY SEPARATION AT HIGH REYNOLDS NUMBERS
Published February 1978
250 pages

This Lecture Series will be devoted to two major aspects of the topic: the physics of flow separation and reattachment, with particular reference to turbulent flows, and a consideration of some practically important types of separated flows which occur in aeronautics. Under both headings lectures will be included on the most recent experimental work, computational techniques and prediction methods, and an attempt made

P.T.O.

AGARD-LS-94

Boundary layer separation
Unsteady flow
Three dimensional flow
Fluid flow
Turbulent flow
Mathematical prediction
Numerical analysis

AGARD Lecture Series No.94
Advisory Group for Aerospace Research and Development, NATO
THREE DIMENSIONAL AND UNSTEADY SEPARATION AT HIGH REYNOLDS NUMBERS
Published February 1978
250 pages

This Lecture Series will be devoted to two major aspects of the topic: the physics of flow separation and reattachment, with particular reference to turbulent flows, and a consideration of some practically important types of separated flows which occur in aeronautics. Under both headings lectures will be included on the most recent experimental work, computational techniques and prediction methods, and an attempt made

P.T.O.

AGARD-LS-94

Boundary layer separation
Unsteady flow
Three dimensional flow
Fluid flow
Turbulent flow
Mathematical prediction
Numerical analysis

AGARD Lecture Series No.94
Advisory Group for Aerospace Research and Development, NATO
THREE DIMENSIONAL AND UNSTEADY SEPARATION AT HIGH REYNOLDS NUMBERS
Published February 1978
250 pages

This Lecture Series will be devoted to two major aspects of the topic: the physics of flow separation and reattachment, with particular reference to turbulent flows, and a consideration of some practically important types of separated flows which occur in aeronautics. Under both headings lectures will be included on the most recent experimental work, computational techniques and prediction methods, and an attempt made

P.T.O.

AGARD-LS-94

Boundary layer separation
Unsteady flow
Three dimensional flow
Fluid flow
Turbulent flow
Mathematical prediction
Numerical analysis

to assess progress and to identify those areas in which further work should be done. Although attention will not be confined to incompressible flows, it is intended that only passing reference should be made to shock-wave boundary layer interaction.

The material in this publication was assembled to support a Lecture Series under the sponsorship of the Fluid Dynamics Panel and the Consultant and Exchange Programme of AGARD presented on 20–24 February at the Von Kármán Institute, Rhode-Saint-Genèse, Belgium.

ISBN 92-835-0210-8

to assess progress and to identify those areas in which further work should be done. Although attention will not be confined to incompressible flows, it is intended that only passing reference should be made to shock-wave boundary layer interaction.

The material in this publication was assembled to support a Lecture Series under the sponsorship of the Fluid Dynamics Panel and the Consultant and Exchange Programme of AGARD presented on 20–24 February at the Von Kármán Institute, Rhode-Saint-Genèse, Belgium.

ISBN 92-835-0210-8

to assess progress and to identify those areas in which further work should be done. Although attention will not be confined to incompressible flows, it is intended that only passing reference should be made to shock-wave boundary layer interaction.

The material in this publication was assembled to support a Lecture Series under the sponsorship of the Fluid Dynamics Panel and the Consultant and Exchange Programme of AGARD presented on 20–24 February at the Von Kármán Institute, Rhode-Saint-Genèse, Belgium.

ISBN 92-835-0210-8

to assess progress and to identify those areas in which further work should be done. Although attention will not be confined to incompressible flows, it is intended that only passing reference should be made to shock-wave boundary layer interaction.

The material in this publication was assembled to support a Lecture Series under the sponsorship of the Fluid Dynamics Panel and the Consultant and Exchange Programme of AGARD presented on 20–24 February at the Von Kármán Institute, Rhode-Saint-Genese, Belgium.

ISBN 92-835-0210-8

AGARD
NATO OTAN
7 RUE ANCELLE · 92200 NEUILLY-SUR-SEINE
FRANCE
Telephone 745.08.10 · Telex 610176

DISTRIBUTION OF UNCLASSIFIED AGARD PUBLICATIONS

AGARD does NOT hold stocks of AGARD publications at the above address for general distribution. Initial distribution of AGARD publications is made to AGARD Member Nations through the following National Distribution Centres. Further copies are sometimes available from these Centres, but if not may be purchased in Microfiche or Photocopy form from the Purchase Agencies listed below.

NATIONAL DISTRIBUTION CENTRES

BELGIUM
Coordonnateur AGARD – VSL
Etat-Major de la Force Aérienne
Quartier Reine Elisabeth
Rue d'Evere, 1140 Bruxelles

CANADA
Defence Scientific Information Service
Department of National Defence
Ottawa, Ontario K1A 0Z2

DENMARK
Danish Defence Research Board
Østerbrogades Kaserne
Copenhagen Ø

FRANCE
O.N.E.R.A. (Direction)
29 Avenue de la Division Leclerc
92 Châtillon sous Bagneux

GERMANY
Zentralstelle für Luft- und Raumfahrtdokumentation und -information
Postfach 860880
D-8 München 86

GREECE
Hellenic Armed Forces Command
D Branch, Athens

ICELAND
Director of Aviation
c/o Flugrad
Reykjavik

ITALY
Aeronautica Militare
Ufficio del Delegato Nazionale all'AGARD
3, Piazzale Adenauer
Roma/EUR

LUXEMBOURG
See Belgium

NETHERLANDS
Netherlands Delegation to AGARD
National Aerospace Laboratory, NLR
P.O. Box 126
Delft

NORWAY
Norwegian Defence Research Establishment
Main Library
P.O. Box 25
N-2007 Kjeller

PORTUGAL
Direccao do Servico de Material
da Forca Aerea
Rua de Escola Politecnica 42
Lisboa
Attn: AGARD National Delegate

TURKEY
Department of Research and Development (ARGE)
Ministry of National Defence, Ankara

UNITED KINGDOM
Defence Research Information Centre
Station Square House
St. Mary Cray
Orpington, Kent BR5 3RE

UNITED STATES
National Aeronautics and Space Administration (NASA),
Langley Field, Virginia 23365
Attn: Report Distribution and Storage Unit

THE UNITED STATES NATIONAL DISTRIBUTION CENTRE (NASA) DOES NOT HOLD STOCKS OF AGARD PUBLICATIONS, AND APPLICATIONS FOR COPIES SHOULD BE MADE DIRECT TO THE NATIONAL TECHNICAL INFORMATION SERVICE (NTIS) AT THE ADDRESS BELOW.

PURCHASE AGENCIES

Microfiche or Photocopy
National Technical
Information Service (NTIS)
5285 Port Royal Road
Springfield
Virginia 22151, USA

Microfiche
Space Documentation Service
European Space Agency
10, rue Mario Nikis
75015 Paris, France

Microfiche
Technology Reports
Centre (DTI)
Station Square House
St. Mary Cray
Orpington, Kent BR5 3RF
England

Requests for microfiche or photocopies of AGARD documents should include the AGARD serial number, title, author or editor, and publication date. Requests to NTIS should include the NASA accession report number. Full bibliographical references and abstracts of AGARD publications are given in the following journals:

Scientific and Technical Aerospace Reports (STAR),
published by NASA Scientific and Technical
Information Facility
Post Office Box 8757
Baltimore/Washington International Airport
Maryland 21240, USA

Government Reports Announcements (GRA),
published by the National Technical
Information Services, Springfield
Virginia 22151, USA

Printed by Technical Editing and Reproduction Ltd
Harford House, 7–9 Charlotte St, London W1P 1HD

ISBN 92-835-0210-8

AD-A050 762 ADVISORY GROUP FOR AEROSPACE RESEARCH AND DEVELOPMENT--ETC F/G 20/4
THREE DIMENSIONAL AND UNSTEADY SEPARATION AT HIGH REYNOLDS NUMB--ETC(U)
FEB 78

UNCLASSIFIED AGARD-LS-94 NL

4 OF 4
AD
A050762

SUPPLEMENTARY

INFORMATION

END
DATE
FILMED
7-78
DDC

SUPPLEMENTARY

INFORMATION

AD-A050 762

NORTH ATLANTIC TREATY ORGANIZATION

ADVISORY GROUP FOR AEROSPACE RESEARCH AND DEVELOPMENT

(ORGANISATION DU TRAITE DE L'ATLANTIQUE NORD)

AGARD Lecture Series No.94

THREE DIMENSIONAL AND UNSTEADY SEPARATION AT HIGH REYNOLDS NUMBERS

ERRATA SHEET

Please note that Figure 22 on page 7-25 is incorrect. An amended page 7-25 is printed on the reverse of this sheet, and should be used to replace the original page 7-25. Your co-operation is appreciated.

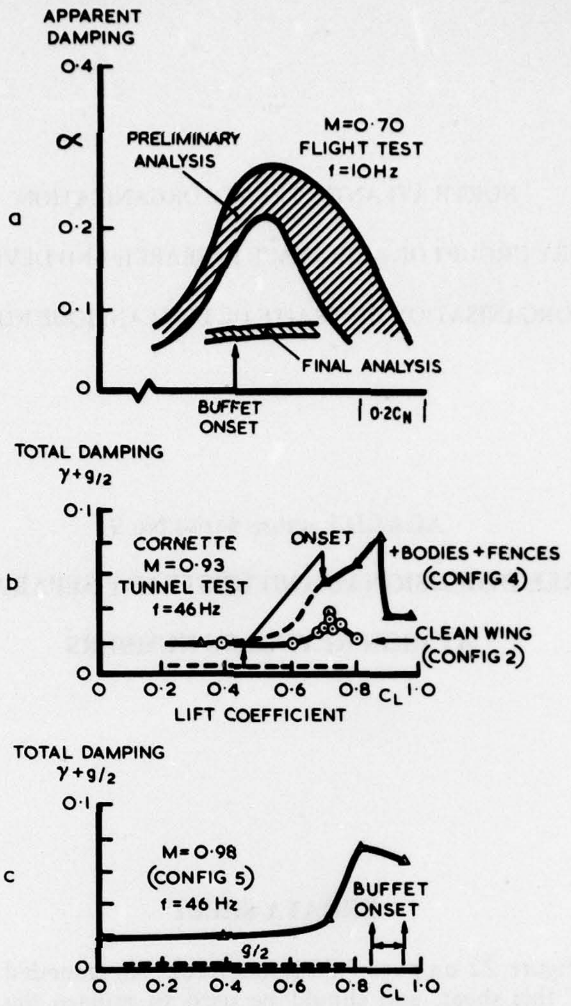

Fig.22 Variation of total damping with lift coefficient

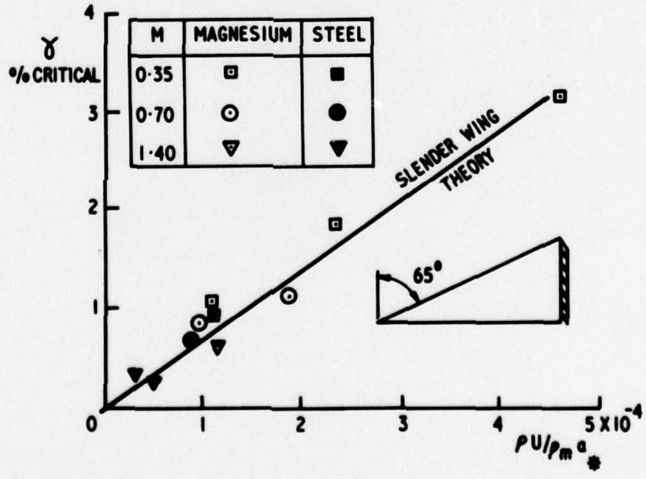

Fig.23 First bending mode – variation of aerodynamic damping with density and velocity